Modelling the Pharmacokinetics and Pharmacodynamics of Macromolecules for the Treatment of Wet AMD



Laurence Hutton-Smith
Pembroke College
University of Oxford

A thesis submitted for the degree of
Doctor of Philosophy

Trinity 2018

To the tens of millions of people who died during the 3 years it took to complete this research, due to lack of access to medicine [1].

Another world is possible.

Acknowledgements

Thank you to my parents for bringing me into existence, this has made a lot of people very angry and been widely regarded as a bad move.

Thank you my supervisors Eamonn Gaffney, Helen Byrne and Philip Maini. The work you have all put in over the years has been immense, it has been an absolute pleasure to work so closely with such esteemed academics, many of whom I looked up to greatly when I was an undergraduate sitting in a lecture hall. I have learnt an enormous amount from you, it has been an honour. Particular thanks must go to Eamonn for the endless hours he spent in discussion with me, as well as his Erdős-esque ability to forgo sleep to read my work - I do not know how you do it. Thank you to The Engineering and Physical Sciences Research Council, The Medical Research Council, and the British taxpayers, for funding the majority (90.4%) of the cost of this research (Grant No. EP/L016044/1). Additional funding (9.6%) was provided by [redacted].

Thank you to all the administrative staff at the Mathematical Institute, particularly Sara Jolliffe, without you our research group couldn't function, as well as Antoinette Elizabeth Drakes and Margaret Dawes for doing an amazing job putting up with me for all these years. Thank you to all the faculty maintenance staff who keep this cathedral to mathematics running, you all deserve a lot more thanks and compensation than you are given.

Thank you to Helen Wright, you have been a source of inspiration throughout my research. It is a testament to the goodness in human nature, that, after all you the world has put you through, you have never stopped giving of yourself to the people. While idlers and the self-interested accrue wealth and power, you are one of the many people who spend their lives helping keep society together, for very little thanks or recognition. I can only hope to emulate you.

Thank you to Larry Sanders, you have been my mentor these past years, you have taught me to never let the fire go out - you have more fight in you in your 80s than most ever do.

You taught me to tell the truth, stand my ground, and to always do what is right - not what is convenient. Thank you for helping me to find meaning in this rather cold world, and inspiring me to spend my life doing work that values human life more than money. Your brother will be the next President of the United States, and will yet have a chance to teach the world what you, and your parents, taught a young Bernard growing up in Brooklyn.

Finally, to those who can hear me, I want to say this - spend your life working for the betterment of the many, not the few. Not for yourself, for others. Do so and make all people your family. It is incumbent upon those with the ability to, to find a way to help those without; to reduce their suffering and by doing so the suffering of all. Do this without compromise or hesitation and you will look back upon on a life well lived. For only together can we make this world the truly wonderful place it should be.

Proletarier aller Länder, vereinigt euch!

Abstract

Wet age related macular degeneration (wet AMD) is a highly debilitating retinal disease, the third leading cause of blindness in the world and one the most expensive ocular conditions to care for. Wet AMD is characterised by the proliferation of neovasculature through the retinal posterior and theorised to be, at least in part, induced and driven by excess vascular endothelial growth factor (VEGF). Many current treatments for wet AMD utilise anti-VEGF macromolecules that bind to VEGF. The retina, however, remains a largely inaccessible, and delicate, anatomical region. Due to difficulties in collecting clinical and experimental data, mathematical modelling is playing an increasingly prominent role in understanding the distribution (Pharmacokinetics, PK) and drug-to-target interactions (Pharmacodynamics, PD) for treatments of wet AMD. This thesis will focus on ordinary/partial differential equation (ODE/PDE) models for the PK/PD of anti-VEGF therapeutics, administered via intravitreal (IVT) injection into the mammalian eye. We start in Chapter 2 with a 2-compartment PK/PD ODE model of drug-VEGF interactions in the eye, analysing a clinical dataset to estimate key binding parameters between VEGF and the typical anti-VEGF molecule, ranibizumab. In Chapter 3, we extend the PK ODE framework of the 2-compartment model to include a mechanistic description of the retina, to estimate retinal permeability to macromolecules used for treating wet AMD. In Chapter 4, using the retinal PK model, we reintroduce VEGF to predict concentrations of free VEGF in the retina post-IVT injection. Chapters 5 and 6 model a hypothetical class of anti-VEGF molecules designed to bind not only VEGF but also existing vitreal superstructures, analysing how dose and binding kinetics impact ocular retention. Alongside these models we present analogous PDE models, addressing whether the assumption that concentrations are homogeneous across anatomical regions, as implicit in ODE models, is appropriate for macromolecular PK/PD in the mammalian eye.

Abbreviations and Definitions

PK	Pharmacokinetics
PD	Pharmacodynamics
AMD	Age related macular degeneration
CNV	Choroidal neovascularization
VEGF	Vascular endothelial growth factor
VA	Visual acuity
OCT	Optical coherence tomography
IVT	Intravitreal
Fab	Fragment antibody
IgG	Full length antibody
Fc	Antibody fragment crystallizable region
RPE	Retinal pigment epithelium
ILM	Inner limiting membrane
MW	Molecular weight
SD	Standard deviation
ODE	Ordinary differential equation
PDE	Partial differential equation
QSS	Quasi-steady state
WLOG	Without loss of generality
Vitreal binders	Molecules capable of binding to existing vitreal/ocular structures/molecules
SVB	Static vitreal binding/binder
nSVB	Non-static vitreal binding/binder
FRV	Free retinal VEGF
FDVD	Freely diffusing vitreal drug
RED	*Reduce* cost, improve *efficacy*, increase *duration* of effect

Pharmacokinetics Commonly referred to as 'what the body does to the drug', pharmacokinetics is the study of the time course of drug absorption, distribution, metabolism, and excretion [2].

Pharmacodynamics Commonly referred to as 'what the drug does to the body', pharmacodynamics is the study of the relationship between drug concentration at the site of action and the resulting effect [2].

Free VEGF Vascular endothelial growth factor molecules that are capable of stimulating angiogenic activity. For example VEGF that is considered 'free' includes active VEGF molecules not bound by a therapeutic agent.

Contents

1 Introduction **1**

1.1 Wet AMD and the application of mathematical modelling 1

1.2 The pathology and treatment of wet AMD 6

1.3 Literature review of relevant previous models 15

1.3.1 Ordinary differential equation ocular models 15

1.3.2 Partial differential equation ocular models 22

1.4 Thesis overview 26

2 Estimation of the *in vivo* binding parameters of ranibizumab using a 2-compartment ODE PK/PD model **29**

2.1 2-compartment model formulation: building on the work of Saunders et al. 30

2.2 Re-analysis of Fauser et al. dataset: an *in vivo* estimate for K_{D} 38

2.3 Impact of binding stoichiometry, rate constants, dose and M_{W} on free VEGF profiles 39

2.4 2-compartment PK/PD ODE model summary 42

3 Mechanistic retinal ODE/PDE PK modelling **44**

3.1 Mechanistic retinal ODE modelling and estimation of retinal permeabilities 44

3.1.1 3-compartment model formulation: semi-mechanistic ocular modelling 46

3.1.2 Estimation of retinal membrane permeabilities using 3-compartment ocular PK data 48

3.1.3 Analytic characterisation of ocular half-life, vitreous-retina concentration ratio and aqueous-retina elimination ratio 51

3.1.4 3-compartment PK ODE model summary 57

3.2 Investigation of the well-mixed assumption using an adaptable, mechanistic, retina-vitreous PDE model 60

3.2.1 Model formulation, geometry and numerical solution 61

3.2.2 Translation from PDE to ODE 68

3.2.3 Estimation of retinal and hyaloidal membrane permeabilities using 3-compartment ocular PK data 69
3.2.4 Comparison of parameter estimation and spatially averaged behaviour of mathematically similar PDE and ODE ocular PK models 73
3.2.5 Analysis of the well mixed assumption 75
3.2.6 One-dimensional caricature PDE model analysis 79
3.2.7 3-compartment PK PDE model summary 89

4 The Retinal PK/PD of anti-VEGF Macromolecules 91
4.1 Free VEGF retinal dynamics post anti-VEGF IVT injection, generated using a semi-mechanistic 3-compartment ocular PK/PD model 91
4.1.1 3-compartment PK/PD model formulation 92
4.1.2 3-compartment reanalysis of Saunders et al. [3] dataset 99
4.1.3 Asymptotic analysis of intermediate time retinal VEGF behaviour . 101
4.1.4 Interpatient half-life and VEGF production variation 106
4.1.5 Retina-aqueous suppression lag 111
4.1.6 Caricature model analysis of retina-aqueous suppression lag 112
4.1.7 Modified retinal permeability PD case studies 120
4.1.8 Effects of dosage and reaction rate modifications 123
4.1.9 3-compartment PK/PD ODE model summary 126
4.2 Analysis of the PK/PD of ocular anti-VEGF macromolecules using a PDE model 132
4.2.1 Model Formulation and Numerical Solution 133
4.2.2 3-compartment PDE analysis of Saunders et al. [3] aggregated dataset 138
4.2.3 Predictive comparison between the ODE and PDE model 140
4.2.4 3-compartment PK/PD PDE model summary 144

5 The ocular PK of vitreal binding macromolecules 146
5.1 Analysis of the PK of vitreal binding macromolecules using an ODE model 146
5.1.1 Model formulation, non-dimensional analysis and solution 147
5.1.2 Half-Life analysis 158
5.1.3 Duration time analysis 171
5.1.4 Repeat dosage analysis 181
5.1.5 Vitreal binding PK ODE model summary 191
5.2 Analysis of the PK of Vitreal Binding Macromolecules Using a PDE Model 192
5.2.1 Model Formulation and Numerical Solution 193
5.2.2 Predictive comparison between the ODE and PDE model 194

6 The ocular PK/PD of bispecific anti-VEGF vitreal binding macromolecules 196
6.1 Model formulation . . . 197
6.2 Asymptotic analysis and PK decoupling . . . 200
6.3 Non-static vitreal binding molecules: modelling the BI-X molecule . . . 205
6.4 PK/PD comparison of static/non-static vitreal binders versus ranibizumab 212
6.5 Static vitreal binding to hyaluronic acid . . . 220
6.6 Repeat dosage analysis . . . 224
6.7 Vitreal binding PK/PD ODE model summary . . . 234

7 Conclusions and future work 240
7.1 Conclusions . . . 240
7.2 Future work . . . 249

A Appendices 253
A.1 Literature compilation of ocular half-Lives and calculated vitreous diffusion times for different animal species and large molecules . . . 254
A.2 Retinal geometric parameter derivations . . . 254
A.3 3-compartment ocular vitreous-aqueous delay PK model with virtual compartment . . . 256
A.4 Fluid flow analysis over human geometry . . . 261
A.5 1D PDE model: orthogonality . . . 263
A.6 R_{h} and $t_{1/2}$ data meta-analysis . . . 263
A.7 Estimation of the hydrodynamic radii of R, V, VR and RVR species . . . 265
A.8 3-compartment PK/PD individual patient plots . . . 266
A.9 Chapter 2 lemma 1 . . . 277
A.10 Caricature model conservation of mass . . . 278
A.11 Caricature model solution for a_1 and a_2, and delay analysis . . . 281
A.12 Caricature model plots: Effect of parameter variation on delay . . . 284
A.13 Chapter 3 lemmas . . . 291
A.14 Analysis of the PK/PD of bispecific anti-VEGF vitreal binding macromolecules using a PDE model . . . 295
A.14.1 Model Formulation and Numerical Solution . . . 295
A.14.2 Predictive comparison between the ODE and PDE model . . . 298
A.15 Extreme parameter value comparison of the ODE and PDE PK/PD static vitreal binding model . . . 301

Bibliography 305

1 Introduction

1.1 Wet AMD and the application of mathematical modelling

Age related macular degeneration (AMD) is a progressive degenerative disease, affecting primarily the macula, a specialised region of the retina responsible for high acuity vision (central vision). Primarily afflicting humans aged 60 or older, AMD presents in two forms, dry and wet AMD. The dry form of AMD develops slowly, over many years, leading to minimal to severe loss of sight. In contrast, once it has presented, the wet form advances swiftly and, if left untreated, will cause blindness [4–7]. Symptoms of wet AMD occur due to the generation of poorly formed, and highly permeable, blood vessels in the posterior of the retina. Leakage from the vessels causes fluid accumulation within the macula, disrupting photoreceptor cell structure and degrading visual acuity. This choroidal neovascularization (CNV), or choroidal angiogenesis, accounts for 90% of all cases of blindness due to AMD [8, 9]. Whereas treatment for dry AMD does not currently exist, treatments administered for the wet form have existed since 2004 [10]. Most current treatments aim to inhibit the action of vascular endothelial cell growth factor (VEGF) to stimulate angiogensis, through the application of antibody therapies. The three most routinely administered antibodies are bevacizumab (2004) [11], ranibizumab (2006) [12] and aflibercept (2011) [13]; bevacizumab and ranibizumab share active sites and, as such, can be considered functionally equivalent molecules [14]. These antibodies bind to VEGF molecules, blocking their interaction with endothelial cells on the surface of the choroidal vasculature, thereby inhibiting further an-

giogenesis [10].

Research directed towards improving our ability to treat wet AMD is of great significance as AMD represents the third leading cause of blindness globally, accounting for 8.7% of all cases of blindness, whereas within developed countries AMD is the number one cause of blindness. Due in some part to an ageing population, the prevalence of AMD is increasing; it is projected that by 2020 196 million people will be suffering from the condition worldwide, rising to 288 million by 2040 [15, 16]. The cost of AMD treatment represents a substantial economic burden; in 2010 the global healthcare cost of AMD came to $254.8 billion, approximately 25% of all healthcare costs due to visual impairment (excluding uncorrected refractive error) [17]. In 2014 the NHS spent £244 million on ranibizuamb, representing the second greatest cost incurred by NHS due to the purchase of medication, and providing treatment for wet AMD remains a considerable cost to this day [18]. In developing countries, due to cost, treatment is typically unavailable to the general public [19], condemning those with the wet form of the disease to blindness.

In addition to the prevalence of AMD and the cost of its treatment, there are other challenges that require investigation. Current treatments are delivered to the vitreous body of the eye (see Figure 1.1), via intravitreal (IVT) injection; such antibodies have an ocular half life in humans of between 7-10 days [20–24], leading to a required injection frequency of 1-2 months [10]. Ocular antibody therapy can induce complications, with 19-24% of patients treated with ranibizumab or bevacizumab reporting serious adverse effects [25]. Severe intraocular inflammation (endophthalmitis) can occur and it is known that the rates of retinal detachment and traumatic cataract occurrence are in proportion to the frequency of vitreal penetration [26]. Such conditions can lead to more severe complications, and may even cause complete vision loss. Patients undergoing frequent IVT injections may also suffer psychological trauma; a 2016 review states *"patients receiving anti-VEGF treatments showed a prevalence rate of depression between 20 and 26%"*, as well as elevated levels of anxiety and stress induced by frequent injections - separate to the condition itself. In addition to these complications, 10-20% of treatment-naive eyes show no marked improvement when treated with ranibizumab or bevacizumab, leaving a *'significant unmet need'* [27] in the treatment outcomes from bevacizumab/ranibizumab therapy.

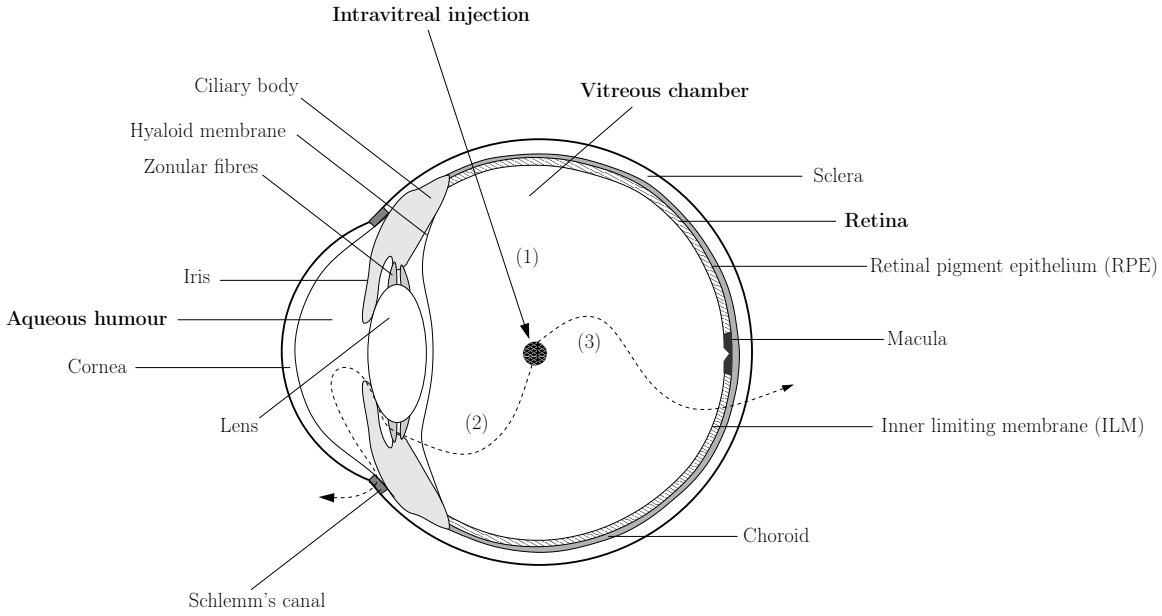

Figure 1.1: Anatomical diagram of the human eye, highlighting key areas involved in the pathogenesis and treatment of wet AMD. (1) Indicates an intravitreal injection of an anti-angiogenic drug; post-injection the drug freely diffuses within the vitreous chamber. (2) The major clearance pathway from the vitreous is through the aqueous humour, at which point it is eliminated via the choroid or Schlemm's canal. (3) The secondary clearance route requires the drug to permeate through the inner limiting membrane of the retina and then through the retinal pigment epithelium into the choroid.

The coupled effects of AMD prevalence within the population, the severity of the condition, the need for frequent injections, and the cost of treatment, makes AMD a serious global problem. This leaves the scientific community with a clear objective - to develop a treatment that can effectively combat the disease, requiring fewer injections, while decreasing the economic burden of access to care. Put succinctly, the real world objectives of AMD research are to Reduce (R) cost, improve Efficacy (E), increase Duration (D) of effect - or 'RED'. The work of this thesis will explore the role of mathematical modelling in helping to achieve these goals.

☆☆☆

Pharmacokinetics (PK) is the study of the time course of drug absorption, distribution, metabolism, and excretion, i.e. 'what the body does to the drug'. By contrast, pharmacodynamics (PD) is the study of the relationship between drug concentration at the site of action and the resulting effect, 'what the drug does to the body' [2]. The study of PK/PD is central in evaluating the performance of a specific drug or treatment, and one that lends itself naturally to mathematical modelling. The study of ocular PK is concerned with the movement of molecules between distinct ocular regions, across various membranes, within

varying levels of fluid flow, typically post IVT injection. Spatially independent/dependent systems of ordinary/partial differential equations (ODE/PDE) can be used to quantitatively describe such molecular transport throughout the eye. Drug-to-target interactions, or PD, can be then integrated into these systems via application of the law of mass action, to create theoretical ocular models to an appropriate level of complexity.

Within this thesis we detail the development of a series of PK/PD spatial and spatially averaged models of the mammalian eye, post-IVT injection, with and without disease activity. Starting from common ocular modelling methodologies we add increasing levels of complexity, building upon standard vitreous-aqueous 2-compartment models [3, 28] (Chapter 2), we integrate increasing biomedical/anatomical accuracy and utilise existing clinical data sets in order to estimate critical model parameters. By building and parametrising these models I create a framework which I can use to address questions related to our RED goals. Possible ways to reduce (R) cost (or equivalently increase treatment access), can be explored by examining if mathematical models predict existing treatments are being utilised in the most efficient manner, or whether performance of hypothetical future molecules can be matched by administering existing drugs using a different treatment protocol. The potential for existing molecules to be used in combination with each other can also be explored, for example a hypothetical new molecule may have two angiogenic targets (for example VEGF-A and angiopoietin 2, a molecule theorised to play a role in angiogensis), the effect of such a molecule may be predicted using modelling to be equivalent to a mixture of two molecule types targeting the angiogenic targets separately. Evaluating and generating hypotheses to improve efficacy (E) can be analysed in several different ways, an ocular PK model can be used to examine which are the most significant molecular properties that determine ocular exposure, and if possible how such properties can be altered to improve quantities such as ocular half-life ($t_{1/2}$). A PK/PD ocular model, including disease activity, can be used to simulate the affect of a therapeutic drug on the concentration of VEGF molecules capable of stimulating angiogenic activity ('unbound' or 'free' VEGF). The concentration of free VEGF is a crucial metric in the evaluation of a drug designed to bind to such free VEGF, while an ocular PK/PD model can be utilised to examine the parameter dependency of the projected free VEGF concentration at the intended site of drug action (in this case the retina). Such a study provides a theoretical foundation for understanding which molecular properties can be manipulated to improve suppression of free VEGF, and, as importantly, which cannot. Perhaps the most central question to be discussed in this thesis is duration (D) of drug effect, and how models can be used predict ways in which it can be increased. In

addition to the PK/PD analysis of current treatments a powerful application of mathematical modelling to this problem is to simulate the PK/PD of hypothetical molecules, which have yet to be developed or are currently undergoing initial testing. We will consider such hypothetical molecules whose design is intended to extend duration. In addition to using PK/PD models of standard treatments to identify the molecular traits which most significantly determine duration of effect, a powerful application of mathematical modelling is to analyse duration of effect of hypothetical molecules with novel and distinct features, which have yet to be developed or are currently undergoing initial testing. Such studies can be valuable as a first step in analysing which potential approaches may yield the best results, and hence provide a theoretical guide as to the most efficient allocation of resources. For example theoretical studies of hypothetical molecules can generate insight into the range of parameter values (if any) for which such molecules improve on existing treatments - an exercise that may be very time-consuming, and expensive, to perform through experimental methods. Additionally if a previously undeveloped drug concept is shown by modelling work to be exceedingly unlikely to be efficacious, not pursing its development would, in addition to saving time and resources, help reduce the quantity of animals sacrificed in preliminary pharmaceutical testing. All of these concepts will be explored in this thesis.

In addition to the real world RED outcomes considered in this work I will also address more abstract problems related to the development of ocular PK/PD models. A key underpinning assumption many widely utilised ocular models is the 'well-mixed' assumption, which states molecular concentration levels within a distinct ocular region can be treated as homogeneous, thus removing the necessity to consider ocular spatial geometry. While such models offer increased computation speed, fewer parameters and more scope for analysis, to our knowledge the applicability of this assumption has never been tested. Within this thesis we examine the suitability of this assumption, as well as the fundamental differences between 'well-mixed' ODE models and spatial PDE models. In addition to this specific study, we will explore the extent to which ocular PK/PD models can be analysed analytically to yield exact or asymptotic solutions. Mathematical models including reactions between chemical species are often non-linear systems, resistant to analytic analysis, as is the case with ocular PK/PD models. Within this work, where possible, we will generate asymptotic solutions to ocular systems, in order to precisely describe the parameter dependency of model behaviour. Not only will this allow more robust analysis of such behaviour, but it will also aid in the parameterisation of more complex models, by allowing us to translate quantifiable biochemical metrics (such as ocular half-life) into model parameters (such as

compartment transfer rates).

Before discussing the projects that comprise this thesis, I summarise the relevant background relating to the pathology and treatment of wet AMD (Section 1.2). In Section 1.3 we review the ocular PK/PD modelling literature in order to place our modelling work in context. We conclude this chapter in Section 1.4 with an overview of the work contained within the five research chapters of this thesis.

1.2 The pathology and treatment of wet AMD

Neovascular age related macular degeneration, or wet AMD, is the advanced form of dry AMD. Both forms of macular degeneration affect the retina, specifically the macula, the region of the retina responsible for central vision. The retina lines the inside of the main body of the human eye, the vitreous chamber (see Figure 1.1) - a virtually acellular region, comprised of over 98% water [30], with gel properties arising from a pervasive extracellular collagen fibril matrix [31]. Figure 1.2 depicts a simplified anatomical diagram of the retina, omitting the biological structures less relevant to the pathology of wet AMD. From Figure 1.2 (a) we see, the retina comprises layers of specialised cells including, light sensitive photoreceptors which are situated above the retinal pigment epithelium (RPE) and face towards the vitreous chamber. Beneath the receptors lie the RPE and Bruch's membrane, which, together, serve as a blood-retinal barrier, separating the choroidal vasculature (which delivers oxygen and nutrients to the retina) from

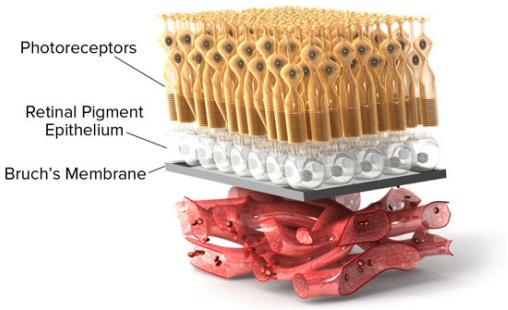

(a) Healthy retina

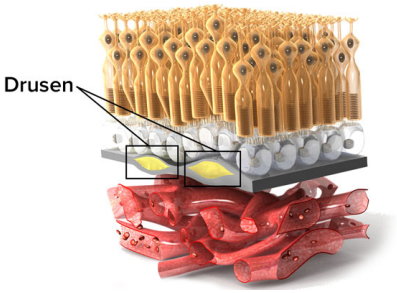

(b) Diseased retina with dry AMD

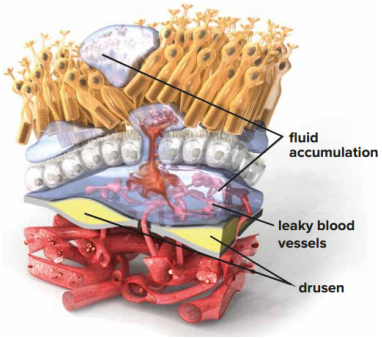

(c) Diseased retina with wet AMD

Figure 1.2: (a) Cross-sectional view of a healthy retina. (b) Diseased retina with dry AMD. (c) Progression of dry AMD to wet AMD. Images reproduced with permission from the Angiogenesis Foundation, showing a simplification of retinal cell structure [29].

the delicate array of photoreceptors [9].

Over time metabolic end products (a collection of proteins and lipids produced by the RPE and choroid), collect inside and above Bruch's membrane, aggregating into deposits known as drusen (Figure 1.2 (b)). Drusen accumulation may disrupt the photoreceptor cells, causing localised retinal thinning, and permanently scar affected regions of the retina. These changes are known as "dry AMD" and can lead to loss of central vision [26].

Dry AMD is the first stage of macular degeneration. The increasing presence of drusen may cause an inflammatory response within the retina, one of the factors theorised to trigger the overproduction of vascular endothelial growth factor (VEGF) within the RPE. The presence of high VEGF concentrations promotes the emergence of new vasculature (neovasculature), from the sub-retinal choroidal space, via a process known as angiogenesis. The new vessels can penetrate the already weakened Bruch's membrane into the retina. They are highly porous and poorly developed. Leakage of fluid and blood from this neovasculature into the posterior retinal space defines the transition from dry to wet AMD [8, 9, 26, 32].

Left untreated, AMD will further degenerate; the fluid may rupture the RPE and accumulate amongst the photoreceptors (see Figure 1.2 (c)), severely disrupting their cellular organisation, and potentially causing permanent damage to nerve endings. In this way wet AMD is highly likely to cause severe central vision loss and eventually central or complete blindness in the affected eye.

Since VEGF was identified as a potent driver of angiogensis of wet AMD, there have been extensive studies to determine its role. In the late 1990s, several landmark *in vivo* and *in vitro* studies [33–36], revealed that VEGF plays a fundamental role for the proliferation of neovasculature, and that its presence is indeed necessary for angiogenesis to occur. Additionally it was demonstrated that VEGF actively increased vascular permeability [37], directly linking it to the fluid leakage central to the pathology of wet AMD. Subsequently VEGF has been the primary target for therapeutic molecules for the treatment of wet AMD.

☆☆☆

While VEGF has been shown to play a key role in the progression of wet AMD, inhibiting its activity remained challenging. The retina is a notoriously difficult target for drug delivery, due to its anatomical location, delicate cell structure and the insular nature of the eye as an organ itself - in fact our ability to view the structure/condition of the retina vastly

surpasses our ability to physically reach it [38]. Additionally, even if it was possible to directly access the retina, any injection of a therapeutic agent would be likely to carry a high risk of cellular damage. Non-invasive procedures, such as topical eye drops and systemic administration, have been shown to be ineffective when used to administer drugs to the retina [39, 40]. This is in part due to the clearance pathways and barriers that exist within the eye. Molecules inside the vitreous primarily exit the eye through the anterior chamber of the eye (Figure 1.1 pathway (2)), and are eliminated into the blood stream through Schlemm's canal, whereas elimination via the retina into the choroid is secondary [26]. Transport through the posterior membranes of the eye is much more challenging for macromolecules than through the anterior hyaloid membrane, and into the aqueous humour, as the inner limiting membrane (ILM) of the retina acts as a barrier to vitreous-retinal transports. Administration of drug systemically is similarly inhibited by the RPE which acts as a blood retinal barrier, and very high levels of an anti-VEGF agent would need to be administered in order to achieve an efficacious concentration in the retina [41]. Additionally, the source of the elevated VEGF concentration is the retina itself, within the RPE [5], making the retina not only the primary target, but also likely to be the necessary target. Due to these considerations, the optimal method of administration for anti-VEGF therapies is widely regarded to be via IVT injection, allowing a molecule to be directly delivered as close to the retina as possible. To understand the current methods of treatment I will briefly summarise the history of anti-VEGF therapies for wet AMD.

Inhibiting VEGF to prevent angiogensis was originally conceived as a treatment for cancer, to prevent host's blood supply becoming integrated into the tumour, such integration being necessary for its continued growth and survival. In 2004, the FDA approved bevacizumab, a recombinant humanized monoclonal antibody (rhuMAb), as a cancer treatment in combination with chemotherapy [10, 11, 42–44]. Bevacizumab is an IgG anti-VEGF antibody with two sites that can to bind to VEGF-A, a member of the VEGF molecular family and a major mediator of angiogenesis and vascular permeability in wet AMD [45]. A schematic of the structure of bevacizumab is shown in Figure 1.3. Throughout this manuscript we will refer to VEGF-A as VEGF.

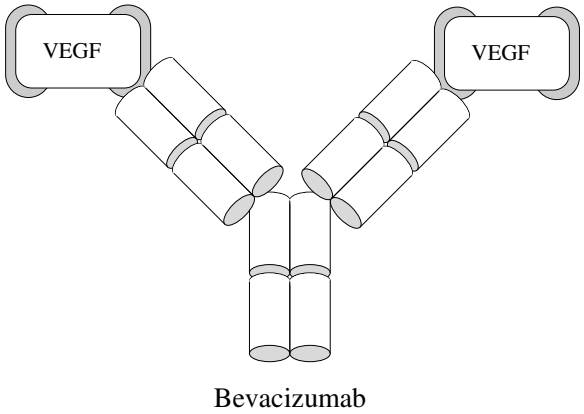

Figure 1.3: Schematic structure of the anti-VEGF IgG antibody bevacizumab, a recombinant humanized monoclonal antibody (rhuMAb) [11, 42–44]. Notice the two active sites (the two arms of the antibody) can bind to VEGF, a major mediator of angiogenesis and vascular permeability in wet AMD. VEGF is depicted bound to each of these sites, notice that each VEGF molecule has two sites to which bevacizumab may bind.

Shortly after the phase I trials of bevacizumab for the treatment of cancer began in 1997, Genentech began development of a similar drug specifically for the treatment of wet AMD, an anti-VEGF recombinant, humanized monoclonal antibody fragment (Fab), which later became known as 'ranibizumab'. Ranibizumab and bevacizumab are derived from the same murine monoclonal anti-VEGF antibody, where ranibizumab is the corresponding fragment of the full length antibody bevacizumab [12, 44, 46], (see Figure 1.4). Between 2006 and 2015 nine randomised controlled trials (3665 participants) comparing the efficacy and safety of IVT bevacizumab and ranibizumab for the treatment of wet AMD were conducted. These trials were then analysed in a systematic review by the Cochrane Collaboration, which concluded that there was between the two compounds no difference in efficacy and no difference in serious, or subsets of, adverse events, aside from an increased rate of gastrointestinal disorders [47].

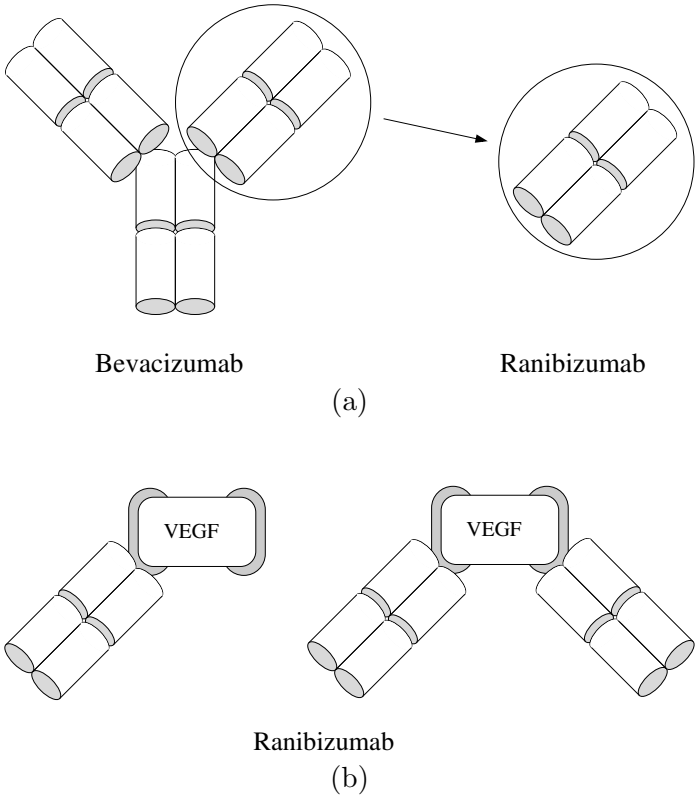

Figure 1.4: (a) Structural similarity of ranibizumab to bevacizumab. (b) Ranibizumab is an anti-VEGF recombinant, humanized monoclonal antibody fragment (Fab), capable of binding to VEGF-A in the same manner as bevacizumab [12]. Notice that two ranibizumab molecules may bind to the same VEGF molecule (bevacizumab is also capable of forming such larger complexes).

Aside from bevacizumab and ranibizumab there exists another viable treatment option for wet AMD, aflibercept, a recombinant fusion protein designed to mimic the VEGF receptors on the surface of vascular endothelial cells (see Figure 1.5). Aflibercept was approved by the FDA in 2011 for the treatment of wet AMD. Aflibercept not only binds to VEGF-A but also VEGF-B and placental growth factor (PlGF). Another major benefit of aflibercept over ranibizumab is that it can be injected every 2 months, instead of every 1 month [10, 13]. Aflibercept has been shown to be at least as efficacious and cost effective as bevacizumab/ranibizumab in several studies. A 2017 systematic review of 28 studies demonstrated that switching from bevacizumab/ranibizumab to aflibercept *"significantly improved anatomical outcomes; however, visual function remained stable, having a comparable effect to other anti-VEGF agents in preservation of vision"* [48], as well as recommending switching to aflibercept may be an effective measure for patients who have developed resistance to treatment.

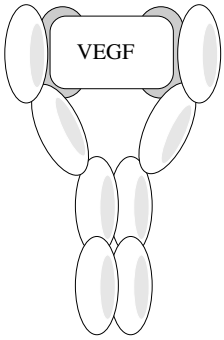

Aflibercept

Figure 1.5: Aflibercept is a recombinant fusion protein designed to mimic the VEGF receptors on the surface of vascular endothelial cells. Aflibercept not only binds to VEGF-A but also VEGF-B and placental growth factor (PlGF) [13].

☆☆☆

There are currently 10-20 prospective treatments of wet AMD undergoing clinical trials, including further anti-VEGF molecules, ocular delivery devices, gradually dissolving delivery gels, topical agents, anti-platelet-derived growth factor therapies, bi/tri-specifc antibodies and anti-angiopoietin molecules [49]. Many other therapies are currently in the preclinical phase, including molecules designed to bind to naturally occurring molecules/structures in the eye (which we will refer to as 'vitreal binders'), in order to prolong duration of effect. For the purpose of this thesis will not review all prospective future treatments, instead, given that ranibizumab is of primary consideration within this thesis, I will consider only the successors to ranibizumab that are currently in clinical trials, as well as preclinical vitreal binding molecules. Specifically I will detail the 'port delivery system' (PDS) [50, 51], the bispecific anti-VEGF/ANG-2 antibody RG7716 [52–57], bispecific anti-VEGF static vitreal binders [58] (SVBs) and the upcoming trispecific anti-VEGF/ANG2 albumin binding BI-X molecule [59].

The 'port delivery system' (PDS), under development by Genentech, is a medical device designed to be implanted in the eye, through the surface of the sclera, beneath the pars plana and subconjunctiva, thus allowing a drug delivery pathway from the surface of the eye into the vitreous chamber (see Figure 1.6). Once implanted, future injections can be performed in a less invasive manner than an IVT injection. In addition, once filled, the PDS is designed to slowly release the drug into the vitreous. The PDS phase I clinical safety trial concluded in 2014, detailing 6 patients with PDS implants over the course of 1 year and 14 over 3 years [51]. For any implanted device complications are always a concern and in

the phase I trial a 10% rate of persistent vitreal haemorrhage* was observed, alongside one occurrence of serious endophthalmitis and 77 other adverse effects. The PDS is currently in the phase II LADDER trial, due to be completed in late 2018 [50].

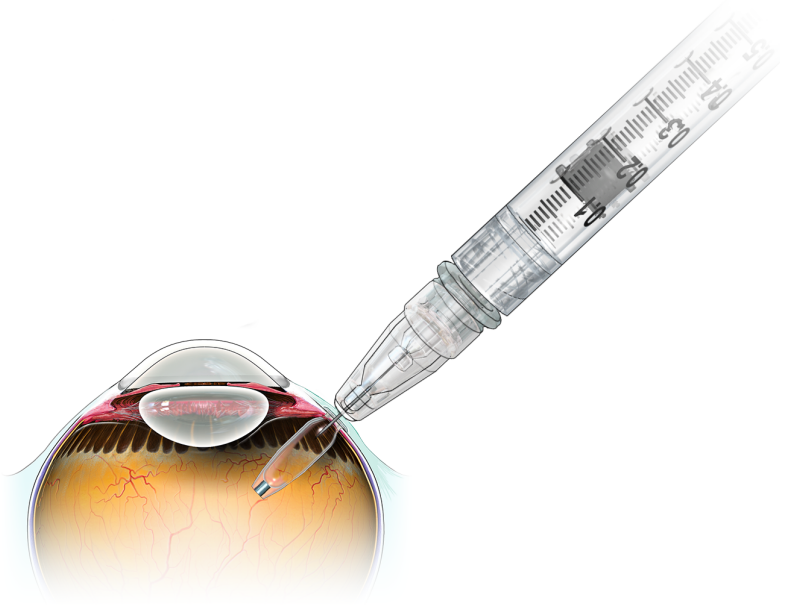

Figure 1.6: Port delivery system (PDS), reproduced from *Breaking the Burden: A New Way to Deliver Anti-VEGF, Review of Optometry, 2018* [60] with permission from Genentech.

Angiopoietin 2 (ANG-2) is theorised to be associated with angiogenesis, and has been found at elevated levels in the aqueous humour of patients with wet AMD. It also appears to play an important role in the development of tumours [55, 61]. Hoffmann-La Roche is developing a bispecific anti-VEGF/ANG-2 antibody currently referred to as RG7716. RG7716 is the fusion of ranibizumab (targeting VEGF) and the anti-ANG-2 molecule LC10 [52] (see Figure 1.7). RG7716 concluded phase I testing in 2017 and at the time of writing it is currently undergoing phase II trials AVENUE [53] and STAIRWAY [62] for the treatment of wet AMD [52–57, 62, 63]. However no results from these studies have yet been published. Roche reported to investors in February 2018 that RG7716 produces statistically significant improvements in VA scores over ranibizumab in the phase II BOULEVARD study [63] for RG7716 as a treatment for diabetic macular edema (DME) [57].

*In comparison 19-24% of patients treated with ranibizumab or bevacizumab report serious adverse effects [25].

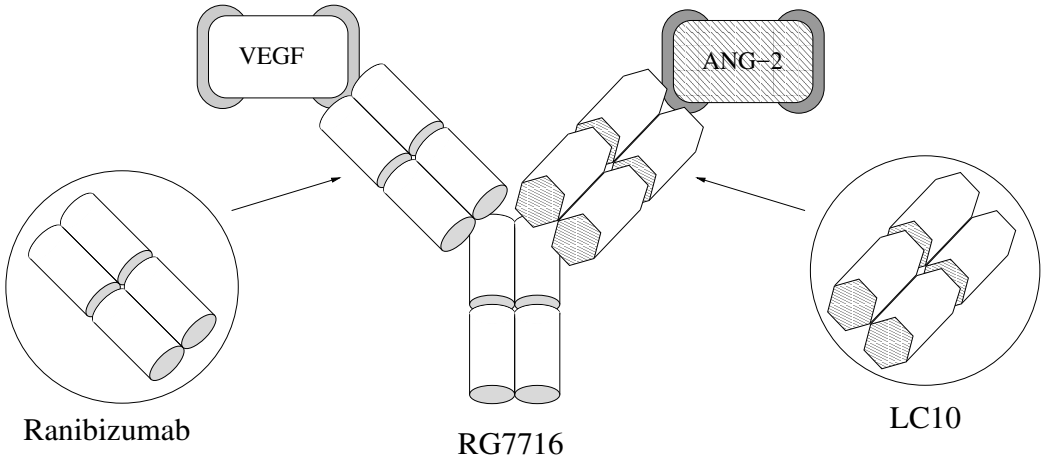

Figure 1.7: RG7716 is a bi-specific therapeutic antibody currently in development, intended to be the successor to ranibizumab. RG7716 is the fusion of ranibizumab (which targets VEGF-A) and LC10, an anti-angiopoietin 2 molecule (ANG-2, as depicted in the diagram) [52–57].

☆☆☆

Alongside the PDS and RG7716, another line of research is focusing on the creation of antibodies that bind to ocular superstructures or large naturally occurring molecules ('vitreal binders'), and, as a result, may possess longer retention times than conventional non-vitreal binding molecules. The vitreous chamber contains a substance known as the 'vitreous gel', comprised of over 98% water with gel properties arising from a pervasive extracellular collagen fibril matrix [31]. Alongside collagen, the vitreous contains albumin, a mobile 66 kDa globular protein [59], and hyaluronic acid, existing in polymer form with a vitreal half-life orders of magnitude greater than antibodies or albumin - and hence can be treated as approximately static [58]. There is currently ongoing preclinical investigation into vitreal binders capable of targeting both hyaluronic acid and albumin, 'long-acting anti-VEGF drugs' (LAVAs) and the BI-X molecule, respectively.

LAVAs are a class of molecules designed to bind to existing hyaluronic acid polymer structures in the vitreous. In a 2017 paper by Ghosh et al. [58], it was detailed how structures of standard therapeutic ocular antibodies can be modified to include an additional hyaluronic binding active site (see Figure 1.8). As described in Ghosh et al. 2017 [58] the LINK domain binds to hyaluronic acid, leaving the remaining active sites of the molecules free to interact with their respective targets, regardless of whether they are bound to hyaluronic acid. Such LAVA molecules have the potential to possess longer vitreal retention times than conventional antibodies as when they are bound to hyaluronic acid their

elimination rate from the eye essentially drops to zero. This raises several interesting questions regarding the strength of the binding to the vitreal network; too weak and the antibody would be equivalent to conventional molecules, too strong and there may never be enough unbound drug free to diffuse into the retina. Investigation of such SVB molecules will be a primary focus of this thesis, and their analysis will be presented in Chapters 3 and 4.

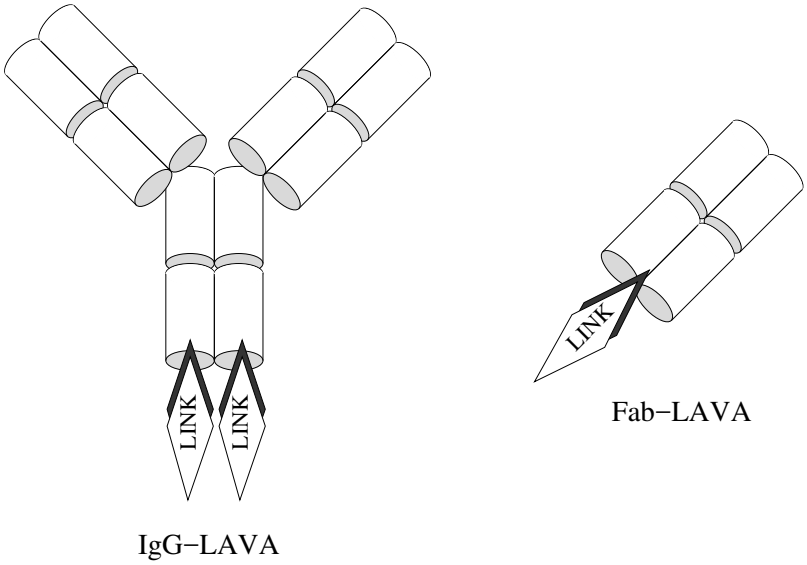

Figure 1.8: Cartoon depiction of the molecular structure of IgG and Fab LAVA molecules. LINK is the site to which hyaluronic acid may bind.

There exists an alternative class of vitreal binder to that of the LAVA molecules; antibodies that are designed to bind not to a superstructure such as collagen or hyaluronic acid, but to naturally occurring ocular proteins. Such non-static vitreal binders (nSVBs) aim to bind to a larger molecule present in the vitreal upon IVT injection, to effectively increase the value of their hydrodynamic radius (R_{h}), decreasing their rate of diffusion and membrane permeability, and hence increasing their ocular half-life ($t_{1/2}$). BI-X, a member of the SVB molecular class, is a trispecific 40 kDa antibody capable of binding to human VEGF, ANG2 and albumin. A preclinical PK study of BI-X in rabbits, performed by Fuchs et al. in 2017 [59], studied the ability of albumin binding to increase ocular $t_{1/2}$. The results were very promising; the ocular $t_{1/2}$ increased from 3.2 to 10 days after the introduction of human albumin into the rabbit model. nSVB such as BI-X have several possible advantages over the static class, such as the previously mentioned LAVA molecules. For example very strong binding to the vitreal target is not a problem, in fact it is ideal - assuming permeation into the retina of the resultant complex is not impeded. Additionally the vitreal target may also be present in the retina, and hence would still retain the $t_{1/2}$ boost gained through

vitreal binding (unlike say a collagen binder). In Chapter 4 will we present PK/PD analysis of the BI-X molecule versus that of the LAVA class.

1.3 Literature review of relevant previous models

1.3.1 Ordinary differential equation ocular models

The ocular PK/PD models relevant to this work can be split into two main groups, models that are based on ordinary differential equations (ODEs), or partial differential equations (PDEs). The ODE models are made up of time-dependent variables, typically describing molecule concentration/quantity in various anatomical regions, which are treated as spatially homogeneous - or 'well-mixed'. ODE models have many advantages over equivalent PDE models - they require substantially less time to solve, they require fewer parameters and, as most collected data are not spatial in resolution, model to the native resolution of available data. In the following text we detail such ODE models, illustrative of the modelling techniques implemented within this thesis.

Mordenti et al. 1999: Comparisons of the Intraocular Tissue Distribution, Pharmacokinetics, and Safety of 125 I-Labeled Full-Length and Fab Antibodies Following Intravitreal Administration [64]

In 1999, Mordenti et al. performed the first intraocular tissue PK study comparing the distribution of IgG and Fab molecules, which, as was noted in Section 1.2, justified the development of the Fab molecule ranibizumab for the treatment of retinal diseases. Alongside the presentation of the experimental results Mordenti et al. also developed an ocular PK model, which has represented an early application of using ODEs to mathematically model ocular antibody PK. Many models share the same basic structure as the model of Mordenti et al. - including the work within this thesis.

The model, depicted schematically in Figure 1.9, was formulated as a system of ODEs (Equations 1.1-1.3), where the amount of drug in the vitreous, plasma and other systemic compartments are given by X_0, X_1 and X_2, respectively, and are functions of time with units of ng. The constants r_{ij} denote the transfer rates between compartments, with units of 1/day. Initially there exists no drug in the systemic compartments, giving $X_1(0) = X_2(0) = 0$, whereas $X_0(0)$ is set equal to the corresponding quantity of drug administered by IVT.

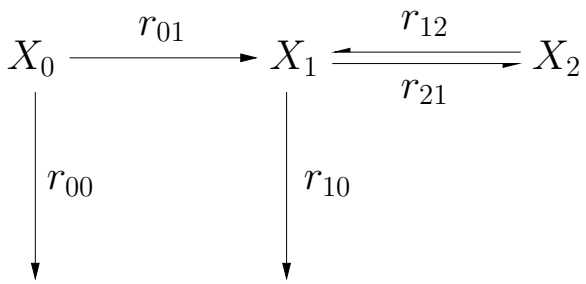

Figure 1.9: Model schematic as presented in Mordenti et al. 1999 [64]. The amount of drug in the vitreous, plasma and other systemic compartments are given by X_0, X_1 and X_2, respectively, with units of moles. The rate constants r_{ij} denote the transfer rates between compartments, with units of 1/day.

$$\frac{\mathrm{d}X_0}{\mathrm{d}t} = -\left(r_{00} + r_{01}\right) X_0, \tag{1.1}$$

$$\frac{\mathrm{d}X_1}{\mathrm{d}t} = r_{01}X_0 - \left(r_{10} + r_{12}\right) X_1 + r_{21}X_2, \tag{1.2}$$

$$\frac{\mathrm{d}X_2}{\mathrm{d}t} = r_{12}X_1 - r_{21}X_2. \tag{1.3}$$

This model describes the vitreal (X_0), serum (X_1) and organ/tissue (X_2) concentration simultaneously, with minimal parameterisation. Drug present in the vitreous is assumed to have two elimination pathways, into the serum at rate r_{01} and into non-plasma regions[†] at rate r_{00}. This latter pathway is typically neglected in current models, where all drug is assumed to enter the bloodstream. Once the drug has moved from the vitreous into the serum it is assumed that the quantity of drug that moves back into the vitreous is negligible. This assumption appears in many ocular models and is based upon the nature of the ocular transport pathways and how they contribute to the insular character of the mammalian eye. Drug circulating in the body via the bloodstream then moves into (at rate r_{12}) and out of (at rate r_{12}) organs/tissue, while being systemically eliminated from the serum at rate r_{10}.

Rhesus monkeys were dosed with IgG and Fab molecules via IVT injection and vitreal/plasma samples were collected at various subsequent times. Measured vitreal and plasma concentrations were treated as X_0/V_0 and X_1/V_1, respectively, where V_0 and V_1 denote the vitreal volume and plasma volume distribution, in (mL). V_0 and V_1 do not appear in the governing equations as X_0, X_1 and X_2 are quantities (mols) not concentrations (M). The numerical solutions of the system were then fitted using a least squares method to this PK dataset, allowing the transfer rates and compartment volumes to be estimated.

[†]The specifics of what this non-plasma region represents are slightly unclear from the text.

Transfer rate estimations carried large uncertainties (roughly twice their estimated values) and volume estimations were found to be larger than would have been expected based on anatomy, however the model captured well the profiles and decay rates exhibited by the dataset.

Overall this model represents a simple starting point for the development of more complex ODE models. As is often the case with PK/PD models this simple PK model is presented outside of a mathematical context due to the general audience of the work. Equations and initial conditions are often left to be inferred from schematic diagrams and most notably linear systems are frequently left unsolved (note that Equations 1.1-1.3 can be solved analytically). Due to this practice models are generally not formulated mechanistically and transfer rate parameters are not interpreted in a biological manner, such as in terms of specific membrane permeabilities. A consequence of this approach to parameter definition is that in order to fit the model to the data parameters can often take biologically unrealistic values, for example in this work the estimated vitreal volume is $\sim$3 times the standard anatomical value. In the work presented in this thesis we attempt to biologically and mechanistically interpret model parameters to the fullest extent possible given the available data.

Gadkar et al. 2015: Design and pharmacokinetic characterization of novel antibody formats for ocular therapeutics [28]

In 2015, Gadkar et al. developed a 3-compartment PK ODE ocular model in order to analyse an extensive antibody PK dataset detailing the PK in the retina, vitreous and aqueous chamber, for a number of antibodies and antibody fragments (ranging from 50-150 kDa), post-IVT injection. The study was performed in rabbits using molecules derived from a human anti-glycoprotein D (anti-gD) antibody, and hence inert in a rabbit model, foregoing the need to account for pharmacodynamic (PD) effects. The modelling work of Gadkar et al. builds upon earlier ocular models such as Mordenti et al. by distinguishing different regions of the eye (the retina, vitreous and anterior aqueous humour). This is of note as this type of model allows for discrimination between experimental concentration samples taken from different ocular regions. As with Mordenti et al. injected drug is cleared from the vitreous by a first order process. However, instead of moving straight into the serum the drug first enters the anterior chamber of the eye, the aqueous humour. This recognises that the major clearance route from the eye is via the aqueous humour, elimination from which is assumed to occur at the rate that aqueous humour is produced from the ciliary

processes of the eye, a production rate that has been studied in great detail across several species. In comparison with the modelling work of Mordenti et al., this represents a step towards a more mechanistic basis for ocular modelling. Additionally this model is one of the first to attempt to account for the retina in addition to other regions of the eye, and the drug concentration of the retina is assumed to be directly proportional to that in the vitreous. This assumption is not based on a mechanistic principle, such as permeation, and represents a physical simplification. Modelling the drug concentration in the retina in this way assumes that the volume of the retina is negligible and, importantly, that no elimination can occur via the RPE into the choroid.

Gadkar et al.'s model was formulated as a system of ODEs, for the concentration (ng/mL) of a general antibody, in the retina c_{ret}, the vitreous c_{vit} and aqueous c_{aq}. The concentration in a phenomenological delay compartment (c_τ), separating the vitreous and aqueous chambers, was introduced to obtain a better fit to the data. The governing equations are given by:

$$c_{\text{ret}} = \alpha c_{\text{vit}} \tag{1.4}$$

$$\frac{\mathrm{d}c_{\text{vit}}}{\mathrm{d}t} = -k_{\text{el}} c_{\text{vit}} \tag{1.5}$$

$$\frac{\mathrm{d}c_\tau}{\mathrm{d}t} = k_{\text{el}} c_{\text{vit}} - \tau c_\tau \tag{1.6}$$

$$\frac{\mathrm{d}c_{\text{aq}}}{\mathrm{d}t} = \left(\frac{V_{\text{vit}}}{V_{\text{aq}}}\right) \tau c_\tau - C_{\text{L}} c_{\text{aq}} \tag{1.7}$$

and the model parameters are defined in Table 1.1.

Parameter	Units	Description
k_{el}	1/day	Vitreous-aqueous elimination
τ	1/day	Vitreous-aqueous delay rate
C_{L}	mL/day	Clearance from the aqueous chamber
V_{vit}	ml	Vitreal volume
V_{aq}	ml	Aqueous volume
α	none	Retina-vitreous concentration ratio

Table 1.1: Model parameters for the model proposed by Gadkar et. al. 2015 [28].

Initially all concentrations are zero, apart from in the vitreous where $c_{\text{vit}}(0)$ is the antibody concentration post-initial IVT injection. When fitting their model, Gadkar et. al. varied k_{el} and τ to fit the data within the vitreous and aqueous compartments. The model was then matched to the retinal data by varying α. The model was found to fit the data well. However, as with Mordenti et al., there was no attempt made to solve the governing

equations analytically.

The modelling work of Gadkar et al. demonstrates the progression of ocular PK modelling using ODEs between 1999 and 2015. The move from 1 to 3 compartments is a notable step forward, allowing for high quality fitting using multiple datasets, as well as greater predictive power. The introduction of the virtual delay compartment was an interesting addition as it was motivated purely by a desire to fit the collected data to the model; its physiological significance however was not considered. While the inclusion of retinal concentration represents an improvement on previous work, the absence of an elimination pathway through the posterior of the retina, or a reduction in vitreal concentration due to transport into the retina, means Gadkar et al.'s model is likely to overestimate clearance of drug through the anterior of the eye. When moving towards a PK/PD model, wherein VEGF is produced in the retina, a mechanistic approach to retinal modelling may be preferable. The development of such a retinal model will be discussed in Chapter 3.

Saunders et al. 2015: A model of the ocular pharmacokinetics involved in the therapy of neovascular age-related macular degeneration with ranibizumab [3]

In 2015, Saunders et. al. [3] presented a two-compartment (vitreous and aqueous) PK/PD ODE ocular model, developed to analyse clinical data collected from patients suffering from neovascular AMD. Data were collected at multiple time points from 31 patients following administration of intravitreal 0.5 mg doses of ranibizumab, free VEGF concentrations were then measured from the aqueous humour samples. The PK aspects of this model are identical to those of Gadkar et al., save for the absence of the phenomenological delay compartment between the vitreous and aqueous, and the lack of an inferred retinal concentration. This model however is the first to link clinically observed free VEGF levels to those in the vitreous chamber, in AMD patients being treated for wet AMD with an anti-VEGF antibody therapy. Put another way, this model utilises a similar PK structure to that of Gadkar et al., but goes further by introducing VEGF-ranibizumab interactions to describe ocular PD.

Within the two compartment model, ranibizumab (R) and free VEGF (V) are assumed to bind and form a VEGF-ranibizumab complex (VR), and reactions are assumed to take place only in the vitreous chamber. It was assumed clearance only took place from the vitreous chamber via the aqueous chamber, at rate k_{el} (1/day). Once in the aqueous humour drug is eliminated at rate $C_{\mathrm{L}}/V_{\mathrm{aq}}$, where C_{L} (mL/day) is the rate at which aqueous humour

is produced, and V_{aq} (mL) is the volume of the aqueous. Figure 1.10 depicts a model schematic for Saunders et al., which can be formulated into the following ODE system

$$\frac{\mathrm{d}v_{\text{vit}}}{\mathrm{d}t} = (k_{\text{off}}c_{\text{vit}} - k_{\text{on}}v_{\text{vit}}r_{\text{vit}}) - k_{\text{el}}v_{\text{vit}} + \frac{V_{\text{in}}}{V_{\text{vit}}}, \tag{1.8}$$

$$\frac{\mathrm{d}r_{\text{vit}}}{\mathrm{d}t} = (k_{\text{off}}c_{\text{vit}} - k_{\text{on}}v_{\text{vit}}r_{\text{vit}}) - k_{\text{el}}r_{\text{vit}}, \tag{1.9}$$

$$\frac{\mathrm{d}c_{\text{vit}}}{\mathrm{d}t} = -(k_{\text{off}}c_{\text{vit}} - k_{\text{on}}v_{\text{vit}}r_{\text{vit}}) - k_{\text{el}}c_{\text{vit}}, \tag{1.10}$$

$$\frac{\mathrm{d}v_{\text{aq}}}{\mathrm{d}t} = \left(\frac{V_{\text{vit}}}{V_{\text{aq}}}\right) k_{\text{el}}v_{\text{vit}} - \frac{C_{\text{L}}}{V_{\text{aq}}}v_{\text{aq}}, \tag{1.11}$$

$$\frac{\mathrm{d}r_{\text{aq}}}{\mathrm{d}t} = \left(\frac{V_{\text{vit}}}{V_{\text{aq}}}\right) k_{\text{el}}r_{\text{vit}} - \frac{C_{\text{L}}}{V_{\text{aq}}}r_{\text{aq}}, \tag{1.12}$$

$$\frac{\mathrm{d}c_{\text{aq}}}{\mathrm{d}t} = \left(\frac{V_{\text{vit}}}{V_{\text{aq}}}\right) k_{\text{el}}c_{\text{vit}} - \frac{C_{\text{L}}}{V_{\text{aq}}}c_{\text{aq}}, \tag{1.13}$$

where v, r and c are the concentrations of V, R and VR respectively (where their subscript indicates their respective compartment), V_{vit} is the vitreal volume and k_{off} and k_{on} are the reaction off and on rates respectively, and V_{in} (pM/day) is the production rate of VEGF.

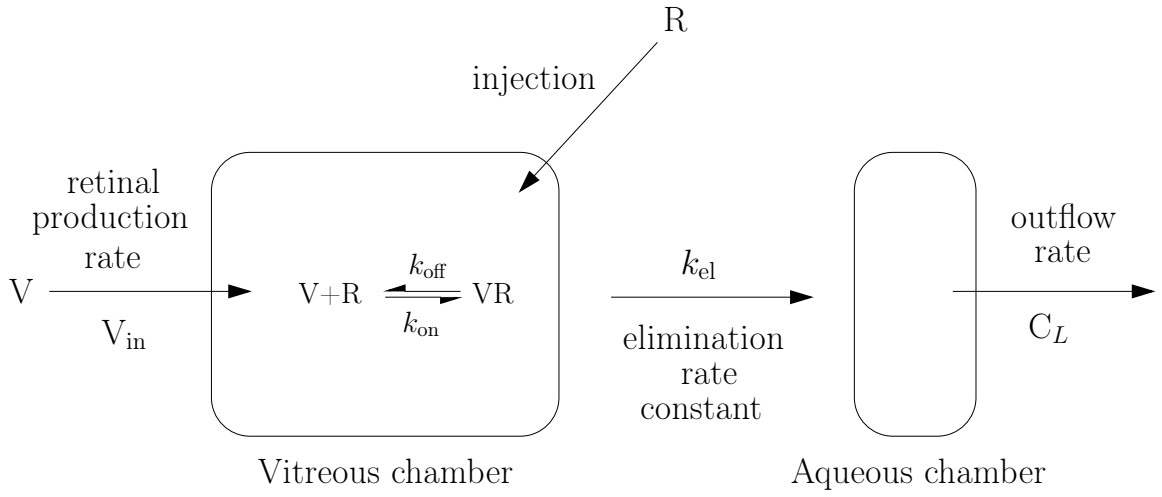

Figure 1.10: Model schematic of model presented in Saunders et al. 2015 [3].

Saunders et al., in order to solve this system, assumed that VEGF and ranibizumab exist in a state of chemical equilibrium within the vitreous, so that

$$v(t) \times r(t) = K_{\text{D}}c(t), \tag{1.14}$$

where K_{D} is the dissociation constant between VEGF and ranibizumab, described in terms of the reaction on and off rates as $K_{\text{D}} = k_{\text{off}}/k_{\text{on}}$. Next, Saunders et. al. defined the

following:

$$v_{\text{tot}} = v_{\text{vit}} + c_{\text{vit}}, \tag{1.15}$$

$$r_{\text{tot}} = r_{\text{vit}} + c_{\text{vit}}, \tag{1.16}$$

for the total VEGF and ranibizumab concentrations respectively. Taking $r(0)$ to be the concentration in the vitreous chamber, equivalent to a dose of 0.5 mg of ranibizumab, one may then write:

$$r_{\text{tot}}(t) = r(0) \times \exp\left(-k_{\text{el}} t\right). \tag{1.17}$$

Similarly one may also write for v_{tot}:

$$v_{\text{tot}} = \frac{V_{\text{in}}}{V_{\text{vit}} k_{\text{el}}}. \tag{1.18}$$

At this point Saunders et. al. solved

$$[v_{\text{tot}}(t) - c_{\text{vit}}(t)] \times [r_{\text{tot}}(t) - c_{\text{vit}}(t)] = K_{\text{D}} c_{\text{vit}}(t), \tag{1.19}$$

for $c_{\text{vit}}(t)$, using the above expressions for $v_{\text{tot}}(t)$ and $r_{\text{tot}}(t)$. If $c_{\text{vit}}(t)$ is known then the solution for $v(t)$ may be obtained via Equation 1.15. The aqueous solution is then determined by making a quasi steady-state (QSS), giving $v_{\text{aq}} = k_{\text{el}} V_{\text{vit}} v_{\text{vit}} / C_{\text{L}}$. This solution was then fitted to patient data, by varying k_{el} and V_{in}. Saunders et. al. made two key simplifying assumptions in their work, firstly they ignored the fact that VEGF has two binding sites for ranibizumab, via which it may form a three molecule complex. Secondly they fixed the value of $K_{\text{D}} = 46$ pM. Through analysis presented in Chapter 2 we demonstrate that fixing $K_{\text{D}} = 46$ pM leads to half-life values for ranibizumab that are inconsistent with experimental values, as Saunders et. al. found. This model does however represent a detailed and novel investigation into the ocular PD of antibody therapies for wet AMD, as well as a starting point for the ODE PK/PD studies contained in this thesis.

Other relevant examples of PK/PD ocular modelling utilising ODEs

Other ODE models of the human eye include Gaudreault et al. 2005 [65], that used a 1-compartment model of the cynomolgus vitreous to analyse *in vivo* PK data. Gaudreault et al. [65] then utilised a non-compartmental method (assumption of proportionality), as in Gadkar et al. [28], to estimate retinal and aqueous concentrations. Gibiansky et al. 2015 [66] presented an ODE model similar to Saunders et al., to analyse *in vivo* cynomolgus PK/PD data, utilising a QSS assumption as well as assuming the system to be in a state

of chemical equilibrium. Similarly to Gaudreault et al. [65] and Gadkar et al. [28], the concentration in the retina was assumed to be proportional to that of the retina, however unlike previous models, in Gibiansky et al. [66] transport from the eye into the serum was assumed to occur via the vitreous, not the aqueous. Additionally, the concentration in the aqueous was assumed to be proportional to the vitreous. Other PK and PK/PD models of drug concentration in the mammalian eye post IVT injection, which utilise comparable mathematical methods to those already discussed and those implemented in this thesis, include Zhu et al. 2008 [43], Xu et al. 2013 [21] and Park et al. 2016 [67].

1.3.2 Partial differential equation ocular models

Ocular PK/PD models built using partial differential equations (PDEs) are more complex than equivalent ODE models, as they not only describe the drug concentration time-course, but also the drug concentration spatial distribution, over whatever ocular geometry is being modelled. PDE models require a higher level of geometric parameterisation, additionally PDE models are also more computationally demanding and therefore slower to solve. However, PDE models do allow for the opportunity to move ocular models closer to physiological reality, and hence, in principle might offer a higher level of predictive accuracy. The question of how ocular ODE and PDE are related to each other has yet to be addressed however, including the suitability of the well-mixed principle utilised in equivalent ODE models.

Friedrich et al. 1997: Drug distribution in the vitreous humor of the human eye: the effects of intravitreal injection position and volume [68]

One of the early ocular PK models developed using PDEs was published in 1997 by Friedrich et al., using a finite element model (FEM) to study the PK of a drug administered via IVT injection in the rabbit eye. We note this model considered only the PK of small molecules, specifically fluorescein and fluorescein glucuronide, rather than the macromolecules which will be the focus of the research presented in this thesis. The geometry of the vitreous body used in the FEM was based on experimentally collected cross-sections of the rabbit eye, and accounted not only for the vitreous body but also a small section of the anterior aqueous humour, alongside the retina, lining the posterior of the vitreous chamber. The vitreous body was separated from the aqueous humour by the hyaloid membrane, through which the drug could permeate. If a molecule passes through this membrane from the vitreous, it is subsequently eliminated by the flow of aqueous humour produced by the ciliary processes. Mass transfer within the model was described by a convective-diffusion equation, incorporating pressure driven flow and movement due to diffusion. Zero

fluid velocity was assumed within the vitreous, hyaloid membrane and retina, as relative to the anterior of the eye the flow in the posterior is very small. Past the anterior hyaloid membrane, the fluid velocity was modelled using a steady state version of the Navier-Stokes equations (Equation 1.20), with incompressibility of the aqueous humour. The distribution of the drug was then determined by solving a convective diffusion equation, as given below by Equation 1.21.

$$\rho\vec{U}\cdot\nabla\vec{U}+\nabla P-\mu\nabla^2\vec{U}=0, \tag{1.20}$$

$$\frac{\partial C}{\partial t}+\vec{U}\cdot\nabla C-D\nabla^2 C=0, \tag{1.21}$$

where C is the concentration of drug (g/mL), D its diffusivity ($\mathrm{cm^2 s^{-1}}$), P the fluid pressure (g $\mathrm{cm^{-1}}$ $\mathrm{s^{-2}}$). $\vec{U}$ is the velocity vector field (cm $\mathrm{s^{-1}}$), μ viscosity (g $\mathrm{s^{-1}}$ $\mathrm{cm^{-1}}$) and ρ density (g $\mathrm{cm^{-3}}$). The pressure field P is determined from incompressibility with prescribed boundary conditions. As previously noted $\vec{U}$ is only non-zero within the aqueous humour, while the eye was assumed to be symmetric along its axis (i.e. alone the line from the centre of the lens to the furthest point of the vitreous), the choice of initial conditions broke this axial symmetry, as the volume of drug introduced via IVT injection was chosen to be off centre, in order to study the effect this would have on the concentration profile of the drug across the vitreous. A no-flux boundary condition was applied to the surface of the lens, and a constant velocity of fluid was assumed to be generated normal to the ciliary processes. The drug was assumed to permeate through the anterior hyaloid membrane of the eye and additionally through the ILM of the retina, with a perfect concentration sink at the RPE (representing choroidal clearance). The diffusivity within the retina was adjusted based upon the estimated permeability of the tissue.

Due to limitations in computation power, this model was solved on a relatively coarse mesh. For example, it seems that the retina was assumed to be one element thick, reducing the precision of the model. The choice to take the posterior of the retina as a perfect sink was perhaps overly simplistic. The RPE acts as a blood-retinal barrier which would mean any drug would have to first permeate through this layer before being eliminated by the choroidal blood flow, therefore choosing the posterior of the retina to be a perfect concentration sink would induce an artificially high concentration gradient across the retina. While the assumption that the vitreous had negligible fluid flow was not justified in this work, the work presented later in this thesis suggests that it was a reasonable approximation (see Section 3.2). In many ways Friedrich et al.'s model was ahead of its time, and impressive given the computational power available at the time; it very much set the stage for the future ocular PDE models discussed below.

Missel 2012: Simulating intravitreal injections in anatomically accurate models for rabbit, monkey, and human eyes [69]

In 2012, Paul Missel published a benchmark paper on the mammalian eye, using anatomically accurate finite element models of the rabbit, monkey and human eyes, in order to study the PK of intravitreally injected molecules. Similar to Friedrich et al., Missel exploited the axial symmetry of the eye. However, unlike Friedrich et al., Missel produced a more complete representation of the eye, modelling the sclera, choroid, retina, vitreous, ciliary body, lens, iris, aqueous and cornea. Missel's work represents the most anatomically detailed *in silico* ocular model to date. Missel based his models on magnetic resonance imaging (MRI) data; measurements taken from these images were then compared to characteristic measurements from the literature.

Missel modelled antibody concentration PK post-IVT injection via a convection-diffusion equation, in the same manner as Friedrich et al.. However, unlike Friedrich et al., Missel accounted for fluid flow within the vitreous chamber. Fluid flow in all non-aqueous regions was modelled by treating by treating the regions as porous media and using Darcy's law,

$$\vec{U} \propto -\nabla p, \tag{1.22}$$

where $\vec{U}$ and p are fluid velocity and the local pressure, respectively. Assuming the fluid is incompressible, the pressure field can then be derived using suitable boundary conditions. Fluid flow in the aqueous humour, as in Friedrich et al., was governed by the Navier-Stokes equations. The modelling work performed in this paper represents the state of the art in ocular PDE modelling, and has been an exceptional resource in our research. The PDE approach presented by Missel gives insight into the conclusions that can be drawn from high level ocular modelling, such as the distribution of intraocular pressure, fluid flow and the early time dynamics of the initial IVT dose. However, as with Friedrich et al., Missel did not comment on the applicability of the well mixed assumption to describe the PK within eye, or how such a PDE model may translate to an ODE model through spatial averaging. The modelling work of Missel, while extremely impressive in its anatomical detail, may represent somewhat of a *'Concorde moment'* due to its shear complexity in comparison to the industry standard of ODE modelling. The geometry alone represents a very large challenge to implement, on top of which the model requires a very large number of parameters, many of which have the potential to contain large uncertainty. This reinforces the need for a rigorous comparison of ODE versus PDE modelling, to justify the use of the

simpler models most frequently used in PK/PD study. Additionally this work posits the need for the development of a simplified adaptable PDE model, whose geometry can easily be adapted for different species simply by changing a handful of parameters.

Other relevant examples of PK/PD ocular modelling utilising PDEs

Other PDE models of the human eye include Kim et al. 2005 [70], which presented a 3D, non-axial symmetric PDE PK model of the rabbit vitreous and retina. Similar to Missel [69] the rate of diffusion of chemical species was set by tissue specific diffusivity. Again, as in Missel [69], fluid flow in the vitreous was determined by Darcy's law, with pressure gradients set by boundary conditions at the anterior and posterior of the model geometry. Molecular concentrations were then determined by a convective diffusion equation in all model geometries. Kotha et al. 2014 [71] presented a 3D PDE PK model of the human eye with a similar level of anatomical accuracy to that of Missel [69], however they omitted consideration of the aqueous chamber and other anteriorial ocular geometry. Additionally this model did not account for transport from the vitreous into the aqueous. Unlike Missel [69] and Kim et al. 2005 [70], Kotha et al. 2014 [71] assumed that there is no molecular transport in the vitreous due to fluid flow, due to there existing only a very small pressure difference across the vitreous. Ferreira et al. 2017 [72] presented a similar model to Kotha et al. [71], however they did not describe the eye using such a high degree of anatomical accuracy. Ferreira et al. [72] modelled the PK of molecules in the vitreous and retina of the eye, modelling fluid flow and diffusion of chemical species in the same manner as Kim et al. [70], however, as was assumed by Kotha et al. [71], they did not find drug transport induced by fluid flow to be significant in comparison to flow driven by diffusion. Ferreira et al. [72] found the pressure gradient across the vitreous of the eye to be relatively constant, in comparison to that across the width of the retina, from the ILM to the RPE. In 2018, Lamminsalo et al. [73], in collaboration with Missel, published a PDE model of the eye, utilising and extending the PK model developed by Missel in 2012 [69]. Using the high degree of anatomical fidelity developed by Missel, Lamminsalo et al compared the PK of drug administered via IVT injection and via injection into the anterior of the eye (the aqueous humour). Lamminsalo et al additionally considered the effects due to temperature induced mixing in the anterior of the eye, a mechanism not considered in previously discussed PDE models. The work of Lamminsalo et al. demonstrates how previously developed PDE models, such as the work of Missel, can be collaboratively extended in order to incorporate further dynamics. This process is particularly necessary for models with a high degree of anatomical accuracy, as much time

can be spent designing, implementing, parametrising and verifying such PDE models. In Section 3.2 we present a highly adaptable ocular geometry of the mammalian eye, requiring little parameterisation, utilisation of such a model may aid those who intend to model the PK of molecules over a simplified ocular geometry, reducing the quantity of parallel model development seen in the work discussed above.

1.4 Thesis overview

This remainder of this thesis comprises 5 chapters of new work, each representing a step towards building and parametrising an ocular PK/PD model of an SVB molecule, capable of mechanistically describing retinal concentrations, simulating interactions with VEGF, as well as binding to a vitreal superstructure. Each model is formulated in terms of a system of ODEs, alongside an equivalent system of PDEs, modelling the identical physiological scenario.

We start in Chapter 2 by extending the vitreous, aqueous (2-compartment) PK/PD ODE model of Saunders et al. [3], creating a similar 2-compartment PK/PD model of ranibizumab post IVT injection. We implement a more biochemically accurate binding stoichiometry between drug and VEGF, and reanalyse a clinical dataset presented by Saunders et al. [3]. By doing so we were able to estimate the *in vivo* value of the dissociation constant between ranibizumab and VEGF.

In Chapter 3, we improve upon the 2-compartment PK ODE framework of the vitreous and aqueous, by integrating mechanistic transport between the retina and vitreous, as well as the introduction of an additional clearance pathway via the retina into the choroid, to build a retina, vitreous, aqueous (3-compartment) ocular PK model. In this chapter, through analysis of a 3-compartment rabbit dataset, we present estimates of the permeabilities of retinal membranes as well as estimating the relative significance of the competing clearance pathways within the eye. Accompanying this numerical analysis we also present an analytic solution to the 3-compartment PK model, and characterise the ocular half-life of chemical species. In addition to the 3-compartment PK ODE model we also study the 3-compartment system using a PDE model. Using this PDE model we investigate the applicability of the well-mixed principle used to justify the use of ocular ODE models.

In Chapter 4, we expand further on the 3-compartment PK ODE model of Chapter 3 through the addition of drug to VEGF binding, in the same manner as in of Chapter 2, therefore creating a 3-compartment PK/PD ocular model. In this chapter we focus our

analysis on the dynamics of free retinal VEGF (FRV) - to what degree does ranibizumab manage to suppress the concentration of FRV, how do the dynamics in the retina differ to that of the remainder of the eye, and what is the role of subretinal permeabilities on FRV suppression? Additionally we present an analysis of how the different parameters that characterise binding between ranibizumab and VEGF influence FRV suppression, as well as how dosage can be optimised to improve such suppression. In the remainder of the chapter we present an extension of the anatomical PK PDE model of Chapter 3, through the introduction of a drug to target interactions, thereby creating an analogous PDE model to that of the ODE 3-compartment PK/PD ODE model. Using this PDE model we repeat the analysis performed on the ODE model to identify any potential disparities in what they predict - as well as investigating the impact of homogeneous versus heterogeneous retinal VEGF production on such results.

In Chapter 5, we return again to the 3-compartment PK model of Chapter 3, this time instead of presenting a PD extension we expand on the PK aspects of the model through the introduction of vitreal binding, in doing so formulating a retina-vitreous PK ODE model for an SVB molecule. We first present an approximate analytic solution of the model, which we then proceed to analyse, considering such factors as ocular half-life and durability of drug concentration. In this chapter the main focus is on the interplay between the quantity of vitreal binding sites in the system and the binding affinity of the drug to such binding sites; we demonstrate that these two parameters almost entirely define the post IVT time-course of the drug concentration. We conclude our analysis of the SVB PK ODE model by analysing the impact of repeat dosages on the accumulation of drug in the vitreous, and whether dosing schemes have the potential to be optimised through dose and frequency, or the incorporation of an initial loading dose, in order to maximise ocular exposure. In addition to the ODE model we perform a comparative analysis of an equivalent PDE model, to identify any predictive disparities.

In Chapter 6, we bring together the core elements of Chapters 2-5 and present the aforementioned retina-vitreous, SVB PK/PD model, formulated by the introduction of VEGF into the SVB PK framework of Chapter 5. In addition to the formulation of the SVB PK/PD model, we also present a PK/PD model for a non-static vitreal binding molecule (nSVB), a type of molecule designed to bind to large - but mobile - elements of the eye, in order to increase its ocular retention. We proceed by presenting a comparison between SVB, nSVB and classical anti-VEGF molecules, for the treatment of wet AMD. As in Chapter 5, we consider how affinity to vitreal binding sites, as well as the quantity of such binding

sites, determines the magnitude and duration of FRV suppression. We additionally present a case study based on a recently published study [58] detailing an SVB molecule designed to bind to vitreal hyaluronic acid, as well as an extended analysis of the impact on FRV suppression due to vitreal drug accumulation and if/how dosing protocols may be optimised. As in Chapters 3-6, we conclude with an analysis of an equivalent PDE model, to identify any predictive disparities between the application of ODE and PDE ocular models.

Finally, we note that Chapters 2-4 are largely based on work published during this thesis. Chapter 2 is based on the 2016 publication Hutton-Smith et al. *"A Mechanistic Model of the Intravitreal Pharmacokinetics of Large Molecules and the Pharmacodynamic Suppression of Ocular Vascular Endothelial Growth Factor Levels by Ranibizumab in Patients with Neovascular Age-Related Macular Degeneration"* [74]. Chapter 3 Section 3.1 is based on the 2017 publication Hutton-Smith et al. *"Ocular Pharmacokinetics of Therapeutic Antibodies Given by Intravitreal Injection: Estimation of Retinal Permeabilities Using a 3 Compartment Semi-Mechanistic Model"* [75]. And finally Chapter 4 Section 4.1 is based on the 2018 publication Hutton-Smith et al. *"Theoretical Insights Into the Retinal Dynamics of VEGF in Patients Treated with Ranibizumab, Based on an Ocular Pharmacokinetic/Pharmacodynamic Model"* [76].

2

Estimation of the *in vivo* binding parameters of ranibizumab using a 2-compartment ODE PK/PD model

The work presented within Chapter 2 is based upon the 2016 publication Hutton-Smith et al. *"A Mechanistic Model of the Intravitreal Pharmacokinetics of Large Molecules and the Pharmacodynamic Suppression of Ocular Vascular Endothelial Growth Factor Levels by Ranibizumab in Patients with Neovascular Age-Related Macular Degeneration"* [74].

As outlined in Section 1.2, the progression and severity of the pathogenesis of wet AMD is primarily mediated by VEGF, which promotes the development of highly permeable vasculature in the retina [32]. Ranibizumab, an anti-VEGF recombinant, humanized monoclonal Fab molecule, is administered by intravitreal (IVT) injection and has been shown to be highly effective in the treatment of wet AMD, halting and even reversing its development [12]. Ranibizumab binds to VEGF, a homodimeric molecule, which neutralises it as a pro-angiogenic factor by blocking its interaction with VEGF receptors, found on the surface of the vascular endothelial cells in the retina. The IVT pharmacokinetics (PK) of ranibizumab and other large molecules that bind VEGF have been studied in humans and pre-clinical animal species by direct analysis of drug levels in the aqueous, vitreous humour or indirect modelling of serum drug levels [20, 21, 24, 28, 45, 65, 77–80]. In a given species, the ocular half-life ($t_{1/2}$) is found to increase modestly with the molecular weight of the compound; comparisons of the same molecule across species show that the $t_{1/2}$ values generally

become larger as the size of the eye increases. For ranibizumab, the half-life ($t_{1/2}$) value in humans has been estimated to be 7.9 days (mean value of two studies; Krohne [20] and Xu [21]) compared to 3.3 and 3.1 days in the monkey [65, 78] and rabbit [28, 79], respectively.

In a series of clinical studies, Fauser's group measured free VEGF levels in aqueous humour samples obtained from patients with wet AMD before and after IVT injections with ranibizumab [3, 81, 82]. Recently the data from 31 patients were published and the time-course of free VEGF levels was modelled by Saunders et al. [3]. In this model, which was described in Section 1.3, the K_{D} value for ranibizumab binding to VEGF was assumed to be 46 pM, this estimate based on an *in vitro* binding study [83] at 25 °C. The half-life of ranibizumab was estimated from the model to be 3.5 days, roughly half the experimentally determined half-life for ranibizumab in humans.

In order to quantitatively understand the biophysical determinants of the IVT $t_{1/2}$ of large molecules and the time-course of VEGF suppression after ranibizumab injection, we develop a mechanistic 2-compartment ODE model of the pharmacokinetics of IVT administration and the pharmacodynamics of VEGF suppression by ranibizumab. Our ranibizumab-VEGF-ranibizumab (RVR) complex PD model is based on Saunders et al.' model but uses the known stoichiometry (2:1) for the binding of ranibizumab to the VEGF homodimer and therefore includes a description of the VEGF-ranibizumab (VR) and RVR complexes. In addition, we treat binding as a dynamic process rather than assuming quasi-equilibrium. Lastly, in view of the variability in *in vitro* K_{D} values for VEGF-ranibizumab binding [83, 84] and the absence of an established *in vivo* K_{D} value in the vitreous humour, we treat K_{D} as a parameter in our model and explore the interrelationship between the *in vivo* K_{D} value and the ranibizumab $t_{1/2}$ in a re-analysis of Saunders et al.'s data.

2.1 2-compartment model formulation: building on the work of Saunders et al.

Following Saunders et al. [3] and Missel [69], we assume that the principal pathway for the ocular clearance of large molecules is by a first-order transfer process from the vitreous to the aqueous chambers. From there the molecules are absorbed into the circulation via Schlemm's Canal by the physiological process of aqueous humour turnover. Figure 2.1 indicates the anterior hyaloid membrane of the vitreous (S_*) through which molecules may travel to enter the aqueous humour. We model this process by assuming molecules are transferred from the vitreous into the aqueous at rate k_{el}. In the aqueous humour we assume that the high rate of flow (relative to the vitreous chamber), prevents transport of

molecules from the aqueous to the vitreous. We denote the concentration of a particular molecule present in the vitreous by $c(t)$, and its concentration at $t = 0$ by c_0. If we assume the molecule is inert (for now) and eliminated into the aqueous humour at rate k_{el}, then:

$$c(t) = c_0 \exp(-k_{\text{el}} t), \tag{2.1}$$

and the half-life ($t_{1/2}$) of the molecule is given by

$$t_{1/2} = \frac{\log 2}{k_{\text{el}}}. \tag{2.2}$$

To estimate k_{el} for molecules of various sizes we hypothesise that $t_{1/2}$ is proportional to the expected time for a particle in the centre of the vitreous to diffuse to the edge (T_{diff}):

$$t_{1/2} \propto T_{\text{diff}}, \tag{2.3}$$

where T_{diff} can be estimated using the Brownian motion description of the mean square displacement of a particle in 3 dimensions, so that:

$$T_{\text{diff}} = \frac{r_{\text{vit}}^2}{6D_{\text{vit}}}. \tag{2.4}$$

The diffusion coefficient, D_{vit}, can be calculated using the Stokes-Einstein relation (Equation 2.5), where k_B and T are, respectively, the Boltzmann constant and absolute temperature and η corresponds to the viscosity of an aqueous solution of 0.15 M NaCl at 37 °C.

$$D_{\text{vit}} = \frac{k_B T}{6\pi\eta R_{\text{h}}}. \tag{2.5}$$

The hydrodynamic radius R_{h} is estimated from the molecular weight (M_{W}), Avogadro's number (N_A) and the partial specific volume of protein (v), taken as 0.73 cm^3/g [85], assuming an equivalent sphere:

$$R_{\text{h}} = \left(\frac{3vM_{\text{W}}}{4\pi N_A}\right)^{1/3}. \tag{2.6}$$

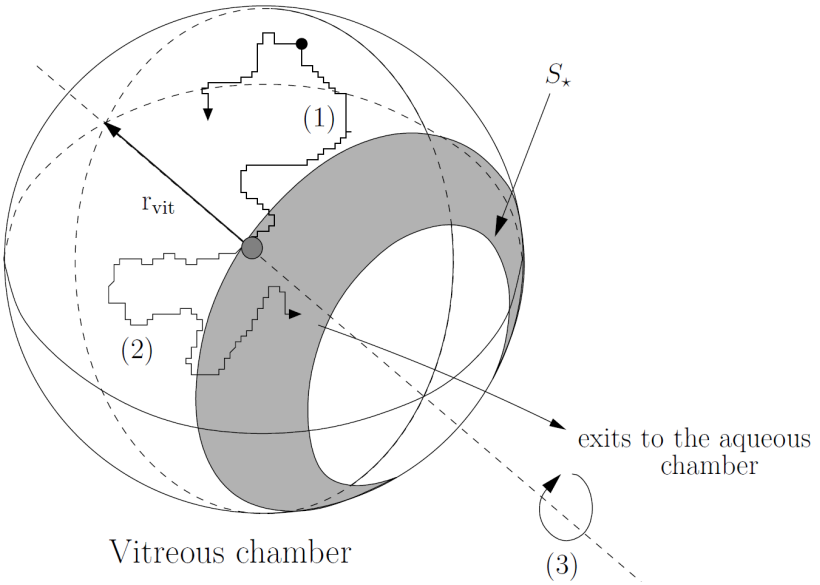

Figure 2.1: Schematic diagram in which the vitreous chamber is viewed as a sphere of radius r_{vit}. S_* is the grey area of the interface through which the vitreous chamber communicates with the aqueous (anterior) chamber. Path (1) shows the random walk of a molecule, originating at the centre, that does not reach the interface. Path (2) shows the random walk of a molecule that reaches S_* and exits to the aqueous chamber. The dashed line passing from the posterior to the anterior of the vitreous chamber (3) is the axis of spherical symmetry.

Molecule	M_{W} (kDa)	R_{h} (nm)	D_{vit} (cm^2 sec^{-1})
Ranibizumab (R), Fab	48.35 [12]	2.4	1.34×10^{-6}
Bevacizumab, IgG	150 [23, 28]	3.51	9.13×10^{-7}
Fab-dimer	100 [28]	3.07	1.05×10^{-6}
VEGF (V)	40 [32]	2.26	1.42×10^{-6}
VR	88.35	2.95	1.09×10^{-6}
RVR	136.7	3.41	9.42×10^{-7}

Table 2.1: Molecular weight (M_{W}), hydrodynamic radius (R_{h}) and diffusion coefficient (D_{vit}) at 37 °C in physiological saline for ranibizumab (R), bevacizumab, a Fab-dimer, VEGF (V), the VEGF-ranibizumab complex (VR) and the ranibizumab-VEGF-ranibizumab complex (RVR).

To investigate the accuracy of our hypothesis (Equation 2.3) we performed a meta-analysis of experimental $t_{1/2}$ data across animal species and molecules, computing the T_{diff} values corresponding to those molecules and species using Equation 2.4. Table A.1 of Appendix A.1 provides a compilation of $t_{1/2}$ data taken from the literature for ranibizumab, Fab fragments, bevacizumab, IgG antibodies and Fab-dimer fragments in the human, monkey, rabbit and rat. Estimates of the vitreous volume (V_{vit}) and radius of the equivalent

vitreous sphere (r_{vit}) are provided for each species, along with the calculated T_{diff} values. In Figure 2.2 we plot the individual $t_{1/2}$ data versus the estimated values of T_{diff}, and observe proportionality as hypothesised by Equation 2.3. Linear regression through the origin gives a slope of 4.3 (95% confidence interval 4.0-4.6).

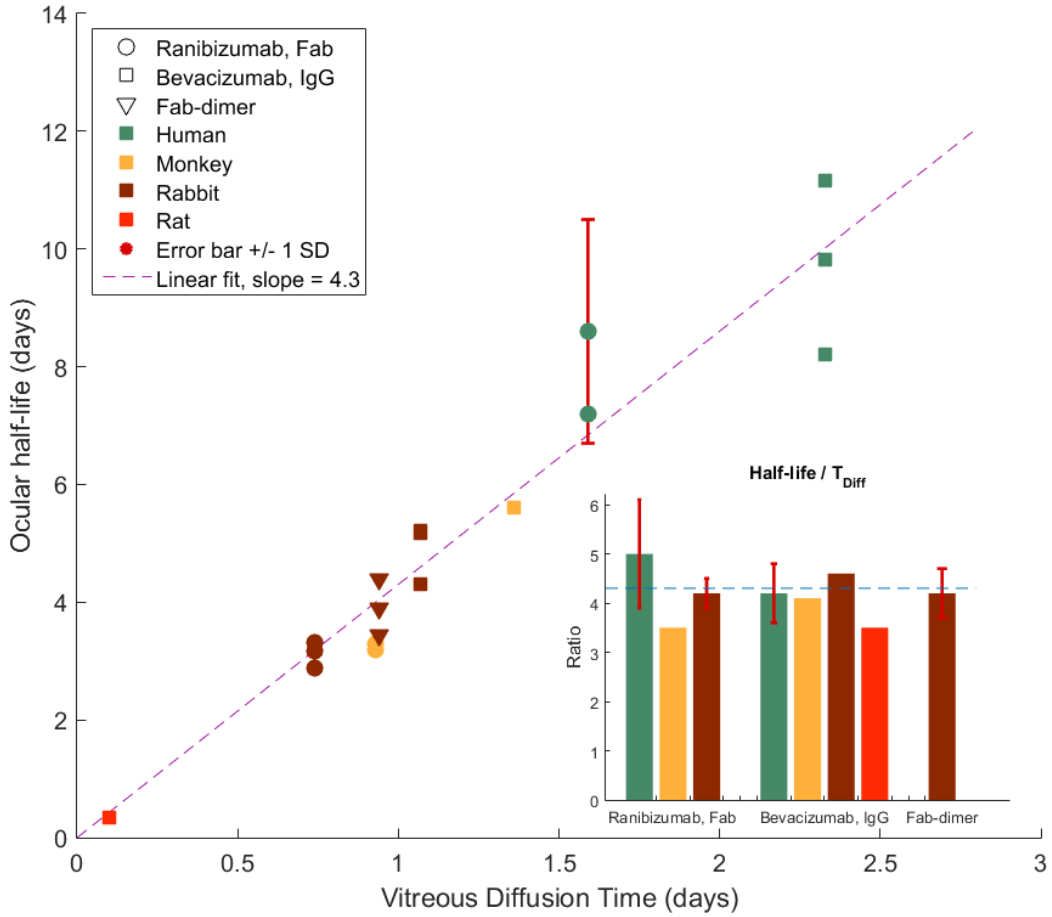

Figure 2.2: Ocular half-life data from individual studies plotted against vitreous diffusion times for various molecules and animal species, using data from Table A.1 of Appendix A.1. Linear regression through the origin yields a line with slope 4.3 (95% confidence interval 4.0-4.6), in close agreement with the relationship predicted by Equation 2.3. The insert depicts the mean ratios $t_{1/2}/T_{\text{diff}}$; the dashed horizontal line equals 4.3.

This meta-analysis provides strong evidence that the experimentally determined ocular half-life of ranibizumab in humans of approximately 7.9 days (mean of two independent studies) is consistent with the relationship predicted by Equation 2.3. Therefore if we assume Equation 2.3 is true, then:

$$t_{1/2} \propto T_{\text{diff}} \propto M_{\text{W}}^{1/3} \tag{2.7}$$

$$\Rightarrow \quad k_{\text{el}} \propto M_{\text{W}}^{-1/3}. \tag{2.8}$$

Hence we may then derive the following scaling relationship for the elimination rates of molecular species i and j:

$$k_{\mathrm{el}}^{(i)} = \left(\frac{M_{\mathrm{W}}^{(j)}}{M_{\mathrm{W}}^{(i)}} \right)^{1/3} k_{\mathrm{el}}^{(j)}. \tag{2.9}$$

Given a value for the vitreal $t_{1/2}$ of ranibizumab, we use Equations 2.2 and 2.9 to estimate the elimination rates for V, VR and RVR.

Pharmacodynamic model of VEGF suppression by ranibizumab - the RVR model

Following Saunders et al. [3], our mathematical model of VEGF suppression is based on the two-compartment representation shown in Figure 2.3. We consider only the vitreous and aqueous chambers of the eye, as the former is the site of ranibizumab injection and the latter is where experimental VEGF samples were collected. VEGF (V), is a homodimer that has two identical binding sites for ranibizumab. Therefore according to the notation in Table 2.2 we define the following sequential reaction scheme,

$$\mathrm{V} + \mathrm{R} \underset{2k_{\mathrm{on}}}{\overset{k_{\mathrm{off}}}{\rightleftharpoons}} \mathrm{VR}, \tag{2.10}$$

$$\mathrm{R} + \mathrm{VR} \underset{k_{\mathrm{on}}}{\overset{2k_{\mathrm{off}}}{\rightleftharpoons}} \mathrm{RVR}. \tag{2.11}$$

Notice that in the first reaction there are two equivalent sites of association, while in the second there are two equivalent sites of dissociation. As a consequence the equilibrium dissociation constant for the first reaction is $K_{\mathrm{D}}/2$ and for the second it is $2K_{\mathrm{D}}$, where $K_{\mathrm{D}} = k_{\mathrm{off}}/k_{\mathrm{on}}$ is the hypothetical value for a single VEGF-ranibizumab binding site. The concentrations of V, R, VR and RVR are given as v, r, c and h, respectively, with subscripts to denote location where appropriate, as defined in Table 2.2.

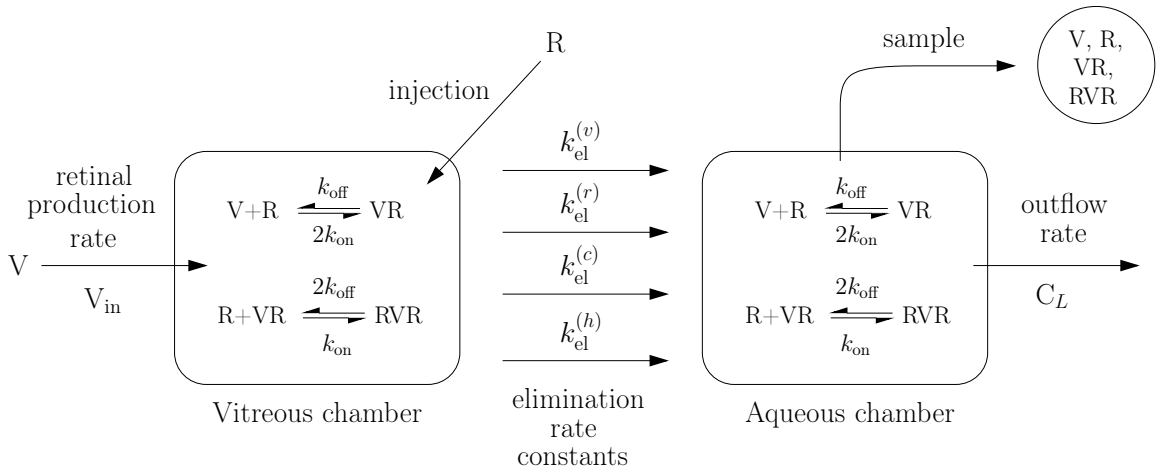

Figure 2.3: Schematic diagram of the two-compartment pharmacodynamic model of VEGF (V) and ranibizumab (R) interactions in the eye which we assume comprises the vitreous and aqueous chambers only. The arrow labelled 'sample' indicates that experimental samples were collected from the aqueous humour.

Chemical species	Chemical notation	Concentration (pM)	
VEGF	V	Vitreous	v_{vit}
		Aqueous	v_{aq}
Ranibizumab	R	Vitreous	r_{vit}
		Aqueous	r_{aq}
VEGF ranibizumab complex	VR	Vitreous	c_{vit}
		Aqueous	c_{aq}
VEGF ranibizumab dimer complex	RVR	Vitreous	h_{vit}
		Aqueous	h_{aq}

Table 2.2: Summary of dependent variables that appear in the 2-compartment model. Concentrations are functions of time (t) with units of pM. Subscripts denote the concentrations of each variable in the vitreous and aqueous chambers.

In patients with wet AMD, VEGF is produced in the retina and then diffuses into the vitreous chamber. Accordingly in our model we combine these effects and assume that V is supplied to the vitreous at a constant rate V_{in} (see the leftmost arrow in Figure 2.3). Ranibizumab is delivered to patients via intravitreal injection; we model this effect by a suitable choice of the initial concentration for $r_{\text{vit}}(t)$. In contrast to the model of Saunders et al., we assume that association and dissociation kinetics occur in both the vitreous and aqueous chambers. As discussed in the previous section (IVT PK model), we suppose that the major pathway of ocular elimination for the four species is via the unidirectional transfer from the vitreous to the aqueous chambers. We represent these processes by the elimination rate constants $k_{\text{el}}^{(v)}$, $k_{\text{el}}^{(r)}$, $k_{\text{el}}^{(c)}$ and $k_{\text{el}}^{(h)}$, which depend on the molecular weight (M_{W}) of each

species (see Table 2.1). Here we neglect both transport from the aqueous to the vitreous chambers and possible elimination of these molecules via the retina. Assuming the system to be well-mixed, the model is described by a coupled system of nonlinear ODEs, in which chemical reactions are described using the law of mass action. In this way we arrive at the following equations for the time-evolution of the dependent variables:

Vitreous

$$\frac{\mathrm{d}v_{\mathrm{vit}}}{\mathrm{d}t} = (k_{\mathrm{off}}c_{\mathrm{vit}} - 2k_{\mathrm{on}}v_{\mathrm{vit}}r_{\mathrm{vit}}) - k_{\mathrm{el}}^{(v)}v_{\mathrm{vit}} + \frac{V_{\mathrm{in}}}{V_{\mathrm{vit}}}, \tag{2.12}$$

$$\frac{\mathrm{d}r_{\mathrm{vit}}}{\mathrm{d}t} = (k_{\mathrm{off}}c_{\mathrm{vit}} - 2k_{\mathrm{on}}v_{\mathrm{vit}}r_{\mathrm{vit}}) + (2k_{\mathrm{off}}h_{\mathrm{vit}} - k_{\mathrm{on}}r_{\mathrm{vit}}c_{\mathrm{vit}}) - k_{\mathrm{el}}^{(r)}r_{\mathrm{vit}}, \tag{2.13}$$

$$\frac{\mathrm{d}c_{\mathrm{vit}}}{\mathrm{d}t} = -(k_{\mathrm{off}}c_{\mathrm{vit}} - 2k_{\mathrm{on}}v_{\mathrm{vit}}r_{\mathrm{vit}}) + (2k_{\mathrm{off}}h_{\mathrm{vit}} - k_{\mathrm{on}}r_{\mathrm{vit}}c_{\mathrm{vit}}) - k_{\mathrm{el}}^{(c)}c_{\mathrm{vit}}, \tag{2.14}$$

$$\frac{\mathrm{d}h_{\mathrm{vit}}}{\mathrm{d}t} = -(2k_{\mathrm{off}}h_{\mathrm{vit}} - k_{\mathrm{on}}r_{\mathrm{vit}}c_{\mathrm{vit}}) - k_{\mathrm{el}}^{(h)}h_{\mathrm{vit}}, \tag{2.15}$$

Aqueous

$$\frac{\mathrm{d}v_{\mathrm{aq}}}{\mathrm{d}t} = (k_{\mathrm{off}}c_{\mathrm{aq}} - 2k_{\mathrm{on}}v_{\mathrm{aq}}r_{\mathrm{aq}}) + \frac{V_{\mathrm{vit}}}{V_{\mathrm{aq}}}k_{\mathrm{el}}^{(v)}v_{\mathrm{vit}} - \frac{C_{\mathrm{L}}}{V_{\mathrm{aq}}}v_{\mathrm{aq}}, \tag{2.16}$$

$$\frac{\mathrm{d}r_{\mathrm{aq}}}{\mathrm{d}t} = (k_{\mathrm{off}}c_{\mathrm{aq}} - 2k_{\mathrm{on}}v_{\mathrm{aq}}r_{\mathrm{aq}}) + (2k_{\mathrm{off}}h_{\mathrm{aq}} - k_{\mathrm{on}}r_{\mathrm{aq}}c_{\mathrm{aq}}) + \frac{V_{\mathrm{vit}}}{V_{\mathrm{aq}}}k_{\mathrm{el}}^{(r)}r_{\mathrm{vit}} - \frac{C_{\mathrm{L}}}{V_{\mathrm{aq}}}r_{\mathrm{aq}}, \tag{2.17}$$

$$\frac{\mathrm{d}c_{\mathrm{aq}}}{\mathrm{d}t} = -(k_{\mathrm{off}}c_{\mathrm{aq}} - 2k_{\mathrm{on}}v_{\mathrm{aq}}r_{\mathrm{aq}}) + (2k_{\mathrm{off}}h_{\mathrm{aq}} - k_{\mathrm{on}}r_{\mathrm{aq}}c_{\mathrm{aq}}) + \frac{V_{\mathrm{vit}}}{V_{\mathrm{aq}}}k_{\mathrm{el}}^{(c)}c_{\mathrm{vit}} - \frac{C_{\mathrm{L}}}{V_{\mathrm{aq}}}c_{\mathrm{aq}}, \tag{2.18}$$

$$\frac{\mathrm{d}h_{\mathrm{aq}}}{\mathrm{d}t} = -(2k_{\mathrm{off}}h_{\mathrm{aq}} - k_{\mathrm{on}}r_{\mathrm{aq}}c_{\mathrm{aq}}) + \frac{V_{\mathrm{vit}}}{V_{\mathrm{aq}}}k_{\mathrm{el}}^{(h)}h_{\mathrm{vit}} - \frac{C_{\mathrm{L}}}{V_{\mathrm{aq}}}h_{\mathrm{aq}}, \tag{2.19}$$

where V_{vit} and V_{aq} denote the volumes of the vitreous and aqueous chambers (mL), respectively, and C_{L} represents the clearance rate from the aqueous chamber (mL/day), taken to be equal to the production rate of aqueous humour. We assume that initially (at $t = 0$) VEGF levels are at the drug-free equilibrium levels predicted by this model and all complexes are absent. In order to simulate a single intravitreal dose the initial vitreous concentration (pM) for ranibizumab is set equal to $r_0 = d_0/(M_{\mathrm{W}}^{(\mathrm{r})}V_{\mathrm{vit}}) \times 10^9$ where d_0 is the ranibizumab dosage (0.5 mg) injected into the vitreous chamber. The initial ranibizumab concentration in the aqueous chamber is set to zero.

Clinical data

We utilized recently published data by Saunders et al. [3], wherein 31 patients with wet AMD were studied following the administration of intravitreal doses of 0.5 mg ranibizumab after various time periods post-injection. Patients were submitted to aqueous humour sampling prior to the time of dosing and at time points over a period of several months. Free

VEGF concentrations were measured from the aqueous samples using Luminex multiplex bead analysis (Luminex, Austin, Texas, USA).

Methods of Parameter Estimation and Optimization

The parameters used in the model, and their values, are stated in Table 2.3. We derived patient specific estimates of $t_{1/2}$ and V_{in} as functions of K_{D} by fitting the patient-specific data over a range of K_{D} values (50 to 60,000 pM); an optimization procedure was used to estimate $t_{1/2}$ and V_{in} for each value of K_{D}. This was achieved using `fmincon` [86] (part of MATLAB's global optimization toolbox) which, for a given function, seeks a local minimum in parameter space by following a local negative gradient. For our purposes we sought to minimize the root mean square error (RMSE) of the solution (solved using MATLAB's stiff ODE solver ode23s) with respect to individual patient data. In order to locate the global minimum, multiple initial estimates of $t_{1/2}$ were taken between 2 and 15 days. An accurate initial estimate for V_{in} was obtained by averaging the VEGF levels at the initial and final time points.

Parameter	Value	Units	Description
k_{off}	0.864 [84]	day^{-1}	Reaction rate of VR $\rightarrow$ V + R
k_{on}	$k_{\text{off}}/K_{\text{D}}$	$\text{day}^{-1}\text{pM}^{-1}$	Reaction rate of R + VR $\rightarrow$ RVR
K_{D}	input	pM	Dissociation constant
C_{L}	3.6 [87]	mL day^{-1}	Aqueous humour clearance rate
V_{in}	estimated	fmol day^{-1}	VEGF production rate
V_{vit}	4.85 [69]	mL	Volume of the vitreous
V_{aq}	0.16 [88, 89]	mL	Volume of the aqueous
d_0	0.5 [81]	mg	Initial dose of ranibizumab
$t_{1/2}$	estimated	days	Ranibizumab vitreal half-life
$k_{\text{el}}^{(v)}$	derived	day^{-1}	Vitreal elimination rate constant for V
$k_{\text{el}}^{(r)}$	derived	day^{-1}	Vitreal elimination rate constant for R
$k_{\text{el}}^{(c)}$	derived	day^{-1}	Vitreal elimination rate constant for VR
$k_{\text{el}}^{(h)}$	derived	day^{-1}	Vitreal elimination rate constant for RVR

Table 2.3: Parameters with stated numerical values were held fixed for all patients. k_{on} is expressed in terms of the dissociation constant $K_{\text{D}} = k_{\text{off}}/k_{\text{on}}$. The value of K_{D} was treated as an input to the model and varied over the range 50 to 60,000 pM. The values of V_{in} and $t_{1/2}$ were estimated for each patient as a function of the input value of K_{D}. Estimates of the rate constants $k_{\text{el}}^{(r)}$, $k_{\text{el}}^{(v)}$, $k_{\text{el}}^{(c)}$ and $k_{\text{el}}^{(h)}$ were derived from $t_{1/2}$ using Equations 2.2 and 2.9.

2.2 Re-analysis of Fauser et al. dataset: an *in vivo* estimate for K_{D}

Figure 2.4 shows the optimized fits of the 2-compartment PK/PD model (Equations 2.12-2.19) to the data for a typical patient (#40) for different input values of K_{D}. As K_{D} increases from 50 to 60,000 pM, the fitted curves change shape and the estimated values of $t_{1/2}$ increase from 3.3 days to 9.8 days. The corresponding RMSE values change only slightly as K_{D} varies (see caption of Figure 2.4).

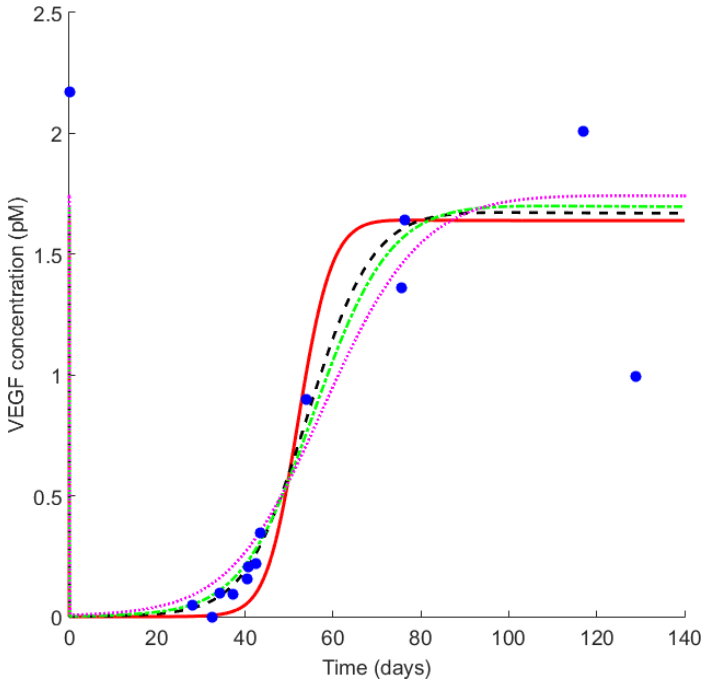

Figure 2.4: Series of optimized fits of the 2-compartment PK/PD model (Equations 2.12-2.19) to the data of patient #40 (blue dots) as K_{D} varies. Key: $K_{\mathrm{D}} = 50$ pM (red solid line, $t_{1/2} = 3.3$ days, RMSE = 0.27 pM), $K_{\mathrm{D}} = 10{,}000$ pM (black dashed line, $t_{1/2} = 6.4$ days, RMSE = 0.25 pM), $K_{\mathrm{D}} = 21{,}000$ pM (green dot/dash line, $t_{1/2} = 7.6$ days, RMSE = 0.25 pM), $K_{\mathrm{D}} = 60{,}000$ pM (purple dotted line, $t_{1/2} = 9.8$ days, RMSE = 0.26 pM).

Varying K_{D} over the same range for all 31 subjects, we show in Figure 2.5 how the mean $\pm$SD of the estimated values of $t_{1/2}$ depends on K_{D} (blue curve and shaded grey region). The relationship between K_{D} and $t_{1/2}$ seen for patient #40 is observed for all patients. We conclude that the VEGF data alone are insufficient to uniquely determine the *in vivo* value of K_{D} and the corresponding distribution of $t_{1/2}$ values. In order to estimate the *in vivo* value of K_{D} in Figure 2.5 we overlay the experimentally determined values of the mean $\pm$SD of $t_{1/2}$ (as indicated by the red line, with SD bounds indicated by dashed lines). From the region of intersection of the experimental range of $t_{1/2}$ with the shaded area, we estimate

the *in vivo* value of K_{D} to lie in the range 18,084-27,361 pM, with an average value of 21,326 pM (21.3 nM).

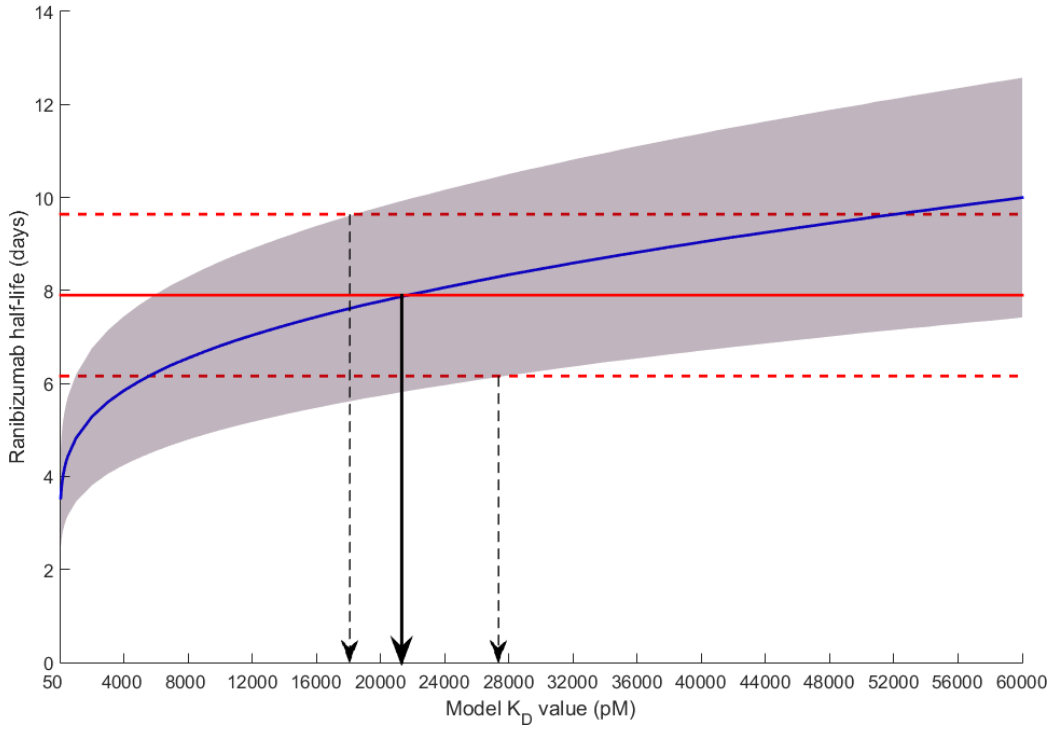

Figure 2.5: Mean (±SD) of model estimated $t_{1/2}$ values (blue curve ±SD in grey area) with respect to a K_{D} range of [50, 60000] pM. The solid red line shows the mean experimental ranibizumab $t_{1/2}$ of 7.9 days in humans, the dashed red lines indicate ± SD (1.74 days). From the points of intersection of the solid and dashed red lines with the blue curve and grey area, we have estimated the *in vivo* value (range) of K_{D} as indicated by the vertical arrows pointing to the x-axis.

2.3 Impact of binding stoichiometry, rate constants, dose and M_{W} on free VEGF profiles

Here we investigate the effect of using the observed 2:1 stoichiometry of ranibizumab binding to VEGF and explore the influence of varying the parameter k_{off} on the VEGF profile. Figure 2.6 (a) shows the VEGF data from patient 40 with two model curves. The solid red line depicts the RVR model fit to the data for a K_{D} value of 21,000 pM, whereas the black dashed line shows the resulting curve if binding is restricted to only the VR binding model and optimized to fit the data. The RVR binding model provides a more accurate representation of the data with a $t_{1/2}$ value of 7.6 days in contrast to the VR binding model with a $t_{1/2}$ value of 9.3 days.

Figure 2.6 (b) shows the effect on the VEGF profile of varying the dissociation rate constant k_{off} from its default value of 0.864 day^{-1} (red curve) while holding K_{D} fixed at 21,000 pM. A 100-fold increase in k_{off} (black dashed curve) shifts the VEGF profile to the left of the red curve, while its shape is maintained. The left-shift results from a rapid redistribution of previously bound R from the VR and RVR species, due to the rapid dilution of all species in the aqueous humour. With a 100-fold decrease in k_{off} (green curve) the VEGF profile shifts further to the left and its shape changes. The altered shape at low k_{off} values results from the slow rates of association and dissociation between the R, V, VR and RVR species which are too slow to achieve the previously attained quasi-equilibrium states in the vitreous humour. Based on these simulations we conclude that for the default value of k_{off} the VEGF profile in the vitreous humour is close to the quasi-equilibrium state while the profile in the aqueous humour reflects a simple dilution of the vitreous profile, as the residence time in the aqueous humour (ca. 0.04 days; ∼1 hour) is too short for redistribution of the bound R. This is consistent with the assumption of chemical equilibrium made by Saunders et al. [3] and shows the subtle influence of k_{off} on the behaviour of the PK/PD model.

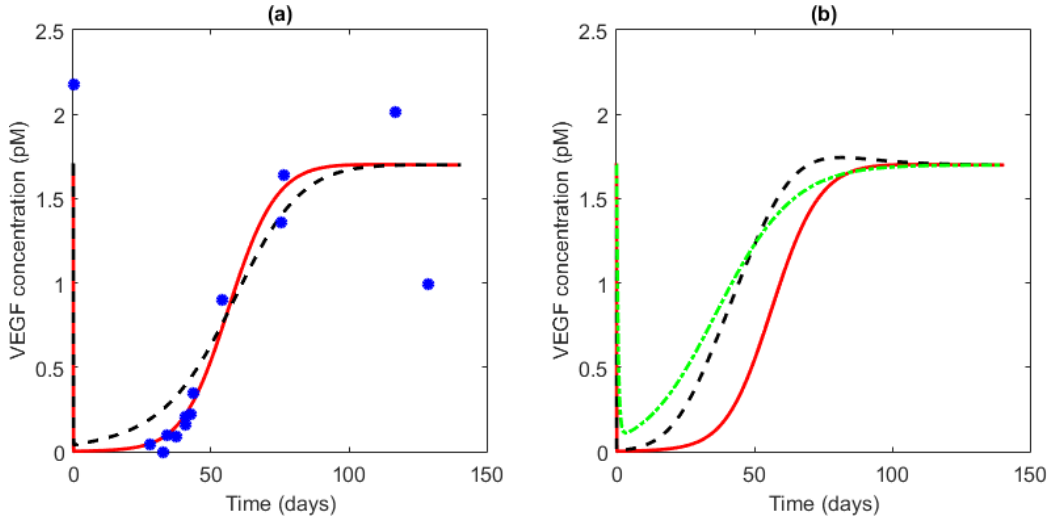

Figure 2.6: Aqueous compartment VEGF concentration profiles, generated from Equations 2.12-2.19. (a) Effect of binding, RVR binding (solid red), VR binding (dashed black), patient #40 data (blue dots); (b) effect of dissociation rate constant, k_{off} = 0.864 day^{-1} (solid red, as in panel a.), 86.4 day^{-1} (dashed black), 0.00864 day^{-1} (dot/dash green).

Using the estimated *in vivo* K_{D} value of 21,000 pM, we demonstrate in Figure 2.7 (a) the effect of increasing the dose of ranibizumab from 0.5 mg (red curve) to 1 mg (dashed black curve) and 2 mg (green dot/dash curve) on the VEGF profiles of patient #40. For each doubling of the dose the profiles shift to the right by approximately 7.6 days (the

ranibizumab $t_{1/2}$ derived for this patient). Figure 2.7 (b) demonstrates the simulated effect in patient #40 of decreasing K_D by factors of 10 and 100 (from the *in vivo* value of 21,000 pM) while keeping a fixed value of $t_{1/2}$ (7.6 days). For each factor of 10 reduction in K_D the VEGF profile shifts to the right by about 26 days.

In Figure 2.7 (c) we simulate the effect of increasing the MW of the VEGF binder from 48.35 kDa (ranibizumab) to 100 kDa, 200 kDa and 500 kDa with a concomitant adjustment of the dose in proportion to MW. By reducing the elimination rate constants for R, VR and RVR in accordance with the $M_W^{-1/3}$ scaling law (Equation 2.9), the curves shift to the right and rise more slowly. In Figure 2.7 (d), the effect of increasing MW at a constant dose of 0.5 mg is shown. At M_W's of 200 and 500 kDa, the curves shift to the left at earlier times and intersect at later times.

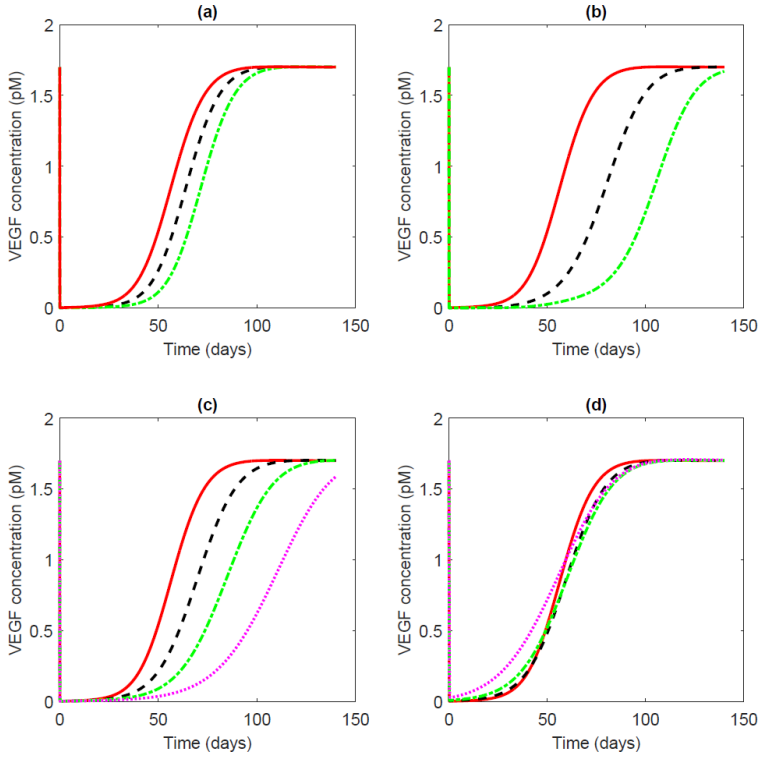

Figure 2.7: Aqueous compartment VEGF profiles, from model Equations 2.12-2.19. (a) Simulated effect of increasing dose 0.5 mg (solid red), 1 mg (dashed black), 2 mg (dot/dash green); (b) simulated effect of lowering K_D with a constant half-life (7.6 days), 21000 pM (solid red), 2100 pM (dashed black), 210 pM (dot/dash green); (c) simulated effect of increasing M_W while adjusting the dose in proportion to M_W: 48.35 kDa (solid red, dose 0.5 mg), 100 kDa (dashed black, 1 mg), 200 kDa (dot/dash green, 2 mg), 500 kDa (dotted purple, 4.5 mg); (d) simulated effect of increasing M_W while keeping dosage constant at 0.5 mg: 48.35 kDa (solid red, 2.3×10^6 pM), 100 kDa (dashed black, 1.1×10^6 pM), 200 kDa (dot/dash green, 5.6×10^5 pM), 500 kDa (dotted purple, 2.2×10^5 pM).

2.4 2-compartment PK/PD ODE model summary

This model provides new mechanistic insights into the intravitreal PK of large molecules like ranibizumab and a reinterpretation of its pharmacodynamic effect on ocular VEGF levels in patients with wet AMD. Through a meta-analysis we have demonstrated that $t_{1/2}$ values for large molecules can be assumed to be proportional to their vitreous diffusion times (T_{diff}), allowing us to create a theoretical basis for estimating $t_{1/2}$ values for molecules with unknown dynamics, based on their M_{W}. This allows us to exploit PK data for well studied molecules, such as ranibizumab, and estimate key PK parameters for unstudied molecule/complexes, such as ranibizumab bound to VEGF.

It is important to note that the experimental $t_{1/2}$ values reported for ranibizumab in humans (7.2 and 8.6 days) are consistent with our theory and data from pre-clinical studies involving small animal species (see Figure 2.2). These values (7.2 and 8.6 days) were derived from two independent clinical studies that used different methodologies, e.g., aqueous humour sampling in a composite data set from patients with different retinal diseases by Krohne et al. [20] and a PK analysis of serum samples by Xu et al. [21]. Our use of the mean value (7.9 days) and the variation around it, estimated from the Xu et al.'s study, is central to the subsequent analysis of the Saunders et al.'s VEGF data.

Using the RVR model of ranibizumab-VEGF binding we provide an alternative analysis of Saunders et al.'s VEGF data in which the interplay between the assumed value of K_{D} and the estimated values of $\text{t}_{1/2}$ has been systematically explored over a wide range of K_{D} values (Figure 2.5). Due to the small variation observed in the quality of fit, we conclude that the VEGF data alone are not sufficient to identify a unique value of K_{D} and the distribution of $t_{1/2}$ values. We have resolved this ambiguity by using the experimentally observed half-life for ranibizumab (7.9 days) to estimate the *in vivo* K_{D} value, which we find to be 21,326 pM (21.3 nM).

The large disparity between our *in vivo* estimate of K_{D} and the *in vitro* value used by Saunders et al. of 46 pM (measured at 25 °C with the Biacore assay) could have a number of possible explanations. First, the Biacore assay is strongly platform dependent and may not reflect the true interaction of ranibizumab and VEGF in solution [84]. In this regard studies of the binding of VEGF to the extracellular domain of the VEGF receptor using Isothermal Titration Calorimetry, a solution-based thermodynamic method, gave K_{D} values of 12-38 nM at 20 °C [90]. Second, at body temperature (37 °C) K_{D} should be larger

than at 25 °C, as the enthalpy of VEGF binding to polypeptides and large molecules is negative [90, 91]. Third, the *in vivo* K_{D} could be influenced by other factors in the eye, e.g., soluble VEGF receptors that could compete with ranibizumab for VEGF molecules [92]. Future experiments on the interaction of ranibizumab and VEGF are needed to resolve this disparity.

We believe it is important to have accurate estimates of $t_{1/2}$ and K_{D} in order to accurately predict the dependence of the VEGF profiles on dose, K_{D} and M_{W}. As illustrated in Figure 2.7 the ability to simulate the effects of these parameters on the VEGF profiles may aid the development of future therapies which prolong the period of VEGF suppression.

In Chapter 3 we extend the base PK structure of the model presented in this chapter to include a mechanistic description of the retina. In Chapter 4 we will further extend this retina, vitreous, aqueous model by reintroduce drug to VEGF binding, presenting a retinal extension to the PK/PD model presented here.

3

Mechanistic retinal ODE/PDE PK modelling

3.1 Mechanistic retinal ODE modelling and estimation of retinal permeabilities

The work presented within Section 3.1 is based on the 2017 publication Hutton-Smith et al. *"Ocular Pharmacokinetics of Therapeutic Antibodies Given by Intravitreal Injection: Estimation of Retinal Permeabilities Using a 3 Compartment Semi-Mechanistic Model"* [75].

Therapeutic antibodies and antibody fragments, administered via intravitreal (IVT) injection, have proved to be efficacious in the treatment of retinal diseases, such as wet AMD. It is assumed that such molecules should be able to penetrate the retina in order to achieve maximum efficacy [93]. The elimination of drugs given by IVT injection primarily occurs by diffusion from the vitreous chamber into the aqueous humour, as we described using a 2-compartment ODE model in Chapter 2. Transport also occurs between the vitreous and retina, and between the retina and choroid, which provides a second ocular elimination pathway [41, 94]. Given the retina is the intended target for such therapeutic molecules, modelling this pathway is a natural PK extension of the 2-compartment model of the previous chapter. The inner limiting membrane (ILM) of the retina separates it from the vitreous, and acts as a biological barrier, impeding macromolecular drug diffusion into the retina. Due to this barrier, and the vitreous-aqueous elimination pathway, much of a drug delivered via IVT injection does not reach the retina. Certain retinal diseases, such as

wet AMD, may require subretinal drug permeation, through the retinal pigment epithelium (RPE) and into the choroid. The RPE itself acts as a tight biological barrier, in a similar manner to the ILM, and is also a major component of the blood-retinal barrier (BRB) [95]. We seek to mechanistically describe and quantify the impact of these phenomena on drug availability within the retina.

In order to improve the properties of IVT-injected drugs, it is crucial to quantitatively understand the pathways and barriers described above. Understanding the influence of molecular size on these processes is also essential in antibody drug design, as well as for potential gene therapies that utilize large adeno-associated virus (AAV) particles for drug encapsulation [96]. In this chapter we extend the 2-compartment model (vitreous chamber and aqueous humour) detailed in Chapter 2, by adding a retinal compartment and incorporating the intraocular transport pathways between vitreous, retina and choroid, and the associated ILM and RPE barriers described above. In Sections 3.1 and 3.2 of this Chapter we present this three compartment model (retina, vitreous, aqueous) in terms of a system of ODEs and PDEs, respectively.

We calibrate our 3-compartment model using the experimental data obtained by Gadkar et. al. [28] in the rabbit with IgG, IgG null, Fc and Fab fragments. These datasets exhibit a common ocular $t_{1/2}$ in the retina, vitreous and aqueous compartments whose value we consider in terms the hydrodynamic radius of the molecule, R_{h}, instead of M_{W} as in Chapter 2. Our model provides a mechanistic basis for this finding and further enables us to derive estimates of the permeability coefficients of the ILM and RPE and their apparent dependence on R_{h}. We compare these estimates to experimental values from the literature [97].

We exploit analytical solutions to the ODE system to determine/derive key pharmacological metrics, such as $t_{1/2}$, in terms of physiological parameters, and comment on how they differ from the standard 2-compartment model of Chapter 2. Lastly we use the model to estimate the ratio of ocular elimination from the aqueous humour to ocular elimination from the retina/choroid as a function of molecular size. A 2017 review of the pharmacokinetic aspects of retinal drug delivery, del Amo et al. [98], describes the various biological barriers within the retina and the difficulty of achieving clinically efficacious drug concentrations there. It further emphasizes the utility of PK models to address this issue and suggests that future models should include descriptions of the retinal tissue itself, as well as the surrounding membranes. We believe that the present 3-compartment, semi-mechanistic

model, incorporating the permeabilities of the ILM and RPE, is an important step towards this goal.

3.1.1 3-compartment model formulation: semi-mechanistic ocular modelling

We utilize data from a recent study by Gadkar et. al. [28], detailing the concentration-time profiles in the retina, vitreous and aqueous, for a number of antibodies and antibody fragments, following IVT injection. Their study was performed in rabbits using molecules derived from a human anti-glycoprotein D (anti-gD) antibody, which is inert in a rabbit model, forgoing the need to account for pharmacodynamic (PD) effects. The particular datasets analysed in this section are for Fab, Fc, IgG and IgG null molecules (noting that IgG null molecules are IgG molecules with fragment crystallizable (Fc) region mutations that prevent binding to neonatal Fc receptor (FcRn)), whose respective parameter values can be found in Table 3.1. Retinal, vitreous and aqueous antibody concentrations were measured at 0.25, 2, 8, 14, 21 and 28 days, excluding the Fc dataset wherein only vitreous and aqueous data were available. The Fab dataset contains retinal data not reported as part of the original study [28], but provided to us by Gadkar et. al. and Genentech.

Antibody	Molecular weight (kDa)	Hydrodynamic radius (nm)	Initial dose (mg)*
Fab	50	2.5	0.615
Fc	50	2.5	0.5
IgG	150	4.9	0.549
IgG null	150	4.9	0.75

Table 3.1: Summary of biophysical properties of antibody and antibody fragments. Weights and doses taken from Gadkar et. al. [28], hydrodynamic radii (R_{h}) taken from Shatz 2016 et. al. [99], specifically the values reported for G10rabFab and G10rabIgG molecules. *Doses correspond to experimental protocol except for IgG null which was estimated from initial vitreous concentrations, assuming a vitreal volume of 1.52 mL (see Table 3.2).

The 3-compartment model, described graphically in Figure 3.1, is comprised of the retina, vitreous and aqueous chambers, with respective antibody concentrations $c_{\mathrm{ret}}(t), c_{\mathrm{vit}}(t)$ and $c_{\mathrm{aq}}(t)$, in pM. An IVT injection is administered at $t = 0$, resulting in an initial vitreal concentration of c_0 pM. The drug is free to move from the vitreous into the aqueous and retina, as well as back from the retina into the vitreous. The drug is cleared from the aqueous humour compartment at a rate corresponding to the aqueous humour production rate (mL/day), and is eliminated from the retina, via the RPE, into the choroid (assumed to be a sink). After elimination from the aqueous compartment or choroid, the drug enters

the systemic circulation where it is eventually cleared from the body; recirculation to the eye is assumed to be negligible. All transport pathways are taken to be first order, and are indicated in Figure 3.1 by arrows with their respective transport rates, given in terms of the parameters in Table 3.2. As we formulated this model in terms of concentrations, all mechanistic transport rates include volume factors to account for compartment size (as shown in Figure 3.1). Note how the transfer rate between the retina and vitreous depends on direction. The original study [28] introduced a phenomenological delay compartment separating the vitreous and aqueous compartments, via first order transport processes. For simplicity we omit this delay in the analysis presented here as it only affects the initial aqueous compartment data points and does not influence significantly aspects of model behaviour in which we are interested (see Appendix A.3 for analysis that includes the delay compartment and justification of this statement). The model is then formulated as a system of linear ODEs, given by Equations 3.1-3.3, with initial conditions $c_{\text{vit}}(0) = c_0$ and $c_{\text{ret}}(0) = c_{\text{aq}}(0) = 0$:

$$\frac{\mathrm{d}c_{\text{ret}}}{\mathrm{d}t} = -\left(\frac{S_{\text{ret}}}{V_{\text{ret}}}\right)\left[p_{\text{ILM}} + p_{\text{RPE}}\right] c_{\text{ret}} + \left(\frac{S_{\text{ret}}}{V_{\text{ret}}}\right) p_{\text{ILM}} c_{\text{ret}}, \tag{3.1}$$

$$\frac{\mathrm{d}c_{\text{vit}}}{\mathrm{d}t} = \left(\frac{S_{\text{ret}}}{V_{\text{vit}}}\right) p_{\text{ILM}} c_{\text{ret}} - \left[\left(\frac{S_{\text{ret}}}{V_{\text{vit}}}\right) p_{\text{ILM}} + k_{\text{el}}\right] c_{\text{vit}}, \tag{3.2}$$

$$\frac{\mathrm{d}c_{\text{aq}}}{\mathrm{d}t} = \left(\frac{V_{\text{vit}}}{V_{\text{aq}}}\right) k_{\text{el}} c_{\text{vit}} - \left(\frac{C_{\text{L}}}{V_{\text{aq}}}\right) c_{\text{aq}}. \tag{3.3}$$

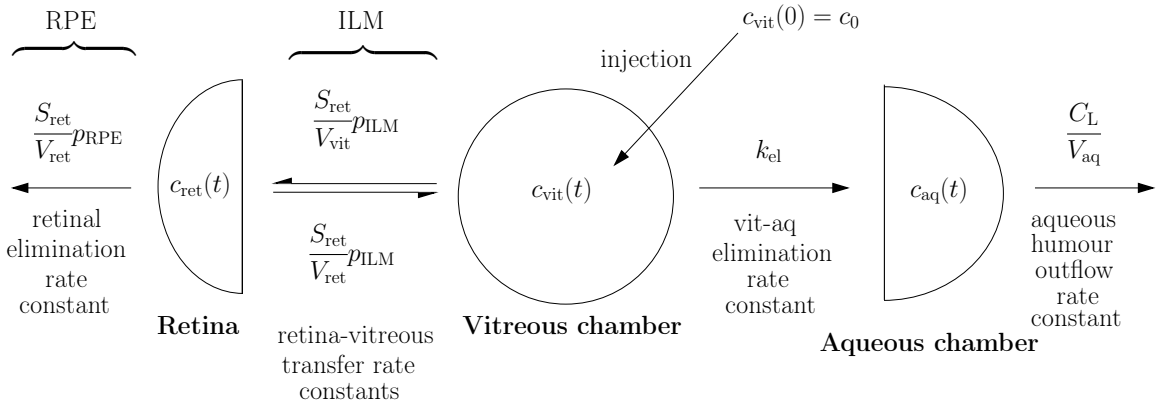

Figure 3.1: 3-compartment PK model for a general antibody, following a single IVT injection. Transport pathways are indicated by arrows, with their respective transfer rate constants. The antibody concentrations in the retina, vitreous and aqueous are denoted, respectively, as $c_{\text{ret}}(t), c_{\text{vit}}(t)$ and $c_{\text{aq}}(t)$. Overbraces indicate the retinal pigment epithelium, RPE, and the inner limiting membrane, ILM, which are situated between the posterior and anterior of the retina, respectively.

Parameter	Value	Units	Description
p_{RPE}	Estimated	cm/sec	Permeability of the retinal pigment epithelium (RPE)
p_{ILM}	Estimated	cm/sec	Permeability of the inner limiting member of the retina (ILM)
k_{el}	Estimated	1/day	Elimination from the vitreous to aqueous chamber
C_{L}	4.32 [69, 100]	ml/day	Clearance from the aqueous chamber
V_{ret}	0.044*	ml	Retinal volume
V_{vit}	1.52 [69]	ml	Vitreal volume
V_{aq}	0.325 [69]	ml	Aqueous volume
S_{ret}	4.35*	cm^2	Retinal surface area

Table 3.2: Summary of model parameters, units and notation. *Estimations of V_{ret} and S_{ret} can be found in Appendix A.2. Estimated parameters were allowed to vary during the fitting protocol and were approximated for each molecule studied.

Equations 3.1-3.3 comprise a linear ODE system with constant coefficients, which can be readily solved to give:

$$c_{\mathrm{ret}}(t) = c_0 \left(\frac{K_2 K_1}{K_1 + K_2}\right)\left[e^{-\lambda_1 t} - e^{-\lambda_2 t}\right], \tag{3.4}$$

$$c_{\mathrm{vit}}(t) = c_0 \left(\frac{1}{K_1 + K_2}\right)\left[K_1 e^{-\lambda_2 t} + K_2 e^{-\lambda_1 t}\right], \tag{3.5}$$

$$c_{\mathrm{aq}}(t) = \frac{c_0 p_{\mathrm{ILM}} k_{\mathrm{el}}}{\lambda_2 - \lambda_1}\left(\frac{S_{\mathrm{ret}}}{V_{\mathrm{aq}}}\right)\left[\frac{K_1}{\frac{C_{\mathrm{L}}}{V_{\mathrm{aq}}} - \lambda_2}\left(e^{-\lambda_2 t} - e^{-\left(\frac{C_{\mathrm{L}}}{V_{\mathrm{aq}}}\right)t}\right) + \frac{K_2}{\frac{C_{\mathrm{L}}}{V_{\mathrm{aq}}} - \lambda_1}\left(e^{-\lambda_1 t} - e^{-\left(\frac{C_{\mathrm{L}}}{V_{\mathrm{aq}}}\right)t}\right)\right], \tag{3.6}$$

where

$$K_1 = \left(\frac{V_{\mathrm{vit}}}{S_{\mathrm{ret}}}\right)\frac{k_{\mathrm{el}} + \left(\frac{S_{\mathrm{ret}}}{V_{\mathrm{vit}}}\right)p_{\mathrm{ILM}} - \lambda_1}{p_{\mathrm{ILM}}}, \quad K_2 = \left(\frac{V_{\mathrm{vit}}}{S_{\mathrm{ret}}}\right)\frac{\lambda_2 - k_{\mathrm{el}} - \left(\frac{S_{\mathrm{ret}}}{V_{\mathrm{vit}}}\right)p_{\mathrm{ILM}}}{p_{\mathrm{ILM}}}, \tag{3.7}$$

and λ_1, λ_2 are defined as

$$\lambda_1 = -\frac{1}{2}\left(\mathrm{Tr}(M) + \sqrt{\mathrm{Tr}(M)^2 - 4\det M}\right), \tag{3.8}$$

$$\lambda_2 = -\frac{1}{2}\left(\mathrm{Tr}(M) - \sqrt{\mathrm{Tr}(M)^2 - 4\det M}\right), \tag{3.9}$$

where $K_1, K_2, \lambda_1, \lambda_2 > 0$, with M defined as

$$M = \begin{pmatrix} -\frac{S_{\mathrm{ret}}}{V_{\mathrm{ret}}}\left(p_{\mathrm{ILM}} + p_{\mathrm{RPE}}\right) & \frac{S_{\mathrm{ret}}}{V_{\mathrm{ret}}}p_{\mathrm{ILM}} \\ \frac{S_{\mathrm{ret}}}{V_{\mathrm{vit}}}p_{\mathrm{ILM}} & -\left(\frac{S_{\mathrm{ret}}}{V_{\mathrm{vit}}}p_{\mathrm{ILM}} + k_{\mathrm{el}}\right) \end{pmatrix}. \tag{3.10}$$

3.1.2 Estimation of retinal membrane permeabilities using 3-compartment ocular PK data

When fitting model solutions to the experimental data, the parameters p_{RPE}, p_{ILM} and k_{el} were allowed to vary, with all other parameters fixed at the values given in Table 3.2. Initial

data points in the aqueous humour, at time 0.25 days, were omitted (see Appendix A.3 for justification). The free parameters were optimized by penalizing the relative mean-square error (MSE) between the logarithmic values of model results and the data, using lsqnonlin [86] (part of MATLAB's optimization toolbox). Confidence intervals were generated using a bootstrap algorithm with re-sampling [101, 102].

Figure 3.2 shows optimized fits for the retina, vitreous and aqueous datasets from Gadkar et. al. [28]. Best fit parameters and confidence intervals can be found in Table 3.3, and their dependence on Rh is illustrated in Figure 3.3. Figure 3.2 demonstrates the model's ability to fit the data, with a common half-life across compartments that is molecule specific. Figure 3.3, in conjunction with Table 3.3, shows that the estimated values of all elimination rate determining parameters (p_{RPE}, p_{ILM}, k_{el}) are higher for molecules of smaller hydrodynamic radius (R_{h}), contributing to a shorter value of the half life ($t_{1/2}$).

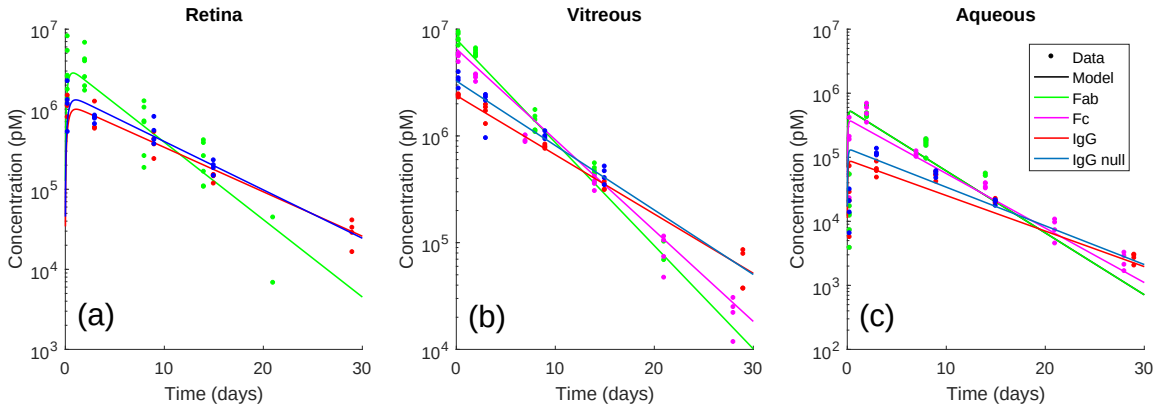

Figure 3.2: Compilation of optimized fits of Equations 3.1-3.3 to the dataset [28]. Coloured markers indicate distinct molecule datasets, whereas coloured lines show the optimized fit. For Fc molecules there were no retina data available, only vitreous and aqueous humour concentrations.

Parameter	Best fit parameter value (95% confidence interval)				Units
	Fab	Fc	IgG	IgG null	
p_{RPE}	2.60 (1.36, 4.04)	n/a	1.84 (1.08, 2.36)	1.91 (1.07, 2.5)	$\times 10^{-7}$ cm/sec
p_{ILM}	1.88 (1.13, 2.81)	n/a	1.7 (0.912, 2.32)	1.65 (0.758, 2.52)	$\times 10^{-7}$ cm/sec
$p_{\mathrm{RPE}}/p_{\mathrm{ILM}}$	1.38 (0.707, 2.21)	n/a	1.08 (0.612, 1.57)	1.16 (0.655, 1.64)	none
k_{el}	0.197 (0.179, 0.219)	0.169 (0.161, 0.178)	0.107 (0.0985, 0.119)	0.118 (0.109, 0.131)	1/day
$t_{1/2}$	3.11	3.54	5.42	4.98	days
RMSE	11.4	4.2	1.8	3.4	$\times 10^5$ pM

Table 3.3: Best fit parameter summary, including 95% confidence intervals obtained via Monte Carlo simulations using error bootstrapping [101] . Due to the lack of retinal data for molecule Fc, estimates for p_{RPE} and p_{ILM} could not be obtained in this case. RMSE, the root mean square error, is taken between the data and the model best fit.

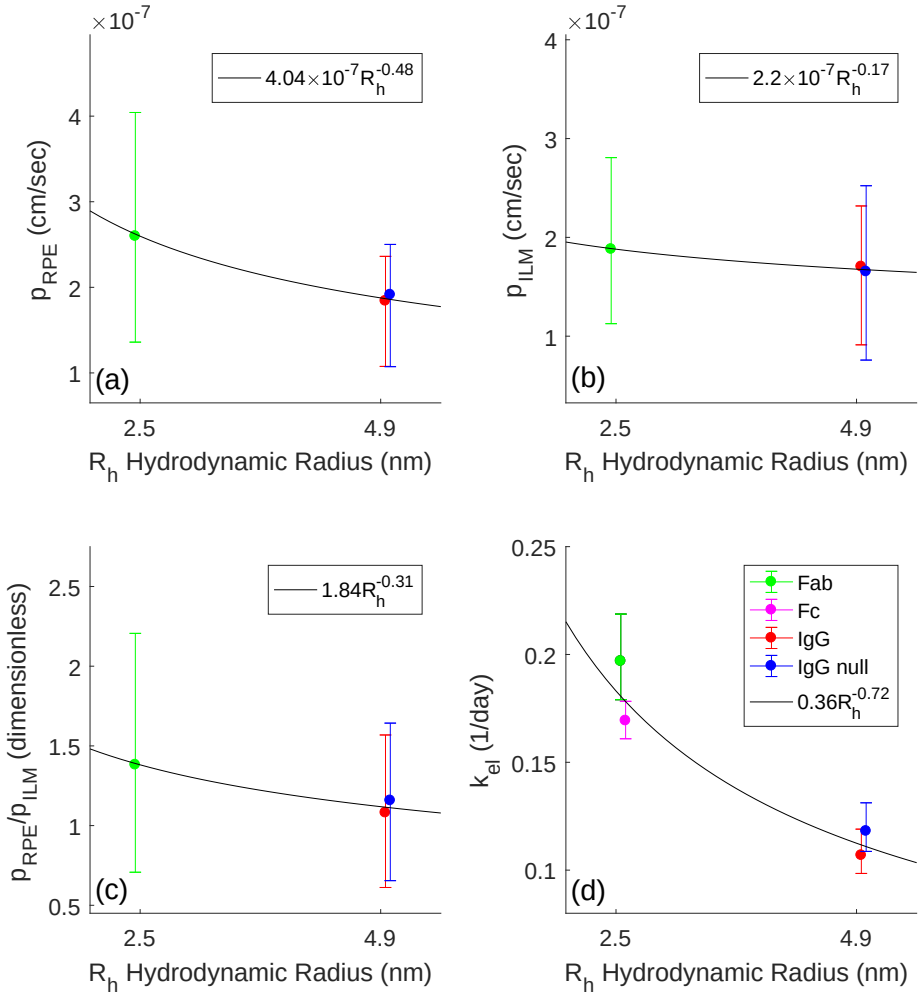

Figure 3.3: Best fit parameters plotted with respect to hydrodynamic radius (R_{h}). Error bars represent 95% confidence intervals obtained via Monte Carlo simulations using bootstrapping [101] . Power law fits, with respect to R_{h}, are shown by the solid lines and the equations corresponding are given in the legend to each subplot. R_{h} values for Fab, IgG and IgG null molecules were taken from [99] . Power laws were chosen here as a means to interpolate within the region of interest.

In Figure 3.4 we compare our estimates of p_{RPE} with results from a study by Pitkanen et al. [97] which analyzed the permeability of the RPE, in bovine eyes, to molecules with R_{h} ranging from 1.3 to 6.4 nm [97]. The model-derived estimates for p_{RPE} (green, red and blue) fit well within the experimentally derived range of RPE permeabilities, occupied by the molecules of similar R_{h}. The solid black curve in Figure 3.4 is a power law, fit to all data points shown.

A 2014 study by Vacca et al. suggests that the ILM of the wild type mouse is less permeable to adeno-associated virus 5 (AAV5) nanoparticles than the retina of mice lacking

the Dp71 gene [103] . The minimum R_{h} for monomeric AAVs is approximately 14 nm [104]. The power law predicted by combining our estimates with the dataset in Pitkanen et. al. [97], yields an upper bound on the permeability of virus particles of approximately 3.05×10^{-8} cm/sec. This value is an order of magnitude smaller than our estimates for full and fragment antibodies.

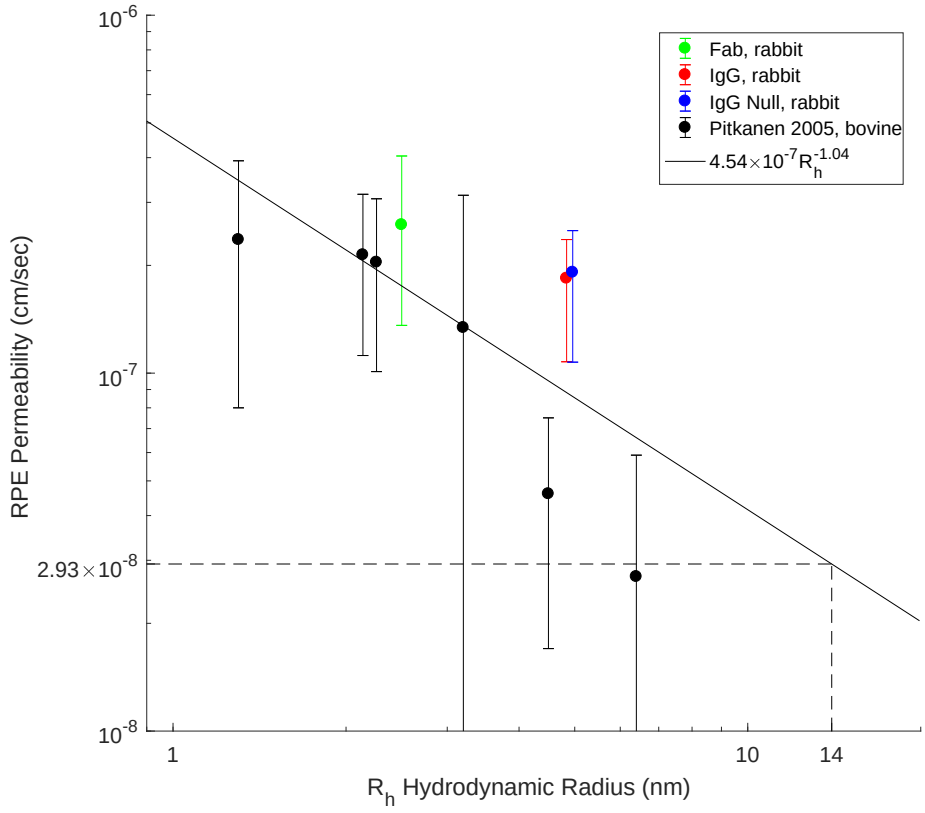

Figure 3.4: Comparison between full experimental bovine dataset [97] and best fit values for RPE permeability, found in Table 3.3. The solid black line denotes a power law fit to these data points, whose parameters, magnitude and exponent (with 95% confidence intervals), are 4.54×10^{-7} $(1.24 \times 10^{-7}, 16.6 \times 10^{-7})$ and -1.04 $(-2.07,\ -0.01)$, respectively. The dashed lines denote the expected permeability (as predicted by the power law) of molecules with hydrodynamic radii of 14 nm.

3.1.3 Analytic characterisation of ocular half-life, vitreous-retina concentration ratio and aqueous-retina elimination ratio

From Table 3.3 we determine that λ_1 & and λ_2 (Equations 3.8 and 3.9) are such that $\lambda_1/\lambda_2 \simeq 0.05 \ll 1$. In this case we can approximate the long time ($t \sim O(1/\lambda_1)$) behaviour

of the system (Equations 3.1-3.3) in the retina and vitreous by the following equations

$$c_{\text{ret}}(t) \simeq c_0 \left(\frac{K_2 K_1}{K_1 + K_2} \right) e^{-\lambda_1 t}, \tag{3.11}$$

$$c_{\text{vit}} \simeq c_0 \left(\frac{K_2}{K_1 + K_2} \right) e^{-\lambda_1 t}, \tag{3.12}$$

$$c_{\text{aq}}(t) \simeq c_0 \left(\frac{p_{\text{ILM}} k_{\text{el}}}{\lambda_2 - \lambda_1} \right) \left(\frac{S_{\text{ret}}}{V_{\text{aq}}} \right) \left(\frac{K_2}{\frac{CL_{\text{aq}}}{V_{\text{aq}}} - \lambda_1} \right) e^{-\lambda_1 t}. \tag{3.13}$$

By dividing Equation 3.12 by 3.11, we can derive an expression for the long-time vitreous retina concentration ratio, given by

$$R_{\text{VR}} \simeq \frac{1}{K_1}. \tag{3.14}$$

Additionally, from Equations 3.11-3.12 note that all compartments share a common decay rate, λ_1, implying they also share a common ocular $t_{1/2}$ given by:

$$t_{1/2} = \frac{\log 2}{\lambda_1}. \tag{3.15}$$

This motivates a deeper understanding of the analytic expression for λ_1, presented below. Recall that λ_1 and λ_2 are defined in Equations 3.8-3.9 in terms of the trace and determinant of matrix M, given by Equation 3.10. We may write $\text{Tr}(M)$ in the following way:

$$\text{Tr}(M) = -\frac{S_{\text{ret}}}{V_{\text{ret}}} \left(\left(1 + \frac{V_{\text{ret}}}{V_{\text{vit}}} \right) p_{\text{ILM}} + p_{\text{RPE}} \right) - k_{\text{el}} \tag{3.16}$$

$$= -\left(\frac{S_{\text{ret}} p_{\text{ILM}}}{V_{\text{ret}}} \right) \left[1 + \frac{p_{\text{RPE}}}{p_{\text{ILM}}} + \frac{V_{\text{ret}}}{V_{\text{vit}}} \left(1 + \frac{V_{\text{vit}} k_{\text{el}}}{S_{\text{ret}} p_{\text{ILM}}} \right) \right]. \tag{3.17}$$

Next note that for a general 2×2 matrix with elements $M = (a_{ij})$, $\text{Tr}M = a_{11} + a_{22}$ and $\det M = a_{11}a_{22} - a_{12}a_{21}$, therefore $(\text{Tr}M)^2 - 4 \det M = (a_{11} - a_{22})^2 + 4a_{12}a_{21}$. Therefore we may write:

$$\sqrt{\text{Tr}(M)^2 - 4 \det M} = \sqrt{\left(\frac{S_{\text{ret}} p_{\text{ILM}}}{V_{\text{ret}}} \right)^2 \left[1 + \frac{p_{\text{RPE}}}{p_{\text{ILM}}} - \frac{V_{\text{ret}}}{V_{\text{vit}}} \left(1 + \frac{V_{\text{vit}} k_{\text{el}}}{S_{\text{ret}} p_{\text{ILM}}} \right) \right]^2 + 4 \frac{(S_{\text{ret}} p_{\text{ILM}})^2}{V_{\text{ret}} V_{\text{vit}}}} \tag{3.18}$$

$$= \left(\frac{S_{\text{ret}} p_{\text{ILM}}}{V_{\text{ret}}} \right) \left[1 + \frac{p_{\text{RPE}}}{p_{\text{ILM}}} - \frac{V_{\text{ret}}}{V_{\text{vit}}} \left(1 + \frac{V_{\text{vit}} k_{\text{el}}}{S_{\text{ret}} p_{\text{ILM}}} \right) \right] \sqrt{1 + \underbrace{\left(\frac{V_{\text{ret}}}{V_{\text{vit}}} \right)}_{\ll 1} \underbrace{\left[\frac{2}{1 + \frac{p_{\text{RPE}}}{p_{\text{ILM}}} - \frac{V_{\text{ret}}}{V_{\text{vit}}} \left(1 + \frac{V_{\text{vit}} k_{\text{el}}}{S_{\text{ret}} p_{\text{ILM}}} \right)} \right]^2}_{\sim O(1)}} \tag{3.19}$$

$$\simeq \left(\frac{S_{\text{ret}} p_{\text{ILM}}}{V_{\text{ret}}} \right) \left[1 + \frac{p_{\text{RPE}}}{p_{\text{ILM}}} - \frac{V_{\text{ret}}}{V_{\text{vit}}} \left(1 + \frac{V_{\text{vit}} k_{\text{el}}}{S_{\text{ret}} p_{\text{ILM}}} \right) \right] \left(1 + \left(\frac{V_{\text{ret}}}{V_{\text{vit}}} \right) \frac{2}{\left[1 + \frac{p_{\text{RPE}}}{p_{\text{ILM}}} - \frac{V_{\text{ret}}}{V_{\text{vit}}} \left(1 + \frac{V_{\text{vit}} k_{\text{el}}}{S_{\text{ret}} p_{\text{ILM}}} \right) \right]^2} \right) \tag{3.20}$$

$$= \left(\frac{S_{\text{ret}} p_{\text{ILM}}}{V_{\text{ret}}} \right) \left[1 + \frac{p_{\text{RPE}}}{p_{\text{ILM}}} - \frac{V_{\text{ret}}}{V_{\text{vit}}} \left(1 + \frac{V_{\text{vit}} k_{\text{el}}}{S_{\text{ret}} p_{\text{ILM}}} \right) \right] + \frac{2}{\left[1 + \frac{p_{\text{RPE}}}{p_{\text{ILM}}} - \frac{V_{\text{ret}}}{V_{\text{vit}}} \left(1 + \frac{V_{\text{vit}} k_{\text{el}}}{S_{\text{ret}} p_{\text{ILM}}} \right) \right]} \left(\frac{S_{\text{ret}} p_{\text{ILM}}}{V_{\text{vit}}} \right). \tag{3.21}$$

We may consider approximations for λ_1 and λ_2. Firstly, let us consider λ_1, as follows:

$$\lambda_1 = -\frac{1}{2}\left(\mathrm{Tr}(M) + \sqrt{\mathrm{Tr}(M)^2 - 4\det M}\right) \tag{3.22}$$

$$\begin{aligned} \simeq -\frac{1}{2}\Bigg(&- \left(\frac{S_{\mathrm{ret}}p_{\mathrm{ILM}}}{V_{\mathrm{ret}}}\right)\left[1 + \frac{p_{\mathrm{RPE}}}{p_{\mathrm{ILM}}} + \frac{V_{\mathrm{ret}}}{V_{\mathrm{vit}}}\left(1 + \frac{V_{\mathrm{vit}}k_{\mathrm{el}}}{S_{\mathrm{ret}}p_{\mathrm{ILM}}}\right)\right] \\ &+ \left(\frac{S_{\mathrm{ret}}p_{\mathrm{ILM}}}{V_{\mathrm{ret}}}\right)\left[1 + \frac{p_{\mathrm{RPE}}}{p_{\mathrm{ILM}}} - \frac{V_{\mathrm{ret}}}{V_{\mathrm{vit}}}\left(1 + \frac{V_{\mathrm{vit}}k_{\mathrm{el}}}{S_{\mathrm{ret}}p_{\mathrm{ILM}}}\right)\right] \\ &+ \frac{2}{\left[1 + \frac{p_{\mathrm{RPE}}}{p_{\mathrm{ILM}}} - \frac{V_{\mathrm{ret}}}{V_{\mathrm{vit}}}\left(1 + \frac{V_{\mathrm{vit}}k_{\mathrm{el}}}{S_{\mathrm{ret}}p_{\mathrm{ILM}}}\right)\right]}\left(\frac{S_{\mathrm{ret}}p_{\mathrm{ILM}}}{V_{\mathrm{vit}}}\right)\Bigg). \end{aligned} \tag{3.23}$$

Therefore, by simplifying Equation 3.23, λ_1 can be approximated by

$$\lambda_1 \simeq k_{\mathrm{el}} + \left(\frac{S_{\mathrm{ret}}p_{\mathrm{ILM}}}{V_{\mathrm{vit}}}\right) - \frac{1}{1 + \frac{p_{\mathrm{RPE}}}{p_{\mathrm{ILM}}} - \frac{V_{\mathrm{ret}}}{V_{\mathrm{vit}}}\left(1 + \frac{V_{\mathrm{vit}}k_{\mathrm{el}}}{S_{\mathrm{ret}}p_{\mathrm{ILM}}}\right)}\left(\frac{S_{\mathrm{ret}}p_{\mathrm{ILM}}}{V_{\mathrm{vit}}}\right). \tag{3.24}$$

Using this approximation we may now express Equation 3.14 as the following:

$$R_{\mathrm{VR}} \simeq 1 + \frac{p_{\mathrm{RPE}}}{p_{\mathrm{ILM}}} - \frac{V_{\mathrm{ret}}}{V_{\mathrm{vit}}}\left(1 + \frac{V_{\mathrm{vit}}k_{\mathrm{el}}}{S_{\mathrm{ret}}p_{\mathrm{ILM}}}\right) \tag{3.25}$$

via the definition of K_1 given in Equation 3.7. Note that, as:

$$1 + \frac{p_{\mathrm{RPE}}}{p_{\mathrm{ILM}}} \gg \frac{V_{\mathrm{ret}}}{V_{\mathrm{vit}}}\left(1 + \frac{V_{\mathrm{vit}}k_{\mathrm{el}}}{S_{\mathrm{ret}}p_{\mathrm{ILM}}}\right), \tag{3.26}$$

is a valid assumption due to the relative volumes of the vitreous and retina, we can approximate Equation 3.25 by the following expression

$$R_{\mathrm{VR}} \simeq 1 + \frac{p_{\mathrm{RPE}}}{p_{\mathrm{ILM}}}, \tag{3.27}$$

and similarly write:

$$\lambda_1 \simeq k_{\mathrm{el}} + \left(\frac{S_{\mathrm{ret}}p_{\mathrm{ILM}}}{V_{\mathrm{vit}}}\right) - \underbrace{\frac{1}{1 + \frac{p_{\mathrm{RPE}}}{p_{\mathrm{ILM}}}}}_{\simeq R_{\mathrm{VR}}}\left(\frac{S_{\mathrm{ret}}p_{\mathrm{ILM}}}{V_{\mathrm{vit}}}\right) \tag{3.28}$$

$$= k_{\mathrm{el}} + \frac{S_{\mathrm{ret}}}{V_{\mathrm{vit}}}\left(\frac{1}{\frac{1}{p_{\mathrm{RPE}}} + \frac{1}{p_{\mathrm{ILM}}}}\right). \tag{3.29}$$

Similarly as for λ_1 we may approximate λ_2 in the following way:

$$\lambda_2 = -\frac{1}{2}\left(\mathrm{Tr}(M) - \sqrt{\mathrm{Tr}(M)^2 - 4\det M}\right) \tag{3.30}$$

$$\simeq -\frac{1}{2}\Bigg(-\left(\frac{S_{\mathrm{ret}}p_{\mathrm{ILM}}}{V_{\mathrm{ret}}}\right)\left[1 + \frac{p_{\mathrm{RPE}}}{p_{\mathrm{ILM}}} + \frac{V_{\mathrm{ret}}}{V_{\mathrm{vit}}}\left(1 + \frac{V_{\mathrm{vit}}k_{\mathrm{el}}}{S_{\mathrm{ret}}p_{\mathrm{ILM}}}\right)\right] \tag{3.31}$$

$$-\left(\frac{S_{\mathrm{ret}}p_{\mathrm{ILM}}}{V_{\mathrm{ret}}}\right)\left[1 + \frac{p_{\mathrm{RPE}}}{p_{\mathrm{ILM}}} - \frac{V_{\mathrm{ret}}}{V_{\mathrm{vit}}}\left(1 + \frac{V_{\mathrm{vit}}k_{\mathrm{el}}}{S_{\mathrm{ret}}p_{\mathrm{ILM}}}\right)\right]$$

$$-\frac{2}{\left[1 + \frac{p_{\mathrm{RPE}}}{p_{\mathrm{ILM}}} - \frac{V_{\mathrm{ret}}}{V_{\mathrm{vit}}}\left(1 + \frac{V_{\mathrm{vit}}k_{\mathrm{el}}}{S_{\mathrm{ret}}p_{\mathrm{ILM}}}\right)\right]}\left(\frac{S_{\mathrm{ret}}p_{\mathrm{ILM}}}{V_{\mathrm{vit}}}\right)\Bigg)$$

$$= \left(\frac{S_{\mathrm{ret}}p_{\mathrm{ILM}}}{V_{\mathrm{ret}}}\right)\left[1 + \frac{p_{\mathrm{RPE}}}{p_{\mathrm{ILM}}}\right] + \frac{1}{\left[1 + \frac{p_{\mathrm{RPE}}}{p_{\mathrm{ILM}}} - \underbrace{\frac{V_{\mathrm{ret}}}{V_{\mathrm{vit}}}}_{\ll 1}\left(1 + \frac{V_{\mathrm{vit}}k_{\mathrm{el}}}{S_{\mathrm{ret}}p_{\mathrm{ILM}}}\right)\right]}\left(\frac{S_{\mathrm{ret}}p_{\mathrm{ILM}}}{V_{\mathrm{vit}}}\right) \tag{3.32}$$

$$\simeq \left[\left(1 + \frac{p_{\mathrm{RPE}}}{p_{\mathrm{ILM}}}\right) + \underbrace{\frac{V_{\mathrm{ret}}}{V_{\mathrm{vit}}}}_{\ll 1}\left(\frac{1}{1 + \frac{p_{\mathrm{RPE}}}{p_{\mathrm{ILM}}}}\right)\right]\left(\frac{S_{\mathrm{ret}}p_{\mathrm{ILM}}}{V_{\mathrm{ret}}}\right) \tag{3.33}$$

$$\simeq \frac{S_{\mathrm{ret}}p_{\mathrm{ILM}}}{V_{\mathrm{ret}}}\left(1 + \frac{p_{\mathrm{RPE}}}{p_{\mathrm{ILM}}}\right), \tag{3.34}$$

as $V_{\mathrm{ret}}/V_{\mathrm{vit}} \ll 1$. We note here that the coefficient in Equation 3.12 for c_{vit} may be written $1/(1+K_1/K_2)$, and via Equation 3.7 we find K_1/K_2 may be approximated, using Equations 3.28 and 3.34, by:

$$K_1/K_2 = \frac{k_{\mathrm{el}} + \left(\frac{S_{\mathrm{ret}}p_{\mathrm{ILM}}}{V_{\mathrm{vit}}}\right) - \lambda_1}{\lambda_2 - k_{\mathrm{el}} - \left(\frac{S_{\mathrm{ret}}p_{\mathrm{ILM}}}{V_{\mathrm{vit}}}\right)} \tag{3.35}$$

$$\simeq \frac{\frac{1}{1+\frac{p_{\mathrm{RPE}}}{p_{\mathrm{ILM}}}}\left(\frac{S_{\mathrm{ret}}p_{\mathrm{ILM}}}{V_{\mathrm{vit}}}\right)}{\lambda_2 - \lambda_1 - \frac{1}{1+\frac{p_{\mathrm{RPE}}}{p_{\mathrm{ILM}}}}\left(\frac{S_{\mathrm{ret}}p_{\mathrm{ILM}}}{V_{\mathrm{vit}}}\right)} \tag{3.36}$$

$$= \frac{1}{\frac{\lambda_2(1-\lambda_1/\lambda_2)}{\frac{1}{1+\frac{p_{\mathrm{RPE}}}{p_{\mathrm{ILM}}}}\left(\frac{S_{\mathrm{ret}}p_{\mathrm{ILM}}}{V_{\mathrm{vit}}}\right)} - 1} \tag{3.37}$$

$$\simeq \frac{1}{\frac{V_{\mathrm{vit}}}{V_{\mathrm{ret}}}\left(1 + \frac{p_{\mathrm{RPE}}}{p_{\mathrm{ILM}}}\right)^2 - 1} \ll 1, \tag{3.38}$$

as $\lambda_1/\lambda_2 \ll 1$ and $V_{\mathrm{vit}}/V_{\mathrm{ret}} \gg 1$. Therefore it follows that we may approximate c_{vit} as a single exponential decay from c_0, as follows:

$$c_{\mathrm{vit}} \simeq c_0 \mathrm{e}^{-\lambda_1 t}. \tag{3.39}$$

The accuracies of the approximations for λ_1, λ_2 and R_{VR}, for the molecules considered, can be found in Table 3.4, where it can be seen they are all close to exact.

Equation 3.27 demonstrates that as p_{RPE} tends to zero, with p_{ILM} held constant, the vitreous and retina approximately equilibrate to the same concentration. Our fitting protocol suggests that the value of $p_{\mathrm{RPE}}/p_{\mathrm{ILM}}$ lies in the range of 1.1-1.4, implying that the antibody concentration of the vitreous is roughly double that of the retina at any given time. In previous 2-compartment models [3, 74] the principle decay rate λ_1 is equal to k_{el}. Equation 3.28 reveals that this will be the case as $p_{\mathrm{ILM}} \to 0$ (i.e. when the 3-compartment model reduces to a 2-compartment model). Notably this is also the case when $p_{\mathrm{RPE}} = 0$, as in this limit the vitreous and retina become indistinguishable (see Figure 3.1). The second term on the right-hand side of Equation 3.28 shows the effect of allowing an additional pathway for transport from the vitreous chamber, through the ILM and into the retina; this term increases the global decay rate by an amount equal to the rate at which transfer takes place, from the vitreous, through the ILM and into the retina ($S_{\mathrm{ret}} p_{\mathrm{ILM}}/V_{\mathrm{vit}}$ 1/day). The third term on the right-hand side of Equation 3.28 describes, in a simple analytic expression, the interplay between the vitreous and retina, which arises due to the bi-directional transport between these 2 compartments. This damping term reduces the decay rate, as molecules which permeate into the retina are then able to return to the main body of the eye. This term is inversely proportional to the vitreous to retina concentration ratio, implying that the bi-directional nature of transport across the ILM dampens the additional decay caused by choroidal elimination by approximately half. Equation 3.29 demonstrates the symmetrical influence of p_{ILM} and p_{RPE} on λ_1 in the limiting cases when either term tends to zero (yielding k_{el}) or infinity (yielding $k_{\mathrm{el}} + (S_{\mathrm{ret}}/V_{\mathrm{vit}}) \times p_{\mathrm{ILM}}$ or p_{RPE}). Notice also the similarity between the second term in Equation 3.29 and the net resistance of two resistors in series, if the reciprocal of permeability is taken as analogous to electrical resistance.

Molecule	Fab	IgG	IgG null
Exact value of R_{VR}	2.26	2.01	2.08
Accuracy of Equation 3.25	99.48%	99.35%	99.39%
Accuracy of Equation 3.27	94.40%	95.95%	95.67%
Exact value of λ_1	0.2224	0.1278	0.1387
Accuracy of Equation 3.24	99.95%	99.90%	99.92%
Accuracy of Equation 3.28	99.51%	99.38%	99.42%
Exact value of λ_2	3.84	3.04	3.06
Accuracy of Equation 3.34	99.46%	99.30%	99.35%

Table 3.4: Accuracy summary of the approximations. All accuracies are relative to the exact values generated from the relevant analytical solutions.

Equations 3.11-3.13 enable us to study the relative influence of the two elimination pathways incorporated into this model; elimination via the choroid versus the aqueous humour. Following IVT injection, the total number of molecules (given in pmols), which exit via the RPE and via the aqueous are given by E_{RPE} and E_{aq}, respectively:

$$E_{\mathrm{RPE}} = S_{\mathrm{ret}} p_{\mathrm{RPE}} \int_0^\infty c_{\mathrm{ret}}(s)\mathrm{d}s \simeq S_{\mathrm{ret}} p_{\mathrm{RPE}} K_1 \left(\frac{S_{\mathrm{ret}}}{V_{\mathrm{vit}}} \frac{c_0 p_{\mathrm{ILM}} K_2}{\lambda_1(\lambda_2 - \lambda_1)} \right), \tag{3.40}$$

$$E_{\mathrm{aq}} = k_{\mathrm{el}} V_{\mathrm{vit}} \int_0^\infty c_{\mathrm{vit}}(s)\mathrm{d}s \simeq k_{\mathrm{el}} V_{\mathrm{vit}} \left(\frac{S_{\mathrm{ret}}}{V_{\mathrm{vit}}} \frac{c_0 p_{\mathrm{ILM}} K_2}{\lambda_1(\lambda_2 - \lambda_1)} \right). \tag{3.41}$$

Their ratio, $E_{\mathrm{aq}}/E_{\mathrm{RPE}}$, is such that:

$$\frac{E_{\mathrm{aq}}}{E_{\mathrm{RPE}}} \simeq \frac{k_{\mathrm{el}} V_{\mathrm{vit}}}{S_{\mathrm{ret}}} \left(\frac{1}{p_{\mathrm{RPE}}} + \frac{1}{p_{\mathrm{ILM}}} \right). \tag{3.42}$$

In Table 3.5 this expression is evaluated for Fab, IgG and IgG null molecules, showing that for each IVT-injected antibody that passes through the RPE into the choroid, 5-7 antibody molecules will be eliminated via the aqueous humour. This justifies the assumption made in previous models [28, 74] that the aqueous humour is the dominant transport pathway and that elimination via the RPE may be neglected.

Molecule	Fab	IgG	IgG null
Percentage of dose exiting through RPE	12.7%	17.6%	16.3%
Percentage of dose exiting through aqueous	87.3%	82.4%	83.7%
$E_{\mathrm{aq}}/E_{\mathrm{RPE}}$	6.87	4.68	5.14

Table 3.5: The aqueous to retinal elimination ratio, $E_{\mathrm{aq}}/E_{\mathrm{RPE}}$, is the ratio of the number of molecules that left the system via the aqueous and the number that left through the RPE, post-transient chemical equilibration.

3.1.4 3-compartment PK ODE model summary

In contrast to the original model used to analyse these data [28], our semi-mechanistic model characterises the membranes on either side of the retina in terms of their permeabilities (p_{ILM} and p_{RPE}), incorporating transport between the vitreous and retina, as well as choroidal elimination. This allows for geometric scaling of this model across species (via adjustment of volumes and surface areas) to, for example, humans, granting applicability of our model to a wider range of experimental and clinical data. Due to the semi-mechanistic nature of our model, the derived half-life ($t_{1/2}$) given by Equations 3.28-3.29 also scales geometrically, giving a valuable physiological relationship that is translatable across species. In this regard, our model predicts (rather than assumes) that a common value of $t_{1/2}$ describes the time-course of drug concentration in the aqueous, vitreous and retina compartments.

While all three compartments exhibit the same apparent $t_{1/2}$ (derived from λ_1), we note that the aqueous and retinal compartments exhibit the pharmacokinetic "flip-flop" phenomenon in comparison to the vitreous compartment. This phenomenon occurs when the rate constant of drug input to a compartment is smaller than the rate of drug elimination [105]. In the aqueous compartment, the rate constant of drug input from the vitreous (k_{el}) is comparable to λ_1, which is on the order of 0.1 to 0.2 day^{-1}, and is much smaller than the elimination rate constant from the aqueous compartment ($CL_{\text{aq}}/V_{\text{aq}} = 13.3$ day^{-1}).

We have shown that the model can be used to estimate permeabilities from 3-compartment PK data. Furthermore, these estimates are similar in magnitude and trend, to those seen in bovine retina by Pitkanen et al. [97]. Additionally we note our RPE permeability estimates are consistent with the predicted values of retina to choroid permeability, generated from a model of the blood-retinal barrier (BRB) [95]. In Tervonen et. al. [95] molecules with radii in the range of 0.5-0.9 nm were studied, and those with a value of $R_{\text{h}} = 0.9$ nm were predicted to have a retina to choroid permeability of approximately 5×10^{-7} cm/sec, which is in line with the power law fit to data in Figure 3.4.

Our estimates of the ILM and RPE permeabilities, as well as their ratio (Table 3.3), suggest p_{ILM} and p_{RPE} are comparable in magnitude and vary weakly with R_{h}. From the structural perspective, the ILM and RPE barriers are both composed of basement membranes containing laminins, proteoglycans and collagens (Halfter et al. [106]) and an adherent cellular layer. In the ILM the cellular layer corresponds to the foot processes of the Muller cells (elongated cells that span a large cross section of the retina, whose anteriorial end, or 'foot', spreads over retinal anterior); while in the RPE it is the pigmented epithelial cells, which

form tight junctions between them. In both cases the cellular layers are anchored to the basement membrane by laminin proteins (see Vacca et. al. [103]). Recent in vitro studies suggest that basement membranes may contribute to the macromolecular barrier properties of epithelia (Vllasaliu et. al. [107]). Transcellular and paracellular pathways also appear to contribute to the permeability of the RPE for Ranibizumab (Fab) and Bevacizumab (IgG) (Terasaki et. al. [108]). Direct measurements of p_{ILM} and p_{RPE} and their components, e.g., basement membranes and cellular layers, are needed to further assess the contribution of these layers as well as the influence of macromolecular size, structure and charge on the respective permeabilities.

Due to the limited available data and uncertainty in our estimated permeabilities for the ILM and RPE we caution against extrapolating the permeability power relations shown in Figure 3.3 much beyond their respective range of R_{h} values. Although the extrapolated estimate of p_{RPE} for the 14 nm AAV particles is consistent with studies in the mouse [103], further experimental data over a range of macromolecular sizes and chemical properties (including charge density) are needed to better define the dependences of p_{RPE}, p_{ILM} and k_{el} on R_{h}. In this regard, we have shown how the 3-compartment PK model can be used to estimate such physiological parameters from ocular PK data obtained in the aqueous, vitreous and retinal compartments.

While acknowledging the limited data available to define the dependence of the parameter k_{el} on R_{h} (Figure 3.3d), we note that it is approximately proportional to $1/R_{\mathrm{h}}$; a result that is consistent with our previous conjecture in Chapter 2. For sufficiently small p_{ILM} (as occurs in the rabbit), Equations 3.28-3.29 imply that the ocular half-life ($t_{1/2}$) will be approximately equal to $1/k_{\mathrm{el}}$ and thus $t_{1/2}$ should increase with R_{h}. Shatz et al. [99] have recently confirmed such a relationship in the rabbit using pegylated Fab molecules with Rh ranging from 2.5 to 6.9 nm. Further development of the theoretical factors that determine k_{el} would be useful for translating the data from rabbits to other species [74].

The analytic approximation for the decay rate λ_1 (Equation 3.28) shows how the retinal elimination pathway and bidirectional transport across the ILM impact λ_1 and, hence, $t_{1/2}$ (Equation 3.15). In comparison to previous 2-compartment models [3, 74] (where $\lambda_1 = k_{\mathrm{el}}$), the additional terms contribute about 11-16% to λ_1 and lead to a similar reduction in the estimated value of k_{el} as that obtained from the 2-compartment model. We further note that the ratio of the retinal permeabilities, pRPE/pILM, appears in the long time decay rate (Equation 3.28), the vitreous-to-retina concentration ratio (Equation 3.27) and the

aqueous-to-retinal elimination ratio (Equation 3.42). This ratio results from the bidirectional transport between the vitreous and retina and is a key determinant of the ocular pharmacokinetics associated with intravitreal administration. Direct measurements of the permeabilities of the ILM and the RPE would be useful to confirm the estimates obtained from the semi-mechanistic PK model.

The recent review of the pharmacokinetic aspects of retinal drug delivery by del Amo et. al. [98] presented a meta-data analysis of intravitreal elimination rates over a wide range of molecules. Using the data presented by Pitkanen et. al. [97] the authors concluded that 3-20% of the injected dose is eliminated through the RPE. We find this to be consistent with our results, given in Table 3.5, which state that 13-18% of molecules exit via the RPE. Our analysis also shows that the magnitude of the aqueous to retinal elimination ratio, Equation 3.42, yields the counter-intuitive finding that molecules with a larger R_{h} value are eliminated at a higher rate through the choroid than molecules with lower R_{h} values. Equation 3.42 reveals that the ratio of the number of molecules eliminated through the aqueous rather than the choroid depends on k_{el}, p_{RPE} and p_{ILM}. Our parameter estimation across molecular species indicates that the magnitude of k_{el} is more sensitive to changes in R_{h} than p_{RPE} and p_{ILM}, which were found to be relatively insensitive. We therefore find that due to the notable drop in the magnitude of k_{el} between Fab and IgG molecules (by approximately 50%), simulated IgG molecules were retained longer within the vitreous, and were hence eliminated at a higher rate through the choroid than Fab molecules. Increasing the number of molecules eliminated via the choroid relative to the aqueous is potentially advantageous from the perspective of drug delivery for many ocular antibodies, which target the posterior of the retina in the treatment of retinal diseases. Due to the magnitude of the confidence intervals for model permeabilities, we suggest that further data are needed to confirm that k_{el} is significantly more sensitive to R_{h} than p_{RPE} and p_{ILM}, and suggest permeability studies of the RPE and ILM in tandem.

Both retinal, vitreal and aqueous PK data are needed to estimate retinal permeabilities. However very few such datasets currently exist. In order to more accurately describe the dependence of p_{ILM}, p_{RPE} and k_{el} on R_{h}, data covering a wider range of hydrodynamic radii are required. With such information our semi-mechanistic model will yield more accurate predictions regarding the effects of molecular size on retinal concentration and choroidal elimination. This 3-compartment PK model can also be readily extended into a PK/PD model, through the inclusion of reaction kinetics, and then used to analyse clinical data. As in Chapter 2, such a PK/PD model could be used to study ranibizumab binding to vascular

endothelial growth factor (VEGF) in the eye. In principle such a model could be used to infer the kinetics of VEGF suppression in the retina, based on the observed suppression of VEGF levels in the aqueous humour.

3.2 Investigation of the well-mixed assumption using an adaptable, mechanistic, retina-vitreous PDE model

The majority of ocular PK modelling, particularly within the pharmaceutical industry itself, is performed using compartment ODE models. Such models are analogous to those implemented by Saunders et al. [3] and Gadkar et al. [28], as well as those presented previously in this thesis (Hutton-Smith et al. 2016 and 2017 [74, 75]). Several spatial PDE convection/diffusion PK/PD studies can be found in the literature [69–72, 109–111], with geometry based upon ocular anatomy. These models have yielded highly detailed predictions regarding vitreal pressure gradients, ocular fluid velocity as well as ocular PK. However, such models have yet to become mainstream in the field of drug development. This can probably be explained by their complexity, and due to their need for some level of anatomical accuracy, and a greater number of parameters. Additionally, such models are challenging to validate, as spatial PK data are technically difficult to acquire.

For these reasons implementation of compartment ODE models has been widespread within the field, but no study has reviewed the accuracy of these spatially averaged (or 'well mixed') models has been performed, to the best of our knowledge. Additionally, no comparison of predictions of mathematically equivalent ODE and PDE ocular PK/PD models has been performed. In this section, through the development of a PDE model that, when spatially averaged reduces to a system of the form implemented in our ODE studies, we are not only able to perform an analysis of the applicability of the well mixed assumption, but also review any disparities between the predictions obtained from ODE and PDE models.

In order to address the intrinsic higher level of complexity of ocular PDE models, we aim to design a model able to generate a suitable level of anatomical detail using as few geometric and mechanistic parameters as possible. In doing so we have aimed to create a model that is easily adapted (through the alteration of a handful of anatomical parameters) to describe a range of mammalian species, thus, increasing its applicability to *in vivo* as well as clinical studies.

3.2.1 Model formulation, geometry and numerical solution

As outlined in Section 1.3 of the Introduction, many published PK models currently within the literature solve a three-dimensional advection-diffusion equation over the geometry of the eye:

$$\frac{\partial C}{\partial t} + \vec{U} \cdot \nabla C - D\nabla^2 C = 0, \tag{3.43}$$

where fluid is assumed to be incompressible, and where $C(\vec{x}, t)$, $\vec{U}$, D, are the drug concentration, fluid velocity and diffusion coefficient, respectively. In the aqueous humour fluid flow rates are substantially higher than in the rest of the eye, in this region the Navier-Stokes equations are typically used to determine $\vec{U}$. Non-aqueous regions of the eye are typically treated as porous media, wherein the fluid velocity is governed by Darcy's law:

$$\vec{U} \propto -\nabla p, \tag{3.44}$$

where p is the local pressure. Assuming the fluid is incompressible, the pressure field can then be derived using suitable boundary conditions. Fluid flow within the eye is driven by two factors, pressure differentials and motion of the ocular body itself (for example by rapid eye movements known as saccades). In the spatial models mentioned above fluid velocity is driven by ocular pressure differentials only. In the work of Missel 2012 [69], one of the most anatomically faithful PDE models of the mammalian eye, aqueous humour is assumed to be produced at a constant rate from the ciliary body; this is modelled by a pressure outlet located in the anterior aqueous humour, which, being of a much greater magnitude than that of the pressure at the choroid or cornea, is the primary driver of fluid flow within the aqueous. Missel demonstrated that the flow is primarily directed along the path from the ciliary body, between the iris and lens, and towards the pressure outlet - and not through the anterior hyaloid membrane separating the vitreous from the aqueous. This result demonstrates the logic that has been used to formulate existing compartment-based models, in which molecular movement from the aqueous humour into the vitreous is assumed to be negligible in comparison to clearance due to the flow of aqueous humour.

In several simulations presented by Missel [69], the pressure differential from the anterior to posterior aqueous humour is found to be of one order of magnitude, whereas across the vitreous chamber it is found to be close to zero. In turn, as fluid velocity in the vitreous is governed by Darcy's law, Missel predicted that the fluid velocity in the aqueous humour would be much greater than that of the vitreous. Missel concludes that vitreal fluid flow (generated by the pressure difference between the anterior and posterior of the vitreous

humour) is *"the most significant impact on the clearance behaviour for the slowly diffusing materials"*, indicating it may be relevant when considering ocular macromolecules, which typically have a vitreal diffusion coefficient of order 10^{-6} cm^2/sec (that of a protein in water). Similarly, Missel in 2002 [111] wrote *"Flow predicted through the vitreous is so small that it contributes to diffusion only for large molecules"*.

Other authors have worked and commented on this consideration in similar PDE models, when modelling the rabbit eye. For example, Friedrich et al. [112] assumed there was no fluid flow within the vitreous. Similarly, in a PDE study of the human eye, Kotha et al. [71] treated fluid flow as negligible, stating *"there is a small pressure difference across vitreous humor, ca. 10 Pa, which causes convective flow towards the retina, but it is shown to be insignificant in the transport equation"*. The justification used by Kotha et al. was derived from an earlier PDE study of the rabbit eye by Kim et al. [70], in which the authors commented: *"our computer simulations show that reducing the convective flow to zero in the model produces insignificant changes in the Gd-DTPA concentration profiles within the vitreous, suggesting that diffusion is the dominant mechanism for transport in our system. Xu et al. [113] calculated Peclet numbers to be 0.4 for a human eye and 0.024 for a mouse eye. Using a nominal velocity at the retinal surface of 3.5×10^{-7} cm s^{-1}, a diffusion coefficient of 2.8×10^{-6} cm^2 s^{-1} in the vitreous, and a nominal length scale of 1.0 cm for the diameter of the vitreous cavity of a rabbit eye, we calculate a Peclet number (vL/D) of approximately 0.09 which implies a dominance of diffusion over flow in affecting the concentration distribution of the Gd-DTPA in the vitreous"*. Given the similarity of the diffusion coefficient of Gd-DTPA to that of ocular anti-VEGF macromolecules, this would imply that the results of Kim et al. [70] indicate diffusion dominates pressure driven convection within the rabbit vitreous. A recent 2017 study by Ferreira et al. [72] simulated pressure induced fluid flow over the human eye. They found that even though the drop in pressure between the aqueous and RPE could be estimated at approximately 800 Pa, over the vitreous the pressure only varied by 10 Pa (1990-2000 Pa). Using this vitreal pressure drop of 10 Pa between the anterior and posterior of the vitreal, as well as the parameters for vitreal hydraulic resistance and viscosity given in Ferreira et al. 2017 [72], we simulated vitreal velocity over the geometry presented in the following sections of this chapter (details of this simulation can be found in Appendix A.4). From this simulation, we found that by interpolating velocity mesh points over a uniform spatial grid, a medium vitreal velocity of 5.6×10^{-7} cm/sec and retinal surface velocity of 1.1×10^{-7} cm/sec, in agreement with the values reported in previous studies.

In conclusion, there is no consensus in the literature regarding the relative contributions of pressure driven fluid flow and diffusion in the transport of macromolecules in the vitreous. We anticipate that pressure driven transport will be important only for molecules much larger than those we will consider in this thesis. Further, given the studies listed above, pressure driven fluid flow appears to be dominated by diffusion through most of the vitreal body. Therefore in our PDE studies we will neglect fluid flow generated by the pressure difference over the vitreal body, and fluid flow from the aqueous humour into the vitreous body. A further step in improving the biological accuracy of this model would be to include this fluid flow. By neglecting fluid flow from the aqueous humour we are able to simplify the ocular geometry and ignore the complex geometry of the anterior of the eye. We therefore only consider the geometry of the vitreous and retina, treating the vitreous as an imperfect sphere, surrounded by a semi-spherical retinal shell.

Generalised ocular geometry of the mammalian eye

Figure 3.5 shows a cross-sectional view of the simplified vitreal and retinal geometry. The vitreous and retinal are represented by domains Ω_{vit} and Ω_{ret}, respectively, the inner limiting membrane (ILM), sub-retinal space, anterior hyaloid membrane and lens are represented by boundaries $\partial\Omega_1, \partial\Omega_1^*, \partial\Omega_2$ and $\partial\Omega_3$, respectively. We treat the vitreous as an imperfect sphere of radius r_0 cm, missing an anterior section due to the presence of the lens. One may view the human eye as a sphere, reducing the geometric complexity even further, however the lens of the rabbit eye (frequently used in *in vivo* studies) occupies a much larger proportion than that of the human eye, hence we retained this anatomical feature to increase cross-species applicability. The boundary of the vitreous is divided into three sections, determined by two angular parameters, θ_1 and θ_2, determining the portions of the vitreal surface in contact with the ILM, anterior hyaloid and lens. We model the retina as a partial-spherical shell of width ε cm, the retinal thickness. We incorporate the lens into the model by removing an ellipsoidal region from Ω_{vit}, the vitreous chamber. The centre of the ellipsoid is defined as the point on the axis of symmetry of the eye directly below the anterior hyaloid membrane. The semi-major axis is then defined as the distance to the anterior hyaloid, and the semi-minor axis by half of the lens thickness, l cm.

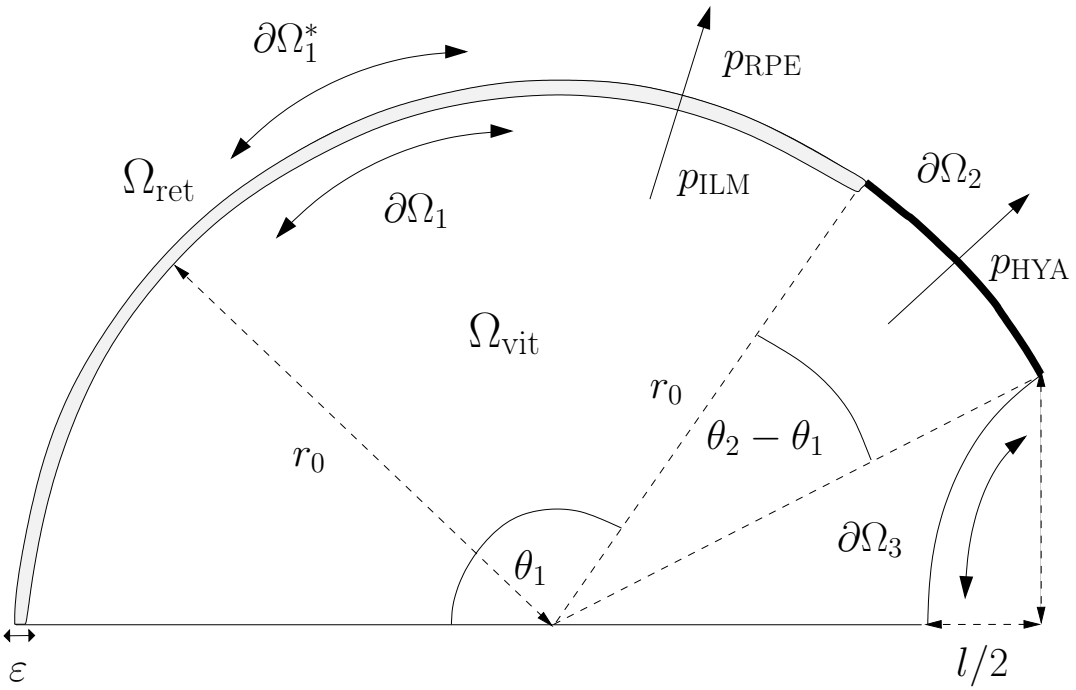

Figure 3.5: Simplified ocular geometry developed for study in this thesis. The vitreous and retina are represented by domains Ω_{vit} and Ω_{ret}, respectively, with the inner limiting membrane (ILM), sub-retinal space, anterior hyaloid membrane and lens represented by boundaries $\partial\Omega_1, \partial\Omega_1^*, \partial\Omega_2$ and $\partial\Omega_3$, respectively. Membrane permeabilities for the hyaloid membrane, RPE and ILM, are given by $p_{\mathrm{HYA}}, p_{\mathrm{RPE}}$ and p_{ILM}, respectively.

Notice that we now describe the geometry of the eye via 5 parameters. Figure 3.6 shows the model geometry evaluated in COMSOL using the rabbit and human parameters listed in Table 3.6. Note that the human eye, while larger, has a smaller lens than the rabbit. Once implemented in a suitable form it is straightforward to numerically derive volumes or surface or surface areas of interest, however they can also be determined via the analytic expressions given in Table 3.7.

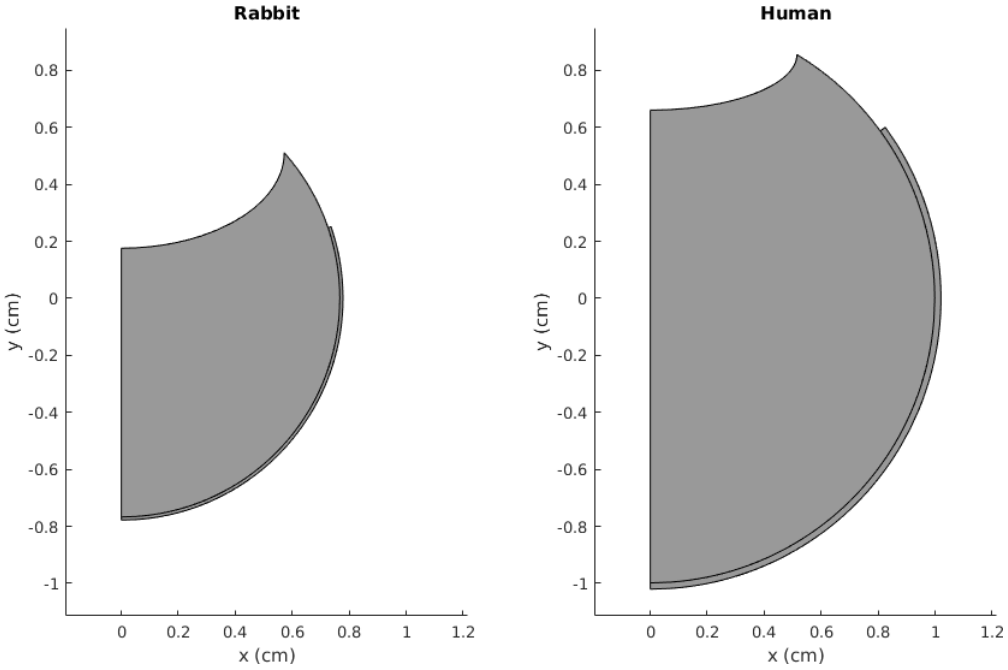

Figure 3.6: Rabbit and human geometries rendered using COMSOL, using geometric parameters found in Table 3.6. See Figure 3.5 for region definitions.

Parameter	Human	Rabbit	Units	Description
r_0	1.0 [74]	0.77 [74]	cm	Radius of the vitreous
ε	0.022 [69]	0.011 [69]	cm	Retinal thickness
l	0.39 [69]	0.67 [69]	cm	Lens thickness
θ_1	2.2 [69]	1.9 [69]	rad	See Figure 3.5
θ_2	2.6 [69]	2.2 [69]	rad	See Figure 3.5
V_{aq}	0.16 [88, 89]	0.33 [69]	cm^3	Volume of the aqueous
C_{L}	3.6 [87]	4.3 [69, 100]	mL/day	Clearance rate from the aqueous chamber

Table 3.6: Parameters for human and rabbit geometry, as well as clearance rate from the aqueous chamber.

Parameter	Value	Units	Description
S_{ret}	$2\pi r_0^2 (1 - \cos\theta_1)$	cm^2	Surface area of the retina
S_{aq}	$2\pi r_0^2 (\cos\theta_1 - \cos\theta_2)$	cm^2	Surface area of anterior hyaloid membrane
V_{vit}	$g(r_0, l, \theta_2)$	cm^3	Volume of the vitreous
V_{ret}	$\frac{2}{3}\pi \{1 - \cos(\theta_1)\} \left[(r_0 + \varepsilon)^3 - r_0^3\right]$	cm^3	Volume of the retina

Table 3.7: Analytic expressions for volumes and surface areas of anatomically relevant ocular regions. The expression for $g(r_0, l, \theta_2)$ is given by Equation 3.45.

Note that $g(r_0, l, \theta_2)$ as described in Table 3.7, is given by

$$g(r_0, l, \theta_2) = \frac{4}{3}\pi r_0^3 - \frac{1}{3}\pi l \left(r_0 \cos\left(\theta_2 - \frac{\pi}{2}\right)\right)^2 - \frac{1}{3}\pi \left(r_0 - r_0 \sin\left(\theta_2 - \frac{\pi}{2}\right)\right)^2 \left(3r_0 - \left(r_0 - r_0 \sin\left(\theta_2 - \frac{\pi}{2}\right)\right)\right). \tag{3.45}$$

Equation 3.45 is derived via taking the differences of the elementary geometric objects that define the ocular geometry of Figure 3.5.

Ocular PDE PK model formulation

We now formulate the model as a 3-dimensional system of time dependent diffusion equations. The diffusion coefficient within the retina is assumed to be different to that of the vitreous (see Equations 3.46 and 3.47). The retina and vitreous are coupled by boundary conditions given by Equations 3.48 and 3.50, and at the posterior of the retina there exists a sink into the choroid via the retinal pigment epithelium (RPE), given by Equation 3.49. Transport from the choroid to the retina is neglected, due to the high rate of blood flow within the choroid. The permeabilities of the ILM and RPE are given by p_{ILM} and p_{RPE}, respectively. From the vitreous, permeation is also allowed into the aqueous humour through the anterior hyaloid membrane of the vitreous - it is assumed to be unidirectional due to the high flow rate found in the anterior of the aqueous humour (as in Chapter 2 and Section 3.1). Transport into the aqueous humour is governed by Equation 3.51 and the permeability of the hyaloid membrane is given by p_{HYA}. Zero diffusive flux is assumed through the lens, given by Equation 3.52. Hence, the model has the form:

$$\frac{\partial c_{\text{ret}}}{\partial t} = D_{\text{ret}} \nabla^2 c_{\text{ret}}, \qquad \text{for } \vec{x} \in \Omega_{\text{ret}}, \tag{3.46}$$

$$\frac{\partial c_{\text{vit}}}{\partial t} = D_{\text{vit}} \nabla^2 c_{\text{vit}}, \qquad \text{for } \vec{x} \in \Omega_{\text{vit}}, \tag{3.47}$$

$$-D_{\text{ret}} \vec{n} \cdot \nabla c_{\text{ret}} = p_{\text{ILM}} \left(c_{\text{ret}} - c_{\text{vit}} \right), \qquad \text{for } \vec{x} \in \partial\Omega_1, \tag{3.48}$$

$$-D_{\text{ret}} \vec{n} \cdot \nabla c_{\text{ret}} = p_{\text{RPE}} c_{\text{ret}}, \qquad \text{for } \vec{x} \in \partial\Omega_1^*, \tag{3.49}$$

$$-D_{\text{vit}} \vec{n} \cdot \nabla c_{\text{vit}} = p_{\text{ILM}} \left(c_{\text{vit}} - c_{\text{ret}} \right), \qquad \text{for } \vec{x} \in \partial\Omega_1, \tag{3.50}$$

$$-D_{\text{vit}} \vec{n} \cdot \nabla c_{\text{vit}} = p_{\text{HYA}} c_{\text{vit}}, \qquad \text{for } \vec{x} \in \partial\Omega_2, \tag{3.51}$$

$$-\vec{n} \cdot \nabla c_{\text{vit}} = 0, \qquad \text{for } \vec{x} \in \partial\Omega_3, \tag{3.52}$$

where $\vec{n}$ is the outward pointing normal and parameter definitions are given in Table 3.8. c_{ret} and c_{vit} have units of pM, and are defined over the various geometric regions of Figure 3.5. Even though the geometry of the aqueous has not been modelled, we can still estimate the concentration in this region by treating it as a well-mixed compartment. Given that the rate of turnover and flow within the aqueous humour is several orders of magnitude greater than that of the vitreous, this seems a reasonable assumption. Therefore the transport of drug into the aqueous is estimated by integrating over $\partial\Omega_2$, the anterior hyaloid membrane

of the vitreous (Equation 3.53):

$$\frac{\mathrm{d}c_{\mathrm{aq}}}{\mathrm{d}t} = \left(\frac{p_{\mathrm{hya}}}{V_{\mathrm{aq}}}\right) \int_{\partial\Omega_2} c_{\mathrm{vit}} \, \mathrm{d}S - \left(\frac{C_{\mathrm{L}}}{V_{\mathrm{aq}}}\right) c_{\mathrm{aq}}. \tag{3.53}$$

Up to this point all aspects of the model have been axisymmetric. This is beneficial for two major reasons, firstly the model can be more simply implemented in any chosen software, but more importantly, computation time will be significantly decreased, as 3D solutions can be derived from 2D axisymmetric solutions. Given that we simulate from the time of IVT injection, initially all drug will be within the vitreous, therefore suitable axisymmetric initial conditions would be a spherical region of non-zero concentration, with volume equivalent to that of the dose injection (centred on the line of rotational symmetry), or uniform initial concentration. In either case the integral over the vitreal domain at $t = 0$ would return a total amount of drug equivalent to that in the injected dose. We tested both of these initial conditions and found negligible difference, a temporal shift was found between the profiles on the order of the time for molecules to diffuse from the centre of the vitreous to the edge, such that at any time significantly greater than this scale the numerical solution using the uniform initial condition was within 97% the value of the solution with homogeneous initial conditions. Additionally in order to investigate the well-mixed assumption the timescale of the initial mixing is not of as much relevance as the longer timescale of drug elimination from the system, which, due to competing sinks at the anterior and posterior of the eye, is theorised to induce a concentration gradient across the vitreous. Therefore the following initial conditions were taken for the IVT PK solution:

$$c_{\mathrm{ret}}(\vec{x}, 0) = 0, \quad \forall \vec{x} \in \Omega_{\mathrm{ret}}, \tag{3.54}$$

$$c_{\mathrm{vit}}(\vec{x}, 0) = c_0, \quad \forall \vec{x} \in \Omega_{\mathrm{vit}}, \tag{3.55}$$

$$c_{\mathrm{aq}}(0) = 0, \tag{3.56}$$

where c_0 (pM) is the vitreal concentration corresponding to the initial dose, relative to the volume of the vitreous.

It remains to estimate the membrane permeabilities (p_{ILM}, p_{RPE} and p_{HYA}) and the vitreal and retinal diffusivities (D_{vit} and D_{ret}). As in Section 3.1, all permeabilities will be considered unknown and be estimated from the Gadkar et al. dataset [28]. The vitreal diffusion coefficient, D_{vit}, for a specific molecule, is calculated using the Stokes-Einstein relation (Equation 2.5). The retinal diffusion coefficient is then estimated following the approach of El-Kareh et al. [114], in which the effective diffusion coefficient for a tissue (D_{eff}) is related to the diffusion coefficient within the intercellular region (D_{int}) and the

proportion of the volume that is intercellular (ϕ, i.e. if a tissue is completely acellular $\phi = 1$). El-Kareh et al. gave the following approximation for D_{eff}:

$$D_{\text{eff}} \simeq D_{\text{int}} \left(\frac{2\phi}{3 - \phi} \right). \tag{3.57}$$

Gabhann et al. [115] extended this idea to consider two tissues, a and b. By assuming both tissues have the same intercellular diffusivity, they derived the following formula relating the effective diffusivities (D_{a} and D_{b}) of the two tissues:

$$D_{\text{a}} = D_{\text{b}} \left\{ \frac{\phi_a}{\phi_b} \right\} \left(\frac{3 - \phi_b}{3 - \phi_a} \right), \tag{3.58}$$

where ϕ_a and ϕ_b are the ϕ values for tissues a & b, respectively. If the vitreous is assumed to be entirely acellular ($\phi_{\text{vit}} = 1$) and the intercellular space of the retina is approximately 30% [115] ($\phi_{\text{ret}} = 0.3$), we deduce from 3.58 the following relationship between D_{ret} and D_{vit}, given by Equation 3.59.

$$D_{\text{ret}} = D_{\text{vit}} \left(\frac{2\phi_{\text{ret}}}{3 - \phi_{\text{ret}}} \right). \tag{3.59}$$

A summary of mechanistic model parameters can be found in Table 3.8.

Parameter	Value	Units	Description
p_{ILM}	Estimated	cm/sec	Permeability of the ILM
p_{RPE}	Estimated	cm/sec	Permeability of the RPE
p_{HYA}	Estimated	cm/sec	Permeability of the anterior hyaloid
D_{vit}	Equation 2.5	cm^2/sec	Diffusion coefficient in the vitreous
D_{ret}	Equation 3.59	cm^2/sec	Diffusion coefficient in the retina

Table 3.8: Mechanistic parameters for PDE model.

3.2.2 Translation from PDE to ODE

As stated at the start of this section, one of the objectives for this work was to build a model which, when spatially averaged assuming the well mixed assumption, reduces to the 3-compartment PK model of Section 3.1. We show that Equations 3.47-3.49 define such a system. We define the spatial average for the vitreous and retina as

$$\bar{c}_{\text{vit}} = \frac{1}{V_{\text{vit}}} \int_{\Omega_{\text{vit}}} c_{\text{vit}} \, \mathrm{d}V, \qquad \bar{c}_{\text{ret}} = \frac{1}{V_{\text{ret}}} \int_{\Omega_{\text{ret}}} c_{\text{ret}} \, \mathrm{d}V. \tag{3.60}$$

Therefore when applied to Equation 3.47 we find

$$\frac{\mathrm{d}\bar{c}_{\text{ret}}}{\mathrm{d}t} = \frac{1}{V_{\text{ret}}} \int_{\Omega_{\text{ret}}} \frac{\partial c_{\text{ret}}}{\partial t} \, \mathrm{d}V = \frac{1}{V_{\text{ret}}} \int_{\Omega_{\text{ret}}} D_{\text{vit}} \nabla^2 c_{\text{ret}} \, \mathrm{d}V \tag{3.61}$$

$$= \frac{1}{V_{\text{ret}}} \int_{\partial\Omega_{\text{ret}}} D_{\text{vit}} \nabla c_{\text{ret}} \cdot \vec{n} \, \mathrm{d}S \tag{3.62}$$

$$= -\frac{p_{\text{ILM}}}{V_{\text{ret}}} \left(\int_{\partial\Omega_1} \left[c_{\text{ret}} - c_{\text{vit}} \right] \, \mathrm{d}S \right) - \frac{p_{\text{RPE}}}{V_{\text{ret}}} \left(\int_{\partial\Omega_1^*} c_{\text{ret}} \, \mathrm{d}S \right), \tag{3.63}$$

and similarly when applied to Equation 3.46 we find

$$\frac{\mathrm{d}\bar{c}_{\mathrm{vit}}}{\mathrm{d}t} = \frac{1}{V_{\mathrm{vit}}}\int_{\Omega_{\mathrm{vit}}} \frac{\partial c_{\mathrm{vit}}}{\partial t}\,\mathrm{d}V = \frac{1}{V_{\mathrm{vit}}}\int_{\Omega_{\mathrm{vit}}} D_{\mathrm{vit}}\nabla^2 c_{\mathrm{vit}}\,\mathrm{d}V \tag{3.64}$$

$$= \frac{1}{V_{\mathrm{vit}}}\int_{\partial\Omega_{\mathrm{vit}}} D_{\mathrm{vit}}\nabla c_{\mathrm{vit}}\cdot\vec{n}\,\mathrm{d}S \tag{3.65}$$

$$= -\frac{p_{\mathrm{ILM}}}{V_{\mathrm{vit}}}\left(\int_{\partial\Omega_1}\left[c_{\mathrm{vit}} - c_{\mathrm{ret}}\right]\,\mathrm{d}S\right) - \frac{p_{\mathrm{HYA}}}{V_{\mathrm{vit}}}\left(\int_{\partial\Omega_2} c_{\mathrm{vit}}\,\mathrm{d}S\right). \tag{3.66}$$

Therefore, by making the well mixed assumption (i.e. $\bar{c}_{\mathrm{vit}} = c_{\mathrm{vit}}$), we derive the following results from Equations 3.63 and 3.66:

$$\frac{\mathrm{d}\bar{c}_{\mathrm{ret}}}{\mathrm{d}t} = -\left(\frac{S_{\mathrm{ret}}}{V_{\mathrm{ret}}}\right)\left[p_{\mathrm{ILM}} + p_{\mathrm{RPE}}\right]\bar{c}_{\mathrm{ret}} + \left(\frac{S_{\mathrm{ret}}}{V_{\mathrm{ret}}}\right)p_{\mathrm{ILM}}\bar{c}_{\mathrm{vit}} \tag{3.67}$$

$$\frac{\mathrm{d}\bar{c}_{\mathrm{vit}}}{\mathrm{d}t} = \left(\frac{S_{\mathrm{ret}}}{V_{\mathrm{vit}}}\right)p_{\mathrm{RPE}}\bar{c}_{\mathrm{ret}} - \left[\left(\frac{S_{\mathrm{ret}}}{V_{\mathrm{vit}}}\right)p_{\mathrm{ILM}} + \left(\frac{S_{\mathrm{aq}}}{V_{\mathrm{vit}}}\right)p_{\mathrm{HYA}}\right]\bar{c}_{\mathrm{vit}}. \tag{3.68}$$

If one defines the following parameter grouping:

$$k_{\mathrm{el}} = \left(\frac{S_{\mathrm{aq}}}{V_{\mathrm{vit}}}\right)p_{\mathrm{HYA}}, \tag{3.69}$$

then the system (Equations 3.67-3.68) can be rewritten in the well-mixed ODE form that was implemented in our previous analysis (as in Section 3.1), as follows:

$$\frac{\mathrm{d}\bar{c}_{\mathrm{ret}}}{\mathrm{d}t} = -\left(\frac{S_{\mathrm{ret}}}{V_{\mathrm{ret}}}\right)\left[p_{\mathrm{ILM}} + p_{\mathrm{RPE}}\right]\bar{c}_{\mathrm{ret}} + \left(\frac{S_{\mathrm{ret}}}{V_{\mathrm{ret}}}\right)p_{\mathrm{ILM}}\bar{c}_{\mathrm{ret}}, \tag{3.70}$$

$$\frac{\mathrm{d}\bar{c}_{\mathrm{vit}}}{\mathrm{d}t} = \left(\frac{S_{\mathrm{ret}}}{V_{\mathrm{vit}}}\right)p_{\mathrm{RPE}}\bar{c}_{\mathrm{ret}} - \left[\left(\frac{S_{\mathrm{ret}}}{V_{\mathrm{vit}}}\right)p_{\mathrm{ILM}} + k_{\mathrm{el}}\right]\bar{c}_{\mathrm{vit}}. \tag{3.71}$$

Equation 3.69 will be the focus of our study on the applicability of the well-mixed assumption. If we can show that our estimated values for p_{HYA}, when adjusted by a factor of $S_{\mathrm{ret}}/V_{\mathrm{ret}}$, match the values predicted for k_{el} in Section 3.1 (along with p_{ILM} and p_{RPE}), then it would add support towards the validity of the well-mixed assumption.

3.2.3 Estimation of retinal and hyaloidal membrane permeabilities using 3-compartment ocular PK data

We utilized data from a recent study by Gadkar et. al. [28], detailing the time courses in the retina, vitreous and aqueous, for a number of antibodies and antibody fragments, following IVT injection. The study was performed in rabbits using molecules derived from a human anti-glycoprotein D (anti-gD) antibody, and hence, inert in a rabbit model, forgoing the need to account for pharmacodynamic (PD) effects. The particular datasets analysed in this study were for Fab, Fc, IgG and IgG null molecules (noting that IgG null molecules are IgG molecules with fragment crystallizable (Fc) region mutations that prevent binding

to neonatal Fc receptor (FcRn)), whose respective parameter values can be found in Table 3.9. Retinal, vitreous and aqueous antibody concentrations were measured at 0.25, 2, 8, 14, 21 and 28 days, excluding the Fc dataset wherein only vitreous and aqueous data were available. The Fab dataset contains retinal data not reported as part of the original study [28], but provided as an additional dataset by Gadkar et. al. and Genentech.

Using this dataset we performed an analysis analogous to that presented in the previous section, and as presented in Section 3.1. As the dataset from Gadkar et al. [28] neglects spatial variation, and focuses on the anatomical regions of the retina, vitreous and aqueous, the average model concentrations for the retina and vitreous, obtained from the spatial model by integrating over the relevant volumes, were fitted to the experimental data. When fitting the model we varied the parameters p_{RPE}, p_{ILM} and p_{HYA}, with all other parameters fixed. The free parameters were optimized by penalizing the relative mean-square error between the logarithmic values of model results and the data, using `lsqnonlin` [86] (part of MATLAB's optimization toolbox). Confidence intervals were generated using a bootstrap algorithm with re-sampling [101, 102].

Antibody	Molecular weight (kDa)	Hydrodynamic radius (nm)	Initial dose (mg)*
Fab	50	3.04	0.615
IgG	150	5.30	0.549
IgG null	150	5.30	0.75

Table 3.9: Summary of biophysical properties of antibody and antibody fragments. Weights and doses taken from Gadkar et. al. [28], hydrodynamic radii (R_{h}) taken from the meta-analysis detailed in Appendix A.6. *Doses correspond to experimental protocol except for IgG null which was estimated from initial vitreous concentrations assuming a vitreal volume of 1.52 mL.

We found upon fitting the model to the data, that the spatial average of the model acted as a single exponential function (past early time), decaying at a constant rate. This profile matches the PK observed within the data, and additionally it corresponds to the exponential behaviour exhibited by the ODE solution. The best fit solutions for each molecule, alongside their respective experimental data, can be seen in Figure 3.7.

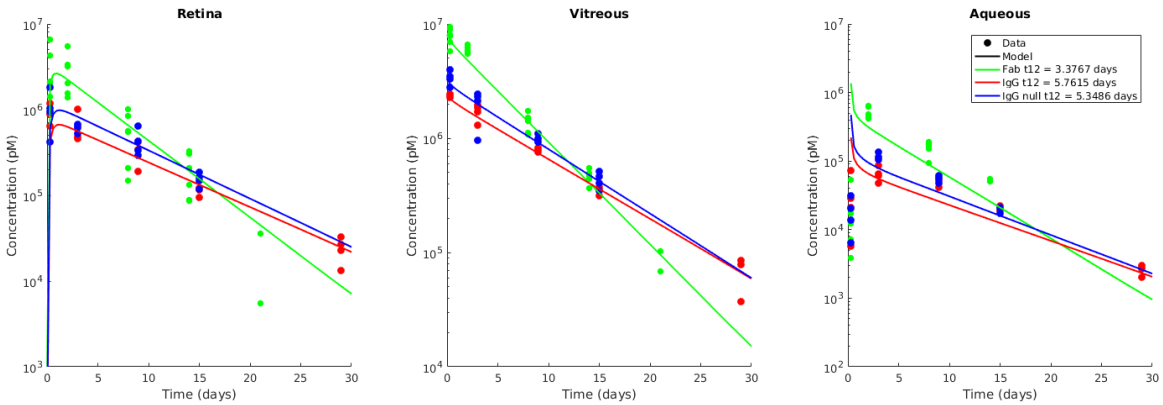

Figure 3.7: Compilation of optimized fits of the PDE model (Equations 3.46-3.52) to the dataset [28]. Coloured markers indicate distinct molecule datasets, whereas coloured lines show the optimized fit. For Fc molecules there were no retina data available, only vitreous and aqueous humour concentrations.

Figure 3.8 shows a heat-map for the concentration of Fab molecules, using best fit parameters, 15 days post IVT injection. This simulation demonstrates that the concentration gradient across the vitreous varies by roughly 1/2 an order of magnitude, being lowest at the anterior hyaloid membrane, and greatest at the most posterior region of the retina. Similarly the retinal concentration, which was found to be relatively constant in the radial direction, can be seen plotted versus θ ($\theta = 0$ represents the furtherest point from the lens), in Figure 3.9. In the θ direction along the retina there is a drop in concentration, by approximately a factor of 3. This appears to be due to the concentration drop in the neighbouring vitreous body. All molecules, post-initial transient behaviour, exhibited similar spatial distributions, and hence similar vitreal and retinal concentration gradients. This is likely due to their similar diffusion coefficients and membrane permeabilities (see Table 3.10).

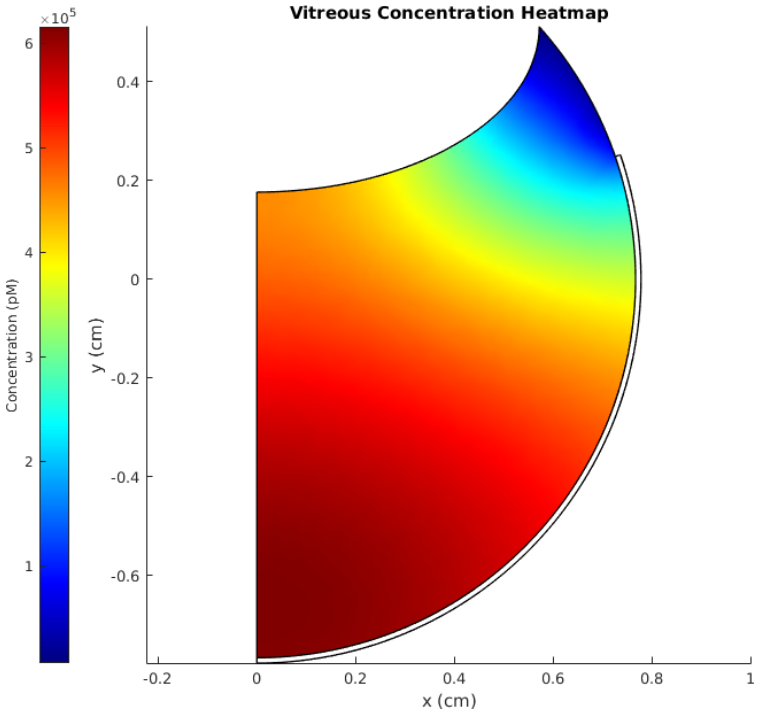

Figure 3.8: Concentration heat-map for Fab molecule IVT PK simulation, at $t = 15$ days. Best fit parameters were used.

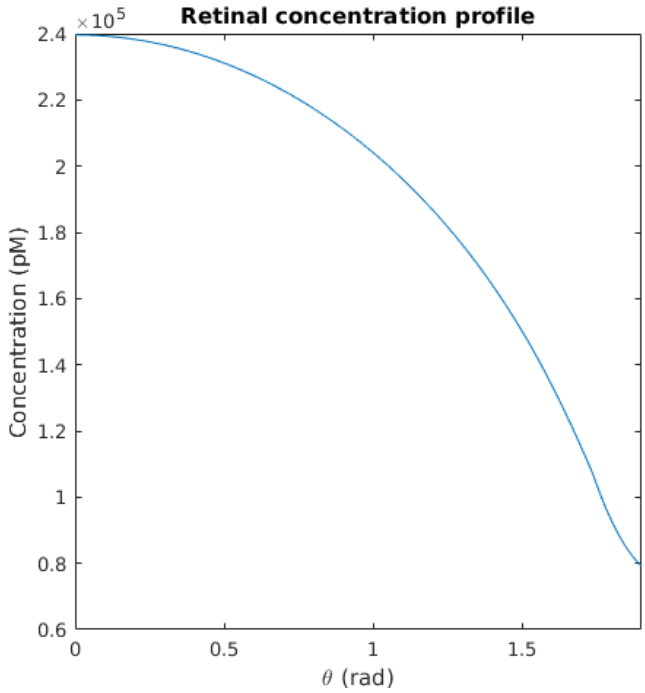

Figure 3.9: Angular variation in concentration profile (where $\theta = 0$ represents the further point from the lens) for Fab molecule IVT PK simulation, at $t = 15$ days. Best fit parameters were used.

Parameter	Best fit parameter value (95% confidence interval)			Units
	Fab	IgG	IgG null	
p_{HYA}	1.91 (1.24, 3.92)	0.874 (0.616, 1.42)	1.72 (0.604, 2.27)	$\times 10^{-5}$ cm/sec
p_{RPE}	2.48 (2.2, 5.35)	2.31 (1.76, 2.98)	2.03 (1.76, 3.55)	$\times 10^{-7}$ cm/sec
p_{ILM}	1.81 (1.25, 2.44)	1.19 (1.12, 1.55)	1.24 (0.922, 1.91)	$\times 10^{-7}$ cm/sec
$t_{1/2}$	3.38	5.76	5.35	days

Table 3.10: Best fit parameter summary, including 95% confidence intervals, obtained via Monte Carlo simulations using error bootstrapping [101, 102].

3.2.4 Comparison of parameter estimation and spatially averaged behaviour of mathematically similar PDE and ODE ocular PK models

Figure 3.10 shows how the estimated values for $p_{\mathrm{HYA}}, p_{\mathrm{RPE}}$ and p_{ILM}, given in Table 3.10, for Fab, IgG and IgG null molecules, depend on their respective hydrodynamic radii, and how these values compare with our earlier estimates of these parameters, derived by fitting the analogous 3-compartment ODE model (Equations 3.70-3.71). We note that the 3-compartment ODE model did not estimate p_{HYA}; it instead estimated the parameter k_{el}. However by using Equation 3.69 (derived by spatially averaging the PDE model) we can estimate values equivalent for p_{HYA}, assuming Equation 3.69 holds. If the ODE model is a good approximation of the PDE model then we would expect the permeability values predicted by the ODE model to match those predicted by fitting the same dataset to the PDE model.

As can be seen from Figure 3.10 there is good agreement between the estimated values for p_{RPE} and p_{ILM} in the PDE and ODE cases. This may lead one to conclude that the ODE model is a good approximation of the PDE model.

However, a major difference in predictions between the PDE and ODE models is found in the estimations for the permeability of the hyaloid membrane, p_{HYA}. Figure 3.10 shows that the predictions for p_{HYA} from the PDE model are an order of magnitude higher than those derived using Equation 3.69. Given that both models were fit to the same dataset, and both fit the data well, this would imply that the order of magnitude difference between the predicted value of p_{HYA} in the ODE case relative to the PDE case is compensating for a fundamental inconsistency between the two models within the parameter regimes considered. Given that the only assumption made in reducing the PDE model to the ODE model was the well-mixed assumption, this must be the cause for this disparity. As the predicted values for p_{RPE} and p_{ILM} are relatively similar between both models, this leads us to deduce that we cannot interpret k_{el} in terms of a hyaloid membrane permeability, and

hence estimates for k_{el} derived from fitting an ODE model to data should be treated as a phenomenological parameter.

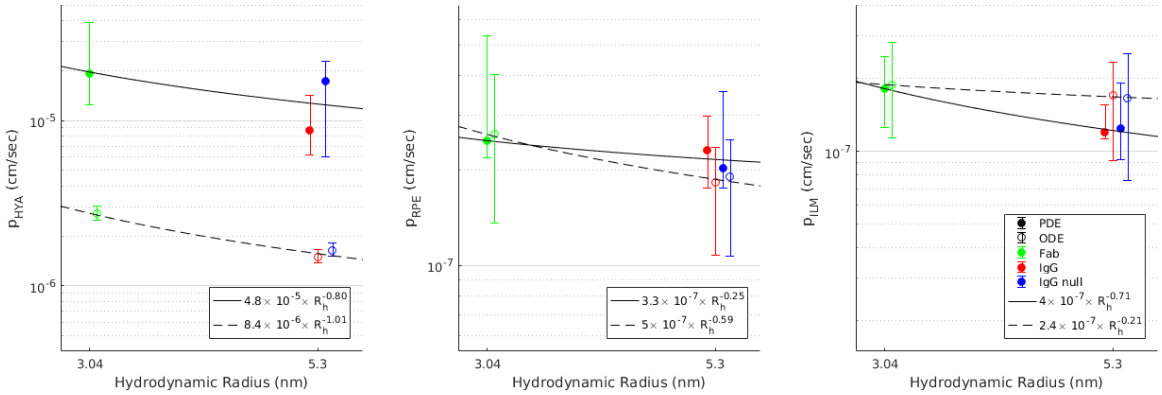

Figure 3.10: Best fit parameters plotted with respect to hydrodynamic radius (R_{h}) using the PDE model, Equations 3.46-3.52 (solid markers/line), and the estimates generated previously using the analogous ODE model, Equations 3.1-3.3 (empty markers and dashed line). The value for p_{HYA} ascribed to the ODE model was generated by using Equation 3.69. Error bars represent 95% confidence intervals obtained via Monte Carlo simulations using error bootstrapping [101, 102]. Power law fits, with respect to R_{h}, are shown by the solid lines, the equations of which are given in each subplots legend. Rh values for Fab, IgG, and IgG null molecules were taken from the meta-analysis in Appendix A.6. Power laws were chosen here as a means to interpolate within the region of interest. Note, power laws differ slightly from Hutton-Smith et al. 2017 [75] as they have been fit using adjusted R_{h} from Appendix A.6.

Before continuing, we note that it is natural to anticipate a discrepancy between results from PDE and ODE models, as molecules in the PDE framework must diffuse to the hyaloid boundary before permeating through it. Hence a higher value of p_{HYA} must be used in the PDE model (relative to the ODE model) to generate the concentration found in aqueous dataset. Molecules in the ODE simulation, where the system is assumed to be well-mixed, have an effectively infinite diffusion coefficient, and hence would require a lower value for p_{HYA} in order to match the aqueous dataset. The same effect is not seen with the predicted retinal permeabilities. It seems unlikely that the same principle does not apply to the estimated value p_{ILM}, however given the uncertainty in its value (see error bars in Figure 3.10) and the similarity of its estimation between the ODE and PDE model, this is not evident. From Figure 3.11 we can see that the PDE estimations for p_{HYA} are approximately two orders of magnitude greater than the estimations for p_{RPE} and p_{ILM}. This would imply that the previously accepted notion (in Saunders et al. [3] for example) that transport is much easier through the anterior of the vitreous into the aqueous than through the retina and into the choroid is reasonable. If we accept for the moment that the majority of flux out of the vitreous occurs via the anterior hyaloid membrane, then it would seem plausible

that this would cause p_{HYA} (and hence k_{el}) to be the most sensitive (relative to p_{RPE} and p_{ILM}) to the rate of diffusion within the vitreous.

Given these results we conclude that estimates for k_{el}, and their corresponding values for p_{HYA} (derived via Equation 3.69), found by fitting the ODE model to data contain information about the diffusional timescale and the permeability of the anterior hyaloid membrane. This suggests that the well-mixed assumption is not a valid assumption to make from a purely mechanistic perspective, however this does not rule out the applicability of well-mixed ODE models, only that estimates for the parameter k_{el} currently lack a mechanistic interpretation.

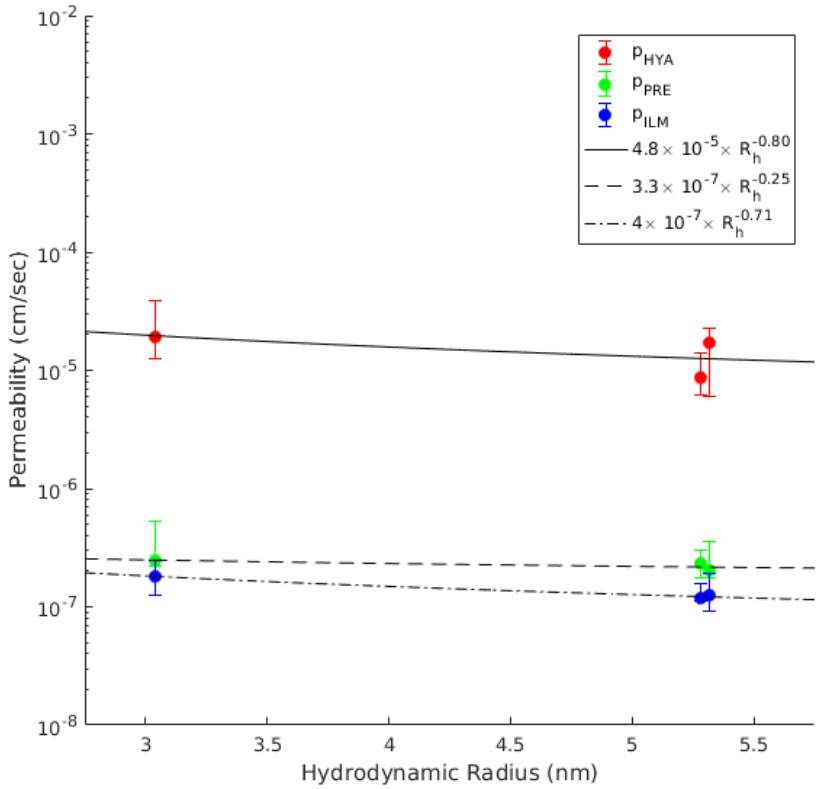

Figure 3.11: Plot showing how best fit parameters, derived from the PDE model (Equations 3.46-3.52), vary with the hydrodynamic radius (R_{h}). This figure contains identical data to Figure 3.10, however permeabilities are plotted relative to each other to highlight their relative orders of magnitude.

3.2.5 Analysis of the well mixed assumption

Even if the ODE model parameter k_{el} has to be treated phenomenologically, the ODE model may still have predictive power. We will investigate this by comparing the estimated

values of the half-life, predicted by the ODE and PDE models. We will assume that the membrane permeabilities of the rabbit are similar to those of the human, and hence use the power laws shown in Figure 3.10 to simulate the permeabilities of the domains $\partial\Omega_1, \partial\Omega_1^*$ and Ω_2 in the human geometry. The power laws for $p_{\mathrm{HYA}}, p_{\mathrm{RPE}}$ and p_{ILM} predicted by fitting the Gadkar et al. dataset [28] to the PDE and ODE model are given by Equations 3.72-3.74 and Equations 3.75-3.77, respectively:

$$p_{\mathrm{HYA}}^{(\mathrm{PDE})} = 4.8 \times 10^{-5} \times R_{\mathrm{h}}^{-0.80}, \tag{3.72}$$

$$p_{\mathrm{RPE}}^{(\mathrm{PDE})} = 3.3 \times 10^{-7} \times R_{\mathrm{h}}^{-0.25}, \tag{3.73}$$

$$p_{\mathrm{ILM}}^{(\mathrm{PDE})} = 4.0 \times 10^{-7} \times R_{\mathrm{h}}^{-0.71}, \tag{3.74}$$

$$p_{\mathrm{HYA}}^{(\mathrm{ODE})} = 8.4 \times 10^{-6} \times R_{\mathrm{h}}^{-1.01}, \tag{3.75}$$

$$p_{\mathrm{RPE}}^{(\mathrm{ODE})} = 5.0 \times 10^{-7} \times R_{\mathrm{h}}^{-0.59}, \tag{3.76}$$

$$p_{\mathrm{ILM}}^{(\mathrm{ODE})} = 2.4 \times 10^{-7} \times R_{\mathrm{h}}^{-0.21}. \tag{3.77}$$

In order to extend the rabbit ODE model (Equations 3.70-3.71) to describe human geometry, new values for the geometric parameters $V_{\mathrm{vit}}, V_{\mathrm{ret}}, S_{\mathrm{ret}}$ and S_{aq} were calculated using the expressions found in Table 3.7. We will consider the half-life ($t_{1/2}$) values for molecules in the human geometry over a range of hydrodynamic radii (which fall within the interpolated region of the molecules in the Gadkar et al. dataset [28]). We first simulate both the PDE and ODE models with human geometrical parameters, using Equations 3.72-3.74 to determine the permeabilities, with the conversion from p_{HYA} to k_{el} given by Equation 3.69 with human geometrical parameters. Analogous ODE simulations were conducted using Equations 3.75-3.77, as well as PDE simulations over a range of D_{vit} values. These results are presented in Figure 3.12.

In Figure 3.12, the red line shows the $t_{1/2}$ values predicted by the PDE model using human geometry and Equations 3.72-3.74. These values for $t_{1/2}$ lie in the biologically reasonable range of 6-11 days. The blue line summarises the results from the ODE model being run with the same permeability interpolation. However, in the ODE model, the hyaloid permeability is a phenomenological parameter containing information about both the hyaloid membrane permeability and the timescale of diffusion. The latter is not compensated for in the PDE interpolation and hence the ODE prediction (blue line) corresponds to a much shorter, and biologically unrealistic, $t_{1/2}$. Next, we consider the effect of increasing the value of D_{vit} in the PDE model, while keeping all other parameters fixed. We see that convergence occurs between the predictions of the ODE and PDE models converge as $D_{\mathrm{vit}} \to \infty$. However, the difference between the red and blue solid lines indicates that for values of D_{vit}

corresponding to therapeutic molecules ($\sim 10^{-6}$ cm^2/sec) the well mixed assumption is not physically realistic for modelling large molecules.

The dashed blue line shows estimates of $t_{1/2}$ when the ODE model is calibrated against the Gadkar et al. dataset [28] via Equations 3.75-3.77. We conclude that even though the well-mixed assumption does not hold, if the ODE model is calibrated to an appropriate dataset, it can generate similar predictions as the PDE model, when geometrically scaled between species.

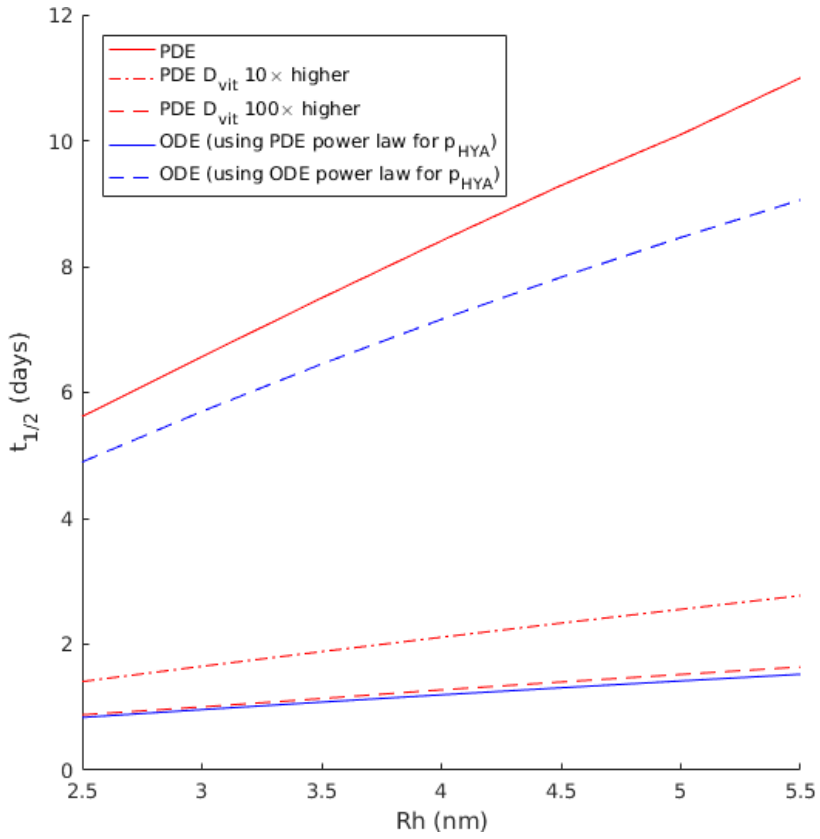

Figure 3.12: Half-life values predicted for the human PDE (red) and ODE model (blue). The solid line uses Equations 3.72-3.74), other red lines use the same parameters aside from D_{vit}, which is scaled by two orders of magnitude. The solid blue line generates parameter values using Equations 3.72-3.74 (derived from fitting the PDE model), whereas the dashed blue line uses Equations 3.75-3.77 (derived from fitting the ODE model).

We will now compare the estimates of $t_{1/2}$ generated from the ODE and PDE models to experimental data. Appendix A.6 details $t_{1/2}$ values for Fab, Fab-dimer (Fab') and IgG molecules in the human and rabbit eye, as well as their reported hydrodynamic radii (R_{h}). In order to compare these values cross species in a meaningful manner, we compare the

predicted $t_{1/2}$ values to their respective vitreal diffusion timescale, T_{diff}, the average time for a particle in the centre of the vitreous to reach the extremity of the vitreous. This value is calculated using the Brownian motion description of the mean square displacement of a particle in three dimensions:

$$T_{\text{diff}} = \frac{r_0^2}{6D_{\text{vit}}}, \tag{3.78}$$

where r_0 is the radius of the vitreous. The values for T_{diff} in the human/rabbit vitreous for Fab, Fab' and IgG are given Table 3.11 - interestingly, due to the relative sizes of the human and rabbit vitreous bodies, T_{diff} for IgG molecules in the rabbit eye is predicted to be similar to that of a Fab molecule in the human eye. Table 3.11 also gives the predicted $t_{1/2}$ for each molecule in the human and rabbit eye (these values are also plotted versus their respective T_{diff} values in Figure 3.13).

Molecule	Rabbit			Human		
	T_{diff} (days)	$t_{1/2}$ (days)		T_{diff} (days)	$t_{1/2}$ (days)	
		PDE	ODE		PDE	ODE
Fab	1.07	3.37	3.07	1.82	6.64	5.71
Fab'	1.39	4.22	3.88	2.35	8.27	7.14
IgG	1.87	5.52	5.1	3.18	10.6	9.28

Table 3.11: Vitreous diffusion timescale (T_{diff}) and half-life values ($t_{1/2}$) corresponding to Figure 3.13.

From Figure 3.13, we can see that both the PDE and ODE models predict values for $t_{1/2}$ that lie within approximately one standard deviation from the mean of available $t_{1/2}$ data. This shows that through calibration to a dataset of a species similar to human (here rabbit), it is possible to build a model that accurately reflects the half-life observed in humans through clinical testing. The predictions of both the ODE and PDE model seem to have similar levels of accuracy. For example, the root mean square error (RMSE) between the PDE predictions for human $t_{1/2}$ values is 1.30 days, whereas for the ODE it is 1.49 days.

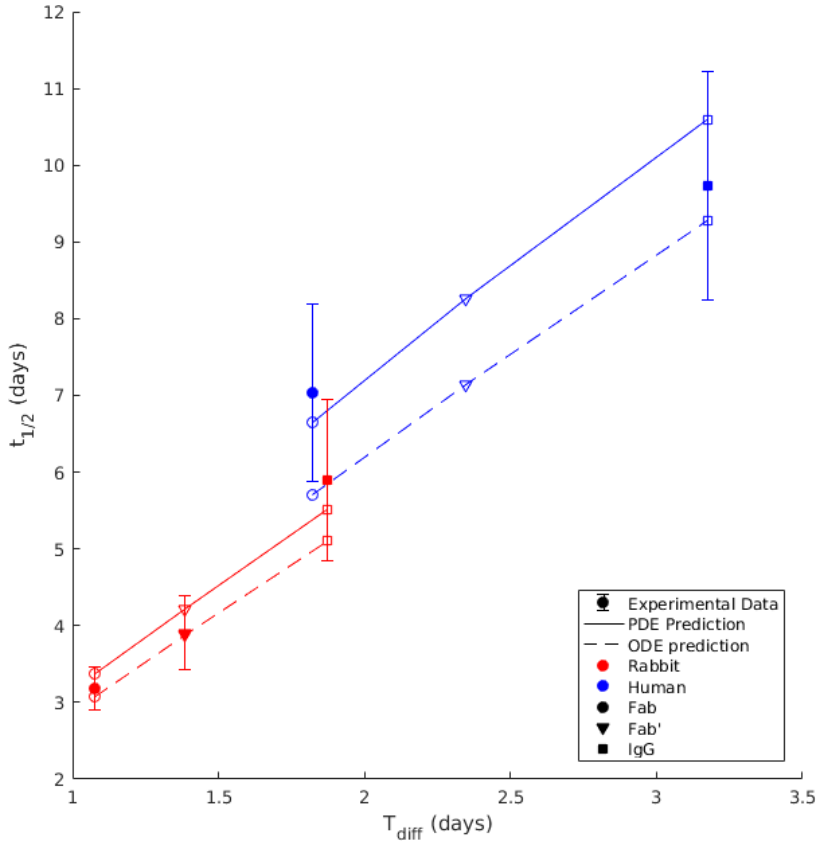

Figure 3.13: A comparison of the predicted $t_{1/2}$ values obtained from the PDE and ODE models to ocular half-life data available in the literature. Error bars represent ±SD from the mean from half-life experimental/clinical data collated in Appendix A.6. PDE and ODE models generated permeability parameter values using Equations 3.72-3.74 and Equations 3.75-3.77, respectively.

3.2.6 One-dimensional caricature PDE model analysis

The geometry presented in Figure 3.5, while less anatomically accurate than Missel's work [69], is still detailed to the point that Equations 3.46-3.53 cannot be solved explicitly. In order to make analytical progress we now simplify the geometry. We present in Figure 3.14 a one-dimensional (1D) representation of the vitreous and retina, from which Equations

3.47-3.49 can be reduced to the following 1D forms, given by Equations 3.79-3.84:

$$\frac{\partial c_{\text{ret}}}{\partial t} = D_{\text{ret}} \frac{\partial^2 c_{\text{ret}}}{\partial x^2}, \qquad \text{for } x \in [-\varepsilon, 0],\ t > 0, \tag{3.79}$$

$$\frac{\partial c_{\text{vit}}}{\partial t} = D_{\text{vit}} \frac{\partial^2 c_{\text{vit}}}{\partial x^2}, \qquad \text{for } x \in [0, r_0],\ t > 0, \tag{3.80}$$

$$D_{\text{ret}} \frac{\partial c_{\text{ret}}}{\partial x} = p_{\text{RPE}} c_{\text{ret}}, \qquad \text{for } x = -\varepsilon,\ t > 0, \tag{3.81}$$

$$-D_{\text{ret}} \frac{\partial c_{\text{ret}}}{\partial x} = p_{\text{ILM}} \left(c_{\text{ret}} - c_{\text{vit}} \right), \qquad \text{for } x = 0,\ t > 0, \tag{3.82}$$

$$D_{\text{vit}} \frac{\partial c_{\text{vit}}}{\partial x} = p_{\text{ILM}} \left(c_{\text{vit}} - c_{\text{ret}} \right), \qquad \text{for } x = 0,\ t > 0, \tag{3.83}$$

$$-D_{\text{vit}} \frac{\partial c_{\text{vit}}}{\partial x} = p_{\text{HYA}} c_{\text{vit}}, \qquad \text{for } x = r_0,\ t > 0, \tag{3.84}$$

with initial conditions:

$$c_{\text{ret}}(0) = 0, \qquad \text{for } x \in [-\varepsilon, 0] \tag{3.85}$$

$$c_{\text{vit}}(0) = c_0, \qquad \text{for } x \in [0, r_0]. \tag{3.86}$$

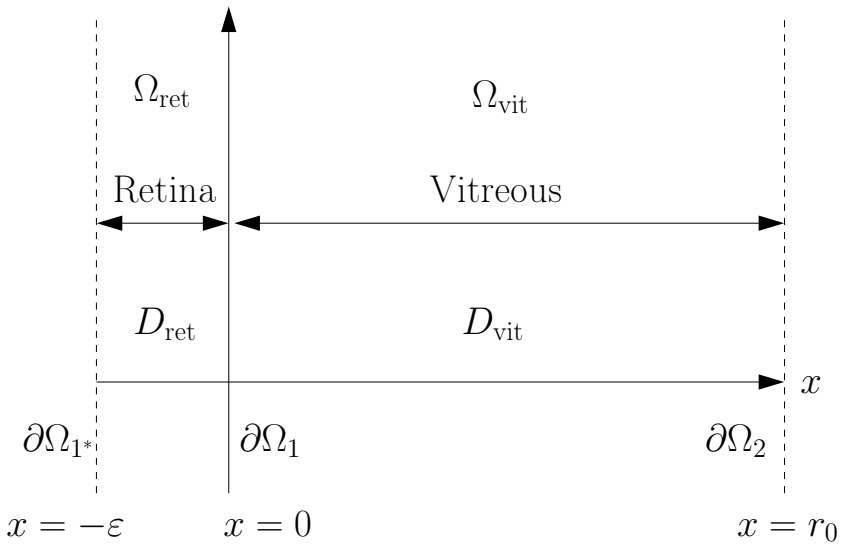

Figure 3.14: An idealised representation of the mammalian eye. Within this one-dimensional model the vitreous and retina are represented by domains Ω_{vit} and Ω_{ret}, respectively, with the inner limiting membrane (ILM), sub-retinal space, and anterior hyaloid membrane represented by boundaries $\partial\Omega_1, \partial\Omega_1^*$ and $\partial\Omega_2$, respectively.

1D well-mixed reduction

The well-mixed analogue of Equations 3.47-3.49 is given by the following equations

$$\frac{\mathrm{d}\bar{c}_{\text{ret}}}{\mathrm{d}t} = -\frac{1}{\varepsilon} \left[p_{\text{RPE}} + p_{\text{ILM}} \right] \bar{c}_{\text{ret}} + \frac{1}{\varepsilon} p_{\text{ILM}} \bar{c}_{\text{vit}} \tag{3.87}$$

$$\frac{\mathrm{d}\bar{c}_{\text{vit}}}{\mathrm{d}t} = \frac{1}{r_0} p_{\text{ILM}} \bar{c}_{\text{ret}} - \frac{1}{r_0} \left[p_{\text{ILM}} + p_{\text{HYA}} \right] \bar{c}_{\text{vit}} \tag{3.88}$$

where

$$\bar{c}_{\text{vit}} = \frac{1}{r_0}\int_0^{r_0} c_{\text{vit}}\ \mathrm{d}V, \qquad \bar{c}_{\text{ret}} = \frac{1}{\varepsilon}\int_{-\varepsilon}^{0} c_{\text{ret}}\ \mathrm{d}V. \tag{3.89}$$

Additionally we note that the decay rate of the 1D well-mixed system, $\bar{\lambda}$, can be expressed as:

$$\bar{\lambda} \simeq \left(\frac{p_{\text{HYA}}}{r_0}\right) + \left(\frac{p_{\text{ILM}}}{r_0}\right) - \frac{1}{1+\frac{p_{\text{RPE}}}{p_{\text{ILM}}}}\left(\frac{p_{\text{ILM}}}{r_0}\right) \tag{3.90}$$

$$= \left(\frac{\frac{1}{p_{\text{RPE}}}+\frac{1}{p_{\text{ILM}}}+\frac{1}{p_{\text{HYA}}}}{\frac{1}{p_{\text{RPE}}}+\frac{1}{p_{\text{ILM}}}}\right)\frac{p_{\text{HYA}}}{r_0}. \tag{3.91}$$

1D dimensional solution: non-dimensionalisation

Before solving Equations 3.79-3.84, we first non-dimensionalise them using the following rescalings:

$$c_{\text{ret}} = c_0 u, \quad c_{\text{vit}} = c_0 v, \quad x = r_0 z, \quad t = \left(\frac{r_0^2}{D_{\text{ret}}}\right)\tau, \tag{3.92}$$

giving:

$$\frac{\partial u}{\partial \tau} = \frac{\partial^2 u}{\partial z^2}, \qquad \text{for } z \in [-\delta, 0],\ \tau > 0, \tag{3.93}$$

$$\frac{\partial v}{\partial \tau} = \Delta\frac{\partial^2 v}{\partial z^2}, \qquad \text{for } z \in [0, 1],\ \tau > 0, \tag{3.94}$$

$$\frac{\partial u}{\partial z} = Au, \qquad \text{for } z = -\delta,\ \tau > 0, \tag{3.95}$$

$$\frac{\partial u}{\partial z} = B\left(v - u\right), \qquad \text{for } z = 0,\ \tau > 0, \tag{3.96}$$

$$\frac{\partial v}{\partial z} = C\left(v - u\right), \qquad \text{for } z = 0,\ \tau > 0, \tag{3.97}$$

$$\frac{\partial v}{\partial z} = -Dv, \qquad \text{for } q = 1,\ \tau > 0, \tag{3.98}$$

where:

$$\Delta = \frac{D_{\text{vit}}}{D_{\text{ret}}}, \quad \delta = \frac{\varepsilon}{r_0}, \tag{3.99}$$

$$A = \frac{r_0 p_{\text{RPE}}}{D_{\text{ret}}}, \quad B = \frac{r_0 p_{\text{ILM}}}{D_{\text{ret}}}, \quad C = \frac{r_0 p_{\text{ILM}}}{D_{\text{vit}}}, \quad D = \frac{r_0 p_{\text{HYA}}}{D_{\text{vit}}}. \tag{3.100}$$

Here we note that we have chosen to rescale t relative to a diffusional timescale, and that we may interpret the constants A, B, C and D as the rate of transport across a membrane, relative to the diffusional timescale; i.e for A we see:

$$A = \left(\frac{p_{\text{RPE}}}{r_0}\right) \Big/ \left(\frac{D_{\text{ret}}}{r_0^2}\right). \tag{3.101}$$

1D dimensional solution: decoupling of the retina

We note here that as the length scale of the retina is much smaller than that of the vitreous, the non-dimensional constant $\delta \ll 1$. Let us next scale z relative to this length scale, by taking $z = \delta q$, and considering the slow timescale T, where $\tau = \delta T$. Then, our retinal equations become:

$$\delta \frac{\partial u}{\partial T} = \frac{\partial^2 u}{\partial q^2}, \qquad \text{for } q \in [-1, 0],\ T > 0, \tag{3.102}$$

$$\frac{\partial u}{\partial q} = \delta A u, \qquad \text{for } q = -1,\ T > 0, \tag{3.103}$$

$$\frac{\partial u}{\partial q} = \delta B \left(v - u \right), \qquad \text{for } z = 0,\ T > 0. \tag{3.104}$$

We seek solutions to Equations 3.102-3.104 of the following form:

$$u = u_0 + \delta u_1 + O(\delta^2), \tag{3.105}$$

which, upon substitution in Equations 3.102-3.104, gives:

$$\delta \frac{\partial u_0}{\partial T} + \delta^2 \frac{\partial u_1}{\partial T} = \frac{\partial^2 u_0}{\partial q^2} + \delta \frac{\partial^2 u_1}{\partial q^2}, \qquad \text{for } q \in [-1, 0],\ T > 0. \tag{3.106}$$

$$\frac{\partial u_0}{\partial q} + \delta \frac{\partial u_1}{\partial q} = \delta A u_0 + \delta^2 A u_1, \qquad \text{for } q = -1,\ T > 0, \tag{3.107}$$

$$\frac{\partial u_0}{\partial q} + \delta \frac{\partial u_1}{\partial q} = \delta B v - \delta B u_0 - \delta^2 B u_1, \qquad \text{for } q = 0,\ T > 0. \tag{3.108}$$

To $O(1)$ this gives

$$0 = \frac{\partial^2 u_0}{\partial q^2} \qquad \text{for } q \in [-1, 0],\ T > 0. \tag{3.109}$$

$$\frac{\partial u_0}{\partial q} = 0, \qquad \text{for } q = -1,\ T > 0, \tag{3.110}$$

$$\frac{\partial u_0}{\partial q} = 0, \qquad \text{for } q = 0,\ T > 0, \tag{3.111}$$

and to $O(\delta)$:

$$\frac{\partial u_0}{\partial T} = \frac{\partial^2 u_1}{\partial q^2}, \qquad \text{for } q \in [-1, 0],\ T > 0. \tag{3.112}$$

$$\frac{\partial u_1}{\partial q} = A u_0, \qquad \text{for } q = -1,\ T > 0, \tag{3.113}$$

$$\frac{\partial u_1}{\partial q} = B v - B u_0, \qquad \text{for } q = 0,\ T > 0. \tag{3.114}$$

Integrating Equation 3.109 gives:

$$\frac{\partial u_0}{\partial q} = \int \frac{\partial^2 u_0}{\partial q^2}\,\mathrm{d}q = f(T) \tag{3.115}$$

$$\left.\frac{\partial u_0}{\partial q}\right|_{q=-1} = 0 = \left.\frac{\partial u_0}{\partial q}\right|_{q=0} \quad \Rightarrow \quad \frac{\partial u_0}{\partial q} = 0, \quad \forall q \in [-1, 0] \tag{3.116}$$

$$\Rightarrow \quad u_0 = u_0(T), \tag{3.117}$$

$$\tag{3.118}$$

therefore u_0 is a function solely of T. Next, we find by integrating 3.112:

$$\frac{\partial u_0}{\partial T} = \int_{-1}^{0} \frac{\partial u_0}{\partial T}\,\mathrm{d}q = \left.\frac{\partial u_1}{\partial q}\right|_{q=0} - \left.\frac{\partial u_1}{\partial q}\right|_{q=-1}, \tag{3.119}$$

therefore:

$$\frac{\partial u_0}{\partial T} = -(A+B)u_0 + Bv|_{q=0}. \tag{3.120}$$

Therefore we find by integrating this equation that:

$$\frac{\partial}{\partial T}\left(u_0 \mathrm{e}^{(A+B)T}\right) = Bv(q,T)|_{q=0}\mathrm{e}^{(A+B)T}, \tag{3.121}$$

$$\Rightarrow \quad u_0 = \underbrace{u_0(0)\mathrm{e}^{-(A+B)T}}_{=0} + B\mathrm{e}^{-(A+B)T}\int_0^T \mathrm{e}^{(A+B)s} v(q,s)|_{q=0}\,\mathrm{d}s \tag{3.122}$$

$$= B\int_0^T v(q,s)|_{q=0}\mathrm{e}^{(A+B)(s-T)}\,\mathrm{d}s. \tag{3.123}$$

Let us expand $v(q,s)|_{q=0}$ near T, for $s < T$, giving:

$$v(q,s)|_{q=0} = v(q,s=T)|_{q=0} + v'(q,s=T)|_{q=0}(s-T) + \cdots \tag{3.124}$$

which upon substitution into u_0 gives:

$$u_0 = B\int_0^T \left\{v(q,s=T)|_{q=0} + v'(q,s=T)|_{q=0}(s-T) + \cdots\right\}\mathrm{e}^{(A+B)(s-T)}\,\mathrm{d}s, \tag{3.125}$$

which, via the substitution $T - s = p$, may be rewritten

$$u_0 = -B\int_T^0 \{v - v'p + \cdots\}\,\mathrm{e}^{-(A+B)p}\,\mathrm{d}p \tag{3.126}$$

$$= B\int_0^T \{v - v'p + \cdots\}\,\mathrm{e}^{-(A+B)p}\,\mathrm{d}p \tag{3.127}$$

$$= Bv\int_0^T \left\{1 - \left(\frac{v'}{v}\right)p + \cdots\right\}\mathrm{e}^{-(A+B)p}\,\mathrm{d}p \tag{3.128}$$

$$= \left(\frac{B}{A+B}\right)v\left[\left\{\left(\frac{1+(A+B)p}{A+B}\right)\frac{v'}{v} - 1\right\}\mathrm{e}^{-(A+B)p} + \cdots\right]_0^T \tag{3.129}$$

$$= \left(\frac{B}{A+B}\right)v\left[\left\{1 - \mathrm{e}^{-(A+B)T}\right\} + \frac{1}{A+B}\left\{(1+(A+B)T)\,\mathrm{e}^{-(A+B)T} - 1\right\}\frac{v'}{v} + \cdots\right], \tag{3.130}$$

where v is evaluated at $s = T$, i.e. $v = v(0,T) = v(q, s = T)|_{q=0}$ and $v' = v'(0,T) = v'(q, s = T)|_{q=0}$. Therefore, in terms of τ, u_0 can be written:

$$u_0 = \left(\frac{B}{A+B}\right) v \left[\left\{1 - \mathrm{e}^{-(A+B)\tau/\delta}\right\} + \frac{1}{A+B}\left\{(1+(A+B)T)\,\mathrm{e}^{-(A+B)\tau/\delta} - 1\right\}\frac{v'}{v} + \cdots\right] \tag{3.131}$$

$$\to \left(\frac{B}{A+B}\right) v \left[1 - \frac{1}{A+B}\left(\frac{v'}{v}\right) + \cdots\right], \quad \text{as } \tau/\delta \to \infty \tag{3.132}$$

for τ sufficiently large to ensure $\exp(-(A+B)\tau/\delta) \ll 1$, which as $A, B \sim O(1)$, means $\tau \gg \delta$. To estimate the error in this expression we proceed to introduce the following ansatz for $v(q,\tau)$, specifically that $\int_0^1 v(q,\tau)\,\mathrm{d}q$ and $v(0,\tau)$ decay exponentially with rate $\mu \sim O(1)$. This ansatz is justified by the numerical solution for $\int_0^1 v(q,\tau)$, shown in Figure 3.15, alongside $v(0,\tau)$. Following from this ansatz we may express v'/v, as in Equation 3.132, in the following way:

$$\frac{v'}{v} = \frac{\partial v(0,T)/\partial T}{v(0,T)} = \frac{\mathrm{d}\tau/\mathrm{d}T\,(\partial v(0,\tau)/\partial\tau)}{v(0,\tau)} = -\delta\mu, \tag{3.133}$$

therefore, as all other terms are $O(1)$ in the limit where $\delta \to 0$, we may take:

$$u_0(\tau) = \left(\frac{B}{A+B}\right) v(q,\tau)|_{q=0} + O(\delta), \tag{3.134}$$

allowing us to express the whole system the following way:

$$u = \left(\frac{B}{A+B}\right) v|_{z=0} \tag{3.135}$$

$$\frac{\partial v}{\partial \tau} = \Delta\frac{\partial^2 v}{\partial z^2}, \qquad \text{for } z \in [0,1],\ \tau > 0 \tag{3.136}$$

$$\frac{\partial v}{\partial z} = Ev, \qquad \text{for } z = 0,\ \tau > 0, \tag{3.137}$$

$$\frac{\partial v}{\partial z} = -Dv, \qquad \text{for } z = 1,\ \tau > 0 \tag{3.138}$$

where

$$E = \frac{AC}{A+B}. \tag{3.139}$$

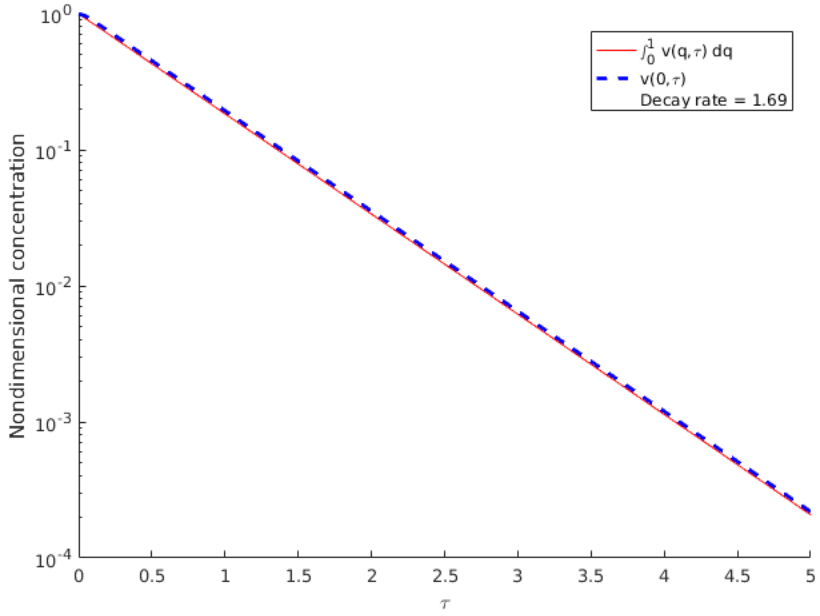

Figure 3.15: Non-dimensional solution for $\int_0^1 v(q,\tau)\,\mathrm{d}q$ and $v(0,\tau)$ to the 1D PDE model (Equations 3.93-3.98), solved using parameters given for the human eye in Section 3.2.1 (setting $r_0 = r_{\text{vit}}$), using the permeabilities estimated for the Fab molecule, given in Table 3.10.

1D dimensional solution: separation of variables

Notice that we have decoupled the retina from the vitreous, allowing us to consider the solution in terms solely of $u(z)$. Let us next separate variables by letting:

$$v = Z(z)T(\tau), \tag{3.140}$$

which upon substitution in Equation 3.136 yields:

$$\frac{1}{\Delta}\frac{\dot{T}}{T} = \frac{Z''}{Z} = \text{ constant } = -\lambda^2, \tag{3.141}$$

where $\cdot = \mathrm{d}/\mathrm{d}T$ and $' = \mathrm{d}/\mathrm{d}z$. Here we note that we take the constant equal to $-\lambda^2$ in order to satisfy our boundary conditions. Solving these two ODEs yields:

$$T \propto \exp\left(-\Delta\lambda^2\tau\right), \tag{3.142}$$

$$Z = a\cos(\lambda z) + b\sin(\lambda z), \tag{3.143}$$

$$Z' = \lambda\left(b\cos(\lambda z) - a\sin(\lambda z)\right), \tag{3.144}$$

where WLOG we may set $a = 1$, as we will later take a linear superposition of these solution functions. On expressing our boundary conditions in terms of Z, Equations 3.137 and 3.138 give

$$\lambda b = E \quad \Rightarrow \quad b = \frac{E}{\lambda}, \tag{3.145}$$

and

$$\lambda\left(\frac{E}{\lambda}\cos(\lambda)-\sin(\lambda)\right)=-D\left(\cos(\lambda)+\frac{E}{\lambda}\sin(\lambda)\right) \tag{3.146}$$

$$\Rightarrow \quad \tan(\lambda)=\frac{(E+D)\,\lambda}{\lambda^2-ED}, \tag{3.147}$$

respectively. The dispersion equation 3.147 has countably infinite solutions λ_i for $i \in \mathbb{N}$, noting if $\lambda_i > 0$ is a solution, then $-\tan(\lambda_i) = -(E+D)\lambda_i/(\lambda_i^2 - ED) \Rightarrow \tan(-\lambda_i) = (E+D)(-\lambda_i)/((-\lambda_i)^2 - ED)$, and hence $-\lambda_i < 0$ is also a solution. We may then express the solution for $v(z,\tau)$ as follows:

$$v(z,\tau)=\sum_{i=1}^{\infty} C_i Z_i(z)\exp\left(-\Delta\lambda_i^2\tau\right), \tag{3.148}$$

where:

$$Z_i(z)=\cos(\lambda_i z)+\left(\frac{E}{\lambda_i}\right)\sin(\lambda_i z). \tag{3.149}$$

Recalling that initially $v(z,0) = 1$ for $z \in [0,1]$, evaluating Equation 3.148 at $\tau = 0$ yields:

$$v(x,0)=\sum_{i=1}^{\infty} C_i Z_i(z)=1. \tag{3.150}$$

If we define the following inner product:

$$\langle f,g\rangle=\int_0^1 f\cdot g\;\mathrm{d}z, \tag{3.151}$$

then it follows for $i \neq j$ that

$$\langle Z_i, Z_j\rangle = 0, \tag{3.152}$$

as shown in Appendix A.5. This implies Z_i and Z_j are orthogonal if $i \neq j$, with respect to the inner product defined by Equation 3.151. Therefore taking the inner product of Equation 3.150 with Z_i gives:

$$1=\langle v(x,0),Z_i\rangle=\sum_{j=1}^{\infty} C_j\langle Z_j,Z_i\rangle \tag{3.153}$$

$$=C_i\langle Z_i,Z_i\rangle \tag{3.154}$$

$$\Rightarrow \quad C_i=\frac{\langle 1,Z_i\rangle}{\langle Z_i,Z_i\rangle}, \tag{3.155}$$

where C_i may be explicitly evaluated in terms of λ_i via integration $\forall i \in \mathbb{N}$. The dispersion relation given by Equation 3.147 may then be solved numerically, allowing us to analyse the analytic solution for $v(z,\tau)$, Equation 3.148, to an arbitrary degree of accuracy. Figure

3.16 shows the non-dimensional solution to the 1D PDE model, solved using parameters given for the human eye in Section 3.2.1 (setting $r_0 = r_{\text{vit}}$), using the permeabilities estimated for Fab molecules given in Table 3.10. Plot (a) shows Equation 3.148 evaluated for $i = 1, 2,$ ... 1000, whereas (b) is only the first term. From these plots we can see that the accuracy of the analytic solution was not largely affected by the assumptions made in order to decouple the retinal compartment, and additionally we see from plot (b) that the solution quickly relaxes to the single term approximation.

1D dimensional solution: principle decay rate

As for $\forall i > 1\ \lambda_1 < |\lambda_i|$, the solution for $v(z, \tau)$ may be approximated, for $t \sim O\left(1/\left(\Delta\lambda_2^2\right)\right)$ and greater, by:

$$v(z, \tau) \simeq \frac{\langle 1, Z_1 \rangle}{\langle Z_1, Z_1 \rangle} Z_1 \exp(-\Delta\lambda_1^2 \tau). \tag{3.156}$$

Therefore the principle decay rate of the system is given by $D_{\text{vit}}\lambda_1^2/r_0^2$, which we may analytically approximate. Considering the set of solutions λ_i for Equation 3.147 we see that the solution with the smallest magnitude, λ_1, must lie in the range $(0, \pi/2)$, as $ED \sim 10^{-1} < \pi/2$, therefore we consider the following continued fraction approximation [116, 117] for $\tan\lambda$:

$$\tan(\lambda) \simeq \frac{\lambda}{1 - \lambda^2/3}, \tag{3.157}$$

accurate for $\lambda \in (0, \pi/2)$. Therefore, using this approximation, we may generate the following approximation for λ_1:

$$\lambda_1^2 \simeq \frac{3\,(E + D + ED)}{3 + E + D}, \tag{3.158}$$

thus the principle decay rate, which we will define as λ, is given by:

$$\lambda := \frac{D_{\text{vit}}\lambda_1^2}{r_0^2} = \frac{\frac{R_p D_{\text{vit}}}{r_0} + 1}{\left(R_p - \frac{1}{p_{\text{HYA}}}\right)\frac{D_{\text{vit}}}{p_{\text{HYA}}} + \frac{R_p r_0}{3}}, \tag{3.159}$$

where R_p is defined as the sum of the permeability 'resistances':

$$R_p = \frac{1}{p_{\text{RPE}}} + \frac{1}{p_{\text{ILM}}} + \frac{1}{p_{\text{HYA}}}. \tag{3.160}$$

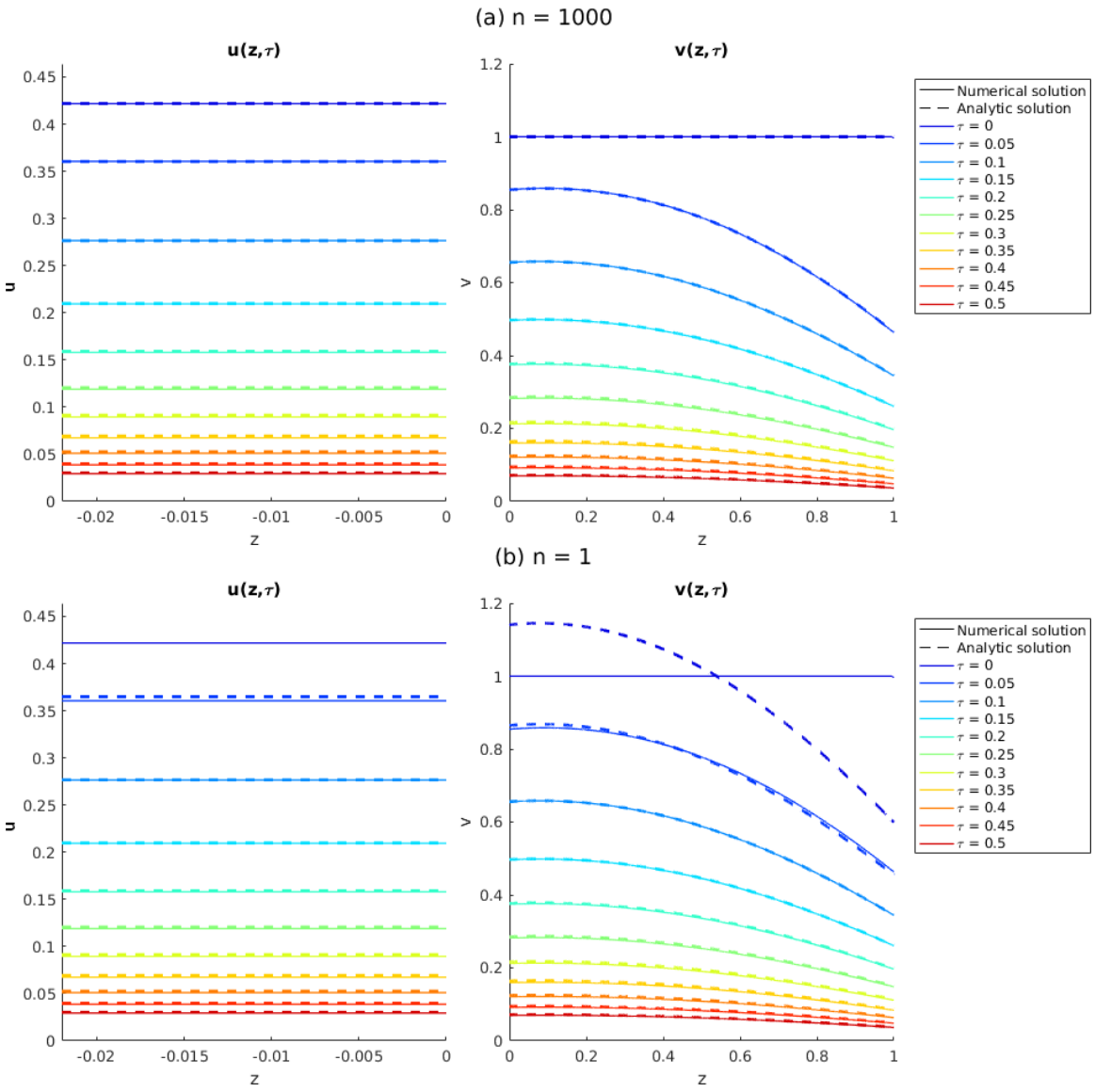

Figure 3.16: Non-dimensional solution to the 1D PDE model, solved using parameters given for the human eye in Section 3.2.1 (setting $r_0 = r_{\text{vit}}$), using the permeabilities estimated for Fab molecules, given in Table 3.10. n refers to the number of terms evaluated in the infinite summation solution for $v(z,\tau)$, given in Equation 3.148 - $u(z,\tau)$ is then generated from $v(z,\tau)$ via Equation 3.135.

Supposing that the timescale of diffusion in the vitreous is much greater than that of the permeabilities, i.e. that $D_{\text{vit}}/r_0^2 \gg r_0/R_p$, allows us to make the following approximation:

$$\frac{R_p D_{\text{vit}}}{r_0} \gg 1 \quad \Rightarrow \quad \lambda \simeq \frac{\frac{R_p D_{\text{vit}}}{r_0}}{\left(R_p - \frac{1}{p_{\text{HYA}}}\right)\frac{D_{\text{vit}}}{p_{\text{HYA}}} + \frac{R_p r_0}{3}}, \tag{3.161}$$

$$\Rightarrow \quad \frac{1}{\lambda} \simeq \underbrace{\left(\frac{\frac{1}{p_{\text{RPE}}} + \frac{1}{p_{\text{ILM}}}}{\frac{1}{p_{\text{RPE}}} + \frac{1}{p_{\text{ILM}}} + \frac{1}{p_{\text{HYA}}}}\right)\frac{r_0}{p_{\text{HYA}}}}_{= 1/\bar{\lambda}} + \frac{r_0^2}{3D_{\text{vit}}}, \tag{3.162}$$

$$\therefore \quad \frac{1}{\lambda} \simeq \frac{1}{\bar{\lambda}} + \frac{r_0^2}{3D_{\text{vit}}}, \tag{3.163}$$

where we recall $\bar{\lambda}$ is the decay rate of the 1D well-mixed system, given by Equation 3.90. If we additionally recall that $\log 2/\lambda = t_{1/2}$ then we may derive the following relationship:

$$t_{1/2} \simeq \bar{t}_{1/2} + \frac{\log 2}{3}\left(\frac{r_0^2}{D_{\text{vit}}}\right), \tag{3.164}$$

where $t_{1/2}$ is the half-life of the 1D PDE model and $\bar{t}_{1/2}$ is the half-life of the corresponding 1D well-mixed system. From this expression we can see the role that diffusion plays in determining the magnitude of the ocular $t_{1/2}$ within a PDE model. We can additionally see that as $D_{\text{vit}} \to \infty$, the half-life $t_{1/2} \to \bar{t}_{1/2}$, as was demonstrated numerically in Figure 3.12. Additionally, Equation 3.164 demonstrates that the smaller the length scale, r_0, of the eye the less diffusion plays a role, and it is the ratio r_0/D_{vit} that determines to what degree the well-mixed assumption is applicable.

3.2.7 3-compartment PK PDE model summary

In this section we have explored the development of a simple PDE model to simulate the PK of an IVT injection of an anti-VEGF antibody. We have managed to describe the geometry of the vitreous, lens, anterior hyaloid membrane and retina with 5 easily collected geometric parameters. The transport mechanisms within the model, diffusion and permeation through 3 distinct membranes are parametrized by a further 4 parameters - one of which, the diffusion coefficient of a molecule within the vitreous, is readily available. Using suitable initial conditions the model may be treated as an axisymmetric problem, significantly reducing computation time, increasing the model's analytic tractability. We have demonstrated through knowledge of the size and rate of turnover of aqueous humour, that three compartment data (such as the dataset presented by Gadkar et al. [28]), may be used (as in Section 3.1) to estimate the 3 remaining membrane permeabilities, allowing for the construction of a fully parametrized system.

Upon spatially averaging the PDE model and analysing the relationship between p_{HYA} and k_{el}, we have determined that the well-mixed assumption strictly only applies for molecules with diffusion coefficients less than or on the order of 10^{-4} cm^2/sec. Therefore upon fitting the ODE model presented within this chapter to a dataset, the parameter k_{el} has no available mechanistic interpretation and must be treated as a phenomenological parameter. However, Figure 3.13 demonstrates that even without a mechanistic interpretation for k_{el}, through geometric scaling via Equation 3.69, it is still possible to produce reasonable PK predictions, similar to those produced by the PDE model.

Additionally, through the analysis of the 1D caricature PDE PK model, we have been able to analyse the role of diffusion and vitreal length scale in the determination of the ocular $t_{1/2}$, and have demonstrated analytically why we do not see parity between the value of k_{el} estimated via an ODE model and the equivalent p_{HYA} value estimated using a PDE model, when fit to the same dataset. Further analysis of geometries more complex than the 1D model presented may shed further light on the explicit relationship between ocular ODE and PDE models.

Given the simplicity of the geometric and mechanistic parametrization, such a model may be of interest in the industrial development of pharmaceutics, which generally favour simple ODE models, with as few parameters and as little complexity as possible. Nonetheless, if one develops a drug that may exhibit significant heterogeneity within its spatial concentration profile, then such a simple PDE model may easily be implemented and explained to shed light on the subject. In Section 4.2 we will consider introducing VEGF and drug-VEGF complexes into this PDE model, once again comparing the pharmacodynamic predictions of the PDE to the ODE, in order to assess the applicability of the ODE model to such a study.

4

The Retinal PK/PD of anti-VEGF Macromolecules

4.1 Free VEGF retinal dynamics post anti-VEGF IVT injection, generated using a semi-mechanistic 3-compartment ocular PK/PD model

The work presented within Section 4.1 is based on the 2018 publication Hutton-Smith et al. *"Theoretical Insights Into the Retinal Dynamics of VEGF in Patients Treated with Ranibizumab, Based on an Ocular Pharmacokinetic/Pharmacodynamic Model"* [76].

It is generally assumed that to achieve maximum angiogenic inhibition, anti-VEGF molecules must bind to VEGF molecules within and below the retina. To do this, after IVT injection, molecules must diffuse to, and penetrate through, the inner limiting membrane (ILM) to enter the retina, and then subsequently through the retinal pigment epithelium (RPE), to enter sub-retinal space. Assessing drug and/or VEGF binding in these tissue layers would require serial retinal biopsies and is not therefore feasible in wet AMD patients. On the other hand serial aqueous humour samples can be obtained in wet AMD patients and have been used by Fauser and colleagues to characterize the VEGF suppression times (VST) associated with different anti-VEGF compounds [82, 118]. While there appears to be a general association between the aqueous humour VST and the suppression of clinical disease activity assessed by optical coherence tomography (OCT) or visual acuity on a population basis, it is presently unknown if the pharmacodynamics (PD) of VEGF suppression

in the retina is similar to the PD observed in aqueous humour and/or whether it would more closely parallel the disease activity in individual patients. The recent observation that the aqueous humour VST is approximately twice as long as the period of suppressed disease activity in a specific subgroup of patients with "persistent CNV activity during anti-VEGF treatment" [118] suggests that the retinal VST could be shorter than the aqueous VST, at least in some patients.

To address these questions we present a PD extension of the 3-compartment PK model detailed in Section 3.1. To predict retinal PD we used the 3-compartment PK/PD model to re-analyse the clinical dataset collected by Saunders et al. [3], detailed in Section 2.1.

The extension from a 2 to 3-compartment PK/PD model grants the ability to compare the simulated free (unbound) VEGF concentration profiles of the retina, vitreous and aqueous compartments. We therefore present an analysis of the temporal behaviour between these three compartments, as well as an analysis of the changes in retinal and aqueous PD, induced through the alteration of dose and binding kinetics. Our analysis shows that under certain conditions a temporal disparity may exist between the suppression of free VEGF levels in the retina and aqueous humour, as well as a difference of the suppression magnitude. Our simulations show that for the reference values of p_{ILM} and p_{RPE}, the simulated duration of VEGF suppression in the retina is approximately 50% shorter than the observed duration of VEGF suppression in the aqueous humour, a finding that may explain the short duration of suppressed disease activity in the high anti-VEGF demand patients reported by Fauser [118]. Alongside these results we also present two case studies addressing relevant biological scenarios, simulation of which was not possible with previous ocular models. Our simulations with the 3-compartment PK/PD model provide new insight into the inter-patient variability in response to anti-VEGF therapy and offer a mechanistic framework for developing treatment regimens and molecules that may prolong the duration of retinal VEGF suppression.

4.1.1 3-compartment PK/PD model formulation

The 3-compartment PK/PD model is described graphically in Figure 4.1, the model is comprised of the retina, vitreous and aqueous humour, between which transport pathways are shown, denoted by arrows, alongside their corresponding transfer rate constant expressions. Reaction kinetics between chemical species can occur within any of the three model compartments, VEGF (V) has two identical binding sites to which ranibizumab (R) can bind [119], to form a VEGF - ranibizumab complex (VR) and subsequently a ranibizumab

- VEGF - ranibizumab complex (RVR). Reactions are governed by Equations 4.1 and 4.2, in which k_{on} and k_{off} (and hence also the dissociation constant $K_{\text{D}} = k_{\text{off}}/k_{\text{on}}$) are reaction rates corresponding to a hypothetical single VEGF binding site.

$$\text{V} + \text{R} \underset{2k_{\text{on}}}{\overset{k_{\text{off}}}{\rightleftharpoons}} \text{VR}, \tag{4.1}$$

$$\text{R} + \text{VR} \underset{k_{\text{on}}}{\overset{2k_{\text{off}}}{\rightleftharpoons}} \text{RVR}. \tag{4.2}$$

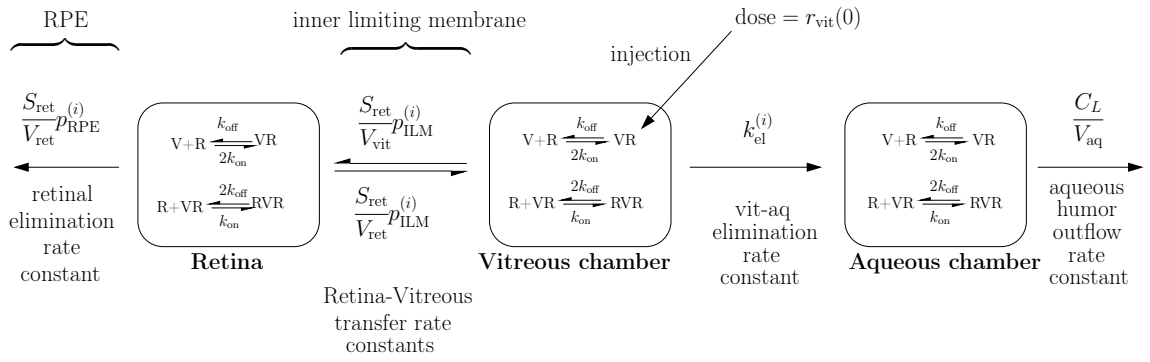

Figure 4.1: 3-compartment reaction model diagram, transport pathways, with their respective transfer rate constants, are indicated by arrows between compartments. Reactions between chemical species, e.g., R, V, VR and RVR, are shown with their respective reaction rates inside compartments, where $S_{\text{ret}}, V_{\text{ret}}, V_{\text{vit}}, V_{\text{aq}}, p_{\text{RPE}}^{(i)}, p_{\text{ILM}}^{(i)}, k_{\text{el}}^{(i)}, C_{\text{L}}$ represent the retinal surface area, retinal volume (including both the intracellular and extracellular spaces), vitreal volume, aqueous volume, RPE permeability, ILM permeability, vitreous-aqueous elimination rate and clearance from the aqueous chamber, respectively. The superscript (i) denotes parameters whose values depend on the the hydrodynamic radius of the particular chemical species. $r_{\text{vit}}(t)$ represents the vitreal concentration of unbound ranibizumab, and $r_{\text{ret}}(0)$ the initial drug concentration.

Chemical species concentrations in each compartment, with units of pM, are denoted by $v(t)$, $r(t)$, $c(t)$ and $h(t)$, for V, R, VR and RVR, respectively. Subscripts on chemical concentrations denote the compartment to which they refer, for example $r_{\text{vit}}(t)$ describes the concentration of R in the vitreous. Full details on concentration notation can be found in Table 4.1. We note that throughout this chapter we will refer to VEGF that is not bound in a VR or RVR complex as 'free VEGF', whereas we refer to unbound ranibizumab simply as 'ranibizumab', as typically the concentration of unbound ranibizumab is several orders of magnitude greater than that of VR or RVR. Initially, prior to IVT injection, VEGF levels are assumed to be at their respective steady state levels in all compartments, and all complexes are assumed to have zero concentration. Ranibizumab is taken to have zero retinal and aqueous concentration initially, and a vitreal concentration $r_{\text{vit}}(0)$ corresponding to a dose

of 0.5 mg, calculated using the molecular weight of ranibizumab, taken to be 48.35 kDa [12].

Species	Conc. (pM)	Description
$\mathrm{V_{ret}}$	v_{ret}	VEGF
$\mathrm{R_{ret}}$	r_{ret}	Ranibizumab
$\mathrm{VR_{ret}}$	c_{ret}	VEGF ranibizumab complex
$\mathrm{RVR_{ret}}$	h_{ret}	Ranibizumab VEGF ranibizumab complex
$\mathrm{V_{vit}}$	v_{vit}	VEGF
$\mathrm{R_{vit}}$	r_{vit}	Ranibizumab
$\mathrm{VR_{vit}}$	c_{vit}	VEGF ranibizumab complex
$\mathrm{RVR_{vit}}$	h_{vit}	Ranibizumab VEGF ranibizumab complex
$\mathrm{V_{aq}}$	v_{aq}	VEGF
$\mathrm{R_{aq}}$	r_{aq}	Ranibizumab
$\mathrm{VR_{aq}}$	c_{aq}	VEGF ranibizumab complex
$\mathrm{RVR_{aq}}$	h_{aq}	Ranibizumab VEGF ranibizumab complex

Table 4.1: Model chemical species. Note, all concentrations are functions of time (t) and are expressed in pM, where subscripts indicate the compartment associated with each concentration.

The model schematic in Figure 4.1 is then formulated, using the parameters listed in Table 4.2, into the following nonlinear system of ordinary differential equations (where $k_{\mathrm{on}} = k_{\mathrm{off}}/K_{\mathrm{D}}$):

Retina

$$\frac{\mathrm{d}v_{\mathrm{ret}}}{\mathrm{d}t} = -\frac{S_{\mathrm{ret}}}{V_{\mathrm{ret}}}\left(p^{(v)}_{\mathrm{ILM}} + p^{(v)}_{\mathrm{RPE}}\right) v_{\mathrm{ret}} + \frac{S_{\mathrm{ret}}}{V_{\mathrm{ret}}} p^{(v)}_{\mathrm{ILM}} v_{\mathrm{vit}} + (k_{\mathrm{off}} c_{\mathrm{ret}} - 2k_{\mathrm{on}} v_{\mathrm{ret}} r_{\mathrm{ret}}) + \frac{V_{\mathrm{in}}}{V_{\mathrm{ret}}}, \quad (4.3)$$

$$\frac{\mathrm{d}r_{\mathrm{ret}}}{\mathrm{d}t} = -\frac{S_{\mathrm{ret}}}{V_{\mathrm{ret}}}\left(p^{(r)}_{\mathrm{ILM}} + p^{(r)}_{\mathrm{RPE}}\right) r_{\mathrm{ret}} + \frac{S_{\mathrm{ret}}}{V_{\mathrm{ret}}} p^{(r)}_{\mathrm{ILM}} r_{\mathrm{vit}} + (k_{\mathrm{off}} c_{\mathrm{ret}} - 2k_{\mathrm{on}} v_{\mathrm{ret}} r_{\mathrm{ret}}) \quad (4.4)$$

$$+ (2k_{\mathrm{off}} h_{\mathrm{ret}} - k_{\mathrm{on}} r_{\mathrm{ret}} c_{\mathrm{ret}}), \quad (4.5)$$

$$\frac{\mathrm{d}c_{\mathrm{ret}}}{\mathrm{d}t} = -\frac{S_{\mathrm{ret}}}{V_{\mathrm{ret}}}\left(p^{(c)}_{\mathrm{ILM}} + p^{(c)}_{\mathrm{RPE}}\right) c_{\mathrm{ret}} + \frac{S_{\mathrm{ret}}}{V_{\mathrm{ret}}} p^{(c)}_{\mathrm{ILM}} c_{\mathrm{vit}} - (k_{\mathrm{off}} c_{\mathrm{ret}} - 2k_{\mathrm{on}} v_{\mathrm{ret}} r_{\mathrm{ret}}) \quad (4.6)$$

$$+ (2k_{\mathrm{off}} h_{\mathrm{ret}} - k_{\mathrm{on}} r_{\mathrm{ret}} c_{\mathrm{ret}}), \quad (4.7)$$

$$\frac{\mathrm{d}h_{\mathrm{ret}}}{\mathrm{d}t} = -\frac{S_{\mathrm{ret}}}{V_{\mathrm{ret}}}\left(p^{(h)}_{\mathrm{ILM}} + p^{(h)}_{\mathrm{RPE}}\right) h_{\mathrm{ret}} + \frac{S_{\mathrm{ret}}}{V_{\mathrm{ret}}} p^{(h)}_{\mathrm{ILM}} h_{\mathrm{vit}} - (2k_{\mathrm{off}} h_{\mathrm{ret}} - k_{\mathrm{on}} r_{\mathrm{ret}} c_{\mathrm{ret}}), \quad (4.8)$$

Vitreous

$$\frac{\mathrm{d}v_{\mathrm{vit}}}{\mathrm{d}t} = \frac{S_{\mathrm{ret}}}{V_{\mathrm{vit}}} p_{\mathrm{ILM}}^{(v)} v_{\mathrm{ret}} - \frac{S_{\mathrm{ret}}}{V_{\mathrm{vit}}} p_{\mathrm{ILM}}^{(v)} v_{\mathrm{vit}} - k_{\mathrm{el}}^{(v)} v_{\mathrm{vit}} + (k_{\mathrm{off}} c_{\mathrm{vit}} - 2k_{\mathrm{on}} v_{\mathrm{vit}} r_{\mathrm{vit}}), \tag{4.9}$$

$$\frac{\mathrm{d}r_{\mathrm{vit}}}{\mathrm{d}t} = \frac{S_{\mathrm{ret}}}{V_{\mathrm{vit}}} p_{\mathrm{ILM}}^{(r)} r_{\mathrm{ret}} - \frac{S_{\mathrm{ret}}}{r_{\mathrm{vit}}} p_{\mathrm{ILM}}^{(r)} r_{\mathrm{vit}} - k_{\mathrm{el}}^{(r)} r_{\mathrm{vit}} + (k_{\mathrm{off}} c_{\mathrm{vit}} - 2k_{\mathrm{on}} v_{\mathrm{vit}} r_{\mathrm{vit}}) \tag{4.10}$$

$$+ (2k_{\mathrm{off}} h_{\mathrm{vit}} - k_{\mathrm{on}} r_{\mathrm{vit}} c_{\mathrm{vit}}), \tag{4.11}$$

$$\frac{\mathrm{d}c_{\mathrm{vit}}}{\mathrm{d}t} = \frac{S_{\mathrm{ret}}}{V_{\mathrm{vit}}} p_{\mathrm{ILM}}^{(c)} c_{\mathrm{ret}} - \frac{S_{\mathrm{ret}}}{c_{\mathrm{vit}}} p_{\mathrm{ILM}}^{(c)} c_{\mathrm{vit}} - k_{\mathrm{el}}^{(c)} c_{\mathrm{vit}} - (k_{\mathrm{off}} c_{\mathrm{vit}} - 2k_{\mathrm{on}} v_{\mathrm{vit}} r_{\mathrm{vit}}) \tag{4.12}$$

$$+ (2k_{\mathrm{off}} h_{\mathrm{vit}} - k_{\mathrm{on}} r_{\mathrm{vit}} c_{\mathrm{vit}}), \tag{4.13}$$

$$\frac{\mathrm{d}h_{\mathrm{vit}}}{\mathrm{d}t} = \frac{S_{\mathrm{ret}}}{V_{\mathrm{vit}}} p_{\mathrm{ILM}}^{(h)} h_{\mathrm{ret}}, - \frac{S_{\mathrm{ret}}}{h_{\mathrm{vit}}} p_{\mathrm{ILM}}^{(h)} h_{\mathrm{vit}} - k_{\mathrm{el}}^{(h)} h_{\mathrm{vit}} - (2k_{\mathrm{off}} h_{\mathrm{vit}} - k_{\mathrm{on}} r_{\mathrm{vit}} c_{\mathrm{vit}}) \tag{4.14}$$

Aqueous

$$\frac{\mathrm{d}v_{\mathrm{aq}}}{\mathrm{d}t} = \frac{V_{\mathrm{vit}}}{V_{\mathrm{aq}}} k_{\mathrm{el}}^{(v)} v_{\mathrm{vit}} - \frac{C_{\mathrm{L}}}{V_{\mathrm{aq}}} v_{\mathrm{aq}} (k_{\mathrm{off}} c_{\mathrm{aq}} - 2k_{\mathrm{on}} v_{\mathrm{aq}} r_{\mathrm{aq}}), \tag{4.15}$$

$$\frac{\mathrm{d}r_{\mathrm{aq}}}{\mathrm{d}t} = \frac{V_{\mathrm{vit}}}{V_{\mathrm{aq}}} k_{\mathrm{el}}^{(r)} r_{\mathrm{vit}} - \frac{C_{\mathrm{L}}}{V_{\mathrm{aq}}} r_{\mathrm{aq}} + (k_{\mathrm{off}} c_{\mathrm{aq}} - 2k_{\mathrm{on}} v_{\mathrm{aq}} r_{\mathrm{aq}}) + (2k_{\mathrm{off}} h_{\mathrm{aq}} - k_{\mathrm{on}} r_{\mathrm{aq}} c_{\mathrm{aq}}), \tag{4.16}$$

$$\frac{\mathrm{d}c_{\mathrm{aq}}}{\mathrm{d}t} = \frac{V_{\mathrm{vit}}}{V_{\mathrm{aq}}} k_{\mathrm{el}}^{(c)} c_{\mathrm{vit}} - \frac{C_{\mathrm{L}}}{V_{\mathrm{aq}}} c_{\mathrm{aq}} - (k_{\mathrm{off}} c_{\mathrm{aq}} - 2k_{\mathrm{on}} v_{\mathrm{aq}} r_{\mathrm{aq}}) + (2k_{\mathrm{off}} h_{\mathrm{aq}} - k_{\mathrm{on}} r_{\mathrm{aq}} c_{\mathrm{aq}}), \tag{4.17}$$

$$\frac{\mathrm{d}h_{\mathrm{aq}}}{\mathrm{d}t} = \frac{V_{\mathrm{vit}}}{V_{\mathrm{aq}}} k_{\mathrm{el}}^{(h)} h_{\mathrm{vit}} - \frac{C_{\mathrm{L}}}{V_{\mathrm{aq}}} h_{\mathrm{aq}} - (2k_{\mathrm{off}} h_{\mathrm{aq}} - k_{\mathrm{on}} r_{\mathrm{aq}} c_{\mathrm{aq}}). \tag{4.18}$$

Transport rate constants between compartments, as noted earlier, are shown in Figure 4.1 next to their respective pathways. Transport is permitted between the vitreous chamber and the retina in either direction, with a rate described via the permeability, p_{ILM} (cm/sec), of the inner limiting membrane (ILM), a basement membrane structure [106] found between the retina and vitreous chamber. Unidirectional transport from the vitreous to the aqueous is also permitted and regulated by the transport rate constant k_{el} (1/day). Clearance firstly occurs in the retina, through the retinal pigment epithelium (RPE), with rate described in terms of the permeability, p_{RPE} (cm/sec), of the RPE, and secondly in the aqueous chamber, at a rate associated with C_{L} (mL/day), the rate of aqueous humour production.

All transport rates, excluding the elimination rate from the aqueous humour, are functions of the hydrodynamic radius, R_{h} (nm), and differ for all chemical species (whose values of R_{h} can be found in Table 4.3). Superscripts on transport rates and permeabilities indicate this chemical species dependence, for example $p_{\mathrm{RPE}}^{(v)}$ would be the permeability of the RPE to VEGF. The equations determining the hydrodynamic radius dependence for retinal permeabilities are taken from Section 3.1, which estimated power law expressions for these parameters using *in vivo* rabbit PK data, for antibody and antibody fragments, collected

by Gadkar et al. [28]. The expression, in terms of hydrodynamic radius, for p_{RPE} is given by,

$$p_{\mathrm{RPE}}^{(i)}(R_{\mathrm{h}}) = 4.04 \times 10^{-7} R_{\mathrm{h}}^{-0.48}, \tag{4.19}$$

and p_{ILM} is found via the following expression:

$$p_{\mathrm{ILM}}^{(i)}(R_{\mathrm{h}}) = 2.2 \times 10^{-7} R_{\mathrm{h}}^{-0.17}, \tag{4.20}$$

where both $p_{\mathrm{RPE}}^{(i)}$ and $p_{\mathrm{ILM}}^{(i)}$ have units of cm/sec, and R_{h} has units of nm. We have investigated the consequences of scaling $p_{\mathrm{RPE}}^{(i)}(R_{\mathrm{h}})$ by factors of 10 and 0.1 in order to illustrate the sensitivity of the model to the magnitude of p_{RPE}, which could conceivably be modified by the penetration of neovascular blood vessels through the RPE and/or the presence of drusen beneath the RPE. We have also investigated the case of a drug that is unable to permeate across the ILM to see how the binding of VEGF in the vitreous influences the retinal concentration of VEGF.

Parameter	Value	Units	Description
k_{off}	0.864 [84]	day^{-1}	Single binding site off rate
k_{on}	$k_{\mathrm{off}}/K_{\mathrm{D}}$	$\mathrm{pM}^{-1}\mathrm{day}^{-1}$	Single binding site on rate
K_{D}	Estimated	pM	Dissociation constant
V_{in}	Disease state dep.	fmol/day	Rate of VEGF production
$t_{1/2}^{(\mathrm{i})}$	R_{h} dep.	days	Ocular half-life
$k_{\mathrm{el}}^{(\mathrm{i})}$	R_{h} dep.	day^{-1}	Vitreous-aqueous elimination rate constant
$p_{\mathrm{RPE}}^{(\mathrm{i})}$	Equation 4.19	cm/sec	RPE permeability
$p_{\mathrm{ILM}}^{(\mathrm{i})}$	Equation 4.20	cm/sec	ILM permeability
C_{L}	3.6 [87]	mL/day	Clearance from the aqueous chamber
V_{ret}	$0.22^{\dagger}$	mL	Retinal volume
V_{vit}	4.5 [24] [43]	mL	Vitreal volume
V_{aq}	0.16 [88] [89]	mL	Aqueous volume
S_{ret}	$9.71^{\dagger}$	cm^2	Retinal surface area

Table 4.2: Model parameters; entries with superscript (i) are chemical species specific where i corresponds to V, R, VR and RVR. †These values were calculated by taking the cross-sectional retinal distance from the posterior to the anterior as 2.37 cm (estimated from Missel [69]), the retinal thickness as 0.022 cm [69] and retinal radius of that equivalent to a sphere of volume 4.5 mL, in the same manner as in Section 3.1.

Chemical species	Notation	R_{h} (nm)	p_{RPE} ($\times 10^{-7}$ cm/sec)	p_{ILM} ($\times 10^{-7}$ cm/sec)
V	$R_{\mathrm{h}}^{(\mathrm{v})}$	2.39	2.66	1.89
R	$R_{\mathrm{h}}^{(\mathrm{r})}$	2.45	2.63	1.89
VR	$R_{\mathrm{h}}^{(\mathrm{c})}$	3.29	2.28	1.79
RVR	$R_{\mathrm{h}}^{(\mathrm{h})}$	4.07	2.06	1.73

Table 4.3: Hydrodynamic radii (R_{h}) and retinal permeabilities for molecular species, calculated by modelling each species as a prolate ellipsoid, the method for which is described in Appendix A.7. Note, these values are taken to be the same as Hutton-Smith et al. 2018, not from the meta-analysis given in Appendix A.6, as this research was performed and submitted for publication prior to the later meta-analysis. Given the small variation in permeability magnitude across the range of R_{h} values concerned here, this will have little effect on quantitative results, and no effect on qualitative results or conclusions (as will be seen in Section 4.2).

To calculate the molecule specific elimination rate constant $k_{\mathrm{el}}^{(i)}$, we note that in Section 2.1 we demonstrated that the $t_{1/2}$ of a molecule can be considered proportional to its T_{diff} value (Equation 2.7), and hence also proportional to its hydrodynamic radius (Equations 2.4 and 2.5). Therefore by fixing a value for the half-life of ranibizumab, $t_{1/2}^{(r)}$, we may estimate $t_{1/2}\left(R_{\mathrm{h}}\right)$ for other chemical species via the following formula:

$$t_{1/2}\left(R_{\mathrm{h}}\right) = \left(\frac{t_{1/2}^{(r)}}{R_{\mathrm{h}}^{(\mathrm{r})}}\right) R_{\mathrm{h}}. \tag{4.21}$$

With a known half-life the long time decay rate λ, for a molecule of hydrodynamic radius R_{h}, can then be described by:

$$\lambda\left(R_{\mathrm{h}}\right) = \frac{\log 2}{t_{1/2}\left(R_{\mathrm{h}}\right)}. \tag{4.22}$$

The vitreous-aqueous rate constant $k_{\mathrm{el}}^{(i)}$ (shown in Figure 4.1) can be estimated by considering the PK analysis of Section 3.1. Recall the matrix M of transport rates between the retina and aqueous, Equation 3.10. The eigenvalues of this matrix gave us the system decay rates λ_1 and λ_2, which are found by solving the following eigenvalue equation:

$$\left(\frac{S_{\mathrm{ret}}}{V_{\mathrm{ret}}}\left(p_{\mathrm{ILM}} + p_{\mathrm{RPE}}\right) - \lambda\right)\left(\frac{S_{\mathrm{ret}}}{V_{\mathrm{vit}}} p_{\mathrm{ILM}} + k_{\mathrm{el}} - \lambda\right) - \frac{S_{\mathrm{ret}}^2}{V_{\mathrm{ret}} V_{\mathrm{vit}}} p_{\mathrm{ILM}}^2 = 0. \tag{4.23}$$

This equation can be rearranged to give k_{el}, in terms of λ, as:

$$k_{\mathrm{el}} = \lambda - \frac{S_{\mathrm{ret}}}{V_{\mathrm{vit}}} p_{\mathrm{ILM}} + \frac{\left(S_{\mathrm{ret}} p_{\mathrm{ILM}}\right)^2}{V_{\mathrm{vit}} S_{\mathrm{ret}}\left(p_{\mathrm{ILM}} + p_{\mathrm{RPE}}\right) - V_{\mathrm{vit}} V_{\mathrm{ret}} \lambda}, \tag{4.24}$$

which allows us to generate a value for k_{el} given $\lambda^{(i)}$, $p_{\mathrm{ILM}}^{(i)}, p_{\mathrm{RPE}}^{(i)}$ and the anatomical factors $V_{\mathrm{vit}}, S_{\mathrm{ret}}$ and V_{ret}. The model is then formulated, in terms of the parameters in Table 4.2,

into a nonlinear system of 12 ordinary differential equations (ODEs).

Parameters for scaled permeability case studies are generated by completing the steps described above, then scaling $p_{\mathrm{RPE}}^{(i)}$ post hoc, in this way $k_{\mathrm{el}}^{(i)}$ remains unchanged, but $t_{1/2}^{(i)}$ and λ are changed. This is achieved via Equation 3.28, which gives λ as a function of k_{el} and the retinal permeabilities. To investigate the effect of modifying dosage and reaction rates we altered parameters $r_{\mathrm{vit}}(0)$, K_{D}, k_{off} and k_{on}, given a fixed half-life and VEGF production rate.

Initial conditions for VEGF can be derived from the steady state solution of Equations 4.3-4.18, in the absence of ranibizumab, giving

$$\begin{pmatrix} v_{\mathrm{ret}}(0) \\ v_{\mathrm{vit}}(0) \\ v_{\mathrm{aq}}(0) \end{pmatrix} = E_Q \begin{pmatrix} 1 + \frac{k_{\mathrm{el}}^{(v)}}{\frac{S_{\mathrm{ret}}}{V_{\mathrm{vit}}} p_{\mathrm{ILM}}^{(v)}} \\ 1 \\ \frac{V_{\mathrm{vit}}}{C_{\mathrm{L}}} k_{\mathrm{el}}^{(v)} \end{pmatrix}, \tag{4.25}$$

where

$$E_Q = \frac{1}{V_{\mathrm{vit}} k_{\mathrm{el}}^{(v)}} \left(\frac{V_{\mathrm{in}}}{\frac{S_{\mathrm{ret}} p_{\mathrm{RPE}}^{(v)}}{V_{\mathrm{vit}} k_{\mathrm{el}}^{(v)}} + 1 + \frac{p_{\mathrm{RPE}}^{(v)}}{p_{\mathrm{ILM}}^{(v)}}} \right), \tag{4.26}$$

with $v_0 \coloneqq v_{\mathrm{ret}}(0), u_0 \coloneqq v_{\mathrm{vit}}(0)$ and $r_0 \coloneqq r_{\mathrm{vit}}(0)$, where $r_{\mathrm{vit}}(0)$ is taken as the initial vitreal concentration of ranibizumab corresponding to the IVT dose.

Equations 4.3-4.18 were solved numerically in MATLAB using ode23s and fit to each of the 31 patient datasets using `lsqnonlin` [86] (part of MATLAB's global optimization toolbox). A range of fixed K_{D} values (between 50 and 50,000 pM) were analysed; during the fitting protocol, a value of K_{D} within this range was taken and kept fixed, while $t_{1/2}^{(r)}$ and V_{in} were varied by the fitting algorithm, penalising the relative mean square error between the logarithms of the numerical solution and the data. This process was repeated for every patient, over the given range of K_{D} values, yielding a distribution of predicted values for $t_{1/2}^{(r)}$ and V_{in}, over the patient sample, for each analysed value of K_{D}. Through this method (identical to that presented in Chapter 2), the resultant values of $t_{1/2}^{(r)}$ were compared to experimental data (7.9 ($\pm$1.74) days, previously compiled in reference [74]), in order to estimate the value of K_{D}. The distribution of predicted $t_{1/2}^{(r)}$ and V_{in} values were fitted to a log-normal distribution using the `lognfit` [86] function of MATLAB.

4.1.2 3-compartment reanalysis of Saunders et al. [3] dataset

The model was found to fit well to the dataset from Saunders et al. [3], a representative patient's fit (patient 40) can be seen in Figure 4.3, with full results from the fitting protocol provided in Appendix A.8, where individual patient fits and parameters are given. The distribution of predicted $t_{1/2}^{(r)}$ values across patients, for values of K_{D} in the range 50-50,000 pM, can be seen in Figure 4.2. For a value of K_{D}, the mean predicted value of $t_{1/2}^{(r)}$ is shown by the solid blue line, while the solid grey region denotes ±SD from the mean. As in Chapter 2, we used the mean experimental value of $t_{1/2}^{(r)}$, 7.9 (±1.74) days, shown respectively by the solid red and dashed lines, to estimate the *in vivo* value for K_{D}, giving 19,000 pM (16,000-25,000 pM), as is shown graphically in Figure 4.2. The dashed blue line denotes the mean $t_{1/2}^{(r)}$, over patients, resulting from the analysis performed in Chapter 3 Section 2, using an analogous two-compartment PK/PD model to analyse the Saunders et al. dataset [3], which predicted an *in vivo* value for K_{D} of 21,000 pM (18,000-27,000 pM).

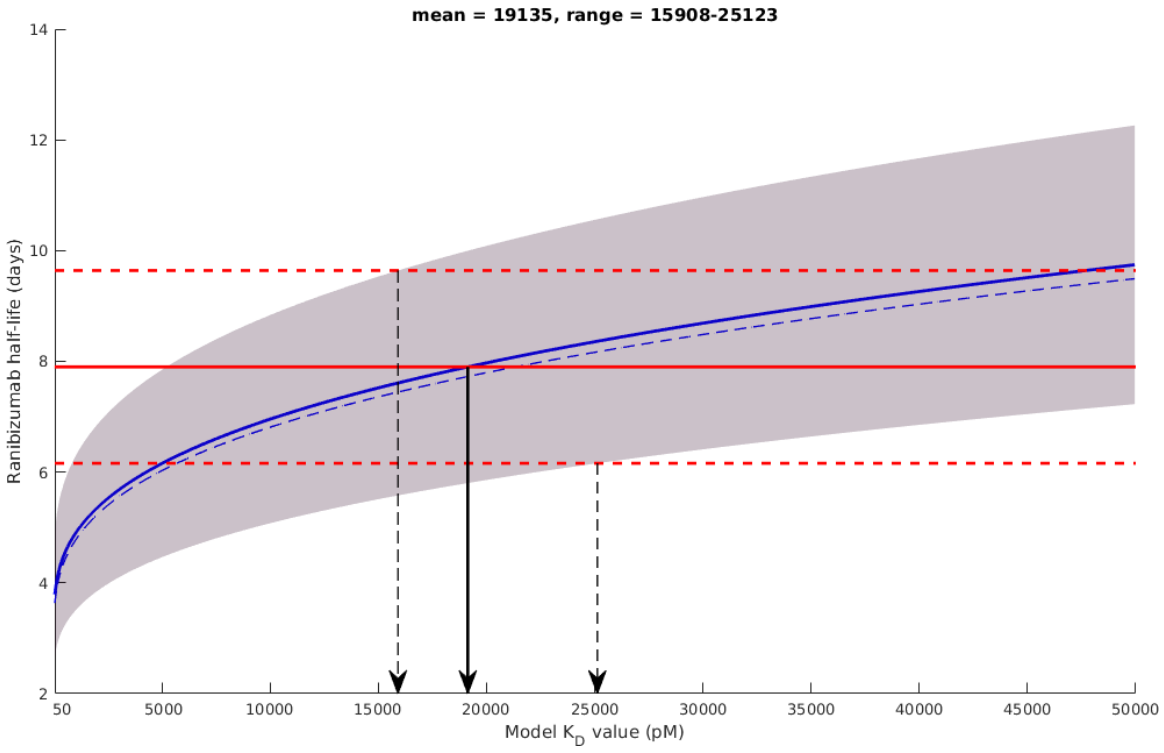

Figure 4.2: Distribution of predicted $t_{1/2}^{(r)}$ values, generated over the prescribed range of K_{D} values (50-50,000 pM) for all 31 patients. The mean patient predicted $t_{1/2}^{(r)}$ value is shown by the solid blue line, with the grey region denoting ±SD. The solid red line shows the experimental mean value of $t_{1/2}^{(r)}$, 7.9 days, with the dashed red line showing ±SD, 1.74 days. The analogous two-compartment mean for $t_{1/2}^{(r)}$, with respect to K_{D}, is shown by the dashed blue line, taken from Chapter 2.

In Figure 4.3 we see the simulated time-dependence of ranibizumab and the free VEGF concentrations in the retina, vitreous and aqueous compartments and the corresponding VEGF data in the aqueous compartment. Ranibizumab decays exponentially at the same rate in all three compartments of the model, and the vitreous concentration is approximately 10× greater than that of the aqueous, and approximately 2× greater than the retina. The free VEGF concentrations in vitreous and aqueous chambers return to their initial values in parallel, however the retina returns to steady state before both the vitreous and aqueous. We also note the initial value of free VEGF in the retina is approximately 3× greater than that of the vitreous, and approximately 30× greater than the aqueous.

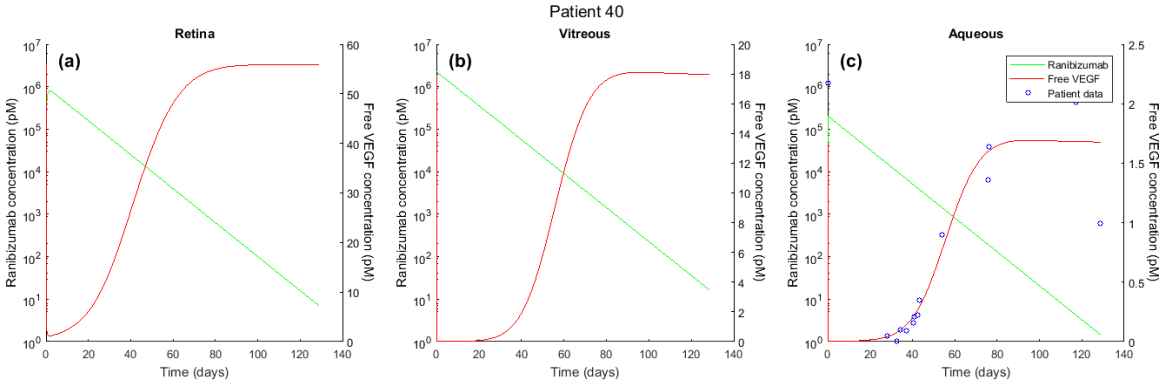

Figure 4.3: Fitting result for patient 40, panels (a)-(c) show the concentration profiles of free VEGF and ranibizumab in the retina, vitreous and aqueous, respectively, plotted with optimal parameters, with values $K_{\mathrm{D}} = 19,000$ pM, $V_{\mathrm{in}} = 18.5$ fmol/day and $t_{12}^{(r)} = 7.5$ days. Patient data can be seen in the aqueous in blue, in all three compartments ranibizumab (log scale, left axis) and VEGF (linear scale, right axis) concentration is shown in green and red, respectively.

Figure 4.4 (a) compares the observed and predicted VEGF data points in the aqueous humour from all patients and observation times, demonstrating that the model performs well across the patient dataset. Figures 4.4 (b) & 4.4 (c) show that the residuals appear to be normally distributed with mean and standard deviation of approximately zero and 0.26 pM, respectively.

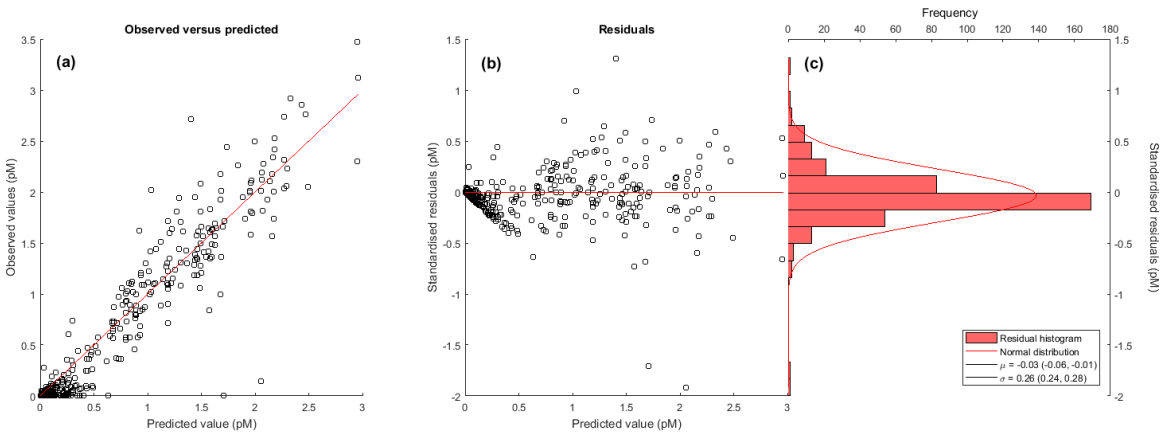

Figure 4.4: Comparison between observed data points for free aqueous VEGF across all 31 patients, and the corresponding predictions made by the model (Equations 4.3-4.18). Panel (a) shows these two quantities plotted versus each other, with the red line representing perfect correlation. Panel (b) shows the difference for each data-point between the predicted and observed value, alongside a plot of their distribution and inferred normal distribution, in panel (c).

4.1.3 Asymptotic analysis of intermediate time retinal VEGF behaviour

In order to further analyse Equations 4.3-4.18 we proceed to non-dimensionalise the vitreous and retinal system equations using the following non-dimensionalisation:

$$v_{\text{ret}} = v_0 x_{\text{ret}}, \quad r_{\text{ret}} = r_0 y_{\text{ret}}, \quad c_{\text{ret}} = v_0 z_{\text{ret}}, \quad h_{\text{ret}} = v_0 w_{\text{ret}}, \tag{4.27}$$

$$v_{\text{vit}} = v_0 x_{\text{vit}}, \quad r_{\text{vit}} = r_0 y_{\text{vit}}, \quad c_{\text{vit}} = v_0 z_{\text{vit}}, \quad h_{\text{vit}} = v_0 w_{\text{vit}}, \tag{4.28}$$

$$t = \frac{1}{k_{\text{off}}}\tau, \tag{4.29}$$

which gives, upon substitution into 4.3-4.18, the following:

Retina

$$\varepsilon\frac{\mathrm{d}x_{\text{ret}}}{\mathrm{d}\tau} = (\varepsilon z_{\text{ret}} - 2x_{\text{ret}}y_{\text{ret}}) + \varepsilon Q^{(v)}x_{\text{vit}} - \varepsilon E^{(v)}x_{\text{ret}} + \varepsilon V, \tag{4.30}$$

$$\frac{\mathrm{d}y_{\text{ret}}}{\mathrm{d}\tau} = \delta\left[(\varepsilon z_{\text{ret}} - 2x_{\text{ret}}y_{\text{ret}}) + (2\varepsilon w_{\text{ret}} - y_{\text{ret}}z_{\text{ret}})\right] + Q^{(r)}y_{\text{vit}} - E^{(r)}y_{\text{ret}}, \tag{4.31}$$

$$\varepsilon\frac{\mathrm{d}z_{\text{ret}}}{\mathrm{d}\tau} = -(\varepsilon z_{\text{ret}} - 2x_{\text{ret}}y_{\text{ret}}) + (2\varepsilon w_{\text{ret}} - y_{\text{ret}}z_{\text{ret}}) + \varepsilon Q^{(c)}z_{\text{vit}} - \varepsilon E^{(c)}z_{\text{ret}}, \tag{4.32}$$

$$\varepsilon\frac{\mathrm{d}w_{\text{ret}}}{\mathrm{d}\tau} = -(2\varepsilon w_{\text{ret}} - y_{\text{ret}}z_{\text{ret}}) + \varepsilon Q^{(h)}w_{\text{vit}} - \varepsilon E^{(h)}w_{\text{ret}}, \tag{4.33}$$

Vitreous

$$\varepsilon\frac{\mathrm{d}x_{\mathrm{vit}}}{\mathrm{d}\tau} = (\varepsilon z_{\mathrm{vit}} - 2x_{\mathrm{vit}}y_{\mathrm{vit}}) + \varepsilon T^{(v)}x_{\mathrm{ret}} - \varepsilon K^{(v)}x_{\mathrm{vit}}, \tag{4.34}$$

$$\frac{\mathrm{d}y_{\mathrm{vit}}}{\mathrm{d}\tau} = \delta\left[(\varepsilon z_{\mathrm{vit}} - 2x_{\mathrm{vit}}y_{\mathrm{vit}}) + (2\varepsilon w_{\mathrm{vit}} - y_{\mathrm{vit}}z_{\mathrm{vit}})\right] + T^{(r)}y_{\mathrm{ret}} - K^{(r)}y_{\mathrm{vit}}, \tag{4.35}$$

$$\varepsilon\frac{\mathrm{d}z_{\mathrm{vit}}}{\mathrm{d}\tau} = -(\varepsilon z_{\mathrm{vit}} - 2x_{\mathrm{vit}}y_{\mathrm{vit}}) + (2\varepsilon w_{\mathrm{vit}} - y_{\mathrm{vit}}z_{\mathrm{vit}}) + \varepsilon T^{(c)}z_{\mathrm{ret}} - \varepsilon K^{(c)}z_{\mathrm{vit}}, \tag{4.36}$$

$$\varepsilon\frac{\mathrm{d}w_{\mathrm{vit}}}{\mathrm{d}\tau} = -(2\varepsilon w_{\mathrm{vit}} - y_{\mathrm{vit}}z_{\mathrm{vit}}) + \varepsilon T^{(h)}w_{\mathrm{ret}} - \varepsilon K^{(h)}w_{\mathrm{vit}}, \tag{4.37}$$

where

$$Q^{(i)} = \frac{1}{k_{\mathrm{off}}}\frac{S_{\mathrm{ret}}}{V_{\mathrm{ret}}}p^{(i)}_{\mathrm{ILM}}, \quad E^{(i)} = \frac{1}{k_{\mathrm{off}}}\frac{S_{\mathrm{ret}}}{V_{\mathrm{ret}}}p^{(i)}_{\mathrm{RPE}} + Q^{(i)} \quad T^{(i)} = \frac{1}{k_{\mathrm{off}}}\frac{S_{\mathrm{ret}}}{V_{\mathrm{vit}}}p^{(i)}_{\mathrm{ILM}}, \tag{4.38}$$

$$K^{(i)} = \frac{k^{(i)}_{\mathrm{el}}}{k_{\mathrm{off}}} + T^{(i)}, \quad H^{(i)} = \frac{k^{(i)}_{\mathrm{el}}V_{\mathrm{vit}}}{k_{\mathrm{off}}V_{\mathrm{aq}}}, \quad V = \frac{V_{\mathrm{in}}}{v_0 k_{\mathrm{off}}V_{\mathrm{ret}}}, \tag{4.39}$$

$$\varepsilon = \frac{K_D}{r_0}, \quad \delta = \frac{v_0}{K_D}, \tag{4.40}$$

noting that all parameters are greater than zero, and $0 < \delta \ll \varepsilon \ll 1$, as $v_0 \sim O(10^1)$ and $r_0 \sim O(10^6)$. All other parameters are $O(1)$. By taking the following asymptotic expansion:

$$y_{\mathrm{ret}} = y^{(0)}_{\mathrm{ret}} + \delta y^{(1)}_{\mathrm{ret}} + O(\delta^2), \tag{4.41}$$

$$y_{\mathrm{vit}} = y^{(0)}_{\mathrm{vit}} + \delta y^{(1)}_{\mathrm{vit}} + O(\delta^2), \tag{4.42}$$

then, to $O(1)$, the system becomes:

$$\frac{\mathrm{d}y^{(0)}_{\mathrm{ret}}}{\mathrm{d}\tau} = -E^{(r)}y^{(0)}_{\mathrm{ret}} + Q^{(r)}y^{(0)}_{\mathrm{vit}}, \tag{4.43}$$

$$\frac{\mathrm{d}y^{(0)}_{\mathrm{vit}}}{\mathrm{d}\tau} = T^{(r)}y^{(0)}_{\mathrm{ret}} - K^{(r)}y^{(0)}_{\mathrm{vit}}. \tag{4.44}$$

Notice that this is a non-dimensional version of the general 3-compartment PK system detailed in Chapter 3 Section 3.1, which, hence, has the following non-dimensional solution:

$$y^{(0)}_{\mathrm{ret}}(\tau) = \frac{K_1K_2}{K_1+K_2}\left[e^{-\bar{\lambda}_1\tau} - e^{-\bar{\lambda}_2\tau}\right], \tag{4.45}$$

$$y^{(0)}_{\mathrm{vit}}(\tau) = \frac{1}{K_1+K_2}\left[K_2e^{-\bar{\lambda}_1\tau} + K_1e^{-\bar{\lambda}_2\tau}\right], \tag{4.46}$$

where

$$K_1 = \frac{K^{(r)} - \bar{\lambda}_1}{T^{(r)}} = \frac{Q^{(r)}}{E^{(r)} - \bar{\lambda}_1}, \tag{4.47}$$

$$K_2 = \frac{\bar{\lambda}_2 - K^{(r)}}{T^{(r)}} = \frac{Q^{(r)}}{\bar{\lambda}_2 - E^{(r)}}, \tag{4.48}$$

and $\bar{\lambda}_1$ and $\bar{\lambda}_2$ are non-dimensional decay rates, given by $\bar{\lambda}_1 = \lambda_1/k_{\mathrm{off}}$ and $\bar{\lambda}_2 = \lambda_2/k_{\mathrm{off}}$, respectively, where λ_1 and λ_2 are given by Equations 3.8 and 3.9, respectively. Equations

4.45-4.46 can be seen to be the nondimensional versions of Equations 3.4-3.5, of the general 3-compartment PK model. In addition to these equations we also note the following:

$$\bar{\lambda}_1 \simeq K^{(r)} - \frac{Q^{(r)}T^{(r)}}{E^{(r)} - K^{(r)}}, \qquad \bar{\lambda}_2 \simeq E^{(r)} + \frac{Q^{(r)}T^{(r)}}{E^{(r)} - K^{(r)}}, \tag{4.49}$$

$$\Rightarrow \quad \lambda_1 \simeq k_{\text{el}}^{(r)} + \left(\frac{S_{\text{ret}}}{V_{\text{vit}}}\right) p_{\text{ILM}}^{(r)} - \left(\frac{S_{\text{ret}} p_{\text{ILM}}^{(r)}}{V_{\text{vit}}}\right) \frac{1}{\left[\left(1 + \frac{p_{\text{RPE}}^{(r)}}{p_{\text{ILM}}^{(r)}}\right) - \frac{V_{\text{ret}}}{V_{\text{vit}}}\left(1 + \frac{V_{\text{vit}} k_{\text{el}}}{S_{\text{ret}} p_{\text{ILM}}^{(r)}}\right)\right]}, \tag{4.50}$$

$$\Rightarrow \quad \lambda_2 \simeq \frac{S_{\text{ret}} p_{\text{ILM}}^{(r)}}{V_{\text{ret}}}\left(1 + \frac{p_{\text{RPE}}^{(r)}}{p_{\text{ILM}}^{(r)}}\right), \tag{4.51}$$

derived via the same expansion process as in Section 3.1.3. Given these equations it follows from our expression for K_1 and K_2 that:

$$K_1 \simeq \frac{Q^{(r)}}{E^{(r)} - K^{(r)}}, \quad K_2 \simeq \frac{E^{(r)} - K^{(r)}}{T^{(r)}} \quad \Rightarrow \quad K_1 K_2 \simeq \frac{Q^{(r)}}{T^{(r)}} = \frac{V_{\text{vit}}}{V_{\text{ret}}}. \tag{4.52}$$

These approximations will be utilised in the following analysis. Next, let us consider the governing equation for x_{ret}:

$$\varepsilon \frac{\mathrm{d}x_{\text{ret}}}{\mathrm{d}\tau} = (\varepsilon z_{\text{ret}} - 2x_{\text{ret}} y_{\text{ret}}) + \varepsilon Q^{(v)} x_{\text{vit}} - \varepsilon E^{(v)} x_{\text{ret}} + \varepsilon V. \tag{4.53}$$

At early time we expect x_{ret} and z_{ret} to be small relative to y_{ret}, due to the large influx of drug into the retina. Any VEGF (x_{ret}) will be bound, and subsequently the VEGF-ranibizumab (z_{ret}) complex will then be bound again to form an RVR complex. As VEGF is produced within the retina we also expect $x_{\text{vit}} \ll x_{\text{ret}}$. Therefore if we take:

$$x_{\text{ret}} = \delta_1 X_{\text{ret}}, \qquad z_{\text{ret}} = \delta_2 Z_{\text{ret}}, \qquad x_{\text{vit}} = \delta_3 X_{\text{vit}}, \tag{4.54}$$

where we assume that

$$\delta_1,\ \delta_2 \ll 1, \qquad \delta_3 \ll \delta_1,\ \delta_2, \tag{4.55}$$

then, upon substitution into Equation 4.53, we may write the following

$$\varepsilon\delta_1 \frac{\mathrm{d}X_{\text{ret}}}{\mathrm{d}\tau} = (\varepsilon\delta_2 Z_{\text{ret}} - 2\delta_1 X_{\text{ret}} y_{\text{ret}}) + \varepsilon\delta_3 Q^{(v)} X_{\text{vit}} - \varepsilon\delta_1 E^{(v)} X_{\text{ret}} + \varepsilon V, \tag{4.56}$$

$$\Rightarrow \quad \varepsilon \frac{\mathrm{d}X_{\text{ret}}}{\mathrm{d}\tau} = \left(\frac{\varepsilon\delta_2}{\delta_1} Z_{\text{ret}} - 2X_{\text{ret}} y_{\text{ret}}\right) + \frac{\varepsilon\delta_3}{\delta_1} Q^{(v)} X_{\text{vit}} - \varepsilon E^{(v)} X_{\text{ret}} + \frac{\varepsilon}{\delta_1} V, \tag{4.57}$$

$$\Rightarrow \quad \underbrace{2X_{\text{ret}} y_{\text{ret}}}_{(1)} + \underbrace{\varepsilon\left(\frac{\mathrm{d}X_{\text{ret}}}{\mathrm{d}\tau} + E^{(v)} X_{\text{ret}}\right)}_{(2)} = \underbrace{\frac{\varepsilon\delta_3}{\delta_1} Q^{(v)} X_{\text{vit}}}_{(3)} + \underbrace{\frac{\varepsilon}{\delta_1} V}_{(4)}, + \underbrace{\frac{\varepsilon\delta_2}{\delta_1} Z_{\text{ret}}}_{(5)}. \tag{4.58}$$

Now, we note the magnitude of the terms in Equation 4.58:

$$\begin{matrix}(1) & (2) & (3) & (4) & (5)\\ \sim O(1), & \sim O(\varepsilon), & \sim O\left(\frac{\varepsilon\delta_3}{\delta_1}\right), & \sim O\left(\frac{\varepsilon}{\delta_1}\right), & \sim O\left(\frac{\varepsilon\delta_2}{\delta_1}\right).\end{matrix} \tag{4.59}$$

As $\delta_3 \ll \delta_1$ term (3) is sub-dominant to $(1), (2), (4)$ and (5), and as δ_2 and δ_1 are both $\ll 1$ we can take $(5) \ll (4)$ (due to the additional factor of δ_2 in (5)). This leaves us with the dominant balance $(1) \sim (4)$, $(2), (3), (5) \ll (1), (4)$, giving us $\delta_1 = \varepsilon$. Therefore taking the following expansion:

$$X_{\text{ret}} = X_{\text{ret}}^{(0)} + \varepsilon X_{\text{ret}}^{(1)} + O(\varepsilon^2) \tag{4.60}$$

we find to $O(1)$ that

$$X_{\text{ret}}^{(0)} = \frac{V}{2y_{\text{ret}}} \tag{4.61}$$

$$\Rightarrow \quad v_{\text{ret}}(t) = \frac{\varepsilon v_0 V}{2}\left(\frac{K_1+K_2}{K_1K_2}\right)\left[\frac{1}{e^{-\lambda_1 t}-e^{-\lambda_2 t}}\right]. \tag{4.62}$$

From Equations 4.47-4.48 and 4.52 we see that:

$$\left(\frac{K_1+K_2}{K_1K_2}\right) \simeq \frac{V_{\text{ret}}}{S_{\text{ret}}p_{\text{ILM}}^{(r)}}\left(\lambda_2-\lambda_1\right), \tag{4.63}$$

which, upon substitution in Equation 4.62, yields the following expression for v_{ret}:

$$v_{\text{ret}}(t) = \frac{1}{2}\left\{\frac{V_{\text{in}}}{r_0 k_{\text{on}}}\right\}\left[\frac{\left(\lambda_2-\lambda_1\right)/S_{\text{ret}}p_{\text{ILM}}^{(r)}}{e^{-\lambda_1 t}-e^{-\lambda_2 t}}\right], \tag{4.64}$$

which, past early time, can be approximated by:

$$v_{\text{ret}}(t) \simeq \frac{1}{2}\left\{\frac{V_{\text{in}}}{r_0 k_{\text{on}}}\right\}\left[\frac{\lambda_2-\lambda_1}{S_{\text{ret}}p_{\text{ILM}}^{(r)}}\right]e^{\lambda_1 t}. \tag{4.65}$$

Notice that Equation 4.65 demonstrates that the rate of return of free VEGF in the retina occurs at the same rate that drug is removed, additionally note that this expression is inversely proportional to dose concentration, r_0, and the binding on rate, k_{on}. From Equation 4.64 we may generate an expression for the minimum free VEGF concentration in the retina, i.e. the maximum level of free VEGF suppression. In order to analyse this quantity note that the approximation of v_{ret} (Equation 4.64) is minimised when y_{ret} is maximised, which occurs at $t_{\min}$, the solution of the following equation:

$$-\lambda_1 e^{-\lambda_1 t_{\min}} + \lambda_2 e^{-\lambda_2 t_{\min}} = 0, \tag{4.66}$$

generated by setting $\mathrm{d}v_{\text{ret}}/\mathrm{d}t = 0$. Solving this equation for $t_{\min}$ yields:

$$t_{\min} = \frac{1}{\lambda_2-\lambda_1}\log\left(\frac{\lambda_2}{\lambda_1}\right). \tag{4.67}$$

Next, via Equation 4.66, we may write

$$e^{-\lambda_1 t_{\min}} - e^{-\lambda_2 t_{\min}} = \left(\frac{\lambda_2 - \lambda_1}{\lambda_1}\right) e^{-\lambda_2 t_{\min}}, \tag{4.68}$$

and via Equation 4.67:

$$e^{\lambda_2 t_{\min}} = e^{\frac{\lambda_2}{\lambda_2 - \lambda_1} \log\left(\frac{\lambda_2}{\lambda_1}\right)} = \left(\frac{1}{\lambda_1/\lambda_2}\right)^{\frac{1}{1-\lambda_1/\lambda_2}}. \tag{4.69}$$

Therefore, using Equations 4.68 and 4.69 we may express the minimum free VEGF retinal concentration, $v_{\text{ret}}(t_{\min})$, in the following way:

$$\Rightarrow \quad v_{\text{ret}}(t_{\min}) = \frac{1}{2} \frac{V_{\text{in}}}{r_0 k_{\text{on}} S_{\text{ret}} p_{\text{ILM}}^{(r)}} \left[\frac{\lambda_2 - \lambda_1}{e^{-\lambda_1 t_{\min}} - e^{-\lambda_2 t_{\min}}}\right] \tag{4.70}$$

$$= \left(\frac{1}{2} \frac{V_{\text{in}}}{r_0 S_{\text{ret}} p_{\text{ILM}}^{(r)} k_{\text{on}}}\right) \lambda_1 e^{\lambda_2 t_{\min}} \tag{4.71}$$

$$= \left(\frac{1}{2} \frac{V_{\text{in}}}{r_0 S_{\text{ret}} p_{\text{ILM}}^{(r)} k_{\text{on}}}\right) \lambda_1 \left(\frac{1}{\lambda_1/\lambda_2}\right)^{\frac{1}{1-\lambda_1/\lambda_2}}. \tag{4.72}$$

Via Lemma A.1 of Appendix A.9, noting $\lambda_1/\lambda_2 \ll 1$, we may approximate $v_{\text{ret}}(t_{\min})$ by:

$$v_{\text{ret}}(t_{\min}) = \frac{1}{2} \left\{\frac{V_{\text{in}}}{r_0 k_{\text{on}}}\right\} \left[\frac{\lambda_2 + \lambda_1 \log\left(\frac{\lambda_2}{\lambda_1}\right) + O\left(\frac{\lambda_1^2}{2\lambda_2} \log^2\left(\frac{\lambda_1}{\lambda_2}\right)\right)}{S_{\text{ret}} p_{\text{ILM}}^{(r)}}\right]. \tag{4.73}$$

Figure 4.5 shows the early time free VEGF concentration profile, the numerical solution is shown in solid red, the full two exponential asymptotic solution is shown in dashed red, and the single exponential asymptotic simplification in dotted red. We also note that Equation 4.73 may be approximated by the following

$$v_{\text{ret}}(t_{\min}) \simeq \frac{1}{2} \left\{\frac{V_{\text{in}}}{r_0 k_{\text{on}}}\right\} \left[\frac{\lambda_2 - \lambda_1 \log\left(\frac{\lambda_1}{\lambda_2}\right)}{S_{\text{ret}} p_{\text{ILM}}^{(r)}}\right] \tag{4.74}$$

$$\simeq \frac{1}{2} \left\{\frac{V_{\text{in}}}{r_0 k_{\text{on}}}\right\} \left[\frac{\lambda_2 - \lambda_1}{S_{\text{ret}} p_{\text{ILM}}^{(r)}}\right], \tag{4.75}$$

as $0 < \lambda_1/\lambda_2 \ll 1$. Therefore Equation 4.65 may be written in terms of $v_{\text{ret}}(t_{\min})$

$$v_{\text{ret}}(t) \simeq \frac{1}{2} \left\{\frac{V_{\text{in}}}{r_0 k_{\text{on}}}\right\} \left[\frac{\lambda_2 - \lambda_1}{S_{\text{ret}} p_{\text{ILM}}^{(r)}}\right] e^{\lambda_1 t} \tag{4.76}$$

$$\simeq v_{\text{ret}}(t_{\min}) e^{\lambda_1 t}. \tag{4.77}$$

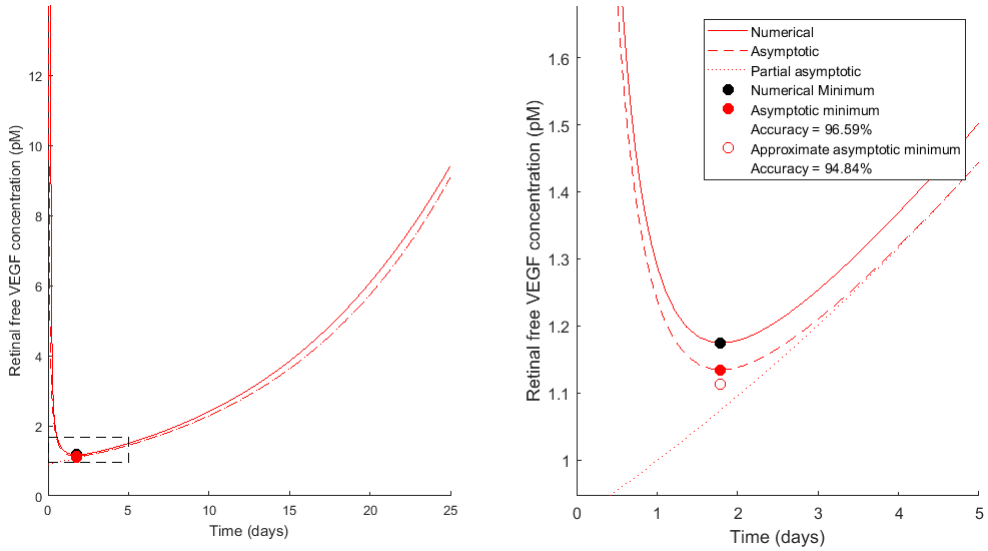

Figure 4.5: Initial free VEGF concentration in the retina, the dashed box in the left-hand panel is the region shown in the right-hand panel. The solid, dashed and dotted red lines denote the numerical, asymptotic (Equation 4.64) and partial asymptotic (Equation 4.65) solutions, respectively, for patient 40 at $K_{\mathrm{D}} = 19,000$ pM and $t_{12}^{(r)} = 7.9$ days. The solid red dot shows the minimum free VEGF concentration, the red circle shows the approximate form of the minimum free VEGF, presented in Equation 4.73, the accuracy of which is given in the figure legend.

4.1.4 Interpatient half-life and VEGF production variation

Figure 4.6 shows the estimates of V_{in} for the present 3-compartment model and the prior 2-compartment model vs. the steady-state aqueous humour VEGF concentration for each subject. The slope for the 3-compartment model is approximately 3-fold larger than for the 2-compartment model, and is described analytically via Equation 4.78, derived from Equation 4.25:

$$V_{\mathrm{in}} = C_{\mathrm{L}} \left(1 + \frac{S_{\mathrm{ret}} p_{\mathrm{RPE}}^{(v)}}{V_{\mathrm{vit}} k_{\mathrm{el}}^{(v)}} + \frac{p_{\mathrm{RPE}}^{(v)}}{p_{\mathrm{ILM}}^{(v)}} \right) v_{\mathrm{aq}}(0). \tag{4.78}$$

Additionally we note the analogue of this relationship derived from the 2-compartment equivalent of this model. Notice, as defined by Equations 2.12-2.19 of Chapter 2, the relationship between V_{in} and $v_{\mathrm{aq}}(0)$ differs to Equation 4.78 in the 2-compartment model, instead being described by Equation 4.79,

$$V_{\mathrm{in}} = C_{\mathrm{L}} v_{\mathrm{aq}}(0). \tag{4.79}$$

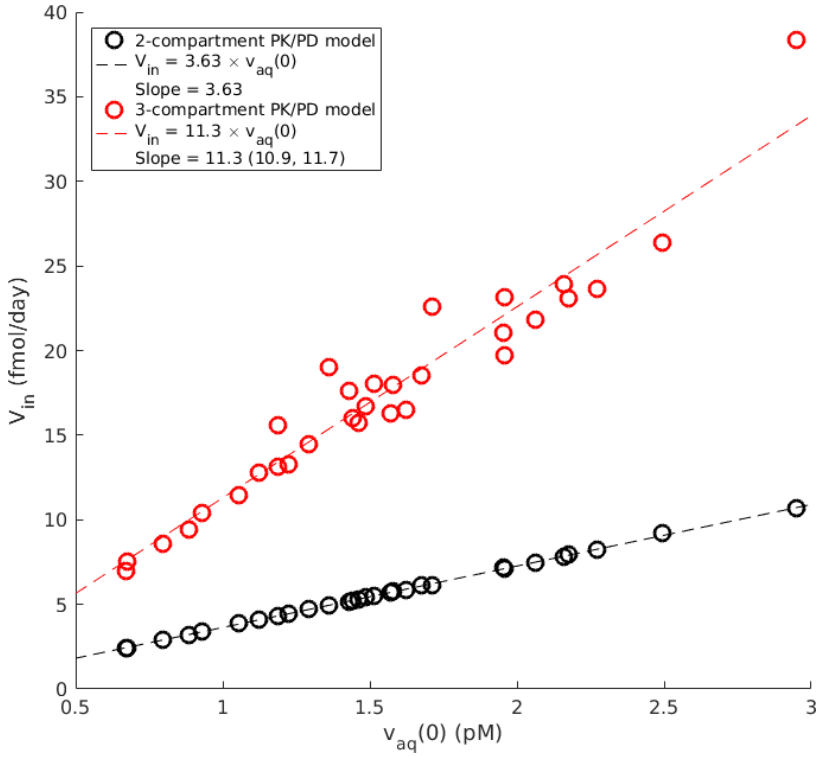

Figure 4.6: Predicted VEGF production rates, V_{in} (fmol/day), over the patient sample, for $K_{\text{D}} = 19,000$ pM. V_{in} is plotted for each patient versus their aqueous free VEGF steady state concentration level, $v_{\text{aq}}(0)$ (pM). Red dots are V_{in} levels predicted by the modelling work performed in this study, black dots are the predicted V_{in} values, derived from the same dataset, by the 2-compartment model presented in Chapter 2.

Figure 4.7 shows the distribution of predicted V_{in} values across the patient sample. Modelling these data with a log normal distribution [120], we find they have mean and standard deviation of 17.5 and 6.9 fmol/day, respectively. This difference in VEGF production implies that approximately 70% of VEGF is eliminated via the choroid relative to 30% eliminated via the aqueous. As shown in Figure 4.6 the variation in these predicted values is a direct consequence of the variation in observed aqueous equilibrium free VEGF concentration, and demonstrates inter-patient variability.

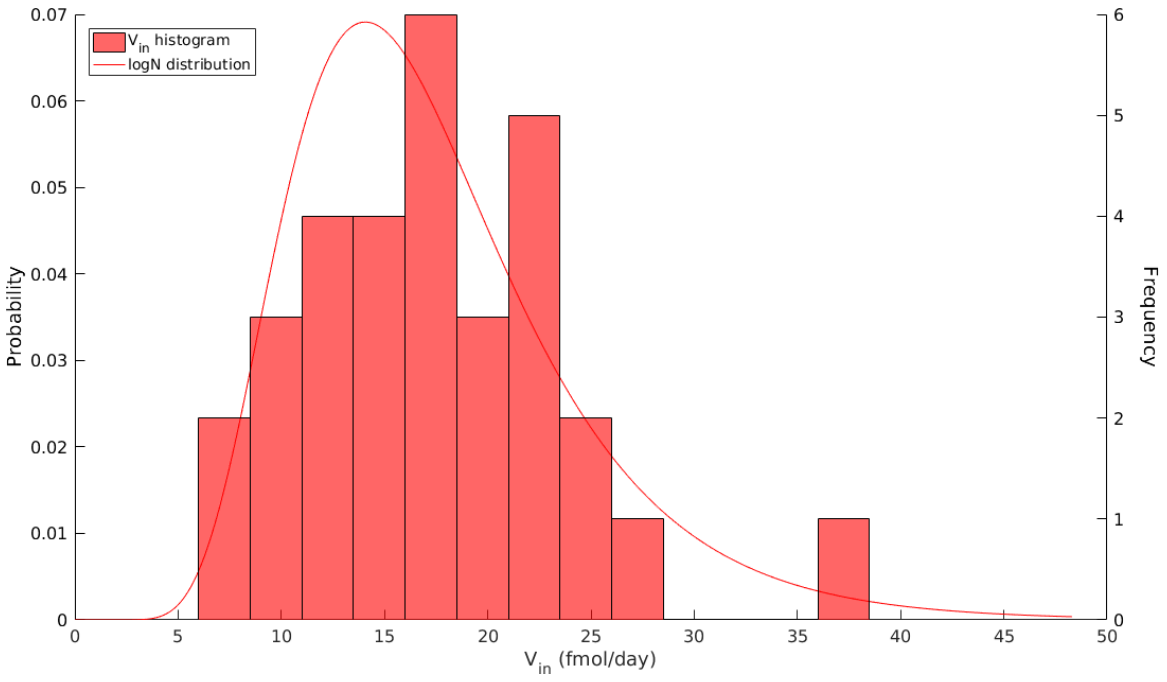

Figure 4.7: Distribution of V_{in} over patient sample, for $K_{\text{D}} = 19,000$ pM. A fit log normal distribution, shown by the red line, is given, with parameters (95% CI) $\mu = 2.76$ (2.65, 2.93) and $\sigma = 0.38$ (0.30, 0.51).

In addition to the VEGF production rate, there is large variation across the patient sample in the time course of the free VEGF profiles. This is quantified by the fitting process (for a fixed value of K_{D}) through variation in the ocular half-life of ranibizumab $t_{1/2}^{(r)}$ and related species. The distribution of predicted values of $t_{1/2}^{(r)}$ is shown in Figure 4.8, also modelled as a log normal distribution [120]. The predicted log normal parameters (as shown in the figure legend), predict a mean $t_{1/2}^{(r)}$ of 7.9 days, with a standard deviation of 2.0 days.

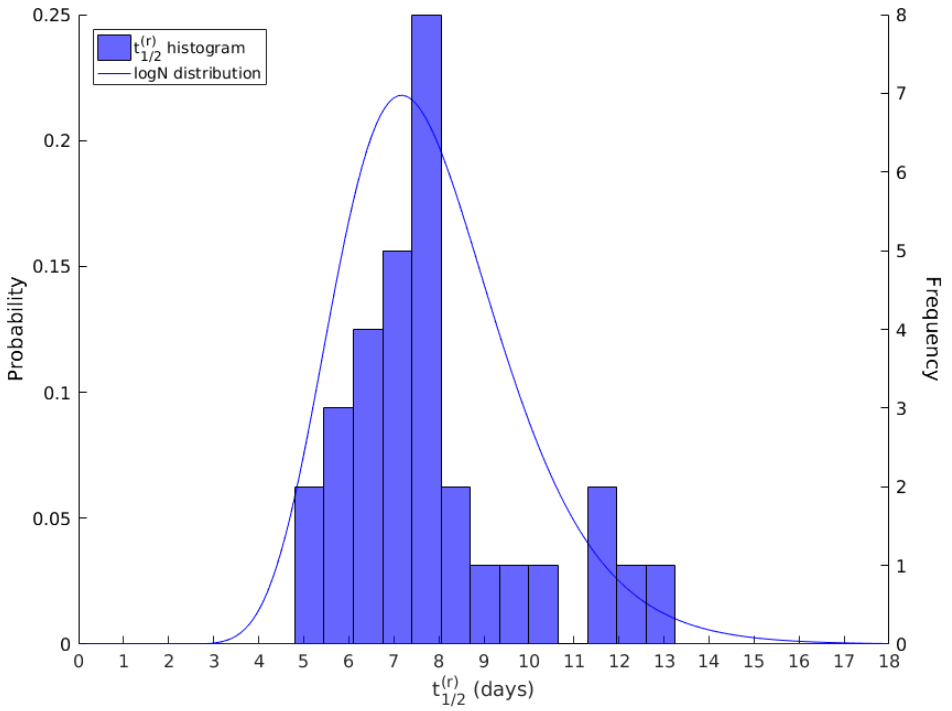

Figure 4.8: Distribution of $t^{(r)}_{1/2}$ over patient sample, for $K_{\mathrm{D}} = 19,000$ pM. The box plot is a histogram, whereas the line shows a log normal distribution, fit to this data, with parameters (95% CI) $\mu = 2.03$ (1.94, 2.12) and $\sigma = 0.25$ (0.20, 0.33).

By rescaling the free VEGF concentration for each patient such that the equilibrium level is unity, the temporal variation of the VEGF dynamics is more readily visualised. The shaded regions shown in Figure 4.9 correspond to the range of simulated free VEGF profiles, the red and blue regions represent the retina and aqueous, respectively. Panel (a) of Figure 4.9 superimposes the normalised clinical data, and one can see the consistency between the distribution of the model fits and the data points. Note the difference in-between panel (a) (aqueous) and (b) (retina) within the first 30 days - we see a distinct difference in behaviour, the aqueous profiles all drop to zero within $0 < t \ll 1$ day, whereas the retina reaches a non-zero minimum in roughly 2 days, at which point the profile starts growing exponentially. We note that in Figure 4.9 data-points that lie outside of the shaded 10-90th percentile region may be either in the 0-10th and 90-100th half-life percentile. Additionally other points may lie outside the range due to variability in determining the baseline VEGF production rate.

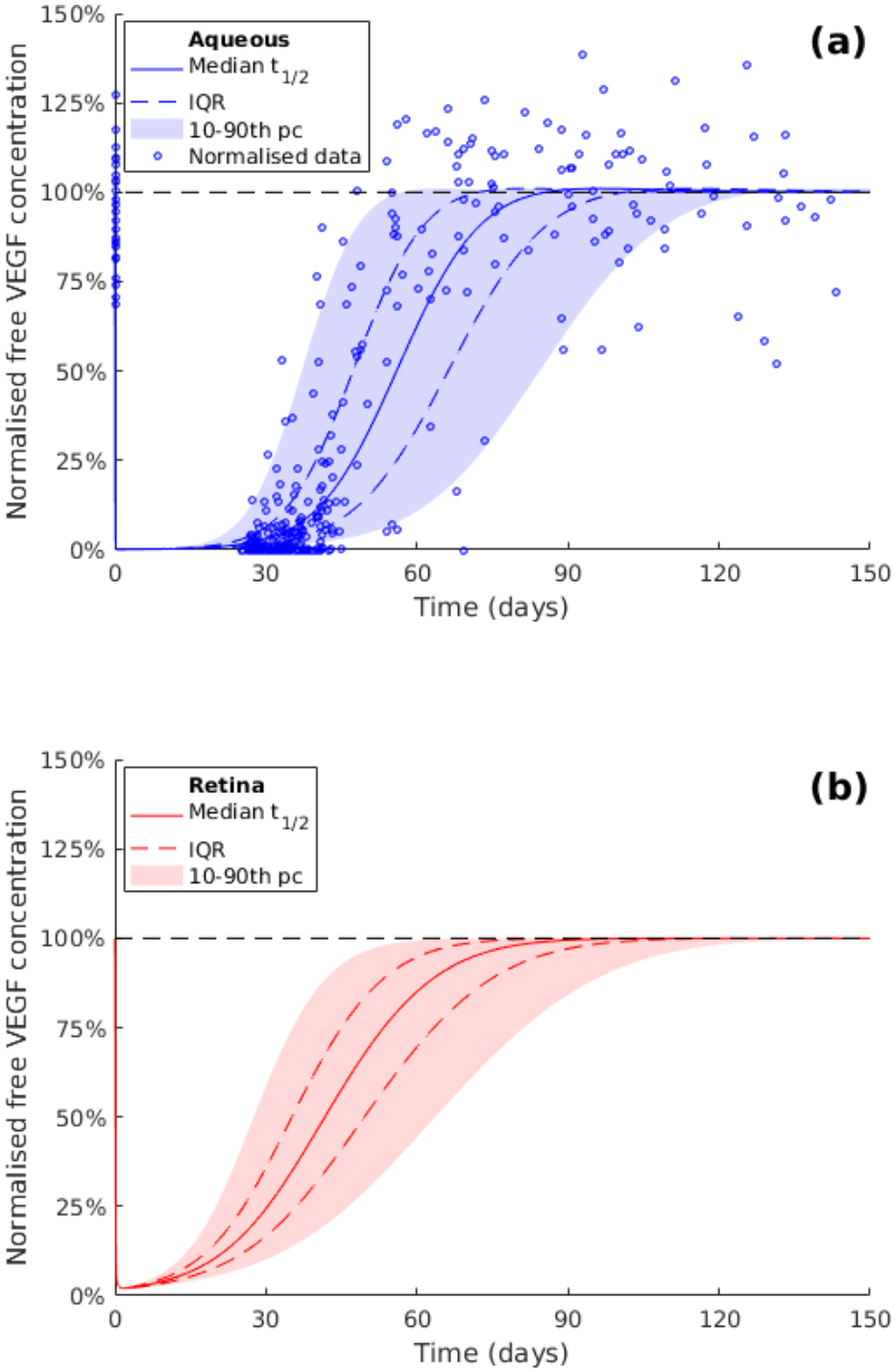

Figure 4.9: Range of normalised free VEGF concentrations across patient sample, the shaded red and blue regions represent the aqueous (panel (a)) and retina (panel (b)), respectively, panel (a) also shows the normalised clinical data. Patient simulations shown are fits corresponding to $K_{\mathrm{D}} = 19,000$ pM.

4.1.5 Retina-aqueous suppression lag

As noted previously the retina begins returning to its free VEGF steady state concentration sooner than the vitreous and aqueous (which return in parallel at a later time). We define $t_{\text{ret}}^{(10\%)}$ and $t_{\text{aq}}^{(10\%)}$ as the time for the retina and aqueous to return to 10% of their respective compartment VEGF steady state concentration. Figure 4.10 shows $t_{\text{ret}}^{(10\%)}$ plotted versus $t_{\text{aq}}^{(10\%)}$ for all 31 patients, demonstrating a strong linear correlation, indicating that the retina reaches 10% of its respective free VEGF concentration approximately twice as fast as the aqueous. We also note that average value of $t_{\text{ret}}^{(10\%)}$ is approximately 20 days shorter than the average value of $t_{\text{aq}}^{(10\%)}$, across the patient sample.

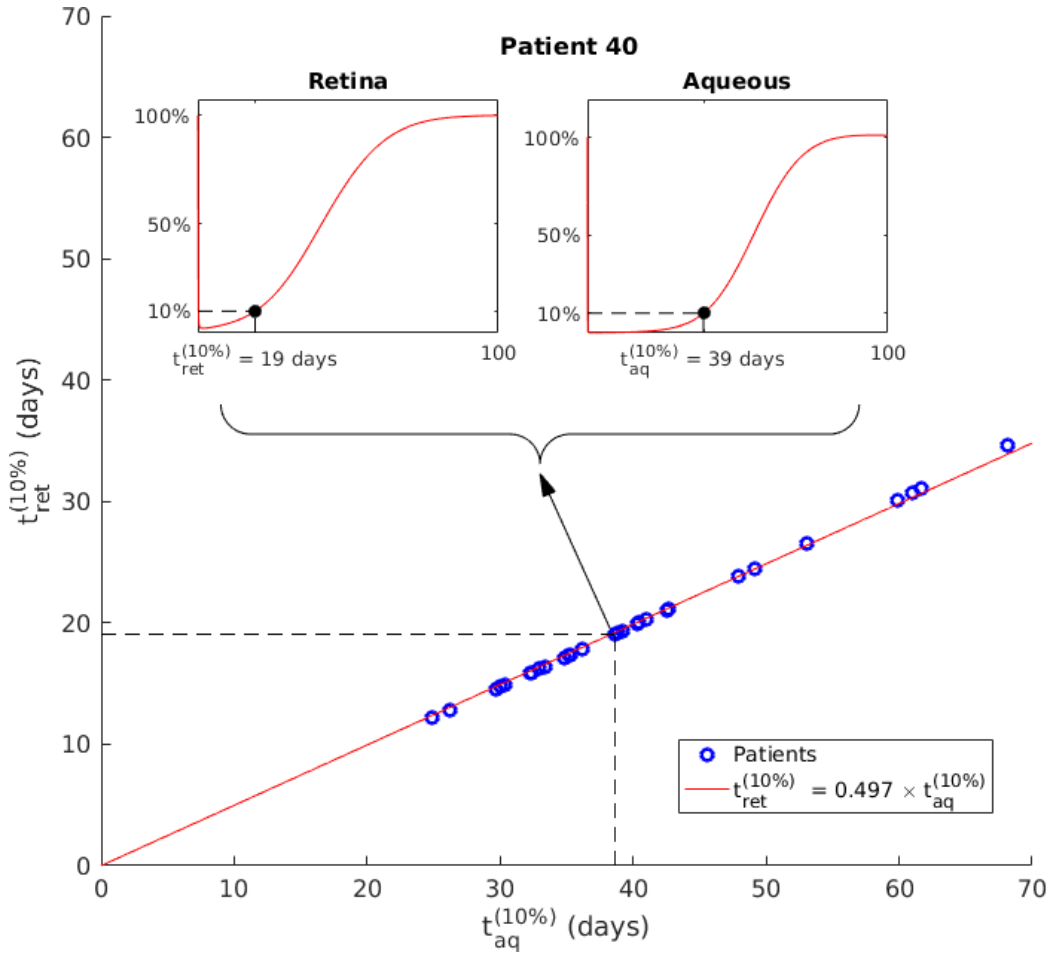

Figure 4.10: Time taken to reach 10% of VEGF steady state concentration in the retina and aqueous, denoted by $t_{\text{ret}}^{(10\%)}$ and $t_{\text{aq}}^{(10\%)}$, respectively, in days. The main plot shows patient $t_{\text{ret}}^{(10\%)}$ values versus $t_{\text{aq}}^{(10\%)}$, with a linear fit through the origin, whose slope (with 95% confidence interval) is found in the legend. Using patient 40 as an example, the inset figure graphically describes how the terms $t_{\text{ret}}^{(10\%)}$ and $t_{\text{aq}}^{(10\%)}$ are defined and how the values in the main plot were generated.

4.1.6 Caricature model analysis of retina-aqueous suppression lag

In order to analyse the observed retina-aqueous suppression lag, detailed across the patient population in Section 4.1.5, we consider a caricature 3-compartment model. In comparison to the 3-compartment model, analytic progress may be made with the caricature 3-compartment model, due to several key simplifications, which we will note while in the model formulation below. We define this caricature model over three chemical species A, B and C, subject to the following chemical reactions:

$$\mathrm{A} + \mathrm{B} \underset{k_{\mathrm{on}}}{\overset{k_{\mathrm{off}}}{\rightleftharpoons}} \mathrm{AB}. \tag{4.80}$$

In this model A, B and C are analogous to V, R and VR, however, unlike the full 3-compartment model, for simplicity we neglect the third chemical species RVR, thus reducing the level of nonlinearity within our system. As the aqueous is mathematically decoupled from the vitreous and retina, in the caricature model we only consider two compartments Ω_1 (with volume V_1) and Ω_2 (with volume V_2), analogous to the retina and vitreous. Surface regions of Ω_1 given by $\delta\Omega_\beta$ and $\delta\Omega_\alpha$ are analogous to the ILM and RPE, respectively, however across these membranes (in contrast to the full 3-compartment model) all molecules have the same permeability, P_β across $\delta\Omega_\beta$ and P_α across $\delta\Omega_\alpha$. This simplification is made as the difference in permeabilities across the range of molecules considered in this thesis is relatively small, and a significant barrier to analytic progress. The surface areas of $\delta\Omega_\beta$ and $\delta\Omega_\alpha$ are both set equal to S. Analogous to the production of VEGF with rate V_{in}, A is produced at rate a_{in} in Ω_1. As in the full 3-compartment model molecules in the vitreous are eliminated into the aqueous at rate k_{el}, in the caricature model molecules in Ω_2 are eliminated at rate K. We may then formulate the caricature model as a system of 6 ODEs, given as follows:

Compartment Ω_1

$$\frac{\mathrm{d}a_1}{\mathrm{d}t} = (k_{\mathrm{off}}c_1 - k_{\mathrm{on}}a_1b_1) - \frac{S}{V_1}(P_\beta + P_\alpha)\,a_1 + \frac{S}{V_1}P_\beta a_2 + \frac{a_{\mathrm{in}}}{V_1}, \tag{4.81}$$

$$\frac{\mathrm{d}b_1}{\mathrm{d}t} = (k_{\mathrm{off}}c_1 - k_{\mathrm{on}}a_1b_1) - \frac{S}{V_1}(P_\beta + P_\alpha)\,b_1 + \frac{S}{V_1}P_\beta b_2, \tag{4.82}$$

$$\frac{\mathrm{d}c_1}{\mathrm{d}t} = -(k_{\mathrm{off}}c_1 - k_{\mathrm{on}}a_1b_1) - \frac{S}{V_1}(P_\beta + P_\alpha)\,c_1 + \frac{S}{V_1}P_\beta c_2, \tag{4.83}$$

Compartment Ω_2

$$\frac{\mathrm{d}a_2}{\mathrm{d}t} = (k_{\text{off}}c_2 - k_{\text{on}}a_2b_2) + \frac{S}{V_2}P_\beta a_1 - \left(\frac{S}{V_2}P_\beta + K\right)a_2, \tag{4.84}$$

$$\frac{\mathrm{d}b_2}{\mathrm{d}t} = (k_{\text{off}}c_2 - k_{\text{on}}a_2b_2) + \frac{S}{V_2}P_\beta b_1 - \left(\frac{S}{V_2}P_\beta + K\right)b_2, \tag{4.85}$$

$$\frac{\mathrm{d}c_2}{\mathrm{d}t} = -(k_{\text{off}}c_2 - k_{\text{on}}a_2b_2) + \frac{S}{V_2}P_\beta c_1 - \left(\frac{S}{V_2}P_\beta + K\right)c_2, \tag{4.86}$$

where all parameters and concentration notation are defined in Tables 4.4 and 4.5, respectively. Initial conditions are given by the following:

$$a_1(0) = a_0, \quad b_1(0) = 0, \quad c_1(0) = 0, \tag{4.87}$$

$$b_2(0) = b_0, \quad a_2(0) = \delta a_0, \quad c_2(0) = 0, \tag{4.88}$$

where b_0 is the initial concentration of molecule B, and where a_0 and δ are derived via solving the steady state problem in the absence of molecule B, and given by:

$$a_0 = \frac{SP_\beta + V_2K}{SP_\beta}\left(\frac{a_{\text{in}}}{SP_\alpha + V_2K\left(1 + \frac{P_\alpha}{P_\beta}\right)}\right), \quad \delta = \frac{SP_\beta}{SP_\beta + V_2K}. \tag{4.89}$$

Species	3-comp analogous species	Conc. (pM)
A_1	V_{ret}	a_1
B_1	R_{ret}	b_1
C_1	VR_{ret}	c_1
A_2	V_{vit}	a_2
B_2	R_{vit}	b_2
C_2	VR_{vit}	c_2

Table 4.4: Model chemical species. Note, all concentrations are functions of time (t) and are expressed in pM, where subscripts indicate the compartment associated with each concentration.

Parameter	3-comp equiv.	Value	Units	Description
k_{off}	k_{off}	1	day^{-1}	Binding site off rate
k_{on}	k_{on}	5×10^{-5}	$\text{pM}^{-1}\text{day}^{-1}$	Binding site on rate
K_{D}	K_{D}	2×10^{4}	pM	Dissociation constant
a_{in}	V_{in}	10	fmol/day	Rate of VEGF production
K	k_{el}	1×10^{-1}	day^{-1}	Vitreous-aqueous elimination rate
P_α	p_{RPE}	1×10^{-7}	cm/sec	RPE permeability
P_β	p_{ILM}	1×10^{-7}	cm/sec	ILM permeability
V_1	V_{ret}	1×10^{-1}	mL	Retinal volume
V_2	V_{vit}	5	mL	Vitreal volume
S	S_{ret}	10	cm^2	Retinal surface area

Table 4.5: Model parameters for the caricature model analogue to the 3-compartment model. Note the second column '3-comp equiv.' detailing how the parameters in the caricature model relate to those of the 3-compartment model. Values given in this table are chosen to be order of magnitude estimates for their typical 3-compartment model analogues, these parameters are taken, and referred to as the baseline parameters used in solving the caricature model throughout this section.

We proceed by using the following non-dimensionalisation:

$$a_1 = a_0 x_1, \quad b_1 = b_0 y_1, \quad c_1 = a_0 z_1, \quad a_2 = \delta a_0 x_2, \quad b_2 = b_0 y_2, \quad c_2 = \delta a_0 z_2, \tag{4.90}$$

where we non-dimensionalise time by letting $t = \tau / k_{\text{off}}$. Upon substitution this yields

Compartment Ω_1

$$\varepsilon \frac{\mathrm{d}x_1}{\mathrm{d}\tau} = (\varepsilon z_1 - x_1 y_1) - \varepsilon(p+q)x_1 + \varepsilon\delta p x_2 + \varepsilon a, \tag{4.91}$$

$$\frac{\mathrm{d}y_1}{\mathrm{d}\tau} = \eta\,(\varepsilon z_1 - x_1 y_1) - (p+q)y_1 + p y_2, \tag{4.92}$$

$$\varepsilon \frac{\mathrm{d}z_1}{\mathrm{d}\tau} = -\,(\varepsilon z_1 - x_1 y_1) - \varepsilon(p+q)z_1 + \varepsilon\delta p z_2. \tag{4.93}$$

Compartment Ω_2

$$\varepsilon \frac{\mathrm{d}x_2}{\mathrm{d}\tau} = (\varepsilon z_2 - x_2 y_2) + \varepsilon \left(\frac{\omega p}{\delta}\right) x_1 - \varepsilon\,(\omega p + k)\,x_2, \tag{4.94}$$

$$\frac{\mathrm{d}y_2}{\mathrm{d}\tau} = \delta\eta\,(\varepsilon z_2 - x_2 y_2) + \omega p y_1 - (\omega p + k)\,y_2, \tag{4.95}$$

$$\varepsilon \frac{\mathrm{d}z_2}{\mathrm{d}\tau} = -\,(\varepsilon z_2 - x_2 y_2) + \varepsilon \left(\frac{\omega p}{\delta}\right) z_1 - \varepsilon\,(\omega p + k)\,z_2, \tag{4.96}$$

where:

$$\varepsilon = \frac{K_{\text{D}}}{b_0}, \quad \omega = \frac{V_1}{V_2}, \quad a = \frac{a_{\text{in}}}{k_{\text{off}} a_0 V_1}, \quad \eta = \frac{a_0}{b_0}, \tag{4.97}$$

$$p = \frac{S}{k_{\text{off}} V_1} P_\beta, \quad q = \frac{S}{k_{\text{off}} V_1} P_\alpha, \quad k = \frac{K}{k_{\text{off}}}. \tag{4.98}$$

By noting that both $\varepsilon, \delta \ll 1$, by the previous analysis of the 3-compartment PK model, presented in Section 3.1, we have the following approximate solution for y_1 and y_2:

$$y_1 \simeq \frac{K_1 K_2}{K_1 + K_2} e^{-\bar{\lambda_1}\tau}, \quad y_2 \simeq \frac{K_2}{K_1 + K_2} e^{-\bar{\lambda_1}\tau}, \tag{4.99}$$

where

$$K_1 = \frac{k + \omega p - \bar{\lambda_1}}{\omega p}, \quad K_2 = \frac{\bar{\lambda_2} - k - \omega p}{\omega p} \tag{4.100}$$

and

$$\bar{\lambda_1} = \frac{1}{k_{\text{off}}}\lambda_1 \simeq \frac{1}{k_{\text{off}}}\left[K + \left(\frac{S}{V_2}\right) P_\beta - \left(\frac{SP_\beta}{V_2}\right) \frac{1}{\left[\left(1 + \frac{P_\alpha}{P_\beta}\right) - \frac{V_1}{V_2}\left(1 + \frac{V_2 K}{S P_\beta}\right)\right]}\right], \tag{4.101}$$

$$\bar{\lambda_2} = \frac{1}{k_{\text{off}}}\lambda_2 \simeq \frac{1}{k_{\text{off}}}\left[\frac{SP_\beta}{V_1}\left(1 + \frac{P_\alpha}{P_\beta}\right)\right]. \tag{4.102}$$

Next, we note that by conservation of mass we may write

$$z_1 = 1 - x_1, \qquad z_2 = 1 - x_2, \tag{4.103}$$

this is (additionally) proven in Appendix A.10. Therefore we can write the system in terms of x_1 and x_2:

Compartment Ω_1

$$\varepsilon \frac{\mathrm{d}x_1}{\mathrm{d}\tau} = -\left[\varepsilon(1 + p + q) + y_1\right] x_1 + \varepsilon \delta p x_2 + \varepsilon(a + 1), \tag{4.104}$$

Compartment Ω_2

$$\varepsilon \frac{\mathrm{d}x_2}{\mathrm{d}\tau} = \varepsilon\left(\frac{\omega p}{\delta}\right) x_1 - \left[\varepsilon\left(\omega p + k + 1\right) + y_2\right] x_1 + \varepsilon. \tag{4.105}$$

As it is known that in the full model the relative magnitudes of k_{el} and k_{off} ($k_{\text{el}} \ll k_{\text{off}}$) cause the vitreous to be in a state of chemical equilibrium, we therefore may further simplify the caricature model equation by assuming $K \ll k_{\text{off}}$, giving the following equation describing chemical equilibrium in Ω_2:

$$x_2 = \frac{1}{1 + y_2/\varepsilon}, \tag{4.106}$$

which reduces the system to the single ODE for x_1:

$$\varepsilon \frac{\mathrm{d}x_1}{\mathrm{d}\tau} = -\left[\varepsilon(1 + p + q) + y_1\right] x_1 + \frac{\varepsilon^2 \delta p}{\varepsilon + y_2} + \varepsilon(a + 1). \tag{4.107}$$

Assuming p and q are large in comparison to ε ($p, q \sim O(1/\varepsilon)$), due to their factor of $1/V_{\text{ret}}$, allows us to make a quasi-steady state (QSS) assumption, giving:

$$x_1 \simeq \frac{\varepsilon\,(a+1) + \varepsilon^2\left(\frac{\delta p}{y_2+\varepsilon}\right)}{y_1 + \varepsilon\,(p+q+1)} \tag{4.108}$$

$$\simeq \frac{\varepsilon\,(a+1)}{y_1 + \varepsilon\,(p+q+1)} \tag{4.109}$$

where we have neglected transport from the vitreous to the retina by assuming $\varepsilon^2(\delta p)/(y_2+\varepsilon) \sim O(\varepsilon^2)$, which, breaks down when $p \sim O(1/(\delta\varepsilon))$ or greater. Appendix A.11 details the generation of the following dimensional expressions for a_1 and a_2, as follows:

$$a_1 \simeq \frac{a_{\text{in}} + k_{\text{off}} V_1 a_0}{k_{\text{off}} V_1 + S(P_\alpha + P_\beta) + V_1 b_0 k_{\text{on}} e^{-\lambda_1 t} \Big/ \left(1 + \frac{P_\alpha}{P_\beta}\right)}, \tag{4.110}$$

$$a_2 \simeq \frac{\delta a_0}{1 + \frac{b_0}{K_{\text{D}}}\left\{1 - \frac{V_1 K}{P_\beta S} \Big/ \left(1 + \frac{P_\alpha}{P_\beta}\right)\right\} e^{-\lambda_1 t}}. \tag{4.111}$$

One can see from Equation 4.110 the similarity between the expression for a_1 and the intermediate time solution for v_{ret}, given by Equation 4.65. Unlike 4.65, as $t \to \infty$ Equation 4.110 converges - however to a value slightly less than the true steady state value of the system. This occurs due to the fact that in moving from Equation 4.108 to Equation 4.109 we neglected vitreous-retina transport, as it was assumed to be $O(\varepsilon^2)$. We tabulate this and the other the assumptions made in generating Equations 4.110-4.111 in Table 4.6.

	Assumption	Compartment	Conditions such that this holds
(1)	Chemical equilibrium	Ω_2	$k_{\text{el}} \ll k_{\text{off}}$
(2)	Quasi steady-state	Ω_1	p or $q \sim O(1/\varepsilon)$
(3)	Vitreal transport is negligible	Ω_1	$p \ll 1/(\delta\varepsilon)$

Table 4.6: Assumptions made in order to generate Equations 4.110-4.111, alongside the theoretical conditions under which such assumptions should hold. See main text for explanations as to why these conditions hold.

In order for us to analyse the suppression lag between the vitreous and retina we define the following:

$$a_1\left(t_1^{(100\alpha\%)}\right) = \alpha a_0 \tag{4.112}$$

$$a_2\left(t_2^{(100\alpha\%)}\right) = \alpha\delta a_0, \tag{4.113}$$

where $\alpha \in [0, 1]$. The suppression delay between Ω_1 and Ω_2 is then described by:

$$\Delta t^{(100\alpha\%)} = t_2^{(100\alpha\%)} - t_1^{(100\alpha\%)}. \tag{4.114}$$

We may then use the solutions for a_1 and a_2 to solve for $t_1^{(100\alpha\%)}$ and $t_2^{(100\alpha\%)}$, and hence $\Delta t^{(100\alpha\%)}$. As detailed in Appendix A.11, the solutions for $t_1^{(100\alpha\%)}, t_2^{(100\alpha\%)}$ and $\Delta t^{(100\alpha\%)}$ can be written:

$$-\lambda_1 t_1^{(100\alpha\%)} = \log\left(\frac{1+\frac{P_\alpha}{P_\beta}}{V_1 b_0 k_{\text{on}}}\left\{\frac{a_{\text{in}}+k_{\text{off}}V_1 a_0}{\alpha a_0} - k_{\text{off}}V_1 - S(P_\alpha+P_\beta)\right\}\right), \tag{4.115}$$

$$\lambda_1 t_2^{(100\alpha\%)} = \log\left(\frac{b_0}{K_{\text{D}}}\left(\frac{\alpha}{1-\alpha}\right)\left\{1-\frac{V_1 K}{P_\beta S}\Big/\left(1+\frac{P_\alpha}{P_\beta}\right)\right\}\right), \tag{4.116}$$

$$\lambda_1 \Delta t^{(100\alpha\%)} = \log(1+g), \tag{4.117}$$

where:

$$g = \frac{P_\alpha}{P_\beta} - \frac{V_1 K}{P_\beta S} + \frac{1}{(1-\alpha)V_1 k_{\text{off}}}\left(1+\frac{P_\alpha}{P_\beta}-\frac{V_1 K}{P_\beta S}\right)\left[\frac{a_{\text{in}}}{a_0} - \alpha S(P_\alpha+P_\beta)\right]. \tag{4.118}$$

Notice we have written Equation 4.117 in this way as, when $g \to 0$, we find that $t_1^{(100\alpha\%)} \to t_2^{(100\alpha\%)}$, and hence $\Delta t^{(100\alpha\%)} \to 0$. Figure 4.11 depicts g and $\Delta t^{(100\alpha\%)}$ plotted over various parameter regimes, modified from baseline (see Table 4.5), for $\alpha = 0.1$. The red line in plot (a) demonstrates that g is increasing in P_α, asymptotes as it tends to zero, tends to infinity as it increases. The red line in plot (b) demonstrates that g is decreasing in P_β, and we see that approximation breaks down for values near the dashed line (where assumption (3) from Table 4.6 breaks down). Plot (b) shows that g is decreasing in k_{off}, and asymptotes as $k_{\text{off}} \to \infty$. We note this does not hold for values lower than K, which is taken to be 10^{-1} 1/day in Figure 4.11. Plots (d) and (e) show these parameter changes similar effects on $\Delta t^{(\alpha)}$ as g. Plot (c) shows g is relatively constant, however there is a large change in $\Delta t^{(\alpha)}$ as K greatly alters λ_1, however this demonstrates that is does not greatly effect g. This result is also evident from plot (f) where we see $\Delta t^{(\alpha)}$ plotted versus K.

Figure 4.12 depicts the toy model solved using the baseline parameters found in Table 4.5, chosen to represent, to order of magnitude, their 3-compartment counterparts. Figure 4.12 demonstrates the accuracy of the approximate solution for a_1 and a_2 (Equations 4.110-4.111), as well as the approximate analytic expression for $t_1^{(100\alpha\%)}$ and $t_2^{(100\alpha\%)}$ (Equations 4.115 and 4.116, respectively) and $\Delta t^{(\alpha)}$ (Equation 4.117). Appendix A.12 fully details the effect of varying $k_{\text{off}}, k_{\text{on}}, K_{\text{D}}, P_\alpha, P_\beta$ and K on the suppression delay between Ω_1 and Ω_2, we reproduce one of these figures, Figure 4.13, as an example of the results found there.

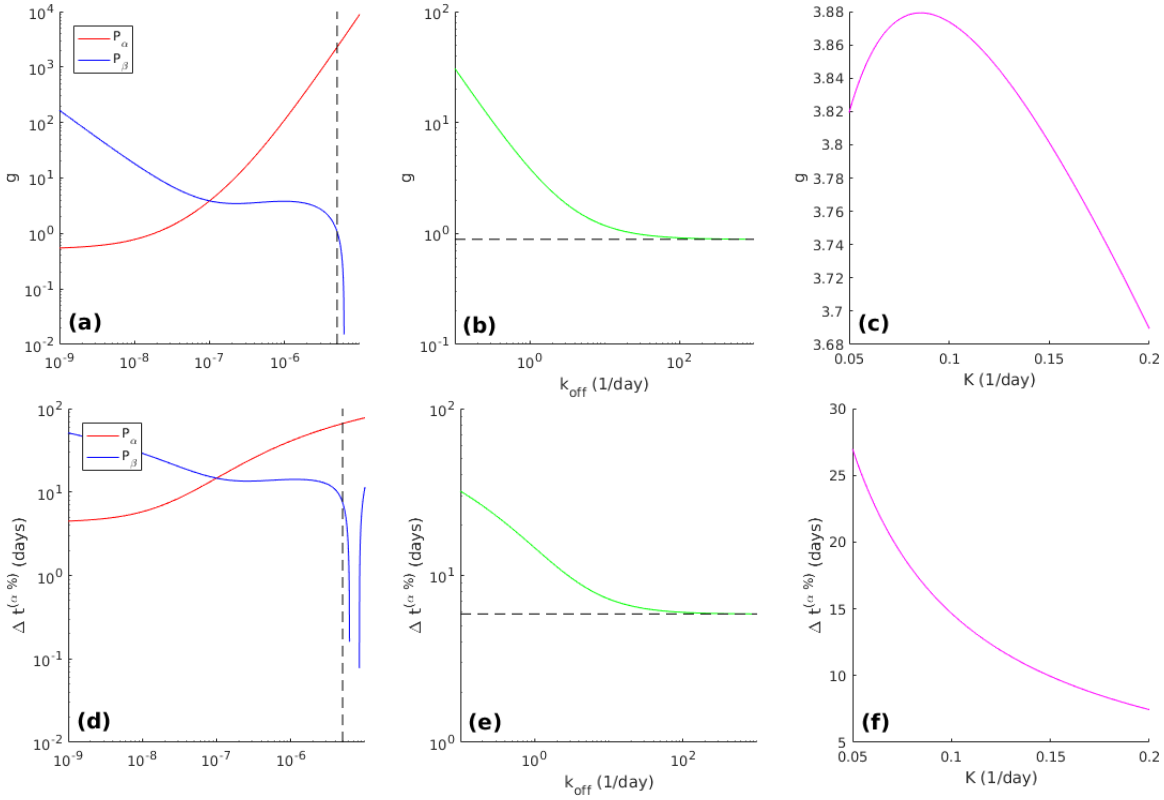

Figure 4.11: Equation 4.118 plotted over various parameter regimes, modified from baseline, for $\alpha = 0.1$. Plots (a), (b) and (c) consider the effect on g due to variation in permeability, k_{off} and K, respectively, plots (d), (e) and (f) show the same for $\Delta t^{(100\alpha\%)}$. The dashed line in plot (a) denotes the point on the horizontal axis equal to the baseline value of P_β (1×10^{-7} cm/sec) divided by ε, i.e. the theoretical point where assumption (3), from Table 4.6, should break down.

The figures in Appendix A.12 under the title *'Caricature model, 3-compartment model comparison'* compare the caricature model with the full 3-compartment model, where both models are solved using parameters for Fab molecules, and human geometry given in Section 4.1.1 (noting molecules A, B and BA in the caricature model are assumed to have transport rates associated with Fab molecules). By repeating the parameter study, this time not only considering the caricature model but also the 3-compartment model, we are able to analyse whether the full model behaves qualitatively in the same manner as the caricature model. While it is evident that the two models are not equivalent (when solved using the same parameter values), we can see from the plots in Appendix A.12 that the two models' behaviour is exceedingly similar with respect to parameter variation. From these results we conclude that the analysis of change in suppression delay in the caricature model holds at least qualitatively for the full 3-compartment model, i.e. that the 3-compartment model concentration profiles will respond in the same way under a parameter change, relative to

the caricature model under the equivalent parameter change. The analysis of the caricature model therefore gives us a mechanistic understanding, through analytic and numerical results, of the suppression delay observed in the full 3-compartment model.

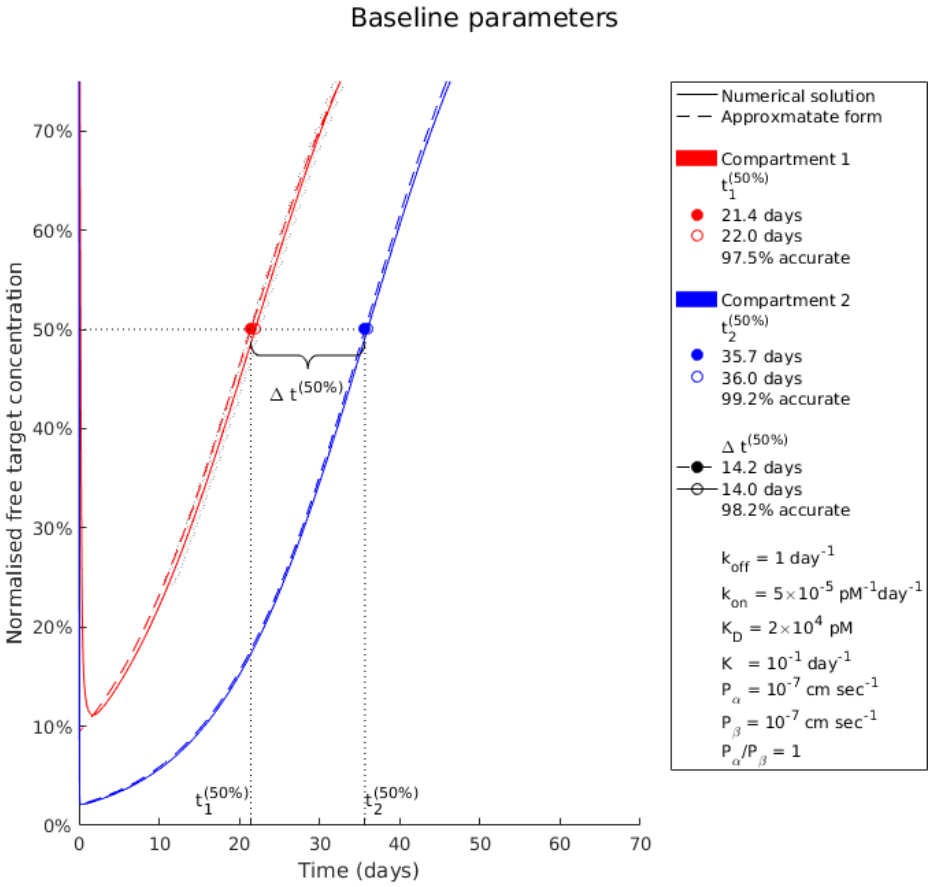

Figure 4.12: Baseline parameter solution for caricature model, depicting numerical (solid, Equations 4.81-4.86) and approximate analytic solution (dashed Equations 4.110-4.111). Solid dots denote exact $t^{100\alpha\%}$ values, whereas empty dots are generated via Equations 4.116-4.116, similarly for $\Delta t^{100\alpha\%}$, where the approximate value is generated from Equation 4.117. Percentage accuracies of these approximate formulae are given in the figure legend.

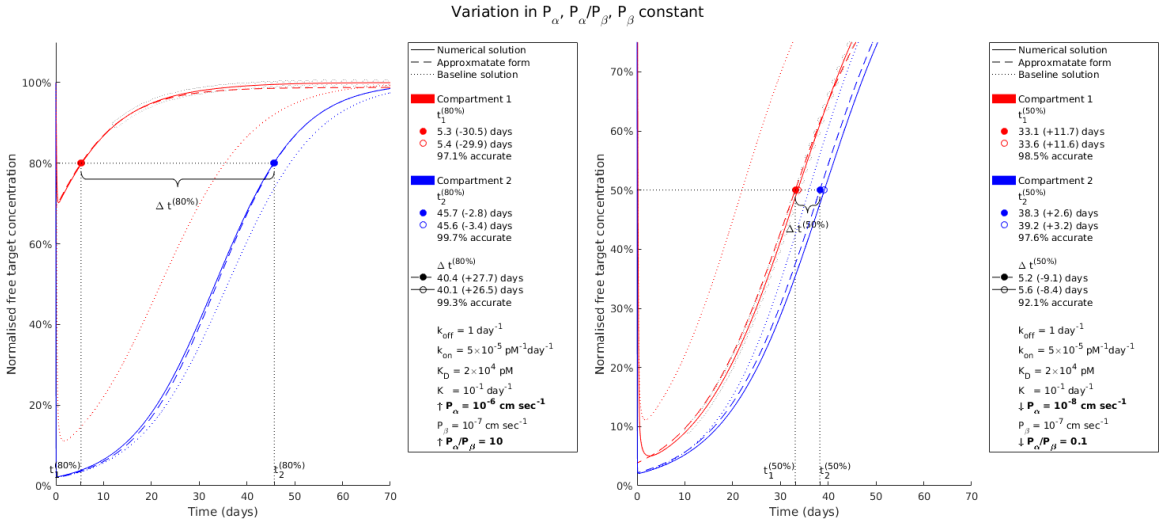

Figure 4.13: Demonstration of parameter variation on the caricature model (Equations 4.81-4.86), approximation solutions and expressions. Here we see the effect of increasing P_α while keeping P_β constant.

4.1.7 Modified retinal permeability PD case studies

Simulated PD for a drug impermeable to the retina

Currently it is assumed that an IVT drug for wet AMD is required to permeate through the ILM and into the retina to be efficacious [121], however it is not known whether a drug that cannot penetrate into the retina can still lower retinal VEGF levels by binding within the vitreous alone. This scenario can be simulated using our model, by setting the ILM permeability to drug and drug-VEGF complexes to zero. By doing so Equation 4.30, the non-dimensional governing equation for retinal free VEGF, reduces to the following:

$$\frac{\mathrm{d}x_{\mathrm{ret}}}{\mathrm{d}\tau} = Q^{(v)}x_{\mathrm{vit}} - E^{(v)}x_{\mathrm{ret}} + V. \tag{4.119}$$

If we assume that the system is in quasi steady-state (via the same logic used to justify previous retinal QSS assumptions), we may write:

$$x_{\mathrm{ret}} = \frac{1}{E^{(v)}}\left(Q^{(v)}x_{\mathrm{vit}} + V\right). \tag{4.120}$$

Therefore, as we expect x_{vit} to be very small post IVT injection, we may approximate x_{ret} to be (initially) equal to a constant, as follows:

$$x_{\mathrm{ret}} \simeq \frac{V}{E^{(v)}} \tag{4.121}$$

$$\Rightarrow \quad v_{\mathrm{ret}} \simeq \frac{V_{\mathrm{in}}}{S_{\mathrm{ret}}\left(p^{(v)}_{\mathrm{ILM}} + p^{(v)}_{\mathrm{RPE}}\right)}. \tag{4.122}$$

This expression does not contain any drug related parameters, therefore the model predicts that if a drug is unable to permeate from the vitreous to the retina, then the concentration to which free VEGF falls in the retina is independent of any properties of the drug, providing it is sufficiently mobile to justify the use of the well-mixed approximation implemented here. The expression given by Equation 4.122 is simply the steady state solution for v_{ret}, derived from Equation 4.3, by setting $v_{\text{vit}} = 0$ in the absence of drug in the retina ($c_{\text{ret}} = r_{\text{ret}} = 0$). This scenario is equivalent to that where all VEGF in the vitreous is initially assumed to be bound.

The numerical solution for retinal free VEGF, of a simulated IVT of 0.5 mg dose of retina-impermeable drug, can be seen in Figure 4.14. As can be seen from the figure, the drop in VEGF concentration is only roughly 15% of the steady state VEGF concentration, after which the concentration of free VEGF returns to steady state.

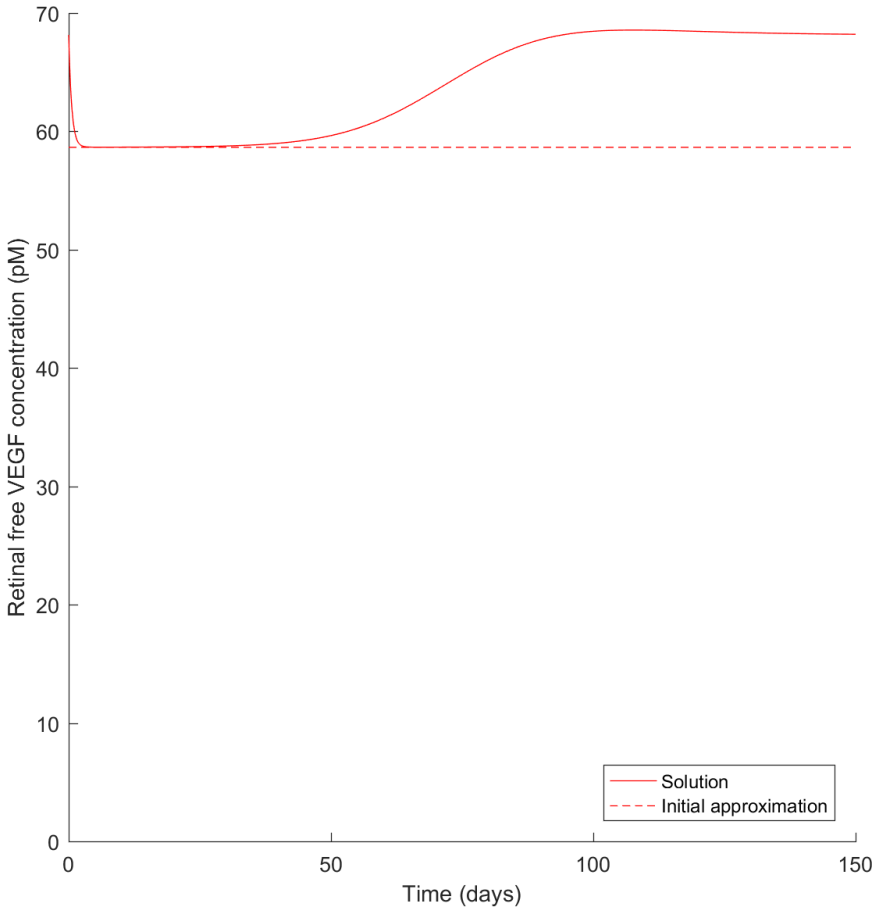

Figure 4.14: Simulated PD for a drug (and drug-VEGF complexes), impermeable to the retina. Numerical solution of Equations 4.3-4.18, for an IVT dose of 0.5 mg, with a K_D of 19,000 pM and half life of 7.5 days, is shown by the solid red line. The approximation given by Equation 4.122 is shown by the dashed line.

Impact of alterations to the permeability of the RPE

The values of the retinal permeabilities, p_{RPE} and p_{ILM}, as noted in section 4.1.1, were estimated from fitting the 3-compartment PK model to experimental data from rabbits with healthy retinas, therefore by using these values we are making two assumptions, that human and rabbit retinal permeabilities are sufficiently similar, and the presence of the disease in humans does not greatly alter these values. Consider an advanced case of wet AMD, such that neovasculature has severally breached the RPE and by doing so increases dramatically the effective permeability from the retina to the choroid. Unfortunately without further information as to which patients may have increased RPE permeability, or to what degree such a retinal breach may increase p_{RPE}, it is not possible to model this scenario in a rigorous manner. We present as a first step towards such an end a simulation where p_{RPE} is increased by a factor of 10 for all molecules. Similarly, for completeness, we consider p_{RPE} is decreased by a factor of 10 for all molecules.

In Figure 4.15 we see the simulated effect of varying p_{RPE} by a factor of 10 and 0.1, relative to the nominal values estimated in the rabbit, for two distinct dosage regimens (0.5 mg and 6 mg). The higher dose of 6 mg was chosen to reflect Phase II trials (BOULEVARD study [63], AVENUE [53] and STAIRWAY [62]), studying RG7716 (an IgG), at such a dosage in the human eye. When p_{RPE} is increased we see a sharp leftward shift in the retinal free VEGF profile, reduced retinal AUC of ranibizumab and decreased $t_{1/2}$, equal to 6.6 days. Relative to the solid red curve, the dashed red curve indicates little free VEGF suppression. Conversely when p_{RPE} is decreased we see increased free VEGF suppression in both the retina and aqueous, as well as an increased $t_{1/2}$, equal to 9.6 days. Note that retinal concentrations are more strongly affected by the value of p_{RPE} than the aqueous concentrations. The blue lines in Figure 4.15 demonstrate the effect of increasing the dose from 0.5 mg to 6 mg. In panels (e) and (f) we see that the blue lines are vertical translations of the corresponding red lines, as would be expected by an increase in dosage. In panels (c) and (d) we see the effect of increasing the dose manifests as a rightward shift in the suppression profiles, increasing the duration and magnitude of free VEGF suppression. In particular we note that the total retinal free VEGF suppressed (by moving from 0.5 mg to 6 mg in the high p_{RPE} case) is increased by $\sim$225%, relative to the 50% increase seen in the aqueous humour.

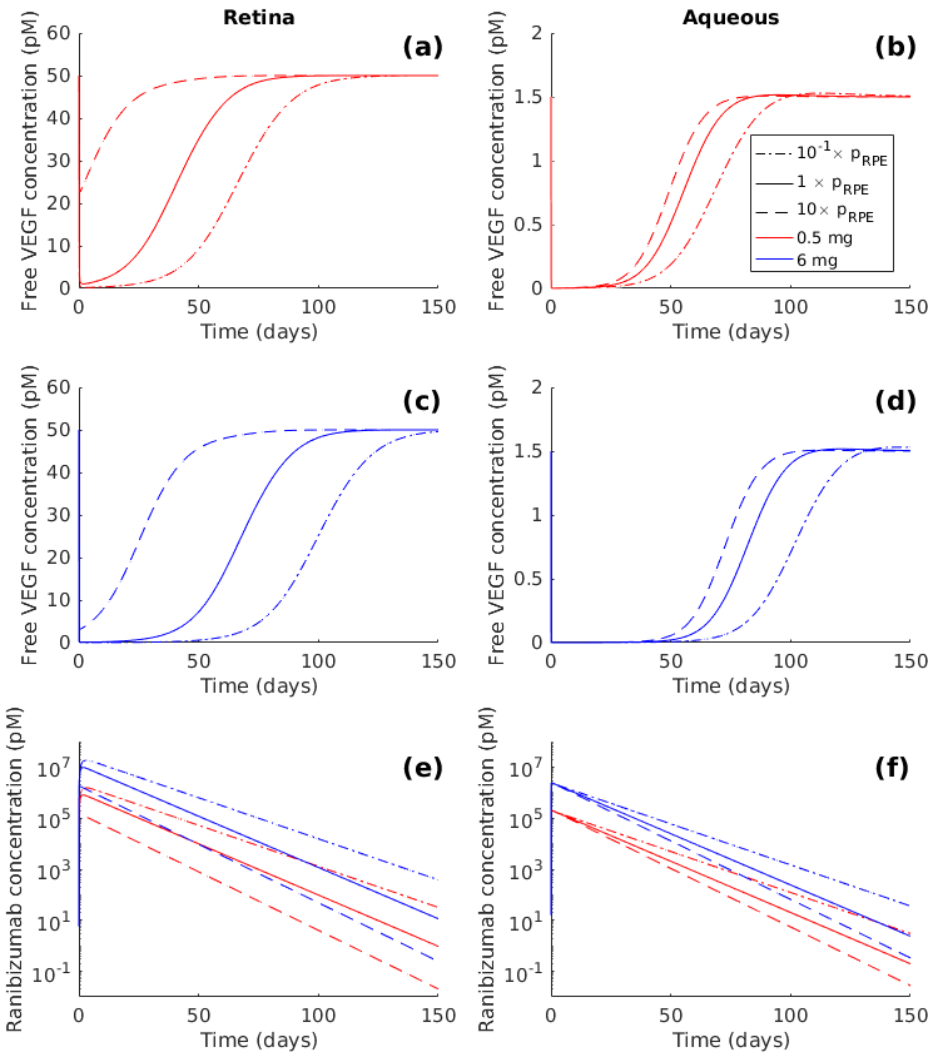

Figure 4.15: In panels (a)-(d), we see free VEGF and in (e)-(f) ranibizumab. Solid curves p_{RPE} set to baseline value as given by Equation 4.19, dashed curves have p_{RPE} set to 10 times as the solid red curve, while the dot-dashed curve has a value of p_{RPE} 10 times less. Red lines represent a dose of 0.5 mg, whereas blue represent a dose of 6 mg. When the value of p_{RPE} is altered so is the value of $t_{1/2}^{(r)}$, the solid, dashed and dot-dashed curves (in the retina and aqueous humour) have $t_{1/2}$ values of 7.5, 6.6 and 9.6 days, respectively. In these simulations $K_{\mathrm{D}} = 19,000$ pM and for each case V_{in} has been adjusted so as to keep the same free VEGF steady state as the base case.

4.1.8 Effects of dosage and reaction rate modifications

The 3-compartment model allows us, for the first time, to compare the simulated free VEGF concentration profiles of the retina and aqueous. We present an analysis examining the dynamical changes in these two compartments resulting from altering dosage and binding kinetics. The left-hand side panels in Figures 4.16-4.19 show the free VEGF concentration in the retinal compartment, alongside a magnification of the first 25 days, whereas the

right-hand side panels show analogous plots for the aqueous compartment. All simulations below used $t_{12}^{(r)} = 7.5$ days and a constant VEGF production rate of 18.5 fmol/day. The boxed regions in each plot have width of 30 days and height corresponding to 10% of their respective compartment free VEGF steady state concentration (this boxed region is then magnified within the panel inset), dots within the retinal inset indicate the minimum free VEGF concentration.

Figures 4.16-4.18 examine the simulated effect of varying parameters determining binding kinetics, namely K_{D}, k_{off} and k_{on}. In Figure 4.16 we see the effect of lowering K_{D} while keeping k_{on} constant (therefore also lowering k_{off}). Here we see a similar shift of the concentration profile of the aqueous as predicted in 2-compartment PK/PD model of Chapter 2 in Figure 2.7, however the model does not predict the same dynamical change in the retina. In the latter, on a longer timescale, we see a rightward temporal shift, however to a much smaller magnitude than is seen in the aqueous. At early time (< 30 days) in the retina we see almost no difference.

In Figure 4.17 we see the effect of increasing k_{on} while keeping K_{D} constant (therefore also increasing k_{off}). On a longer timescale we see very little change in either the retina or aqueous, suggesting these compartments are in a state of chemical equilibrium. At early time in the retina we see a decrease in the minimum suppression of free VEGF, as well as a decrease in the rate of return from suppression - this follows the same dynamical change that is presented when the dosage is increased.

In Figure 4.18 we see the effect of increasing k_{on} while keeping k_{off} constant (therefore also lowering K_{D}). We see a congruent shift to the right of free VEGF profiles between the retina and aqueous, resulting in an equal increase in $t_{\mathrm{ret}}^{(10\%)}$ in both compartments. In the retina, in addition to increasing the suppression time, we also see a decrease in the minimum suppression of free VEGF. Figure 4.19 demonstrates the effect of increasing the dose, from the standard dose of 0.5 mg, up to 4 mg. Here we see an almost exact reflection of the dynamical change observed by increasing k_{on} while keeping k_{off} constant; a rightward temporal shift observed in both the retina and aqueous, a decrease in the minimum achieved free VEGF retinal concentration, as well as a decreased rate of return from suppression.

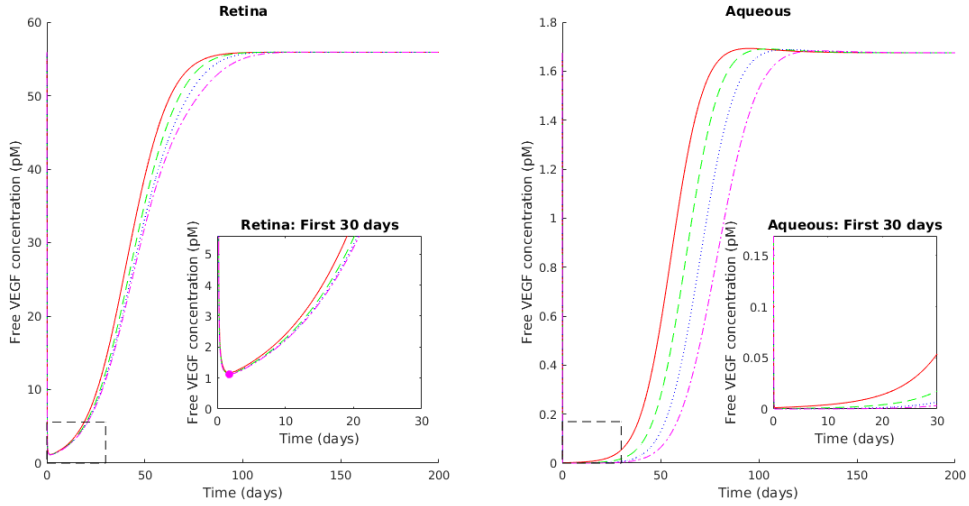

Figure 4.16: Simulated effect of decreasing K_{D} and k_{off} so as to keep k_{on} fixed, on the solution to Equations 4.3-4.18. Plots shown correspond to $K_{\mathrm{D}} = 19{,}000$ pM (solid red), $K_{\mathrm{D}} = 9{,}500$ pM (dashed green), $K_{\mathrm{D}} = 4{,}750$ pM (dotted blue) and $K_{\mathrm{D}} = 1900$ pM (dot-dash magenta).

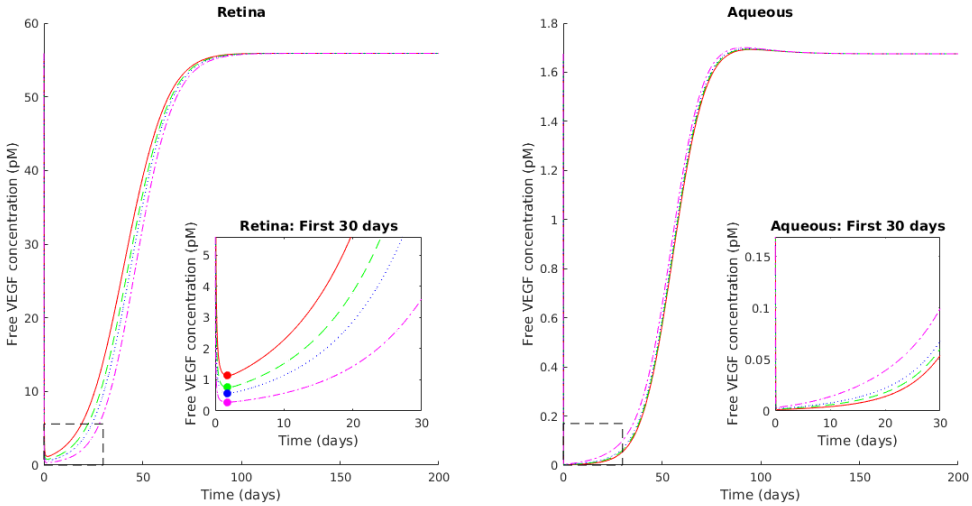

Figure 4.17: Simulated effect of increasing k_{on} and k_{off} so as to keep K_{D} fixed at 19,000 pM, on the solution to Equations 4.3-4.18. Plots shown correspond to $k_{\mathrm{off}} = 0.864$ 1/day (solid red), $k_{\mathrm{off}} = 1.296$ 1/day (dashed green), $k_{\mathrm{off}} = 1.728$ 1/day (dotted blue) and $k_{\mathrm{off}} = 3.456$ 1/day (dot-dash magenta).

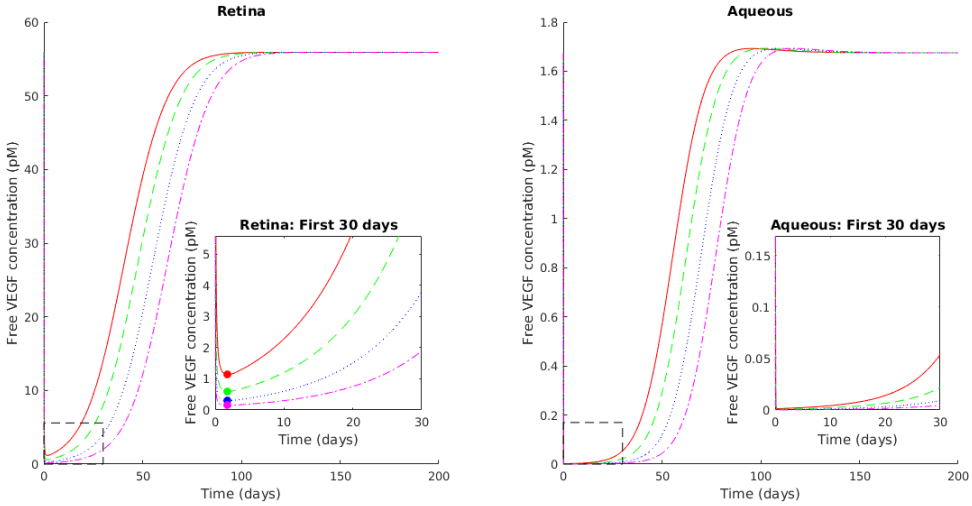

Figure 4.18: Simulated effect of increasing k_{on} and decreasing K_{D} so as to keep k_{off} fixed at 0.864 1/day, on the solution to Equations 4.3-4.18. Plots shown correspond to $K_{\text{D}} =$ 19,000 pM (solid red), $K_{\text{D}} = 10{,}000$ pM (dashed green), $K_{\text{D}} = 5{,}000$ pM (dotted blue) and $K_{\text{D}} = 2{,}500$ pM (dot-dash magenta).

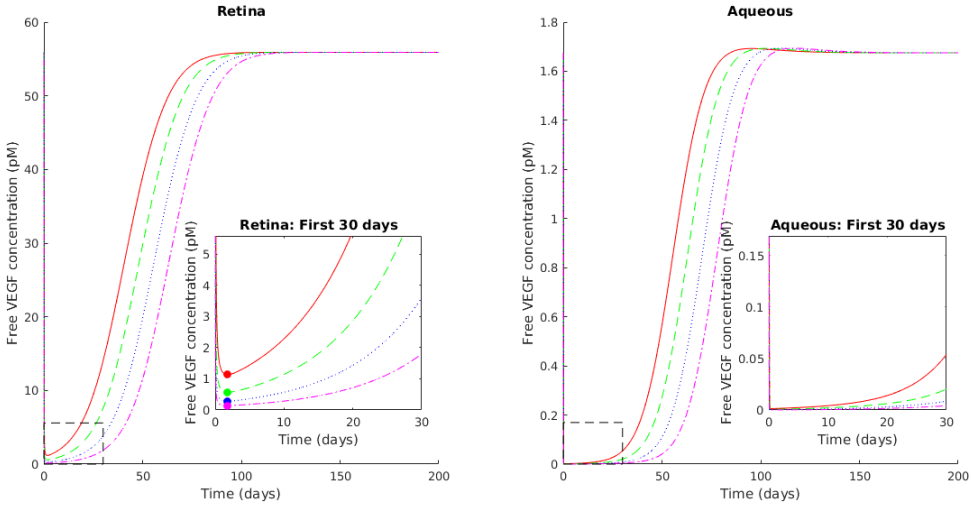

Figure 4.19: Simulated effect of increasing the dose from 0.5 mg (solid red), to 1 mg (dashed green), 2 mg (dotted blue) and 4 mg (dot-dash magenta), on the solution to Equations 4.3-4.18. Plotted with $K_{\text{D}} = 19{,}000$ pM.

4.1.9 3-compartment PK/PD ODE model summary

We have shown how, through the additional estimation of retinal permeabilities, the 2-compartment PK/PD model presented by Chapter 2 may be extended to also provide a window into retinal PD. This 3-compartment PK/PD model provides the first insights into the predicted behaviour of free VEGF concentrations in the retina, in a way that cannot be directly observed clinically in humans. OCT measurements allow for the direct observation

of the effect of anti-VEGF therapy on retinal disease activity, however the relationship of OCT parameters, e.g. central retinal thickness, to retinal or aqueous humour VEGF levels has not been established - a metric that, if possible to measure clinically, would be useful in evaluating the performance of anti-VEGF molecules. The 3-compartment model offers several key findings regarding an observed temporal disparity between the PD observed in the retina and aqueous humour, as well as its dependence on key parameters. This is of particular note as previous models [3, 28, 74] have assumed that the behaviour of free VEGF in the vitreous and aqueous is identical to that of the retina, however our findings suggest this is not necessarily the case.

It is important to bear in mind that the results presented in this chapter are simulated predictions and are subject to the accuracy of our model assumptions. The underlying PK structure of the model was based upon the work detailed in Section 3.1. A key assumption in this work was that human and rabbit retinal permeabilities are sufficiently similar - this uncertainty motivated the sensitivity study (under the heading *'Impact of alterations to the permeability of the RPE'* of Section 4.1.7) regarding the magnitude of p_{RPE}. Figure 4.15 demonstrates that, as the value of p_{RPE} is varied over two orders of magnitude, there is a large variation in the degree to which retinal free VEGF is suppressed, as well as in the value of $t_{1/2}^{(r)}$, ranging from 6.6 - 9.6 days. This variation in $t_{1/2}^{(r)}$ due to the variation in p_{RPE} may explain, to some degree, the level of variation, for a fixed value of K_{D}, observed in the estimated $t_{1/2}^{(r)}$ value within the Saunders et al. dataset [3] (see Figure 4.8).

In Figure 4.14 we show the predicted retinal free VEGF profile in the case where no drug, or drug bound VEGF molecule, is able to permeate into the retina. This result demonstrates that if the drug is restricted from entering the retina its ability to suppress retinal free VEGF is largely compromised, reducing the concentration by only 14% from the steady state in Figure 4.14. It is known from *in vivo* and *in vitro* studies that full length and fragment antibody molecules are able to permeate retinal membranes [28, 97], and given that bevacizumab is known to be an efficacious treatment for wet AMD [47], we conclude this result is not relevant to anti-VEGF macromolecules currently used in treatment. However, given that the model predicts vitreous to retina penetration is necessary to maximize retinal free VEGF suppression, this may be important to consider in the development of future anti-VEGF molecules, for example macromolecules intentionally developed to have a large hydrodynamic radius (for example through pegylation etc. [122]).

A disparity observed in our model between the retina and aqueous humour time at which the free VEGF is predicted to return to baseline (or a percentage thereof) has been observed. Figure 4.10 shows the time taken for the concentration of free VEGF to return to 10% of its steady-state value, $t_{\text{ret}}^{(10\%)}$ and $t_{\text{aq}}^{(10\%)}$, for the retina and aqueous, respectively. From this we can see that the time taken for the concentration of free retinal VEGF to return to 10% is half of that of the aqueous. This temporal disparity, alongside the decrease in absolute retinal free VEGF suppression relative to the aqueous, is non-optimal given that the retina is the intended site of drug action - hence we believe investigation into the existence of this predicted phenomenon may be warranted. A study that may give credence to these predictions was conducted in a population of wet AMD patients responding poorly to anti-VEGF treatment (characterized as having a "high anti-VEGF-A demand"), by Fauser et al. in 2016 [118]. Here it was demonstrated that the duration of drug efficacy was 14 ($\pm$12) days, as inferred using OCT measurements for a 0.5 mg dosing regimen of ranibizumab. This duration was approximately half of the VEGF suppression time measured in the aqueous humour of these patients. The return of disease activity in the retina observed by Fauser et al. appears to follow the return of retinal free VEGF that our model predicts, for our base values of p_{RPE} (Figure 4.10). Although there is uncertainty in the levels of retinal VEGF that are needed to drive disease activity, as well as the potential for inter-patient variation in p_{RPE}, our simulations provide a plausible mechanism based hypothesis for the apparent temporal difference in retinal disease activity and aqueous VEGF suppression observed in this particular subpopulation of wet AMD patients.

In contrast to the subset of "high anti-VEGFA demand" patients, Fauser's group (Muether et al. 2012 [81]) has previously shown that the recurrence of disease activity in the majority of wet AMD patients generally occurs after the suppression of aqueous humour VEGF levels has ended, and in some cases may be delayed considerably. In the present model the duration of retinal suppression of VEGF approaches the duration of aqueous humour suppression at very low values of p_{RPE} but never exceeds it (Figure 4.15). Thus retinal VEGF levels appear to be necessary but not sufficient to drive disease activity in some patients.

The concept of what it means for free VEGF to be clinically 'suppressed' is not well defined. Saunders et al. [3] stated any observed concentration in the aqueous *"below the lower limit of quantification, LOQ, (4 pg/mL, or 0.1 pM) of the Luminex xMAP assay"*, to be considered to indicate a clinically suppressed state. The predicted minimum free VEGF concentration in the retina averaged roughly 1 pM across the patient sample; this value is

10 times greater than the previously considered 'suppressed level' of 0.1 pM used in Saunders et al. [3]. All simulations indicated this minimum was achieved at early time (roughly 2 days), and was subsequently followed by exponential increase in free VEGF, at a rate equal to that of the removal of ranibizumab from the system. A potential hypothesis for the biologically relevant free VEGF suppression level may be derived from considering the dissociation constant between VEGF and VEGF receptor molecules. Levels of free retinal VEGF below this dissociation constant would correspond to a majority of VEGF receptors left unbound, and hence, may represent a biologically relevant threshold. Literature on K_{D} for VEGF-R binding shows a wide variation from nM values [123–125] to pM values [83]. More data are needed to clarify this key parameter in order to assess the biological relevance of the retinal suppression curves.

Our 3-compartment model allows us to predict the effect of altering antibody-VEGF binding parameters on retinal PD, something that in previous model generations was assumed to mirror that observed in vitreous concentrations [3, 74]. The question of whether changes in PD observed in the aqueous humour are an accurate measure of changes in the retina is one of interest. Figure 4.16 shows the simulated effect of decreasing K_{D} and k_{off} so as to keep k_{on} fixed. This scenario was analogously studied in the 2-compartment model in Chapter 2, in which we commented that as K_{D} and k_{off} were simultaneously decreased, the aqueous chamber suppression time increased. This effect is also present in the 3-compartment model, however the effect observed in the aqueous chamber is not predicted to be mirrored in the retina. Equations 4.65 and 4.73 describe the early time behaviour of the retinal free VEGF (the minimum concentration achieved and initial exponential return, up to approximately 30-40 days) is inversely proportional to k_{on} and the initial dose. Therefore, with respect to the previously mentioned simulation, as k_{on} is held constant the minimum free VEGF concentration and initial return of free VEGF remains unchanged in the retina. The time $t_{\mathrm{ret}}^{(10\%)}$ remains approximately constant, however due to the change in the aqueous chamber the difference between $t_{\mathrm{ret}}^{(10\%)}$ and $t_{\mathrm{aq}}^{(10\%)}$ increases from 38 days to 58 days. This modelling result further indicates that changes in PD observed in the aqueous may be misleading if they are simply extrapolated to describe the retina. Additionally this leads us to conclude that the model predicts that without increasing the value of k_{on} for a specific antibody, a parameter partially dependent on the random chance of two molecules encountering each other (i.e. regulated by diffusion), there will be little change in its ability to suppress retinal free VEGF.

Figure 4.17 (containing simulations of increasing k_{on} and k_{off} so as to keep K_{D} fixed), shows limited improvement in free VEGF suppression at later times (>30 days). This would indicate that the retinal compartment at later time relaxes to a state of quasi-equilibrium, and hence, as K_{D} remains unchanged, the improved VEGF suppression seen at early time does not carry through much past 30 days. It therefore follows from Figure 4.18 (wherein k_{on} is increased and K_{D} is decreased so as to keep k_{off} fixed), that the model predicts the only scenario in which improvement in retinal free VEGF suppression is possible, at both early and late time, is via a simultaneous increase and decrease of k_{on} and K_{D}, respectively. Equations 4.65 and 4.73 tell us that early time retinal PD is not only inversely proportional to k_{on}, but additionally to dosage. The simulated effects of increased dosage are shown in Figure 4.19, these simulations show that, assuming the accuracy of the model, it is possible to produce the same qualitative behaviour as is achieved by increasing k_{on} and decreasing K_{D} (shown in Figure 4.18) by solely increasing the dose. This is of note as it implies the, theoretically, if there existed two antibodies A and B with similar binding mechanisms (for example one site with which to bind to VEGF) and the same value of k_{off} and $t_{1/2}^{(r)}$, then if antibody B possessed, relative to A, a higher and lower value of k_{on} and K_{D}, respectively, antibody A could achieve the same retinal free VEGF suppression as B by simply increasing its dose relative to B. We stress this is a theoretical result based on numerical and analytic analysis of our model and hence requires validation.

Finally, as previously shown in Figure 4.15, if the permeability of the RPE is higher than the baseline value primarily studied here, then the ability of the treatment to suppress retinal free VEGF is greatly reduced. It is possible this may be the case for patients with severely compromised retina-choroid membranes, due to pervasive neovasculature, and therefore may be a contributing factor towards variation in the response to anti-VEGF treatment. In such a scenario the model predicts that a higher dose of the drug could be an effective technique to counteract the negative effects of a higher rate of retina to choroid transfer, as can be seen from Figure 4.15, where, by moving from 0.5 mg to 6 mg in the high p_{RPE} case, the total retinal free VEGF suppressed is increased by $\sim$225% (relative to the 50% increase seen in the aqueous humour). Although there has been little study to date regarding the efficacy of high dose (>0.5mg) ranibizumab treatment, two clinical studies (HARBOR and SAVE) have investigated the effects of 2 mg vs. 0.5 mg doses of ranibizumab in monthly and/or PRN (as needed) regimens in patients with wet AMD. At the 24-month endpoint of the HARBOR study (Ho et al. 2014 [126]) the mean number of injections administered to patients who completed the study was 11.9 in the 2 mg PRN group vs. 14.2 in the 0.5 mg PRN group. The corresponding average interval between

injections was 12.5 weeks in the 2 mg PRN group vs. 9.9 weeks in the 0.5 mg PRN group, a difference of 2.6 weeks. The two PRN treatment groups had comparable results on the visual acuity end points (change from baseline in BCVA*) at the 12 and 24-month evaluations, approximately +8 letters. According to the model, a 4-fold increase in dose should increase the duration of VEGF suppression after each injection by approximately 2 half-lives, which for ranibizumab is about 16 days (2.3 weeks). This prediction is consistent with the longer injection interval observed in the HARBOR study for the 2 mg PRN group. In the SAVE study (Brown et al 2013 [27]) patients failing to respond to treatment (referred to as recalcitrant patients), who, while receiving standard monthly doses of ranibizumab (0.5 mg) or bevacizumab (1.25 mg), still suffered from persistent leakage, were given 3 consecutive monthly doses of 2 mg ranibizumab and evaluated one month after each dose. At these time points the average change in BCVA from the baseline level achieved on standard dosing ranged between +3.3 to +3.9 letters. This finding would be consistent with a longer or deeper retinal VEGF suppression at the 2 mg dose, as would be expected from Figures 4.19 and 4.15. As suggested by Brown et al. patients failing to respond to treatment may either have a shorter ocular half-life of ranibizumab or require a greater degree of VEGF blockade. In terms of the 3-compartment model, such patients could conceivably have a higher RPE permeability that would shorten their ocular half-life and result in a lower degree of retinal VEGF suppression. Figure 4.15 demonstrates that for such patients a higher dosage may be required.

As noted throughout this discussion these results are based upon theoretical using parameters derived from both human and rabbit data, therefore the conclusions made within this chapter, formulated upon the basis of our results, require validation. As mentioned in the introduction on this chapter, data concerning retinal free VEGF concentrations, from patients being treated for wet AMD, are currently impossible to obtain clinically. Additionally such data are technically challenging to acquire experimentally from animal models, and only limited data exist. These facts however motivated the development of our model, as a first step towards understanding and predicting the PD of free VEGF in a highly inaccessible, yet clinically relevant, anatomical region. Our model provides several hypotheses regarding the PD of retinal free VEGF, the implications of which may be observable through future data collection, as well as motivating the collection of such data. In the parameter regimes considered, the model has predicted the existence of a retinal-aqueous suppression lag, as well as dissimilar retina-aqueous responses upon alterations to binding parameters.

*Best corrected visual acuity (BCVA) is a measure of VA improvement with units of 'letters'.

Thus, we are led to conclude the time profile of free VEGF concentrations acquired via aqueous humour sampling may not always match (via some scaling factor), that of the retina. Our analysis of altering binding parameters leads us to conclude that a high dose of an anti-VEGF macromolecule may achieve the same retinal free VEGF suppression as a similar macromolecule with superior binding characteristics, administered at a relatively lower dose. Additionally this study demonstrates the model predicts that without the ability to increase k_{on} (for a hypothetical molecule), increased retinal free VEGF suppression would not be possible by changing k_{off} and K_{D} alone. Finally our case study concerning a higher than baseline p_{RPE} value demonstrated very poor retinal free VEGF suppression; as noted previously, patients with highly advanced neovascularization may possess higher effective p_{RPE} values, and hence may be predisposed respond poorly to treatment. Hence, studies similar to that conducted by Fauser et al. [118], focusing on patients responding poorly to anti-VEGF treatment, may reveal valuable information regarding physiological/pathological factors that differentiate them from the rest of the population.

4.2 Analysis of the PK/PD of ocular anti-VEGF macromolecules using a PDE model

In Section 3.2 we demonstrated how a PDE model of the eye may be used to simulate an IVT injection of an anti-VEGF macromolecule and study the resultant PK. In this section we will build on this model to introduce interactions between the drug and target, in order to analyse pharmacodynamic (PD) predictions. As previously studied, we will be considering ranibizumab, a Fab molecule with one binding site with which to associate to vascular endothelial growth factor, or VEGF, produced within the retina. This scenario was previously analysed using an analogous 3 compartment PK/PD ODE model; again, we will be comparing and contrasting the predictions generated by using the PDE and ODE model. We found in the case of the PK model, of Section 3.2, there was very little difference in the applicability and predictions of the ODE and PDE model, however, given the introduction of multiple chemical species and binding kinetics, the same need not hold a priori for the PK/PD model.

Another aspect we will explore in this section is the potential for heterogeneity in retinal VEGF production. The progression of dry AMD to wet AMD when the presence of VEGF triggers the production of choroidal neovasculature, penetrating the basement layers of the retina. The exact pathology of wet AMD is not understood, but it is assumed that the production of VEGF is triggered by local inflammation due to the presence of drusen (a collection of metabolic end products and lipids) within Bruch's membrane. Drusen can

appear anywhere within the retina, however in many cases it appears to congregate primarily near the macula region of the retina. This tendency of drusen deposition entails it is plausible that retinal inflammation, and hence VEGF production, may also be somewhat localised to the macula. In this study we will consider homogeneous and heterogeneous VEGF production within the retina, in order to access the potential for any variation in model predictions, between the spatially heterogeneous and homogeneous PDE model, as well as the ODE model.

As in the 3-compartment PK/PD ODE study we will consider the Saunders et al. dataset [3], detailing 31 patients suffering with neovascular age-related macular degeneration (wet AMD). Aqueous humour samples were collected at several time points post-intravitreal (IVT) injection of 0.5 mg of ranibizumab, as well as the pre-treatment baseline value. As this dataset contains data only for human, we will not be considering the rabbit geometry in this analysis.

4.2.1 Model Formulation and Numerical Solution

The model geometry remains unchanged from that of the PK PDE model, presented in Section 3.2, apart from the addition of the macula region. The macula lies towards the most posterior region of the vitreous, therefore we will model it by the section of the retina denoted by Ω_M, as shown in Figure 4.20.

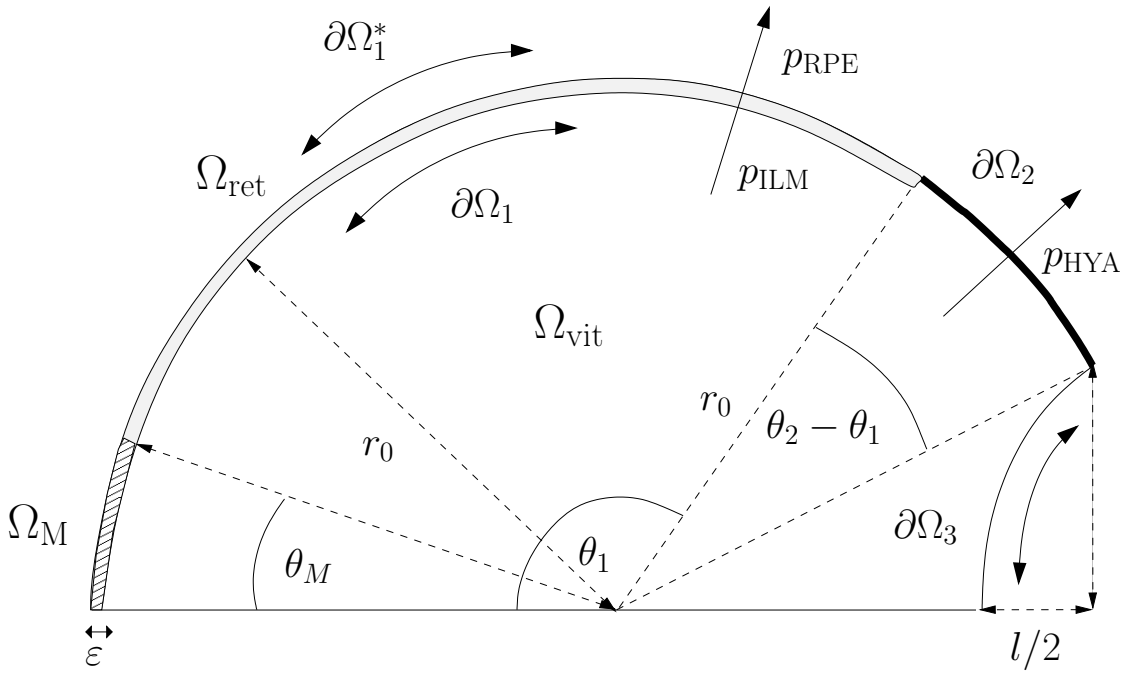

Figure 4.20: Identical ocular geometry as presented in Figure 3.6, with the addition of the macula region of the retina, denoted by Ω_M. We note that $\Omega_M \subset \Omega_{\mathrm{ret}}$, and hence the boundaries $\partial\Omega_1$ and $\partial\Omega_1^*$ cover Ω_M.

As in Section 3.2 the model is formulated as a system of PDEs (for the retina and vitreous), whereas spatially independent ODEs are utilized to infer the concentration within the aqueous. As in Section 4.1 reaction kinetics between chemical species can occur within any of the three model compartments, VEGF (V) has two identical binding sites to which ranibizumab (R) can bind [119], to form a VEGF - ranibizumab complex (VR) and subsequently a ranibizumab - VEGF - ranibizumab complex (RVR). Reactions are governed by Equations 4.1-4.2, in which k_{on} and k_{off} (and hence also the dissociation constant $K_{\mathrm{D}} = k_{\mathrm{off}}/k_{\mathrm{on}}$) are reaction rates corresponding to a hypothetical single VEGF binding site. The model is then formulated by Equations 4.123-4.154, as follows:

VEGF (V, $\mathrm{v}(\vec{x},t)$)

$$\frac{\partial v_{\mathrm{ret}}}{\partial t} = D_{\mathrm{ret}}^{(v)}\nabla^2 v_{\mathrm{ret}} + (k_{\mathrm{off}}c_{\mathrm{ret}} - 2k_{\mathrm{on}}v_{\mathrm{ret}}r_{\mathrm{ret}}) + \frac{V_{\mathrm{in}}}{V_{\mathrm{ret}}}\delta_{\vec{x}}\left(\Omega_M\right), \quad \text{for } \vec{x}\in\Omega_{\mathrm{ret}}, \tag{4.123}$$

$$\frac{\partial v_{\mathrm{vit}}}{\partial t} = D_{\mathrm{vit}}^{(v)}\nabla^2 v_{\mathrm{vit}} + (k_{\mathrm{off}}c_{\mathrm{vit}} - 2k_{\mathrm{on}}v_{\mathrm{vit}}r_{\mathrm{vit}}), \quad \text{for } \vec{x}\in\Omega_{\mathrm{vit}}, \tag{4.124}$$

$$-D_{\mathrm{ret}}\vec{n}\cdot\nabla v_{\mathrm{ret}} = p_{\mathrm{ILM}}^{(v)}\left(v_{\mathrm{ret}} - v_{\mathrm{vit}}\right), \quad \text{for } \vec{x}\in\partial\Omega_1, \tag{4.125}$$

$$-D_{\mathrm{ret}}\vec{n}\cdot\nabla v_{\mathrm{ret}} = p_{\mathrm{RPE}}^{(v)}v_{\mathrm{ret}}, \quad \text{for } \vec{x}\in\partial\Omega_1^*, \tag{4.126}$$

$$-D_{\mathrm{vit}}\vec{n}\cdot\nabla v_{\mathrm{vit}} = p_{\mathrm{ILM}}^{(v)}\left(v_{\mathrm{vit}} - v_{\mathrm{ret}}\right), \quad \text{for } \vec{x}\in\partial\Omega_1, \tag{4.127}$$

$$-D_{\mathrm{vit}}\vec{n}\cdot\nabla v_{\mathrm{vit}} = p_{\mathrm{HYA}}^{(v)}v_{\mathrm{vit}}, \quad \text{for } \vec{x}\in\partial\Omega_2, \tag{4.128}$$

$$-\vec{n}\cdot\nabla v_{\mathrm{vit}} = 0, \quad \text{for } \vec{x}\in\partial\Omega_3, \tag{4.129}$$

$$\frac{\mathrm{d}v_{\mathrm{aq}}}{\mathrm{d}t} = \left(\frac{p_{\mathrm{HYA}}^{(v)}}{V_{\mathrm{aq}}}\right)\int_{\partial\Omega_2} v_{\mathrm{vit}}\ \mathrm{d}S - \left(\frac{C_{\mathrm{L}}}{V_{\mathrm{aq}}}\right)v_{\mathrm{aq}} + (k_{\mathrm{off}}c_{\mathrm{aq}} - 2k_{\mathrm{on}}v_{\mathrm{aq}}r_{\mathrm{aq}}), \tag{4.130}$$

Drug (R, $\mathrm{r}(\vec{x},t)$)

$$\frac{\partial r_{\mathrm{ret}}}{\partial t} = D_{\mathrm{ret}}^{(r)}\nabla^2 r_{\mathrm{ret}} + (k_{\mathrm{off}}c_{\mathrm{ret}} - 2k_{\mathrm{on}}v_{\mathrm{ret}}r_{\mathrm{ret}}), \quad \text{for } \vec{x}\in\Omega_{\mathrm{ret}}, \tag{4.131}$$
$$+ (2k_{\mathrm{off}}h_{\mathrm{ret}} - k_{\mathrm{on}}c_{\mathrm{ret}}r_{\mathrm{ret}})$$

$$\frac{\partial r_{\mathrm{vit}}}{\partial t} = D_{\mathrm{vit}}^{(r)}\nabla^2 r_{\mathrm{vit}} + (k_{\mathrm{off}}c_{\mathrm{vit}} - 2k_{\mathrm{on}}v_{\mathrm{vit}}r_{\mathrm{vit}}), \quad \text{for } \vec{x}\in\Omega_{\mathrm{vit}}, \tag{4.132}$$
$$+ (2k_{\mathrm{off}}h_{\mathrm{vit}} - k_{\mathrm{on}}c_{\mathrm{vit}}r_{\mathrm{vit}})$$

$$-D_{\mathrm{ret}}\vec{n}\cdot\nabla r_{\mathrm{ret}} = p_{\mathrm{ILM}}^{(r)}\left(r_{\mathrm{ret}} - r_{\mathrm{vit}}\right), \quad \text{for } \vec{x}\in\partial\Omega_1, \tag{4.133}$$

$$-D_{\mathrm{ret}}\vec{n}\cdot\nabla r_{\mathrm{ret}} = p_{\mathrm{RPE}}^{(r)}r_{\mathrm{ret}}, \quad \text{for } \vec{x}\in\partial\Omega_1^*, \tag{4.134}$$

$$-D_{\mathrm{vit}}\vec{n}\cdot\nabla r_{\mathrm{vit}} = p_{\mathrm{ILM}}^{(r)}\left(r_{\mathrm{vit}} - r_{\mathrm{ret}}\right), \quad \text{for } \vec{x}\in\partial\Omega_1, \tag{4.135}$$

$$-D_{\mathrm{vit}}\vec{n}\cdot\nabla r_{\mathrm{vit}} = p_{\mathrm{HYA}}^{(r)}r_{\mathrm{vit}}, \quad \text{for } \vec{x}\in\partial\Omega_2, \tag{4.136}$$

$$-\vec{n}\cdot\nabla r_{\mathrm{vit}} = 0, \quad \text{for } \vec{x}\in\partial\Omega_3, \tag{4.137}$$

$$\frac{\mathrm{d}r_{\mathrm{aq}}}{\mathrm{d}t} = \left(\frac{p_{\mathrm{HYA}}^{(r)}}{V_{\mathrm{aq}}}\right)\int_{\partial\Omega_2} r_{\mathrm{vit}}\ \mathrm{d}S - \left(\frac{C_{\mathrm{L}}}{V_{\mathrm{aq}}}\right)v_{\mathrm{aq}} + (k_{\mathrm{off}}c_{\mathrm{aq}} - 2k_{\mathrm{on}}v_{\mathrm{aq}}r_{\mathrm{aq}}) \tag{4.138}$$
$$+ (2k_{\mathrm{off}}h_{\mathrm{aq}} - k_{\mathrm{on}}c_{\mathrm{aq}}r_{\mathrm{aq}}),$$

VEGF-drug (VR, c($\vec{x},t$))

$$\frac{\partial c_{\text{ret}}}{\partial t} = D_{\text{ret}}^{(c)}\nabla^2 c_{\text{ret}} - (k_{\text{off}}c_{\text{ret}} - 2k_{\text{on}}v_{\text{ret}}r_{\text{ret}}), \qquad \text{for } \vec{x}\in\Omega_{\text{ret}}, \tag{4.139}$$
$$+ (2k_{\text{off}}h_{\text{ret}} - k_{\text{on}}c_{\text{ret}}r_{\text{ret}})$$

$$\frac{\partial c_{\text{vit}}}{\partial t} = D_{\text{vit}}^{(c)}\nabla^2 c_{\text{vit}} - (k_{\text{off}}c_{\text{vit}} - 2k_{\text{on}}v_{\text{vit}}r_{\text{vit}}), \qquad \text{for } \vec{x}\in\Omega_{\text{vit}}, \tag{4.140}$$
$$+ (2k_{\text{off}}h_{\text{vit}} - k_{\text{on}}c_{\text{vit}}r_{\text{vit}})$$

$$-D_{\text{ret}}\vec{n}\cdot\nabla c_{\text{ret}} = p_{\text{ILM}}^{(c)}\left(c_{\text{ret}} - c_{\text{vit}}\right), \qquad \text{for } \vec{x}\in\partial\Omega_1, \tag{4.141}$$

$$-D_{\text{ret}}\vec{n}\cdot\nabla c_{\text{ret}} = p_{\text{RPE}}^{(c)}c_{\text{ret}}, \qquad \text{for } \vec{x}\in\partial\Omega_1^*, \tag{4.142}$$

$$-D_{\text{vit}}\vec{n}\cdot\nabla c_{\text{vit}} = p_{\text{ILM}}^{(c)}\left(c_{\text{vit}} - c_{\text{ret}}\right), \qquad \text{for } \vec{x}\in\partial\Omega_1, \tag{4.143}$$

$$-D_{\text{vit}}\vec{n}\cdot\nabla c_{\text{vit}} = p_{\text{HYA}}^{(c)}c_{\text{vit}}, \qquad \text{for } \vec{x}\in\partial\Omega_2, \tag{4.144}$$

$$-\vec{n}\cdot\nabla c_{\text{vit}} = 0, \qquad \text{for } \vec{x}\in\partial\Omega_3, \tag{4.145}$$

$$\frac{\mathrm{d}c_{\text{aq}}}{\mathrm{d}t} = \left(\frac{p_{\text{HYA}}^{(c)}}{V_{\text{aq}}}\right)\int_{\partial\Omega_2} c_{\text{vit}}\ \mathrm{d}S - \left(\frac{C_{\text{L}}}{V_{\text{aq}}}\right)v_{\text{aq}} - (k_{\text{off}}c_{\text{aq}} - 2k_{\text{on}}v_{\text{aq}}r_{\text{aq}}) \tag{4.146}$$
$$+ (2k_{\text{off}}h_{\text{aq}} - k_{\text{on}}c_{\text{aq}}r_{\text{aq}}),$$

Drug-VEGF-drug (RVR, h($\vec{x},t$))

$$\frac{\partial h_{\text{ret}}}{\partial t} = D_{\text{ret}}^{(h)}\nabla^2 h_{\text{ret}} - (2k_{\text{off}}h_{\text{ret}} - k_{\text{on}}c_{\text{ret}}r_{\text{ret}}), \qquad \text{for } \vec{x}\in\Omega_{\text{ret}}, \tag{4.147}$$

$$\frac{\partial h_{\text{vit}}}{\partial t} = D_{\text{vit}}^{(h)}\nabla^2 h_{\text{vit}} - (2k_{\text{off}}h_{\text{vit}} - k_{\text{on}}c_{\text{vit}}r_{\text{vit}}), \qquad \text{for } \vec{x}\in\Omega_{\text{vit}}, \tag{4.148}$$

$$-D_{\text{ret}}\vec{n}\cdot\nabla h_{\text{ret}} = p_{\text{ILM}}^{(h)}\left(h_{\text{ret}} - h_{\text{vit}}\right), \qquad \text{for } \vec{x}\in\partial\Omega_1, \tag{4.149}$$

$$-D_{\text{ret}}\vec{n}\cdot\nabla h_{\text{ret}} = p_{\text{RPE}}^{(h)}h_{\text{ret}}, \qquad \text{for } \vec{x}\in\partial\Omega_1^*, \tag{4.150}$$

$$-D_{\text{vit}}\vec{n}\cdot\nabla h_{\text{vit}} = p_{\text{ILM}}^{(h)}\left(h_{\text{vit}} - h_{\text{ret}}\right), \qquad \text{for } \vec{x}\in\partial\Omega_1, \tag{4.151}$$

$$-D_{\text{vit}}\vec{n}\cdot\nabla h_{\text{vit}} = p_{\text{HYA}}^{(h)}h_{\text{vit}}, \qquad \text{for } \vec{x}\in\partial\Omega_2, \tag{4.152}$$

$$-\vec{n}\cdot\nabla h_{\text{vit}} = 0, \qquad \text{for } \vec{x}\in\partial\Omega_3, \tag{4.153}$$

$$\frac{\mathrm{d}h_{\text{aq}}}{\mathrm{d}t} = \left(\frac{p_{\text{HYA}}^{(h)}}{V_{\text{aq}}}\right)\int_{\partial\Omega_2} h_{\text{vit}}\ \mathrm{d}S - \left(\frac{C_{\text{L}}}{V_{\text{aq}}}\right)v_{\text{aq}} - (2k_{\text{off}}h_{\text{aq}} - k_{\text{on}}c_{\text{aq}}r_{\text{aq}}), \tag{4.154}$$

where $\vec{n}$ is the outward pointing normal, and the units of concentration are pM. Parameter values and definitions, for human geometry, are the same as in Section 3.2, given in Table 3.6. Permeability values were calculated using the power laws estimated from Section 3.2, and given by Equations 3.72-3.74. Additional parameters related to binding kinetics are given in Table 4.7. Hydrodynamic radii for V,VR and RVR are taken from Section 4.1, whereas the value for R is taken from the meta-analysis in Appendix A.6. Molecule specific diffusion coefficients were then calculated using the Stokes-Einstein relation. Initial conditions for all drug-VEGF complexes are initially zero, the drug is assumed only to be initially present in the vitreous, with concentration corresponding to the initial dose (d_0) given by

$$r_{\text{vit}}(\vec{x},t=0) = \frac{d_0}{M_W V_{\text{vit}}}\times 10^9 \ \ (\text{pM}), \quad \text{for } \vec{x}\in\Omega_{\text{vit}}, \tag{4.155}$$

where M_{W} is the molecule weight of ranibizumab, taken to be 48.35 kDa [12]. Initial conditions for VEGF in all model regions, $v_{\mathrm{ret}}, v_{\mathrm{vit}}$ and v_{aq}, are given by their solution to the spatial steady state problem, i.e. where $d_0 = 0$.

Parameter	Value	Units	Description
V_{in}	Patient specific	fmol/day	VEGF production rate
k_{off}	0.864 [84]	1/day	Binding off rate
k_{on}	$k_{\mathrm{off}}/K_{\mathrm{D}}$	$(\mathrm{pMday})^{-1}$	Binding on rate
K_{D}	Estimated	pM	Dissociation constant
$M_{\%}$	0.04 [127]	none	Macula percentage
θ_{M}	$h(\theta_1, M_{\%})$ (Equation 4.156)	rad	Macular angle
V_{M}	$\frac{2}{3}\pi\left\{1-\cos(\theta_{\mathrm{M}})\right\}\left[(r_0+\varepsilon)^3 - r_0^3\right]$	cm^3	Volume of the macula

Table 4.7: Additional parameters used for the PDE PK/PD model relative to the PDE PK model, including binding parameters for ranibizumab, VEGF production and values defining the geometry of the macula. Macula percentage refers to the percentage of retinal surface occupied by the macula, whereas θ_{M} is defined in Figure 4.20. Parameters r_0 and ε denote the vitreal radius and retinal thickness, values for which are given in Table 3.6.

The value of θ_M is generated by the following formula:

$$h(\theta_1, M_{\%}) = \cos^{-1}\left(1 - \left(1 - \cos\left(\theta_1\right)\right) M_{\%}\right), \tag{4.156}$$

$$\therefore \quad h(\theta_1 = 2.2, M_{\%} = 0.04) = 0.3583... \simeq 0.36 \text{ rad}. \tag{4.157}$$

We additionally note that the concentration of VEGF in the macula and in non-macula region of the retina are defined by

$$v_{\mathrm{M}}(\vec{x}, t) = v_{\mathrm{ret}}(\vec{x}, t) \quad \text{for } \vec{x} \in \Omega_{\mathrm{M}}, \tag{4.158}$$

$$v_{\not{\mathrm{M}}}(\vec{x}, t) = v_{\mathrm{ret}}(\vec{x}, t) \quad \text{for } \vec{x} \in \Omega_{\mathrm{ret}} \backslash \Omega_{\mathrm{M}}, \tag{4.159}$$

respectively. We can define the spatial average, for a general chemical species C, over the macula, non-macula region, retina and vitreous as

$$\bar{C}_{\mathrm{M}} = \frac{1}{V_{\mathrm{M}}} \int_{\Omega_{\mathrm{M}}} C_{\mathrm{ret}} \, \mathrm{d}V, \qquad \bar{C}_{\not{\mathrm{M}}} = \frac{1}{V_{\mathrm{ret}} - V_{\mathrm{M}}} \int_{\Omega_{\mathrm{ret}} \backslash \Omega_{\mathrm{M}}} C_{\mathrm{ret}} \, \mathrm{d}V \tag{4.160}$$

$$\bar{C}_{\mathrm{ret}} = \frac{1}{V_{\mathrm{ret}}} \int_{\Omega_{\mathrm{ret}}} C_{\mathrm{ret}} \, \mathrm{d}V, \tag{4.161}$$

$$\bar{C}_{\mathrm{vit}} = \frac{1}{V_{\mathrm{vit}}} \int_{\Omega_{\mathrm{vit}}} C_{\mathrm{vit}} \, \mathrm{d}V, \tag{4.162}$$

respectively. We therefore define two distinct models via Equations 4.123-4.154; the standard (non-macula) model, wherein $\theta_M = \theta_1$, and the macula model, where $\theta_M = 0.36$ rad. The standard model therefore represents retinal-wide VEGF production, whereas the macula model isolated VEGF production to the macula region of the retina, as shown in Figure

4.20.

For the analysis presented in this section we utilised the 2015 dataset, published by Saunders et al. [3] and previously analysed in Chapter 2 and Section 4.1, detailing 31 patients suffering with neovascular age-related macular degeneration (wet AMD). In contrast to how we have previously utilised this dataset, by fitting the model to each of the 31 patient datasets, we fit the model to the dataset in aggregate, for computational reasons. This was achieved by non-dimensionaling each patient dataset, using their free aqueous VEGF equilibrium level. Once this was done for each patient, their respective datasets were aggregated. The value of the parameter V_{in} was then set so that the spatial average, of steady free VEGF state solution, in the aqueous was equal to unity. This was done for both the standard (homogeneous VEGF production) and macula (heterogeneous VEGF production) PDE models. The model was then fitted to the data, allowing a fitting algorithm to vary the value of K_{D} (the only non-prescribed parameter), while penalising the relative mean square error between the numerical solution and the data.

4.2.2 3-compartment PDE analysis of Saunders et al. [3] aggregated dataset

Upon fitting the PDE models to the aggregated dataset, we found that the standard and macula model both estimated similar values of K_{D}, 13,851 (11,687, 16,015) pM and 15,950 (14,064, 17,837) pM, respectively. Figure 4.21 shows the free VEGF profiles, in the retina and aqueous, of both PDE models, using their respective best fit value for K_{D}. The retinal profiles plotted correspond to the spatial average equations, given by Equations 4.160-4.161, whereas the aqueous profile corresponds to the numerical solution of v_{aq}. These profiles are plotted normalised by their respective steady state VEGF concentration.

By considering the normalized profiles of each model we can easily compare the different PD exhibited by each. As can be seen in the aqueous humour, both the standard and macula model fit Saunders et al. [3] dataset well, and with almost identical profiles. In the retina we can see that $\bar{C}_{\text{ret}}$ for the standard and macula model, again, have very similar retinal free VEGF profiles. In the case of the macula model $\bar{C}_{\text{M}}$ is, when normalised, slightly higher than $\bar{C}_{\text{ret}}$, whereas $\bar{C}_{\not{M}}$ is slightly lower, as one would expect. However, when normalised, $\bar{C}_{\text{ret}}$ and $\bar{C}_{\text{M}}$ have very similar profiles, implying that the heterogeneity in VEGF production does not greatly alter the PD of the drug.

The only major difference observed between the standard and macula models was regarding the magnitude of the VEGF production rate, V_{in}. In the macula model, as the volume of retinal tissue producing VEGF is smaller, the value of V_{in} required in order to produce a given aqueous equilibrium concentration is larger. However this value was found to be approximately equal to that of the standard model, multiplied by the ratio of volumes of VEGF producing tissues between the two models, $V_{\text{ret}}/V_{\text{M}}$. Therefore the total molar production rate is approximately the same in both models, and further suggests the introduction of the heterogeneity in VEGF production does not greatly affect the behaviour of the model.

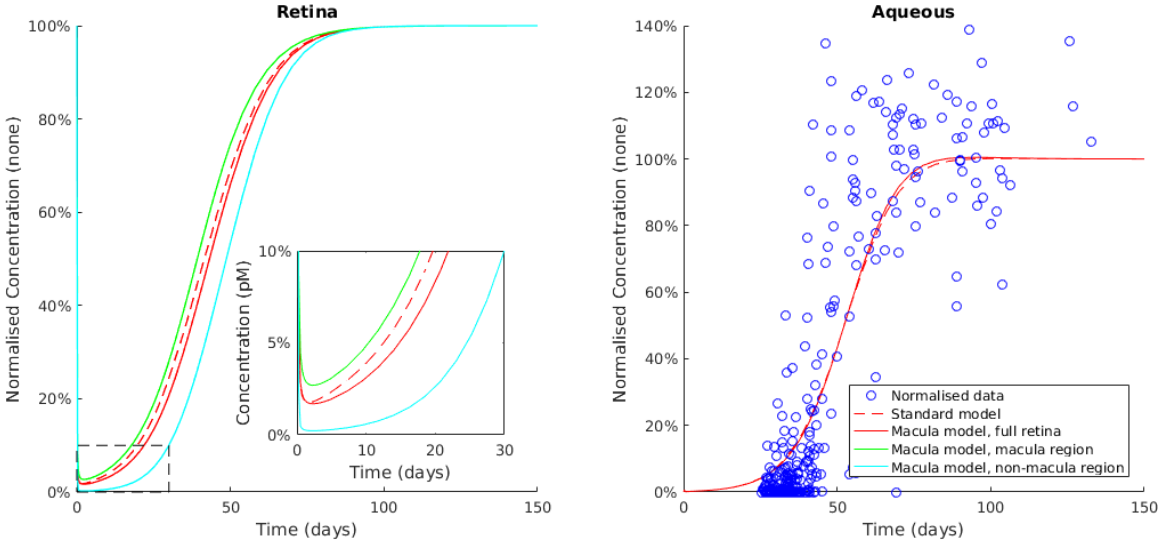

Figure 4.21: Fits to the Fauser dataset, $K_{\text{D}} = 13,851$ $(11,687, 16,015)$ pM for the homogeneous VEGF production model, and $K_{\text{D}} = 15950$ $(14,064, 17,837)$ pM for the heterogeneous macula VEGF production model.

To examine further the differing characteristics of the standard and macula model we present in Figure 4.22 a comparison of the retinal and vitreal free VEGF concentration problems of the standard PDE, macula PDE, and ODE models, over a range of K_{D} values. Each model is solved using their respective best fit K_{D} values (as in Figure 4.21), decreased by one order of magnitude down in plot (a) and increased by one order of magnitude in plot (b). From Figure 4.22 we see that over two orders of magnitude for K_{D} there is little change in the fidelity of the macula concentration of the macula model to the retinal concentration in the standard model, hence in further analysis we will only consider the standard model.

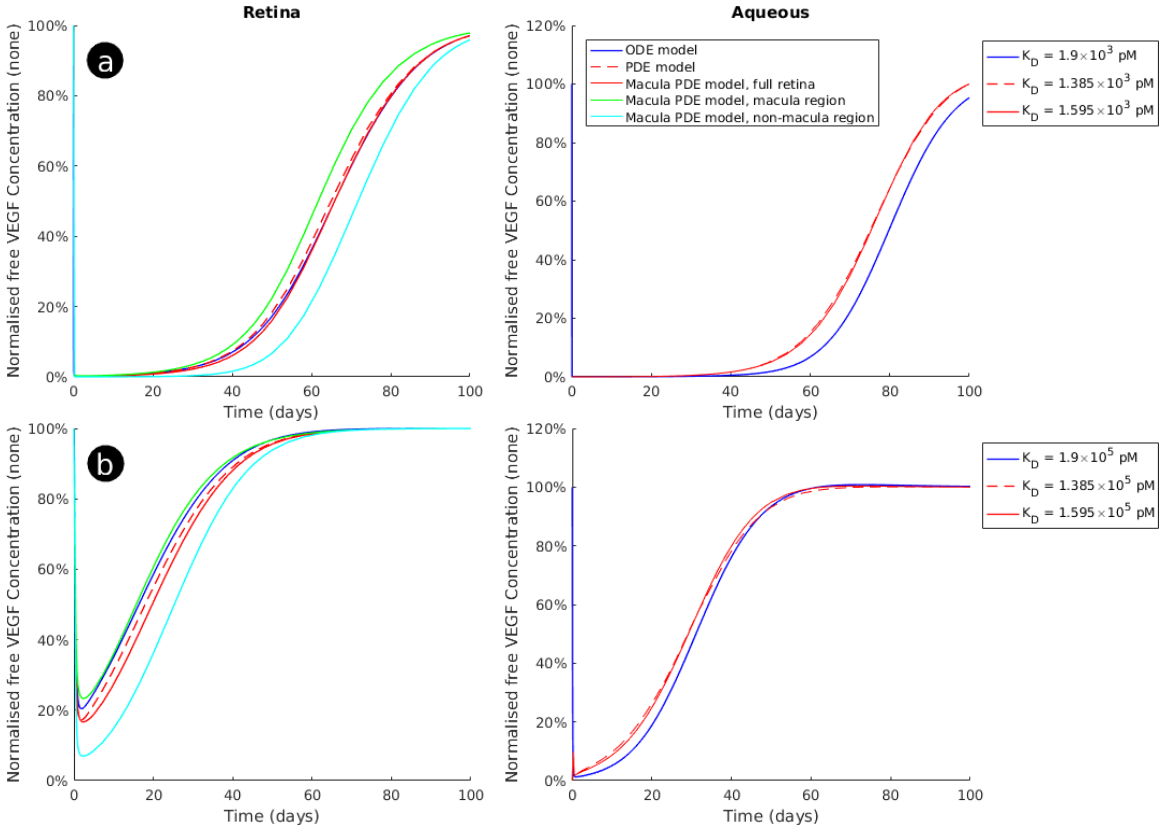

Figure 4.22: Comparison of the retinal and vitreal free VEGF concentration problems of the standard PDE, macula PDE, and ODE models, over a range of K_{D} values. Each model is solved using their respective best fit K_{D} values (as given in Figure 4.21), decreased by one order of magnitude down in plot (a) and increased by one order of magnitude in plot (b).

4.2.3 Predictive comparison between the ODE and PDE model

Figure 4.23 shows free VEGF concentrations for the standard PDE model best fit, alongside the ODE model of Section 4.1, the latter solved with a K_{D} value of 19,000 pM and a half-life of 7.5 days. 7.5 days was chosen as it is was the median half-life value derived from fitting the dataset of each patient to the ODE model. As can be seen the PD predicted by both these models is almost identical, both exhibit a retina-aqueous delay and a lack of retinal free VEGF suppression (the implications of which are discussed in Section 4.1). Additionally, the value of V_{in} required to generate a fixed equilibrium concentration was also found to be approximately the same between the two models.

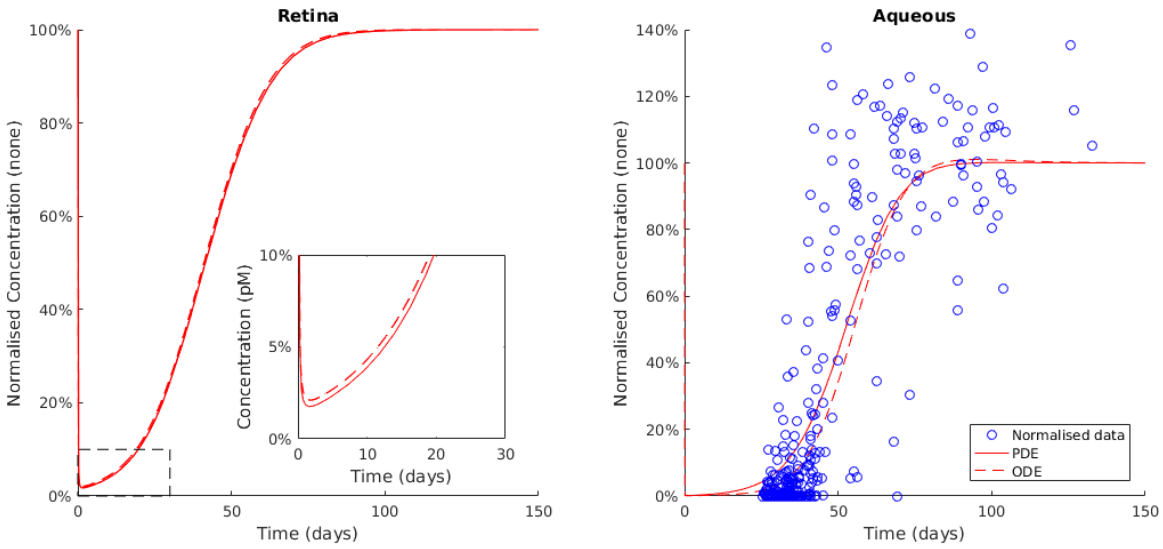

Figure 4.23: Comparison of the ODE fit, with $K_{\mathrm{D}} = 19,000$ pM, using parameters from MS3, (half-life of 7.5 days, the median half life estimated in Section 4.1), and the homogeneous PDE model, using standard parameters.

So far in our comparison of the PK/PD PDE model and the PK/PD ODE model we have found almost identical behaviour between the two. In Section 4.1 a number of relevant case studies were investigated; in order to properly access whether the ODE and PDE models generate distinct predictions we will also consider replicating these case studies using the standard PDE model. Figure 4.24 demonstrates that when the permeability of the RPE is greatly increased (by a factor of 10), both the ODE and PDE model predict greatly reduced free VEGF suppression in the retina, and exhibit very similar profiles. Similarly, in Figure 4.25 we see almost identical behaviour when the permeability of the ILM is reduced to zero for the drug and drug-VEGF complexes.

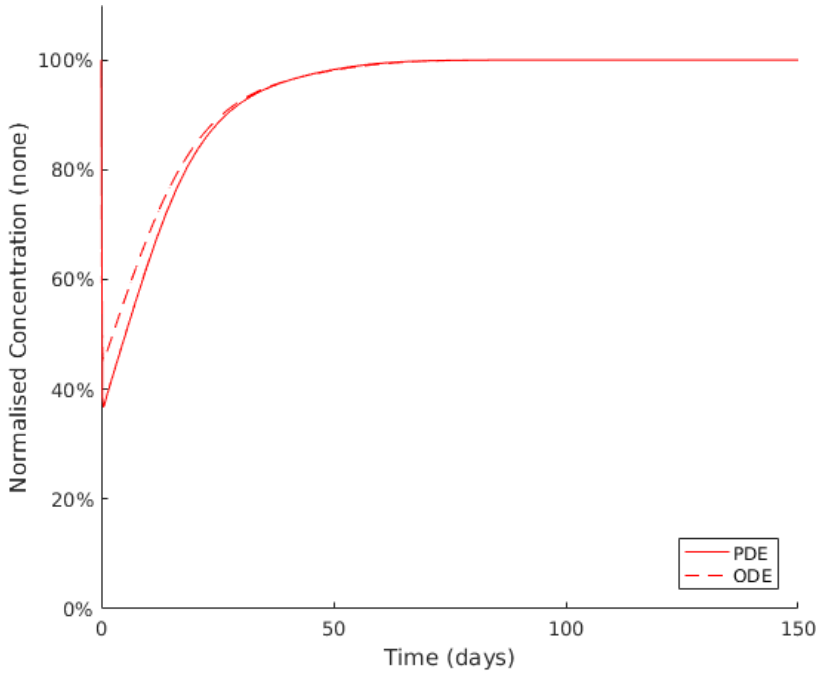

Figure 4.24: Simulated retinal PD for values of p_{RPE} 10 times greater than those predicted in Section 3.2. Numerical solution for the ODE IVT dose of 0.5 mg, with a K_D of 19,000 pM. The half life in the ODE case was reduced from 7.5 days to 6.6, and in the PDE case from 6.6 to 6.0 days.

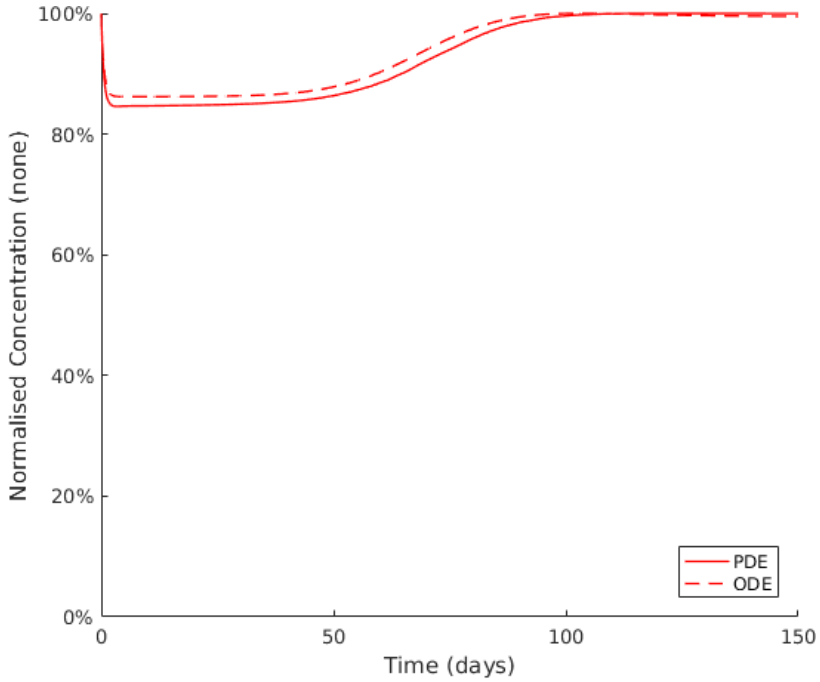

Figure 4.25: Simulated PD for a drug (and drug-VEGF complexes), impermeable to the retina. Numerical solution for the ODE IVT dose of 0.5 mg, with a K_D of 19,000 pM and half life of 7.5 days, with all other parameters taken from Section 4.1.

A key study featured in Section 4.1 was the analysis of the effects of altering binding and dosage parameters. These simulations were replicated using the standard PDE model, shown in Figures 4.26-4.29, and were subsequently found to exhibit no difference in qualitative behaviour.

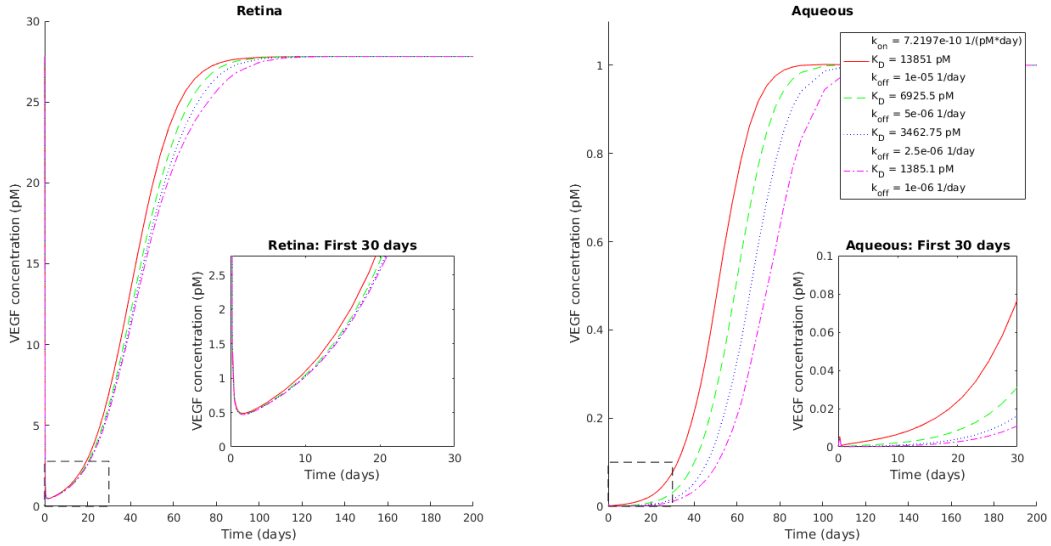

Figure 4.26: Simulated effect of decreasing K_{D} and k_{off} so as to keep k_{on} fixed, according to the standard PDE model. Plots shown correspond to K_{D} = 19,000 pM (solid red), K_{D} = 9,500 pM (dashed green), K_{D} = 4,750 pM (dotted blue) and K_{D} = 1900 pM (dot-dash magenta).

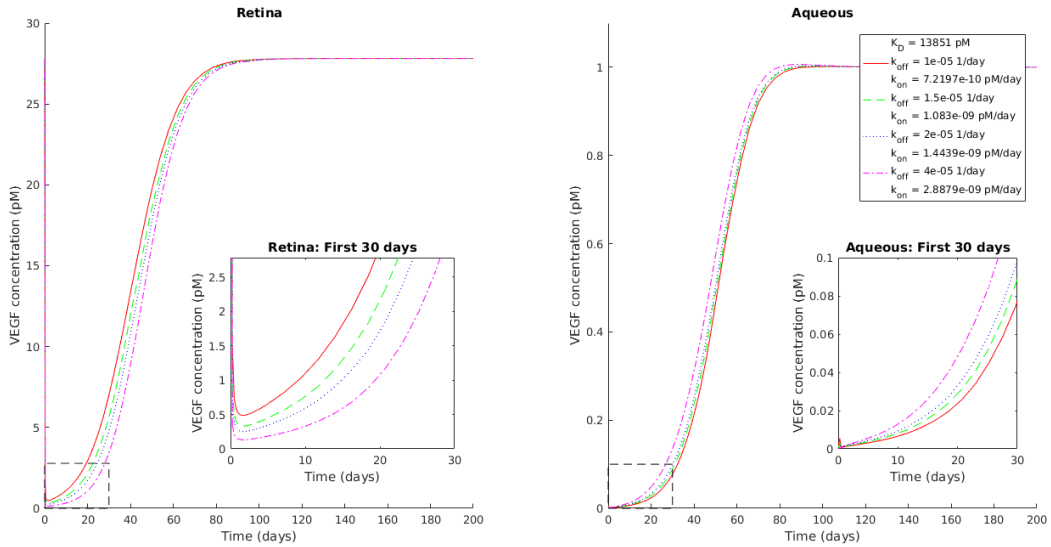

Figure 4.27: Simulated effect of increasing k_{on} and k_{off} so as to keep K_{D} fixed at 19,000 pM. Plots shown correspond to k_{off} = 0.864 1/day (solid red), k_{off} = 1.296 1/day (dashed green), k_{off} = 1.728 1/day (dotted blue) and k_{off} = 3.456 1/day (dot-dash magenta).

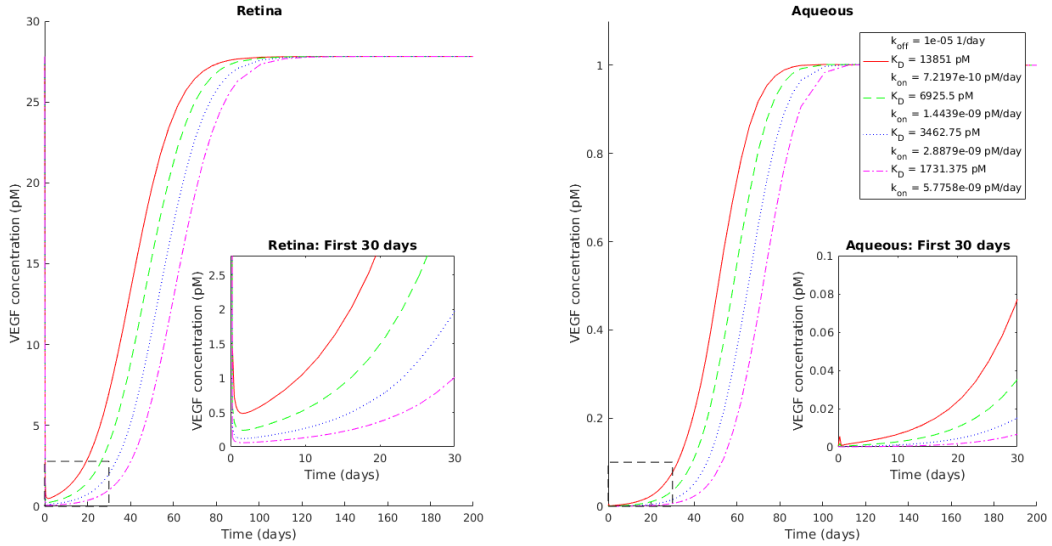

Figure 4.28: Simulated effect of increasing k_{on} and decreasing K_{D} so as to keep k_{off} fixed at 0.864 1/day. Plots shown correspond to K_{D} = 19,000 pM (solid red), K_{D} = 10,000 pM (dashed green), K_{D} = 5,000 pM (dotted blue) and K_{D} = 2,500 pM (dot-dash magenta).

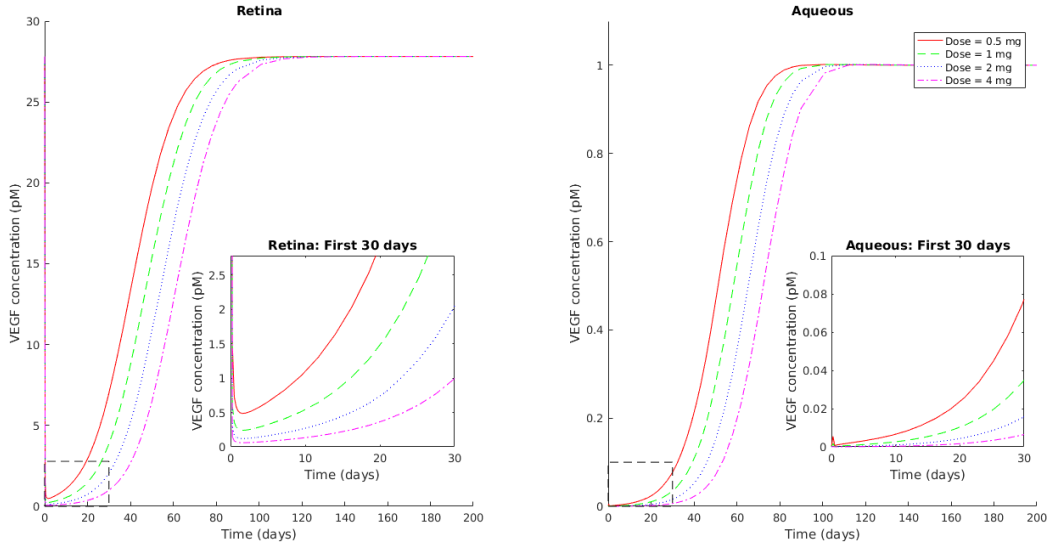

Figure 4.29: Simulated effect of increasing the dose from 0.5 mg (solid red), to 1 mg (dashed green), 5 mg (dotted blue) and 10 mg (dot-dash magenta). Plotted with K_{D} = 19,000 pM.

4.2.4 3-compartment PK/PD PDE model summary

By examining both homogeneous and heterogeneous VEGF production PDE models we are able to demonstrate that restricting the region of VEGF production to the macula does not have a large effect, and hence can be assumed to be homogeneous for simplicity. The reanalysis of the PK/PD system using the PDE model yielded predictions almost identical to that of the ODE model. The standard PDE model predicted a value for K_{D} of the same

order of magnitude as the ODE model, as well as exhibiting analogous behaviour in the number of case studies analysed. This comparison analysis has shown that the ODE model has a high degree of robustness with regard to its predictive ability, in comparison to its more complex PDE analogue, over a large relevant range of parameters including permeabilities, binding parameters and dosage. This supports the primary conclusion that the ODE and PDE models have equal numerical predictive ability with respect to this physical scenario.

The ODE model however has several advantages over its PDE analogue, alongside the increased computation speed, the ODE model also offers many opportunities for analytic investigation, allowing for greater mathematical insight, through asymptotics. However, this similarity in behaviour does not necessarily indicate that the same will be true after the introduction of drug-vitreal binding, as this may increase the level of heterogeneity within the system by lowering the effective diffusion coefficient [128]. The investigation of this possibility will examined in Chapter 5.

5

The ocular PK of vitreal binding macromolecules

5.1 Analysis of the PK of vitreal binding macromolecules using an ODE model

As mentioned in the Introduction (Chapter 1) the primary goal of this thesis is to mathematically model the PK/PD of vitreal binding molecules, designed for use in the human eye. Vitreal binding antibodies for therapeutic use in the eye are designed to be multi-specific, i.e. they are able to target more than one species of molecule. Where vitreal binders differ from other multi-specific binders (such as RG7716, see Figure 1.7) is that in addition to binding to molecules involved in a signalling pathway of interest (primary targets), they can also bind to non-pathological molecules (secondary targets), such as ocular super-structures or molecules naturally present in the vitreous. By binding to such super-structures or other molecules the vitreal binder is thought to be retained longer in the eye, hence extending its therapeutic capabilities. Vitreal binding molecules fall into two categories - static and non-static binders - static binders (SVBs) bind to ocular super-structures (such as collagen fibrils or hyaluronic acid polymers) whereas non-static binders (nSVBs) bind to molecules on the same scale as themselves (such has albumin). In this chapter we will present the theoretical PK of SVBs.

The initial analysis within this chapter will consider SVB molecules in terms of a retinal and vitreal ODE model, and will consider a theoretical molecule with one binding site with

which to bind to a single type of ocular super-structure. As the turn-over rate of ocular super-structures in the eye is so low, in comparison to the half-life of non-vitreal binding antibodies, we will assume the concentration of such structures to be constant with respect to the timescales of interest and that they cannot diffusive between model compartments. Importantly it then follows that when an SVB molecule is bound to a superstructure it cannot move between compartments. Additionally we will assume that when bound to a super-structure, a therapeutic antibody will still be able to bind to other molecules (vitreal VEGF, for example), although no drug-to-primary target interactions will be considered until Chapter 6.

We will address several important questions regarding SVBs, in the context of anti-VEGF therapy for wet AMD. Given that the goal of SVB molecules is to increase ocular retention, we will first consider how the introduction of vitreal binding alters the molecule's ocular $t_{1/2}$, and how this can be optimised. In Chapter 4 we demonstrated that, theoretically, an anti-VEGF antibody injected into the vitreous must be able to penetrate into the retina in order for there to be meaningful suppression of VEGF (see Figure 4.14). An SVB will always remain in the vitreous for as long as or longer than, its non-vitreal binding counterpart, however, this does not guarantee there will be a high enough concentration of the antibody freely diffusing in the vitreous (and hence be able to permeate into the retina) for there to a high enough retinal concentration for it to be efficacious. Therefore, secondly, we will analyse the concentration of unbound SVB molecules, and what role the strength of vitreal binding and binding site availability has in determining this. Finally we will consider what would be the effect of repeat dosing of such molecules: we will examine whether the drug accumulates within the vitreous over the course of multiple injections, what effect this would have on the concentration of free drug, and whether bolus doses of the drug at the start of treatment have the potential to reduce injection frequency even further.

5.1.1 Model formulation, non-dimensional analysis and solution

Model formulation

To formulate the model let us first define the concentration of unbound drug (C) in the retina and vitreous by c_{ret}, c_{vit} (pM) respectively, and the concentration of unbound (N) and bound binding sites (CN) by n and b (pM), respectively. Therefore the following chemical

reactions may take place within the system:

$$\mathrm{C} + \mathrm{N} \underset{k_{\mathrm{on}}^{(n)}}{\overset{k_{\mathrm{off}}^{(n)}}{\rightleftharpoons}} \mathrm{CN}. \tag{5.1}$$

We then formulate the model by modifying the 3-compartment PK ODE model (Equations 3.1-3.2), to include the ability for c_{vit} to bind to n. Additionally, as there do not exist any available aqueous experimental/clinical data, we omit the aqueous compartment. The PK SVB model, of the concentration of an SVB molecule post IVT injection, is then described by Equations 5.2-5.5 as follows:

$$\frac{\mathrm{d}c_{\mathrm{ret}}}{\mathrm{d}t} = -\left(\frac{S_{\mathrm{ret}}}{V_{\mathrm{ret}}}\right)\left[p_{\mathrm{ILM}} + p_{\mathrm{RPE}}\right] c_{\mathrm{ret}} + \left(\frac{S_{\mathrm{ret}}}{V_{\mathrm{ret}}}\right) p_{\mathrm{ILM}} c_{\mathrm{vit}}, \tag{5.2}$$

$$\frac{\mathrm{d}c_{\mathrm{vit}}}{\mathrm{d}t} = \left(\frac{S_{\mathrm{ret}}}{V_{\mathrm{vit}}}\right) p_{\mathrm{ILM}} c_{\mathrm{ret}} - \left[\left(\frac{S_{\mathrm{ret}}}{V_{\mathrm{vit}}}\right) p_{\mathrm{ILM}} + k_{\mathrm{el}}\right] c_{\mathrm{vit}} + k_{\mathrm{off}}^{(n)} b - k_{\mathrm{on}}^{(n)} n c_{\mathrm{vit}}, \tag{5.3}$$

$$\frac{\mathrm{d}n}{\mathrm{d}t} = k_{\mathrm{off}}^{(n)} b - k_{\mathrm{on}}^{(n)} n c_{\mathrm{vit}}, \tag{5.4}$$

$$\frac{\mathrm{d}b}{\mathrm{d}t} = -k_{\mathrm{off}}^{(n)} b + k_{\mathrm{on}}^{(n)} n c_{\mathrm{vit}}, \tag{5.5}$$

with:

$$c_{\mathrm{ret}}(0) = 0, \quad c_{\mathrm{vit}}(0) = c_0, \quad n(0) = n_0, \quad b(0) = 0, \tag{5.6}$$

where c_0 is the initial concentration of drug, resulting from a dose of d_0 mg, and n_0 is the total concentration of binding sites. Other parameter definitions can be found in Table 5.1, and follow from those defined in Chapters 3 and 4. The transfer rate k_{el} from the vitreous to the aqueous is defined via the following equation, as given by Equation 4.24 in Section 4.1:

$$k_{\mathrm{el}} = \lambda - \frac{S_{\mathrm{ret}}}{V_{\mathrm{vit}}} p_{\mathrm{ILM}} + \frac{\left(S_{\mathrm{ret}} p_{\mathrm{ILM}}\right)^2}{V_{\mathrm{vit}} S_{\mathrm{ret}} \left(p_{\mathrm{ILM}} + p_{\mathrm{RPE}}\right) - V_{\mathrm{vit}} V_{\mathrm{ret}} \lambda}, \tag{5.7}$$

where

$$\lambda\left(R_{\mathrm{h}}\right) = \frac{\log 2}{t_{1/2}^{(0)}}. \tag{5.8}$$

We note that λ and $t_{1/2}^{(0)}$ are the principle decay rate and half-life, of the molecule in the *absence* of vitreal binding, respectively. The value of R_{h} was taken to be that of a Fab molecule, 3.04 nm, as found using the meta-analysis presented in Appendix A.6.

Parameter	Value	Units	Description
k_{off}	variable	day^{-1}	Single binding site off rate
k_{on}	variable	$\text{pM}^{-1}\text{day}^{-1}$	Single binding site off rate
$K_{\text{D}}^{(n)}$	variable	pM	Dissociation constant
R_{h}	3.04 (App A.6)	nm	Hydrodynamic radius
k_{el}	Equation 5.7	day^{-1}	Vitreous-aqueous elimination rate constant
λ	Equation 5.8	day^{-1}	Ocular decay rate without vitreal binding
p_{RPE}	Equation 3.76	cm/sec	RPE permeability
p_{ILM}	Equation 3.77	cm/sec	ILM permeability
C_{L}	3.6 [87]	mL/day	Clearance from the aqueous chamber
V_{ret}	$0.22^{\dagger}$	mL	Retinal volume
V_{vit}	4.5 [24], [43]	mL	Vitreal volume
V_{aq}	0.16 [88], [89]	mL	Aqueous volume
S_{ret}	$9.71^{\dagger}$	cm^2	Retinal surface area

Table 5.1: SVB model parameter values and definitions, molecule specific parameters are presented for Fab molecules. †These values were calculated by taking the cross-sectional retinal distance from the posterior to the anterior as 2.37 cm (estimated from Missel [69]), the retinal thickness as 0.022 cm and retinal radius of that equivalent to a sphere of volume 4.5 mL, in the same manner as presented in Section 3.1.

As total binding sites (unoccupied and occupied) are conserved with respect to time we find, by taking the sum of Equations 5.4-5.5, the following conservation relationship:

$$\frac{\text{d}}{\text{d}t}\left(n+b\right)=0, \tag{5.9}$$

$$\Rightarrow \quad n+b=n_0, \tag{5.10}$$

$$\Rightarrow \quad b=n_0-n. \tag{5.11}$$

Upon substitution into Equations 5.2-5.5 the system is reduced to:

$$\frac{\text{d}c_{\text{ret}}}{\text{d}t}=-\left(\frac{S_{\text{ret}}}{V_{\text{ret}}}\right)\left[p_{\text{ILM}}+p_{\text{RPE}}\right]c_{\text{ret}}+\left(\frac{S_{\text{ret}}}{V_{\text{ret}}}\right)p_{\text{ILM}}c_{\text{vit}}, \tag{5.12}$$

$$\frac{\text{d}c_{\text{vit}}}{\text{d}t}=\left(\frac{S_{\text{ret}}}{V_{\text{vit}}}\right)p_{\text{ILM}}c_{\text{ret}}-\left[\left(\frac{S_{\text{ret}}}{V_{\text{vit}}}\right)p_{\text{ILM}}+k_{\text{el}}\right]c_{\text{vit}}+k_{\text{off}}^{(n)}(n_0-n)-k_{\text{on}}^{(n)}nc_{\text{vit}}, \tag{5.13}$$

$$\frac{\text{d}n}{\text{d}t}=k_{\text{off}}^{(n)}(n_0-n)-k_{\text{on}}^{(n)}nc_{\text{vit}}. \tag{5.14}$$

Model non-dimensionalisation

Let us use the following non-dimensionalisation:

$$c_{\text{ret}}=c_0x, \quad c_{\text{vit}}=c_0y, \quad n=n_0z, \quad t=\frac{1}{k_{\text{off}}^{(n)}}\tau, \tag{5.15}$$

$$\Rightarrow \quad x(0)=0, \quad y(0)=1, \quad z(0)=1, \tag{5.16}$$

which upon substitution into Equations 5.12-5.14 yields:

$$\frac{\mathrm{d}x}{\mathrm{d}\tau} = -Ax + By, \tag{5.17}$$

$$\frac{\mathrm{d}y}{\mathrm{d}\tau} = Cx - Dy + \left(\frac{1}{\alpha}\right)\left[(1-z) - \left(\frac{\alpha}{\beta}\right)zy\right], \tag{5.18}$$

$$\frac{\mathrm{d}z}{\mathrm{d}\tau} = (1-z) - \left(\frac{\alpha}{\beta}\right)zy, \tag{5.19}$$

where:

$$A = \frac{1}{k_{\mathrm{off}}^{(n)}}\left(\frac{S_{\mathrm{ret}}}{V_{\mathrm{ret}}}\right)[p_{\mathrm{ILM}} + p_{\mathrm{RPE}}], \quad B = \frac{1}{k_{\mathrm{off}}^{(n)}}\left(\frac{S_{\mathrm{ret}}}{V_{\mathrm{ret}}}\right)p_{\mathrm{ILM}}, \tag{5.20}$$

$$C = \frac{1}{k_{\mathrm{off}}^{(n)}}\left(\frac{S_{\mathrm{ret}}}{V_{\mathrm{vit}}}\right)p_{\mathrm{ILM}}, \quad D = \frac{1}{k_{\mathrm{off}}^{(n)}}\left[\left(\frac{S_{\mathrm{ret}}}{V_{\mathrm{vit}}}\right)p_{\mathrm{ILM}} + k_{\mathrm{el}}\right], \tag{5.21}$$

$$\alpha = \frac{c_0}{n_0}, \quad \beta = \frac{K_{\mathrm{D}}^{(n)}}{n_0}. \tag{5.22}$$

We note that α and β have very particular interpretations that will be of importance in the proceeding analysis. The relative magnitude of the initial dose to the number of binding sites is given by α, whereas the relative magnitude of the dissociation constant and the number of binding sites is given by β, with physical interpretations of their values are discussed in Table 5.2.

Parameter group	Value	Interpretation
$\alpha = \frac{c_0}{n_0}$	$\ll 1$	Very little binding
	< 1	Saturation not possible
	$= 1$	Perfect binding would lead to saturation
	> 1	Saturation possible
	$\gg 1$	Binding sites likely saturated
$\beta = \frac{K_{\mathrm{D}}^{(n)}}{n_0}$	$\ll 1$	Almost all C bound
	< 1	More than half of C bound
	$= 1$	Half of C bound
	> 1	Less than half of C
	$\gg 1$	Almost none of C bound

Table 5.2: Physical interpretation of the values of the model critical parameter groupings, α and β, where C denotes the unbound drug. The term 'saturation' refers to binding site occupation, e.g. if the binding sites within the vitreous are 'saturated' then they are all occupied. Interpretation of $K_{\mathrm{D}}^{(n)}$ assumes chemical equilibrium, and uses the standard results demonstrated in Lemma A.2 of Appendix A.13.

Before we proceed with the small time solution, we additionally note the following parameter relationship between A, B, C and D which will introduce a small parameter into

our system:

$$D - \frac{BC}{A} = \frac{1}{k_{\text{off}}^{(n)}} \left[k_{\text{el}} + \left(\frac{S_{\text{ret}}}{V_{\text{vit}}} \right) p_{\text{ILM}} - \frac{1}{1 + \frac{p_{\text{RPE}}}{p_{\text{ILM}}}} \left(\frac{S_{\text{ret}}}{V_{\text{vit}}} \right) p_{\text{ILM}} \right] \tag{5.23}$$

$$= \frac{\lambda}{k_{\text{off}}^{(n)}}, \tag{5.24}$$

where λ is the principle decay rate in the absence of vitreal binding, as shown by Equation 3.28 of Section 3.1. Therefore let us define

$$\varepsilon \coloneqq \frac{\lambda}{k_{\text{off}}^{(n)}}. \tag{5.25}$$

We will consider the distinguished limit representing chemical equilibrium wherein $k_{\text{off}}^{(n)}, k_{\text{on}}^{(n)} \to \infty$, with $K_{\text{D}}^{(n)}$ fixed. In this limit $\varepsilon \to 0^+$, as binding occurs on a much faster timescale than decay. Additionally, by noting that $\lambda \sim O(10^{-1})$ 1/day (see Table 3.4), we may scale A, B, C and D in the following way:

$$A = \varepsilon \hat{A}, \quad B = \varepsilon \hat{B}, \quad C = \varepsilon \hat{C}, \quad D = \varepsilon \hat{D}. \tag{5.26}$$

where we note, as their exists a factor of $1/V_{\text{ret}}$ in $\hat{A}, \hat{B}$ and $1/V_{\text{vit}}$ in $\hat{C}, \hat{D}$ we find that:

$$\hat{C}, \hat{D} \ll \hat{A}, \hat{B} \ll 1/\varepsilon, \tag{5.27}$$

since $V_{\text{ret}}/V_{\text{vit}} \ll 1$.

Small time solution (τ)

To solve this system we first consider the small time behaviour (on the timescale of $\tau = t/k_{\text{off}}$), as this will give us the slow timescale initial conditions. Upon injection, on a timescale faster than that of transport between compartments, there is a very fast transition to a state of chemical equilibrium (assuming $\varepsilon \ll 1$), whereby the concentration of injected drug (y) binds to the static vitreal network (z). By substituting the scaled parameters in Equation 5.26 into the nondimensional governing Equations 5.17-5.19 we find the following:

$$\frac{\mathrm{d}x}{\mathrm{d}\tau} = -\varepsilon \hat{A} x + \varepsilon \hat{B} y, \tag{5.28}$$

$$\frac{\mathrm{d}y}{\mathrm{d}\tau} = \varepsilon \hat{C} x - \varepsilon \hat{D} y + \left(\frac{1}{\alpha} \right) \left[(1 - z) - \left(\frac{\alpha}{\beta} \right) zy \right], \tag{5.29}$$

$$\frac{\mathrm{d}z}{\mathrm{d}\tau} = (1 - z) - \left(\frac{\alpha}{\beta} \right) zy. \tag{5.30}$$

Therefore on the fast timescale of τ (where inter-compartmental transport and elimination can be neglected), as $\varepsilon \to 0^+$, the system reduces to:

$$\frac{\mathrm{d}x}{\mathrm{d}\tau} = 0, \tag{5.31}$$

$$\frac{\mathrm{d}y}{\mathrm{d}\tau} = \left(\frac{1}{\alpha}\right)\left[(1-z) - \left(\frac{\alpha}{\beta}\right) zy\right], \tag{5.32}$$

$$\frac{\mathrm{d}z}{\mathrm{d}\tau} = (1-z) - \left(\frac{\alpha}{\beta}\right) zy. \tag{5.33}$$

Noting the initial conditions we therefore have $x(\tau) = 0$, together with:

$$\frac{\mathrm{d}y}{\mathrm{d}\tau} = \left(\frac{1}{\alpha}\right)\frac{\mathrm{d}z}{\mathrm{d}\tau}, \tag{5.34}$$

$$\Rightarrow \quad y - \left(\frac{1}{\alpha}\right) z = \text{constant}, \tag{5.35}$$

$$\Rightarrow \quad y = \left(\frac{1}{\alpha}\right) z + \left(1 - \frac{1}{\alpha}\right). \tag{5.36}$$

Therefore, upon substitution of this into $\mathrm{d}z/\mathrm{d}\tau$ we find

$$\frac{\mathrm{d}z}{\mathrm{d}\tau} = -\left(\frac{1}{\beta}\right) z^2 + \left(\frac{1}{\beta} - \frac{\alpha}{\beta} - 1\right) z + 1, \tag{5.37}$$

giving the small time steady-state concentration of z, z_0, one the fast timescale as:

$$z_0 \coloneqq \lim_{\tau\to\infty} z(\tau) = \frac{1}{2}\left[(1-\alpha-\beta) + \sqrt{4\beta + (1-\alpha-\beta)^2}\right], \tag{5.38}$$

where z_0 can be shown to be stable in $\mathrm{d}z/\mathrm{d}\tau$, z space as $\mathrm{d}z/\mathrm{d}\tau > 0$, $\mathrm{d}z/\mathrm{d}\tau < 0$ implies $z < z_0$, $z > z_0$, respectively. Therefore it follows from Equation 5.36 that the small time steady-state concentration of y, y_0 is given by:

$$y_0 = \frac{1}{2}\left[\left(1 - \frac{1+\beta}{\alpha}\right) + \sqrt{\frac{4\beta}{\alpha^2} + \left(\frac{1-\beta}{\alpha} - 1\right)^2}\right]. \tag{5.39}$$

We can also express y_0 in terms of the dimensional parameters, as is given by Equation 5.40 below:

$$y_0 = \frac{1}{2}\left[\left\{1 - \left(\frac{n_0 + K_{\mathrm{D}}^{(n)}}{c_0}\right)\right\} + \sqrt{\frac{4n_0K_{\mathrm{D}}^{(n)}}{c_0^2} + \left\{1 - \left(\frac{n_0 - K_{\mathrm{D}}^{(n)}}{c_0}\right)\right\}^2}\right]. \tag{5.40}$$

This expression for y_0 will be an important quantity in our analysis, as c_0y_0 represents the concentration of free drug, remaining after the fast chemical equilibration post IVT injection. We will refer to c_0y_0 as the 'effective initial concentration' of freely diffusing vitreal drug (FDVD), where y_0 represents the proportion of the initial dose remaining

unbound, after the initial chemical equilibration between the SVB molecules and the vitreal super-structure.

Slow timescale chemical equilibrium ($\varepsilon\tau$)

After the initial fast chemical equilibration (on timescale τ) we consider transport between compartments, and therefore rescale to a slow timescale, T, such that

$$\tau = \frac{T}{\varepsilon}, \tag{5.41}$$

giving

$$\frac{\mathrm{d}x}{\mathrm{d}T} = -\hat{A}x + \hat{B}y, \tag{5.42}$$

$$\frac{\mathrm{d}y}{\mathrm{d}T} = \hat{C}x - \hat{D}y + \frac{1}{\varepsilon}\left(\frac{1}{\alpha}\right)\left[(1-z) - \left(\frac{\alpha}{\beta}\right)zy\right], \tag{5.43}$$

$$\frac{\mathrm{d}z}{\mathrm{d}T} = \frac{1}{\varepsilon}\left[(1-z) - \left(\frac{\alpha}{\beta}\right)zy\right], \tag{5.44}$$

where $x(0) = 0$, $y(0) = y_0$ and $z(0) = z_0$. Additionally let us note that we may rewrite expression 5.43 using 5.44, giving:

$$\frac{\mathrm{d}y}{\mathrm{d}T} - \left(\frac{1}{\alpha}\right)\frac{\mathrm{d}z}{\mathrm{d}T} = \hat{C}x - \hat{D}y. \tag{5.45}$$

In order for us to generate a definite integral via utilisation of an integrating factor, let us next make the substitution $w(T) = 1 - z(T)$ into Equation 5.44, where $w(T)$ represents the non-dimensional concentration of occupied binding sites. This substitution gives:

$$\frac{\mathrm{d}}{\mathrm{d}T}\left(1 - w(T)\right) = \frac{1}{\varepsilon}\left[w(T) - \left(\frac{\alpha}{\beta}\right)(1-w(T))y(T)\right], \tag{5.46}$$

$$\Rightarrow \quad \frac{1}{\varepsilon}w(T) + \frac{\mathrm{d}w}{\mathrm{d}T} = \frac{1}{\varepsilon}\left(\frac{\alpha}{\beta}\right)(1-w(T))y(T), \tag{5.47}$$

$$\Rightarrow \quad \frac{\mathrm{d}}{\mathrm{d}T}\left(\mathrm{e}^{T/\varepsilon}w(T)\right) = \frac{1}{\varepsilon}\left(\frac{\alpha}{\beta}\right)(1-w(T))y(T)\mathrm{e}^{T/\varepsilon}, \tag{5.48}$$

$$\Rightarrow \quad w(T) = \frac{1}{\varepsilon}\left(\frac{\alpha}{\beta}\right)\int_0^T (1-w(s))y(s)\mathrm{e}^{-(T-s)/\varepsilon}\,\mathrm{d}s + w(0)\mathrm{e}^{-T/\varepsilon}, \tag{5.49}$$

$$\Rightarrow \quad w(T) = \frac{1}{\varepsilon}\left(\frac{\alpha}{\beta}\right)\int_0^T (1-w(s))y(s)\mathrm{e}^{-(T-s)/\varepsilon}\,\mathrm{d}s + (1-z_0)\mathrm{e}^{-T/\varepsilon}. \tag{5.50}$$

By next expanding $(1-w(s))y(s)$ around $s = T$, for $s < T$ and $T - s \sim O(\varepsilon)$, we find:

$$(1-w(s))y(s) = \left[(1-w(s))y(s)\right]\Big|_{s=T} + \left[(1-w(s))y(s)\right]'\Big|_{s=T}(s-T) + O\left((s-T)^2\right), \tag{5.51}$$

which, upon substitution into our definite integral expression for $w(T)$, yields:

$$w(T) = \frac{1}{\varepsilon}\left(\frac{\alpha}{\beta}\right)\int_0^T \left\{[(1-w(s))y(s)]\Big|_{s=T} + [(1-w(s))y(s)]'\Big|_{s=T}(s-T) + O\left((s-T)^2\right)\right\} \mathrm{e}^{-(T-s)/\varepsilon}\,\mathrm{d}s \quad (5.52)$$
$$+ (1-z_0)\mathrm{e}^{-T/\varepsilon}.$$

By changing variables such that $T - s = \varepsilon p$ (where $p \sim O(1)$), Equation 5.53 becomes:

$$w(T) = -\left(\frac{\alpha}{\beta}\right)\int_{T/\varepsilon}^0 \left\{[(1-w(p))y(p)]\Big|_{p=0} - [(1-w(p))y(p)]'\Big|_{p=0}\varepsilon p + O(\varepsilon^2)\right\}\mathrm{e}^{-p}\,\mathrm{d}p + (1-z_0)\mathrm{e}^{-T/\varepsilon} \quad (5.53)$$

$$= \left(\frac{\alpha}{\beta}\right)\int_0^{T/\varepsilon} \left\{[(1-w(p))y(p)]\Big|_{p=0} - [(1-w(p))y(p)]'\Big|_{p=0}\varepsilon p + O(\varepsilon^2)\right\}\mathrm{e}^{-p}\,\mathrm{d}p + (1-z_0)\mathrm{e}^{-T/\varepsilon} \quad (5.54)$$

$$\to \left(\frac{\alpha}{\beta}\right)[(1-w(p))y(p)]\Big|_{p=0}\int_0^\infty \mathrm{e}^{-p}\,\mathrm{d}p + O(\varepsilon), \qquad \text{as } \varepsilon \to 0. \quad (5.55)$$

Therefore we find the following to $O(1)$:

$$w(T) = \left(\frac{\alpha}{\beta}\right)(1-w(T))y(T) + O(\varepsilon). \quad (5.56)$$

This expression can be recognised as the equation for chemical equilibrium between z and y in the vitreous, and holds as long as $\varepsilon \ll 1$, with error $O(\varepsilon)$. Therefore as $z = 1 - w$ we may write:

$$1 - z = \left(\frac{\alpha}{\beta}\right)zy + O(\varepsilon) \quad (5.57)$$

$$\Rightarrow \quad z(y) = \frac{1}{1 + (\alpha/\beta)\,y} + O(\varepsilon). \quad (5.58)$$

Therefore now we have z in terms of y, by differentiating $z(y)$ and substituting it into Equation 5.45, we may write the system (Equations 5.42-5.44) in terms of only x and y, as follows:

$$\frac{\mathrm{d}x}{\mathrm{d}T} = -\hat{A}x + \hat{B}y, \quad (5.59)$$

$$\left(1 + \frac{\beta}{(\beta+\alpha y)^2}\right)\frac{\mathrm{d}y}{\mathrm{d}T} = \hat{C}x - \hat{D}y. \quad (5.60)$$

Retinal quasi-steady state

Recall the relative scales between $\hat{C}, \hat{D}$ and $\hat{A}, \hat{B}$ (Equation 5.27), due to their respective volumetric factors: $\hat{A}, \hat{B} \propto 1/V_{\text{ret}}$ and $\hat{C}, \hat{D} \propto 1/V_{\text{vit}}$. Defining $\delta = V_{\text{ret}}/V_{\text{vit}}$, we then make the following scaling:

$$\bar{A} = \delta\hat{A}, \quad \bar{B} = \delta\hat{B}, \quad (5.61)$$

such that:

$$\bar{A},\ \bar{B} \sim O(\hat{C}, \hat{D}). \quad (5.62)$$

Additionally, as $\delta \sim O(10^{-2})$ and ε can be made arbitrary small by tending $k_{\text{off}}^{(n)} \to \infty$, we may assume $\varepsilon \ll \delta$, therefore:

$$\hat{C}, \hat{D} \ll \hat{A}, \hat{B} \sim O\left(\frac{1}{\delta}\right) \ll 1/\varepsilon. \tag{5.63}$$

We may then write our system in the following way:

$$\delta \frac{\mathrm{d}x}{\mathrm{d}T} = -\bar{A}x + \bar{B}y, \tag{5.64}$$

$$\left(1 + \frac{\beta}{(\beta + \alpha y)^2}\right) \frac{\mathrm{d}y}{\mathrm{d}T} = \hat{C}x - \hat{D}y. \tag{5.65}$$

Therefore in the limit where $\delta, \varepsilon \to 0$ we find

$$x \simeq \left(\frac{\bar{B}}{\bar{A}}\right) y. \tag{5.66}$$

Upon substitution of this expression into Equation 5.65, we obtain:

$$\left(1 + \frac{\beta}{(\beta + \alpha y)^2}\right) \frac{\mathrm{d}y}{\mathrm{d}T} \simeq -\left(\hat{D} - \frac{\hat{B}\hat{C}}{\hat{A}}\right) y, \tag{5.67}$$

where we have used $\hat{B}/\bar{A} = \bar{B}/\hat{A}$. Therefore in terms of τ we may fully describe x, y and z by the following equations:

$$x = \left(\frac{B}{A}\right) y, \tag{5.68}$$

$$\left(1 + \frac{\beta}{(\beta + \alpha y)^2}\right) \frac{\mathrm{d}y}{\mathrm{d}\tau} = -\varepsilon y, \tag{5.69}$$

$$z = \frac{1}{1 + (\alpha/\beta)\, y}, \tag{5.70}$$

where $y(0) = y_0$. We note that x and z are both functions of y, and $\mathrm{d}y/\mathrm{d}\tau$ is a function solely of y.

Slow timescale solution for y

We may solve Equation 5.69 for y as follows:

$$\frac{\mathrm{d}y}{\mathrm{d}\tau} = -\varepsilon \left(\frac{y}{1 + \frac{\beta}{(\beta+\alpha y)^2}}\right), \tag{5.71}$$

$$\Rightarrow \quad -\varepsilon\tau = \int \frac{1 + \frac{\beta}{(\beta+\alpha y)^2}}{y}\, \mathrm{d}y \tag{5.72}$$

$$= \log(y) + \left(\frac{1}{\beta}\right)\left[\frac{\beta}{\alpha y + \beta} + \log\left(\frac{\alpha y}{\alpha y + \beta}\right)\right] - C_0. \tag{5.73}$$

Therefore

$$-\varepsilon\tau + C_0 = \log(y) + \left(\frac{1}{\beta}\right)\left[\frac{\beta}{\alpha y + \beta} + \log\left(\frac{\alpha y}{\alpha y + \beta}\right)\right], \tag{5.74}$$

where

$$C_0 = \log(y_0) + \left(\frac{1}{\beta}\right)\left[\frac{\beta}{\alpha y_0 + \beta} + \log\left(\frac{\alpha y_0}{\alpha y_0 + \beta}\right)\right]. \tag{5.75}$$

We note that Equation 5.74 cannot be explicitly inverted to give $y = y(\tau)$. We may also re-dimensionalise this expression to give t in terms of c, by the following expression:

$$-\lambda t + C_0 = \log\left(\frac{c}{c_0}\right) + \frac{n_0}{K_{\mathrm{D}}^{(n)}}\left[\frac{K_{\mathrm{D}}^{(n)}}{c + K_{\mathrm{D}}^{(n)}} + \log\left(\frac{c}{c + K_{\mathrm{D}}^{(n)}}\right)\right], \tag{5.76}$$

where Equation 5.75 becomes:

$$C_0 = \log(y_0) + \frac{n_0}{K_{\mathrm{D}}^{(n)}}\left[\frac{K_{\mathrm{D}}^{(n)}}{c_0 y_0 + K_{\mathrm{D}}^{(n)}} + \log\left(\frac{c_0 y_0}{c_0 y_0 + K_{\mathrm{D}}^{(n)}}\right)\right]. \tag{5.77}$$

Notice that in Equation 5.76 as $n_0/K_{\mathrm{D}}^{(n)} \to 0$ (and in Equation 5.74 as $\beta \to \infty$) we recover Equation 3.39 from Chapter 3, for the standard 3-compartment PK model, which gave the concentration in the vitreous as $c_0 \mathrm{e}^{-\lambda t}$ (noting that as $n_0/K_{\mathrm{D}}^{(n)} \to 0$ we find $C_0 \to 0$, as $y_0 \to 1$).

Initial characterisation of the SVB PK model and validation of analytics

Plots (a)-(d) of Figure 5.1 show 5.76 evaluated using parameters from Table 5.1, across a range of parameter values for n_0 and $K_{\mathrm{D}}^{(n)}$, at a dose of 0.5 mg and where $k_{\mathrm{off}}^{(n)}$ has been set to be very much larger than λ ($k_{\mathrm{off}}^{(n)} \sim O(10)$). In addition to the numerical and analytic solution to the SVB PK model (solid and dashed lines, respectively) we also compare to the non-vitreal binding model (dot-dashed line), as given in Chapter 3 by Equations 3.1-3.3, using the same parameter values for both models. Parameter values for n_0 and $K_{\mathrm{D}}^{(n)}$ were chosen to demonstrate the range of behaviour exhibited by the model.

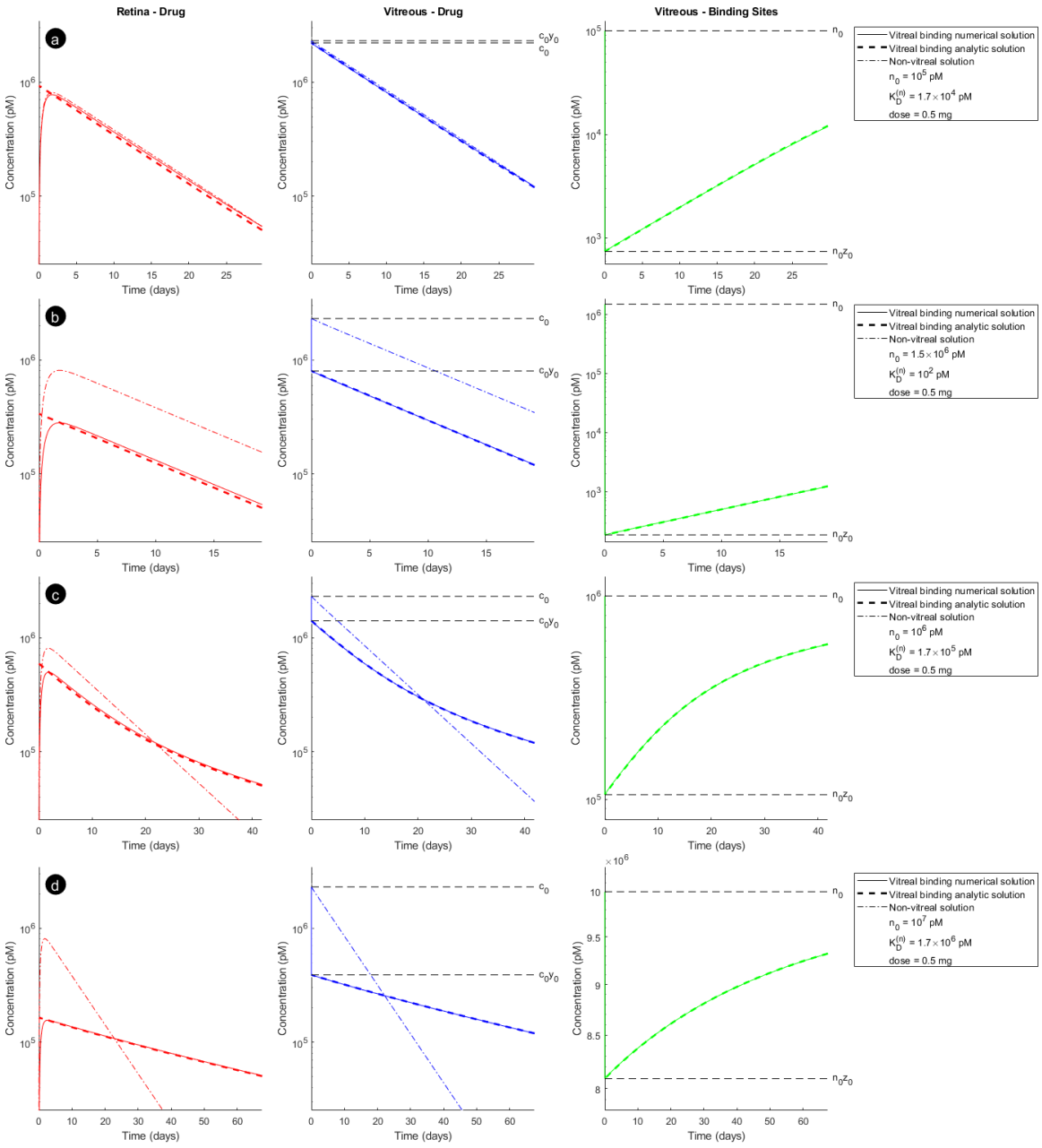

Figure 5.1: Plots (a)-(d) show the SVB model solved numerically, Equations 5.2-5.5, and analytically, Equation 5.76, (solid and dashed lines, respectively), alongside the equivalent non-vitreal binding model (dot-dashed line), Equations 3.1-3.3. Concentration profiles are given for $c_{\text{ret}}, c_{\text{vit}}$ and n, in red, blue and green, respectively. Both models in (a)-(d) are solved using the same parameters, given in Table 5.1, aside from n_0 and $K_{\text{D}}^{(n)}$ which vary between plots, with values given in individual plot legends. Given the accuracy of the asymptotics relative to the numerics, the dashed and solid lines overlap almost exactly in all plots.

In all plots (a)-(d) we see good agreement between the analytic solution and the numerics, verifying the analysis performed within this section for these regions in parameter

space. In plot (a) of Figure 5.1 the model exhibits exponential decay with very little difference between the SVB model and the non-vitreal binding model, $y_0 \simeq 1$ and the decay rate of the system is approximately equal to λ. In plot (b) we see similar exponential decay as in plot (a), at the same rate as the non-vitreal model, however the value of y_0 has reduce dramatically relative to (a). In plot (c) we see the vitreal model exhibit non-exponential decay, where the gradient of the logarithmic vitreal concentration becomes less negative with time, i.e. the rate of decay decreases with time. At time $t = 0$ the mode has a similar instantaneous decay rate as the non-vitreal binding model, and starts off with an effective initial concentration lower than c_0, however as the rate of decay decreases with time for these values of n_0 and $K_{\mathrm{D}}^{(n)}$, the vitreal and non-vitreal binding models intersect around $t = 20$ days, from which point the SVB model retains a higher concentration of free drug. Finally, in plot (d), unlike in plot (c), we see exponential decay, however here the SVB model is decaying at a much slower rate than that of the non-vitreal binding model, retaining a higher concentration of free drug past approximately $t = 20$ days, despite the SVB model's considerably lower effective initial concentration.

Analysis performed in Sections 5.1.2-5.1.3 will demonstrate plots (a)-(d) of Figure 5.1 represent the 4 characteristic types of behaviour exhibited by the SVB model. In the following analysis we will proceed to explain under what parameter regimes these occur, and why.

5.1.2 Half-Life analysis

Concentration dependent half-life

As was demonstrated by plot (c) of Figure 5.1 the concentration of free drug in the vitreal-binding model does not necessarily decay exponentially, and hence does not necessarily have a constant half-life. Motivated by this, let us consider half-life a function of concentration, $\tau_{1/2}(y)$, in the following way:

$$y(\tau) = y, \tag{5.78}$$

$$y(\tau + \tau_{1/2}(y)) = \frac{y}{2}. \tag{5.79}$$

$$\tag{5.80}$$

Using the solution for $\tau_{1/2}(y)$ given by Equation 5.74, we may solve Equations 5.78-5.79 for $\tau_{1/2}(y)$, to give:

$$\varepsilon\tau_{1/2}(y) = \log(2) + \frac{1}{\beta}\left[\log\left(1 + \frac{\beta}{\alpha y + \beta}\right) + \frac{\beta}{\alpha y + \beta} - \frac{2\beta}{\alpha y + 2\beta}\right]. \tag{5.81}$$

Redimensionalising 5.81 gives $t_{1/2}(c) = \tau_{1/2}(y/c_0)/k_{\text{off}}^{(n)}$, the dimensional concentration dependent half-life, described by the following equation:

$$t_{1/2}(c) = t_{1/2}^{(0)} + \frac{t_{1/2}^{0}}{\log(2)} \left\{ \frac{n_0}{K_{\text{D}}^{(n)}} \right\} \left[\log\left(1 + \frac{K_{\text{D}}^{(n)}}{c + K_{\text{D}}^{(n)}} \right) + \frac{K_{\text{D}}^{(n)}}{c + K_{\text{D}}^{(n)}} - \frac{2K_{\text{D}}^{(n)}}{c + 2K_{\text{D}}^{(n)}} \right], \quad (5.82)$$

recalling $\lambda = \log 2/t_{1/2}^{(0)}$, where we reiterate $t_{1/2}^{(0)}$ is the half-life in the absence of vitreal binding. Let us define the following function:

$$F(c/K_{\text{D}}^{(n)}) = \frac{1}{\log 2} \left[\log\left(1 + \frac{1}{c/K_{\text{D}}^{(n)} + 1} \right) + \frac{1}{c/K_{\text{D}}^{(n)} + 1} - \frac{2}{c/K_{\text{D}}^{(n)} + 2} \right], \quad (5.83)$$

implying that we may write:

$$t_{1/2}(c) = t_{1/2}^{(0)} \left(1 + \left\{ \frac{n_0}{K_{\text{D}}^{(n)}} \right\} F(c/K_{\text{D}}^{(n)}) \right). \quad (5.84)$$

Notice as $c/K_{\text{D}}^{(n)} \to 0$, $F(c/K_{\text{D}}^{(n)}) \to 1$, and similarly as $c/K_{\text{D}}^{(n)} \to \infty$, $F(c/K_{\text{D}}^{(n)}) \to 0$, as can be seen from Figure 5.2, where Equation 5.83 is shown plotted over $c/K_{\text{D}}^{(n)} \in [10^{-3}, 10^{3}]$. Notice the principle phase shift from 1 to 0 occurs, as would be expected from Equation 5.83, when $c \sim K_{\text{D}}^{(n)}$. This firstly tells us that $t_{1/2}(c)$ is bounded in the following way:

$$t_{1/2}(c) \in \left(t_{1/2}^{(0)}, t_{1/2}^{(0)} \left(1 + \left\{ \frac{n_0}{K_{\text{D}}^{(n)}} \right\} \right) \right) \quad (5.85)$$

assuming that $n_0, K_{\text{D}}^{(n)} > 0$. From Equation 5.85 we see the principle component in determining the magnitude of the half-life of the system is the ratio $n_0/K_{\text{D}}^{(n)}$, and the half-life cannot exceed $t_{1/2}^{(0)} \left(1 + \left\{ n_0/K_{\text{D}}^{(n)} \right\} \right)$. Additionally, we see from Equation 5.83 that as $c \to 0$, $F(c/K_{\text{D}}^{(n)}) \to 1$, hence given enough time the system will always maximise $t_{1/2}(c)$ (as given enough time $c \to 0$). Importantly however, Equation 5.83 demonstrates that the half-life of a SVB system is dependent not only on the ratio $n_0/K_{\text{D}}^{(n)}$, but also on the relative magnitude of the free drug concentration, c, and the value of $K_{\text{D}}^{(n)}$. We will explore this further in the following subsections.

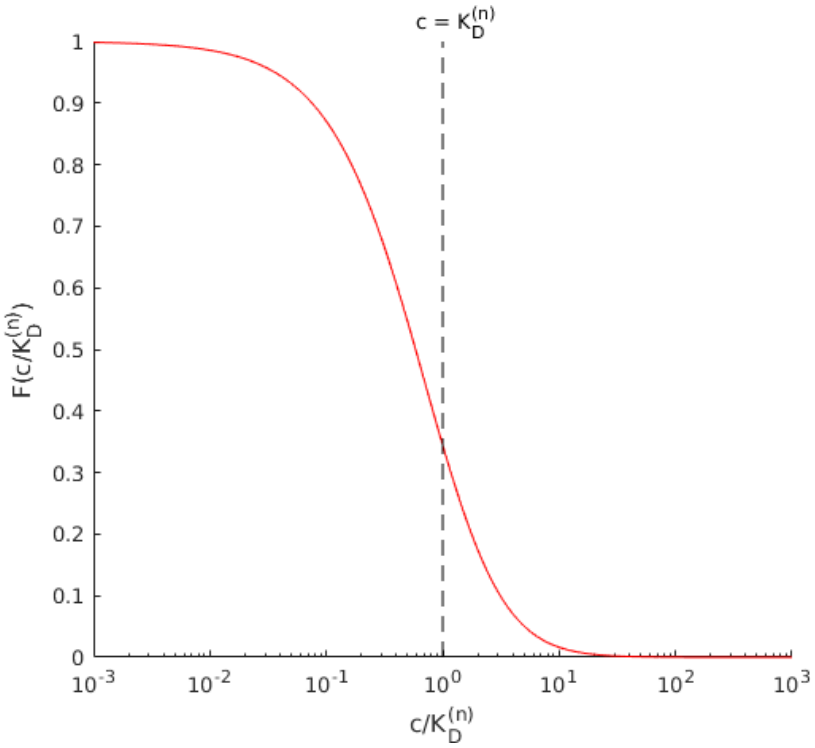

Figure 5.2: Equation 5.83 plotted for $c/K_{\mathrm{D}}^{(n)} \in [10^{-3}, 10^{3}]$. Note the dashed line denoting where $c = K_{\mathrm{D}}^{(n)}$.

Initial half-life

Given that we have previously demonstrated the existence of concentration dependent half-life, an important metric in determining the duration for which the drug is retained in the vitreous would be the time taken for the drug concentration to reach half of the effective initial concentration ($c_0 y_0$), which we shall refer to as the 'initial half-life'. Therefore the initial half-life is given by $t_{1/2}^{(\mathrm{init})} \coloneqq t_{1/2}(c_0 y_0)$, which, via Equation 5.82, may be written in terms of y_0 as:

$$t_{1/2}^{(\mathrm{init})} = t_{1/2}^{(0)} + \frac{t_{1/2}^{(0)}}{\log(2)} \left\{ \frac{n_0}{K_{\mathrm{D}}^{(n)}} \right\} \left[\log\left(2 - c_0\left(1 - y_0\right)/n_0\right) - \left(\frac{1 - c_0\left(1 - y_0\right)/n_0}{2 - c_0\left(1 - y_0\right)/n_0} \right) c_0\left(1 - y_0\right)/n_0 \right], \quad (5.86)$$

derived by using the following relation:

$$c_0 y_0 / K_{\mathrm{D}}^{(n)} + 1 = \frac{1}{1 - c_0\left(1 - y_0\right)/n_0}, \quad (5.87)$$

generated by Equations 5.36 and 5.57. Let us now define ζ as:

$$\zeta = c_0 \left(\frac{1 - y_0}{n_0} \right), \quad (5.88)$$

therefore we may express $t_{1/2}^{(\mathrm{init})}$ as:

$$t_{1/2}^{(\mathrm{init})} = \left(1 + \left\{\frac{n_0}{K_{\mathrm{D}}^{(n)}}\right\} f\left(\zeta\right)\right) t_{1/2}^{(0)}, \tag{5.89}$$

where $f(\zeta)$ is defined as:

$$f\left(\zeta\right) = \frac{1}{\log 2}\left[\log\left(2-\zeta\right) - \left(\frac{1-\zeta}{2-\zeta}\right)\zeta\right]. \tag{5.90}$$

To analyse Equation 5.89 we first note Lemma A.3 of Appendix A.13, which tells us that we may express ζ in terms of α and β as follows:

$$\zeta(\alpha,\beta) = \frac{1}{2}\left[1+\alpha+\beta-\sqrt{\left(\alpha+\beta\right)^2+2(\beta-\alpha)+1}\right], \tag{5.91}$$

and additionally demonstrating $\forall\alpha,\beta>0$ that $\zeta\in(0,1)$, hence implying that $f(\zeta)\in(0,1)$ also, as $f'(\zeta)<0\ \forall\zeta\in(0,1)$ and $f(0)=1$, $f(1)=0$. Figure 5.3 depicts Equations 5.91, $\zeta(\alpha,\beta)$, and 5.90, $f(\zeta)$, over α,β parameter space, which behave as expected. Notice that as $\beta\to 0$ we find $\zeta\to 1$ and $f(\zeta)\to 0$ only when $\alpha\geq 1$, indicating that whether $\alpha\geq 1$ or <1 may be significant in determining the model's behaviour. Figure 5.4 depicts Equation 5.89, $t_{1/2}^{(\mathrm{init})}$, evaluated over the same range of parameter space as in Figure 5.3. As expected $t_{1/2}^{(\mathrm{init})} > t_{1/2}^{(0)}$, as can be seen from Equation 5.89, where $t_{1/2}^{(0)}$ is taken to equal 7.04 days. Unlike ζ and $f(\zeta)$, there exists stationary point for $t_{1/2}^{(\mathrm{init})}$ with respect to β - and that this stationary point appears (in Figure 5.89) to only seems to exist for $\alpha>1$, whereas for $\alpha<1$ the initial half-life $\to\infty$ as $\beta\to 0$. This tells us that position in α,β space determines, and potentially bounds, the possible values of $t_{1/2}^{(\mathrm{init})}$ - how it does so we will considered in the following subsection.

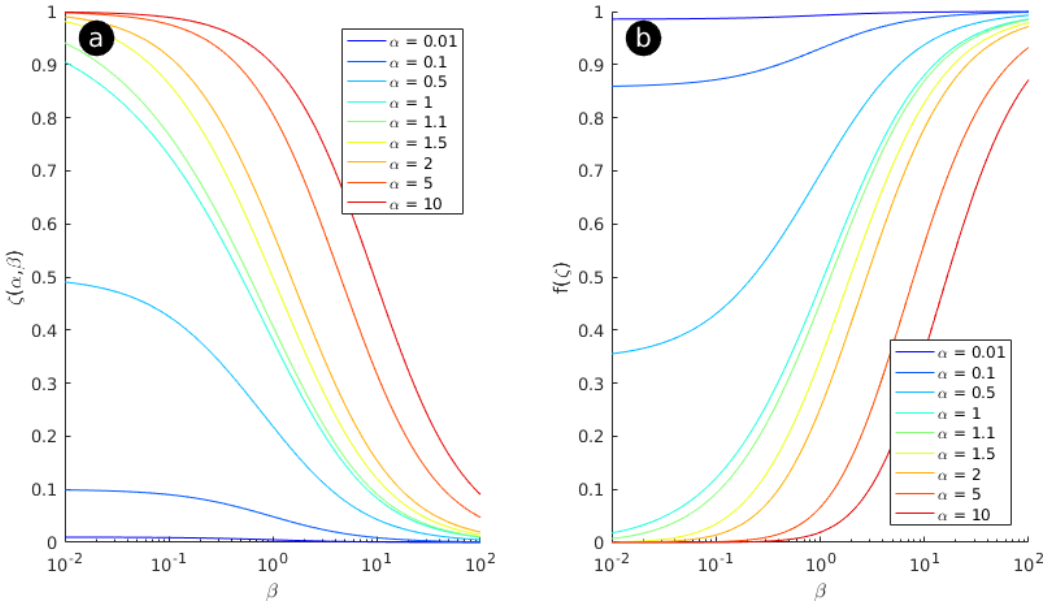

Figure 5.3: Equations 5.91, $\zeta(\alpha, \beta)$, and 5.90, $f(\zeta)$, plotted (in (a) and (b), respectively), over a range of β values, for various constant α values, given in the legend.

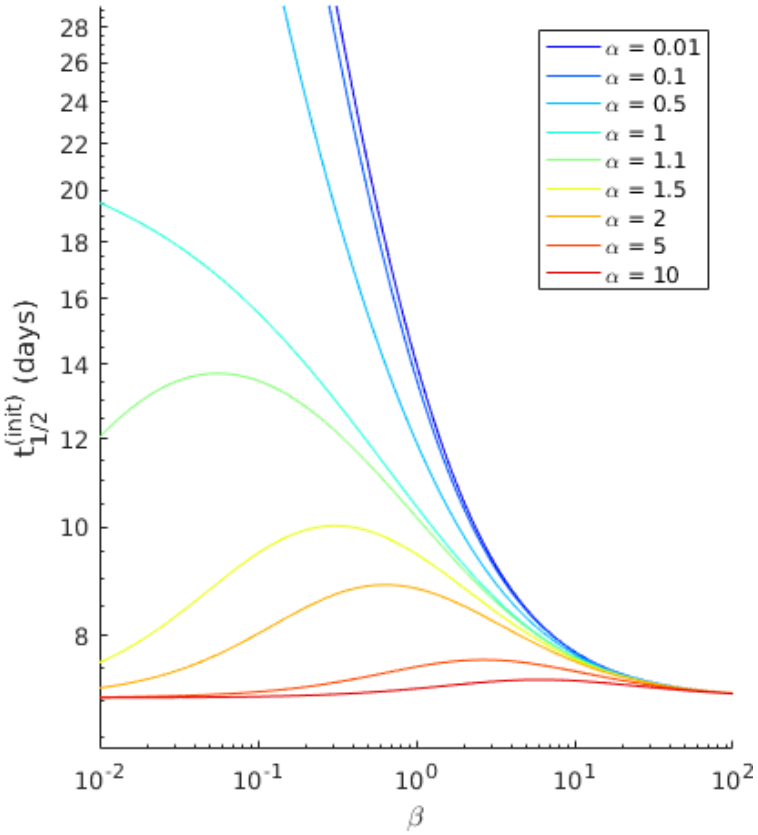

Figure 5.4: Equation 5.89, $t_{1/2}^{(\text{init})}$, plotted over a range of β values, for various constant α values, given in the legend.

Initial half-life optimisation

From Figure 5.4 it appears that there can exist a maximal stationary value of $t_{1/2}^{(\text{init})}$ with respect to β - we will proceed by analysing for what values of α and β this can occur. To analyse this we first consider the derivative of $t_{1/2}^{(\text{init})}$ with respect to β; as shown in Lemma A.4 we find:

$$\frac{\partial t_{1/2}^{(\text{init})}}{\partial \beta} = 0 \quad \iff \quad A(\zeta, \alpha) = g(\zeta), \tag{5.92}$$

where

$$A(\zeta, \alpha) = \frac{\alpha - \zeta}{\alpha - \zeta^2} \tag{5.93}$$

$$g(\zeta) = \frac{(1-\zeta)(2-\zeta)\zeta - (2-\zeta)^2 \log(2-\zeta)}{\zeta(\zeta-4)(\zeta-1)^2}. \tag{5.94}$$

We can now consider $\partial t_{1/2}^{(\text{init})}/\partial\beta = 0$ as equivalent to when the functions $A(\zeta, \alpha)$ and $g(\zeta)$ intersect, which we will analyse in Lemma 5.1.

Lemma 5.1. *The following holds:*

$$\exists \beta_0 > 0 : \left.\frac{\partial t_{1/2}^{(init)}}{\partial \beta}\right|_{\beta_0} = 0 \iff \alpha \geq 1. \tag{5.95}$$

Proof. Lemma A.4 demonstrates the above statement is equivalent to the existence of an intersection of functions $A(\zeta, \alpha)$ and $g(\zeta)$, given by Equations 5.93 and 5.94, respectively. If we first consider $g(\zeta)$ we see that Figure 5.5 numerically demonstrates that $g(\zeta)$ is monotonically decreasing. It can be seen from Equation 5.94 that $g(\zeta)$ tends to infinity as ζ tends to 0, and via L'Hospital's rule it can be shown that $g(\zeta)$ tends to $1/2$ as ζ tends to 1, as below:

$$\lim_{\zeta \to 1} g(\zeta) = \lim_{\zeta \to 1} \left(\frac{4\log(2-\zeta) - 7\zeta - 2\zeta\log(2-\zeta) + 3\zeta^2 + 4}{4\zeta^3 - 18\zeta^2 + 18\zeta - 4} \right) \tag{5.96}$$

$$= \lim_{\zeta \to 1} \left(\frac{6\zeta - 2\log(2-\zeta) - 9}{12\zeta^2 - 36\zeta + 18} \right) \tag{5.97}$$

$$= \frac{1}{2}. \tag{5.98}$$

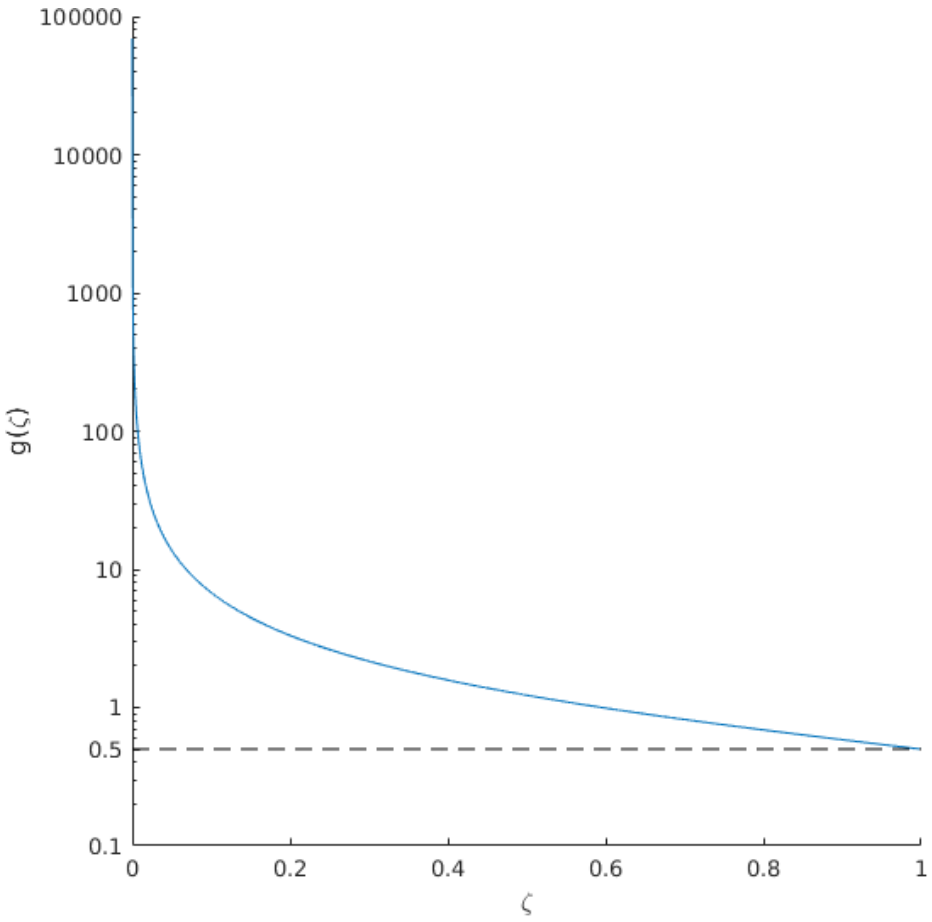

Figure 5.5: $g(\zeta)$ over the range of possible ζ values, notice it tends to $1/2$ as $\zeta \to 1$ and infinity as $\zeta \to 0$.

In order to analyse $A(\zeta, \alpha)$ we first notice that $A(0, \alpha) = 1 \ \forall \alpha$ and asymptotes to $-\infty, +\infty$ as $\zeta \nearrow \sqrt{\alpha}$, $\zeta \searrow \sqrt{\alpha}$, respectively. Additionally let us note that the derivative of $A(\zeta, \alpha)$ with respect to ζ is given by:

$$\frac{\partial A(\zeta, \alpha)}{\partial \zeta} = \frac{-(\alpha - \zeta)^2 + \alpha(\alpha - 1)}{(\alpha - \zeta^2)^2}, \tag{5.99}$$

and finally that $A(\zeta \to 1, \alpha) = 1 \ \forall \alpha \neq 1$ - whereas when $\alpha = 1$ we find $A(\zeta \to 1, 1) = 1/2$, as follows from L'Hospital's rule:

$$\lim_{\zeta \to 1} A(\zeta, 1) = \lim_{\zeta \to 1} \frac{1 - \zeta}{1 - \zeta^2} \tag{5.100}$$

$$= \lim_{\zeta \to 1} \frac{-1}{-2\zeta} \tag{5.101}$$

$$= \frac{1}{2}. \tag{5.102}$$

We now consider whether $A(\zeta, \alpha)$ and $g(\zeta)$ intersect case-wise with respect to α.

Case (1): $\alpha > 1$

When $\alpha > 1$, $\sqrt{\alpha} \notin [0,1]$, implying $A(\zeta,\alpha)$ is continuous over ζ. Therefore for $\alpha > 1$, as $A(0,\alpha) = 1 = A(1,\alpha)$ and $g(1) = 1/2$, A and g must cross. Therefore there exists a solution to $A(\zeta,\alpha) = g(\zeta)$.

Case (2): $\alpha = 1$

When $\alpha = 1$ $A(\zeta,1)$ can be written:

$$A(\zeta,1) = \frac{1}{1+\zeta}. \tag{5.103}$$

We have previously shown that $A(1,1) = 1/2$, therefore $A(1,1) = g(1)$. We next note that the derivative $\partial A(\zeta,1)/\partial\zeta$ is strictly negative, as:

$$\frac{\partial A(\zeta,1)}{\partial\zeta} = -\frac{1}{(1+\zeta)^2} < 0, \tag{5.104}$$

and hence, as $1/(1+\zeta)$ and $g(\zeta)$ are both convex functions over $\zeta \in (0,1)$, we find when $\alpha = 1$ $A(\zeta,1)$ and $g(\zeta)$ intersect once, when $\zeta = 1$. However as can be deduced from Equation 5.91, for $\alpha = 1$ we find ζ can only equal 1 when $\beta = 0$, which cannot occur as $\beta > 0$.

Case (3): $\alpha < 1$

Notice that from the first derivative of α with respect to ζ we have shown the following

$$\frac{\partial A(\zeta,\alpha)}{\partial\zeta} < 0 \quad \forall\zeta \in [0,1], \text{ for } \alpha < 1, \tag{5.105}$$

therefore $A(\zeta,\alpha)$ is monotonically decreasing over ζ. Additionally note that

$$\lim_{\zeta\downarrow\sqrt{\alpha}} A(\zeta,\alpha) = +\infty, \tag{5.106}$$

therefore as $A(1,\alpha) = 1$ and $g(1) = 1/2$, there cannot exist an intersection of $A(\zeta,\alpha)$ and $g(\zeta)$ for $\zeta > \sqrt{\alpha}$. Hence, let us attempt to bound $A(\zeta,\alpha)$ by $A(\zeta,1)$ $\forall\zeta \in [0,\sqrt{\alpha})$, $\forall\alpha < 1$, because if this is the case then $A(\zeta,\alpha)$ and $g(\zeta)$ cannot intersect in this region, as we have already shown $A(\zeta,\alpha)$ cannot intersect $g(\zeta)$ for $\alpha = 1$. By making the substitution $\alpha = 1-\delta$, where $\delta \in (0,1)$, we see if $A(\zeta,1) > A(\zeta,\alpha)$ $\forall\zeta \in [0,\sqrt{\alpha})$, $\forall\alpha < 1$ then $A(\zeta,1-\delta)/A(\zeta,1)$

should be $\in [0,1]$ $\forall \delta \in (0,1)$ and $\zeta \in (0, \sqrt{1-\delta})$. If this is the case then the following expression must be less than 0:

$$\frac{A(\zeta, 1-\delta)}{A(\zeta,1)} - 1 = \frac{\overbrace{\delta\zeta}^{>0}}{\underbrace{\left(\zeta + \sqrt{1-\delta}\right)}_{>0}\underbrace{\left(\zeta - \sqrt{1-\delta}\right)}_{<0}} < 0. \tag{5.107}$$

Hence, if $\alpha < 1$, then $A(\zeta, \alpha)$ and $g(\zeta)$ also do not intersect. Cases (1)-(3) are illustrated in Figures 5.6 and 5.7. □

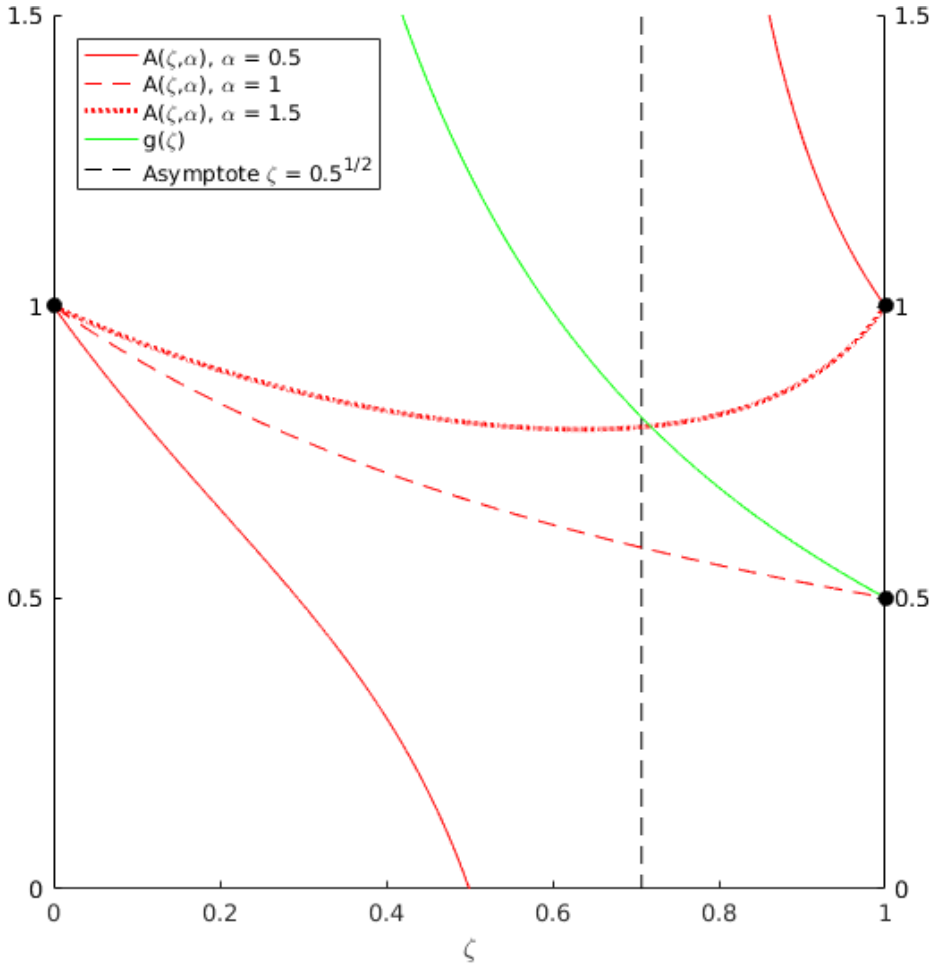

Figure 5.6: $A(\zeta, \alpha)$ (Equation 5.93) and $g(\zeta)$ (Equation 5.94) plotted for various values of α. Notice for all values of α $A(0,\alpha) = 1$ and for all values of $\alpha \neq 1$, $A(1,\alpha) = 1$. When $\alpha = 1$, $A(1,1) = 1/2$. The vertical dashed line, $\zeta = \sqrt{0.5}$, shows the asymptote of $A(\zeta,\alpha)$ in the case where $\alpha = 0.5$.

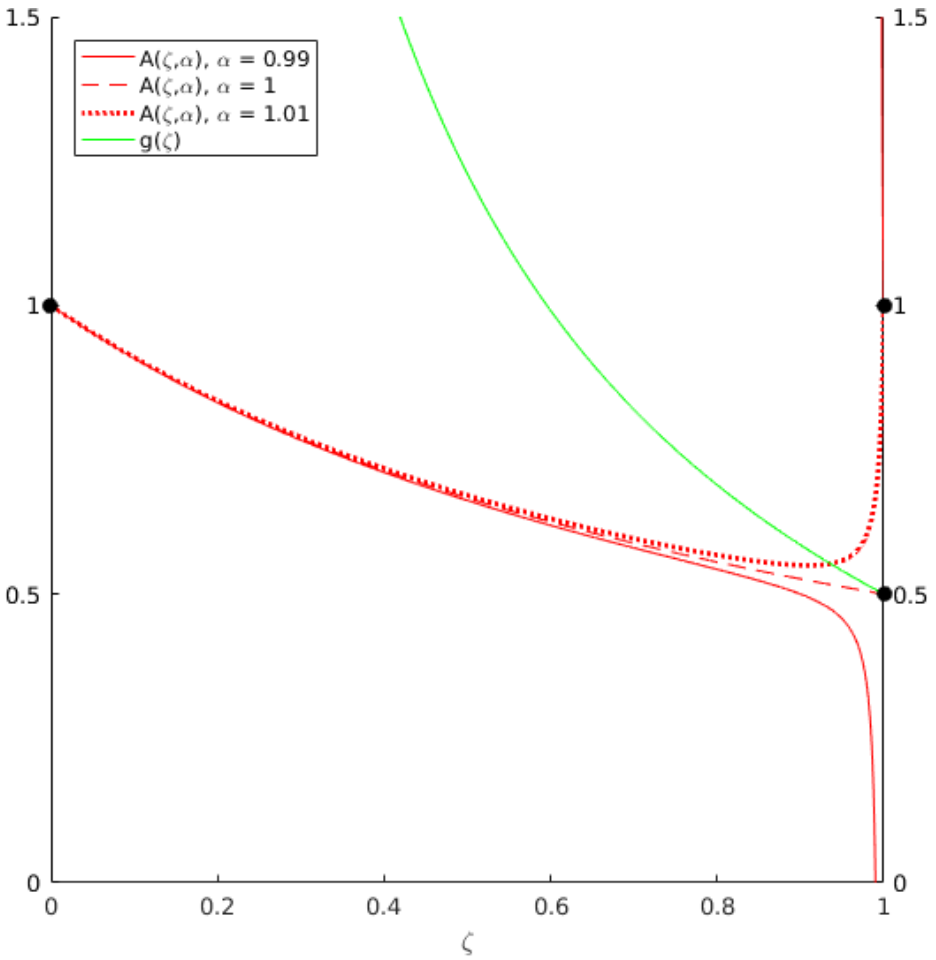

Figure 5.7: $A(\zeta, \alpha)$ (Equation 5.93) and $g(\zeta)$ (Equation 5.94) plotted for various values of α. Here we see how the behaviour of $A(\zeta, \alpha)$ changes when α crosses over $\alpha = 1$.

Therefore we have shown that there exists a stationary point in $t_{1/2}^{(\text{init})}$ with respect to β if and only if $\alpha > 1$, and that there exists a stationary point at $\beta \to 0$ for $\alpha = 1$. The numerics shown in Figure 5.4 not only postulated this, but additionally that in the case where $\alpha < 1$, $t_{1/2}^{(\text{init})}$ is maximised by minimizing β; the proof that this is indeed the case is given in Lemma 5.2.

Lemma 5.2. *For $\alpha < 1$, $t_{1/2}^{(init)}$ is maximised by minimizing β.*

Proof. Let us now consider the limit of $t_{1/2}^{(\text{init})}$ for $\alpha < 1$ as $\beta \to 0$, or equivalently the limit of $f(\zeta)/\beta$. Writing β in terms of α and ζ (see Lemma A.3) we may consider the limit of $f(\zeta)/\beta$ as $\beta \to 0$ in terms of ζ and α as follows:

$$\lim_{\beta \to 0} \left\{ \frac{1}{\beta} f(\zeta) \right\} = \lim_{\beta \to 0} \left\{ \frac{1}{\log 2} \left(\frac{\zeta}{\zeta^2 - (1+\alpha)\zeta + \alpha} \right) \left[\log(2-\zeta) - \left(\frac{1-\zeta}{2-\zeta} \right) \zeta \right] \right\}. \quad (5.108)$$

To evaluate this limit we consider the limit of ζ as $\beta \to 0$,

$$\zeta(\alpha,\beta)\Big|_{\beta=0} = \frac{1}{2}\left[1+\alpha-\left|\sqrt{\alpha^2-2\alpha+1}\right|\right] \tag{5.109}$$

$$= \frac{1}{2}\left[1+\alpha-|\alpha-1|\right] \tag{5.110}$$

$$= \begin{cases} \alpha & \alpha < 1, \\ 1 & \alpha \geq 1. \end{cases} \tag{5.111}$$

Therefore, for $\alpha < 1$, as $\zeta \to \alpha$ as $\beta \to 0$, allows us to evaluate 5.108, giving:

$$\lim_{\beta\to 0}\left\{\frac{1}{\beta}f(\zeta)\right\} = \frac{1}{\log 2}\underbrace{\left[\log(2-\alpha)-\left(\frac{1-\alpha}{2-\alpha}\right)\alpha\right]}_{\in(0,\infty)}\lim_{\zeta\to\alpha}\left(\frac{\zeta}{\zeta^2-(1+\alpha)\zeta+\alpha}\right) \tag{5.112}$$

$$\propto \lim_{\zeta\to\alpha}\left(\frac{\zeta}{\zeta^2-(1+\alpha)\zeta+\alpha}\right) = \infty. \tag{5.113}$$

Therefore we have shown that $t_{1/2}^{(\text{init})} \to \infty$ as $\beta \to 0$. Hence, as Lemma 5.1 has shown that there cannot exist a turning point for $t_{1/2}^{(\text{init})}$ with respect to β for $\alpha < 1$, we have shown that as $t_{1/2}^{\text{init}}$ tends to infinity as $\beta \to 0$, $t_{1/2}^{(\text{init})}$ can be maximised by minimizing β. □

The analysis of $t_{1/2}^{(\text{init})}$ can be summarised by considering $t_{1/2}^{(\text{init})}$ evaluated over dimensional parameter space ($K_{\text{D}}^{(n)}, n_0$ as opposed to α, β), shown in Figures 5.8 and 5.9. In Figure 5.8 notice the two black lines partitioning $\left(K_{\text{D}}^{(n)}, n_0\right)$ parameter space. To the left of the line $n_0 = c_0$ is the region where $\alpha > 1$, whereas to the right is $\alpha < 1$. Similarly above the line $K_{\text{D}}^{(n)} = n_0$ represents the region where $\beta > 1$ and below where $\beta < 1$. We see that as the ratio $K_{\text{D}}^{(n)}/n_0$ is minimised, in the region where $n_0 > c_0$, $t_{1/2}^{(\text{init})}$ is $O(n_0/K_{\text{D}}^{(n)})$, which tends to infinity as $K_{\text{D}}^{(n)}/n_0 \to 0$. In order to properly visualise the behaviour of $t_{1/2}^{(\text{init})}$ in the red region of Figure 5.8 we present Figure 5.9, a ribbon plot where n_0 has been restricted to be in the region $n_0 \in [10^4, c_0]$. From Figure 5.9 we see again the existence of the stationary point predicted by the analysis within this subsection, as well as the stationary point that exists for when $n_0 = c_0$ ($\alpha = 1$) and $K_{\text{D}}^{(n)}/n_0 \to 0$ ($\beta \to 0$).

From this we can see that the greatest increase in $t_{1/2}^{(\text{init})}$ from $t_{1/2}^{(0)}$ occurs when $n_0 > c_0$, where $t_{1/2}^{(\text{init})}$ can be extended arbitrarily depending on the ratio of $K_{\text{D}}^{(n)}$ and n_0. When $n_0 \leq c_0$ we have found, from Figure 5.9, then there exists an optimal relationship between $K_{\text{D}}^{(n)}$ and n_0, to maximise $t_{1/2}^{(\text{init})}$. We will derive an expression for the optimal $K_{\text{D}}^{(n)}, n_0$ relationship in Section 5.1.3.

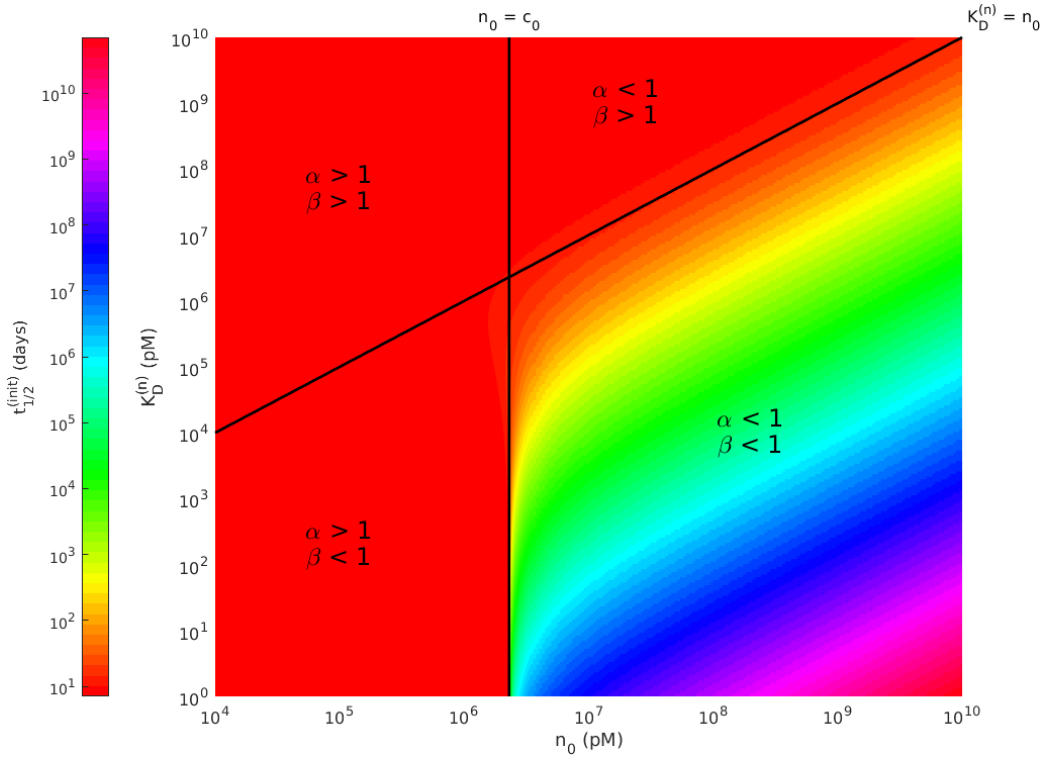

Figure 5.8: Plot of $t_{1/2}^{(\text{init})}$ (Equation 5.89) for $n_0 \in [10^4, 10^{10}]$ and $K_{\text{D}}^{(n)} \in [10^0, 10^{10}]$. See text for details.

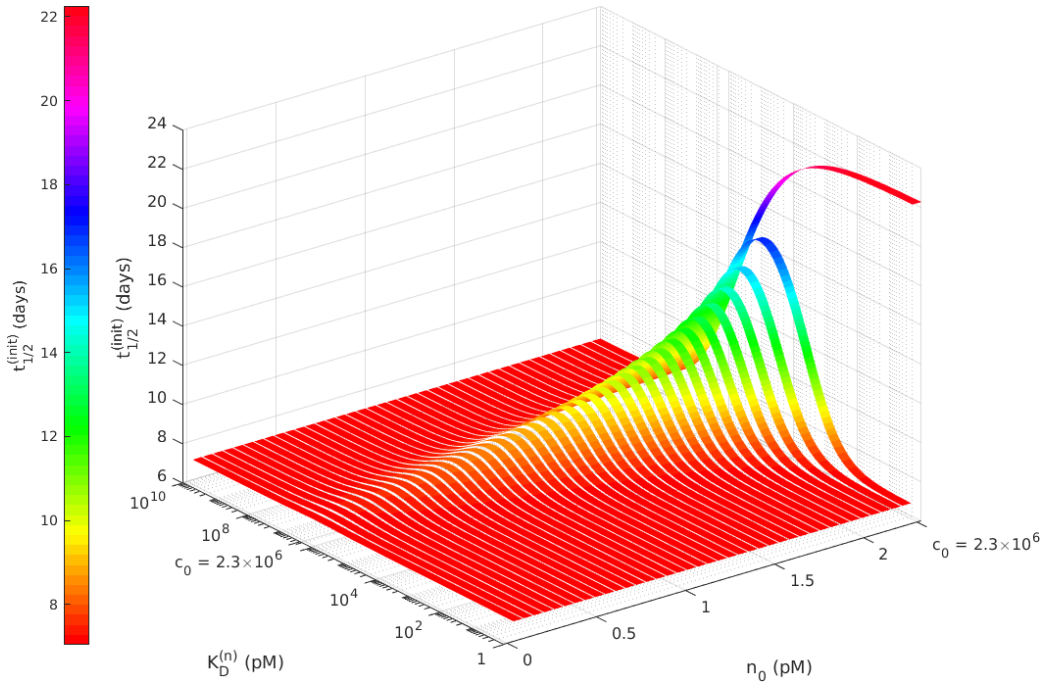

Figure 5.9: Ribbon of $t_{1/2}^{(\text{init})}$ (Equation 5.89) for $n_0 \in [10^4, c_0]$ and $K_{\text{D}}^{(n)} \in [10^0, 10^{10}]$, i.e. for $\alpha > 1$.

Logarithmic gradient half-life analysis

To conclude the analysis of $t_{1/2}$ in this section we present a short analysis of the logarithmic gradient of $c(t)$ with respect to time, given by $\mathrm{d}(\log c)/\mathrm{d}t$. To explain why this is a quantity of interest we consider the system in the absence of vitreal binding, $c = c_0 \exp(-\lambda t)$, where we make the substitution $u = \log(c)$:

$$c = c_0 \exp(-\lambda t) \quad \Rightarrow \quad -\lambda t = \log\left(\frac{c}{c_0}\right) \tag{5.114}$$

$$= u - \log(c_0), \tag{5.115}$$

$$\Rightarrow \quad \frac{\mathrm{d}u}{\mathrm{d}t} = -\lambda, \tag{5.116}$$

$$\Rightarrow \quad \frac{\mathrm{d}}{\mathrm{d}t}(\log c) = -\lambda, \tag{5.117}$$

$$\Rightarrow \quad \left|\frac{\mathrm{d}}{\mathrm{d}t}(\log c)\right| = \frac{\log 2}{t_{1/2}^{(0)}}, \tag{5.118}$$

$$\Rightarrow \quad t_{1/2}^{(0)} = \log 2 \left(\left|\frac{\mathrm{d}}{\mathrm{d}t}(\log c)\right|\right)^{-1}. \tag{5.119}$$

Therefore the larger the magnitude of the logarithmic gradient the smaller the half-life of the system, as expected. Motivated by this we will therefore define the quantity on the right hand side of Equation 5.119 as the logarithmically derived half-life, $t_{1/2}^{(\log)}$, as follows:

$$t_{1/2}^{(\log)} = \log 2 \left(\left|\frac{\mathrm{d}}{\mathrm{d}t}(\log c)\right|\right)^{-1}. \tag{5.120}$$

Therefore let us consider the equivalent expression for the SVB model, given below:

$$-\lambda t + C_0 = \log\left(\frac{c}{c_0}\right) + \frac{n_0}{K_{\mathrm{D}}^{(n)}}\left[\frac{K_{\mathrm{D}}^{(n)}}{c + K_{\mathrm{D}}^{(n)}} + \log\left(\frac{c}{c + K_{\mathrm{D}}^{(n)}}\right)\right] \tag{5.121}$$

$$= u - \log(c_0) + \frac{n_0}{K_{\mathrm{D}}^{(n)}}\left[\frac{K_{\mathrm{D}}^{(n)}}{\exp u + K_{\mathrm{D}}^{(n)}} + \log\left(\frac{\exp u}{\exp u + K_{\mathrm{D}}^{(n)}}\right)\right], \tag{5.122}$$

$$\Rightarrow \quad -\lambda\frac{\mathrm{d}t}{\mathrm{d}u} = \frac{n_0 K_{\mathrm{D}}^{(n)}}{(K_{\mathrm{D}}^{(n)} + \exp u)^2} + 1 \tag{5.123}$$

$$= \frac{n_0/K_{\mathrm{D}}^{(n)}}{(1 + c/K_{\mathrm{D}}^{(n)})^2} + 1, \tag{5.124}$$

$$\Rightarrow \quad \frac{1}{\log 2}\left|\frac{\mathrm{d}}{\mathrm{d}t}(\log c)\right| = \frac{1}{t_{1/2}^{(0)}}\left(\frac{n_0/K_{\mathrm{D}}^{(n)}}{(1 + c/K_{\mathrm{D}}^{(n)})^2} + 1\right)^{-1}, \tag{5.125}$$

therefore the logarithmically derived half-life for the full system is given by:

$$t_{1/2}^{(\log)} = t_{1/2}^{(0)}\left(\frac{n_0/K_{\mathrm{D}}^{(n)}}{(1 + c/K_{\mathrm{D}}^{(n)})^2} + 1\right). \tag{5.126}$$

The expression for the logarithmic gradient given by Equation 5.126 gives us several important insights into the behaviour of the system. Again, as shown in the previous subsection, we see that minimising the ratio K_{D}/n_0 leads to a maximal system half-life, however this expression sheds some light on the concentration dependence of the half-life by demonstrating the importance of the relative magnitude of the concentration of the drug and $K_{\mathrm{D}}^{(n)}$. For example if $c \gg K_{\mathrm{D}}^{(n)}$ or $c \ll K_{\mathrm{D}}^{(n)}$, then the half-life expressed by the system switches between $t_{1/2}^{(0)}$ and $t_{1/2}^{(0)}(1 + K_{\mathrm{D}}/n_0)$, respectively, somewhat mirroring Equation 5.89. Therefore Equation 5.126 predicts the half-life of the system can only be concentration dependent when $c \sim K_{\mathrm{D}}^{(n)}$. This explains the previously noticed switching between exponential and non-exponential decay, as seen in Figure 5.1.

5.1.3 Duration time analysis

From the half-life analysis in Subsection 5.1.2 it may appear that in order to maximise the efficacy of drug all one needs to do is minimise $K_{\mathrm{D}}^{(n)}/n_0$, as doing so increases the half-life of the system to an arbitrarily high level. However as $K_{\mathrm{D}}^{(n)} \to 0$ while $n_0 \to \infty$ the effective initial concentration $c_0 y_0 \to 0$, as there ultimately exists a surplus of binding sites, with which the drug may bind with high affinity. This can be seen from Figure 5.10.

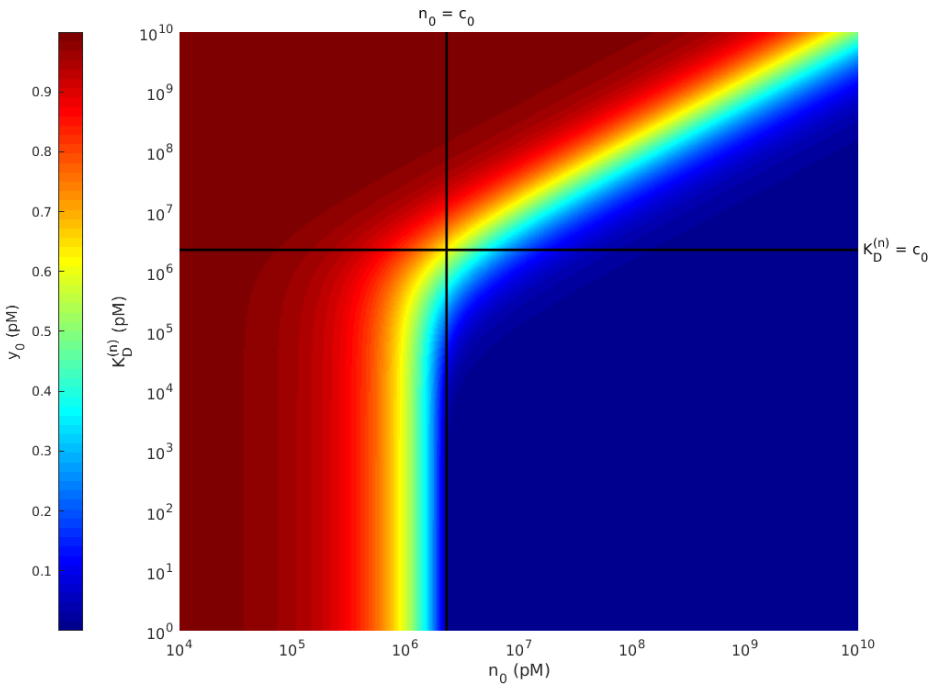

Figure 5.10: Plot of y_0 (Equation 5.40) for $K_{\mathrm{D}}^{(n)} \in [10^0, 10^{10}]$ and $n_0 \in [10^4, 10^{10}]$, for a dose of 0.5 mg.

As noted at the start of this chapter, the retinal impermeability study of Chapter 4 (Figure 4.14) demonstrated that without the ability of a drug (and drug-target complexes) to permeate into the retina, meaningful retinal free VEGF suppression is not achievable. Therefore if $y_0 \to 0$ then, although the total drug in the vitreous remains close to c_0 for a very long time relative to the non-vitreal binding drug, as it is bound to the vitreal superstructure it is trapped there, and hence unable to enter the retina.

Figure 5.1 suggests that there exists a 'sweet spot' in $\left(K_{\mathrm{D}}^{(n)}, n_0\right)$ parameter space, in which we see that even though initially the concentration of the drug is much lower than the equivalent non-vitreal binding molecule, over time it maintains a higher vitreal concentration as the $t_{1/2}$ of the drug has been substantially increased. In this scenario the $K_{\mathrm{D}}^{(n)}$ is large enough to allow for sufficient binding and unbinding of the drug between the vitreal superstructure, thereby maintaining a large concentration of freely diffusing drug in the vitreous, able to enter the retina. The concentration of freely diffusing drug required in the vitreous to adequately suppress free retinal VEGF is not well defined, and likely to vary between patients, however, for the purposes of this section we will estimate a likely minimum required concentration. Using this minimum required concentration we will analyse, using the model, the time taken for the concentration of free vitreal drug to reach this concentration, which we will define as the 'duration time' of the drug, or t_{dur}.

In this chapter we only consider the PK of an SVB molecule, therefore we will estimate the minimum concentration of free drug in the vitreous required in order to maintain adequate suppression of free VEGF in the retina, to match the expected concentration of ranibizumab post IVT injection, at which another injection is assumed to be required. Standard procedure is to inject 0.5 mg of ranibizumab every month [129], therefore assuming a vitreal volume of 4.5 ml, the initial concentration of ranibizumab is given by:

$$c_0^{(r)} \simeq 2.2981 \times 10^6 \text{ pM}. \tag{5.127}$$

Hence, the concentration $c^{(r)}(t)$, after time $t > 0$, assuming a half-life of $t_{1/2}^{(0)}$, is given by

$$c^{(r)}(t) = c_0^{(r)} e^{-t \log(2)/t_{1/2}^0}. \tag{5.128}$$

Taking $t_{1/2}^{(0)} = 7.04$ days (the estimated half-life for a Fab molecule given in Appendix A.6) and assuming the drug becomes ineffective after 30 days (as this is the point at which standard protocol would dictate another injection is required), the theoretical minimum

concentration required to suppress free retinal VEGF is given by $c_{30}^{(r)}$, as follows:

$$c_{30}^{(r)} \coloneqq c^{(r)}(30) \tag{5.129}$$

$$\simeq 1.1983 \times 10^5 \text{ pM}. \tag{5.130}$$

We will proceed using $c_{30}^{(r)}$ for the minimum concentration of free drug required in the vitreous, implicitly assuming the binding properties between bispecific SVB molecule and VEGF to match that of ranibizumab (this will be explored further in Chapter 6).

Therefore recalling the solution of the system, $t(c)$, given by Equation 5.76, we define the duration time of the system by:

$$t_{\text{dur}}(c_{30}^{(r)}; d_0, K_{\text{D}}^{(n)}, n_0) \coloneqq t(c_{30}^{(r)}), \tag{5.131}$$

which we will consider a function of $c_{30}^{(r)}$ as well as d_0, $K_{\text{D}}^{(n)}$, and n_0. This function can be seen plotted over $K_{\text{D}}^{(n)} \in [10^0, 10^{10}]$ and $n_0 \in [10^4, 10^{10}]$ for a dose of 0.5 mg in Figure 5.11. From the distribution of t_{dur} over $\left(K_{\text{D}}^{(n)}, n_0\right)$ parameter space in Figure 5.11 we can see resultant effect of the competing influences of of $t_{1/2}$ (Figure 5.8) and y_0 (Figure 5.10). Figure 5.8 demonstrated that the $t_{1/2}^{(\text{init})}$ of the system can be increased to extremely high levels in the region of $K_{\text{D}}^{(n)}, n_0$ parameter space where $n_0 > c_0$, however, Figure 5.10 demonstrated that in this region y_0 plunges to zero. If one was to consider Figures 5.9 and 5.10 side by side, one may intuitively guess that there exists a common region in $K_{\text{D}}^{(n)}, n_0$ parameter space, whereby $t_{1/2}^{(\text{init})}$ starts growing rapidly, but also where y_0 is transitioning from $1 \to 0$, and that in this region we may long vitreal retention times while a high proportion of the drug is maintain free to diffuse into the retina. Figure 5.11 demonstrates that this region exists as a 'hill' in $\left(K_{\text{D}}^{(n)}, n_0\right)$ parameter space, where $K_{\text{D}}^{(n)} \geq c_{30}^{(r)}$ and $n_0 > c_0$, where the duration time of the drug is maximised at ∼2-3 times greater than that of its non-vitreal binding counterpart. However, below this hill we see a swift drop to $t_{\text{dur}} = 0$, as in this region $c_0 y_0 < c_{30}^{(r)}$. The region where $n_0 < c_0$, wherein there exists optimal or stationary $t_{1/2}^{(0)}$ values, as shown in Figure 5.12, we see $t_{\text{dur}} < 30$ days for $K_{\text{D}}^{(n)} < c_{30}^{(r)}$, indicating that in this region the drug under-performs its non-vitreal binding counterpart. However in the region $K_{\text{D}}^{(n)} \in (c_{30}^{(r)}, c_0)$ we see the origin of the aforementioned 'hill' in $\left(K_{\text{D}}^{(n)}, n_0\right)$ parameter space, which, from Figure 5.12, can be seen to match the region in $\left(K_{\text{D}}^{(n)}, n_0\right)$ parameter space wherein $t_{1/2}^{(\text{init})}$ is optimised.

From Figure 5.11 we see that t_{dur} divides the $\left(K_{\text{D}}^{(n)}, n_0\right)$ parameter space into 3 regions, (1) $K_{\text{D}}^{(n)} \ll c_{30}^{(r)}$, (2) $K_{\text{D}}^{(n)} \in [c_{30}^{(r)}, c_0]$ and (3) $K_{\text{D}}^{(n)} \gg c_0$. In region (1) t_{dur} appears independent of $K_{\text{D}}^{(n)}$, and $t_{\text{dur}} \leq 30$ days - this region we will consider as the 'overly strong binding

region'. Equation 5.126, the logarithmically derived half-life, $t_{1/2}^{(\log)}$, predicts that in region (1), for $n_0 < c_0$, we expect to find that $t_{1/2} \sim t_{1/2}^{(0)}$. Region (2) appears to be a transitional region - here we find the region of parameter space that optimises $t_{1/2}^{(\text{init})}$ for $n_0 < c_0$ (the origin of the hill), as well as the lower region of the hill. Equation 5.126 predicts that in this region we should find non-exponential decay exhibited by the model, as $c_0 \sim K_{\text{D}}^{(n)}$. In region (3) we find the majority of the t_{dur} hill, where above and below the hill we find $t_{\text{dur}} = 30$ days and $t_{\text{dur}} = 0$, respectively. Additionally, Equation 5.126 predicts that in region (3) the half-life obtains its maximal value: $t_{1/2}^{(0)}(1 + K_{\text{D}}^{(n)}/n_0)$. In order to further analyse Equation 5.131 let us attempt to approximate the solution of the system, $t(c)$ (Equation 5.76), in regions (1) and (3) - by doing so, as $t_{\text{dur}} = t(c_{30}^{(r)})$, we will also generate approximations for t_{dur}.

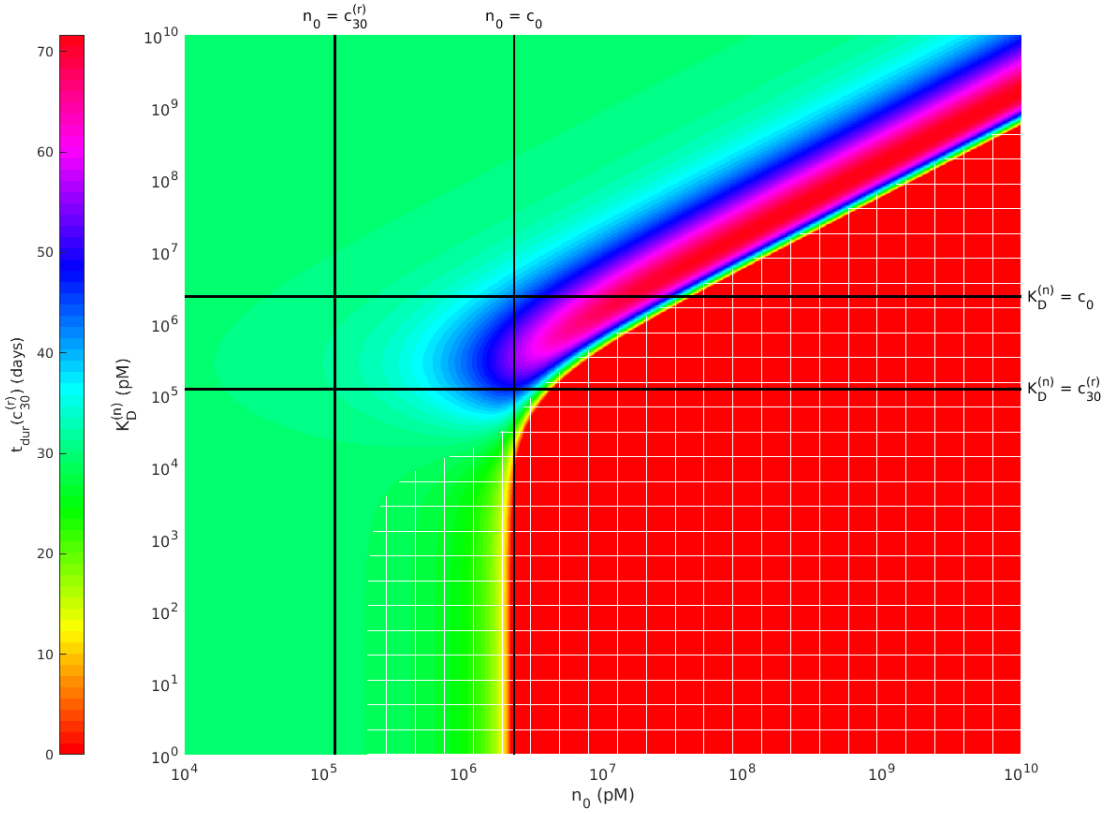

Figure 5.11: Equation 5.131, t_{dur}, plotted over $K_{\text{D}}^{(n)} \in [10^0, 10^{10}]$ and $n_0 \in [10^4, 10^{10}]$. The white mesh intersecting in the t_{dur} coloured surface is a x, y plane plotted at $z = 30$ days, representing the duration time of the non-vitreal binding drug. $t_{\text{dur}} < 30$ days in any region where the white mesh is visible.

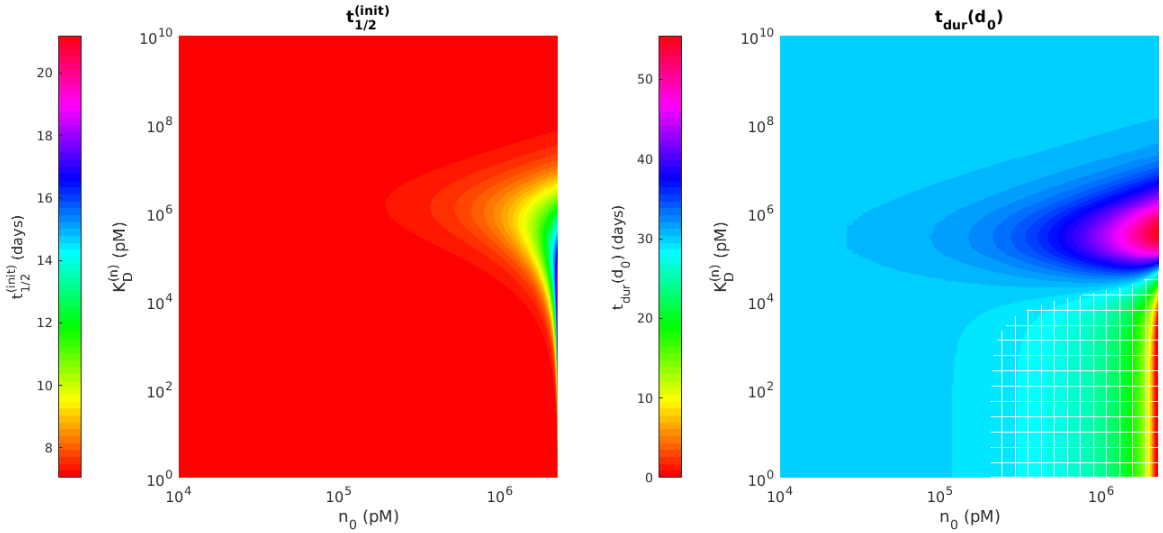

Figure 5.12: Equation 5.89, $t_{1/2}^{(\text{init})}$ and Equation 5.131, $t_{\text{dur}}(0.5; K_{\text{D}}^{(n)}, n_0)$, plotted over $K_{\text{D}}^{(n)} \in [10^0, 10^{10}]$ and $n_0 \in [10^4, c_0]$. $t_{\text{dur}} < 30$ days in any region where the white mesh is visible.

Region (3): $K_{\text{D}}^{(n)} \gg c_0$

We will first consider approximating $t(c)$ (in order to approximate t_{dur}) in region (3), as it is within this region of $\left(K_{\text{D}}^{(n)}, n_0\right)$ parameter space that t_{dur} obtains its maximal value. Let us define $\bar{\varepsilon} = c_0/K_{\text{D}}^{(n)}$ such that in region (3) we have $\bar{\varepsilon} \ll 1$; we may therefore rewrite y_0, Equation 5.40, by Taylor expansion, in the following way:

$$y_0 = \frac{1}{2}\left[\left\{1 - \frac{1}{\bar{\varepsilon}}\left(\frac{1+\beta}{\beta}\right)\right\} + \frac{1}{\bar{\varepsilon}}\sqrt{\left(\frac{1+\beta}{\beta}\right)^2 - 2\bar{\varepsilon}\left(\frac{1-\beta}{\beta}\right) + \bar{\varepsilon}^2}\right] \tag{5.132}$$

$$= \frac{1}{\frac{1}{\beta}+1} + O(\bar{\varepsilon}) \tag{5.133}$$

$$= \frac{1}{\left(\frac{n_0}{K_{\text{D}}^{(n)}}+1\right)}. \tag{5.134}$$

Therefore we may substitute this expression for y_0 into $t(c)$, Equation 5.76, giving:

$$\frac{\log(2)}{t_{1/2}^0}t(c) = \log\left(\frac{1}{1+\frac{1}{\beta}}\right) + \frac{1}{\beta}\left[\underbrace{\frac{\left(\frac{\beta}{1+\beta}\right)}{\bar{\varepsilon}+\left(\frac{\beta}{1+\beta}\right)}}_{\simeq 1} - \underbrace{\frac{1}{\bar{\varepsilon}+1}}_{\simeq 1} + \log\left(\frac{c_0}{c}\underbrace{\left\{\frac{\bar{\varepsilon}+1}{\bar{\varepsilon}+\left(1+\frac{1}{\beta}\right)}\right\}}_{\simeq 1/(1+1/\beta)}\right)\right], \tag{5.135}$$

therefore we find, in dimensional terms, that:

$$\frac{\log(2)}{t_{1/2}^0}t(c) \simeq \left(1+\frac{n_0}{K_{\text{D}}^{(n)}}\right)\log\left(\frac{c_0}{c}\left\{\frac{1}{1+\frac{n_0}{K_{\text{D}}^{(n)}}}\right\}\right), \tag{5.136}$$

where, similarly to region (1), we have used the fact that if $c_0 \ll K_{\mathrm{D}}^{(n)}$ then it implies that $c \ll K_{\mathrm{D}}^{(n)}$, $\forall t > 0$, and hence have taken $c \sim c_0$. Using this equation we may also then write the solution for $c(t)$, as given by the following equation:

$$c(t) \simeq \frac{c_0}{\left(\frac{n_0}{K_{\mathrm{D}}^{(n)}} + 1\right)} \exp\left\{ -\frac{\log(2)}{t_{1/2}^{(0)}\left(\frac{n_0}{K_{\mathrm{D}}^{(n)}} + 1\right)} t \right\}. \tag{5.137}$$

Equation 5.137 demonstrates that in region (3) the half-life of the model has achieved the maximal value of $t_{1/2}^{(0)}\left(n_0/K_{\mathrm{D}}^{(n)} + 1\right)$, and the effective initial concentration is inversely proportional to $\left(n_0/K_{\mathrm{D}}^{(n)} + 1\right)$. Notice that this implies that, in this region of $\left(K_{\mathrm{D}}^{(n)}, n_0\right)$ parameter space, the SVB model initially under-performs the non-vitreal binding model, however given the increased $t_{1/2}$ in the SVB system, at some later point, defined to be $t_\star$, it overtakes the non-vitreal binding model. This behaviour can be seen in Figure 5.1 plot (d). We can solve for $t_\star$, giving:

$$t_\star = \frac{t_{1/2}^{(0)}}{\log 2}\left(\frac{K_{\mathrm{D}}^{(n)}}{n_0} + 1\right)\log\left(\frac{n_0}{K_{\mathrm{D}}^{(n)}} + 1\right), \tag{5.138}$$

which we notice is proportional to $\left(K_{\mathrm{D}}^{(n)}/n_0 + 1\right)$, as would be expected based on y_0.

Returning to our analysis of t_{dur}, we note that numerically it appears that the hill in Figure 5.11 lies parallel (in log-log space) to $K_{\mathrm{D}}^{(n)} = n_0$, in $\left(K_{\mathrm{D}}^{(n)}, n_0\right)$ parameter space. This hypothesis also suggested by the $t_{1/2}$ analysis of the Section 5.1.2 that demonstrated $t_{1/2}^{(\mathrm{init})}$ is maximised by minimising the ratio $K_{\mathrm{D}}^{(n)}/n_0$. We also note that Equation 5.136 is, other than c_0, dependant only on the ratio of n_0 and $K_{\mathrm{D}}^{(n)}$. Therefore to analyse this hypothesis we proceed to consider stationary points of Equation 5.136 with respect to to β, as follows:

$$\frac{\partial t\,(c)}{\partial \beta} = 0 \quad \Leftrightarrow \quad \log\left(\frac{c_0}{c}\left\{\frac{1}{1+\frac{1}{\beta}}\right\}\right) = 1 \tag{5.139}$$

$$\Rightarrow \quad \beta = \frac{\mathrm{e}}{c_0/c - \mathrm{e}} \tag{5.140}$$

$$\Rightarrow \quad \frac{K_{\mathrm{D}}^{(n)}}{n_0} = \left(\frac{\mathrm{e}}{c_0/c - \mathrm{e}}\right), \tag{5.141}$$

demonstrating that $t(c)$ is maximised for a specific ratio of $K_{\mathrm{D}}^{(n)}$ and n_0, noting that we have numerically demonstrated the existence of a maximum for $t(c)$ in $\left(K_{\mathrm{D}}^{(n)}, n_0\right)$ parameter space, and hence know this represents a maximal value for $t(c)$. Additionally, we note this expression is always greater than zero, as $\min\{c_0/c\} = c_0/c(0) = 1/y_0 = n_0/K_{\mathrm{D}}^{(n)} \gg 1$,

hence, $c_0/c - \mathrm{e} > 0 \; \forall t > 0$. Therefore, given Equation 5.141, if $K_{\mathrm{D}}^{(n)} \gg c_0$ then the ratio of $K_{\mathrm{D}}^{(n)}$ and n_0 that maximises $t_{\mathrm{dur}}\left(c_{30}^{(r)}\right)$ is given by:

$$\Theta(c_0) \coloneqq \frac{\mathrm{e}}{c_0/c_{30}^{(r)} - \mathrm{e}}, \tag{5.142}$$

which we define as $\Theta(c_0)$. For a dose of 0.5 mg, $\Theta(c_0) \sim 0.17$, indicating it is ideal to have a $K_{\mathrm{D}}^{(n)}$ roughly an order of magnitude less than n_0. We also note here that the stationary values for $t_{1/2}^{(\mathrm{init})}$, for $c_0 < n_0$, were found with respect to β, indicating that they lie parallel to the hill in parameter space, and hence that they represent the origin of the hill in the transitional region in region (2). The line $K_{\mathrm{D}}^{(n)} = \Theta(c_0)n_0$, as shown in Figure 5.13, verifies that Equation 5.142 gives the optimal $K_{\mathrm{D}}^{(n)}$, n_0 ratio, explicitly giving us the $\left(K_{\mathrm{D}}^{(n)}, n_0\right)$ coordinates lying atop the hill in $\left(K_{\mathrm{D}}^{(n)}, n_0\right)$ parameter space.

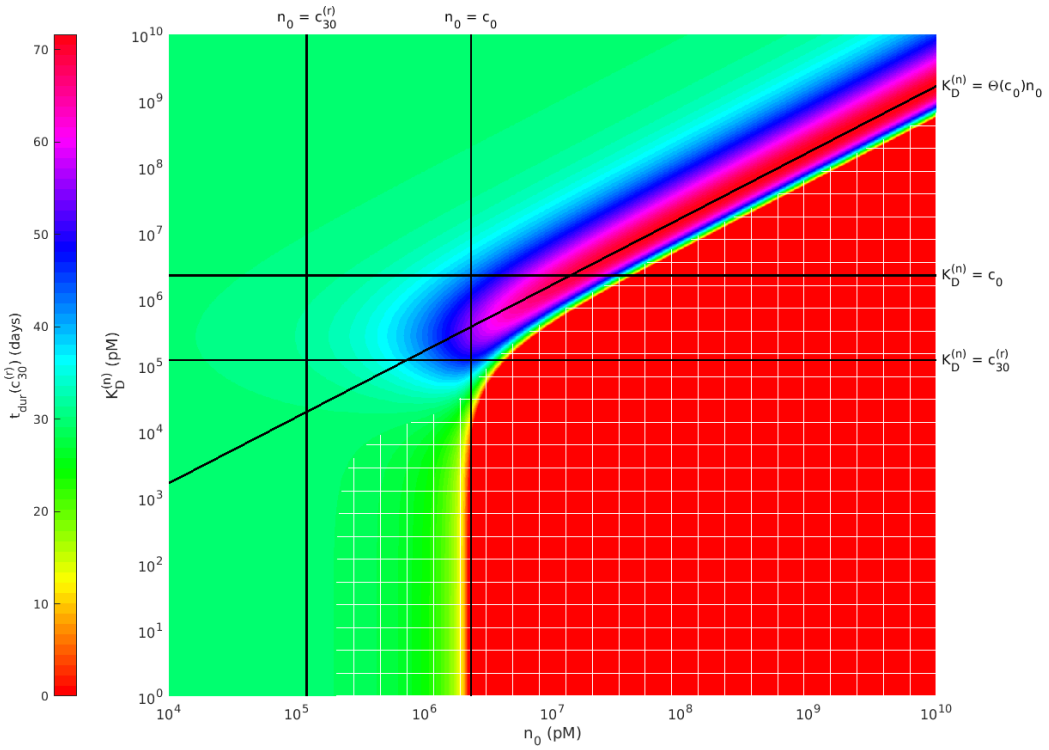

Figure 5.13: $t_{\mathrm{dur}}(c_{30}^{(r)})$ (Equation 5.131) plotted over $K_{\mathrm{D}}^{(n)} \in [10^0, 10^{10}]$ and $n_0 \in [10^4, 10^{10}]$, as in Figure 5.11, including the line $K_{\mathrm{D}}^{(n)} = \Theta(c_0)n_0$, as given by Equation 5.142, for a dose of 0.5 mg.

Region (1): $K_{\mathrm{D}}^{(n)} \ll c_0$

Let us define $\bar{\varepsilon} = K_{\mathrm{D}}^{(n)}/c_0$ and assume that $\bar{\varepsilon} \ll 1$, therefore we may rewrite y_0, Equa-

tion 5.40, in the following way:

$$y_0 = \frac{1}{2}\left[1 - \bar{\varepsilon}\left(\left(\frac{1}{\beta}\right)+1\right) + \left\{1 - \bar{\varepsilon}\left(\left(\frac{1}{\beta}\right)-1\right)\right\}\sqrt{1 + \frac{4\left(\frac{1}{\beta}\right)\bar{\varepsilon}^2}{\{1 - \bar{\varepsilon}\left(\left(\frac{1}{\beta}\right)-1\right)\}^2}}\right] \tag{5.143}$$

$$\simeq \frac{1}{2}\left[1 - \bar{\varepsilon}\left(\left(\frac{1}{\beta}\right)+1\right) + 1 - \bar{\varepsilon}\left(\left(\frac{1}{\beta}\right)-1\right) + \frac{2\left(\frac{1}{\beta}\right)\bar{\varepsilon}^2}{1 - \bar{\varepsilon}\left(\left(\frac{1}{\beta}\right)-1\right)}\right] \tag{5.144}$$

$$\simeq 1 - \bar{\varepsilon}\left(\frac{1}{\beta}\right) + O(\bar{\varepsilon}^2), \tag{5.145}$$

where we recall that $\beta = K_{\mathrm{D}}^{(n)}/n_0$. We then substitute this expression for y_0 into $t(c)$, Equation 5.76, giving:

$$\frac{\log(2)}{t_{1/2}^0} t(c) \simeq -\log\left(\frac{c}{c_0(1-\bar{\varepsilon}/\beta)}\right) + \frac{1}{\beta}\left[-\frac{K_{\mathrm{D}}^{(n)}}{c + K_{\mathrm{D}}^{(n)}} - \log\left(\frac{c}{c + K_{\mathrm{D}}^{(n)}}\right)\right]. \tag{5.146}$$

Under our assumption that $\bar{\varepsilon} \ll 1$, as $c(0) = c_0$ then for suitably small time $K_{\mathrm{D}}^{(n)} \ll c(t)$, also. Therefore we may write:

$$\frac{\log(2)}{t_{1/2}^0} t(c) \simeq -\log\left(\frac{c}{c_0(1-\bar{\varepsilon}/\beta)}\right). \tag{5.147}$$

To summarise we may approximate y_0 by the following:

$$y_0 = 1 - \frac{n_0}{c_0}, \tag{5.148}$$

$t(c)$ as

$$t(c) \simeq \frac{t_{1/2}^0}{\log(2)} \log\left(\frac{c_0 - n_0}{c}\right), \tag{5.149}$$

and by inverting $t(c)$ we may write $c(t)$ as:

$$c(t) \simeq c_0\left(1 - \frac{n_0}{c_0}\right)\exp\left\{-\frac{\log(2)}{t_{1/2}^0} t\right\}. \tag{5.150}$$

Equation 5.150 demonstrates that in this region, as predicted numerically by Figure 5.1 plot (b) and analytically by Equation 5.126, we see exponential decay with half-life $t_{1/2}^{(0)}$. In region (1) for $n < c_{30}^{(r)}$ in Figure 5.11 we see the SVB model approximately match the non-vitreal binding model, this can be understood from Equation 5.150 as here $\frac{n_0}{c_0} \ll 1$.

As noted above, Equations 5.149 and 5.150 only hold for $t > 0$ such that $K_{\mathrm{D}}^{(n)} \ll c(t)$, in addition to $K_{\mathrm{D}}^{(n)} \ll c_0$.

Composite approximations and error for t_{dur} in regions (1) and (3)

We have now derived approximations for t_{dur}, based on the relative magnitudes of $K_{\text{D}}^{(n)}$ and n_0, for regions (1) and (3), given by Equations 5.149 and 5.136, respectively. Figure 5.14 shows Equations 5.149 and 5.136 evaluated over $K_{\text{D}}^{(n)} \in [10^0, 10^{10}]$ and $n_0 \in [10^4, 10^{10}]$ and Figure 5.15 depicts the relative errors of both functions with respect to the exact function for t_{dur}, as given by Equation 5.131. We can see that the approximations of t_{dur} for $K_{\text{D}}^{(n)} \ll c_0$ and $K_{\text{D}}^{(n)} \gg c_0$ are approximately exact within their respective regions of $\left(K_{\text{D}}^{(n)}, n_0\right)$ parameter space. This motivates a non-continuous composite approximate solution for t_{dur}, where t_{dur} is defined by Equation 5.149 for $K_{\text{D}}^{(n)} > c_{30}^{(r)}$ and 5.136 $K_{\text{D}}^{(n)} \leq c_{30}^{(r)}$, shown in Figure 5.16, alongside its error. Figure 5.16 demonstrates that the approximations for t_{dur} in regions (1) and (3), as well as y_0 and $c(t)$ are generally highly accurate over $\left(K_{\text{D}}^{(n)}, n_0\right)$ parameter space, aside from the transitional region (2) where $K_{\text{D}}^{(n)} \in [c_{30}^{(r)}, c_0]$, and non-exponential decay is observed.

This concludes our analysis on the duration time of the SVB molecule. Within this section we have demonstrated the impact of $K_{\text{D}}^{(n)}$ and n_0 on the persistence of freely diffusing vitreal drug. We have shown the ratio of these values, alongside their relative magnitudes to c_0 and $c_{30}^{(r)}$ determine the duration of time the concentration of free drug remains at theoretically efficacious levels. The interplay between the effect of these parameters on determining the effective initial concentration ($c_0 y_0$) and extending the ocular half-life have been shown to be cross purposes, e.g. increasing the ocular half-life, generally, decreases the quantity of freely diffusing drug available in the vitreous. We theorised and demonstrated the existence of a region of $\left(K_{\text{D}}^{(n)}, n_0\right)$ parameter space wherein t_{dur} is optimised, showing that this region is defined for $n_0 > c_0$ and for the ratio of $K_{\text{D}}^{(n)}$ and n_0 to be approximately 0.2.

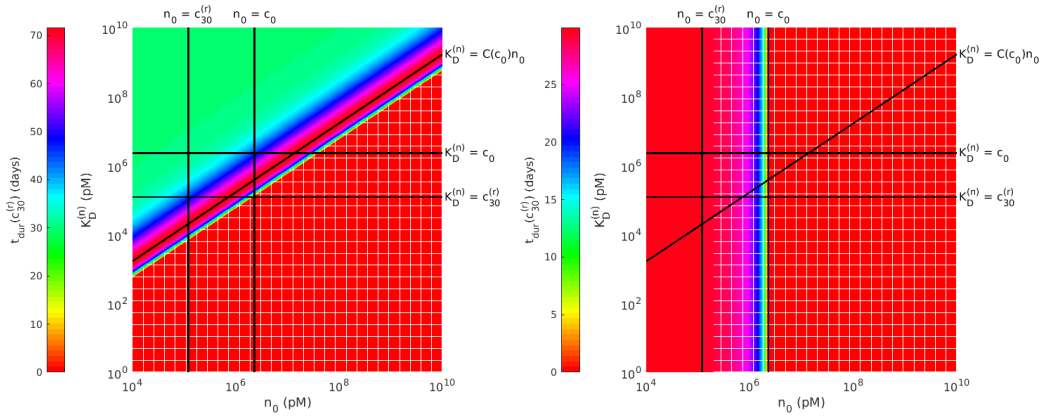

Figure 5.14: t_{dur}, as approximated by Equations 5.149 (region (1), right) and 5.136 (region (3), left) evaluated over $K_{\text{D}}^{(n)} \in [10^0, 10^{10}]$ and $n_0 \in [10^4, 10^{10}]$.

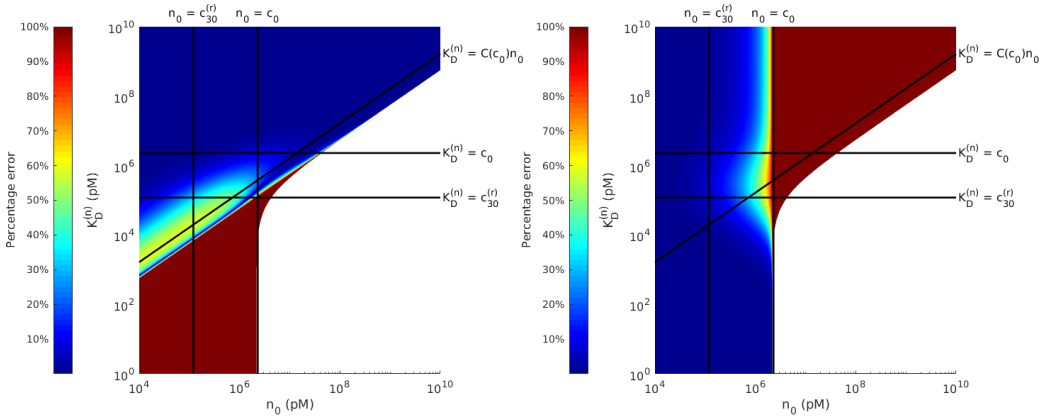

Figure 5.15: The relative error between the exact expression for t_{dur}, given by Equation 5.131, and t_{dur} as approximated by Equations 5.149 (region (1), right) and 5.136 (region (3), left) evaluated over $K_{\text{D}}^{(n)} \in [10^0, 10^{10}]$ and $n_0 \in [10^4, 10^{10}]$.

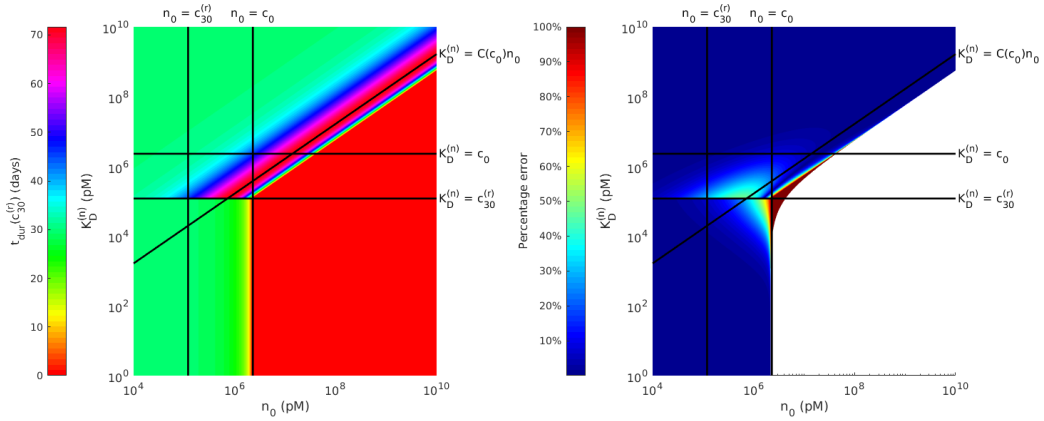

Figure 5.16: Composite definition t_{dur}, defined by Equation 5.149 for $K_{\text{D}}^{(n)} > c_{30}^{(r)}$ and 5.136 $K_{\text{D}}^{(n)} \leq c_{30}^{(r)}$.

5.1.4 Repeat dosage analysis

Within this section we explore the effect of repeat dosing on drug retention in the vitreous. As the total number of binding sites remains constant between injections it is possible that over time the PK in the system could behave differently depending on the quantity and dosage of previous injections, relative to a treatment naive eye. It may be the case that drug accumulates bound to vitreal binding sites between injections - if that is the case, then dosage protocols have the potential to be optimised to maximise the time vitreal concentration of free drug remains above $c_{30}^{(r)}$.

We will consider how the position in $\left(K_{\mathrm{D}}^{(n)}, n_0\right)$ parameter space affects the behaviour of the model solution; over the course of multiple doses which regions have the potential to be exploited to increase drug retention, and whether the available free drug in regions where $t_{\mathrm{dur}} < 30$ days can be increased by accumulating drug bound to binding sites over time. In addition we will also explore whether, and to what degree, an initial bolus injection (a super-high initial dose) could aid in prolonging drug retention. The $K_{\mathrm{D}}^{(n)}$ and n_0 values analysed in the following 13 plots are shown in Figure 5.17, depicted in the context of $t_{\mathrm{dur}}(c_{30}^{(r)})$. All standard doses (non-loading doses) are taken to be 0.5 mg, and all doses are administered every 60 days. The concentration of free vitreal drug in the SVB PK model will be shown in each plot alongside the concentration of vitreal drug in the non-vitreal binding PK model (Chapter 3 Section 3.1), to demonstrate PK alteration due to addition of vitreal binding.

In Figures 5.18 and 5.19, we see the model evaluated for multiple doses for $n_0 = 1 \times 10^7$ pM and $K_{\mathrm{D}}^{(n)} = 1 \times 10^1$ pM, i.e. in the red zone of Figure 5.17, where $t_{\mathrm{dur}} = 0$. In this region of $\left(K_{\mathrm{D}}^{(n)}, n_0\right)$ parameter space we have very extensive binding and a large quantity of available binding sites. Due to this, post IVT injection, all drug is immediately bound and remains bound. For every subsequent dose the number of unoccupied binding sites in the vitreous reduces by the equivalent number of drug molecules injected, until, at around 250 days (or the 5th injection), all binding sites are occupied - at which point all excess drug is free and decays with half-life $t_{1/2}^{(0)}$. We can see that after the 6th injection the SVB model starts to match the non-vitreal binding model (dashed and solid lines overlap). Figure 5.19 demonstrates that by using a loading dose of 2 mg it is possible to more quickly occupy all vitreal binding sites, but due to the strength of the binding there is little exchange between bound and unbound drug, causing the concentration of free drug molecules to decay at the same rate as in the non-vitreal binding model. This demonstrates that molecules that lie in this region of parameter space will always under-perform, or equal the performance of their

non-vitreal binding equivalents. Figure 5.20 strengthens this hypothesis, showing the model solved using the same parameters as in Figures 5.18 and 5.19, with a value of n_0 10 times higher. In this scenario we see it takes 10 times as long to saturate all the binding sites, and for the SVB molecule to equal the performance of the non-vitreal binding molecule.

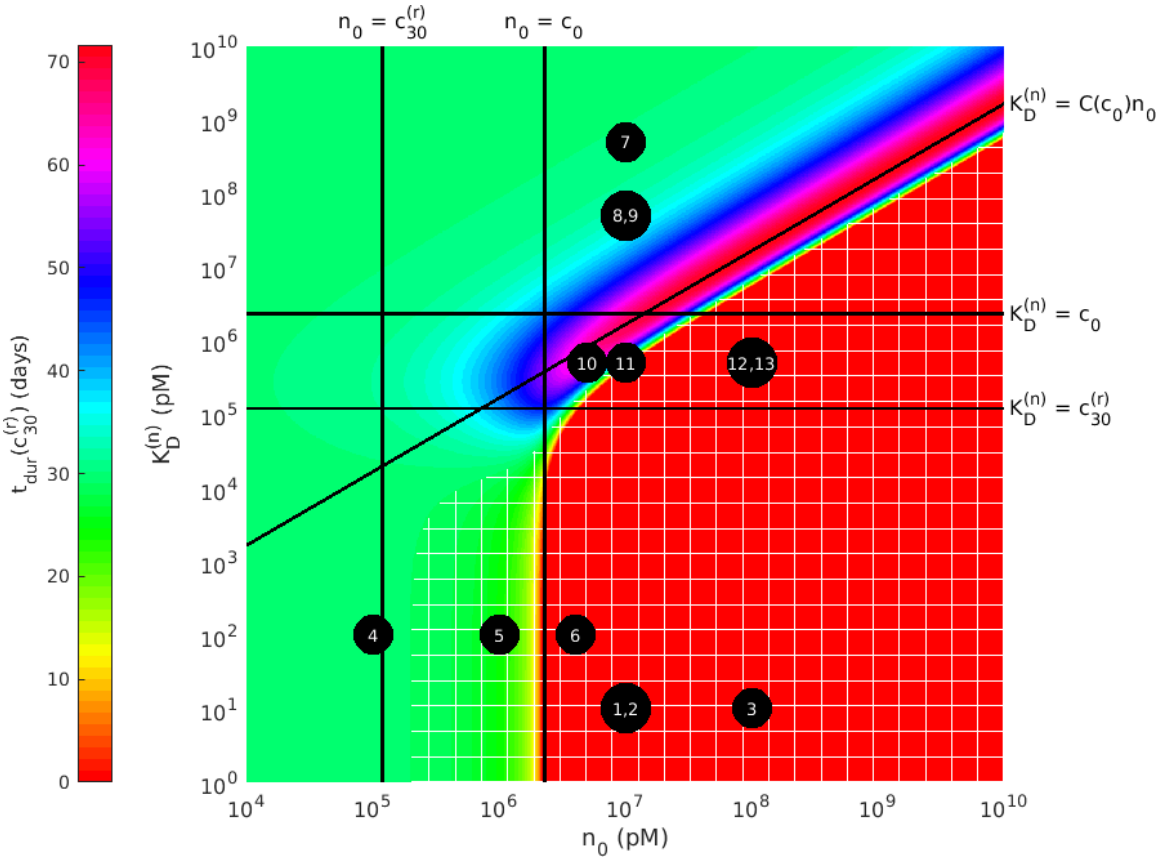

Figure 5.17: $\left(K_{\mathrm{D}}^{(n)}, n_0\right)$ parameter space map for Figures 5.18-5.30. Identical to Figure 5.11 ($t_{\mathrm{dur}}(c_{30}^{(r)})$ evaluated for a dose of 0.5 mg), with the addition of labels, (i), denoting the $K_{\mathrm{D}}^{(n)}$, n_0 parameter values for Figures 5.18-5.30.

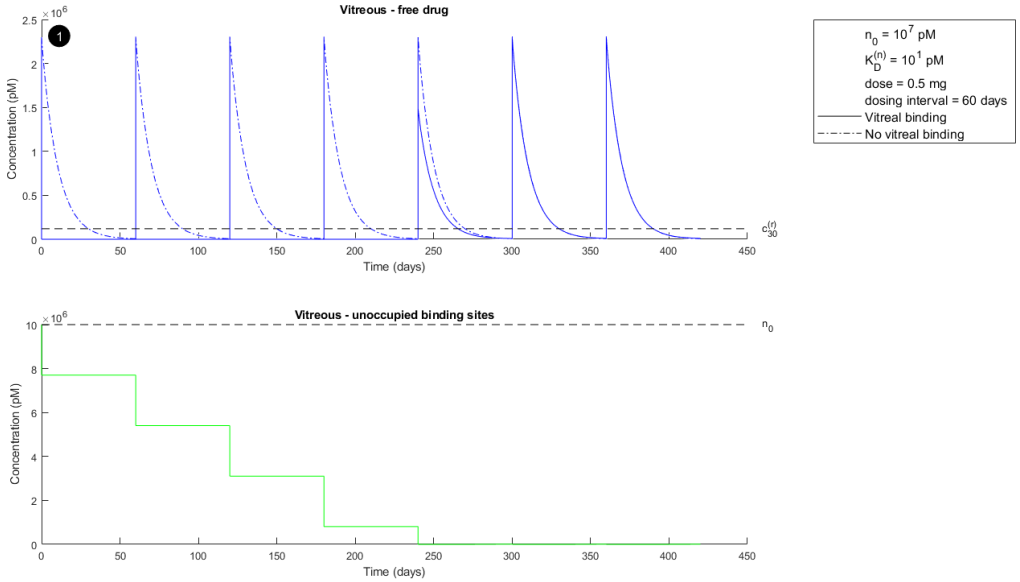

Figure 5.18: Multiple dosing solution for the SVB model, where $K_{\mathrm{D}}^{(n)} = 10^1$ pM, $n_0 = 10^7$ pM. Dosage protocol can be found in the figure legend. Near perfect capture of drug by vitreal binding sites resulting in either no free drug, or free drug decaying with half-life $t_{1/2}^{(0)}$.

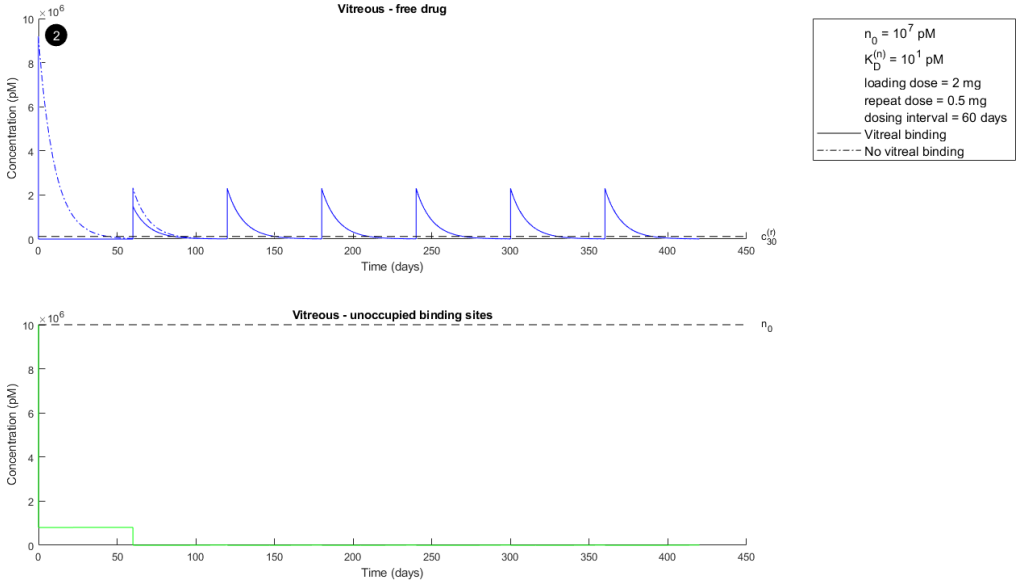

Figure 5.19: Multiple dosing solution for the SVB model, where $K_{\mathrm{D}}^{(n)} = 10^1$ pM, $n_0 = 10^7$ pM. Dosage protocol can be found in the figure legend. Near perfect capture of drug by vitreal binding sites resulting in either no free drug, or free drug decaying with half-life $t_{1/2}^{(0)}$. The loading dose proves to be an ineffective measure to increase persistence of free vitreal drug.

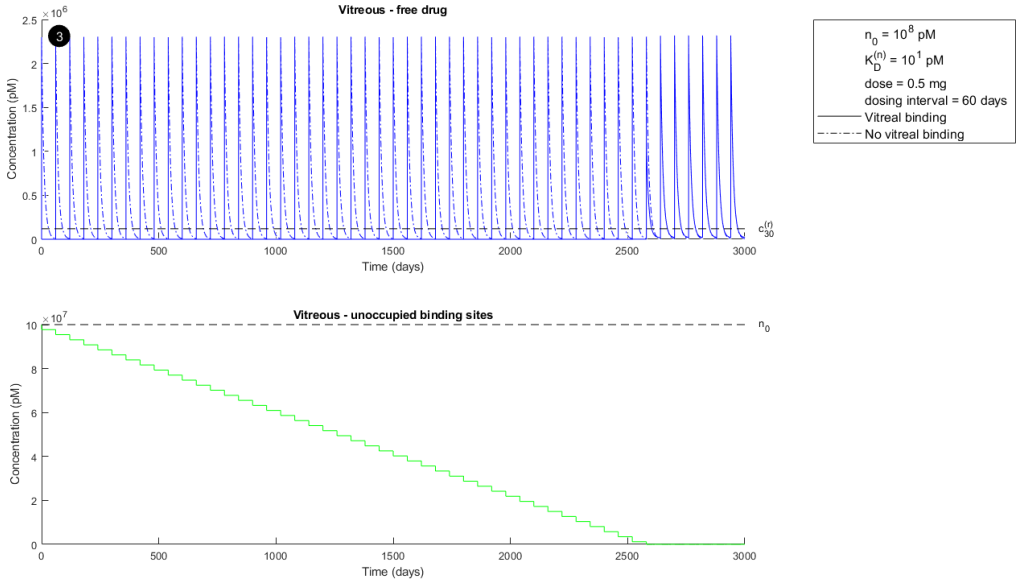

Figure 5.20: Multiple dosing solution for the SVB model, where $K_{\mathrm{D}}^{(n)} = 10^1$ pM, $n_0 = 10^8$ pM. Dosage protocol can be found in the figure legend. Similar to Figures 5.18 and 5.19, however the increased quantity of vitreal binding sites increases the time time required for the concentration of free vitreal binder to match those of the non-vitreal binding molecule.

Figures 5.21-5.23 are all solved for $K_{\mathrm{D}}^{(n)} = 10^2$ pM, for various n_0 values. In Figure 5.21, for $n_0 = 10^5 < c_{30}^{(r)}$ pM, we see almost no difference between the SVB model and the non-vitreal binding model - not surprising given that t_{dur} at this point is 30 days. As we increase the value of n_0 to 4×10^6 pM (Figure 5.23), we notice y_0 has decreased from approximately 1 and that for small concentrations of c the $t_{1/2}$ of the system increases. Repeat dosages improve the performance of the SVB molecule relative to the non-vitreal binding molecule, however these improvements are very minor and do not increase t_{dur} past the first injection. Increasing n_0 to 10^6, past c_0 (Figure 5.23), we see a return to the step-function-like behaviour of Figures 5.18-5.20, as in this region of parameter space there exist sufficient vitreal binding sites to completely bind all injected drug. Here we see that given multiple doses, all unoccupied vitreal binding sites are eventually able to be bound, and the molecule returns to decaying at a similar half-life to that of the non-vitreal binding molecule.

In Figures 5.18-5.23 we have detailed the characteristic behaviour of the model when $K_{\mathrm{D}}^{(n)} < c_{30}^{(r)}$ and c_0, and that the persistence of free drug molecules in the vitreous is consistently lower or equal to that of the non-vitreal binding molecules. This indicates in this region of parameter space, due to the tight binding between the molecule and the vitreal binding sites, all SVB molecules will under-perform their classic non-vitreal binding counterparts. Note, that these results are reinforced by the approximations made for t_{dur} and $c(t)$, given by Equations 5.149 and 5.150, respectively.

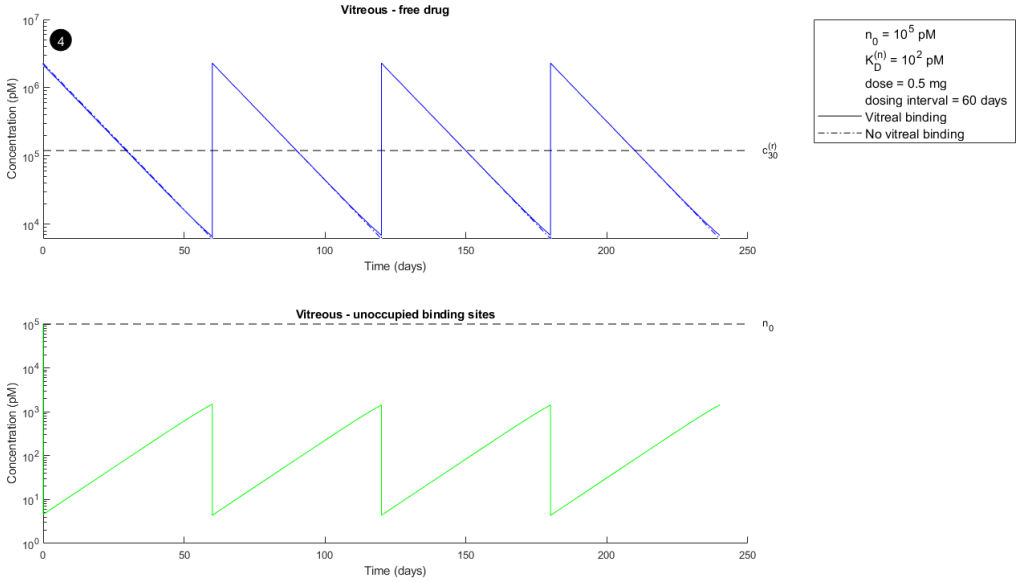

Figure 5.21: Multiple dosing solution for the SVB model, where $K_{\mathrm{D}}^{(n)} = 10^2$ pM, $n_0 = 10^5$ pM. Dosage protocol can be found in the figure legend. We see that there is approximately no difference between the vitreal and non-vitreal binding model solutions for the concentration of free vitreal drug.

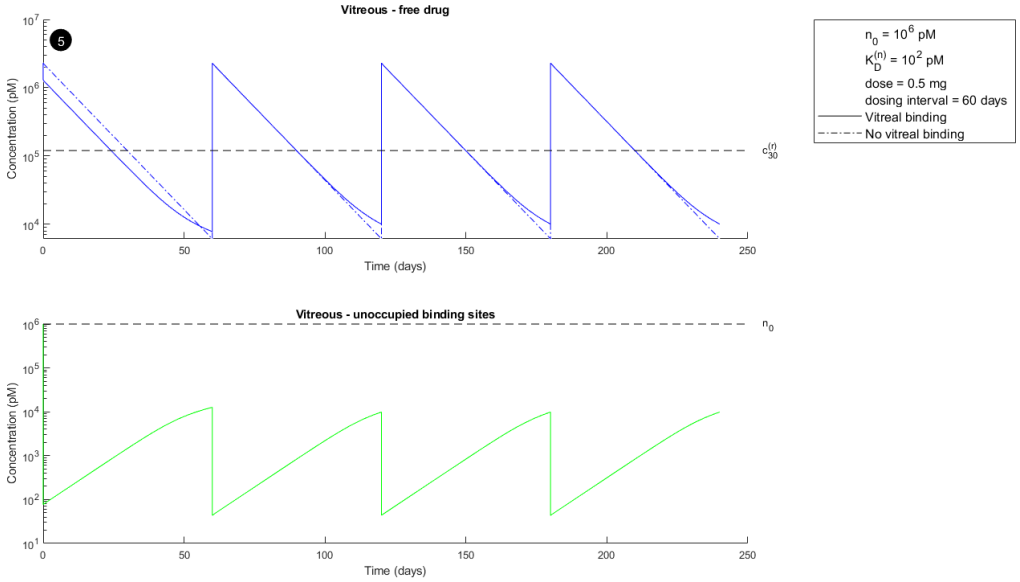

Figure 5.22: Multiple dosing solution for the SVB model, where $K_{\mathrm{D}}^{(n)} = 10^2$ pM, $n_0 = 10^6$ pM. Dosage protocol can be found in the figure legend. The vitreal and non-vitreal model solutions for free vitreal drug both decay at the same rate, however between 1st and 2nd dose there exist less available vitreal binding drug, due to the decreased value of y_0 from 1.

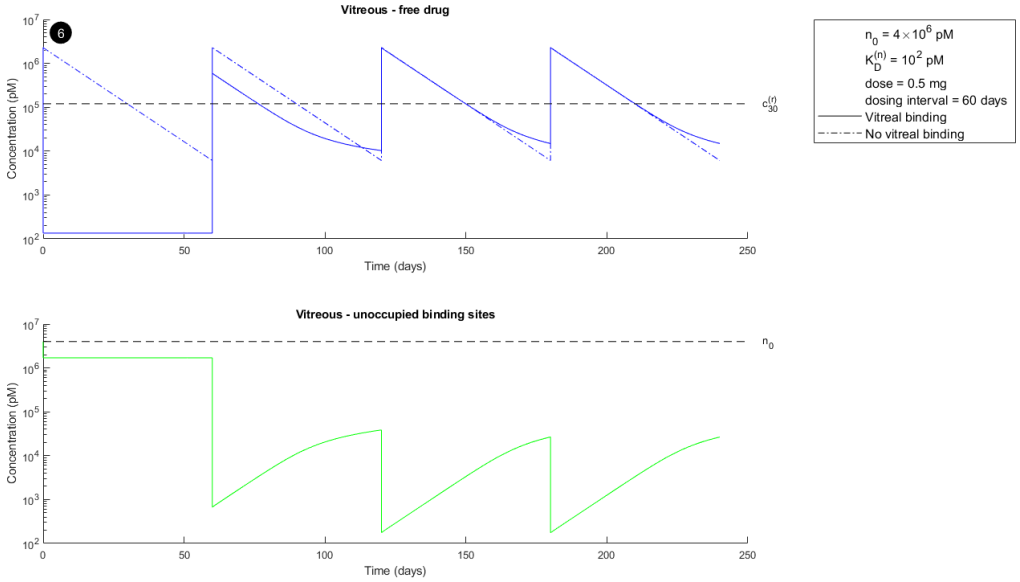

Figure 5.23: Multiple dosing solution for the SVB model, where $K_{\mathrm{D}}^{(n)} = 10^2$ pM, $n_0 = 4 \times 10^6$ pM. Dosage protocol can be found in the figure legend. Initially all vitreal binders are captured by the vitreal binding sites, until binding site saturation is reached, at this point the concentration profiles behave analogously to those in Figures 5.21 and 5.22.

We will next discuss Figures 5.24-5.30 which detail the behaviour of the model, subject to repeat dosing, for $K_{\mathrm{D}}^{(n)} > c_{30}^{(r)}$, i.e. above and on the hill in $\left(K_{\mathrm{D}}^{(n)}, n_0\right)$ parameter space. Figures 5.24-5.25 demonstrate that as the ratio of $K_{\mathrm{D}}^{(n)}$ to n_0 is lowered, the values of y_0 and $t_{1/2}$ decrease and increase, respectively. This behaviour is in accordance with the predictions drawn from the approximations of t_{dur} and $c(t)$ in region (3), given by Equations 5.136 and 5.137, respectively. We notice that as we move closer to the hill in $\left(K_{\mathrm{D}}^{(n)}, n_0\right)$ parameter space the concentration profile of the free drug molecules in the SVB model rises above that of the non-vitreal binding model, and hence outperforms it. It is important to note here that the behaviour of the model is not affected by multiple doses, indicating that the response to treatment would likely remain consistent over time. Figure 5.26 investigates the same scenario as in Figure 5.25, however, with the addition of a loading dose of 10 mg. Here we see that the loading dose has little effect after the second injection, and hence does not appear to be a viable strategy for increasing the persistence of free drug concentration levels.

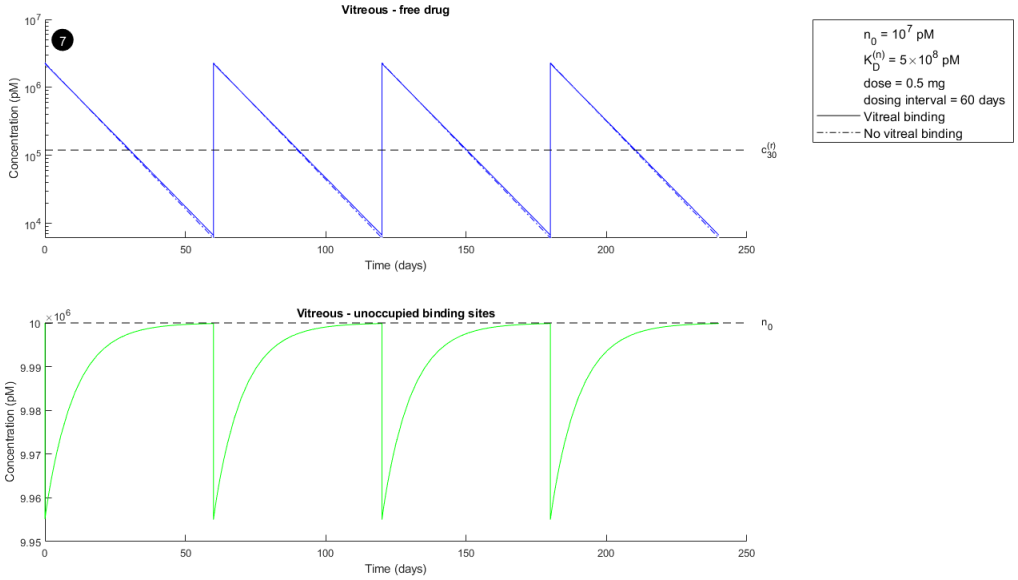

Figure 5.24: Multiple dosing solution for the SVB model, where $K_{\mathrm{D}}^{(n)} = 5 \times 10^8$ pM, $n_0 = 10^7$ pM. Dosage protocol can be found in the figure legend. We see that there is approximately no difference between the vitreal and non-vitreal binding model solutions for the concentration of free vitreal drug.

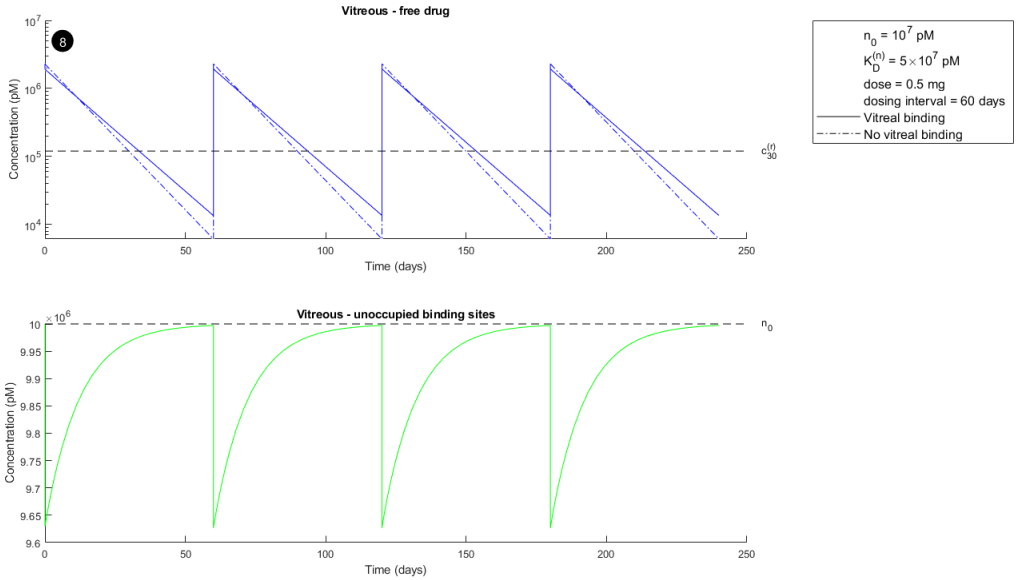

Figure 5.25: Multiple dosing solution for the SVB model, where $K_{\mathrm{D}}^{(n)} = 5 \times 10^7$ pM, $n_0 = 10^7$ pM. Dosage protocol can be found in the figure legend. We see an increased half-life exhibited by the vitreal binding model.

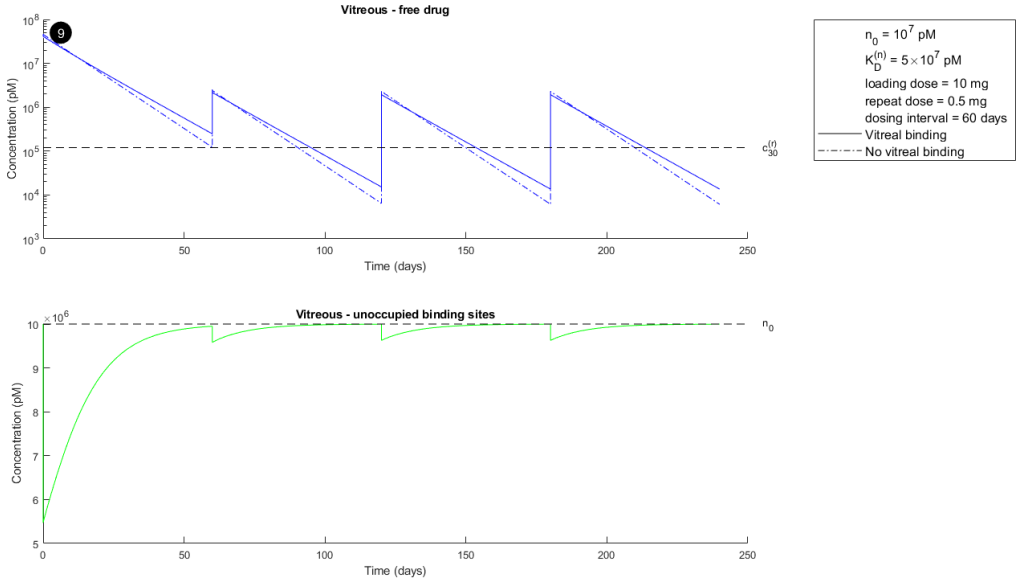

Figure 5.26: Multiple dosing solution for the vitreal binding model, where $K_{\mathrm{D}}^{(n)} = 5 \times 10^7$ pM, $n_0 = 10^7$ pM. Dosage protocol can be found in the figure legend. The loading dose is found to not produce any lasting increase in drug concentration.

Figures 5.27-5.30 consider the region of $\left(K_{\mathrm{D}}^{(n)}, n_0\right)$ parameter space on or near the hill. Figure 5.27 shows the model solutions for values of $K_{\mathrm{D}}^{(n)}$ and n_0 very close to the optimal ratio predicted by Equation 5.142. Here we see that the free concentration of the drug remains above $c_{30}^{(r)}$ for over 60 days, and is retained for longer than 60 days from the 2nd injection onwards. In this parameter regime we see a much longer $t_{1/2}$ relative to the non-vitreal binding molecule, which more than compensates for the decrease in initial effective concentration from c_0. If these parameter values were achievable this molecule would likely be twice or more effective than its classical counterpart. Figure 5.28 shows the model solved using the same value of $K_{\mathrm{D}}^{(n)}$, however with n_0 twice as high. This region in parameter space represents the steep drop off the hill in Figure 5.17 into the red zone. From the resultant decay after the first injection we see that, although the drug decays with a very large half-life, the decrease in y_0 causes t_{dur} to drop to roughly 30 days - the same as the non-vitreous binding molecule. It is important to note here that $c_{30}^{(r)}$ is only a rough estimate for the minimum required free drug concentration in the vitreous, and the solution here vastly outperforms the non-vitreal binding model at retaining concentrations of free drug lower than $c_{30}^{(r)}$. From the 2nd dose onwards we see a great improvement in the persistence of vitreal free drug concentration, as over time each subsequent dose further saturates the number of available binding sites, effectively reducing the instantaneous value of n_0, bringing the behaviour of the model back to that shown in Figure 5.27.

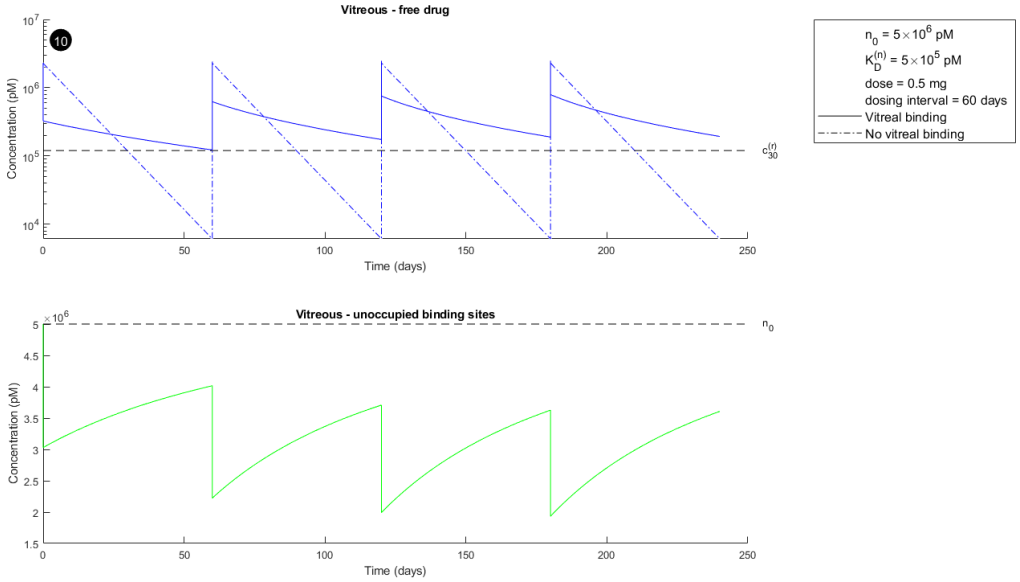

Figure 5.27: Multiple dosing solution for the SVB model, where $K_{\mathrm{D}}^{(n)} = 5 \times 10^5$ pM, $n_0 = 5 \times 10^6$ pM. Dosage protocol can be found in the figure legend. We see a greatly increased persistence of freely diffusing vitreal drug.

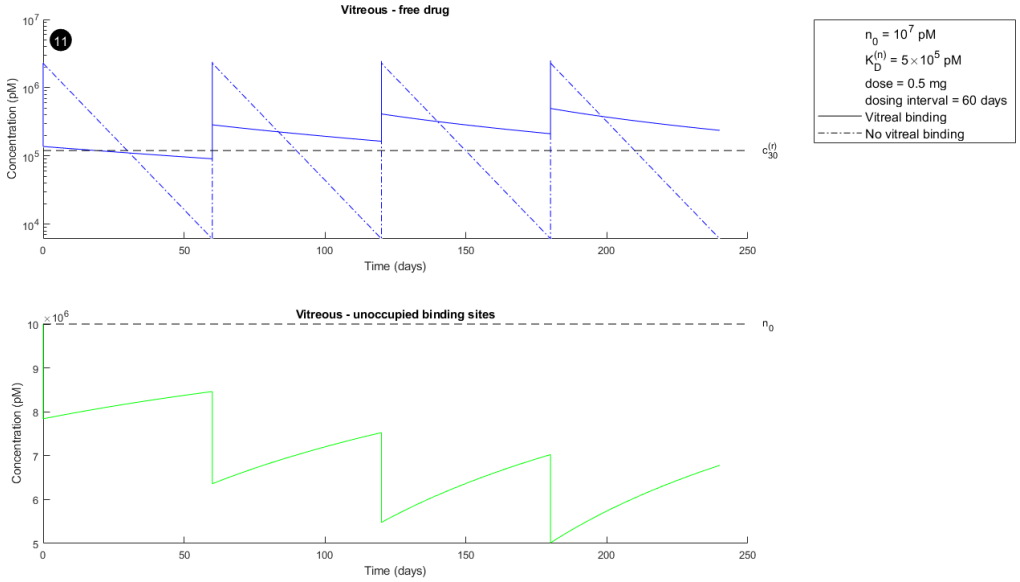

Figure 5.28: Multiple dosing solution for the SVB model, where $K_{\mathrm{D}}^{(n)} = 5 \times 10^5$ pM, $n_0 = 10^7$ pM. Dosage protocol can be found in the figure legend. We see a greatly increased persistence of freely diffusing vitreal drug, with subsequent doses increasing vitreal concentration levels through binding site saturation.

Finally we consider Figures 5.29-5.30, whose $K_{\mathrm{D}}^{(n)}$ and n_0 values both lie in the red zone of parameter space, to the right of the hill. In Figure 5.29 we see step function behaviour presented by both vitreal binding sites and free vitreal drug concentration; for every subsequent injection the number of unoccupied binding sites decreases and, due to chemical equilibrium and the magnitude of $K_{\mathrm{D}}^{(n)}$, the concentration of free vitreal drug

increases noticeably. In order to examine the behaviour at higher levels of binding site saturation Figure 5.30 demonstrates the same scenario with an initial loading dose of 6 mg. Here we see an immediate transition to a state where a sufficiently large number of vitreal binding sites are occupied to maintain a large quantity of free vitreal drug, and in comparison to the non-vitreal binding model there is little to no decay over the 60 day interval. We note that these two plots show the model solved for the same value of n_0 as in Figure 5.20, however due to the 5 orders of magnitude difference between $K_{\mathrm{D}}^{(n)}$ values we see very different behaviour, indicating that even given a very large n_0 value, with a high enough value of $K_{\mathrm{D}}^{(n)}$, favourable behaviour can be achieved. Once all binding sites are saturated the concentration level of free vitreal drug retained in the vitreous can be kept sufficiently greater than $c_{30}^{(r)}$, and hence, theoretically, remain highly efficacious.

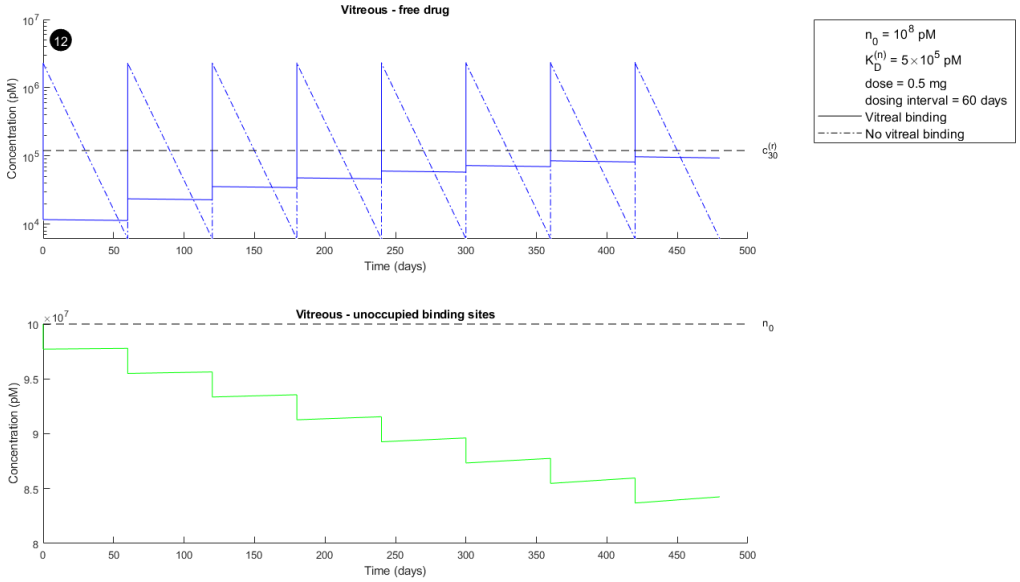

Figure 5.29: Multiple dosing solution for the SVB model, where $K_{\mathrm{D}}^{(n)} = 5\times10^5$ pM, $n_0 = 10^8$ pM. Dosage protocol can be found in the figure legend. Exceedingly long half-life exhibited by the SVB model relative to the non-vitreal binding model, repeat dosages consistently increase the concentration of freely diffusing drug in the vitreous.

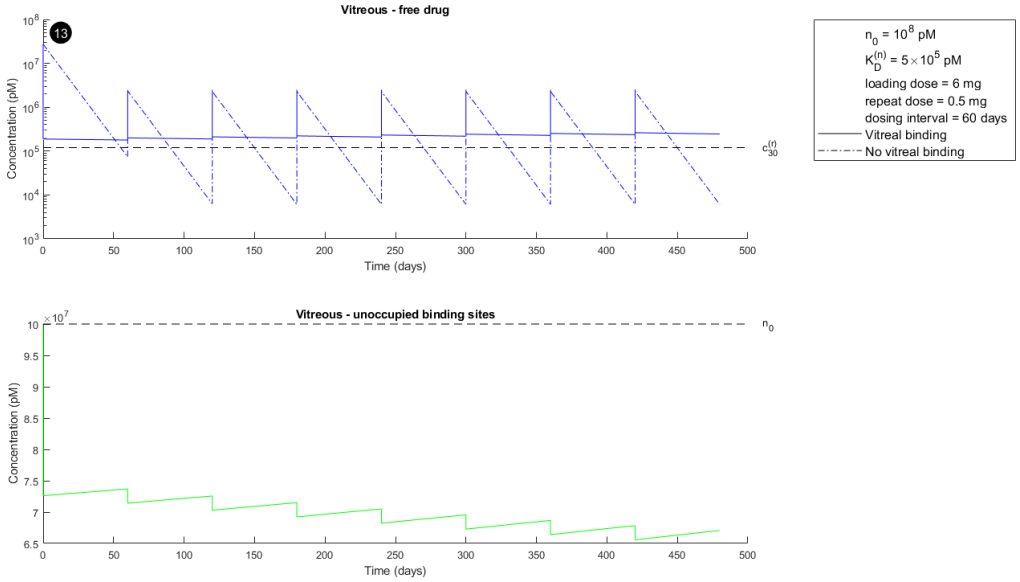

Figure 5.30: Multiple dosing solution for the SVB model, where $K_{\mathrm{D}}^{(n)} = 5 \times 10^5$ pM, $n_0 = 10^8$ pM. Dosage protocol can be found in the figure legend. The same result as in Figure 5.29, however we have demonstrated the use of a loading dose to hasten binding site saturation, and hence decrease the required time for the concentration of freely diffusing vitreal drug to reach levels greater than $c_{30}^{(r)}$.

5.1.5 Vitreal binding PK ODE model summary

In this section we have taken the first steps towards modelling the behaviour of SVB molecules, for therapeutic use in the eye. Our PK analysis, using a vitreous-retina ODE model, has demonstrated that there exists great potential for SVB molecules to improve upon the retention times of their classic counterparts, but also that this effect is highly dependent on $\left(K_{\mathrm{D}}^{(n)}, n_0\right)$ parameter space, and alongside the potential for improvement, large parts of $\left(K_{\mathrm{D}}^{(n)}, n_0\right)$ parameter space in fact worsen the retention. Within this section we note, based on results in Chapter 4, that the PK metric critically related to drug efficacy is the concentration of freely diffusing drug in the vitreous - the magnitude of this concentration determines the availability of drug in the retina to bind to VEGF. We have shown that SVB molecules, in order to be as efficacious as their classical counterparts, must not only be able to access a large quantity of vitreal binding sites, but must also bind weakly enough in order to maintain a sufficiently large concentration of free vitreal drug.

We have also presented an analytic solution to the model (Equation 5.76) alongside an extensive study of the possible $t_{1/2}$ values achievable within the vitreal binding system. We have shown that the $t_{1/2}$ of an SVB molecule is always greater than or equal to $t_{1/2}^{(0)}$, the $t_{1/2}$ of its classical counterpart, that it can never exceed $\left(1 + n_0/K_{\mathrm{D}}^{(n)}\right) t_{1/2}^{(0)}$, and that in certain parts of parameter space it always achieves this maximum value - and can there-

fore, theoretically, be increased arbitrarily within physical reason. However, the ability to increase $t_{1/2}$ needs to be considered in tandem with the decrease in effective initial concentration of the system, $c_0 y_0$, which bounds the maximum possible free vitreal drug in the PK subsequent to IVT injection, which decreases inversely proportional to $t_{1/2}$ (Equation 5.134).

We have demonstrated the model exhibits 3 characteristic types of behaviour, depending on its position in $\left(K_{\mathrm{D}}^{(n)}, n_0\right)$ parameter space: (1) exponential decay at the same rate as the classical molecule, (2) non-exponential decay with a $t_{1/2}$ increasing with time, and (3) exponential decay with a maximal $t_{1/2}$. We have shown that type (1) behaviour is induced through strong binding between drug and binding sites, and that a molecule with these properties is likely to under-perform against its classical counterpart. Behaviour of types (2) and (3) are highly dependent on the magnitude of n_0 relative to c_0 as well its ratio to $K_{\mathrm{D}}^{(n)}$. SVB molecules exhibiting these behaviour types have the potential to greatly outperform those of their classical counterparts. For $n_0 > c_0$ assuming strength of binding can be controlled, it is theoretically possible to achieve persistently high concentrations of free drug for up to 2 or 3 times as long as the non-vitreal binding drug.

Our PK analysis has shown that if the molecule binds too strongly (high $K_{\mathrm{D}}^{(n)}$) we find that bound drug is essentially removed from the system once bound to a vitreal binding site, and that any excess drug injected after all the binding sites have been saturated simply decays in the same manner as the classical drug. Similarly if the binding is too weak (low $K_{\mathrm{D}}^{(n)}$) then there is no interaction between and binding sites and the drug again decays in the same manner as the classical drug. In addition to constraints on $K_{\mathrm{D}}^{(n)}$ we have additionally demonstrated that in order for a molecule to outperform its classical counterpart (at the same dose) there must be an excess of available binding sites, i.e. $n_0 > c_0$. It is possible to see an increase in duration time while $n_0 < c_0$, however this region in parameter space is reasonably specific, requiring $K_{\mathrm{D}} \in (c_{30}^{(r)}, c_0)$ and n_0 to also be greater than $c_{30}^{(r)}$. We have shown analytically that t_{dur} depends only on the ratio of $K_{\mathrm{D}}^{(n)}$ and n_0 (Equation 5.137), that there exists an optimal ratio of $K_{\mathrm{D}}^{(n)}$ to n_0, and that to maximise duration time $K_{\mathrm{D}}^{(n)}/n_0 \sim O(10^{-1})$ (Equation 5.142).

5.2 Analysis of the PK of Vitreal Binding Macromolecules Using a PDE Model

In this section, as in Sections 3.2 and 4.2, we consider the PDE analogue of the ODE model considered in this section, specifically the SVB extension of the 3-compartment PDE model

considered in Section 3.2 (omitting the aqueous compartment). Sections 3.2 and 4.2 have both demonstrated the similarity in PK/PD, as well as predictive capacity of the ODE models relative to their PDE analogues. However we present this analysis for completeness, and as a verification of continued equivalence between ODE and PDE ocular models. In this section we will compare the PK of ODE and PDE SVB models over the large parameter range ($K_{\mathrm{D}}^{(n)} \in [10^0, 10^{10}]$ and $n_0 \in [10^4, 10^{10}]$) considered in Section 5.1, and assess the similarities and differences in PK between the two models.

5.2.1 Model Formulation and Numerical Solution

In order to formulate the SVB PK PDE model we will extend Equations 3.47-3.49 of Section 3.2, which define the retina-vitreous PDE PK model. The model is then defined by Equations 5.151-5.159:

Drug (C, c($\vec{x}, t$))

$$\frac{\partial c_{\mathrm{ret}}}{\partial t} = D_{\mathrm{ret}} \nabla^2 c_{\mathrm{ret}}, \qquad \text{for } \vec{x} \in \Omega_{\mathrm{ret}}, \tag{5.151}$$

$$\frac{\partial c_{\mathrm{vit}}}{\partial t} = D_{\mathrm{vit}} \nabla^2 c_{\mathrm{vit}} + k_{\mathrm{off}}^{(n)} b - k_{\mathrm{on}}^{(n)} n c_{\mathrm{vit}}, \qquad \text{for } \vec{x} \in \Omega_{\mathrm{vit}}, \tag{5.152}$$

$$-D_{\mathrm{ret}} \vec{n} \cdot \nabla c_{\mathrm{ret}} = p_{\mathrm{ILM}} \left(c_{\mathrm{ret}} - c_{\mathrm{vit}} \right), \qquad \text{for } \vec{x} \in \partial\Omega_1, \tag{5.153}$$

$$-D_{\mathrm{ret}} \vec{n} \cdot \nabla c_{\mathrm{ret}} = p_{\mathrm{RPE}} c_{\mathrm{ret}}, \qquad \text{for } \vec{x} \in \partial\Omega_1^*, \tag{5.154}$$

$$-D_{\mathrm{vit}} \vec{n} \cdot \nabla c_{\mathrm{vit}} = p_{\mathrm{ILM}}, \left(c_{\mathrm{vit}} - c_{\mathrm{ret}} \right), \qquad \text{for } \vec{x} \in \partial\Omega_1, \tag{5.155}$$

$$-D_{\mathrm{vit}} \vec{n} \cdot \nabla c_{\mathrm{vit}} = p_{\mathrm{HYA}} c_{\mathrm{vit}}, \qquad \text{for } \vec{x} \in \partial\Omega_2, \tag{5.156}$$

$$-\vec{n} \cdot \nabla c_{\mathrm{vit}} = 0, \qquad \text{for } \vec{x} \in \partial\Omega_3, \tag{5.157}$$

Unoccupied Binding Site (N, n($\vec{x}, t$))

$$\frac{\partial n}{\partial t} = k_{\mathrm{off}}^{(n)} b - k_{\mathrm{on}}^{(n)} n c_{\mathrm{vit}}, \qquad \text{for } \vec{x} \in \Omega_{\mathrm{vit}}, \tag{5.158}$$

Occupied Vitreal Binding Site (CN, b($\vec{x}, t$))

$$\frac{\partial n}{\partial t} = -\left(k_{\mathrm{off}}^{(n)} b - k_{\mathrm{on}}^{(n)} n c_{\mathrm{vit}} \right), \qquad \text{for } \vec{x} \in \Omega_{\mathrm{vit}}. \tag{5.159}$$

We solve the model for a Fab molecule, with hydrodynamic radius $R_{\mathrm{h}} = 3.04$ nm, dosed a 0.5 mg, over human geometry, as defined in Figure 3.5 and Table 3.6. Initially the drug is assumed to be at zero concentration in the retina, and uniform concentration in the vitreous, alongside the concentration of unbound binding sites. All parameters, aside from $k_{\mathrm{off}}^{(n)}, k_{\mathrm{on}}^{(n)}$ and n_0, are generated in the same manner as in the PDE PK/PD model, as defined in Section 4.2. The binding off rate, $k_{\mathrm{off}}^{(n)}$, is taken to be much greater than the decay

rate of the system such that $k_{\text{off}}^{(n)} \sim O(10)$ 1/day, as in Section 5.1. We then fix $K_{\text{D}}^{(n)}$ and generate the binding on rate via $k_{\text{on}}^{(n)} = k_{\text{off}}^{(n)}/K_{\text{D}}$. Similarly to $K_{\text{D}}^{(n)}$, the total concentration of binding sites, n_0, is set arbitrarily.

5.2.2 Predictive comparison between the ODE and PDE model

In order to compare the SVB PK PDE model to the ODE model discussed in Section 5.1, we modify the value of k_{el} so as the generate the same PK (specifically the $t_{1/2}$ of the system) in the absence of vitreal binding, i.e. when $k_{\text{on}}^{(n)} = 0$. We do this so as when comparing the ODE and PDE model over $\left(K_{\text{D}}^{(n)}, n_0\right)$ parameter space, we may analyse PK differences due solely to the introduction of vitreal binding. The ODE model is then solved using the same $K_{\text{D}}^{(n)}$ and n_0 values as the PDE, over $K_{\text{D}}^{(n)} \in [10^0, 10^{10}]$ and $n_0 \in [10^4, 10^{10}]$, where all remaining parameters are set in the same manner as in Section 5.1.

Figure 5.31 shows the percentage error between the ODE and PDE SVB PK models' retinal and vitreal solutions. The error was calculated by considering the relative magnitude of the spatially averaged PDE solution to the ODE model at equally spaced intervals. We solved the system over $K_{\text{D}}^{(n)} \in [10^0, 10^{10}]$ pM and $n_0 \in [10^4, 10^{10}]$ pM, at equally spaced logarithmic intervals, totalling 4928 combinations (88 $K_{\text{D}}^{(n)}$ values, 56 n_0 values). As can be seen from Figure 5.31 the error across $\left(K_{\text{D}}^{(n)}, n_0\right)$ parameter space between the ODE and PDE retinal and vitreal solutions is below 6% and 9%, respectively. Given this high fidelity between the ODE and PDE models we will limit our analysis to that conducted on the ODE model presented in Section 5.1.

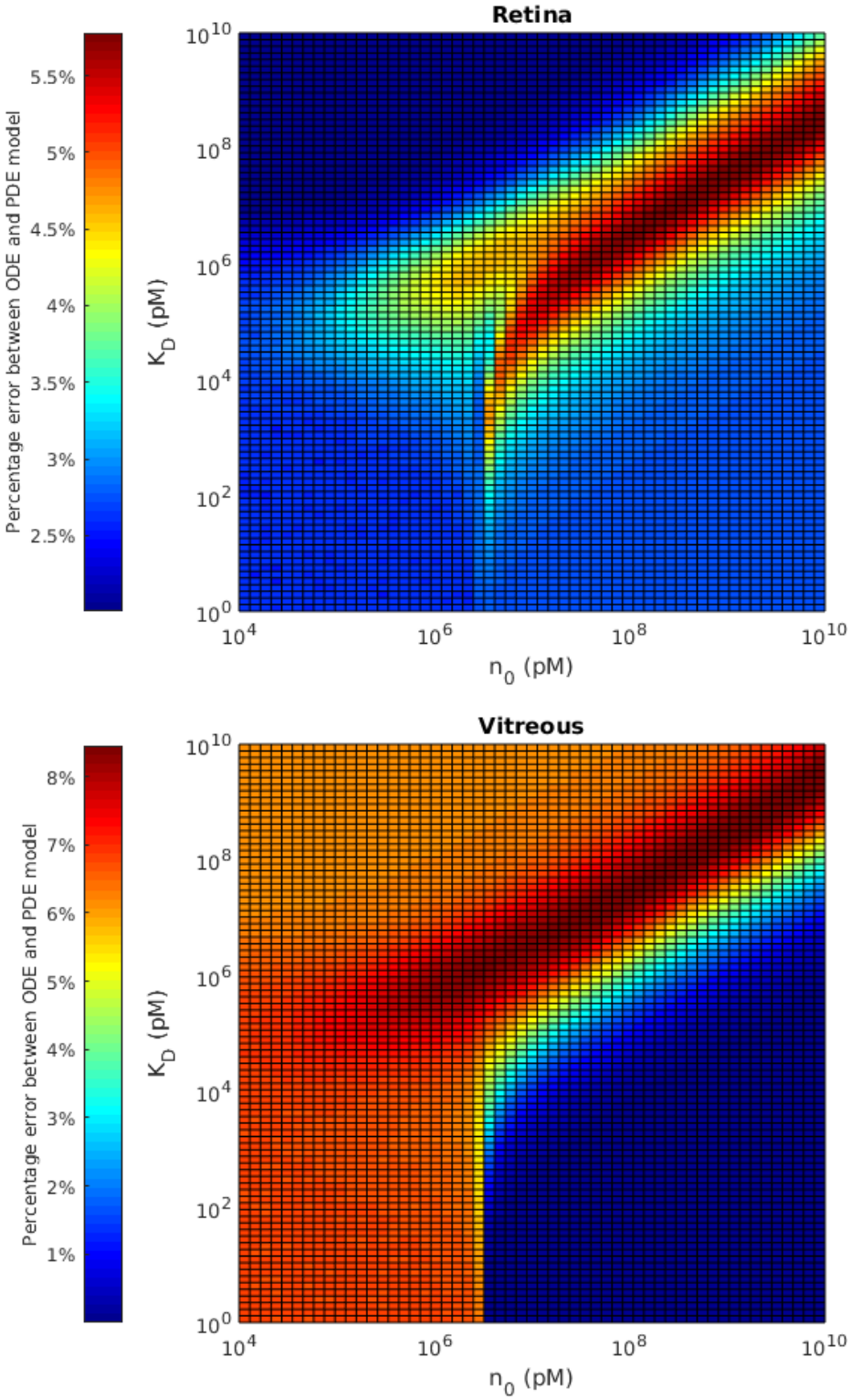

Figure 5.31: Percentage error between the ODE (Equations 5.2-5.5) and PDE (Equations 5.151-5.159) SVB PK models, in the retina (upper plot) and vitreous (lower plot). The error was calculated by considering the relative magnitude of the spatially averaged PDE solution to the ODE model at equally spaced intervals. We solved over $K_{\mathrm{D}}^{(n)} \in [10^0, 10^{10}]$ pM and $n_0 \in [10^4, 10^{10}]$ pM, at equally spaced logarithmic intervals, totalling 4928 combinations.

6

The ocular PK/PD of bispecific anti-VEGF vitreal binding macromolecules

In this chapter we present a retina-vitreous ODE model of the PK/PD of a bispecific vitreal binding, anti-VEGF molecule, not only describing the PK induced by vitreal binding, but additionally incorporating drug-VEGF interactions. By doing so we will be able to emulate the analysis of free retinal VEGF (FRV) concentrations, as in Chapter 5, and compare the theoretical efficacy of a bispecific, vitreal binding anti-VEGF molecule, to its classical counterpart.

We will do this by extending the static vitreal binding (SVB) ODE model presented in Chapter 5 to include binding to VEGF molecules, in the same manner as we extended the 3-compartment PK ODE model (Section 3.1) to a 3-compartment PK/PD model (Section 4.1). Unlike the 3-compartment PK/PD model, due to the presence of a third chemical species (N, in addition to V and R), larger complexes will be able to be formed within the model, such as a VEGF molecule, bound to a drug molecule, bound to a vitreal binding site (VRN).

Given the PK analysis performed in Chapter 5, which demonstrated that the position in $\left(K_{\mathrm{D}}^{(n)}, n_0\right)$ parameter space greatly affects the behaviour of the model, we expect to find a wide variation in FRV levels, dependent on the values of $K_{\mathrm{D}}^{(n)}$ and n_0. In the vitreous

however, as molecules bound to the vitreal binding sites can still bind to VEGF, we expect there always to be a level of free VEGF suppression greater than or equal to that of the monospecific anti-VEGF molecule. Given we have already demonstrated that the presence of drug in the retina is crucial to suppress the concentration of FRV, we expect to find that, even when free VEGF is completely suppressed in the vitreous, the retina may still possess relatively high FRV concentrations. We will investigate what values of $K_{\mathrm{D}}^{(n)}$ and n_0 provide optimal retinal free VEGF suppression.

In addition to the consideration of the static SVB molecule, whose PK we detailed in Chapter 5, we will also consider the other class of vitreal binder discussed in the Introduction (Section 1.2), nSVB. Specifically we will model the BI-X molecule, an anti-VEGF/ANG-2 human albumin binding nSVB molecule [59]. By developing a PK framework for this molecule we will be able to compare the efficacy of SVB and nSVB molecules.

Unlike Chapters 3-5 we do not present the PDE model analogous to the PK/PD ODE SVB model. Instead, as we found there to be little difference between the ODE and equivalent PDE model, we present this model in Appendix A.14.

6.1 Model formulation

The vitreal binding PK/PD model consists of three base chemical species: drug, VEGF and vitreal binding sites, R,V and N, respectively. To formulate the model we must first consider which complexes/reactions are possible given these three base species; it follows from Chapters 3-5 that the following reactions can occur:

$$\mathrm{V}+\mathrm{R} \underset{2k_{\mathrm{on}}^{(v)}}{\overset{k_{\mathrm{off}}^{(v)}}{\rightleftharpoons}} \mathrm{VR}, \quad \mathrm{R}+\mathrm{VR} \underset{k_{\mathrm{on}}^{(v)}}{\overset{2k_{\mathrm{off}}^{(v)}}{\rightleftharpoons}} \mathrm{RVR}, \quad \mathrm{R}+\mathrm{N} \underset{k_{\mathrm{on}}^{(n)}}{\overset{k_{\mathrm{off}}^{(n)}}{\rightleftharpoons}} \mathrm{RN}, \tag{6.1}$$

where $k_{\mathrm{off}}^{(v)}/k_{\mathrm{on}}^{(v)}$ and $k_{\mathrm{off}}^{(n)}/k_{\mathrm{on}}^{(n)}$ denote drug binding kinetics with respect to VEGF and vitreal binding sites, respectively. In addition to these interactions we also assume that once an RN complex is formed, a VEGF molecule may attach forming a VRN complex. We also assume a VRN complex can be formed by a VR complex attaching to a vitreal binding site; these two reactions are given by:

$$\mathrm{VR}+\mathrm{N} \underset{k_{\mathrm{on}}^{(n)}}{\overset{k_{\mathrm{off}}^{(n)}}{\rightleftharpoons}} \mathrm{VRN}, \quad \mathrm{V}+\mathrm{RN} \underset{2k_{\mathrm{on}}^{(v)}}{\overset{k_{\mathrm{off}}^{(v)}}{\rightleftharpoons}} \mathrm{VRN}. \tag{6.2}$$

Similarly a RVRN complex can be formed by the following reactions:

$$\mathrm{RVR}+\mathrm{N} \underset{2k_{\mathrm{on}}^{(n)}}{\overset{k_{\mathrm{off}}^{(n)}}{\rightleftharpoons}} \mathrm{RVRN}, \quad \mathrm{VR}+\mathrm{RN} \underset{k_{\mathrm{on}}^{(v)}}{\overset{k_{\mathrm{off}}^{(v)}}{\rightleftharpoons}} \mathrm{RVRN}, \quad \mathrm{R}+\mathrm{VRN} \underset{k_{\mathrm{on}}^{(v)}}{\overset{k_{\mathrm{off}}^{(v)}}{\rightleftharpoons}} \mathrm{RVRN}. \tag{6.3}$$

Theoretically it may be possible for a NRVRN complex to form, whereby an RVR molecule binds to two vitreal bindings sites simultaneously. However, detailed structural knowledge of both RVR and the frequency/distribution of vitreal binding sites would be required in order to examine whether two binding sites exist sufficiently close to each other in vitreal space for an RVR complex to bind. We would also require knowledge of the conformation formed by RVR complexes, in order to access the maximum reach of both R "arms" of the RVR complex. Therefore, for simplicity we will omit the possibility of the complex forming. The chemical species considering in this model are given in Table 6.1, alongside their concentration notation.

Species	Conc. (pM)	Description
V	v	VEGF
R	r	Drug
VR	c	VEGF, drug complex
RVR	h	Drug, VEGF, drug complex
N	n	Vitreal binding site
RN	m	Drug, binding site complex
VRN	f	VEGF, ranibizumab, drug binding site complex
RVRN	g	Drug, VEGF, drug, binding site complex

Table 6.1: Model chemical species. Note, all concentrations are functions of time (t) and are expressed in pM. This notation will additionally include subscripts to denote to which compartment each concentrations refers, e.g. v_{ret} is the concentration of V in the retina, whereas v_{vit} is the concentration of V in the vitreous.

In order to formulate the model into a system of ODEs we simply extend the SVB PK ODE model, given by Equations 5.12-5.14, to incorporate the possible system reactions, in an analogous manner as was implemented to extend the 3-compartment PK ODE (Equations 3.1-3.3) to the 3-compartment PK/PD model (Equations 4.3-4.18). Therefore the model is formulated as the ODE system given by Equations 6.4-6.15, below:

Retina

$$\frac{\mathrm{d}v_{\text{ret}}}{\mathrm{d}t} = -\left(\frac{S_{\text{ret}}}{V_{\text{ret}}}\right)\left[p^{(v)}_{\text{ILM}} + p^{(v)}_{\text{RPE}}\right] v_{\text{ret}} + \left(\frac{S_{\text{ret}}}{V_{\text{ret}}}\right) p^{(v)}_{\text{ILM}} v_{\text{vit}} + \left(k^{(v)}_{\text{off}} c_{\text{ret}} - 2k^{(v)}_{\text{on}} v_{\text{ret}} r_{\text{ret}}\right) + \frac{V_{\text{in}}}{V_{\text{ret}}}, \tag{6.4}$$

$$\frac{\mathrm{d}r_{\text{ret}}}{\mathrm{d}t} = -\left(\frac{S_{\text{ret}}}{V_{\text{ret}}}\right)\left[p^{(r)}_{\text{ILM}} + p^{(r)}_{\text{RPE}}\right] r_{\text{ret}} + \left(\frac{S_{\text{ret}}}{V_{\text{ret}}}\right) p^{(r)}_{\text{ILM}} r_{\text{vit}} + \left(k^{(v)}_{\text{off}} c_{\text{ret}} - 2k^{(v)}_{\text{on}} v_{\text{ret}} r_{\text{ret}}\right) + \left(2k^{(v)}_{\text{off}} h_{\text{ret}} - k^{(v)}_{\text{on}} r_{\text{ret}} c_{\text{ret}}\right), \tag{6.5}$$

$$\frac{\mathrm{d}c_{\mathrm{ret}}}{\mathrm{d}t} = -\left(\frac{S_{\mathrm{ret}}}{V_{\mathrm{ret}}}\right)\left[p^{(c)}_{\mathrm{ILM}} + p^{(c)}_{\mathrm{RPE}}\right] c_{\mathrm{ret}} + \left(\frac{S_{\mathrm{ret}}}{V_{\mathrm{ret}}}\right) p^{(c)}_{\mathrm{ILM}} c_{\mathrm{vit}} - \left(k^{(v)}_{\mathrm{off}} c_{\mathrm{ret}} - 2k^{(v)}_{\mathrm{on}} v_{\mathrm{ret}} r_{\mathrm{ret}}\right) + \left(2k^{(v)}_{\mathrm{off}} h_{\mathrm{ret}} - k^{(v)}_{\mathrm{on}} r_{\mathrm{ret}} c_{\mathrm{ret}}\right), \tag{6.6}$$

$$\frac{\mathrm{d}h_{\mathrm{ret}}}{\mathrm{d}t} = -\left(\frac{S_{\mathrm{ret}}}{V_{\mathrm{ret}}}\right)\left[p^{(h)}_{\mathrm{ILM}} + p^{(h)}_{\mathrm{RPE}}\right] h_{\mathrm{ret}} + \left(\frac{S_{\mathrm{ret}}}{V_{\mathrm{ret}}}\right) p^{(h)}_{\mathrm{ILM}} h_{\mathrm{vit}} - \left(2k^{(v)}_{\mathrm{off}} h_{\mathrm{ret}} - k^{(v)}_{\mathrm{on}} r_{\mathrm{ret}} c_{\mathrm{ret}}\right), \tag{6.7}$$

Vitreous

$$\frac{\mathrm{d}v_{\mathrm{vit}}}{\mathrm{d}t} = \left(\frac{S_{\mathrm{ret}}}{V_{\mathrm{vit}}}\right) p^{(v)}_{\mathrm{ILM}} v_{\mathrm{ret}} - \left[\left(\frac{S_{\mathrm{ret}}}{V_{\mathrm{vit}}}\right) p^{(v)}_{\mathrm{ILM}} + k^{(v)}_{\mathrm{el}}\right] v_{\mathrm{vit}} + \left(k^{(v)}_{\mathrm{off}} c_{\mathrm{vit}} - 2k^{(v)}_{\mathrm{on}} v_{\mathrm{vit}} r_{\mathrm{vit}}\right) + \left(k^{(v)}_{\mathrm{off}} f - 2k^{(v)}_{\mathrm{on}} v_{\mathrm{vit}} m\right), \tag{6.8}$$

$$\frac{\mathrm{d}r_{\mathrm{vit}}}{\mathrm{d}t} = \left(\frac{S_{\mathrm{ret}}}{V_{\mathrm{vit}}}\right) p^{(r)}_{\mathrm{ILM}} r_{\mathrm{ret}} - \left[\left(\frac{S_{\mathrm{ret}}}{V_{\mathrm{vit}}}\right) p^{(r)}_{\mathrm{ILM}} + k^{(r)}_{\mathrm{el}}\right] r_{\mathrm{vit}} + \left(k^{(v)}_{\mathrm{off}} c_{\mathrm{vit}} - 2k^{(v)}_{\mathrm{on}} v_{\mathrm{vit}} r_{\mathrm{vit}}\right) + \left(2k^{(v)}_{\mathrm{off}} h_{\mathrm{vit}} - k^{(v)}_{\mathrm{on}} r_{\mathrm{vit}} c_{\mathrm{vit}}\right) + \left(k^{(n)}_{\mathrm{off}} m - k^{(n)}_{\mathrm{on}} r_{\mathrm{vit}} n\right) + \left(k^{(v)}_{\mathrm{off}} g - k^{(v)}_{\mathrm{on}} r_{\mathrm{vit}} f\right), \tag{6.9}$$

$$\frac{\mathrm{d}c_{\mathrm{vit}}}{\mathrm{d}t} = \left(\frac{S_{\mathrm{ret}}}{V_{\mathrm{vit}}}\right) p^{(c)}_{\mathrm{ILM}} c_{\mathrm{ret}} - \left[\left(\frac{S_{\mathrm{ret}}}{V_{\mathrm{vit}}}\right) p^{(c)}_{\mathrm{ILM}} + k^{(c)}_{\mathrm{el}}\right] c_{\mathrm{vit}} - \left(k^{(v)}_{\mathrm{off}} c_{\mathrm{vit}} - 2k^{(v)}_{\mathrm{on}} v_{\mathrm{vit}} r_{\mathrm{vit}}\right) + \left(2k^{(v)}_{\mathrm{off}} h_{\mathrm{vit}} - k^{(v)}_{\mathrm{on}} r_{\mathrm{vit}} c_{\mathrm{vit}}\right) + \left(k^{(n)}_{\mathrm{off}} f - k^{(n)}_{\mathrm{on}} c_{\mathrm{vit}} n\right) + \left(k^{(v)}_{\mathrm{off}} g - k^{(v)}_{\mathrm{on}} c_{\mathrm{vit}} m\right), \tag{6.10}$$

$$\frac{\mathrm{d}h_{\mathrm{vit}}}{\mathrm{d}t} = \left(\frac{S_{\mathrm{ret}}}{V_{\mathrm{vit}}}\right) p^{(h)}_{\mathrm{ILM}} h_{\mathrm{ret}} - \left[\left(\frac{S_{\mathrm{ret}}}{V_{\mathrm{vit}}}\right) p^{(h)}_{\mathrm{ILM}} + k^{(h)}_{\mathrm{el}}\right] h_{\mathrm{vit}} - \left(2k^{(v)}_{\mathrm{off}} h_{\mathrm{vit}} - k^{(v)}_{\mathrm{on}} r_{\mathrm{vit}} c_{\mathrm{vit}}\right) + \left(k^{(n)}_{\mathrm{off}} g - 2k^{(n)}_{\mathrm{on}} h_{\mathrm{vit}} n\right), \tag{6.11}$$

$$\frac{\mathrm{d}n}{\mathrm{d}t} = + \left(k^{(n)}_{\mathrm{off}} m - k^{(n)}_{\mathrm{on}} r_{\mathrm{vit}} n\right) + \left(k^{(n)}_{\mathrm{off}} f - k^{(n)}_{\mathrm{on}} c_{\mathrm{vit}} n\right) + \left(k^{(n)}_{\mathrm{off}} g - 2k^{(n)}_{\mathrm{on}} h_{\mathrm{vit}} n\right), \tag{6.12}$$

$$\frac{\mathrm{d}m}{\mathrm{d}t} = - \left(k^{(n)}_{\mathrm{off}} m - k^{(n)}_{\mathrm{on}} r_{\mathrm{vit}} n\right) + \left(k^{(v)}_{\mathrm{off}} f - 2k^{(v)}_{\mathrm{on}} v_{\mathrm{vit}} m\right) + \left(k^{(v)}_{\mathrm{off}} g - k^{(v)}_{\mathrm{on}} c_{\mathrm{vit}} m\right), \tag{6.13}$$

$$\frac{\mathrm{d}f}{\mathrm{d}t} = - \left(k^{(n)}_{\mathrm{off}} f - k^{(n)}_{\mathrm{on}} c_{\mathrm{vit}} n\right) - \left(k^{(v)}_{\mathrm{off}} f - 2k^{(v)}_{\mathrm{on}} v_{\mathrm{vit}} m\right) + \left(k^{(v)}_{\mathrm{off}} g - k^{(v)}_{\mathrm{on}} r_{\mathrm{vit}} f\right), \tag{6.14}$$

$$\frac{\mathrm{d}g}{\mathrm{d}t} = - \left(k^{(n)}_{\mathrm{off}} g - 2k^{(n)}_{\mathrm{on}} h_{\mathrm{vit}} n\right) - \left(k^{(v)}_{\mathrm{off}} g - k^{(v)}_{\mathrm{on}} c_{\mathrm{vit}} m\right) - \left(k^{(v)}_{\mathrm{off}} g - k^{(v)}_{\mathrm{on}} r_{\mathrm{vit}} f\right), \tag{6.15}$$

where we have initial conditions:

$$v_{\text{ret}}(0) = v_0, \quad r_{\text{ret}}(0) = c_{\text{ret}}(0) = h_{\text{ret}}(0) = 0, \tag{6.16}$$

$$v_{\text{vit}}(0) = u_0, \quad r_{\text{vit}}(0) = r_0, \quad c_{\text{vit}}(0) = h_{\text{vit}}(0) = 0, \tag{6.17}$$

$$n(0) = n_0, \quad m(0) = f(0) = g(0) = 0. \tag{6.18}$$

All parameter definitions utilised in the model can be found in Tables 4.2 and 5.1 of Chapters 4 and 5, respectively. The vitreous to aqueous clearance parameter, k_{el}, is generated in the same manner as in Chapter 4, via Equations 4.21, 4.22 and 4.24. We model the drug as a Fab, and therefore take $t_{1/2} = 7.04$ days and $R_{\text{h}} = 3.04$ nm, as given in Appendix A.6. R_{h} values for VEGF and drug-VEGF complexes are given in Table 4.3 of Chapter 4. Permeabilities are generated using Equations 3.76 and 3.77, as in Chapter 5. The initial conditions for VEGF in the retina and vitreous are given by Equation 4.25, as the steady state solution in the absence of drug is not affected by the presence of vitreal binding sites. We assume that drug-VEGF binding occurs with the same binding kinetics as for ranibizumab, i.e. $k_{\text{off}}^{(v)} = 0.861$ 1/day and $K_{\text{D}}^{(v)} = 19000$ pM, as was approximated in Chapter 4. As in Chapter 5 we will assume that $K_{\text{D}}^{(n)}$ and n_0 are unknown and will be varied throughout the analysis, alongside dosage. Notice that as total binding sites are conserved, by adding Equations 6.12-6.15 we find:

$$\frac{\text{d}}{\text{d}t}\left(n + m + f + g\right) = 0, \tag{6.19}$$

$$\Rightarrow \quad n + m + f + g = n_0, \tag{6.20}$$

and hence we may write g in terms of n_0, n, m and f as follows:

$$g = n_0 - \left\{n + m + f\right\}. \tag{6.21}$$

We will analyse the system equations further in the following subsection.

6.2 Asymptotic analysis and PK decoupling

In order to analyse Equations 6.4-6.15 we first nondimensionalise the system using the following nondimensionalisation:

$$t = \frac{\tau}{k_{\text{off}}^{(n)}}, \tag{6.22}$$

$$v_{\text{ret}} = v_0 x_{\text{ret}}, \quad r_{\text{ret}} = r_0 y_{\text{ret}}, \quad c_{\text{ret}} = v_0 z_{\text{ret}}, \quad h_{\text{ret}} = v_0 w_{\text{ret}}, \tag{6.23}$$

$$v_{\text{vit}} = u_0 x_{\text{vit}}, \quad r_{\text{vit}} = r_0 y_{\text{vit}}, \quad c_{\text{vit}} = u_0 z_{\text{vit}}, \quad h_{\text{vit}} = u_0 w_{\text{vit}}, \tag{6.24}$$

$$n = n_0\phi, \quad m = n_0\psi, \quad f = u_0\zeta, \quad g = u_0\xi, \tag{6.25}$$

which allows us to rewrite Equations 6.4-6.15 in the following way:

Retina

$$\varepsilon_1 \frac{\mathrm{d}x_{\mathrm{ret}}}{\mathrm{d}\tau} = -\varepsilon_1 F^{(v)} x_{\mathrm{ret}} + \delta\varepsilon_1 P^{(v)} x_{\mathrm{vit}} + \kappa\left(\varepsilon_1 z_{\mathrm{ret}} - 2x_{\mathrm{ret}} y_{\mathrm{ret}}\right) + \varepsilon_1 V, \tag{6.26}$$

$$\frac{\mathrm{d}y_{\mathrm{ret}}}{\mathrm{d}\tau} = -F^{(r)} y_{\mathrm{ret}} + P^{(r)} y_{\mathrm{vit}} + \varepsilon_2\kappa\left(\varepsilon_1 z_{\mathrm{ret}} - 2x_{\mathrm{ret}} y_{\mathrm{ret}}\right) + \varepsilon_2\kappa\left(2\varepsilon_1 w_{\mathrm{ret}} - y_{\mathrm{ret}} z_{\mathrm{ret}}\right), \tag{6.27}$$

$$\varepsilon_1 \frac{\mathrm{d}z_{\mathrm{ret}}}{\mathrm{d}\tau} = -\varepsilon_1 F^{(c)} z_{\mathrm{ret}} + \delta\varepsilon_1 P^{(c)} z_{\mathrm{vit}} - \kappa\left(\varepsilon_1 z_{\mathrm{ret}} - 2x_{\mathrm{ret}} y_{\mathrm{ret}}\right) + \kappa\left(2\varepsilon_1 w_{\mathrm{ret}} - y_{\mathrm{ret}} z_{\mathrm{ret}}\right), \tag{6.28}$$

$$\varepsilon_1 \frac{\mathrm{d}w_{\mathrm{ret}}}{\mathrm{d}\tau} = -\varepsilon_1 F^{(h)} w_{\mathrm{ret}} + \delta\varepsilon_1 P^{(h)} w_{\mathrm{vit}} - \kappa\left(2\varepsilon_1 w_{\mathrm{ret}} - y_{\mathrm{ret}} z_{\mathrm{ret}}\right), \tag{6.29}$$

Vitreous

$$\varepsilon_1 \frac{\mathrm{d}x_{\mathrm{vit}}}{\mathrm{d}\tau} = \beta\nu\varepsilon_1 P^{(v)} x_{\mathrm{ret}} - \varepsilon_1 G^{(v)} x_{\mathrm{vit}} + \kappa\left(\varepsilon_1 z_{\mathrm{vit}} - 2x_{\mathrm{vit}} y_{\mathrm{vit}}\right) + \kappa\left(\varepsilon_1\zeta - \frac{2}{\alpha} x_{\mathrm{vit}}\psi\right), \tag{6.30}$$

$$\frac{\mathrm{d}y_{\mathrm{vit}}}{\mathrm{d}\tau} = \nu P^{(r)} y_{\mathrm{ret}} - G^{(r)} y_{\mathrm{vit}} + \frac{\varepsilon_2\kappa}{\beta}\left(\varepsilon_1 z_{\mathrm{vit}} - 2x_{\mathrm{vit}} y_{\mathrm{vit}}\right) + \frac{\varepsilon_2\kappa}{\beta}\left(2\varepsilon_1 w_{\mathrm{vit}} - y_{\mathrm{vit}} z_{\mathrm{vit}}\right) + \left(\frac{1}{\alpha}\psi - \frac{1}{\beta} y_{\mathrm{vit}}\phi\right) + \frac{\varepsilon_2\kappa}{\beta}\left(\varepsilon_1\xi - y_{\mathrm{vit}}\zeta\right), \tag{6.31}$$

$$\varepsilon_1 \frac{\mathrm{d}z_{\mathrm{vit}}}{\mathrm{d}\tau} = \beta\nu\varepsilon_1 P^{(c)} z_{\mathrm{ret}} - \varepsilon_1 G^{(c)} z_{\mathrm{vit}} - \kappa\left(\varepsilon_1 z_{\mathrm{vit}} - 2x_{\mathrm{vit}} y_{\mathrm{vit}}\right) + \kappa\left(2\varepsilon_1 w_{\mathrm{vit}} - y_{\mathrm{vit}} z_{\mathrm{vit}}\right) + \varepsilon_1\left(\zeta - \frac{1}{\beta} z_{\mathrm{vit}}\phi\right) + \kappa\left(\varepsilon_1\xi - \frac{1}{\alpha} z_{\mathrm{vit}}\psi\right), \tag{6.32}$$

$$\varepsilon_1 \frac{\mathrm{d}w_{\mathrm{vit}}}{\mathrm{d}t} = \beta\nu\varepsilon_1 P^{(c)} w_{\mathrm{ret}} - \varepsilon_1 G^{(h)} w_{\mathrm{vit}} - \kappa\left(2\varepsilon_1 w_{\mathrm{vit}} - y_{\mathrm{vit}} z_{\mathrm{vit}}\right) + \varepsilon_1\left(\xi - \frac{2}{\beta} w_{\mathrm{vit}}\phi\right), \tag{6.33}$$

$$\frac{\mathrm{d}\phi}{\mathrm{d}\tau} = +\left(\psi - \frac{\alpha}{\beta}y_{\mathrm{vit}}\phi\right) + \varepsilon_3\left(\zeta - \frac{1}{\beta}z_{\mathrm{vit}}\phi\right) + \varepsilon_3\left(\xi - \frac{2}{\beta}w_{\mathrm{vit}}\phi\right), \tag{6.34}$$

$$\frac{\mathrm{d}\psi}{\mathrm{d}\tau} = -\left(\psi - \frac{\alpha}{\beta}y_{\mathrm{vit}}\phi\right) + \kappa\left(\varepsilon_3\zeta - \frac{2}{\beta}\varepsilon_2 x_{\mathrm{vit}}\psi\right) + \kappa\left(\varepsilon_3\xi - \frac{1}{\beta}\varepsilon_2 z_{\mathrm{vit}}\psi\right), \tag{6.35}$$

$$\varepsilon_1\varepsilon_3\frac{\mathrm{d}\zeta}{\mathrm{d}\tau} = -\varepsilon_1\varepsilon_3\left(\zeta - \frac{1}{\beta}z_{\mathrm{vit}}\phi\right) - \kappa\varepsilon_1\left(\varepsilon_3\zeta - \frac{2}{\beta}\varepsilon_2 x_{\mathrm{vit}}\psi\right) + \kappa\varepsilon_3\left(\varepsilon_1\xi - y_{\mathrm{vit}}\zeta\right), \tag{6.36}$$

$$\varepsilon_1\varepsilon_3\frac{\mathrm{d}\xi}{\mathrm{d}\tau} = -\varepsilon_1\varepsilon_3\left(\xi - \frac{2}{\beta}w_{\mathrm{vit}}\phi\right) - \kappa\varepsilon_1\left(\varepsilon_3\xi - \frac{1}{\beta}\varepsilon_2 z_{\mathrm{vit}}\psi\right) - \kappa\varepsilon_3\left(\varepsilon_1\xi - y_{\mathrm{vit}}\zeta\right), \tag{6.37}$$

where:

$$F^{(i)} = \frac{1}{k_{\mathrm{off}}^{(n)}}\left(\frac{S_{\mathrm{ret}}}{V_{\mathrm{ret}}}\right)\left[p_{\mathrm{ILM}}^{(i)} + p_{\mathrm{RPE}}^{(i)}\right], \tag{6.38}$$

$$P^{(i)} = \frac{1}{k_{\mathrm{off}}^{(n)}}\left(\frac{S_{\mathrm{ret}}}{V_{\mathrm{ret}}}\right)p_{\mathrm{ILM}}^{(i)}, \tag{6.39}$$

$$G^{(i)} = \frac{1}{k_{\mathrm{off}}^{(n)}}\left[\left(\frac{S_{\mathrm{ret}}}{V_{\mathrm{vit}}}\right)p_{\mathrm{ILM}}^{(i)} + k_{\mathrm{el}}^{(i)}\right], \tag{6.40}$$

with $i \in \{v, r, c, h\}$ and

$$\kappa = \frac{k_{\mathrm{off}}^{(v)}}{k_{\mathrm{off}}^{(n)}}, \quad V = \frac{V_{\mathrm{in}}}{v_0 k_{\mathrm{off}}^{(n)} V_{\mathrm{ret}}}, \quad \nu = \frac{V_{\mathrm{ret}}}{V_{\mathrm{vit}}}, \quad \delta = \frac{u_0}{v_0}, \tag{6.41}$$

$$\alpha = \frac{r_0}{n_0}, \quad \beta = \frac{K_{\mathrm{D}}^{(n)}}{n_0}, \tag{6.42}$$

$$\varepsilon_1 = \frac{K_{\mathrm{D}}^{(v)}}{r_0}, \quad \varepsilon_2 = \frac{v_0}{K_{\mathrm{D}}^{(v)}}, \quad \varepsilon_3 = \frac{u_0}{n_0}. \tag{6.43}$$

Let us now consider the orders of magnitude of these parameter groupings. We first note that α and β are defined in the same manner as in Chapter 5 (Equation 5.22). Parameters $F^{(i)}, P^{(i)}, G^{(i)}$, with $i \in \{v, r, c, h\}$ and V, κ, δ are $O(1)$. The ratio of the retinal and vitreal volumes, hence, ν, is small, and on the order of $O(10^{-2})$. For a typical dose of ranibizumab, i.e. 0.5 mg, ε_1 is $O(10^{-2})$, whereas ε_2 is $O(10^{-3})$. Notice that v_0 and $K_{\mathrm{D}}^{(v)}$ will frequently remain constant in this analysis, whereas r_0 will increase if a dose larger than 0.5 mg is considered, therefore we note that ε_1 is $O(10^{-2})$ or smaller for doses larger than 2 mg.

Finally we consider ε_3; for standard VEGF production u_0 is of $O(10^1)$ pM, therefore given that we will only be considering values of n_0 greater than 10^4 pM, ε_3 can be assumed to be less than $O(10^{-3})$, and in most cases, much less than $O(10^{-3})$. Therefore, under standard parameter regimes we can assume the following relationship between $\varepsilon_1, \varepsilon_2$ and ε_3:

$$0 < \varepsilon_3 \ll \varepsilon_2 \sim \varepsilon_1 \ll 1. \tag{6.44}$$

Therefore let us define $\varepsilon \coloneqq \varepsilon_1$ and take the following asymptotic expansions in ε of the form:

$$\chi = \chi^{(0)} + \varepsilon\chi^{(1)} + O(\varepsilon^2), \tag{6.45}$$

where $\chi \in \{x_{\text{ret}}, y_{\text{ret}}, z_{\text{ret}}, w_{\text{ret}}, x_{\text{vit}}, y_{\text{vit}}, z_{\text{vit}}, w_{\text{vit}}, \phi, \psi, \zeta\}$. Upon substitution of this expansion, into Equations 6.26-6.37 we expand to $O(1)$ to find the system is given by:

Retina

$$\frac{\mathrm{d}y_{\text{ret}}^{(0)}}{\mathrm{d}\tau} = -F^{(r)}y_{\text{ret}}^{(0)} + P^{(r)}y_{\text{vit}}^{(0)}, \tag{6.46}$$

Vitreous

$$\frac{\mathrm{d}y_{\text{vit}}^{(0)}}{\mathrm{d}\tau} = \nu P^{(r)}y_{\text{ret}}^{(0)} - G^{(r)}y_{\text{vit}}^{(0)} + \left(\frac{1}{\alpha}\psi^{(0)} - \frac{1}{\beta}y_{\text{vit}}^{(0)}\phi^{(0)}\right), \tag{6.47}$$

$$\frac{1}{\alpha}\frac{\mathrm{d}\phi^{(0)}}{\mathrm{d}\tau} = \left(\frac{1}{\alpha}\psi^{(0)} - \frac{1}{\beta}y_{\text{vit}}^{(0)}\phi^{(0)}\right), \tag{6.48}$$

$$\frac{1}{\alpha}\frac{\mathrm{d}\psi^{(0)}}{\mathrm{d}\tau} = -\left(\frac{1}{\alpha}\psi^{(0)} - \frac{1}{\beta}y_{\text{vit}}^{(0)}\phi^{(0)}\right). \tag{6.49}$$

Here we additionally note that initially:

$$n(0) + m(0) + f(0) + g(0) = n_0 \tag{6.50}$$

$$\Rightarrow \quad \phi(0) + \psi(0) + \varepsilon_3\left(\zeta(0) + \xi(0)\right) = 1 \tag{6.51}$$

$$\Rightarrow \quad \phi^{(0)}(0) + \psi^{(0)}(0) + \varepsilon\left(\phi^{(1)}(0) + \psi^{(1)}(0)\right) + O(\varepsilon_3) = 1 \tag{6.52}$$

$$\Rightarrow \quad \phi^{(0)}(0) + \psi^{(0)}(0) + O(\varepsilon_3) = 1, \tag{6.53}$$

via the non-dimensionalisation given in Equation 6.25. Therefore to $O(1)$ we may take $\phi^{(0)}(0) + \psi^{(0)}(0) = 1$. Noting this result, we find by adding Equations 6.48 and 6.49:

$$\frac{\mathrm{d}}{\mathrm{d}\tau}\left(\psi^{(0)} + \phi^{(0)}\right) = 0 \tag{6.54}$$

$$\Rightarrow \quad \phi^{(0)}(\tau) + \psi^{(0)}(\tau) = 1; \tag{6.55}$$

therefore we may take $\psi^{(0)} = 1 - \phi^{(0)}$. Substituting this expression into Equations 6.46-6.49 gives the system to $O(1)$ as:

Retina

$$\frac{\mathrm{d}y_{\text{ret}}^{(0)}}{\mathrm{d}\tau} = -F^{(r)}y_{\text{ret}}^{(0)} + P^{(r)}y_{\text{vit}}^{(0)}. \tag{6.56}$$

Vitreous

$$\frac{\mathrm{d}y_{\mathrm{vit}}^{(0)}}{\mathrm{d}\tau} = \nu P^{(r)} y_{\mathrm{ret}}^{(0)} - G^{(r)} y_{\mathrm{vit}}^{(0)} + \left(\frac{1}{\alpha}\right)\left[\left(1-\phi^{(0)}\right) - \left(\frac{\alpha}{\beta}\right) y_{\mathrm{vit}}^{(0)}\phi^{(0)}\right], \tag{6.57}$$

$$\frac{\mathrm{d}\phi^{(0)}}{\mathrm{d}\tau} = \left(1-\phi^{(0)}\right) - \left(\frac{\alpha}{\beta}\right) y_{\mathrm{vit}}^{(0)}\phi^{(0)}. \tag{6.58}$$

Therefore we have demonstrated that the non-dimensional system described to first order, as given by Equations 6.56-6.58, is identical to that of the non-dimensional vitreal binding PK ODE model, given by Equations 5.17-5.19, Chapter 5. This can be seen by setting $y_{\mathrm{ret}}^{(0)} = x, y_{\mathrm{vit}}^{(0)} = y$ and $\phi^{(0)} = z$, and noting that the parameter groupings $F^{(r)}, P^{(r)}, \nu P^{(r)}$ and $G^{(r)}$ are precisely equal to A, B, C and D (Equations 5.20-5.21), respectively. Therefore, noting that the same non-dimensionalisation was used in both models, we have demonstrated that the system, to first order, describes the PK of an SVB molecule in the absence of drug. This allows us to decouple the PK from the system; i.e. the PD is slave to PK, and thereby we inherit all the results of Chapter 5. Notably, Equations 5.68, 5.74 and 5.70 of Chapter 5 gives us analytic solutions for $y_{\mathrm{ret}}^{(0)}, y_{\mathrm{vit}}^{(0)}$ and $\phi^{(0)}$, respectively, given by Equations 6.59-6.61 below:

$$y_{\mathrm{ret}}^{(0)} = \left(\frac{P^{(r)}}{F^{(r)}}\right) y_{\mathrm{vit}}^{(0)}, \tag{6.59}$$

$$-\mu\tau + C_0 = \log(y_{\mathrm{vit}}^{(0)}) + \frac{1}{\beta}\left[\frac{\beta}{\alpha y_{\mathrm{vit}}^{(0)} + \beta} + \log\left(\frac{\alpha y_{\mathrm{vit}}^{(0)}}{\alpha y_{\mathrm{vit}}^{(0)} + \beta}\right)\right], \tag{6.60}$$

$$\phi^{(0)}(0) = \frac{1}{1 + (\alpha/\beta)\, y_{\mathrm{vit}}^{(0)}}, \tag{6.61}$$

where

$$\mu = \frac{1}{k_{\mathrm{off}}^{(n)}}\left(\frac{\log 2}{t_{1/2}^{(0)}}\right), \tag{6.62}$$

$$C_0 = \log(y_0) + \frac{1}{\beta}\left[\frac{\beta}{\alpha y_0 + \beta} + \log\left(\frac{\alpha y_0}{\alpha y_0 + \beta}\right)\right], \tag{6.63}$$

$$y_0 = \frac{1}{2}\left[\left(1 - \frac{1+\beta}{\alpha}\right) + \sqrt{\frac{4\beta}{\alpha^2} + \left(\frac{1-\beta}{\alpha} - 1\right)^2}\right]. \tag{6.64}$$

Notice that in Chapter 4, Section 4.1.3, we decoupled PK from PD in the 3-compartment PK/PD model, in an analogous way as we have done here. Therefore, in addition to inheriting the PK solution from Chapter 5, given that the retinal equations (Equations 6.26-6.29) are unchanged from those of Chapter 4 (Equations 4.30-4.33), we also inherit the asymptotic analysis performed on v_{ret} in Chapter 4, Section 4.1.3, up to and including

Equation 4.61. Therefore the intermediate solution for v_{ret} is given by:

$$v_{\text{ret}} \simeq \frac{V_{\text{in}}}{2k_{\text{on}}^{(v)} r_0 V_{\text{ret}}} \left(1 + \frac{p_{\text{RPE}}^{(r)}}{p_{\text{ILM}}^{(r)}}\right) \frac{1}{y_{\text{vit}}^{(0)}(t)}, \tag{6.65}$$

via Equation 6.59. Notice now, using our approximations for $y_{\text{vit}}^{(0)}$, given by Equations 5.150 and 5.137 of Section 5.1.3, for $K_{\text{D}}^{(n)}/r_0 \ll 1$ and $K_{\text{D}}^{(n)}/r_0 \gg 1$, respectively, we may approximate v_{ret} by the piecewise function, as follows:

$$v_{\text{ret}} \simeq \begin{cases} \frac{V_{\text{in}}}{2k_{\text{on}}^{(v)}(r_0 - n_0)V_{\text{ret}}} \left(1 + \frac{p_{\text{RPE}}^{(r)}}{p_{\text{ILM}}^{(r)}}\right) \exp\left\{\left(\frac{\log(2)}{t_{1/2}^{(0)}}\right) t\right\} & \text{for } K_{\text{D}}^{(n)}/r_0 \ll 1, \\ \frac{V_{\text{in}}}{2k_{\text{on}}^{(v)} r_0 V_{\text{ret}}} \left(1 + \frac{p_{\text{RPE}}^{(r)}}{p_{\text{ILM}}^{(r)}}\right) \frac{1}{y_{\text{vit}}^{(0)}(t)} & \text{for } K_{\text{D}}^{(n)}/r_0 \sim 1, \\ \frac{V_{\text{in}}}{2k_{\text{on}}^{(v)} r_0 V_{\text{ret}}} \left(1 + \frac{p_{\text{RPE}}^{(r)}}{p_{\text{ILM}}^{(r)}}\right) \left(\frac{n_0}{K_{\text{D}}^{(n)}} + 1\right) \exp\left\{\left(\frac{\log(2)}{\left(\frac{n_0}{K_{\text{D}}^{(n)}} + 1\right) t_{1/2}^{(0)}}\right) t\right\} & \text{for } K_{\text{D}}^{(n)}/r_0 \gg 1. \end{cases} \tag{6.66}$$

Equations 6.65 and 6.66 demonstrate how the PK behaviour directly prescribes the early time concentration profile of v_{ret}, providing evidence for our hypothesis that the vitreal concentration of the freely diffusing drug, and hence the vitreal effective initial concentration ($c_0 y_0$) and the vitreal half-life ($t_{1/2}$), determine the free VEGF suppression in the retina. In tandem with these effects related to the vitreal binding, we see also that, as in Chapter 4, the concentration of FRV is also inversely proportional to $k_{\text{on}}^{(v)}$ and r_0 - except when $K_{\text{D}}^{(n)} \ll c_0$, whereby instead of being inversely proportional to r_0 it is inversely proportional to $r_0 - n_0$, the remaining non-bound drug post-IVT.

6.3 Non-static vitreal binding molecules: modelling the BI-X molecule

Before we present further analysis of the SVB PK/PD model, we will detail in this section a PK/PD model for an nSVB, in order to compare the theoretical efficacy of both classes of vitreal binders. nSVB molecules aim to bind to larger molecules naturally present in the vitreous (such as albumin), to effectively increase the value of their R_{h} value, decreasing their rate of diffusion and membrane permeability, and hence increasing their ocular $t_{1/2}$. BI-X, a member of the SVB molecule class, is a trispecific 40 kDa antibody capable of binding to human VEGF, ANG-2 and albumin. A preclinical PK study of BI-X in rabbits, performed by Fuchs et al. in 2017 [59], investigated the ability of albumin binding to increase ocular $t_{1/2}$. The results were very promising; the ocular $t_{1/2}$ increased from 3.2 to 10 days after the introduction of human albumin into the rabbit model. We will consider the BI-X in our modelling of nSVB, in comparison to Fab SVB discussed up to this point.

Given the limited information available regarding the BI-X molecule, we will make a variety of simplifications in our modelling of it, however, all simplifications made will only decrease the potential efficacy of the molecule, therefore any simulations will be underestimations of the molecule's performance - not exaggerations of it. The first simplification we will make will be to omit any BI-X ANG-2 interactions. Given that the molecule can simultaneously bind VEGF and ANG-2, the portion of BI-X molecules bound to ANG-2 will have a larger R_{h} value, and hence decay at a slower rate, increasing their $t_{1/2}$, and hence (as we have demonstrated at numerous times during this thesis) increasing their efficacy. Therefore by omitting BI-X ANG-2 binding we will be underestimating the BI-X molecule's anti-VEGF ability. We will assume that the BI-X molecule (B), given its molecular weight of 40 kDa, has a similar R_{h} value to that of a Fab molecule, and therefore take it to be equal to 3.04 nm, as in Appendix A.6. Similarly we will assume VEGF-BI-X (VB) complexes have the same R_{h} values as VEGF-Fab complexes, given in Table 4.3 of Chapter 4, as well as all larger complexes (BVBA and ABVBA). Finally, given the lack of information regarding a BI-X molecule bound to both VEGF and albumin (A) we will assume a VBA complex possesses the same R_{h} value as a BA complex. Again this simplification will only cause a decrease in drug efficacy, as theoretically a VBA complex, with a larger R_{h} value than a BA complex, should decay more slowly. The chemical species present within the system are detailed in Table 6.2, alongside their R_{h} values.

Species	Conc. (pM)	R_{h} (nm)	Description
V	$v(t)$	2.39*	VEGF
B	$b(t)$	3.04†	BI-X
VB	$c(t)$	3.29*	VEGF-BI-X complex
BVB	$d(t)$	4.07*	BI-X-VEGF-BI-X complex
A	$a(t)$	7.8 [130]	Albumin
BA	$f(t)$	$R_{\mathrm{h}}^{(\mathrm{BA})}$	BI-X-albumin complex
VBA	$g(t)$	$R_{\mathrm{h}}^{(\mathrm{BA})}$	VEGF-BI-X-albumin complex
BVBA	$h(t)$	$R_{\mathrm{h}}^{(\mathrm{BA})}$	BI-X-VEGF-BI-X-albumin complex
ABVBA	$j(t)$	$R_{\mathrm{h}}^{(\mathrm{BA})}$	Albumin-BI-X-VEGF-BI-X-albumin complex

Table 6.2: Model chemical species. R_{h} denotes molecular hydrodynamic radii. Note, all concentrations are functions of time (t) and are expressed in pM. This notation will additionally include subscripts to denote to which compartment each concentration refers, e.g. v_{ret} is the concentration of V in the retina, whereas v_{vit} is the concentration of V in the vitreous. *These values are taken from Table 4.3, where the R_{h} values of VR and VB are assumed to be the same. †The R_{h} value for the BI-X molecule was assumed to be the same as that for the Fab molecule, as given in Appendix A.6.

Given the chemical species in Table 6.2 the chemical reactions possible within the system

are defined as follows:

$$\mathrm{V} + \mathrm{B} \underset{2k_{\mathrm{on}}^{(v)}}{\overset{k_{\mathrm{off}}^{(v)}}{\rightleftharpoons}} \mathrm{VB}, \qquad \mathrm{B} + \mathrm{A} \underset{k_{\mathrm{on}}^{(a)}}{\overset{k_{\mathrm{off}}^{(a)}}{\rightleftharpoons}} \mathrm{BA}, \tag{6.67}$$

$$\mathrm{B} + \mathrm{VB} \underset{k_{\mathrm{on}}^{(v)}}{\overset{2k_{\mathrm{off}}^{(v)}}{\rightleftharpoons}} \mathrm{BVB}, \qquad \mathrm{VB} + \mathrm{A} \underset{k_{\mathrm{on}}^{(a)}}{\overset{k_{\mathrm{off}}^{(a)}}{\rightleftharpoons}} \mathrm{VBA}, \qquad \mathrm{V} + \mathrm{BA} \underset{2k_{\mathrm{on}}^{(v)}}{\overset{k_{\mathrm{off}}^{(v)}}{\rightleftharpoons}} \mathrm{VBA}, \tag{6.68}$$

$$\mathrm{BVB} + \mathrm{A} \underset{2k_{\mathrm{on}}^{(a)}}{\overset{k_{\mathrm{off}}^{(a)}}{\rightleftharpoons}} \mathrm{BVBA}, \qquad \mathrm{VB} + \mathrm{BA} \underset{k_{\mathrm{on}}^{(v)}}{\overset{k_{\mathrm{off}}^{(v)}}{\rightleftharpoons}} \mathrm{BVBA}, \qquad \mathrm{B} + \mathrm{VBA} \underset{k_{\mathrm{on}}^{(v)}}{\overset{k_{\mathrm{off}}^{(v)}}{\rightleftharpoons}} \mathrm{BVBA}, \tag{6.69}$$

$$\mathrm{ABVB} + \mathrm{A} \underset{k_{\mathrm{on}}^{(a)}}{\overset{2k_{\mathrm{off}}^{(a)}}{\rightleftharpoons}} \mathrm{ABVBA}, \qquad \mathrm{VBA} + \mathrm{BA} \underset{k_{\mathrm{on}}^{(v)}}{\overset{2k_{\mathrm{off}}^{(v)}}{\rightleftharpoons}} \mathrm{ABVBA}, \tag{6.70}$$

where reaction rates $k_{\mathrm{off}}^{(a)}$ and $k_{\mathrm{on}}^{(a)}$ are the off and on binding rates between the BI-X molecule and albumin, respectively. In order to formulate a PK/PD ODE model for the BI-X molecule we extend the 3-compartment PK model of Section 3.1 to additionally describe reaction kinetics between the drug, VEGF and albumin, as defined by Equations 6.67-6.70. We do this in an analogous manner to how we extended the 3-compartment PK model to the 3-compartment PK/PD model of Chapter 5. As there are no available data on the binding affinity between BI-X and VEGF, we assume the VEGF binding site of the BI-X molecule to be identical to the theoretical single ranibizumab binding site, i.e. the off and on binding rates between BI-X and VEGF are given by $k_{\mathrm{off}}^{(v)}$ and $k_{\mathrm{on}}^{(v)}$, respectively, as in Equations 6.4-6.15. Additionally, we model a source of albumin within the retina, to represent influx of albumin via the choroid at rate A_{in} fmol/day. The BI-X model is then defined by the nonlinear ODE system, Equations 6.71-6.89:

Retina

$$\begin{aligned}\frac{\mathrm{d}v_{\mathrm{ret}}}{\mathrm{d}t} = &-\frac{S_{\mathrm{ret}}}{V_{\mathrm{ret}}}\left(p_{\mathrm{ILM}}^{(v)} + p_{\mathrm{RPE}}^{(v)}\right) v_{\mathrm{ret}} + \frac{S_{\mathrm{ret}}}{V_{\mathrm{ret}}} p_{\mathrm{ILM}}^{(v)} v_{\mathrm{vit}} + \left(k_{\mathrm{off}}^{(v)} c_{\mathrm{ret}} - 2k_{\mathrm{on}}^{(v)} v_{\mathrm{ret}} b_{\mathrm{ret}}\right) \\ &+ \left(k_{\mathrm{off}}^{(v)} g_{\mathrm{ret}} - 2k_{\mathrm{on}}^{(v)} v_{\mathrm{ret}} f_{\mathrm{ret}}\right) \\ &+ \frac{V_{\mathrm{in}}}{V_{\mathrm{ret}}},\end{aligned} \tag{6.71}$$

$$\begin{aligned}\frac{\mathrm{d}b_{\mathrm{ret}}}{\mathrm{d}t} = &-\frac{S_{\mathrm{ret}}}{V_{\mathrm{ret}}}\left(p_{\mathrm{ILM}}^{(b)} + p_{\mathrm{RPE}}^{(b)}\right) b_{\mathrm{ret}} + \frac{S_{\mathrm{ret}}}{V_{\mathrm{ret}}} p_{\mathrm{ILM}}^{(b)} b_{\mathrm{vit}} + \left(k_{\mathrm{off}}^{(v)} c_{\mathrm{ret}} - 2k_{\mathrm{on}}^{(v)} v_{\mathrm{ret}} b_{\mathrm{ret}}\right) \\ &+ \left(k_{\mathrm{off}}^{(a)} f_{\mathrm{ret}} - k_{\mathrm{on}}^{(a)} b_{\mathrm{ret}} a_{\mathrm{ret}}\right) \\ &+ \left(2k_{\mathrm{off}}^{(v)} d_{\mathrm{ret}} - k_{\mathrm{on}}^{(v)} c_{\mathrm{ret}} b_{\mathrm{ret}}\right) \\ &+ \left(k_{\mathrm{off}}^{(v)} h_{\mathrm{ret}} - k_{\mathrm{on}}^{(v)} b_{\mathrm{ret}} g_{\mathrm{ret}}\right),\end{aligned} \tag{6.72}$$

$$\frac{\mathrm{d}c_{\mathrm{ret}}}{\mathrm{d}t} = -\frac{S_{\mathrm{ret}}}{V_{\mathrm{ret}}}\left(p^{(c)}_{\mathrm{ILM}} + p^{(c)}_{\mathrm{RPE}}\right)c_{\mathrm{ret}} + \frac{S_{\mathrm{ret}}}{V_{\mathrm{ret}}}p^{(c)}_{\mathrm{ILM}}c_{\mathrm{vit}} - \left(k^{(v)}_{\mathrm{off}}c_{\mathrm{ret}} - 2k^{(v)}_{\mathrm{on}}v_{\mathrm{ret}}b_{\mathrm{ret}}\right) + \left(k^{(a)}_{\mathrm{off}}g_{\mathrm{ret}} - k^{(a)}_{\mathrm{on}}c_{\mathrm{ret}}a_{\mathrm{ret}}\right) + \left(2k^{(v)}_{\mathrm{off}}d_{\mathrm{ret}} - k^{(v)}_{\mathrm{on}}c_{\mathrm{ret}}b_{\mathrm{ret}}\right) + \left(k^{(v)}_{\mathrm{off}}h_{\mathrm{ret}} - k^{(v)}_{\mathrm{on}}c_{\mathrm{ret}}f_{\mathrm{ret}}\right), \tag{6.73}$$

$$\frac{\mathrm{d}d_{\mathrm{ret}}}{\mathrm{d}t} = -\frac{S_{\mathrm{ret}}}{V_{\mathrm{ret}}}\left(p^{(d)}_{\mathrm{ILM}} + p^{(d)}_{\mathrm{RPE}}\right)d_{\mathrm{ret}} + \frac{S_{\mathrm{ret}}}{V_{\mathrm{ret}}}p^{(d)}_{\mathrm{ILM}}d_{\mathrm{vit}} - \left(2k^{(v)}_{\mathrm{off}}d_{\mathrm{ret}} - k^{(v)}_{\mathrm{on}}c_{\mathrm{ret}}b_{\mathrm{ret}}\right) + \left(k^{(a)}_{\mathrm{off}}h_{\mathrm{ret}} - 2k^{(a)}_{\mathrm{on}}d_{\mathrm{ret}}a_{\mathrm{ret}}\right), \tag{6.74}$$

$$\frac{\mathrm{d}a_{\mathrm{ret}}}{\mathrm{d}t} = -\frac{S_{\mathrm{ret}}}{V_{\mathrm{ret}}}\left(p^{(a)}_{\mathrm{ILM}} + p^{(a)}_{\mathrm{RPE}}\right)a_{\mathrm{ret}} + \frac{S_{\mathrm{ret}}}{V_{\mathrm{ret}}}p^{(a)}_{\mathrm{ILM}}a_{\mathrm{vit}} + \left(k^{(a)}_{\mathrm{off}}f_{\mathrm{ret}} - k^{(a)}_{\mathrm{on}}b_{\mathrm{ret}}a_{\mathrm{ret}}\right) + \left(k^{(a)}_{\mathrm{off}}g_{\mathrm{ret}} - k^{(a)}_{\mathrm{on}}c_{\mathrm{ret}}a_{\mathrm{ret}}\right) + \left(k^{(a)}_{\mathrm{off}}h_{\mathrm{ret}} - 2k^{(a)}_{\mathrm{on}}d_{\mathrm{ret}}a_{\mathrm{ret}}\right) + \left(2k^{(a)}_{\mathrm{off}}j_{\mathrm{ret}} - k^{(a)}_{\mathrm{on}}a_{\mathrm{ret}}h_{\mathrm{ret}}\right) + \frac{A_{\mathrm{in}}}{V_{\mathrm{ret}}}, \tag{6.75}$$

$$\frac{\mathrm{d}f_{\mathrm{ret}}}{\mathrm{d}t} = -\frac{S_{\mathrm{ret}}}{V_{\mathrm{ret}}}\left(p^{(f)}_{\mathrm{ILM}} + p^{(f)}_{\mathrm{RPE}}\right)f_{\mathrm{ret}} + \frac{S_{\mathrm{ret}}}{V_{\mathrm{ret}}}p^{(f)}_{\mathrm{ILM}}f_{\mathrm{vit}} - \left(k^{(a)}_{\mathrm{off}}f_{\mathrm{ret}} - k^{(a)}_{\mathrm{on}}b_{\mathrm{ret}}a_{\mathrm{ret}}\right) + \left(k^{(v)}_{\mathrm{off}}g_{\mathrm{ret}} - 2k^{(v)}_{\mathrm{on}}v_{\mathrm{ret}}f_{\mathrm{ret}}\right) + \left(k^{(v)}_{\mathrm{off}}h_{\mathrm{ret}} - k^{(v)}_{\mathrm{on}}c_{\mathrm{ret}}f_{\mathrm{ret}}\right) + \left(2k^{(v)}_{\mathrm{off}}j_{\mathrm{ret}} - k^{(v)}_{\mathrm{on}}g_{\mathrm{ret}}f_{\mathrm{ret}}\right), \tag{6.76}$$

$$\frac{\mathrm{d}g_{\mathrm{ret}}}{\mathrm{d}t} = -\frac{S_{\mathrm{ret}}}{V_{\mathrm{ret}}}\left(p^{(g)}_{\mathrm{ILM}} + p^{(g)}_{\mathrm{RPE}}\right)g_{\mathrm{ret}} + \frac{S_{\mathrm{ret}}}{V_{\mathrm{ret}}}p^{(g)}_{\mathrm{ILM}}g_{\mathrm{vit}} - \left(k^{(a)}_{\mathrm{off}}g_{\mathrm{ret}} - k^{(a)}_{\mathrm{on}}c_{\mathrm{ret}}a_{\mathrm{ret}}\right) - \left(k^{(v)}_{\mathrm{off}}g_{\mathrm{ret}} - 2k^{(v)}_{\mathrm{on}}v_{\mathrm{ret}}f_{\mathrm{ret}}\right) + \left(k^{(v)}_{\mathrm{off}}h_{\mathrm{ret}} - k^{(v)}_{\mathrm{on}}b_{\mathrm{ret}}g_{\mathrm{ret}}\right) + \left(2k^{(v)}_{\mathrm{off}}j_{\mathrm{ret}} - k^{(v)}_{\mathrm{on}}g_{\mathrm{ret}}f_{\mathrm{ret}}\right), \tag{6.77}$$

$$\frac{\mathrm{d}h_{\mathrm{ret}}}{\mathrm{d}t} = -\frac{S_{\mathrm{ret}}}{V_{\mathrm{ret}}}\left(p^{(h)}_{\mathrm{ILM}} + p^{(h)}_{\mathrm{RPE}}\right)h_{\mathrm{ret}} + \frac{S_{\mathrm{ret}}}{V_{\mathrm{ret}}}p^{(h)}_{\mathrm{ILM}}h_{\mathrm{vit}} - \left(k^{(a)}_{\mathrm{off}}h_{\mathrm{ret}} - 2k^{(a)}_{\mathrm{on}}d_{\mathrm{ret}}a_{\mathrm{ret}}\right) - \left(k^{(v)}_{\mathrm{off}}h_{\mathrm{ret}} - k^{(v)}_{\mathrm{on}}c_{\mathrm{ret}}f_{\mathrm{ret}}\right) - \left(k^{(v)}_{\mathrm{off}}h_{\mathrm{ret}} - k^{(v)}_{\mathrm{on}}b_{\mathrm{ret}}g_{\mathrm{ret}}\right) + \left(2k^{(a)}_{\mathrm{off}}j_{\mathrm{ret}} - k^{(a)}_{\mathrm{on}}a_{\mathrm{ret}}h_{\mathrm{ret}}\right), \tag{6.78}$$

$$\frac{\mathrm{d}j_{\mathrm{ret}}}{\mathrm{d}t} = -\frac{S_{\mathrm{ret}}}{V_{\mathrm{ret}}}\left(p^{(j)}_{\mathrm{ILM}} + p^{(j)}_{\mathrm{RPE}}\right) j_{\mathrm{ret}} + \frac{S_{\mathrm{ret}}}{V_{\mathrm{ret}}} p^{(j)}_{\mathrm{ILM}} j_{\mathrm{vit}} - \left(2k^{(a)}_{\mathrm{off}} j_{\mathrm{ret}} - k^{(a)}_{\mathrm{on}} a_{\mathrm{ret}} h_{\mathrm{ret}}\right) - \left(2k^{(v)}_{\mathrm{off}} j_{\mathrm{ret}} - k^{(v)}_{\mathrm{on}} g_{\mathrm{ret}} f_{\mathrm{ret}}\right), \tag{6.79}$$

Vitreous

$$\frac{\mathrm{d}v_{\mathrm{vit}}}{\mathrm{d}t} = \frac{S_{\mathrm{ret}}}{V_{\mathrm{vit}}} p^{(v)}_{\mathrm{ILM}} v_{\mathrm{ret}} - \left(\frac{S_{\mathrm{ret}}}{V_{\mathrm{vit}}} p^{(v)}_{\mathrm{ILM}} + k^{(v)}_{\mathrm{el}}\right) v_{\mathrm{vit}} + \left(k^{(v)}_{\mathrm{off}} c_{\mathrm{vit}} - 2k^{(v)}_{\mathrm{on}} v_{\mathrm{vit}} b_{\mathrm{vit}}\right) + \left(k^{(v)}_{\mathrm{off}} g_{\mathrm{vit}} - 2k^{(v)}_{\mathrm{on}} v_{\mathrm{vit}} f_{\mathrm{vit}}\right), \tag{6.80}$$

$$\frac{\mathrm{d}b_{\mathrm{vit}}}{\mathrm{d}t} = \frac{S_{\mathrm{ret}}}{V_{\mathrm{vit}}} p^{(b)}_{\mathrm{ILM}} b_{\mathrm{ret}} - \left(\frac{S_{\mathrm{ret}}}{V_{\mathrm{vit}}} p^{(b)}_{\mathrm{ILM}} + k^{(b)}_{\mathrm{el}}\right) b_{\mathrm{vit}} + \left(k^{(v)}_{\mathrm{off}} c_{\mathrm{vit}} - 2k^{(v)}_{\mathrm{on}} v_{\mathrm{vit}} b_{\mathrm{vit}}\right) + \left(k^{(a)}_{\mathrm{off}} f_{\mathrm{vit}} - k^{(a)}_{\mathrm{on}} b_{\mathrm{vit}} a_{\mathrm{vit}}\right) + \left(2k^{(v)}_{\mathrm{off}} d_{\mathrm{vit}} - k^{(v)}_{\mathrm{on}} c_{\mathrm{vit}} b_{\mathrm{vit}}\right) + \left(k^{(v)}_{\mathrm{off}} h_{\mathrm{vit}} - k^{(v)}_{\mathrm{on}} b_{\mathrm{vit}} g_{\mathrm{vit}}\right), \tag{6.81}$$

$$\frac{\mathrm{d}c_{\mathrm{vit}}}{\mathrm{d}t} = \frac{S_{\mathrm{ret}}}{V_{\mathrm{vit}}} p^{(c)}_{\mathrm{ILM}} c_{\mathrm{ret}} - \left(\frac{S_{\mathrm{ret}}}{V_{\mathrm{vit}}} p^{(c)}_{\mathrm{ILM}} + k^{(c)}_{\mathrm{el}}\right) c_{\mathrm{vit}} - \left(k^{(v)}_{\mathrm{off}} c_{\mathrm{vit}} - 2k^{(v)}_{\mathrm{on}} v_{\mathrm{vit}} b_{\mathrm{vit}}\right) + \left(k^{(a)}_{\mathrm{off}} g_{\mathrm{vit}} - k^{(a)}_{\mathrm{on}} c_{\mathrm{vit}} a_{\mathrm{vit}}\right) + \left(2k^{(v)}_{\mathrm{off}} d_{\mathrm{vit}} - k^{(v)}_{\mathrm{on}} c_{\mathrm{vit}} b_{\mathrm{vit}}\right) + \left(k^{(v)}_{\mathrm{off}} h_{\mathrm{vit}} - k^{(v)}_{\mathrm{on}} c_{\mathrm{vit}} f_{\mathrm{vit}}\right), \tag{6.82}$$

$$\frac{\mathrm{d}d_{\mathrm{vit}}}{\mathrm{d}t} = \frac{S_{\mathrm{ret}}}{V_{\mathrm{vit}}} p^{(d)}_{\mathrm{ILM}} d_{\mathrm{ret}} - \left(\frac{S_{\mathrm{ret}}}{V_{\mathrm{vit}}} p^{(d)}_{\mathrm{ILM}} + k^{(d)}_{\mathrm{el}}\right) d_{\mathrm{vit}} - \left(2k^{(v)}_{\mathrm{off}} d_{\mathrm{vit}} - k^{(v)}_{\mathrm{on}} c_{\mathrm{vit}} b_{\mathrm{vit}}\right) + \left(k^{(a)}_{\mathrm{off}} h_{\mathrm{vit}} - 2k^{(a)}_{\mathrm{on}} d_{\mathrm{vit}} a_{\mathrm{vit}}\right), \tag{6.83}$$

$$\frac{\mathrm{d}a_{\mathrm{vit}}}{\mathrm{d}t} = \frac{S_{\mathrm{ret}}}{V_{\mathrm{vit}}} p^{(a)}_{\mathrm{ILM}} a_{\mathrm{ret}} - \left(\frac{S_{\mathrm{ret}}}{V_{\mathrm{vit}}} p^{(a)}_{\mathrm{ILM}} + k^{(a)}_{\mathrm{el}}\right) a_{\mathrm{vit}} + \left(k^{(a)}_{\mathrm{off}} f_{\mathrm{vit}} - k^{(a)}_{\mathrm{on}} b_{\mathrm{vit}} a_{\mathrm{vit}}\right) + \left(k^{(a)}_{\mathrm{off}} g_{\mathrm{vit}} - k^{(a)}_{\mathrm{on}} c_{\mathrm{vit}} a_{\mathrm{vit}}\right) + \left(k^{(a)}_{\mathrm{off}} h_{\mathrm{vit}} - 2k^{(a)}_{\mathrm{on}} d_{\mathrm{vit}} a_{\mathrm{vit}}\right) + \left(2k^{(a)}_{\mathrm{off}} j_{\mathrm{vit}} - k^{(a)}_{\mathrm{on}} a_{\mathrm{vit}} h_{\mathrm{vit}}\right), \tag{6.84}$$

$$\frac{\mathrm{d}f_{\mathrm{vit}}}{\mathrm{d}t} = \frac{S_{\mathrm{ret}}}{V_{\mathrm{vit}}} p^{(f)}_{\mathrm{ILM}} f_{\mathrm{ret}} - \left(\frac{S_{\mathrm{ret}}}{V_{\mathrm{vit}}} p^{(f)}_{\mathrm{ILM}} + k^{(f)}_{\mathrm{el}}\right) f_{\mathrm{vit}} - \left(k^{(a)}_{\mathrm{off}} f_{\mathrm{vit}} - k^{(a)}_{\mathrm{on}} b_{\mathrm{vit}} a_{\mathrm{vit}}\right) + \left(k^{(v)}_{\mathrm{off}} g_{\mathrm{vit}} - 2k^{(v)}_{\mathrm{on}} v_{\mathrm{vit}} f_{\mathrm{vit}}\right) + \left(k^{(v)}_{\mathrm{off}} h_{\mathrm{vit}} - k^{(v)}_{\mathrm{on}} c_{\mathrm{vit}} f_{\mathrm{vit}}\right) + \left(2k^{(v)}_{\mathrm{off}} j_{\mathrm{vit}} - k^{(v)}_{\mathrm{on}} g_{\mathrm{vit}} f_{\mathrm{vit}}\right), \tag{6.85}$$

$$\frac{\mathrm{d}g_{\mathrm{vit}}}{\mathrm{d}t} = \frac{S_{\mathrm{ret}}}{V_{\mathrm{vit}}} p^{(g)}_{\mathrm{ILM}} g_{\mathrm{ret}} - \left(\frac{S_{\mathrm{ret}}}{V_{\mathrm{vit}}} p^{(g)}_{\mathrm{ILM}} + k^{(g)}_{\mathrm{el}}\right) g_{\mathrm{vit}} - \left(k^{(a)}_{\mathrm{off}} g_{\mathrm{vit}} - k^{(a)}_{\mathrm{on}} c_{\mathrm{vit}} a_{\mathrm{vit}}\right) - \left(k^{(v)}_{\mathrm{off}} g_{\mathrm{vit}} - 2k^{(v)}_{\mathrm{on}} v_{\mathrm{vit}} f_{\mathrm{vit}}\right) + \left(k^{(v)}_{\mathrm{off}} h_{\mathrm{vit}} - k^{(v)}_{\mathrm{on}} b_{\mathrm{vit}} g_{\mathrm{vit}}\right) + \left(2k^{(v)}_{\mathrm{off}} j_{\mathrm{vit}} - k^{(v)}_{\mathrm{on}} g_{\mathrm{vit}} f_{\mathrm{vit}}\right), \tag{6.86}$$

$$\frac{\mathrm{d}h_{\mathrm{vit}}}{\mathrm{d}t} = \frac{S_{\mathrm{ret}}}{V_{\mathrm{vit}}} p^{(h)}_{\mathrm{ILM}} h_{\mathrm{ret}} - \left(\frac{S_{\mathrm{ret}}}{V_{\mathrm{vit}}} p^{(h)}_{\mathrm{ILM}} + k^{(h)}_{\mathrm{el}}\right) h_{\mathrm{vit}} - \left(k^{(a)}_{\mathrm{off}} h_{\mathrm{vit}} - 2k^{(a)}_{\mathrm{on}} d_{\mathrm{vit}} a_{\mathrm{vit}}\right) - \left(k^{(v)}_{\mathrm{off}} h_{\mathrm{vit}} - k^{(v)}_{\mathrm{on}} c_{\mathrm{vit}} f_{\mathrm{vit}}\right) - \left(k^{(v)}_{\mathrm{off}} h_{\mathrm{vit}} - k^{(v)}_{\mathrm{on}} b_{\mathrm{vit}} g_{\mathrm{vit}}\right) + \left(2k^{(a)}_{\mathrm{off}} j_{\mathrm{vit}} - k^{(a)}_{\mathrm{on}} a_{\mathrm{vit}} h_{\mathrm{vit}}\right), \tag{6.87}$$

$$\frac{\mathrm{d}j_{\mathrm{vit}}}{\mathrm{d}t} = \frac{S_{\mathrm{ret}}}{V_{\mathrm{vit}}} p^{(j)}_{\mathrm{ILM}} j_{\mathrm{ret}} - \left(\frac{S_{\mathrm{ret}}}{V_{\mathrm{vit}}} p^{(j)}_{\mathrm{ILM}} + k^{(j)}_{\mathrm{el}}\right) j_{\mathrm{vit}} - \left(2k^{(a)}_{\mathrm{off}} j_{\mathrm{vit}} - k^{(a)}_{\mathrm{on}} a_{\mathrm{vit}} h_{\mathrm{vit}}\right) - \left(2k^{(v)}_{\mathrm{off}} j_{\mathrm{vit}} - k^{(v)}_{\mathrm{on}} g_{\mathrm{vit}} f_{\mathrm{vit}}\right). \tag{6.88}$$

All parameters in Equations 6.71-6.89 not already discussed are defined in Table 4.2 and are identically defined and generated as those in Chapter 4, i.e. permeabilities are generated via Equations 4.19-4.20, and k_{el} from Equation 4.24. The initial conditions of the system are then given by:

$$v_{\mathrm{ret}}(0) = v_0^{(\mathrm{ret})}, \quad b_{\mathrm{ret}}(0) = 0, \quad c_{\mathrm{ret}}(0) = 0, \tag{6.89}$$

$$d_{\mathrm{ret}}(0) = 0, \quad a_{\mathrm{ret}}(0) = a_0^{(\mathrm{ret})}, \quad f_{\mathrm{ret}}(0) = 0, \tag{6.90}$$

$$g_{\mathrm{ret}}(0) = 0, \quad h_{\mathrm{ret}}(0) = 0, \quad j_{\mathrm{ret}}(0) = 0, \tag{6.91}$$

$$v_{\mathrm{vit}}(0) = v_0^{(\mathrm{vit})}, \quad b_{\mathrm{vit}}(0) = b_0, \quad c_{\mathrm{vit}}(0) = 0, \tag{6.92}$$

$$d_{\mathrm{vit}}(0) = 0, \quad a_{\mathrm{vit}}(0) = a_0^{(\mathrm{vit})}, \quad f_{\mathrm{vit}}(0) = 0, \tag{6.93}$$

$$g_{\mathrm{vit}}(0) = 0, \quad h_{\mathrm{vit}}(0) = 0, \quad j_{\mathrm{vit}}(0) = 0, \tag{6.94}$$

where b_0 is the initial concentration of BI-X, and $v_0^{(\mathrm{ret})}, v_0^{(\mathrm{vit})}, a_0^{(\mathrm{ret})}$ and $a_0^{(\mathrm{vit})}$ are determined by solving the system in the absence of drug (see Equation 4.25). If the equilibrium concentration of albumin in the vitreous, $a_0^{(\mathrm{vit})}$, is known it is possible to generate a value for A_{in}, and hence find $a_0^{(\mathrm{ret})}$. From Fuchs et al. [59] we take the total quantity of albumin in one human vitreous to be 20 nmols, allowing us to find $a_0^{(\mathrm{vit})}(0)$, from which we can determine A_{in}. Additionally as $K_{\mathrm{D}}^{(a)} = 1.4$ nM [59], by setting $k_{\mathrm{off}}^{(a)} \gg k_{\mathrm{el}}^{(a)}$, i.e. assuming the albumin and BI-X are in chemical equilibrium, we may generate a value for $k_{\mathrm{on}}^{(a)}$ using $k_{\mathrm{off}}^{(a)}/K_{\mathrm{D}}^{(a)}$.

All that remains to be done to fully parametrise this system, given these assumptions, is to estimate the hydrodynamic radius of the BA complex, $R_{\mathrm{h}}^{(\mathrm{BA})}$. We do this in a similar manner to which we estimated the half-life of a molecule with a known hydrodynamic radius, using Equation 4.21 of Chapter 4. Rearranging Equation 4.21 we find $R_{\mathrm{h}}^{(\mathrm{BA})}$ may be estimated via:

$$R_{\mathrm{h}}^{(\mathrm{BA})} = \left(\frac{t_{1/2}^{(\mathrm{BA,\ rabbit})}}{t_{1/2}^{(\mathrm{Fab,\ rabbit})}} \right) \times R_{\mathrm{h}}^{(\mathrm{Fab})} = 9.56 \text{ nm} \tag{6.95}$$

where $t_{1/2}^{(\mathrm{BA,\ rabbit})} = 10$ days, $t_{1/2}^{(\mathrm{Fab,\ rabbit})} = 3.18$ days and $R_{\mathrm{h}}^{(Fab)} = 3.04$ nm are the half-life of the BA complex in the rabbit (from Fuchs et al. 2017 [59]), the half-life of a Fab molecule in the rabbit (Appendix A.6), and the hydrodynamic radius of a Fab molecule (Appendix A.6), respectively. This value of 9.56 nm is very high in comparison to the R_{h} values detailed in Appendix A.6; the authors of Fuchs et al. [59] note this apparent non-conformity, stating: *"This demonstrates that an apparent M_W increase increases the ocular half-life and the increase is more pronounced for BI-X (with and without albumin) compared to other molecules between 40 and 150 kDa."*. Using this value for $R_{\mathrm{h}}^{(\mathrm{BA})}$ we then estimate the half-life of the BA complex in the human, $t_{1/2}^{(\mathrm{BA,\ human})}$, to be:

$$t_{1/2}^{(\mathrm{BA,\ human})}\left(R_{\mathrm{h}}^{(\mathrm{BA})}\right) = \left(\frac{t_{1/2}^{(\mathrm{Fab,\ rabbit})}}{R_{\mathrm{h}}^{(\mathrm{Fab})}} \right) \times R_{\mathrm{h}}^{(\mathrm{BA})} \tag{6.96}$$

$$= \left(\frac{t_{1/2}^{(\mathrm{Fab,\ human})}}{t_{1/2}^{(\mathrm{Fab,\ rabbit})}} \right) \times t_{1/2}^{(\mathrm{BA,\ rabbit})} \simeq 22.1 \text{ days} \tag{6.97}$$

as in Equation 4.21 of Chapter 4, which we can see is independent of our estimated value for $R_{\mathrm{h}}^{(\mathrm{BA})}$.

Finally, before presenting a comparison between the BI-X PK/PD model solution and that of the SVB, we first detail the following PK results. As $a_0^{(\mathrm{vit})}(0) \sim O(10^7)$ pM and $b_0 \sim O(10^6)$ pM, we may take $b_0 \ll a_0^{(\mathrm{vit})}$, which allows us to approximate $a(t)$ and $f(t)$ by the following

$$a_{\mathrm{vit}}(t) \simeq a_0^{(\mathrm{vit})}, \tag{6.98}$$

$$f_{\mathrm{vit}}(t) \simeq b_0 \mathrm{e}^{-\lambda^{(\mathrm{BA})}t}, \tag{6.99}$$

where $\lambda^{(\mathrm{BA})}$ is the decay rate associated with BA. Therefore assuming that our system

remains in chemical equilibrium, i.e. that $\lambda^{(\mathrm{BA})} \ll k_{\mathrm{off}}^{(\mathrm{a})}$, the following holds

$$K_{\mathrm{D}}^{(a)} f_{\mathrm{vit}} \simeq a_{\mathrm{vit}} b_{\mathrm{vit}} \tag{6.100}$$

$$\Rightarrow \quad b_{\mathrm{vit}} \simeq \left(\frac{b_0 K_{\mathrm{D}}^{(a)}}{a_0^{(\mathrm{vit})}} \right) \mathrm{e}^{-\lambda^{(\mathrm{BA})} t}. \tag{6.101}$$

Equations 6.99 and 6.101 demonstrate that both B and BA molecules decay in the vitreous with the extended half-life of the BA molecule. Additionally, as the concentration of the retina can be taken as proportional to that of the vitreous, we conclude B and BA decay in the retina at the same rate as that of the vitreous. We will now move on to compare and discuss the simulated PK/PD of the BI-X molecule, an SVB equivalent of ranibizumab, and ranibizumab.

6.4 PK/PD comparison of static/non-static vitreal binders versus ranibizumab

In this section we will discuss Figures 6.1-6.7, compare the theoretical PK/PD, after a single IVT injection of, SVB molecules (Equations 6.4-6.15), nSVB BI-X molecules (Equations 6.71-6.89) and ranibizumab (Equations 4.3-4.18). In all simulations each molecule is dosed at 0.5 mg at $t = 0$, and the binding kinetics of each molecule with VEGF are assumed to be that of ranibizumab, characterised in Chapter 4, such that $k_{\mathrm{off}}^{(v)} = 0.864$ 1/day and $K_{\mathrm{D}}^{(v)} = 19000$ pM. We note that as each molecule has exactly one VEGF binding site, an equal dosage comparison is equivalent to an equal binding site comparison. Additionally, in all solutions V_{in} is taken as 20 fmol/day, a representative value from the analysis presented in Figure 4.6 in Chapter 4. Each figure details the model solutions for 5 distinct locations in $\left(K_{\mathrm{D}}^{(n)}, n_0\right)$ parameter space, given explicitly in the figure legend, with their locations marked on a plot of t_{dur} (Equation 5.131) in the bottom-rightmost sub-plot. Recall from Chapter 5 that t_{dur} represents the time taken for the concentration of the SVB to reach a specific value. Here t_{dur} is evaluated for $r_{5\%} = 0.05 \times r_0$, 5% of the initially injected concentration, where we note that $c_{30}^{(r)} = 0.0539 \times r_0$. We shall refer to the ith SVB model solution, in each subsequent figure, as plot (i). Finally we note that in each figure, as dose remains constant and ranibizumab and the BI-X molecule are independent of $\left(K_{\mathrm{D}}^{(n)}, n_0\right)$ parameter space, the solutions for these models will be identical between Figures 6.1-6.7.

In Figures 6.1-6.7, as well as Figures 6.8-6.10 and 6.12-6.22, of Sections 6.5 and 6.6, respectively, dashed lines show solutions for the nSVB model (Equations 4.3-4.18), solid coloured lines (denoted as black in the figure legend to indicate model specific line style) show solutions to SVB PK/PD model (Equations 6.4-6.15) and dotted lines show solution

to BI-X model (Equations 6.71-6.89). Retinal and vitreal free VEGF solutions for all models are given by the variables v_{ret} and v_{vit}, respectively. Drug concentration for the nSVB and SVB models, in the retina and vitreous, are given by r_{ret} and r_{vit}, respectively. For the BI-X molecule we take the drug concentration in the retina and vitreous to be equal to $b_{\text{ret}} + f_{\text{ret}}$ and $b_{\text{vit}} + f_{\text{vit}}$, respectively, i.e. both B and BA, as typically $b(t) \ll f(t)$. The additional green solid line in Figures 6.12-6.22 of Section 6.6 denote the concentration of unbound free vitreal binding sites, $n(t)$.

Figure 6.1 show the model solutions for a range of n_0 values greater than r_0, and $K_{\text{D}}^{(n)} = 10^8$ pM. Similarly, in Figure 6.2, $K_{\text{D}}^{(n)}$ is held constant at 10^7 pM, and n_0 varies over a range of values, exactly one order of magnitude lower than those of Figure 6.1, such that the ratio $K_{\text{D}}^{(n)}/n_0$ is the same for plot (i) between Figures 6.1 and 6.2. From our PK analysis of the SVB (Section 5.1.2) we know that in this region of $\left(K_{\text{D}}^{(n)}, n_0\right)$ parameter space the drug decays with a half-life of $t_{1/2}^{(0)}\left(1 + n_0/K_{\text{D}}^{(n)}\right)$ (Equation 5.137), and from our duration time analysis (Section 5.1.3) we know that for $K_{\text{D}}^{(n)}/n_0 \sim O(10^{-1})$ the duration time, t_{dur}, is maximised. As n_0 increases we see from Figure 6.1 that the behaviour of the SVB molecule radically changes; in plot (1) the SVB decays in a similar manner to ranibizumab (with a slightly higher $t_{1/2}$), and hence suppresses VEGF in a similar manner. As n_0 increases the half-life of the drug steadily increases alongside t_{dur}. For plots (3) and (4) t_{dur} is close to its maximal value, hence, here we see that there remains available a large quantity of freely diffusing drug for an extended time period, relative to ranibizumab. Due to this, we see in plots (3) and (4) that the SVB suppresses the concentration of free retinal VEGF to much greater level than ranibizumab. Notice that in plot (3) the SVB consistently suppresses free retina VEGF to a greater degree than ranibizumab, whereas initially ranibizumab outperforms the SVB in plot (4) (i.e. ranibizumab suppresses FRV to a greater degree than the SVB initially). This is due to the low effective initial concentration of plot (4) - while (4) maintains a very long half-life, initially the drug exists at lower concentrations than ranibizumab and (3). However, given a suitably long period of time, (4) will outperform both ranibizumab and (3), due to the previously mentioned (Chapter 5) trade-off between half-life and effective initial concentration that SVB molecules must make, i.e. modifying $(K_{\text{D}}^{(n)}, n_0)$ to yield an increased half-life typically reduces the effective initial concentration. The effect of this trade-off becomes further pronounced in plot (5) whereby the half-life of the drug (on the timescale considered) is essentially infinite, however the effective initial concentration is so low that the suppression of free VEGF in the retina is less than 50% $\forall t > 0$. Given that the efficacious duration time of ranibizumab is estimated to be ~ 30 days, it is unlikely that this level of retinal free VEGF suppression is

of a great enough magnitude to inhibit disease activity. This is, of course, not surprising considering $t_{\text{dur}} = 0$ at (5), i.e. (5) lives in the 'red zone' of $\left(K_{\text{D}}^{(n)}, n_0\right)$ parameter space.

Figure 6.1 demonstrates that the BI-X molecule substantially outperforms ranibizumab, noting the solutions for ranibizumab and the BI-X molecule are identical for Figures 6.1-6.7. This is primarily due to the greatly increased half-life of the BI-X molecule, when bound with albumin, of 22 days. We can also see from Figure 6.1 that the free VEGF retinal suppression achieved using the BI-X molecule outperforms all plots (1)-(5), aside from plots (4) and (5) at late time. This demonstrates the advantage a nSVB has over a SVB by being able prolong its ocular retention in all parts of the eye - not only the vitreous.

Figure 6.2 is included here to demonstrate that in this region of $\left(K_{\text{D}}^{(n)}, n_0\right)$ parameter space the SVB is dependent only on the ratio $K_{\text{D}}^{(n)}/n_0$, as we note the resultant plots (1)-(5) are identical between both Figures 6.1 and 6.2.

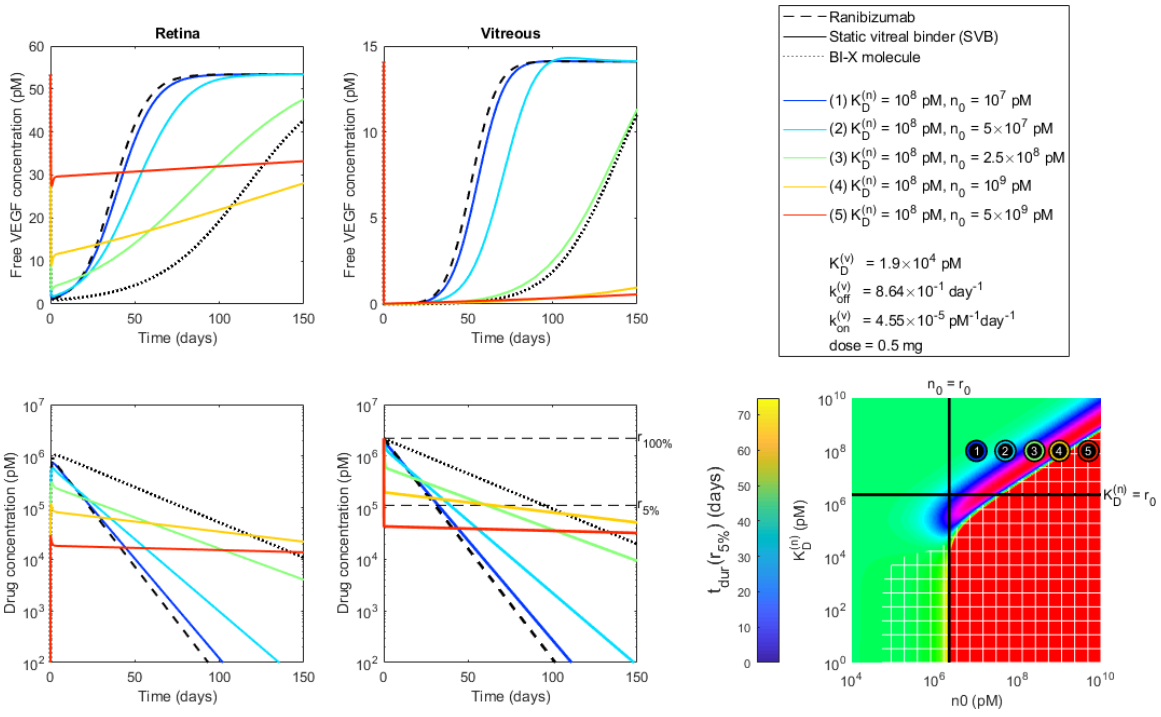

Figure 6.1: The solution to the SVB PK/PD model (Equations 6.4-6.15), for the 5 $(K_{\text{D}}^{(n)}, n_0)$ pairs indicated in the legend, are shown by the 5 coloured lines (plots (1)-(5)). The solution to the BI-X model (Equations 6.71-6.89) is shown by the dotted line. The solution to the non-vitreal binding model (Equations 4.3-4.18) is shown by the dashed line. Here $K_{\text{D}}^{(n)}$ is high relative to r_0, and we see a range of behaviours dependent on the magnitude of n_0.

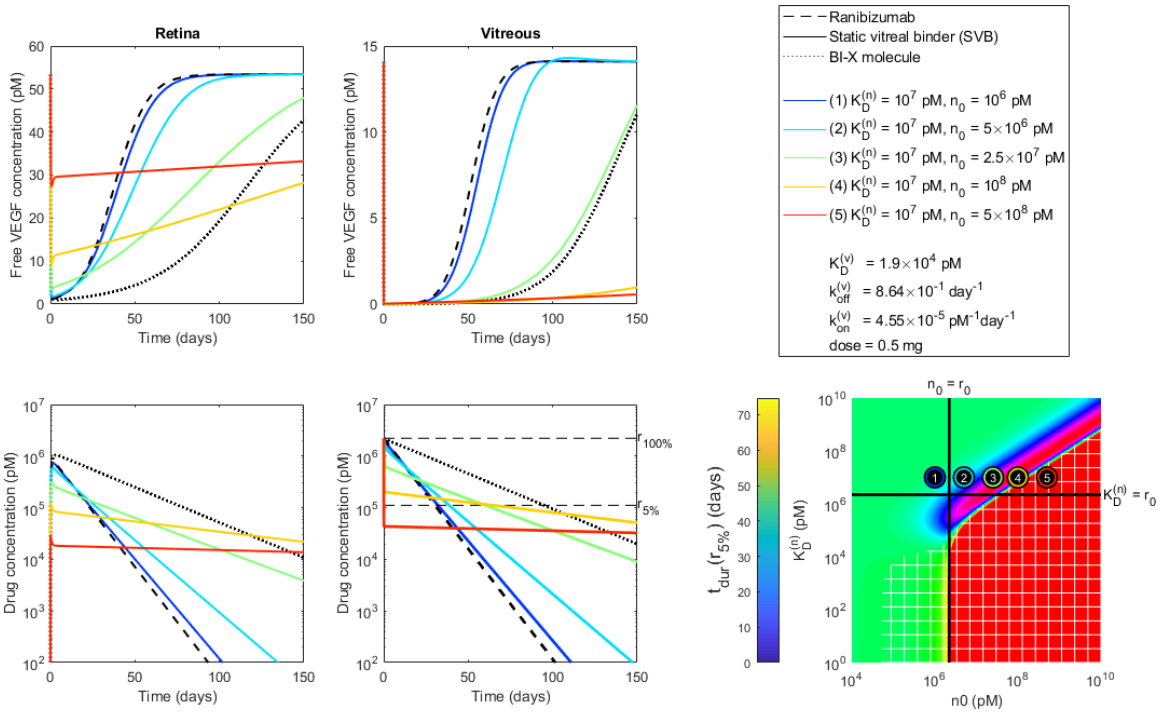

Figure 6.2: The solution to the SVB PK/PD model (Equations 6.4-6.15), for the 5 $(K_{\mathrm{D}}^{(n)}, n_0)$ pairs indicated in the legend, are shown by the 5 coloured lines (plots (1)-(5)). The solution to the BI-X model (Equations 6.71-6.89) is shown by the dotted line. The solution to the non-vitreal binding model (Equations 4.3-4.18) is shown by the dashed line. Here we vary $K_{\mathrm{D}}^{(n)}$ and n_0, but keep the ratio $K_{\mathrm{D}}^{(n)}/n_0$ constant relative to Figure 6.1, i.e. the ratio $K_{\mathrm{D}}^{(n)}/n_0$ for plots (1) is the same in Figures 6.1 and 6.2. We note that the plots are identical to the corresponding plots in Figure 6.1, demonstrating that in this region of parameter space $(K_{\mathrm{D}}^{(n)} \gg r_0)$ the behaviour of the SVB model only depends on the ratio of $K_{\mathrm{D}}^{(n)}$ and n_0.

In contrast to Figures 6.1 and 6.2, which examined a value of $K_{\mathrm{D}}^{(n)}$ much greater than r_0, Figure 6.3 will consider $K_{\mathrm{D}}^{(n)} \ll r_0$. In this region of parameter space, as the binding between the SVB molecules and vitreal binding sites is so tight, we see the unbound SVB decay with half-life $t_{1/2}^{(0)}$ (Equation 5.150) for a portion of the time-course of the drug's decay. Plots (1)-(4) demonstrate that past the time that the concentration of the drug is no longer much greater than $K_{\mathrm{D}}^{(n)}$, the decay rate of the SVB transitions from decaying with rate $t_{1/2}^{(0)}$, to non-exponential decay, to that of a rate $t_{1/2}^{(0)}\left(1 + n_0/K_{\mathrm{D}}^{(n)}\right)$. However, given that this occurs when the concentration of the drug is so low that it is unable to suppress free retinal VEGF to a meaningful degree, we conclude that there is no positive effect gained from this late time increase in half-life. Notice also, as n_0 increases the effective initial concentration of the SVB decreases, such that the effective initial concentration of plot (5) is close to zero. We see that in this figure the BI-X molecule greatly outperforms the SVB molecule.

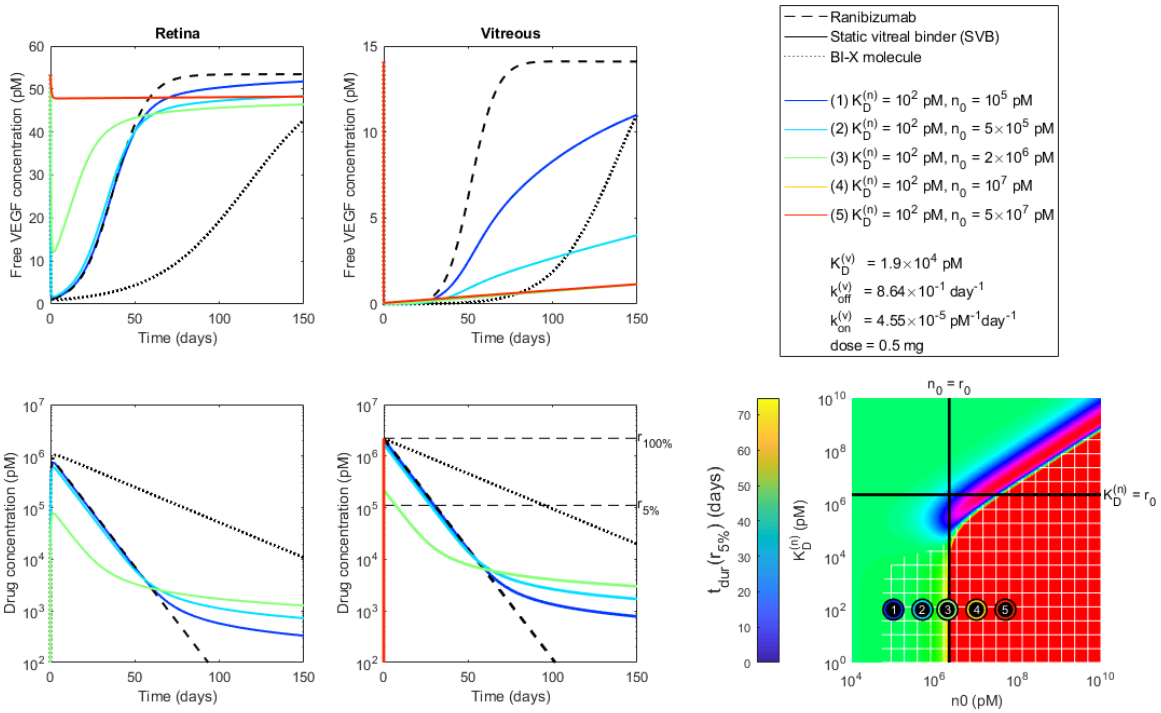

Figure 6.3: The solution to the SVB PK/PD model (Equations 6.4-6.15), for the 5 $(K_{\mathrm{D}}^{(n)}, n_0)$ pairs indicated in the legend, are shown by the 5 coloured lines (plots (1)-(5)). The solution to the BI-X model (Equations 6.71-6.89) is shown by the dotted line. The solution to the non-vitreal binding model (Equations 4.3-4.18) is shown by the dashed line. Here we see the effect of strong binding over wide range of n_0 values. No meaningful improvement on ranibizumab. Here the BI-X molecule is much more effective at suppressing FRV than the SVB molecule. Note free VEGF plots of (4) and (5) are approximately equal, hence the yellow line of plot (4) is obscured by the red line of (5). This is also the case for the unbound drug concentration of plots (4) and (5), however given it is approximately zero it is not visible on the log scale plotted here.

Given the significance of the ratio $K_{\mathrm{D}}^{(n)}/n_0$ Figures 6.4-6.7 will examine the variation of behaviour of the SVB model along lines where the ratio of $K_{\mathrm{D}}^{(n)}/n_0$ is held constant, i.e. parallel (in log-log space) to the slope of the hill (the region of $\left(K_{\mathrm{D}}^{(n)}, n_0\right)$ parameter space such that t_{dur} is maximised). The ith plot of Figures 6.4-6.7 is solved for the same n_0 value, however the ratio $K_{\mathrm{D}}^{(n)}/n_0$ decreases between each figure, such that $K_{\mathrm{D}}^{(n)}/n_0 = 15.7, 1.57, 0.157, 1.57\times10^{-2}, 1.57\times10^{-3}$, for Figures 6.4-6.7, respectively. In this way, the value of $K_{\mathrm{D}}^{(n)}$ for the ith plot is decreased by a factor of 10 between each figure, where we note that $K_{\mathrm{D}}^{(n)}/n_0$ is chosen such that t_{dur} is maximised for Figure 6.6.

In Figure 6.4 we see almost no difference between the SVB molecule and ranibizumab. We can see from the t_{dur} that all plots (1)-(5), while lying outside of the red or meshed regions, lie far enough above the hill in $\left(K_{\mathrm{D}}^{(n)}, n_0\right)$ parameter space such that there is little positive effect from the addition of vitreal binding to the classical molecule. In physical terms we have a combination of weak binding and an insufficient quantity of binding sites, i.e. K_{D} is too high, n_0 is too low, and hence their ratio $K_{\mathrm{D}}^{(n)}/n_0$ is too high for there to

be an increased ocular retention of the drug due to vitreal binding. Moving to Figure 6.5 we can see that reducing $K_{\mathrm{D}}^{(n)}$ and the ratio $K_{\mathrm{D}}^{(n)}/n_0$ by one order of magnitude starts to noticeably differentiate the SVB from ranibizumab. As expected plots (1)-(5) eventually all decay at the same rate, however for early time plots (1)-(3) decay with half-life equal to $t_{1/2}^{(0)}$ and hence have reduced retinal suppression relative to (4) and (5) at later times.

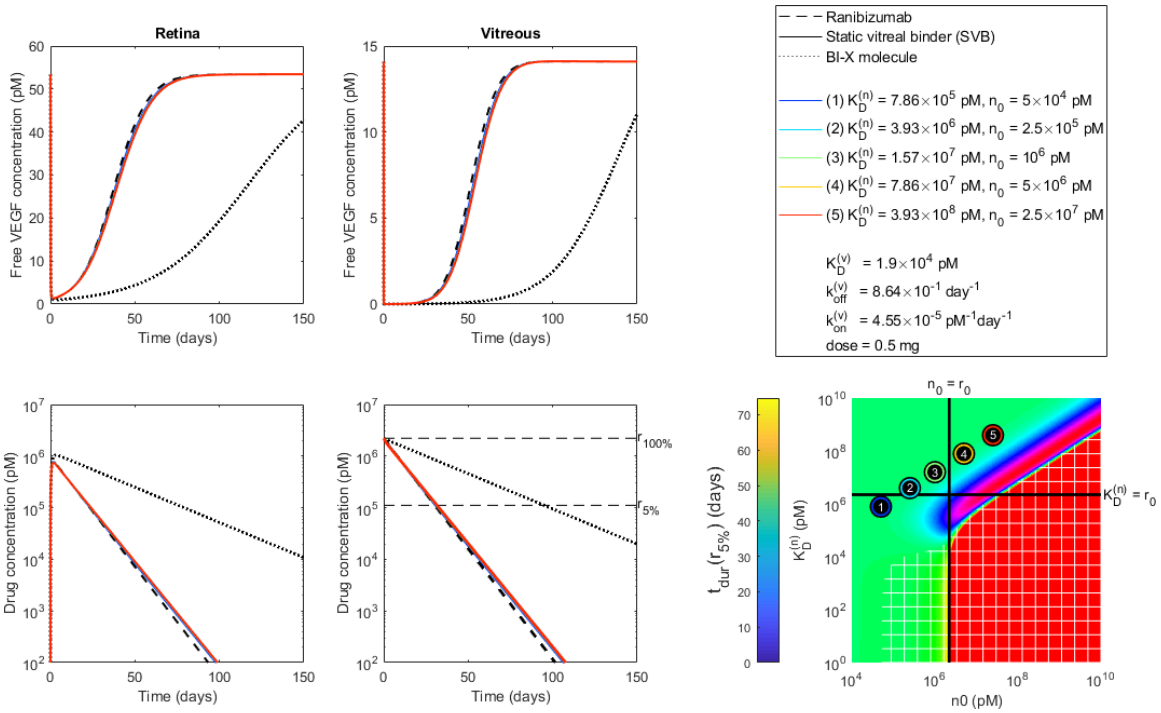

Figure 6.4: The solution to the SVB PK/PD model (Equations 6.4-6.15), for the 5 $(K_{\mathrm{D}}^{(n)}, n_0)$ pairs indicated in the legend, are shown by the 5 coloured lines (plots (1)-(5)). The solution to the BI-X model (Equations 6.71-6.89) is shown by the dotted line. The solution to the non-vitreal binding model (Equations 4.3-4.18) is shown by the dashed line. Here we see little to no difference between the SVB and ranibizumab, as the ratio $K_{\mathrm{D}}^{(n)}/n_0$ is too high for the SVB to be effective, i.e. K_{D} is too high, n_0 is too low, and hence their ratio $K_{\mathrm{D}}^{(n)}/n_0$ is too high for there to be a increased ocular retention of the drug due to vitreal binding. Note here that as plots (1)-(5) are approximately the same, it is not possible to tell them apart in the plot as each of their curves overlap.

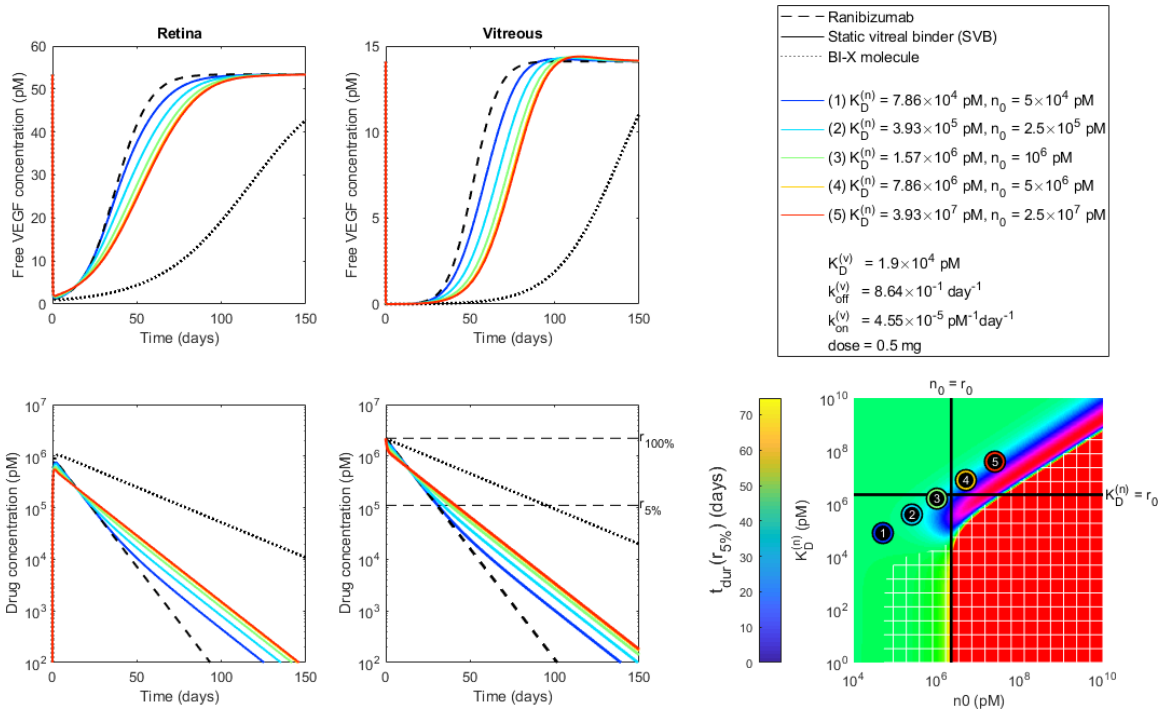

Figure 6.5: The solution to the SVB PK/PD model (Equations 6.4-6.15), for the 5 $(K_{\mathrm{D}}^{(n)}, n_0)$ pairs indicated in the legend, are shown by the 5 coloured lines (plots (1)-(5)). The solution to the BI-X model (Equations 6.71-6.89) is shown by the dotted line. The solution to the non-vitreal binding model (Equations 4.3-4.18) is shown by the dashed line. Here we see concentration profiles for the SVB molecule and ranibizumab diverge relative to Figure 6.4, as the effect of vitreal binding becomes more pronounced. However the increase in FRV suppression of the SVB molecule is not greatly increased relative ranibizumab, and still greatly outperformed by the BI-X molecule.

By reducing $K_{\mathrm{D}}^{(n)}$ by one order of magnitude further (Figure 6.6) we find $K_{\mathrm{D}}^{(n)}/n_0 = 0.157$ - the $K_{\mathrm{D}}^{(n)}$, n_0 ratio that maximises t_{dur} (as determined by Equation 5.142, substituting $c_{30}^{(r)}$ for $r_{5\%}$). Therefore plots (4)-(5), which lie to the right of $n_0 = r_0$, lie precisely atop the hill in $\left(K_{\mathrm{D}}^{(n)}, n_0\right)$ parameter space - given we have demonstrated that in this region of parameter space the model is only dependent on the ratio $K_{\mathrm{D}}^{(n)}/n_0$, we see (4) and (5) have almost identical concentration profiles ((4) and (5) are not identical as the n_0 value of (4) is not sufficiency greater than r_0). In plots (4) and (5) we see that for times greater than zero the free drug decays with half-life in $(t_{1/2}^{(0)}, t_{1/2}^{(0)}(1+n_0/K_{\mathrm{D}}^{(n)})$, whereas plots (1)-(3) exhibit a transition from decaying with half-life $t_{1/2}^{(0)}$ (for approximately the first 25 days) to decaying at the same rate as (4) and (5). Because of this range of half-life values between plots (1)-(5), we see the level of suppression of the free VEGF in the retina increase as we move from plots (1) to (5), in line with the duration time prediction. We see that plot (5) has the optimal relationship between half-life and effective initial concentration to maintain a concentration of freely diffusing drug in the vitreous, as we decrease $K_{\mathrm{D}}^{(n)}$ by an order of magnitude further (Figure 6.7), we see plot (5) fall off the edge of the hill and into the red

zone - here, even though the half-life of (5) is incredibly high, the effective initial concentration is so low it remains below $r_{5\%}$ for all time, as is also the case for (4). We see from this that (4) and (5) both fail to effectively suppress the free VEGF concentration in the retina, being outperformed by plots (1)-(3) as well as ranibizumab and the BI-X molecule. This of course assumes that decreasing the concentration of free VEGF in the retina from ~ 55 pM to ~ 30 pM is not sufficient to inhibit disease activity. Understanding how free VEGF concentration is linked to disease activity will be discussed as future work.

For Figures 6.7 the behaviour of plots (1)-(3) remains relatively unchanged - this is due to the fact that when both $K_{\mathrm{D}}^{(n)}$ and n_0 are both much less than r_0, the concentration of freely diffusing vitreal drug (FDVD) decays at the same rate as ranibizumab (as long as $r_{\mathrm{vit}} \gg K_{\mathrm{D}}^{(n)}$, see Section 5.1.3). This further indicates that this region of $\left(K_{\mathrm{D}}^{(n)}, n_0\right)$ parameter space is highly likely to not be capable of efficaciously suppressing free retinal VEGF.

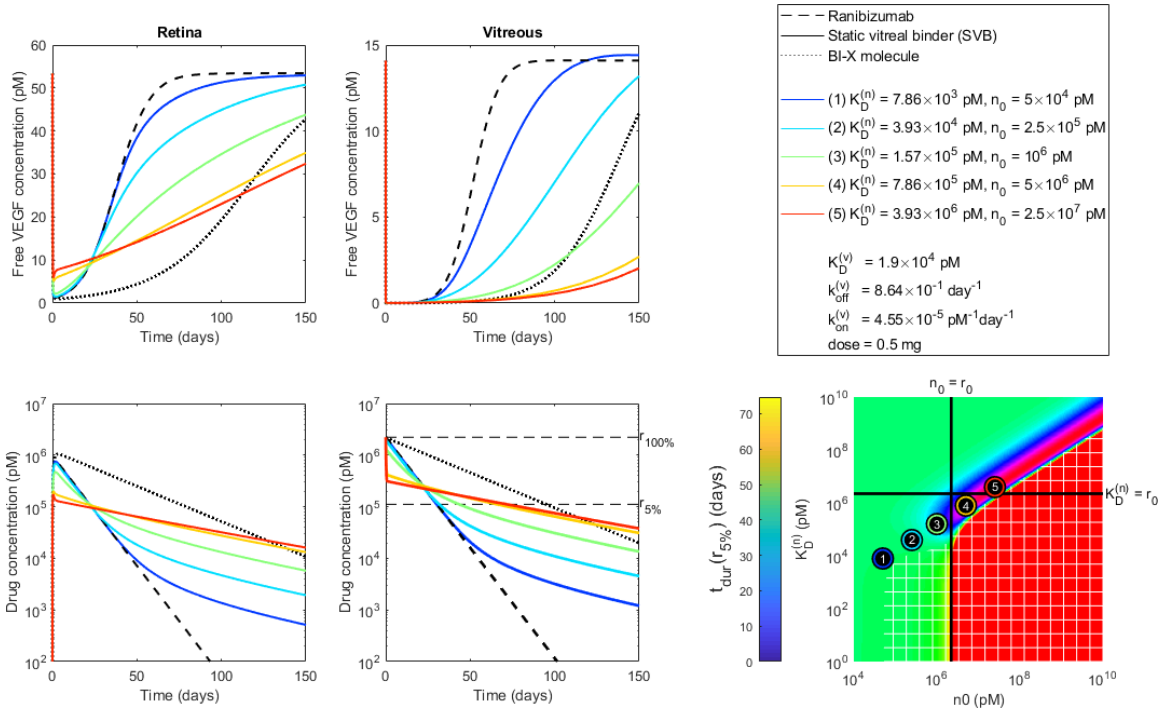

Figure 6.6: The solution to the SVB PK/PD model (Equations 6.4-6.15), for the 5 $(K_{\mathrm{D}}^{(n)}, n_0)$ pairs indicated in the legend, are shown by the 5 coloured lines (plots (1)-(5)). The solution to the BI-X model (Equations 6.71-6.89) is shown by the dotted line. The solution to the non-vitreal binding model (Equations 4.3-4.18) is shown by the dashed line. Here are taken to have the optimal ratio $K_{\mathrm{D}}^{(n)}$ and n_0, as determined by Equation 5.142. We see persistent and high levels of free retinal VEGF suppression observed for solutions such that $n_0 > r_0$ (plots (4) and (5)).

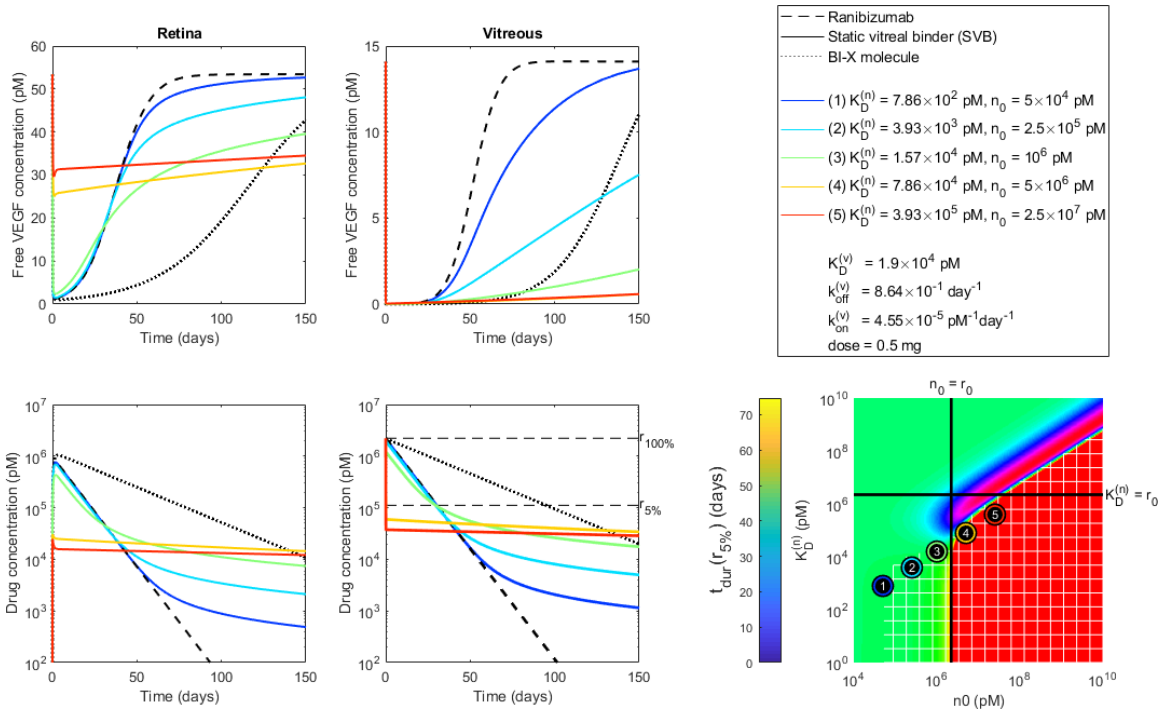

Figure 6.7: The solution to the SVB PK/PD model (Equations 6.4-6.15), for the 5 $(K_D^{(n)}, n_0)$ pairs indicated in the legend, are shown by the 5 coloured lines (plots (1)-(5)). The solution to the BI-X model (Equations 6.71-6.89) is shown by the dotted line. The solution to the non-vitreal binding model (Equations 4.3-4.18) is shown by the dashed line. Here we see the SVB model solution exhibits either FRV suppression similar to that of ranibizumab (plots (1)-(3)), or greatly reduced suppression relative to ranibizumab (plots (4)-(5)).

6.5 Static vitreal binding to hyaluronic acid

Similar to collagen, hyaluronic acid forms large space filling networks within the vitreous, generally adopting stiff coil configurations [31]. The median concentration of hyaluronic acid in the human eye has been shown to be between 34-700 μg mL^{-1}, with a median value of 130 μg mL^{-1} [131]. Due to these features hyaluronic acid is being considered as a target for SVB molecules. A 2017 study [58] combined a 97-amino-acid hyaluronic acid binder with therapeutic antibodies and proteins, in order to access the potential of hyaluronic acid as a target of a SVB. Based on rabbit and monkey studies, it was estimated that the human vitreous has a carrying capacity of up to 2mg of a Fab molecule. Therefore, assuming the molecular weight of a Fab molecule to be 50 kDa, and the human vitreous to have a volume of 4.5 mL, the concentration of hyaluronic acid binding sites, n_0, available to bind to is therefore equal to 8.89×10^6 pM. The concentration of hyaluronic acid binding over time is then given by $n(t)$, as in Equations 6.4-6.15.

In Figures 6.8-6.10, keeping n_0 is fixed, we will consider a hyaluronic acid binding SVB

molecule with a range of $K_{\mathrm{D}}^{(n)}$ values, in comparison to ranibizumab and the BI-X molecule. The SVB model is evaluated for 8 $K_{\mathrm{D}}^{(n)}$ values, identical between plots (1)-(8) in Figures 6.8-6.10. We will compare the resultant dynamics from initial doses of 0.5 mg, 2 mg and 8 mg in Figures 6.8, 6.9 and 6.10, respectively. Alongside each plot, we will show t_{dur} evaluated at 5% of the initial dose.

In Figure 6.8 we see the hyaluronic SVB evaluated at the standard dose of 0.5 mg. Here we find that as $n_0 < r_0$, depending on the value of $K_{\mathrm{D}}^{(n)}$, we can lie in the favourable region of $\left(K_{\mathrm{D}}^{(n)}, n_0\right)$ parameter space, with respect to t_{dur} (i.e. the region where $t_{\mathrm{dur}} > 30$ days as shown in Figure 6.8). For plots (1)-(3) we can see, as they lie in the red zone with respect to t_{dur}, that they exhibit exceedingly strong binding to hyaluronic acid, as well as greatly extended half-lives, however they are largely unable to suppress free retinal VEGF. Plots (4)-(7) span the region of $\left(K_{\mathrm{D}}^{(n)}, n_0\right)$ parameter space such that $t_{\mathrm{dur}} > 50$ days (i.e. the aforementioned 'hill' in $\left(K_{\mathrm{D}}^{(n)}, n_0\right)$ parameter space), where we expect from our analysis in Chapter 5 to see the greatest ability of the SVB to suppress free retinal VEGF. Plot (4), lying on the steep transition from the red zone to the peak of the hill, possesses sufficiently weak binding to hyaluronic acid to outperform all other plots by day 100 - however, from previous discussion on this topic, this level of VEGF suppression seems unlikely to inhibit disease progression. Plot (5) sits exactly at the peak of the hill - this model solution manages to suppress free retinal VEGF to a high degree at early and late times, and therefore represents the ideal SVB molecule, with respect to single dose performance on a treatment naive eye. This molecule more than doubles the duration time of ranibizumab, and could therefore, at least theoretically, reduce the frequency of injections from 1 to 2 months.

As $K_{\mathrm{D}}^{(n)}$ is increased further, in plots (6)-(7), we see the magnitude of free VEGF suppression in the retina decrease, and become more similar to that of ranibizumab, where finally in plot (8) we see almost identical behaviour between the two molecules. In comparison to the SVB, the BI-X molecule outperforms every one of plots (1)-(8), aside from plots (4) and (5) at late time. This indicates that the BI-X molecule may be more consistent in its treatment outcomes than a SVB class molecule, or at least less sensitive to kinetic properties.

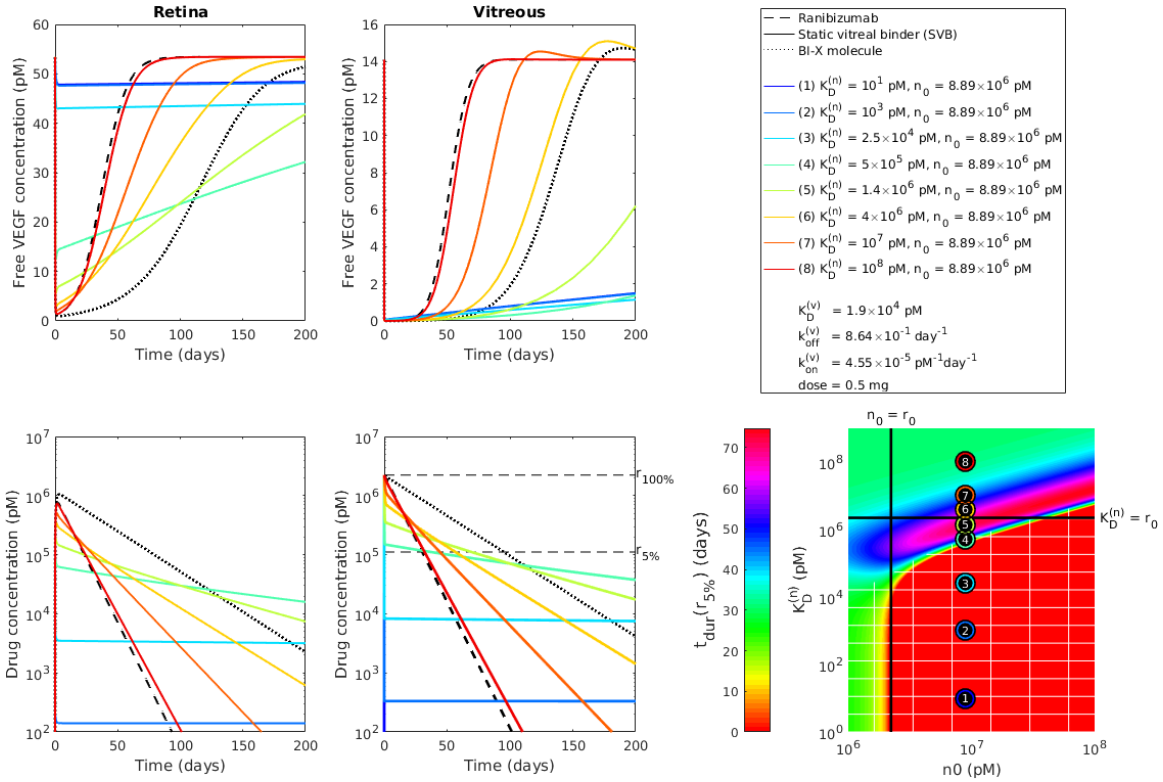

Figure 6.8: The solution to the SVB PK/PD model (Equations 6.4-6.15), for the 5 $(K_{\mathrm{D}}^{(n)}, n_0)$ pairs indicated in the legend, are shown by the 5 coloured lines (plots (1)-(5)). The solution to the BI-X model (Equations 6.71-6.89) is shown by the dotted line. The solution to the non-vitreal binding model (Equations 4.3-4.18) is shown by the dashed line. Here we see a 0.5 mg dose of the hyaluronic acid SVB, plotted alongside ranibizumab and the BI-X molecule administered at the same dose. Plots (4)-(7) exhibit favourable free VEGF suppression relative to ranibizumab, whereas plots (1)-(3) and (8) fail to meaningfully improve on the level of FRV suppression achieved by ranibizumab. The BI-X molecule exhibits greater levels of FRV suppression than all other simulations.

In Figure 6.9 we replicate the simulations of Figure 6.8, however we increase the dose from 0.5 mg to 2 mg (the theoretical carrying capacity of hyaluronic acid), thereby setting $n_0 = r_0$. As we increase $K_{\mathrm{D}}^{(n)}$ between plots (1)-(3) we see a substantial increase in FRV suppression, especially relative to Figure 6.8. We see similar changes in the behaviour of plots (4)-(7), as the concentration profiles of FRV for these plots become shallower and sustained at a lower level for a longer time. The same cannot be said for plot (8), where we see the concentration profile of FRV again mirror that of ranibizumab, simply being shifted right along the time axis.

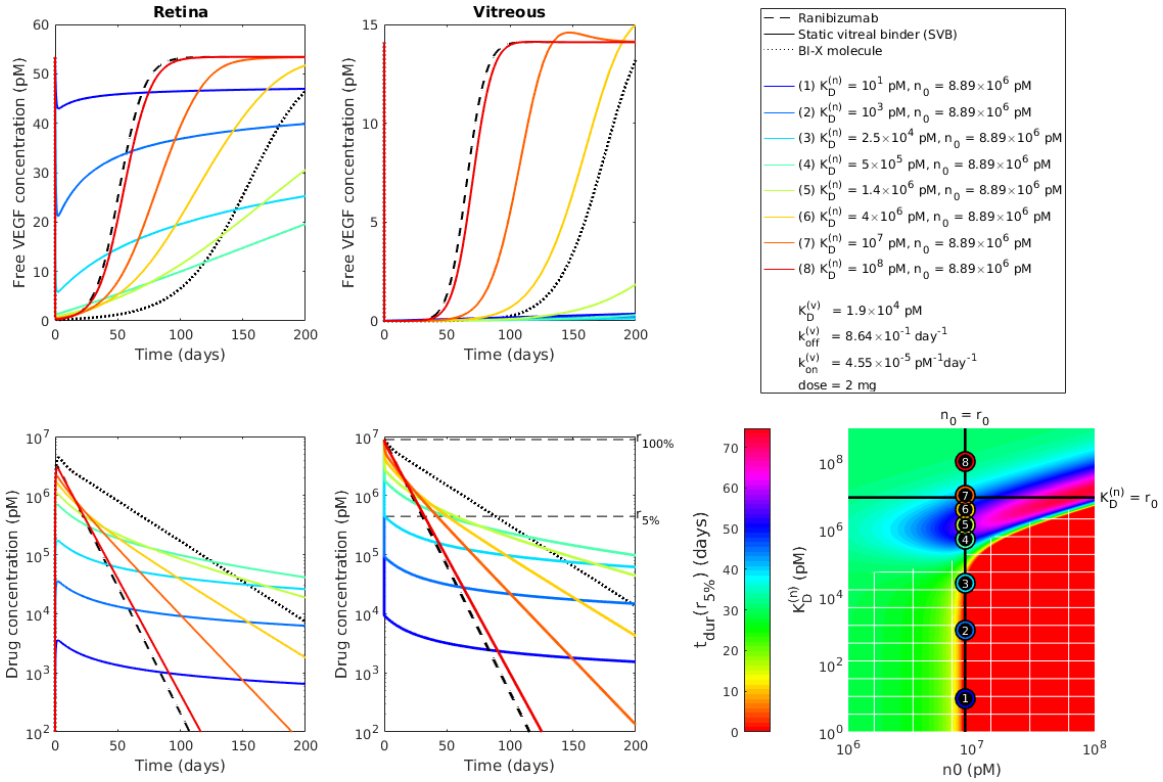

Figure 6.9: The solution to the SVB PK/PD model (Equations 6.4-6.15), for the 5 $(K_{\mathrm{D}}^{(n)}, n_0)$ pairs indicated in the legend, are shown by the 5 coloured lines (plots (1)-(5)). The solution to the BI-X model (Equations 6.71-6.89) is shown by the dotted line. The solution to the non-vitreal binding model (Equations 4.3-4.18) is shown by the dashed line. Here we see a 2 mg dose of hyaluronic acid SVB, plotted alongside ranibizumab and the BI-X molecule administered at the same dose. Plots (3)-(7) exhibit favourable free VEGF suppression relative to ranibizumab, whereas plots (1)-(2) and (8) fail to meaningfully improve on the level of FRV suppression achieved by ranibizumab. The BI-X molecule exhibits greater levels of FRV suppression that all other simulations.

As we increase the dose further to 8 mg we now note that all plots (1)-(8) lie to the left of $n_0 = r_0$ and away from the hill with respect to t_{dur}. Here we see that, initially, plots (1)-(8) perform similarly to ranibizumab - this is due to the injected dose being 4 times that of the carrying capacity of hyaluronic acid. After this initial phase, plots (3)-(7) quickly differentiate themselves from ranibizumab, exhibiting extended half-lives, much in the same manner as in Figures 6.8-6.9. Plots (1)-(2) follow the concentration profile of ranibizumab for a long time (given that their values of $K_{\mathrm{D}}^{(n)}$ are much less than r_0), and at a later time they begin to decay with a half-life more similar to that of plots (3)-(7). We note here that in 6.8-6.9 the BI-X molecule, in almost all cases, outperforms the hyaluronic SVB molecule - only in the regions such that t_{dur} is close to its maximal point do we see the SVB generate a greater level of FRV suppression, but only at very late times ($t > 100$ days). This again

indicates its reliability over the SVB molecule class.

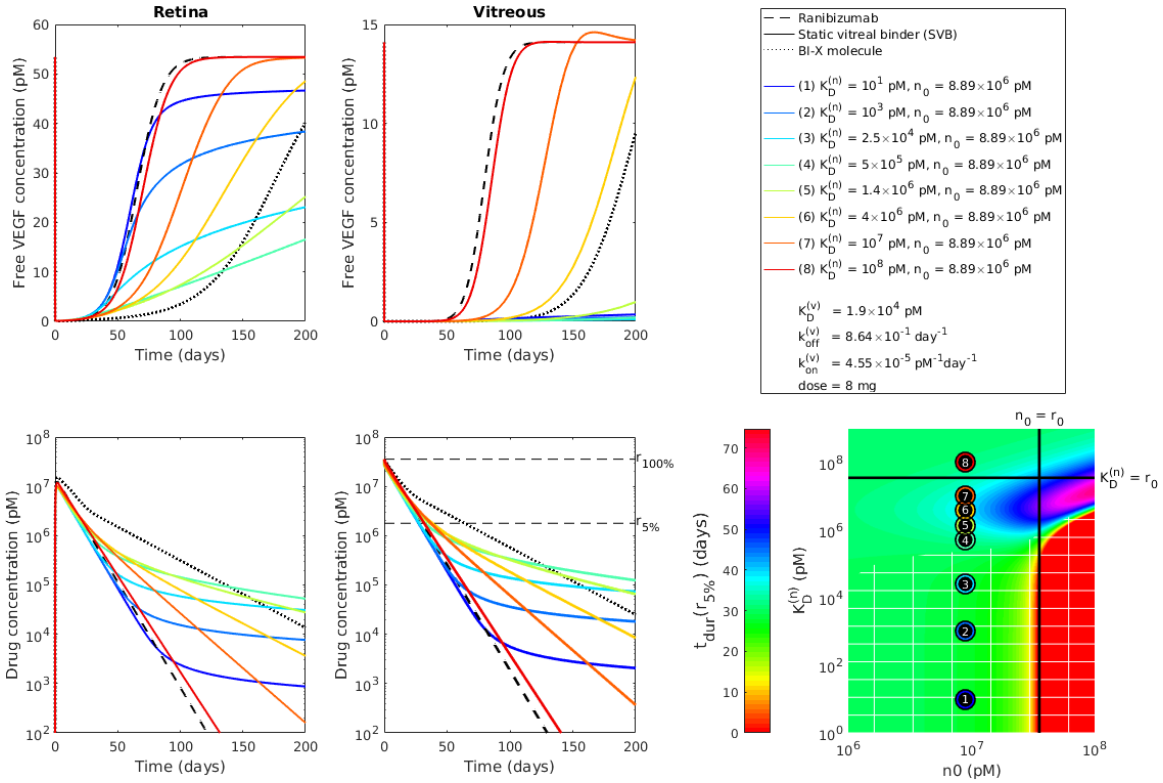

Figure 6.10: The solution to the SVB PK/PD model (Equations 6.4-6.15), for the 5 $(K_D^{(n)}, n_0)$ pairs indicated in the legend, are shown by the 5 coloured lines (plots (1)-(5)). The solution to the BI-X model (Equations 6.71-6.89) is shown by the dotted line. The solution to the non-vitreal binding model (Equations 4.3-4.18) is shown by the dashed line. Here we see a 8 mg dose of the hyaluronic acid SVB, plotted alongside ranibizumab and the BI-X molecule administered at the same dose. Plots (3)-(7) exhibit favourable free VEGF suppression relative to ranibizumab, whereas plots (1)-(2) and (8) fail to meaningfully improve on the level of FRV suppression achieved by ranibizumab. The BI-X molecule exhibits greater levels of FRV suppression that all other simulations.

6.6 Repeat dosage analysis

As in Section 5.1.4 of Chapter 5, in this section we will consider the resultant PD following repeat dosages of the SVB molecule. We will present a comparison between the SVB molecule, the BI-X molecule and ranibizumab (has been done in previous sections of this chapter), using identical dosage protocols. In Section 5.1.4 we explored the idea that after each subsequent dose SVB molecules may accumulate on vitreal binding sites, hence, a change in behaviour may be observed at later time from that exhibited after the first injection in a treatment naive eye. We demonstrated in Section 5.1.4 that this is indeed the case and how, and to what degree, the resultant PK differs at later doses is highly dependent

on location in $\left(K_{\mathrm{D}}^{(n)}, n_0\right)$ parameter space. We also demonstrated that the concentration of freely diffusing vitreal drug (FDVD) can only be positively impacted, i.e. increased, by this phenomenon. In Section 5.1.4 we also demonstrated that a loading dose injected at $t = 0$ could be used to jump-start the system, decreasing the number of injections required before the benefits of drug accumulation are observed.

In Figures 6.12-6.22 we discuss various hypothetical dosage protocols, using a range of doses and loading doses, administered at 90 day intervals. We consider 6 locations in $\left(K_{\mathrm{D}}^{(n)}, n_0\right)$ parameter space, the values for which are shown in Figure 6.11; each figure's corresponding number can be found in the left top left of its plot.

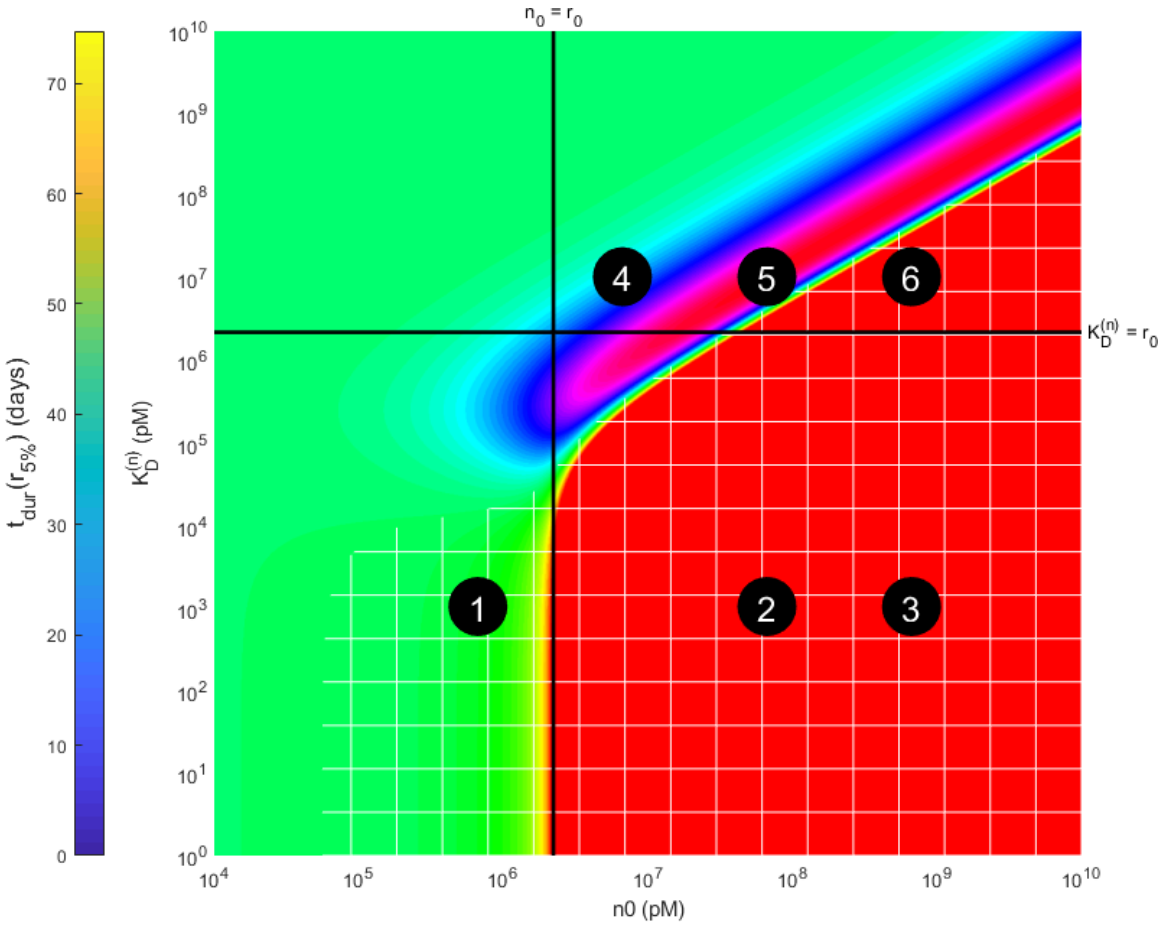

Figure 6.11: Duration time to reach 5% of a 0.5 mg dose, hence, here r_0 corresponds to the concentration resulting from a dose of 0.5 mg. The labels (1)-(5) indicate the $\left(K_{\mathrm{D}}^{(n)}, n_0\right)$ values for which the SVB model (Equations 6.4-6.15) were solved using, in the Figures 6.12-6.22.

In Figures 6.12-6.15 we solve the SVB model using a value of $K_{\mathrm{D}}^{(n)}$ of order $\sim O(10^3)$ at a dose of 5 mg (10 mg in Figure 6.15), such that $K_{\mathrm{D}}^{(n)} \ll r_0$. In Figure 6.12 we see the

SVB molecule decays in a manner very similar to ranibizuamb (until the concentration of free binding sites becomes on a par with FDVD). Additionally we observe no noticeable effect due to accumulation of drug on vitreal binding sites. Therefore, until such later time that the SVB's decay rate increases from $t_{1/2}^{(0)}$, the suppression of FRV is not increased relative to ranibizumab, and hence location (1) in $\left(K_{\mathrm{D}}^{(n)}, n_0\right)$ parameter space appears to be largely as efficacious as ranibizuamb - even for a dose of 5 mg. As has been previously discussed, this is primarily due to the binding strength between the SVB and the vitreal binding site; here the binding affinity is so high that it does not allow for a sufficiently high concentration of FDVD to permeate into the retina, to maintain suppression of FRV. We also note here that the BI-X molecule outperforms both the SVB molecule and ranibizuamb.

In Figure 6.13 we solve the SVB model using a value of n_0 two orders of magnitude greater than in Figure 6.12. Here we see similar behaviour to that of Figure 6.12, however, a noticeable transition in behaviour is observed between each dose. We firstly note that the rate at which the concentration of FRV increases is exactly that at which the concentration of FDVD decreases (as has been demonstrated in Section 6.2). We see the PK of the model transition through the three stages of behaviour predicted in Section 5.1.2; initially, while there are many more free binding sites than SVB molecules the system decays extremely slowly, with $t_{1/2} = t_{1/2}^{(0)}\left(1 + n_0/K_{\mathrm{D}}^{(n)}\right)$. As the number of unbound binding sites reaches parity with the FDVD (due to the accumulation of drug from repeated injections) we see the half-life decrease, finally, from the 4th injection onwards, as there exists now a large surplus of drug with respect to free binding sites, the drug decays with half-life $t_{1/2}^{(0)}$. We can see by the 4th injection that the suppression of FRV becomes quite high relative to that of ranibizumab. A loading dose of 20 mg at $t = 0$ could be used to generate this effect at the time of the first injection. However, even at its best performance, the SVB molecule is still greatly outperformed by the BI-X molecule, which inhibits the concentration of FRV by over 3 times as much as the SVB. This further indicates that strong binding can seriously impact the ability of an SVB to suppress FRV.

Finally, in our analysis of low $K_{\mathrm{D}}^{(n)}$ SVB molecules, in Figure 6.14 we solve the SVB model using a value of n_0 one order of magnitude greater still than that used in Figure 6.13. Here we see almost no suppression of FRV at all, due to the relatively complete absence of any FDVD. As was demonstrated in Section 5.1.4, an SVB sitting in this location of $\left(K_{\mathrm{D}}^{(n)}, n_0\right)$ parameter space would require ten times as long to exhibit the behaviour of Figure 6.13. It can be seen from Figure 6.15, even while utilising a loading dose of 100 mg

(a dose highly likely to be impossible to be formulated in practice) and dosing with 10 mg each 90 days, it still requires approximately 500 days before positive results are observed.

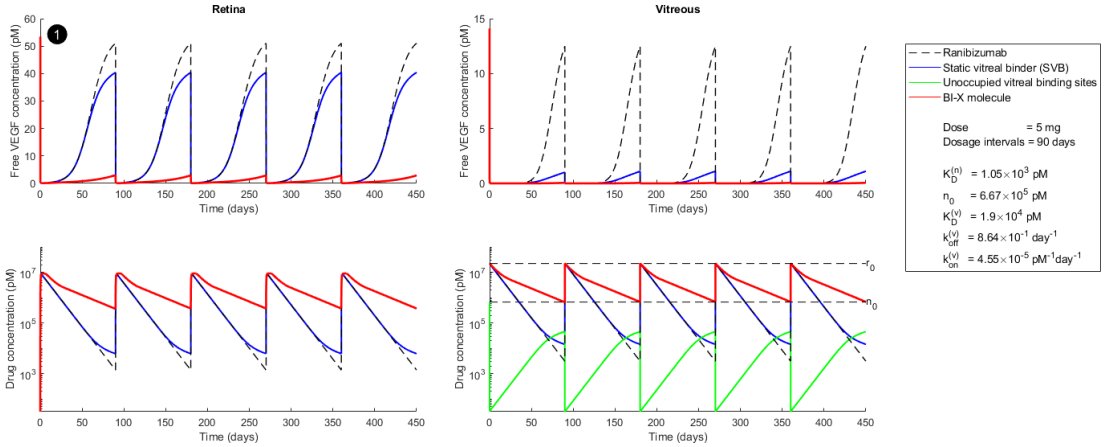

Figure 6.12: The solution to the SVB PK/PD model (Equations 6.4-6.15) is shown by the blue line. The concentration of unbound vitreal binding sites are shown by the solid green line, plotted alongside the concentration of vitreal drug. The solution to the BI-X model (Equations 6.71-6.89) is shown by the red line. The non-vitreal binding model (Equations 4.3-4.18) is shown by the dashed line. Here we see the SVB model solved for $K_{\mathrm{D}}^{(n)} = 10^3$ pM, $n_0 = 6.7 \times 10^5$ pM. Doses of 5 mg administered every 90 days. Models for ranibizumab and the BI-X molecule were run using an identical dosage protocol. Extremely poor FRV suppression resulting from treatment with SVB molecule.

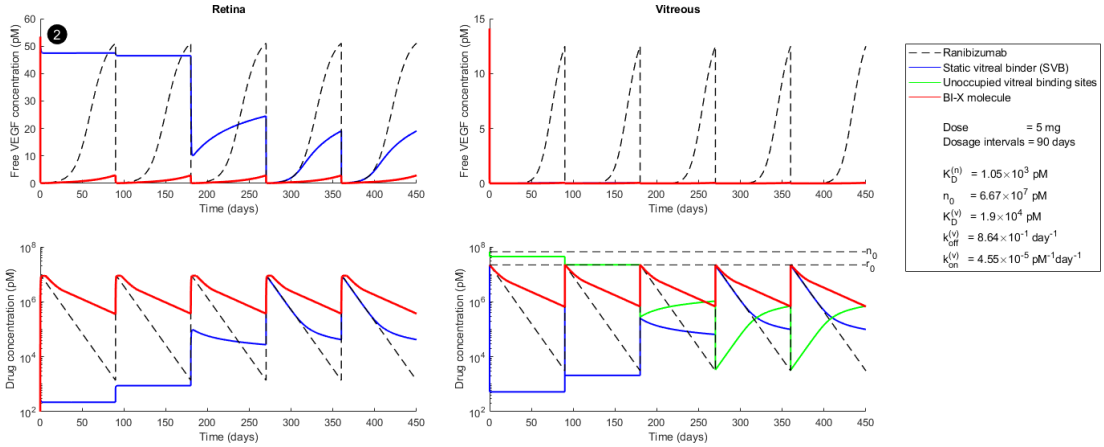

Figure 6.13: The solution to the SVB PK/PD model (Equations 6.4-6.15) is shown by the blue line. The concentration of unbound vitreal binding sites are shown by the solid green line, plotted alongside the concentration of vitreal drug. The solution to the BI-X model (Equations 6.71-6.89) is shown by the red line. The non-vitreal binding model (Equations 4.3-4.18) is shown by the dashed line. Here we see the SVB model solved for $K_{\mathrm{D}}^{(n)} = 10^3$ pM, $n_0 = 6.7 \times 10^7$ pM. Doses of 5 mg administered every 90 days. Models for ranibizumab and the BI-X molecule were run using an identical dosage protocol. Again, extremely poor FRV suppression resulting from treatment with the SVB molecule, until later time such that the drug has accumulated in the vitreous. At this later time (after the 4th injection) the SVB molecule suppresses FRV to a much greater degree than ranibizumab, however not to the degree that the BI-X molecule achieves at the same dose.

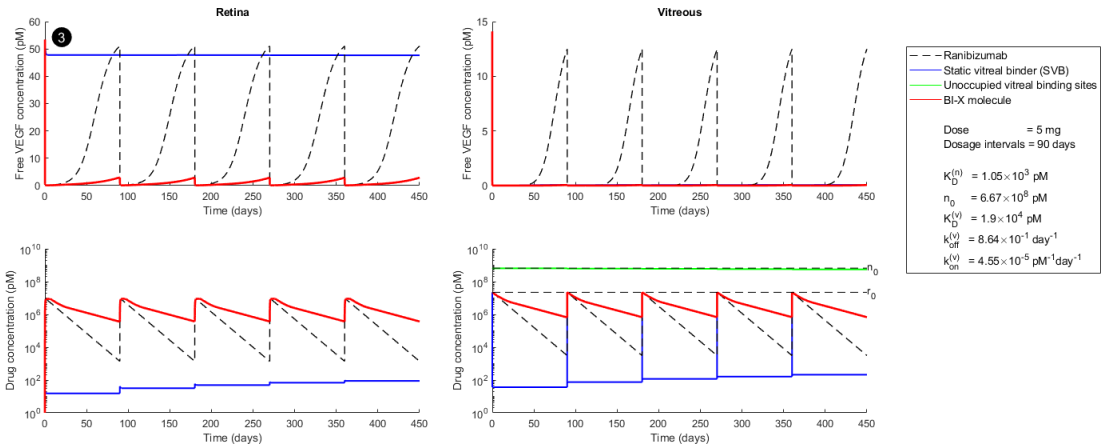

Figure 6.14: The solution to the SVB PK/PD model (Equations 6.4-6.15) is shown by the blue line. The concentration of unbound vitreal binding sites are shown by the solid green line, plotted alongside the concentration of vitreal drug. The solution to the BI-X model (Equations 6.71-6.89) is shown by the red line. The non-vitreal binding model (Equations 4.3-4.18) is shown by the dashed line. Here we see the SVB model solved for $K_{\mathrm{D}}^{(n)} = 10^3$ pM, $n_0 = 6.7 \times 10^8$ pM. Doses of 5 mg administered every 90 days. Models for ranibizumab and the BI-X molecule were run using an identical dosage protocol. Extremely poor FRV suppression resulting from treatment with SVB molecule.

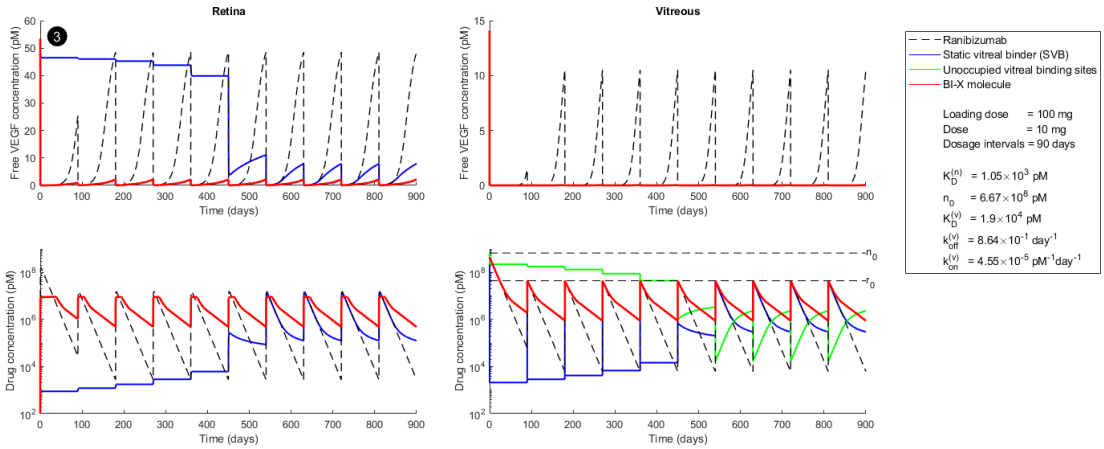

Figure 6.15: The solution to the SVB PK/PD model (Equations 6.4-6.15) is shown by the blue line. The concentration of unbound vitreal binding sites are shown by the solid green line, plotted alongside the concentration of vitreal drug. The solution to the BI-X model (Equations 6.71-6.89) is shown by the red line. The non-vitreal binding model (Equations 4.3-4.18) is shown by the dashed line. Here we see the SVB model solved for $K_{\mathrm{D}}^{(n)} = 10^3$ pM, $n_0 = 6.7 \times 10^8$ pM. Doses of 10 mg administered every 90 days, with a loading dose of 100 mg administered at $t = 0$ days. Models for ranibizumab and the BI-X molecule were run using an identical dosage protocol. The SVB molecule exhibits similar behaviour as it did in Figure 6.13, however a greater number of injections are required before increased FRV suppression is observed, relative to ranibizumab.

In Figures 6.16-6.22 the SVB model is solved for $K_{\mathrm{D}}^{(n)} \sim O(10^3)$ at various doses, such that for all Figures 6.16-6.22 $K_{\mathrm{D}}^{(n)} \gg r_0$. In Figure 6.16 the SVB model is solved for a dose of 0.5 mg, at a position in $\left(K_{\mathrm{D}}^{(n)}, n_0\right)$ parameter space that yields a value of t_{dur} elevated by approximately 15 days from that of ranibizumab, as can be seen from Figure 6.11. We can see from the rate at which the SVB molecule decays that the half-life of the SVB

molecule has increased from $t_{1/2}^{(0)}$, and that the SVB molecule is now able to suppress FRV to a greater degree than that of ranibizuamb. However, it is evident that the increase in FRV suppression relative to ranibizuamb is modest, and that the BI-X molecule suppresses FRV by over three times that of the SVB molecule. We also note there is no noticeable accumulation effect observed after multiple doses, due to the concentration of available binding sites being of similar magnitude to each dose.

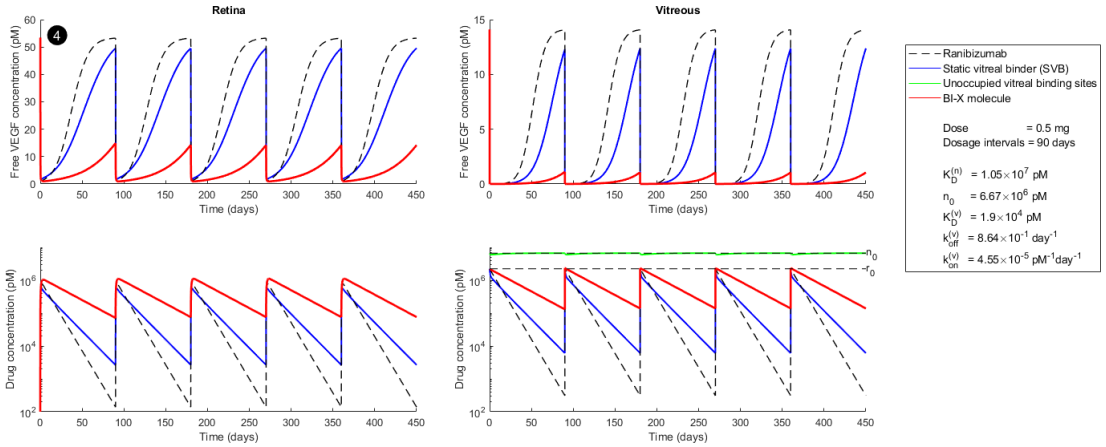

Figure 6.16: The solution to the SVB PK/PD model (Equations 6.4-6.15) is shown by the blue line. The concentration of unbound vitreal binding sites are shown by the solid green line, plotted alongside the concentration of vitreal drug. The solution to the BI-X model (Equations 6.71-6.89) is shown by the red line. The non-vitreal binding model (Equations 4.3-4.18) is shown by the dashed line. Here we see the SVB model solved for $K_D^{(n)} = 10^7$ pM, $n_0 = 6.7 \times 10^6$ pM. Doses of 0.5 mg administered every 90 days. Models for ranibizumab and the BI-X molecule were run using an identical dosage protocol. The SVB molecule decays at a slower rate than ranibizumab, and hence suppresses FRV to a greater degree than it. However the improvement in FRV suppression relative to ranibizumab is still not as great as is achieved by the BI-X molecule.

In Figure 6.17 the SVB model is solved for a dose of 0.5 mg, at a position in $\left(K_D^{(n)}, n_0\right)$ parameter space such that t_{dur} is maximised for a dose of 0.5 mg (see Figure 6.11). Subsequently we observe a greatly extended ocular half-life, alongside persistently high concentrations of FDVD, sufficient to suppress concentrations of FRV. While not seeing an effect due to repeat dosing, the SVB molecule is able to outperform ranibizumab, and more closely match the FRV suppression of the BI-X molecule. for approximately 50% of the dose interval. We also note that, in comparison to Figures 6.12-6.15 where we considered doses greater than or equal to 5 mg, here we dose with the standard ocular dose of 0.5 mg, and yet observe a higher level of FRV suppression. The same simulation is then shown in Figure 6.18, however we have now increased the dose to 5 mg. Figure 6.18 demonstrates that at this higher dose the level of FRV suppression is increased even further relative to that of ranibizumab, and performs almost identically to the BI-X molecule. Given the proven safety of 5 mg antibody injections into the human eye [54] it appears 5 mg or higher would

be a highly recommendable dosage. Figure 6.19 examines the same position in $\left(K_{\mathrm{D}}^{(n)}, n_0\right)$ parameter space, however now with an initial loading dose of 20 mg, followed by subsequent injections of 0.5 mg. Here we see that initially the loading dose is highly effective in suppressing the FRV. However, due to the lack of available vitreal binding sites we do not see an accumulation effect, and by the 4th dose the dynamics of the system have returned to that of Figure 6.17.

In Figure 6.20 the SVB model is solved for a dose of 0.5 mg, at a position in $\left(K_{\mathrm{D}}^{(n)}, n_0\right)$ parameter space such that $t_{\mathrm{dur}} = 0$ for a dose of 0.5 mg (see Figure 6.11), i.e. after the first injection the value of effective initial concentration of FDVD ($y_0 r_0$) is less than 5% of the equivalent concentration of the drug injected (r_0). Single dose analysis of this position in $\left(K_{\mathrm{D}}^{(n)}, n_0\right)$ parameter space has indicated it is unable to sufficiently suppress FRV, as although the ratio $n_0/K_{\mathrm{D}}^{(n)} \sim O(10^4)$ (hence generating an exceedingly large half-life), the capture of FDVD by vitreal binding sites is to such a degree that there exists an insufficient concentration of drug present in the retina to suppress FRV. However, in contrast to these previous findings, Figure 6.20 demonstrates that due to the large quantity of available binding sites, along with the relatively high value of $K_{\mathrm{D}}^{(n)}$, over many subsequent injections we observe an accumulated quantity of FDVD, increasing with every subsequent injection. Notice that, as the half-life on this timescale is effectively infinite, after each injection the concentration of FRV decreases similar to a step function. The magnitude of the drop in FRV after each injection decreases each time, showing that the positive effect due to the accumulation of drug on vitreal binding sites is diminishing in its returns - yet it is sufficiently high to start to bring the concentration of FRV below that achieved via the BI-X molecule.

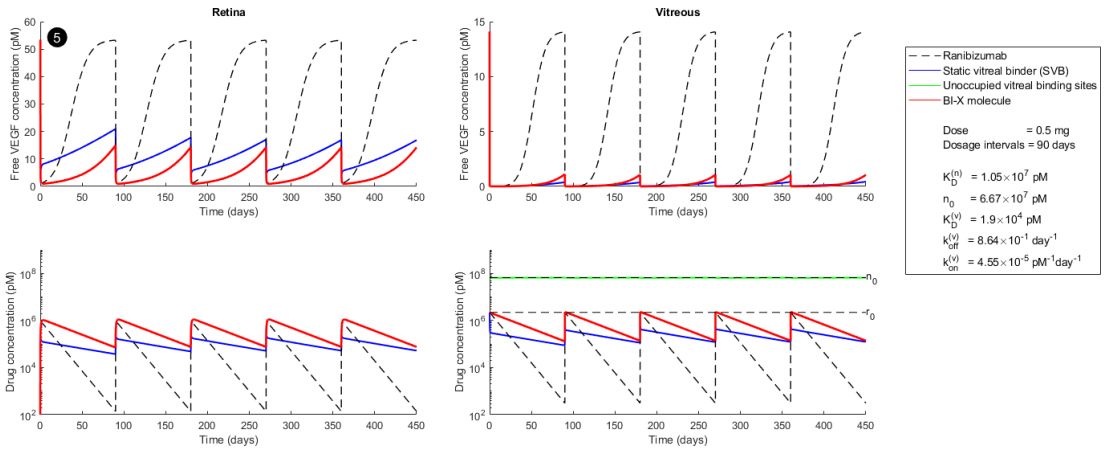

Figure 6.17: The solution to the SVB PK/PD model (Equations 6.4-6.15) is shown by the blue line. The concentration of unbound vitreal binding sites are shown by the solid green line, plotted alongside the concentration of vitreal drug. The solution to the BI-X model (Equations 6.71-6.89) is shown by the red line. The non-vitreal binding model (Equations 4.3-4.18) is shown by the dashed line. Here we see the SVB model solved for $K_{\mathrm{D}}^{(n)} = 10^7$ pM, $n_0 = 6.7 \times 10^7$ pM. Doses of 0.5 mg administered every 90 days. Models for ranibizumab and the BI-X molecule were run using an identical dosage protocol. High concentrations of FDVD are retained for a long time, leading to greatly increased FRV suppression, resultant from treatment with the SVB molecule, relative to ranibizumab. The BI-X molecule, however, is still able to suppress concentrations of FRV to a greater degree than the SVB molecule.

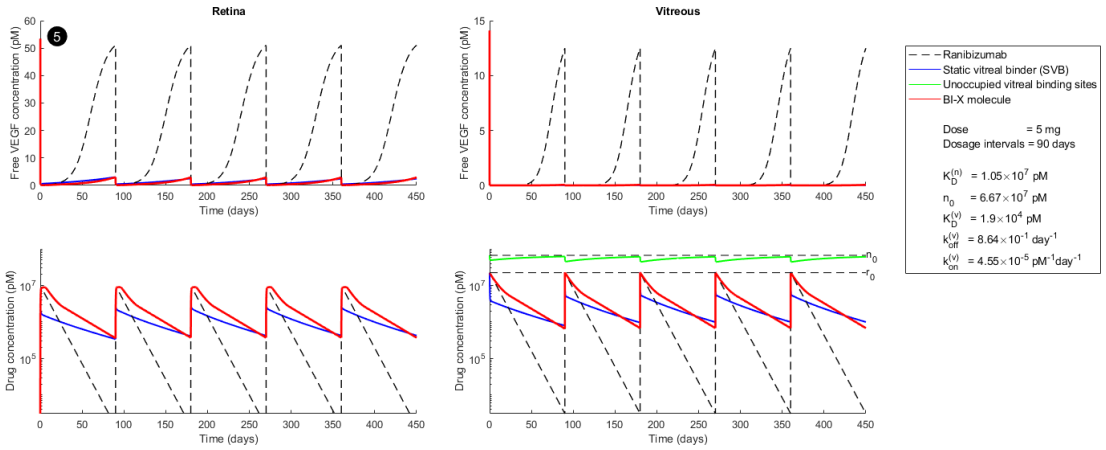

Figure 6.18: The solution to the SVB PK/PD model (Equations 6.4-6.15) is shown by the blue line. The concentration of unbound vitreal binding sites are shown by the solid green line, plotted alongside the concentration of vitreal drug. The solution to the BI-X model (Equations 6.71-6.89) is shown by the red line. The non-vitreal binding model (Equations 4.3-4.18) is shown by the dashed line. Here we see the SVB model solved for $K_{\mathrm{D}}^{(n)} = 10^7$ pM, $n_0 = 6.7 \times 10^7$ pM. Doses of 5 mg administered every 90 days. Models for ranibizumab and the BI-X molecule were run using an identical dosage protocol. The SVB and BI-X molecules exhibit almost identical levels of FRV suppression, both greatly superior to that achieved by ranibizumab.

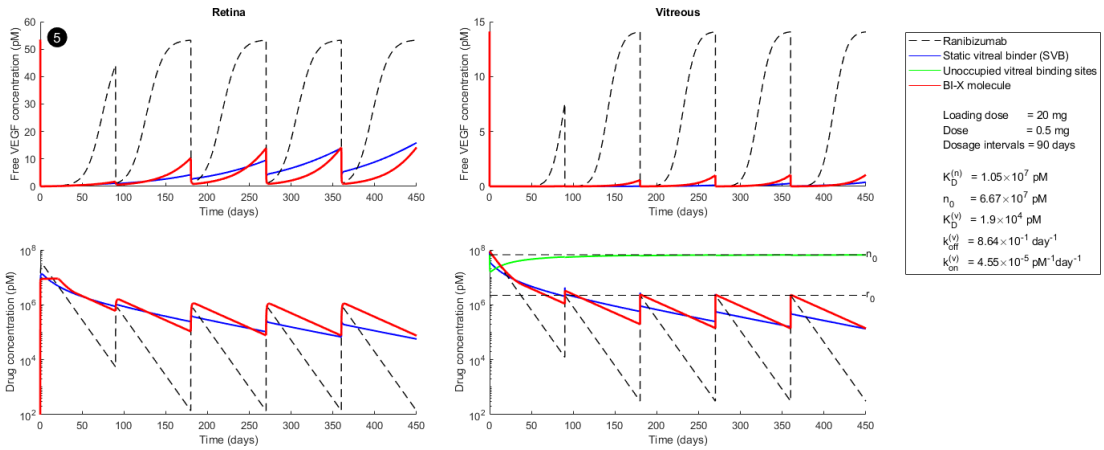

Figure 6.19: The solution to the SVB PK/PD model (Equations 6.4-6.15) is shown by the blue line. The concentration of unbound vitreal binding sites are shown by the solid green line, plotted alongside the concentration of vitreal drug. The solution to the BI-X model (Equations 6.71-6.89) is shown by the red line. The non-vitreal binding model (Equations 4.3-4.18) is shown by the dashed line. Here we see SVB model solved for $K_{\mathrm{D}}^{(n)} = 10^7$ pM, $n_0 = 6.7 \times 10^7$ pM. Doses of 0.5 mg administered every 90 days, with a loading dose of 20 mg administered at $t = 0$ days. Models for ranibizumab and the BI-X molecule were run using an identical dosage protocol. The loading dose fails to meaningfully increase the level of FRV suppression after the 3rd injection.

Figure 6.21 replicates the simulation of Figure 6.20 for a dose of 5 mg, one order of magnitude higher than that of the dose in Figure 6.20. Here we see similar behaviour as in Figure 6.20, however magnified greatly - the level of FRV suppression after the first injection is approximately half of that after the 5th dose in Figure 6.20. After the first dose we again see a noticeable positive effect on FRV suppression due to the accumulation of drug bound to vitreal binding sites - as can be seen from the concentration of FDVD, shortly after the first 4-5 injections the concentration of FDVD converges close to a seemingly steady level. This concentration of FDVD is sustained for all subsequent times, and is sufficiently high to almost completely suppress FRV, outperforming ranibizumab and replicating the magnitude of suppression achieved by the BI-X molecule. If this was able to be achieved in practice, it may be possible to only require 1 injection for every 3 injections required when treating with ranibizumab.

Finally, Figure 6.21 replicates the simulation of Figure 6.20 simulating repeated doses of 2 mg, with a loading dose of 10 mg at $t = 0$. Here we see that initially the loading dose is highly effective at jump-starting the accumulation effect, relative to Figures 6.19 and 6.20, by immediately pushing the concentration of FDVD close to the long time concentration achievable through repeat dosing. We note here that (as expected) the loading dose of the BI-X molecule does not carry a benefit through to later injections, however the BI-X molecule is able to maintain a lower suppression of FDVD at time just past that of each

injection. The simulation of Figure 6.21 demonstrates that for an SVB molecule lying at this point in $\left(K_{\mathrm{D}}^{(n)}, n_0\right)$ parameter space, it is possible to generate a prolonged suppression of FRV, substantially greater than that of ranibizumab.

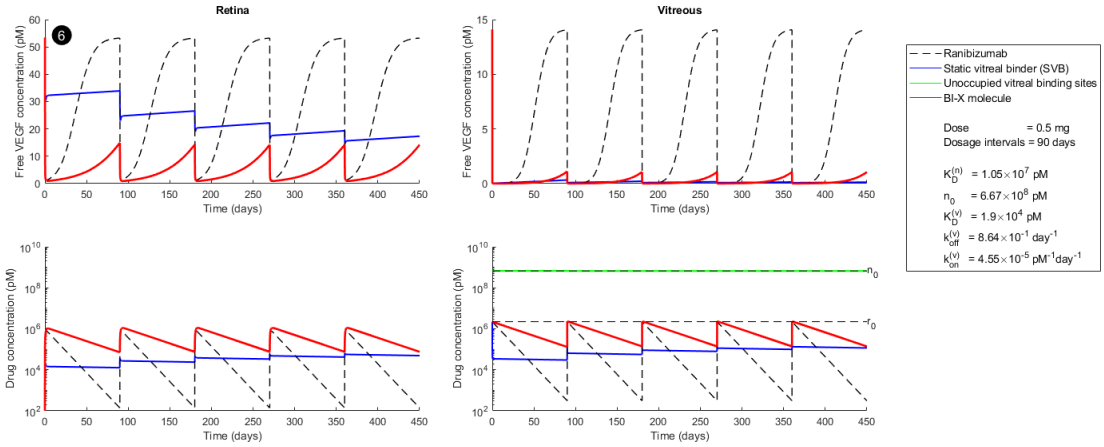

Figure 6.20: The solution to the SVB PK/PD model (Equations 6.4-6.15) is shown by the blue line. The concentration of unbound vitreal binding sites are shown by the solid green line, plotted alongside the concentration of vitreal drug. The solution to the BI-X model (Equations 6.71-6.89) is shown by the red line. The non-vitreal binding model (Equations 4.3-4.18) is shown by the dashed line. Here we see the SVB model solved for $K_{\mathrm{D}}^{(n)} = 10^7$ pM, $n_0 = 6.7 \times 10^8$ pM. Doses of 0.5 mg administered every 90 days. Models for ranibizumab and the BI-X molecule were run using an identical dosage protocol. Over time the quantity of FDVD increases, due to drug accumulation on vitreal binding sites, we see through repeated dosing a greater level of FRV suppression is able to be achieved.

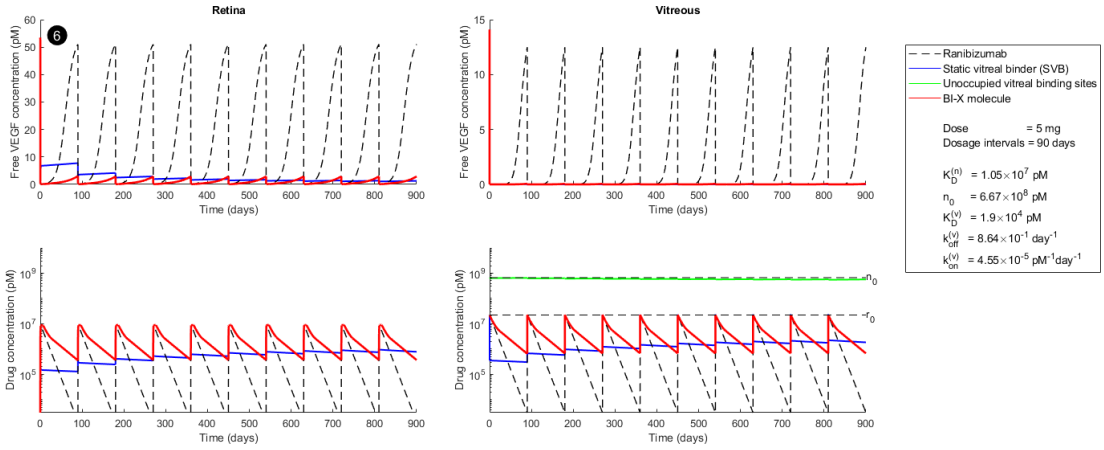

Figure 6.21: The solution to the SVB PK/PD model (Equations 6.4-6.15) is shown by the blue line. The concentration of unbound vitreal binding sites are shown by the solid green line, plotted alongside the concentration of vitreal drug. The solution to the BI-X model (Equations 6.71-6.89) is shown by the red line. The non-vitreal binding model (Equations 4.3-4.18) is shown by the dashed line. Here we see the SVB model solved for $K_{\mathrm{D}}^{(n)} = 10^7$ pM, $n_0 = 6.7 \times 10^8$ pM. Doses of 5 mg administered every 90 days. Models for ranibizumab and the BI-X molecule were run using an identical dosage protocol. The same effect as in Figure 6.20, however, due to the increased dose, the effect is more pronounced, greatly increasing the FRV suppression induced by the SVB beyond that achieved by the BI-X molecule.

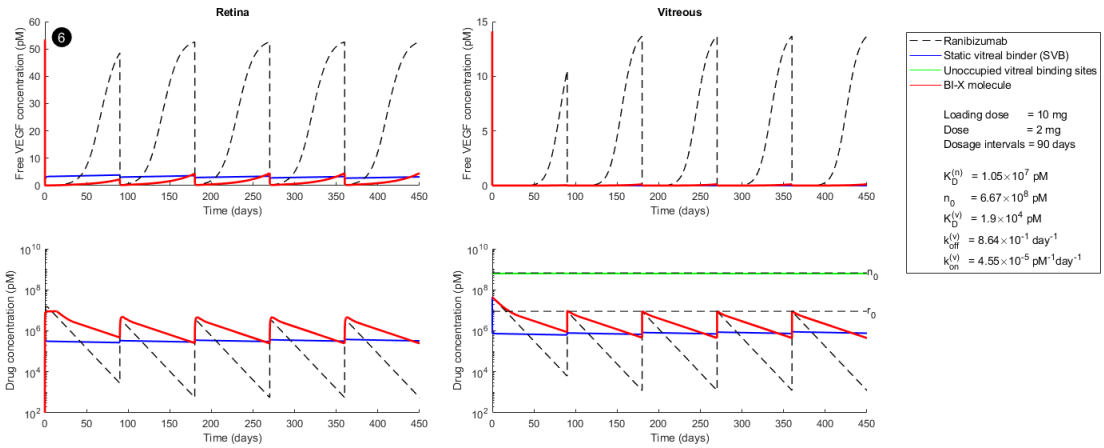

Figure 6.22: The solution to the SVB PK/PD model (Equations 6.4-6.15) is shown by the blue line. The concentration of unbound vitreal binding sites are shown by the solid green line, plotted alongside the concentration of vitreal drug. The solution to the BI-X model (Equations 6.71-6.89) is shown by the red line. The non-vitreal binding model (Equations 4.3-4.18) is shown by the dashed line. Here we see the SVB model solved for $K_{\mathrm{D}}^{(n)} = 10^7$ pM, $n_0 = 6.7 \times 10^8$ pM. Doses of 2 mg administered every 90 days, with a loading dose of 10 mg administered at $t = 0$ days. Models for ranibizumab and the BI-X molecule were run using an identical dosage protocol. Similar behaviour to that observed in Figures 6.20 and 6.21, however, through the utilisation of a loading dose at time $t = 0$, the number of doses required to utilise the accumulation effect is reduced.

6.7 Vitreal binding PK/PD ODE model summary

In this chapter we have presented the final ODE model of this thesis, which represents the fusion of the ODE models discussed in Chapters 2-5, to describe the PK/PD of a SVB. This model incorporates the mechanistic PK retinal framework of Chapter 3, the RVR binding PD model of Chapters 2 and 4 and, crucially, the SVB PK model of Chapter 5. By combining these models we had to account for the possibility of the formation of larger molecular groups, such as a RVRN complex - thus greatly increasing the complexity of the model relative to those from which it was generated. Despite this increased level of complexity, in Section 6.2 we demonstrated that the PK of the model (the concentration time-courses for R, N and RN) could be decoupled from the rest of the model, allowing us to describe the concentration of FDVD using the SVB PK ODE model of Chapter 5. This step in our analysis allows the utilisation of the PK results of Chapter 5, including our analysis on the half-life of a SVB molecule (Section 5.1.2) and its duration time (Section 5.1.3). The analysis of Section 6.2 additionally allowed us to analyse the FRV dynamics of the SVB PK/PD model, in an analogous manner to Section 4.1.3. This demonstrated that, as in Section 4.1.3, the concentration of FRV is inversely proportional to the concentration of unbound drug in the retina, and hence also inversely proportional to the concentration of FDVD. This result tells us that through understanding both the proportionality constant between FRV (discussed in Section 4.1.3) and the concentration time-course of FDVD (Chapter 5),

one may fully characterise the suppression of FRV - and hence the efficacy of the drug.

In this chapter, in addition to modelling the PK/PD of the SVB molecule, we also formulated a model for, and analysed, the PK/PD of a second class of vitreal binding molecule, an nSVB molecule - specifically the BI-X molecule [59]. In Section 6.3 we formulate the BI-X PK/PD model, an nSVB molecule capable of binding to ocular albumin. In Fuchs et al. [59] it was stated that the BI-X molecule (in addition to an injection of a surplus of human albumin) was able to achieve an ocular half-life of 10 days in the rabbit, over 3 times greater than that of a standard Fab molecule. Our analysis of the BI-X molecule hinges on the accuracy of our estimate for the value of the human ocular half-life of the BI-X-albumin complex, generated by scaling the half-life of the BI-X-albumin complex in the rabbit, relative to that of the Fab in the rabbit and human. Given that the half-life of a Fab molecule increases by a factor of 2.21 between the rabbit and human, our meta-analysis of the relationship between vitreal diffusion time and half-life (Chapter 2) suggests that the half-life of the BI-X-albumin complex will also scale by that factor between the rabbit and human, hence, yielding our estimate of 22.1 days for the value of the half-life of the BI-X-albumin complex in the human. Therefore, as can be seen, although this is a very high value, it is generated in a manner consistent with our previous work, and is based upon the assumptions of the scaling analysis in Chapters 2 and 4, as well as the accuracy of the reported values in Fuchs et al. [59].

In Sections 6.4-6.6 we compare the solutions to the models of the SVB, BI-X molecule and ranibizumab, for various locations in $\left(K_{\mathrm{D}}^{(n)}, n_0\right)$ parameter space, to demonstrate the impact of the PK behaviour types discussed in Chapter 5. In Section 6.4 we see that depending on the location in $\left(K_{\mathrm{D}}^{(n)}, n_0\right)$ parameter space the suppression of FRV varies greatly - for weak binding and few binding sites the SVB molecule suppresses FRV behaves in a very similar fashion to that of ranibizumab and for strong binding with a large quantity of binding sites the SVB molecule exhibits an extremely long half-life, but possesses an effective initial concentration of FDVD insufficiently large to suppress FRV. Between these two extremes lies a region of $\left(K_{\mathrm{D}}^{(n)}, n_0\right)$ parameter space, as outlined in Chapter 5, where the ratio of $K_{\mathrm{D}}^{(n)}$ and n_0 is such that a concentration of FDVD, sufficiently high to suppress FRV, is maintained for an extended period of time, relative to ranibizumab. From Figures 6.1-6.7 we can see that for SVB molecules whose values of $K_{\mathrm{D}}^{(n)}$ and n_0 lie in this region of parameter space, the SVB molecule is able to suppress the concentration of FRV up to 2-3 times as long as ranibizumab.

In Section 6.5 we presented a case study for an SVB molecule proposed and studied by Ghosh et al. [58], capable of binding to vitreal hyaluronic acid. Following the work of Ghosh et al. we assumed that the human vitreous has a carrying capacity of 2 mg of a Fab based SVB molecule, and considered a range of $K_{\mathrm{D}}^{(n)}$ values based on this quantity of binding sites, at doses of 0.5 mg, 2 mg and 8 mg. We can see from Figures 6.8-6.10 that, for this fixed value of n_0 ($\sim O(10^7)$), for values of $K_{\mathrm{D}}^{(n)}$ between 10^6 and 10^7 a level of FRV suppression greatly superior to ranibizumab can be achieved. We found that increasing the dose from 0.5 mg to 2 mg resulted in a large positive effect on the suppression of FRV, and increasing the dose from 2 to 8 mg, while also improving the suppression of FRV, did not reduce its concentration to the degree observed by increasing the dose from 0.5 mg to 2 mg. This was to be expected given that the carrying capacity of the hyaluronic acid was modelled as 2 mg - therefore any dose greater than 2 mg would yield diminishing returns with respect to FRV suppression.

In Section 6.6, we presented an analogous study to that of Section 5.1.4, detailing the effect of repeat doses of the SVB molecule, to analyse the consequence of drug accumulation on vitreal binding sites, alongside the possible application of loading doses. Figures 6.12-6.22 detail various hypothetical dosage protocols, using a range of doses and loading doses, administered at 90 day intervals, comparing the SVB model evaluated at various places in $\left(K_{\mathrm{D}}^{(n)}, n_0\right)$ parameter space, alongside ranibizumab and the BI-X molecule. From this analysis we found for values of $K_{\mathrm{D}}^{(n)}$ much less than the minimum vitreal concentration of ranibizumab required to sufficiently suppress FRV, there was no location in $\left(K_{\mathrm{D}}^{(n)}, n_0\right)$ parameter space such that it was capable of outperforming ranibizumab, at any dose. For this region in parameter space, due to the strength of the binding between the SVB and the vitreal binding sites, the only times when the SVB model exhibited a decay rate greater than ranibizumab were when its concentration was already much less than that required to sufficiently suppress FRV. When a large dose, or loading dose, was administered the excess quantity of SVB molecules simply decayed in line with ranibizumab, hence yielding no increase in FRV suppression. For $K_{\mathrm{D}}^{(n)}$ values of order 10^6 pM or greater we found those with maximal t_{dur} values (locations (4) and (5) of Figure 6.11) were able to maintain FRV suppression levels greatly superior to ranibizumab and on par with the BI-X molecule, however they did not appear to benefit from any drug to vitreal binding site accumulation effect. In location (6) of Figure 6.11, in the 0.5 mg t_{dur} red zone ($t_{\mathrm{dur}} = 0$ days), it was found that due to the large quantity of vitreal binding sites and relatively weak binding, the concentration of FDVD would accumulate significantly between doses. We demonstrated that after a certain quantity of the drug had been administered, it was possible to maintain

an almost complete and stable suppression of FRV, and that this could be achieved using either high doses or through a large loading dose at $t = 0$ days. This result demonstrates that t_{dur} analysis alone is not sufficient to analyse the performance of an SVB molecule relative to $\left(K_{\text{D}}^{(n)}, n_0\right)$ parameter space and that perhaps the duration time of a SVB drug should be considered after the nth injection.

In all sections of this chapter we have considered the performance of the SVB molecule relative to the BI-X molecule, in which the BI-X molecule almost universally managed to suppress FRV to a greater degree than the SVB molecule. The BI-X molecule is in many ways a simpler concept than that of the SVB molecule - instead of attempting to bind in the vitreous to prolong its duration, (yielding a 'sweet spot' in parameter space), the BI-X molecule attempts only to increase its hydrodynamic radius (and hence its half-life) by binding to large mobile molecules naturally occurring within the vitreous. It appears that, within the limitations of the models presented in this work, the BI-X molecule consistently outperforms the SVB molecule. This is clear from the results presented here, however there are potential issues with how our BI-X model was constructed - as noted previously the performance of the BI-X molecule is primarily due to our estimated human half-life of 22.1 days, which requires validation. Additionally, given the large hydrodynamic radius predicted for BA or larger albumin complexes, relative to the antibodies considered in Chapter 3 Section 3.1, we cannot comment on the likelihood of these complexes permeating into the retina. Further experimental investigation is required in order to validate our estimated human half-life and assumption of retinal permeation. We strongly encourage that it is confirmed whether the BI-X molecule, as part of a larger complex, is able to permeate into the retina, as our earlier theoretical work in Chapter 4 demonstrated that, without retinal permeation of drug or drug-target complexes, meaningful FRV suppression is not achievable.

We also note here that the superiority of the BI-X molecule relative to the SVB is strongly dependent on the assumption that the retina does not also contain sites to which the SVB molecule could bind. This assumption is, of course, a key component of the formulation of the SVB model, such a static vitreous-retina binding molecule (SVRB) would be described by a different mathematical framework - however it is not biologically unreasonable to imagine that structures to which a molecule is designed to bind to in the vitreous, may also be present in the retina. From our analysis of the SVB model, we can state that it seems possible that a SVRB model may predict more favourable FRV suppression, however such a molecule would still require a sufficiently high concentration of FDVD in order to generate a concentration of drug in the retina sufficiently high to suppress FRV - with or

without the capability of retinal binding. However, for such a molecule it seems likely that repeat injections would have a much more significant effect, as retinal binding site saturation may be possible to achieve. For a sufficiently low value of $K_{\mathrm{D}}^{(n)}$ and a sufficiently high concentration of retinal binding sites, it seems plausible that after a certain number of doses it would be possible for such an SVRB molecule to achieve almost complete FRV suppression - however this requires confirmation. Analysis of such a model we suggest as future work.

Finally, in our discussion regarding the simulations of the SVB molecule we have generally only considered the free VEGF suppression in the retina - as this is the site of disease activity - however in Sections 6.4-6.6 we additionally provide VEGF concentration profiles in the vitreous. In Chapter 4 we demonstrated that the concentration of VEGF in the aqueous humour is proportional to that of the vitreous, it therefore follows that if the SVB molecule completely suppresses the concentration of free VEGF within the vitreous, then the concentration of free VEGF within aqueous humour will also be suppressed. However, as we have demonstrated within this chapter, it is possible for the concentration of free VEGF in the vitreous to be almost completely suppressed, while the concentration of FRV remains close its steady state concentration, i.e. barely affected by the presence of the drug in the eye (see Figure 6.8 plots (1) and (2)). This is particularly seen in our simulations for SVB molecules with high binding affinities to vitreal binding sites, and often occurs alongside the exhibition of an extremely long half-life. Given the knowledge that the concentrations of molecular species in the aqueous mirror those of the vitreous, if one was to sample the aqueous (as previously done [81, 118]) to measure either free VEGF concentration, or to study PK (i.e. characterise the half-life), of an SVB molecule post-IVT injection, in a patient suffering from wet AMD, it may be possible to find very a low concentration of free VEGF, alongside a very long ocular drug half-life. These would both be very promising results, however we have demonstrated that both these phenomena can occur while the concentration of FRV has been barely reduced from steady state, hence, these phenomena can be observed while the drug is having absolutely no meaningful effect on disease activity. This demonstrates that if a clinical trial was conducted using aqueous (or vitreal) free VEGF, or drug longevity (i.e. half-life) as secondary outcomes, then the trial could yield false positives. Additionally given that molecules are not typically designed to have extremely weak binding, i.e $K_{\mathrm{D}}^{(n)} \sim O(10^6)$ or greater, assuming the findings of the model to be correct, it is potentially not unlikely for such a false positive to occur. Historically several experimental treatments have gone on to be approved after yielding positive secondary outcomes, despite having shown little or no improvement in their primary clinical outcome [132]. Due to this

we strongly caution against using ocular half-life, or free VEGF concentrations measured from aqueous humour sampling, as indicators of efficacy in any clinical or experimental trial of an SVB molecule, as in the absence of favourable visual acuity scores or an observable reduction in disease activity (over an equivalent non-vitreal binding molecule) these may indicate a false positive. Additionally, if such a false positive was to occur, it is likely that the level of FRV suppression would in fact be much lower than an equivalent non-vitreal binding molecule, hence, if approved, leading patients to be treated with a sub-standard drug relative to standard of care. We note, these conclusions are only as accurate as our model, which requires further experimental data to validate, and hence must be viewed in such a context.

7 Conclusions and future work

7.1 Conclusions

As mentioned in the introduction, wet AMD is a highly debilitating retinal disease, causing central visions loss and, if left untreated, a considerable reduction in the quality of life of those afflicted [4–7]. Currently, wet AMD represents the third leading cause of blindness across the globe, and over the following decades the number with the disease is expected to rise by almost 100 million [15, 16]. In addition to the severity and prevalence of wet AMD, providing those suffering from the condition with treatment represents a significant economic burden on the provider of care, primarily due to the price of treatment. In 2010 the global healthcare cost of AMD came to $254.8 billion, approximately 25% of all healthcare costs due to visual impairment (excluding uncorrected refractive error) [17], and in 2014 the NHS spent £244 million on ranibizuamb, representing the second greatest cost incurred by NHS due to the purchase of medication [18]. Severity, prevalence and cost to treat, together, make wet AMD a problem to be contended with on a global scale. In this thesis we have developed a number of PK/PD models to systematically investigate aspects of current and future treatments for wet AMD.

PK/PD modelling of therapeutic macromolecules in the eye represents a key tool to be used in the fight against retinal conditions, such as wet AMD. Ocular PK/PD modelling, in combination with experimental and clinical study, gives us the ability to look further into the eye than can be done clinically; giving us a window into the dynamics occurring

between our data points, that our instruments cannot reach. Using ODE and PDE models we can interrogate experimental data to retrieve key physiological or biochemical parameters, allowing us to characterise and compare treatment protocols. Using the same models we can then look outwards from our data, to generate and test hypotheses, as well as make treatment predictions. In doing so, we hope to guide future experimental/clinical studies by attempting to predict which avenues or research will yield fruitful results - and which may not. As well as testing future, undeveloped therapeutic molecules, we can examine modifications of an existing molecule or its treatment protocol *in silico*, with an aim to improve on, or optimise, its design or application. I now return to the RED goals (*Reduce* cost, improve *efficacy*, increase *duration* of effect) of this thesis, described in the introduction, and discuss how this work, using the methodology outlined above, can help achieve them.

In Chapter 2, we presented a 2-compartment, vitreous-aqueous, model of the human eye. By building on the work of Saunders et al. [3], we demonstrated how to introduce a higher level of biochemical accuracy through the introduction of the RVR binding model, and hence showed a relatively simple way in which the model could be made more realistic. Through re-examination of the clinical dataset of patients being treated with ranibizumab for wet AMD, presented in Saunders et al. [3], we determined how, when fitting to the data, the value of $K_{\mathrm{D}}^{(v)}$ (the dissociation constant between ranibizumab and VEFG) determines the ocular half-life predicted during the fitting process. By sweeping over many $K_{\mathrm{D}}^{(v)}$ values we determined that when $K_{\mathrm{D}} \simeq 21,000$ pM the 2-compartment model predicted a half-life distribution, across the 31 patients, most closely reflecting the experimentally recorded half-life of ranibizumab in humans (Section 2.2). This value of $K_{\mathrm{D}}^{(v)}$, $21,000$ pM, was greater than that assumed by Saunders et al., who took $K_{\mathrm{D}}^{(v)} = 46$ pM, and hence implies that the affinity with which ranibizumab binds to VEGF was much less than previously thought.

In Chapter 3 we extended the 2-compartment model to describe the PK within the retina, by considering the permeability of molecules to the ILM and RPE. By calibrating this 3-compartment model to experimental 3-compartment PK data (Gadkar et al. [28]) we were able to estimate the permeabilities of the ILM and RPE (Section 3.1.2), and hence fully parametrise the 3-compartment model with respect to a range of different macromolecules. In addition to the estimation of the retinal permeabilities in the 3-compartment model we also derived the analytic solution of the 3-compartment model, allowing us to characterise the ocular half-life in terms of model parameters (Equations 3.15 and 3.24), which demonstrated that, as previously assumed (for example in Chapter 2, Saunders et al. [3], Gadkar et al. [28]), the rate of clearance via the anterior chamber of the eye primarily determines

the rate of a molecule's decay within the eye.

Due to the addition of the choroidal clearance pathway, we were able to estimate the relative quantity of molecules eliminated via the choroid versus via the anterior chamber. This is of significance since, as we have previously noted, a large proportion of molecules injected into the vitreous are lost via this anterior pathway, before they are able to reach the retina - their intended target. Using the 3-compartment model to quantity this aqueous-retina elimination ratio may then estimate the proportion of a dose to which the retina/choroid is being exposed, and hence the proportion of molecules injected that are likely to bind to VEGF in the retina or choroid. This analysis (Section 3.1.3) concluded that, due to the notable drop in the magnitude of k_{el} between Fab and IgG molecules (by approximately 50%), simulated IgG molecules were retained longer within the vitreous, and were hence eliminated at a higher rate through the choroid than Fab molecules. This indicates that larger molecules, such as bevacizumab, may have the counter-intuitive ability to gain a greater degree of retinal exposure - even while possessing lower retinal permeabilities than smaller molecules, such as ranibizumab. Experimental study would help confirm whether this is the case, and whether this phenomenon could be exploited to improve treatment outcomes, and hence treatment *efficacy*.

Also in Chapter 3 we presented an equivalent 3-compartment PK PDE model of the retina, vitreous and aqueous, and performed the same fitting procedure to the Gadkar et al. [28] dataset (Section 3.2), that was performed using the 3-compartment ODE model. In this PDE model transport from the vitreous to aqueous, modelled by the parameter k_{el} in the ODE model, was instead based on the permeability of the anterior hyaloid membrane, p_{HYA}. By spatially averaging the PDE model we derived Equation 3.69 relating k_{el} and p_{HYA}, under the well-mixed assumption (used in the ODE models). This equation can be used to calculate the values of p_{HYA}, as predicted by the 3-compartment ODE, using its estimated values for k_{el}. We found that both the ODE and PDE models predicted similar permeabilities of the RPE and ILM, however the values of p_{HYA} estimated by the PDE model were much lower than those predicted by the ODE model (Section 3.2.4). This indicates that, while we demonstrated that both the ODE and PDE models (when calibrated to the same 3-compartment PK dataset) possess similar predictive capacity, the parameter k_{el} of the ODE model should be treated as a phenomenological parameter whose value, when estimated, contains information regarding both p_{HYA} and the vitreal diffusion coefficient, D_{vit} (Section 3.2.5). In Section 3.2.6 we attempted to characterise the relationship between k_{el}, p_{HYA} and D_{vit} using a one-dimensional caricature of the ocular

PDE model. By solving this model we derived Equation 3.164 relating the half-life of the one-dimensional PDE model to the half-life of the equivalent well-mixed model and D_{vit}, demonstrating that while the timescale of diffusion across the vitreous is on the order of, or greater than, the timescale of permeation through ocular membranes, the parameter k_{el} of the ODE model will remain phenomenological. Section 4.2 of Chapter 4 compares the 3-compartment PK/PD ODE model, to an equivalent PDE model, in a similar manner to Section 3.2. This analysis found no notable difference between the solutions and predictive capabilities of the ODE and PDE models, further strengthening the conclusions from Section 4.2 that ODE models can reliably model the PK/PD of macromolecules within the eye.

In Chapter 4 we used the 3-compartment model of Chapter 3 to reanalyse the clinical dataset considered in Chapter 2, through integrating the RVR binding model into the PK structure of the 3-compartment model, thus creating a 3-compartment PK/PD model for ranibizumab. Through numerical analysis of the model, we demonstrated that the model predicts the magnitude of free VEGF suppression in the retina is generally lower than that of the aqueous (Section 4.1.3), as well as predicting the existence of a retina-aqueous suppression lag, such that the concentration of free VEGF returns to steady state sooner than in the vitreous and aqueous (Section 4.1.5). We demonstrated that increasing the permeability of the RPE made both of these effects more pronounced (Section 4.1.7), and this dependence on p_{RPE} could also be demonstrated analytically (Section 4.1.6), using the solution to a simplified 3-compartment PK/PD model (Equations 4.110 and 4.118). The existence of this predicted suppression lag may explain the findings of Fauser et al. [118] that demonstrated, in a subset of patients responding poorly to ranibizumab, that the duration of drug efficacy was approximately half of that for which free VEGF was suppressed in the aqueous humour.

In an attempt to find a way to improve the performance of ranibizumab in the retina, we conducted a study examining the effect on FRV suppression due to variation in binding rate parameters ($k_{\text{off}}, k_{\text{on}}$ and $K_{\text{D}}^{(v)}$), as well as dosage modifications (Section 4.1.8). This study concluded that the only scenario in which improvement in retinal free VEGF suppression is possible, at both early and late time, is via a simultaneous increase and decrease of k_{on} and $K_{\text{D}}^{(v)}$, respectively. Achieving this would, in practice, be challenging, as the magnitude of k_{on} is partially dependent on the random chance of the drug meeting its target. However, dosage analysis demonstrated it is possible to produce the same qualitative behaviour as is achieved by increasing k_{on} and decreasing $K_{\text{D}}^{(v)}$ by solely increasing the dose - therefore implying that the simplest method (increasing dosage), to increase the magnitude of FRV suppression (of a standard anti-VEGF molecule such as ranibizumab), may also be the

most likely to be effective. In Section 4.1.7 we demonstrated that when the permeability of the RPE was taken higher than baseline, increasing the dose of ranibizumab from 0.5 mg to 6 mg, increased the total retinal free VEGF suppressed by ∼225% - relative to the 50% increase seen in the aqueous humour. This implies that in patients with high RPE permeabilities - which could be the case in patients with advanced cases of wet AMD due to pervasive neovasculature - such an increased the dose may substantially increase the ability of the treatment to suppress FRV.

As patients with advanced neovascularization may possess higher effective p_{RPE} values, such patients may be predisposed to respond poorly to treatment. Hence, studies similar to that conducted by Fauser et al. [118], focusing on patients responding poorly to anti-VEGF treatment, may reveal valuable information regarding physiological/pathological factors that differentiate them from the rest of the population. Our research suggests that such poor responders may respond well to an increased dosage of the nature simulated in Section 4.1.7, and we believe this would be worthwhile to investigate. Given that 10-20% of treatment-naive eyes show no marked improvement when treated with ranibizumab or bevacizumab at standard doses, such a treatment alternative may address the '*significant unmet need*' in treatment outcomes noted by Brown et al. [27]. Brown et al. [27] additionally suggested higher dosages may fulfil this need, stating "*we hypothesize that a higher dose of ranibizumab might improve efficacy, leading to better outcomes for patients who are "incomplete responders" to conventional monthly therapy.*", a hypothesis congruent with our own. The safety of such an increased dose would, of course, have to be rigorously investigated - however the 6 mg IgG ocular safety trial of RG7716, conducted in 2017 by Chakravarthy et al. [54], determined such an injection to be completely safe. A 6 mg treatment protocol, such as this, has the potential to not only increase *efficacy*, but also *reduce* cost, as the patents on ranibizumab have been estimated to expire in 2022/20 (UK/US) [133], and hence ranibizumab could soon be produced generically at a fraction of the current price (currently £742/$2000 for 0.5 mg in the UK/US [134–136]). Such a treatment protocol may achieve similar or greater efficacy to the upcoming RG7716 molecule, which when dosed at 6 mg has the equivalent anti-VEGF capability of a 2 mg dose of ranibizumab (as for each 1 mg of ranibizumab there exist 3 times as many anti-VEGF binding sites as for each 1 mg of RG7716, additionally noting ranibizumab is a constituent molecule of RG7716, see Figure 1.7). Independent and state-funded clinical trials of this nature, testing safety and efficacy, are not unprecedented, due to their potential to reduce the economic burden of providing care, for example see the 2014 systematic review of 9 independent trials (3665 participants) comparing the safety and efficacy of bevacizumab versus ranibizumab [47]. The economic

burden of providing care is particularly great for wet AMD, which in 2010 amounted to approximately 25% of all healthcare costs due to visual impairment (excluding uncorrected refractive error) [17]. Therefore reducing the cost of wet AMD treatment could have a profound global effect, and potentially make treatment available in less wealthy nations, wherein treatment for wet AMD is essentially non-existent [19].

In Chapters 5 and 6 we shifted our analysis from that of existing anti-VEGF antibodies, to multi-specific antibodies, capable of binding to other molecules in addition to VEGF. Specifically, we considered antibodies designed to bind to ocular super-structures (SVBs) or large naturally occurring molecules (nSVBs), in order to increase the *duration* of time a dose is retained in the eye. In Chapter 5 we formulated a retina-vitreous PK model for such an SVB molecule, by extending the 3-compartment PK ODE model of Chapter 3 to include additional chemical species denoting the concentration of unbound and bound static vitreal binding sites. In deriving the analytic solution to the model (Section 5.1.1) we demonstrated that, due to a fast initial chemical equilibration between the drug and vitreal binding sites, shortly after the drug is injected the concentration of FDVD drops to reach a concentration we referred to as an 'effective initial concentration', strictly lower than the concentration corresponding to the initial injection, the 'dosage concentration'. The relative magnitude of the effective initial concentration and the dosage concentration varies between 0 and 1, and is a function of $c_0, K_{\mathrm{D}}^{(n)}$ and n_0 (Equation 5.40).

We note that during this analysis we focused primarily on the concentration of FDVD, not the total drug in the vitreous, as Section 4.1.7 demonstrated that, in the absence of drug/drug-target complexes to retinal permeation, an anti-VEGF molecule's capability to suppress FRV was almost entirely compromised. Therefore, using the analytic solution to the SVB PK ODE model we analysed the half-life of FDVD, and how it compared in magnitude to that of the equivalent non-vitreal binding, classical, molecule (Section 5.1.2). We demonstrated that the half-life of an SVB molecule could be increased arbitrarily by increasing the number of available vitreal binding sites, as well as the molecule's binding affinity to such sites, i.e. increasing the ratio $n_0/K_{\mathrm{D}}^{(n)}$. Additionally we demonstrated that the half-life exhibited by an SVB molecule is a monotonically decreasing function in concentration (Equation 5.84), confirming the intuitive conclusion that the lower the concentration of the drug, the more binding sites are available for individual drug molecules to bind to - hence over time the half-life of the system will increase as the drug is eliminated.

We next returned to the concept of effective initial concentration, demonstrating that when $n_0/K_{\mathrm{D}}^{(n)} \to \infty$ while the half-life tends to infinity, the effective initial concentration tends to zero. Noting our previous comment regarding the requirement of FDVD to maintain efficacious FRV suppression, it is possible for a molecule (with a very high $n_0/K_{\mathrm{D}}^{(n)}$ value) to have an exceptionally long half-life, while being entirely ineffective. Given that the concentration of FDVD is monotonically decreasing, this tells us that if the effective initial concentration is below a hypothetical concentration of FDVD required to efficaciously suppress FRV, then the treatment will be ineffective for all time. Additionally the amount of time the concentration of FDVD spends above this value, is the amount of time that the treatment is theoretically efficacious. We analysed the time such that the concentration of FDVD remained greater than a theoretical minimum efficacious concentration, which we defined as the 'duration time' (t_{dur}) of the drug (Section 5.1.3). This analysis (see Figure 5.11) determined that t_{dur}, for a fixed dose, is determined by location in $\left(K_{\mathrm{D}}^{(n)}, n_0\right)$ parameter space. For $K_{\mathrm{D}}^{(n)} \sim O(c_0)$ and greater we found there to exist values of t_{dur} up to 2.3 times greater than that of an equivalent non-vitreal binding molecule. These values lay along a line in log-log $\left(K_{\mathrm{D}}^{(n)}, n_0\right)$ parameter space - a region we refer to as 'the hill' of $\left(K_{\mathrm{D}}^{(n)}, n_0\right)$ parameter space.

To analyse which values of $K_{\mathrm{D}}^{(n)}$ and n_0 generate maximal t_{dur} values we generated approximate solutions for t_{dur} and the concentration of FDVD, $c(t)$, given by Equations 5.137 and 5.150, respectively. Using these equations we demonstrated that when $K_{\mathrm{D}}^{(n)} \gg c_0$, t_{dur} and $c(t)$ depend only on the ratio $K_{\mathrm{D}}^{(n)}/n_0$, and that t_{dur} is maximised for a specific ratio determined by the dose and minimum efficacious concentration (Equation 5.142), approximately equal to 0.2. Additionally we demonstrated that in this region $c(t)$ exhibits exponential decay with the maximal half-life achievable within the system.

Using this knowledge of the SVB PK behaviour over $\left(K_{\mathrm{D}}^{(n)}, n_0\right)$ parameter space, we moved on to consider dosing protocols, and notably the effect of repeat dosing, at various locations in $\left(K_{\mathrm{D}}^{(n)}, n_0\right)$ parameter space (Section 5.1.4). Due to the ability of the SVB molecule to bind to static superstructures in the vitreous we hypothesised that, after multiple doses, drug may accumulate on vitreal binding sites, and hence be a higher concentration of FDVD may be able to be maintained after multiple doses, relative to after a single dose. Through investigation of high affinity binding between the SVB and the vitreal binding sites we identified two characteristic behaviour types; the decay either exhibited no noticeable difference in decay rate between SVB and classical counterpart for all time, or we found the concentration of FDVD was approximately zero. In the latter case the binding was so tight

that any drug bound to a vitreal binding site is essentially removed from the system (zero effective initial concentration). Hence, we conclude that SVB molecules lying in this region of $\left(K_{\mathrm{D}}^{(n)}, n_0\right)$ parameter space have the potential to be only as efficacious as their classical counterpart, and are in fact likely to under-perform in comparison.

Figures 5.18-5.23 examined the effect of repeat dosing for lower affinity binding between the SVB and the vitreal binding sites than in Figures 5.24-5.30. As predicted in Section 5.1.3 the SVB molecule exhibited favourable increasing in decay rate, while possessing an effective initial concentration greatly above $c_{30}^{(r)}$. We found SVB molecules whose $\left(K_{\mathrm{D}}^{(n)}, n_0\right)$ pairs lay on or near to the hill of $\left(K_{\mathrm{D}}^{(n)}, n_0\right)$ parameter space maintained an efficacious concentration of FDVD for the longest, as predicted by our duration time analysis - however we found minimal increase in FDVD concentration due to drug accumulation in the vitreous. Unexpectedly, SVB molecules whose $\left(K_{\mathrm{D}}^{(n)}, n_0\right)$ pairs lay in the region of $\left(K_{\mathrm{D}}^{(n)}, n_0\right)$ parameter space such that $t_{\mathrm{dur}} = 0$, while initially exhibiting FDVD concentration well below the theoretical efficacious level, benefited exceedingly positively from the accumulation effect.

Finally in Chapter 6, we studied the PK/PD of anti-VEGF SVB and nSVB molecules, relative to their classical counterpart, ranibizumab. Alongside the PD extension of the SVB PK model we presented a PK/PD model for a nSVB, specifically the BI-X molecule, an antibody similar in size to ranibizumab, designed to bind to naturally occurring ocular albumin, as well as VEGF (Section 6.3).

In Figures 6.1-6.7 of Section 6.4 compare the theoretical PK/PD, after a single IVT injection of, static vitreal binding (SVB) molecules (Equations 6.4-6.15), non-static vitreal binding (nSVB) BI-X molecules (Equations 6.71-6.89) and ranibizumab (Equations 4.3-4.18). From this analysis we found that the underling PK of the FDVD, as outlined in Chapter 5, completely dictates the suppression of FRV. We found that the SVB was able to suppress FRV to a greater degree, relative to ranibizumab, at precisely the locations predicted by the duration time analysis of Chapter 5, i.e. when the SVB model was evaluated on or near the hill in $\left(K_{\mathrm{D}}^{(n)}, n_0\right)$ parameter space, the suppression of FRV achieved was far superior to that of ranibizumab. We found when evaluating the SVB model away from this region, either the binding between the SVB molecule and the vitreal binding sites was too great (and hence trapped the FDVD leading to a lack of any FRV suppression at all), or the alteration in PK/PD, due to the addition vitreal binding functionality to the classic molecule, was so minor the concentration time profiles of FRV and FDVD almost exactly

matched those of ranibizumab. The hill region of $\left(K_{\mathrm{D}}^{(n)}, n_0\right)$ parameter space therefore represents a 'sweet spot', wherein sufficient concentrations of FDVD are present in order to efficaciously suppress FRV. While the SVB molecule was able to outperform ranibizumab in a subset of $\left(K_{\mathrm{D}}^{(n)}, n_0\right)$ parameter space, due to the substantially increased half-life of the BI-X-albumin complex, the SVB molecule did not manage to suppress FRV to a greater degree than the BI-X molecule - except at very late time ($t > 100$ days). As can be seen from plots (4) and (5) of Figure 6.6, even when the duration time of the SVB molecule is maximised, and it is decaying at half-life greater than that of the BI-X molecule, as the effective initial concentration of the SVB molecule is lower than that of the BI-X molecule (due to vitreal trapping of SVB molecules), it maintains a lower FDVD concentration for the majority of the time-course of the simulation, and hence suppresses FRV to a lesser degree. This phenomenon represents a potential stumbling block in the design of the SVB molecule.

In Section 6.6 of Chapter 6 we presented an analogous study to that of Section 5.1.4, detailing the effect of repeat doses of the SVB molecule, to analyse the consequence of drug accumulation on vitreal binding sites, alongside the possible application of loading doses. As expected from the repeat dosage PK analysis of Section 5.1.4, high affinity binding between the SVB molecule and the vitreal binding sites either produces FRV equal to or less than that achieved by ranibizumab. When the binding affinity is reduced, and the SVB molecule is evaluated at $\left(K_{\mathrm{D}}^{(n)}, n_0\right)$ pairs near or on the hill in $\left(K_{\mathrm{D}}^{(n)}, n_0\right)$ parameter space, we find superior FRV suppression - however neither repeat doses or loading doses were found to be able to exploit vitreal accumulation of the drug. In all cases mentioned up to this point, as in Section 6.4, the BI-X molecule achieved FRV suppression to a much greater degree than the SVB molecule, again indicating that the concept of simply extending the ocular half-life proves highly effective at suppressing FRV. However, as was noted in Section 5.1.4, for $\left(K_{\mathrm{D}}^{(n)}, n_0\right)$ pairs such that $t_{\mathrm{dur}} = 0$ (time such that the concentration of FDVD remains at or above a theoretically efficacious level), for $K_{\mathrm{D}}^{(n)} \sim O(r_0)$ or greater (i.e. low binding affinity), after multiple injections the model predicted that the concentration of SVB in the vitreous would be compounded, and hence allow the formulation of dosage protocols to exploit this accumulation effect. Figures 6.20-6.22 demonstrate just this, showing that over many subsequent injections (or through the utilisation of a loading dose at time $t = 0$), the concentration of FDVD increases to the point where it is able suppress FRV to a degree even greater than the BI-X molecule, administered using the same dosage protocol. Additionally, due to the magnitude of $n_0/K_{\mathrm{D}}^{(n)}$ in this region of $\left(K_{\mathrm{D}}^{(n)}, n_0\right)$ parameter space the half-life exhibited by the SVB molecule is (on the timescale of the injection intervals) essentially infinite, and hence highly effective at suppressing FRV. We conclude by stating if this later

behaviour was possible to replicate clinically it would offer the potential to achieve great increase in both *efficacy* (via deeper sustained FRV suppression relative to ranibizumab) and *duration* (via the exceedingly long half-life).

Finally, in our discussion of the results of Chapter 6 we reiterate our earlier warning of the possibility of false positives, when performing clinical or experimental studies using SVB molecules. If one was to sample the aqueous (as previously done [81, 118]) to measure either free VEGF concentration, or to study PK (i.e. characterise the half-life), of a SVB molecule post-IVT injection, it may be possible to find very a low concentration of free VEGF, alongside a very long ocular drug half-life. These would both be very promising results, however we have demonstrated that both these phenomena can occur while the concentration of FRV has been barely reduced from steady state, hence, these phenomena can be observed whilst the drug is having absolutely no meaningful effect on FRV suppression. This demonstrates that if a clinical trial was conducted using aqueous (or vitreal) free VEGF, or drug longevity (i.e. half-life) as secondary outcomes, then these trial outcomes could yield false positives. Due to this we strongly caution against using ocular half-life, or free VEGF concentrations measured from aqueous humour sampling, as indicators of efficacy in any clinical or experimental trial of an SVB molecule, as in the absence of favourable visual acuity scores or an observable reduction in disease activity (over an equivalent non-vitreal binding molecule) these may indicate a false positive. Additionally, if such a false positive was to occur, it is likely that the level of FRV suppression would in fact be much lower than an equivalent non-vitreal binding molecule, hence, if approved, leading patients to be treated with a sub-standard drug relative to standard of care. We note, these conclusions are only as accurate as our model, which requires further experimental data to validate, and hence must be viewed in such a context.

7.2 Future work

We will now discuss the future research that we believe would be a suitable extension to the work discussed within this thesis. The models in this thesis which were explored least using analytic methods were those implemented using PDE systems. We did not devote much time within this work attempting to analytically solve the PDE systems presented here, due to their inherent complexity relative to equivalent ODE models, however we believe the simplest anatomical PDE model detailed in this work (Equations 3.46-3.52) may be possible to analyse. A solution to this system would allow much more detailed analysis of the well-mixed assumption than that presented in Section 3.2.5. Additionally, such a

solution would also allow for analysis of the decay rate of the system, analogous to that presented in our discussion of the 1D PDE model - such analysis would allow for a much more meaningful discussion of exactly how diffusion impacts the relationship between the ODE and PDE ocular PK models. Further analytic analysis to extend this work could also be a more detailed asymptotic analysis of the 3-compartment PK/PD model, expanding upon the work presented in Section 4.1.3. With further work it may be possible to characterise the concentration of FRV over the whole time-course of the treatment protocol, as opposed to only intermediate time. This may be possible to achieve using a direct exact/approximate solution or via the use of asymptotic matching.

A substantial drawback in modelling anti-VEGF therapies for angiogenic conditions, such as wet AMD, is that we currently have no way to determine how the level of free VEGF concentration determines the level of disease activity. This is likely to be a highly non-linear process, involving many signalling pathways in addition to VEGF, and hence modelling VEGF alone may not be sufficient to determine the state of the disease. A step towards achieving this goal would be to incorporate the subretinal and choroidal space into the models presented here, and to model the interactions between VEGF and VEGF receptors. Expanding the work presented here to not only consider the therapeutic molecules and their targets, but also the state of the disease, would be both a great step forward and a great challenge.

The work within this thesis has the potential to be simply extended to analyse a multitude of theoretical treatments, inspired, in part, by the findings of our research. As mentioned in our discussion of Chapter 6 the SVB molecule has the potential to suppress FRV to a degree much greater than ranibizumab, however, if it becomes trapped in the vitreous, it can also cease to suppress FRV to any meaningful degree. A way to solve this problem would be to destabilise the LAVA links from the main antibody molecule, causing them to decay on a timescale similar to that of the treatment protocol. Such a decaying SVB molecule would work by binding tightly to a vitreal super-structure, immediately post-IVT injection. Then at some later time the main body of the antibody would detach from the vitreal binding LAVA portion - leaving the main body of the antibody (with, for example, anti-VEGF capability) free to diffuse within the vitreous. Through this methodology it may be possible to more easily maintain a sufficiently high concentration of FDVD, without the need to worry about drug capture within the vitreous. When considering a molecule of this design it is of substantial importance to consider the potential for patients to become resistant to treatment after repeat dosing. There is the distinct possibility that,

after several injections, LAVA vitreal binding ligands (once separated from the main body of their original complex) may be bound to a large proportion of their target vitreal super-structure binding sites, therefore, molecules administered in further injections would not have access to a sufficient quantity of vitreal binding sites, and hence would not decay on an extended timescale. To circumvent the problem of vitreal capture altogether I suggest another hypothetical antibody, a static retinal binder (SRB). Such a molecule would act in exactly the same way as the SVB class antibodies, except instead of binding to vitreal super-structure, it would bind to a structure (or cell type) within the retina. By doing so such a molecule would effectively create a surplus of 'dummy' VEGF receptor molecules within the vitreous, reducing the quantity of VEGF able to activate genuine VEGF receptors. A molecule of this type could have the potential to be disruptive to the cellular processes occurring within the retina, and hence would require extensive toxicology and safety screening. Such safety screening would need to consider the safety of injecting such a drug over the course of many years, as the chance of any adverse effects may increase with each injection, due to accumulation of the drug in the retina. Additionally, such a molecule may actively accumulate the total quantity of VEGF within the retina, as once bound to a fixed SRB molecule it would then not be able to leave the retina. Such an effect may, as with the decaying SVB molecule, lead to patients developing resistance to treatment. Therefore, I conclude that while both of these hypothetical molecules carry the possibility for great increases in efficacy, they also may prove ineffective, or at worst dangerous, to the patient. Studies of such molecules would therefore need to be performed with the utmost caution with consideration to these potential issues.

A major addition to the modelling presented in this thesis would be, in addition to modelling the PD of VEGF and anti-VEGF molecules, to also model the PD of ANG-2 and anti-ANG-2 therapies. This is particularly relevant given the current trend in upcoming wet-AMD treatments to target ANG-2 in addition to VEGF (see the BI-X molecule and RG7716). By extending our modelling work to also consider ANG-2 binding we would be able to more thoroughly simulate such antibodies currently in development, for example the upcoming RG7716 molecule - a bispecific antibody combining ranibizumab and LC10 (an anti-ANG-2 molecule). A potential limitation of this therapy is that at any dose of RG7716 the ratio of anti-VEGF to anti-ANG-2 binding sites is fixed at 1:1. There exists the potential that a ratio of anti-VEGF to anti-ANG2 binding sites other than 1:1 may be more efficacious - such a different ratio could be achieved using a ranibizumab-LC10 combination therapy (a mixture of separate ranibizumab and LC10 molecules). Investigation of what binding site ratio achieves optimal VEGF/ANG-2 suppression would be an ideal

target for mathematical analysis, utilising such a VEGF/ANG-2 PD model. Additionally, given the structure of the RG7716 molecule, it may be possible to generate similar efficacy to the RG7716 molecule by simply injecting a 1:1 mixture of ranibizumab and LC10 - such a therapy could also be analysed in comparison to RG7716 using a mathematical model. As previously mentioned, as the patent of ranibizumab is due to expire in the early 2020s, such a ranibizumab-LC10 combination therapy may be possible to produce at a fraction of the cost of RG7716*. I therefore suggest there could be great value in investigating RG7716, not only in comparison to ranibizumab and the BI-X molecule, but also against a ranibizumab-LC10 combination therapy.

We conclude this thesis by stating that we believe mathematical modelling has a large and ever-increasing role to play in the optimisation of existing treatment protocols, as well as in the development and critique of proposed future therapies. We hope that the work presented here has contributed to this end, and that this work continues to be built upon to aid further improvements in quality and accessibility of care. I believe if scientific research is aligned to the RED goals outlined in this thesis, then the prognosis for future sufferers of wet AMD will be bright. That all - not just those living in developed countries - will have access to affordable, efficacious and long acting treatment for wet AMD, allowing them to retain arguably one of the most important and necessary aspects of the human experience; sight.

*Given that US patent for LC10 was filed in 2009 [52] generic production of the molecule would not be possible until the late 2020s, unlike ranibizumab.

A

Appendices

A.1 Literature compilation of ocular half-Lives and calculated vitreous diffusion times for different animal species and large molecules

This appendix section contains material reproduced from Hutton-Smith et al. 2016 [74].

Species			Ranibizumab, Fab		
Name	v_{vit} (mL)	r_{vit} (cm)	$t_{1/2}$ (days)	T_{diff} (days)	$t_{1/2}/T_{\text{diff}}$
Human (76kg)	4.5 [69]	1.03	7.9 (1.74) [20, 21]	1.59	5.0 (1.1)
Monkey (2.2-4.5kg)	2.17 [69]	0.8	3.25 (0.06) [65, 78]	0.93	3.5 (0.1)
Rabbit (2.5-3kg)	1.52 [69]	0.71	3.12 (0.21) [28, 79]	0.74	4.2 (0.3)
Rat (0.25-0.35 kg)	0.042 [137]	0.22	n/a	n/a	n/a

Species			Bevacizumab, IGg		
Name	v_{vit} (mL)	r_{vit} (cm)	$t_{1/2}$ (days)	T_{diff} (days)	$t_{1/2}/T_{\text{diff}}$
Human (76kg)	4.5 [69]	1.03	9.73 (1.48) [23, 24, 77]	2.33	4.2 (0.6)
Monkey (2.2-4.5kg)	2.17 [69]	0.8	5.6 [78]	1.36	4.1
Rabbit (2.5-3kg)	1.52 [69]	0.71	4.9 (0.04) [28, 45]	1.07	4.6 (0.03)
Rat (0.25-0.35 kg)	0.042 [137]	0.22	0.341 [74, 80]	0.1	3.5

Species			Fab-dimer		
Name	v_{vit} (mL)	r_{vit} (cm)	$t_{1/2}$ (days)	T_{diff} (days)	$t_{1/2}/T_{\text{diff}}$
Human (76kg)	4.5 [69]	1.03	n/a	n/a	n/a
Monkey (2.2-4.5kg)	2.17 [69]	0.8	n/a	n/a	n/a
Rabbit (2.5-3kg)	1.52 [69]	0.71	3.91 (0.48)	0.94	4.2 (0.5)
Rat (0.25-0.35 kg)	0.042 [137]	0.22	n/a	n/a	n/a

Table A.1: Half-lives correspond to mean (SD) of the values from the individual studies referenced. Vitreous diffusion times were calculated from Equation 2.5 using the D_{vit} values of Table 1 and the r_{vit} value for each species. Values in parentheses denote SDs where available; r_{vit} values were obtained by approximating the vitreous chamber as a sphere.

A.2 Retinal geometric parameter derivations

Consider the vitreous as described by a sphere, partially covered by the retina, as shown in Figure A.1 below, which depicts a circular cross-section through the vitreous. Using this simple geometric model we will derive estimates for V_{ret} and S_{ret}. Relevant geometric parameters are given in Table A.2.

Parameter	Value	units	Description
V_{ret}	unknown	mL	Retinal volume
V_{vit}	1.52 [69]	mL	Vitreal volume
S_{ret}	unknown	cm^2	Retinal surface area
r	0.713*	cm	Vitreal radius
ε	0.01 [69]	cm	Retinal thickness
L	1.385†	cm	Cross-sectional arc length of retina
θ	L/r	rad	Cross-sectional sector angle

Table A.2: Geometric parameters for the rabbit eye. *The radius r is the radius of the sphere with volume V_{vit}, where the latter was taken from [69]. †This value was estimated from the scale diagrams found in [69].

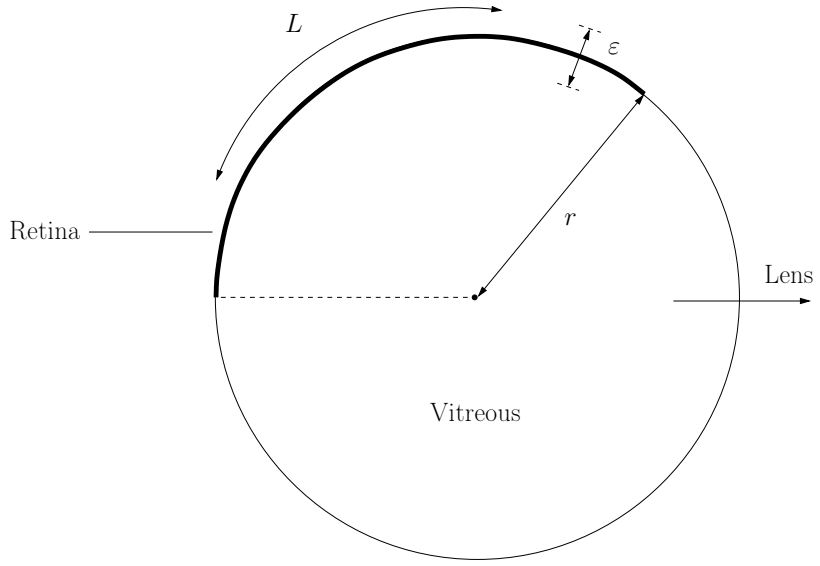

Figure A.1: Geometric model used to derive parameters relating to the retina. The eye is orientated such that the lens is pointing in the positive x axis and the portion of the vitreous in contact with the retina is in bold.

Therefore, assuming azimuthal symmetry around the normal to the lens, the percentage of the vitreous in contact with the retina is given by

$$\Delta = \frac{1}{4\pi r^2} \int_0^{2\pi} \int_0^{\theta_r} r^2 \sin\theta \, \mathrm{d}\theta \mathrm{d}\phi \tag{A.1}$$

$$= \frac{1}{2} \left(1 - \cos\theta_r\right) \tag{A.2}$$

$$\simeq 0.681 \tag{A.3}$$

where $\theta_r = L/r$. Therefore we can approximate S_{ret} and V_{ret} by

$$S_{\text{ret}} = \Delta \times 4\pi r^2 \simeq 4.35 \text{ cm}^2 \tag{A.4}$$

$$V_{\text{ret}} = \Delta \times \frac{4}{3}\pi \left[(r+\varepsilon)^3 - r^3\right] \simeq 0.044 \text{ cm}^3. \tag{A.5}$$

We emphasize that we assume that the surface area S_{ret} is the same on either side of the retina, i.e. for both the RPE and ILM. This approximation is reasonable due to the relative magnitudes of ocular radius (r) and retinal thickness (ε).

A.3 3-compartment ocular vitreous-aqueous delay PK model with virtual compartment

The delay model is given by the following linear system

$$\frac{\mathrm{d}c_{\text{ret}}}{\mathrm{d}t} = \frac{S_{\text{ret}}}{V_{\text{ret}}}\left[-\left(p_{\text{ILM}} + p_{\text{RPE}}\right)c_{\text{ret}} + p_{\text{ILM}}c_{\text{vit}}\right], \tag{A.6}$$

$$\frac{\mathrm{d}c_{\text{vit}}}{\mathrm{d}t} = \left(\frac{S_{\text{ret}}}{V_{\text{vit}}}\right)p_{\text{ILM}}c_{\text{ret}} - \left(\left(\frac{S_{\text{ret}}}{V_{\text{vit}}}\right)p_{\text{ILM}} + k_{\text{el}}\right)c_{\text{vit}}, \tag{A.7}$$

$$\frac{\mathrm{d}c_{\mu}}{\mathrm{d}t} = \left(\frac{V_{\text{vit}}}{V_{\text{aq}}}\right)k_{\text{el}}c_{\text{vit}} - \mu c_{\mu}, \tag{A.8}$$

$$\frac{\mathrm{d}c_{\text{aq}}}{\mathrm{d}t} = \mu c_{\mu} - \left(\frac{CL_{\text{aq}}}{V_{\text{aq}}}\right)c_{\text{aq}}, \tag{A.9}$$

where $c_{\text{ret}}(0) = c_{\mu}(0) = c_{\text{aq}}(0) = 0$ and $c_{\text{vit}}(0) = c_0$ representing the initial concentration corresponding to the intravitreal injection, and where μ (with units of 1/day) is the rate of transfer from the virtual delay compartment into the aqueous, as shown in Figure A.2.

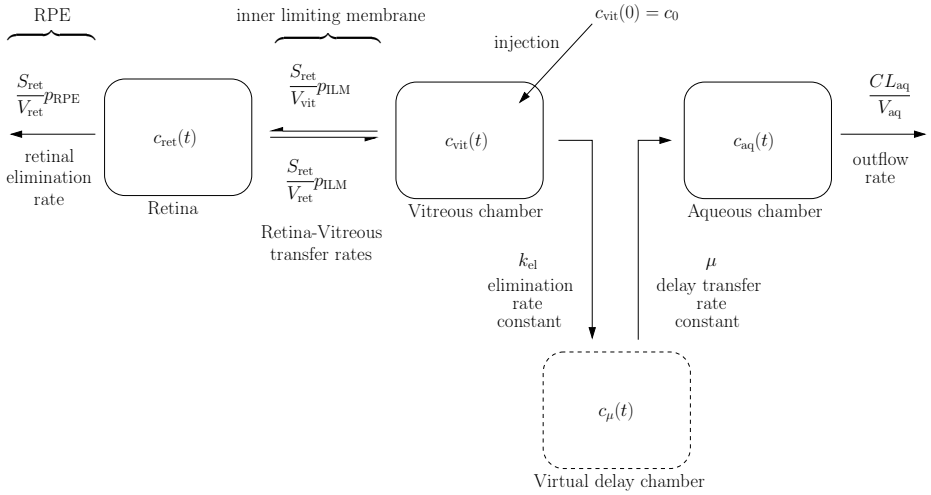

Figure A.2: 3-compartment PK model for a general antibody, with concentration $c(t)$, injected into the vitreous chamber and which may transit from the vitreous into the aqueous or retina. Subscripts on $c(t)$ indicate the notation for each compartments respective concentration. Note the virtual delay compartment, separating the vitreous and the aqueous; for large values of mu we can consider the model as not to include this virtual compartment.

Parameter	Non-delay model				Delay model				Units
	Fab	Fc	IgG	IgG null	Fab	Fc	IgG	IgG null	
p_{RPE} ($\times 10^{-7}$)	2.60 (1.36, 4.04)	n/a	1.84 (1.08, 2.36)	1.91 (1.07, 2.50)	2.71 (1.38, 4.39)	n/a	1.86 (1.10, 2.45)	2.34 (1.34, 3.20)	cm/sec
p_{ILM} ($\times 10^{-7}$)	1.88 (1.13, 2.81)	n/a	1.70 (0.912, 2.32)	1.65 (0.758, 2.52)	2.12 (1.26, 3.34)	n/a	1.87 (1.06, 2.64)	2.05 (1.02, 3.14	cm/sec
$p_{\mathrm{RPE}}/p_{\mathrm{ILM}}$	1.38 (0.71, 2.21)	n/a	1.08 (0.61, 1.57)	1.16 (0.65, 1.64)	1.27 (0.66, 2.02)	n/a	0.99 (0.54, 1.45)	1.14 (0.69, 1.59)	none
k_{el}	0.197 (0.179, 0.219)	0.169 (0.161, 0.178)	0.107 (0.0985, 0.119)	0.118 (0.109, 0.131)	0.200 (0.18, 0.225)	0.173 (0.165, 0.184)	0.109 (0.1, 0.122)	0.117 (0.106, 0.131)	1/day
μ	n/a	n/a	n/a	n/a	0.765 (0.468, 1.42)	1.61 (0.589, 2.5)	1.12 (0.42, 2.5)	0.674 (0.441, 1.24)	1/day
λ_1	0.223	0.196	0.128	0.139	0.228	0.20	0.131	0.143	1/day
λ_2	3.84	3.96	3.04	3.06	4.14	4.00	3.21	3.76	1/day
$t_{1/2}$	3.11	3.54	5.42	4.98	3.04	3.47	5.30	4.86	days

Table A.3: Optimized parameter summary across delay and non-delay models, including 95% confidence intervals obtained via Monte Carlo simulations using error bootstrapping. Due to the lack of retinal data for molecule Fc, estimates for p_{RPE}, p_{ILM} and hence their ratio were not able to be obtained.

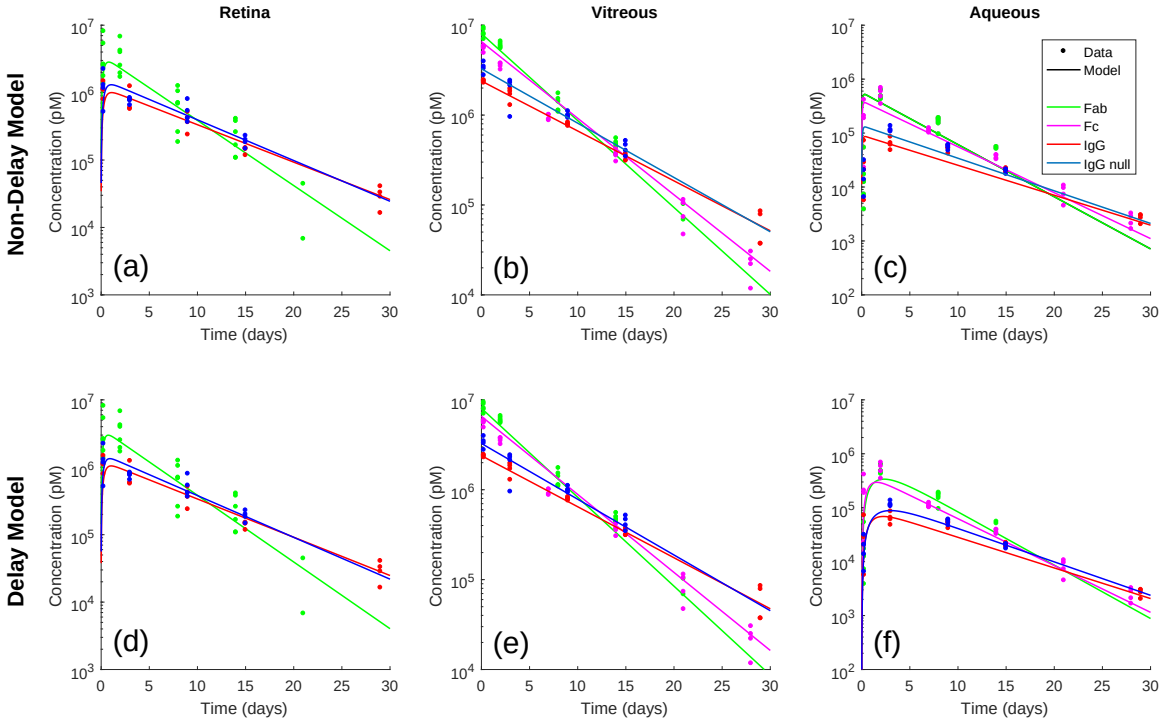

Figure A.3: Compilation of optimized fits to the dataset [28]. Coloured markers indicate distinct molecule data sets, whereas coloured lines show the optimized fit. (a-c) were fit using the non-delay model and (d-f) using the delay model. Note that as there were no available data for Fc in the retina, this dataset was fit purely using vitreous and aqueous data.

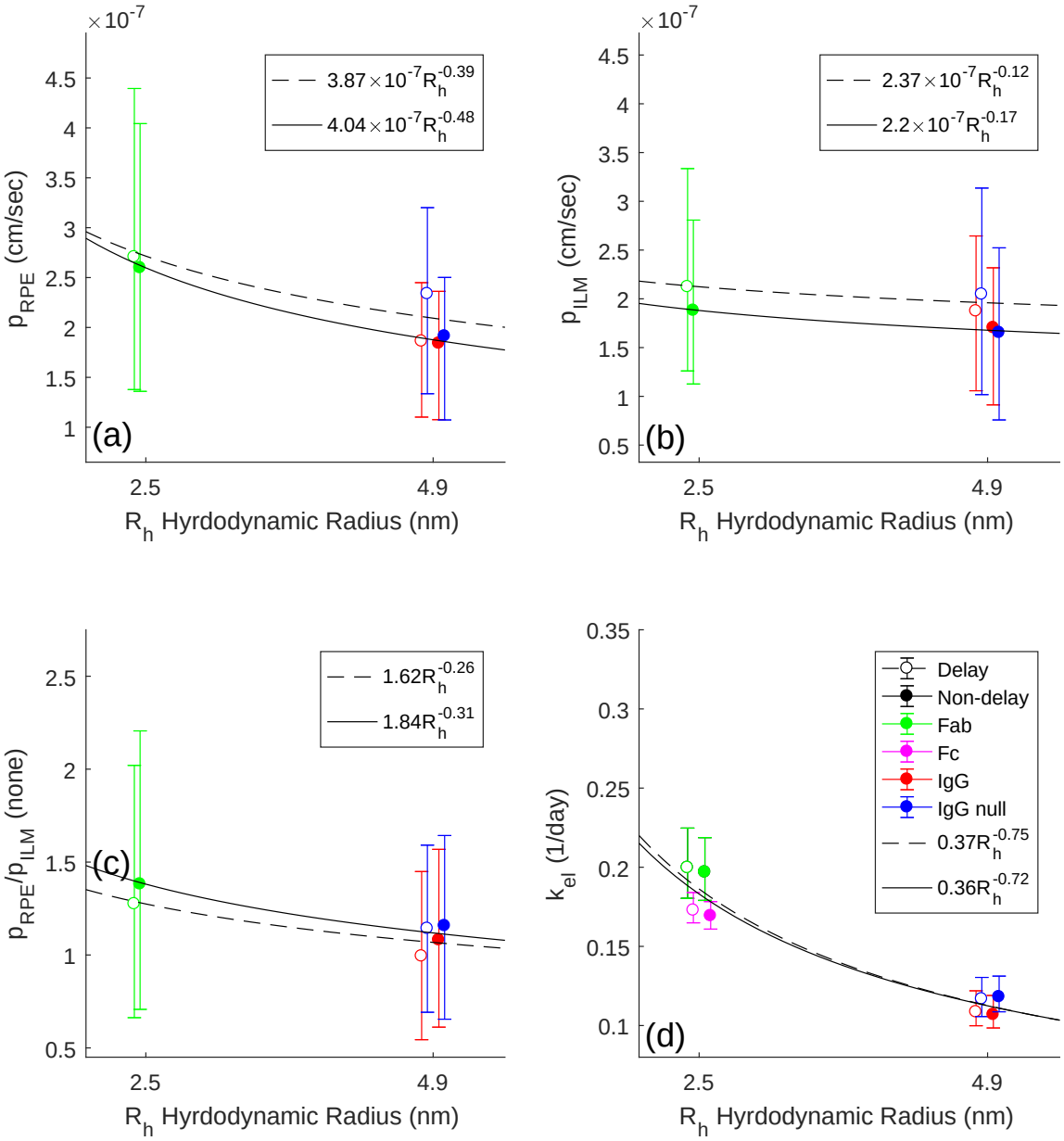

Figure A.4: Optimized parameters across delay and non-delay models, unfilled and solid markers respectively, plotted with respect to hydrodynamic radius (R_{h}).

As for the non-delay model, Equations A.10-A.14 define a linear ODE system with

constant coefficients, with solution for the concentrations of the retina, vitreous and aqueous:

$$c_{\mathrm{ret}}(t) = \frac{c_0 p_{\mathrm{ILM}}}{\lambda_2 - \lambda_1} \left(\frac{S_{\mathrm{ret}}}{V_{\mathrm{vit}}}\right) K_2 K_1 \left[e^{-\lambda_1 t} - e^{-\lambda_2 t}\right], \tag{A.10}$$

$$c_{\mathrm{vit}}(t) = \frac{c_0 p_{\mathrm{ILM}}}{\lambda_2 - \lambda_1} \left(\frac{S_{\mathrm{ret}}}{V_{\mathrm{vit}}}\right) \left[K_1 e^{-\lambda_2 t} + K_2 e^{-\lambda_1 t}\right], \tag{A.11}$$

$$c_{\mathrm{aq}}(t) = \frac{c_0 p_{\mathrm{ILM}} k_{\mathrm{el}}}{\lambda_2 - \lambda_1} \left(\frac{S_{\mathrm{ret}}}{V_{\mathrm{aq}}}\right) \Bigg[\frac{1}{\frac{CL_{\mathrm{aq}}}{V_{\mathrm{aq}}} - \lambda_2} \frac{K_1}{1 - \lambda_2/\mu} \left(e^{-\lambda_2 t} - e^{-\left(\frac{CL_{\mathrm{aq}}}{V_{\mathrm{aq}}}\right)t}\right) \tag{A.12}$$

$$+ \left(\frac{1}{\frac{CL_{\mathrm{aq}}}{V_{\mathrm{aq}}} - \lambda_1}\right) \left(\frac{K_2}{1 - \lambda_1/\mu}\right) \left(e^{-\lambda_1 t} - e^{-\left(\frac{CL_{\mathrm{aq}}}{V_{\mathrm{aq}}}\right)t}\right) \tag{A.13}$$

$$- \frac{1}{\frac{CL_{\mathrm{aq}}}{V_{\mathrm{aq}}} - \mu} \left[\frac{K_1}{1 - \lambda_2/\mu} + \frac{K_2}{1 - \lambda_1/\mu}\right] \left(e^{-\mu t} - e^{-\left(\frac{CL_{\mathrm{aq}}}{V_{\mathrm{aq}}}\right)t}\right) \Bigg], \tag{A.14}$$

where

$$K_1 = 1 + \left(\frac{V_{\mathrm{vit}}}{S_{\mathrm{ret}}}\right) \frac{k_{\mathrm{el}} - \lambda_1}{p_{\mathrm{ILM}}}, \quad K_2 = -1 + \left(\frac{V_{\mathrm{vit}}}{S_{\mathrm{ret}}}\right) \frac{\lambda_2 - k_{\mathrm{el}}}{p_{\mathrm{ILM}}}, \tag{A.15}$$

and λ_1, λ_2 are defined as

$$\lambda_1 = -\frac{1}{2}\left(\mathrm{Tr}(M) + \sqrt{\mathrm{Tr}(M)^2 - 4\det M}\right), \tag{A.16}$$

$$\lambda_2 = -\frac{1}{2}\left(\mathrm{Tr}(M) - \sqrt{\mathrm{Tr}(M)^2 - 4\det M}\right), \tag{A.17}$$

$$M = \begin{pmatrix} -\frac{S_{\mathrm{ret}}}{V_{\mathrm{ret}}}\left(p_{\mathrm{ILM}} + p_{\mathrm{RPE}}\right) & \frac{S_{\mathrm{ret}}}{V_{\mathrm{ret}}} p_{\mathrm{ILM}} \\ \frac{S_{\mathrm{ret}}}{V_{\mathrm{vit}}} p_{\mathrm{ILM}} & -\left(\frac{S_{\mathrm{ret}}}{V_{\mathrm{vit}}} p_{\mathrm{ILM}} + k_{\mathrm{el}}\right) \end{pmatrix}. \tag{A.18}$$

Figure A.3 shows optimized fits (of the delay and non-delay model) for the retina, vitreous and aqueous data sets from Gadkar et al. 2015 [28], obtained using the fitting protocol described in the methods section. A summary of the optimized parameters and confidence intervals for both models can be found in Table A.3, as well as in Figure A.4.

The retinal and vitreal compartments are almost identical for the non-delay (a-c) and delay (d-f) models, the major difference between the two models appears in the aqueous compartment. The addition of the virtual delay compartment introduces a post-transient peak (on a timescale of the order of $1/\lambda$) in the aqueous compartment, allowing the curve to pass through the initial aqueous data points at $t = 0.25$ days.

In contrast, the non-delay model was found to not be able to be fit accurately with the inclusion of these initial aqueous data points, motivating the need for the delay term. However, by excluding the data corresponding to $t = 0.25$ days during the fitting protocol the non-delay model could not only be fit successfully, but returned very similar parameter values as the delay model, without the need for the introduction of the additional delay parameter μ, as can be seen in Table A.3. As can be seen from Figure A.4 the optimized parameters for the delay and non-delay models also indicate similar parameter dependencies on hydrodynamic radius.

A.4 Fluid flow analysis over human geometry

By using Darcy's law, and assuming fluid incompressibility, we were able to simulate the pressure and velocity profiles which would be generated using our simplified geometry of the human eye. Darcy's law for porous media, given by Equation A.19, is used to model fluid flow within the vitreous, where K and η were taken from Ferreira et al. 2017 [72], with values of 8.4×10^{-14} m^2 and 10^{-3} kg m^{-1} s^{-1}, respectively.

$$\vec{v} = -\frac{K}{\eta}\nabla p \tag{A.19}$$

By assuming the vitreal fluid is incompressible we are able to generate a steady state pressure profile, using Equation A.20, with suitable boundary conditions. In Ferreira et al. 2017 [72] it was found that the pressure differential over the vitreous body was roughly 10 Pa, with an anterior and posterior pressure of 2000 Pa and 1990 Pa, respectively, these values were used as boundary conditions on $\delta\Omega_2$ and $\delta\Omega_1$.

$$\nabla \cdot \vec{v} = 0 \quad \Rightarrow \quad \nabla^2 p = 0 \tag{A.20}$$

The resultant pressure and velocity magnitude profiles can be seen in Figures A.5 and A.6. By interpolating the velocity profile mesh points over a uniform spatial grid we were able to take a spatial median, which gave us a median vitreal velocity of 5.6×10^{-7} cm/sec, a retinal surface velocity of 1.1×10^{-7} cm/sec, as well as a global minimum of 3.0×10^{-9} cm/sec. By taking the length scale of the human eye as 1 cm and diffusion as 10^{-6} cm^2/sec, this generates Peclet numbers $\ll 1$, indicating fluid transport is primarily due to diffusion.

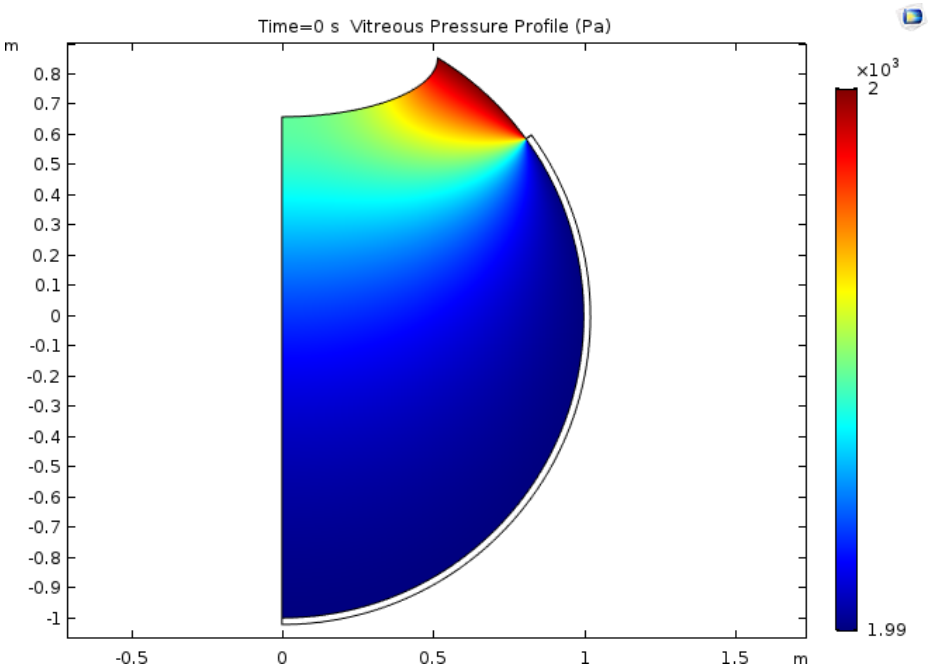

Figure A.5: Simulated vitreal pressure profile, derived using Equation A.20, with units Pa

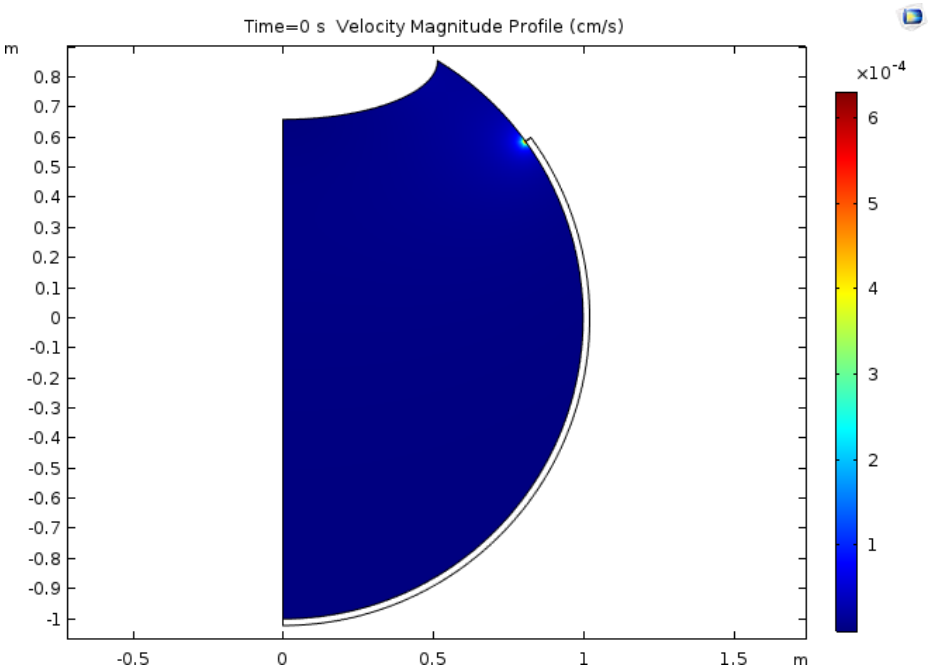

Figure A.6: Simulated vitreal velocity magnitude profile, derived using Equation A.19, with units cm/sec

A.5 1D PDE model: orthogonality

Following from Equation 3.151 we find, for $i \neq j$ that:

$$\langle Z_i, Z_j \rangle = \int_0^1 Z_i Z_j \, \mathrm{d}z \tag{A.21}$$

$$= \frac{1}{\lambda_i^2 - \lambda_j^2} \int_0^1 \left(\lambda_i^2 - \lambda_j^2\right) Z_i Z_j \, \mathrm{d}z \tag{A.22}$$

$$= \frac{1}{\lambda_i^2 - \lambda_j^2} \int_0^1 \lambda_i^2 Z_i Z_j - \lambda_j^2 Z_i Z_j \, \mathrm{d}z \tag{A.23}$$

$$= \frac{1}{\lambda_i^2 - \lambda_j^2} \int_0^1 Z_i'' Z_j - Z_i Z_j'' \, \mathrm{d}z \tag{A.24}$$

$$= \frac{1}{\lambda_i^2 - \lambda_j^2} \int_0^1 \frac{\mathrm{d}}{\mathrm{d}z} \left(Z_i' Z_j - Z_i Z_j'\right) \, \mathrm{d}z \tag{A.25}$$

$$= \frac{1}{\lambda_i^2 - \lambda_j^2} \left(Z_i' Z_j - Z_i Z_j'\right) \Big|_0^1 \tag{A.26}$$

$$= \frac{1}{\lambda_i^2 - \lambda_j^2} \big(- DZ_i(1)Z_j(1) + DZ_i(1)Z_j(1) \tag{A.27}$$

$$+ EZ_i(0)Z_j(0) - EZ_i(0)Z_j(0)\big)$$

$$\therefore \quad \langle Z_i, Z_j \rangle = 0, \tag{A.28}$$

implying Z_i and Z_j are orthogonal if $i \neq j$, with respect to the inner product defined by Equation 3.151.

A.6 R_h and $t_{1/2}$ data meta-analysis

Tabulated data used to calculate estimated values of R_h (Table A.4) and $t_{1/2}$ (Table A.5) for Fab, Fab' and IgG molecules.

Molecule	Fab	Fab'	IgG
M_W (kDa)	50 [69]	100 [69]	150 [69]
R_h (nm)	2.75 [138]	4.48 [139]	4.58 [138]
	2.40 [138]	4.2 [99]	3.5 [138]
	2.77 [138]	3.07 [74]	3.85 [138]
	3.52 [138]		5.49 [138]
	4.20 [138]		6.3 [138]
	4.10 [138]		6.5 [138]
	3.19 [139]		5.41 [139]
	2.45 [76]		5.29 [139]
	2.50 [99]		5.9 [140]
	2.80 [99]		5.45 [140]
	2.80 [99]		5.45 [141]
			5.83 [142]
			6.02 [142]
			4.9 [99]
			4.8 [99]
			5.2 [99]
			5.5 [143]
			5.5 [143]
Mean (nm)	**3.04**	**3.92**	**5.30**
SD (nm)	0.64	0.75	0.77

Table A.4: Literature values for the R_h values of Fab, Fab' and IgG molecules.

	Human		Rabbit		
Molecule	Fab	IgG	Fab	Fab'	IgG
M_W (kDa)	50 [69]	150 [69]	50 [69]	100 [69]	150 [69]
$t_{1/2}$ (days)	7.19 [20]	8.21 [23]	3.11 [74]	4.39 [28]	5.42 [74]
	8.6 [21]	11.17 [23]	3.54 [74]	3.44 [28]	4.98 [74]
	6.24* [22]	9.82 [24]	2.88 [79]	3.89 [28]	4.31 [79]
	6.11* [22]		3.2 [99]		6.99 [144]
					7.06 [144]
					5.95 [39]
					6.61 [145]
Mean (days)	**7.04**	**9.73**	**3.18**	**3.91**	**5.90**
SD (days)	1.15	1.48	0.27	0.48	0.31

Table A.5: Literature values for the R_h values of Fab, Fab' and IgG molecules, in humans and rabbits. *Given the absence of an active FcRn region in a Fab, these values were inferred from PK serum data, assuming flip-flop kinetics between the vitreous and serum. Such behaviour is seen in [28] for Fab molecules in rabbits.

A.7 Estimation of the hydrodynamic radii of R, V, VR and RVR species

The hydrodynamic radii (R_h values) of the VEGF dimer (V), Ranibizumab Fab (R), VR and RVR species were estimated by representing each species as a prolate ellipsoid and applying Perrins formula (given below) [146]. The dimensions of the ellipsoid were estimated from Ferrara's structural representation of the RVR species [119], as follows.

Axial ratios of each species were first estimated by drawing lines corresponding to the apparent length and apparent width of each species and taking their ratio (width/length) as shown in Figure A.7.

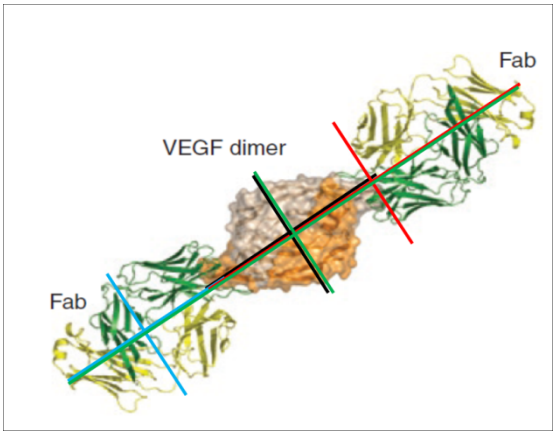

Figure A.7: RVR structure taken from Ferrara [119]. Coloured line segments superimposed on figure were drawn by eye to estimate the apparent lengths (longer segments) and widths (shorter segments) of the different species: V (black), R (blue), VR (red) and RVR (green) species. The axial ratio (dimensionless) was taken as the ratio of the width/length.

The molecular weights (M_W) of the VEGF dimer and ranibizumab were taken as 44000 and 48000 Daltons, respectively, from literature values [147, 148] and the values of the VR and RVR species calculated additively. The volume of each species was computed from the corresponding molecular weight assuming a protein density of 1.33 g/mL [149] and was set equal to that of a prolate ellipsoid with semi-major axis a and semi-minor axis b, i.e. $V_{\text{prolate}} = (4/3)ab^2$. The values of a and b were computed from the volume and the previously estimated axial ratios (set equal to b/a).

Perrin's formula for prolate ellipsoids [146] was used to calculate R_h from the values of

a and b:

$$R_{\mathrm{h}} = \frac{a\sqrt{1-\left(\frac{b}{a}\right)^2}}{\log\left[\left\{1+\sqrt{1-\left(\frac{b}{a}\right)^2}\right\}\Big/\frac{b}{a}\right]}. \tag{A.29}$$

The resulting R_{h} values and related parameters are given in Table A.6.

	Units	**V**	**R**	**VR**	**RVR**
Molecular Weight	Da	44,000	48,000	92,000	140,000
Volume*	$10^4\times$Å	5.50	6.00	11.5	17.5
Axial ratio (b/a)	none	0.68	0.74	0.37	0.26
Semi-major axis (a)	Å	30.5	29.7	58.1	85.4
Semi-minor axis (b)	Å	20.7	22.0	21.7	22.1
Hydrodynamic radius (R_{h})	nm	2.39	2.45	3.29	4.07

Table A.6: Hydrodynamic radii of each species and related parameters used to calculate them. *Assumes protein density of 1.33 g/mL.

The estimated R_{h} for ranibizumab (2.45 nm) is in excellent agreement with the experimental value (2.5 nm) for a Fab molecule determined from dynamic light scattering measurements by Shatz et al. [99]; while the R_{h} estimated for the RVR species (4.07 nm) is similar to the experimental value reported in [99] for an IgG molecule (4.9 nm), which has a comparable M_{W}.

A.8 3-compartment PK/PD individual patient plots

The following 31 figures A.8-A.38 show the individual plots for each patient in the retina and aqueous, the solid red lines represent the numerical solution for the 3-compartment PK/PD model (Equations 4.3-4.18), presented in the Section 4.1 (for $K_{\mathrm{D}} = 19{,}000$), whereas the dashed black line in the aqueous shows the corresponding 2-compartment PK/PD fit (Equations 2.12-2.19), presented in Chapter 2. All fit parameters for a specific patient can be found in the figure legend. The dashed red line in the retina shows the asymptotic solution for free VEGF in the retina, as given by Equation 4.64. The solid blue line represents the total concentration of VEGF in each compartment, i.e. in the retina the total VEGF is given by $v_{\mathrm{ret}} + c_{\mathrm{ret}} + h_{\mathrm{ret}}$.

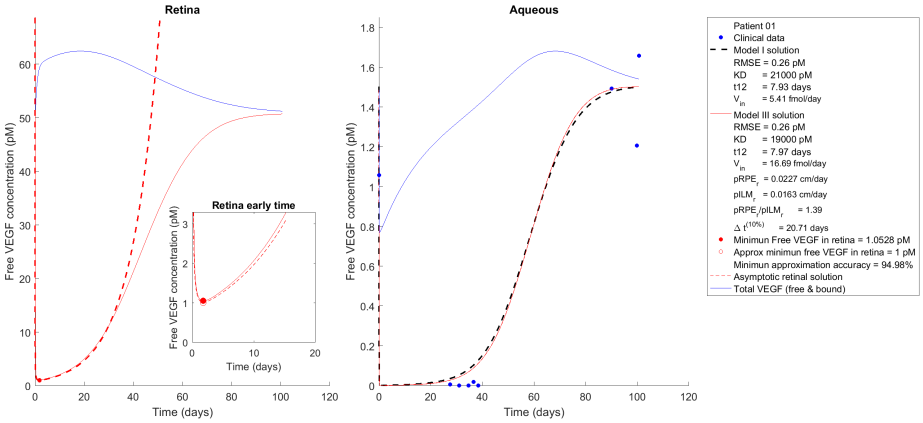

Figure A.8: Patient 01

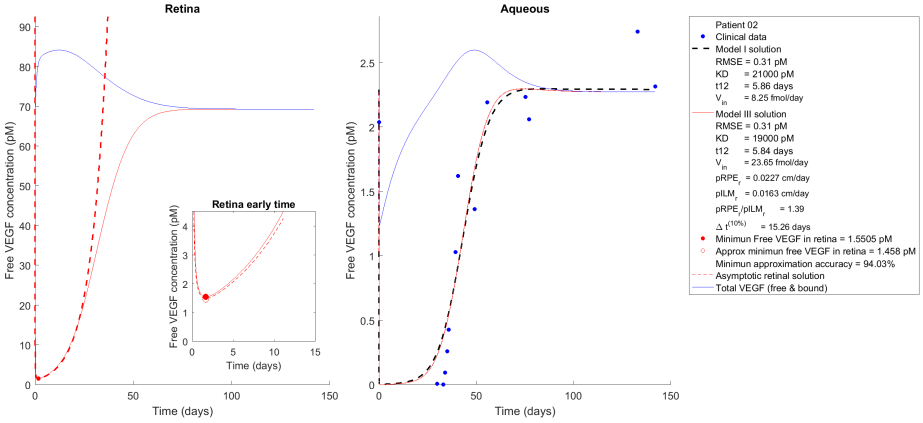

Figure A.9: Patient 02

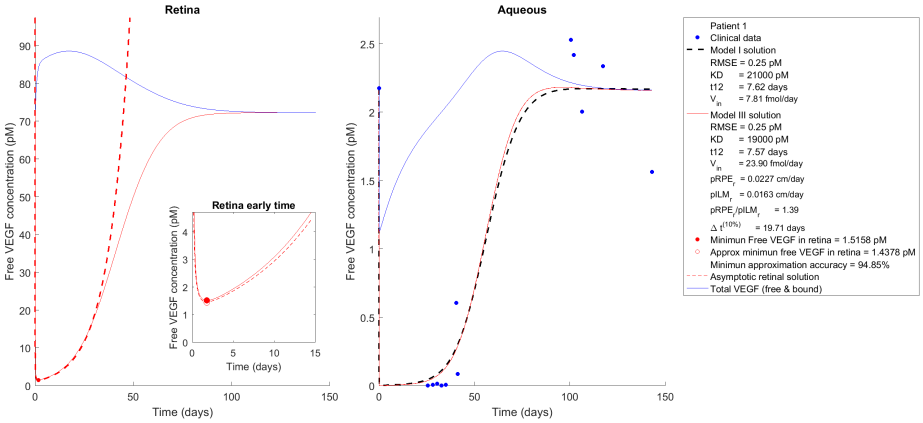

Figure A.10: Patient 1

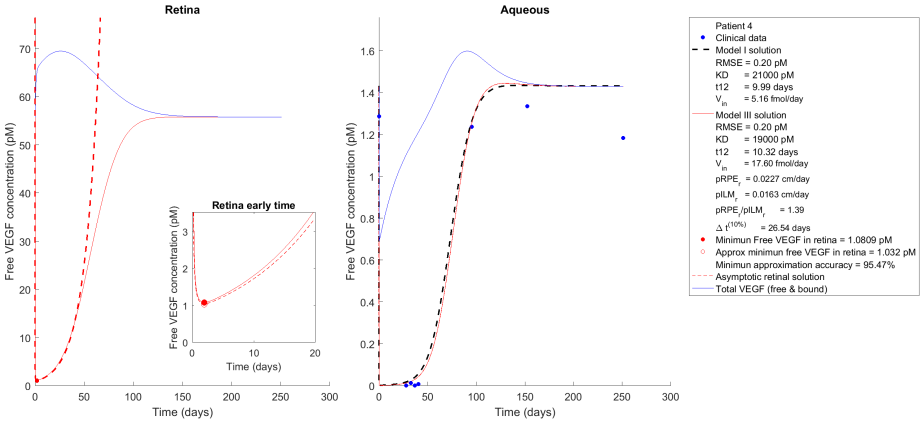

Figure A.11: Patient 4

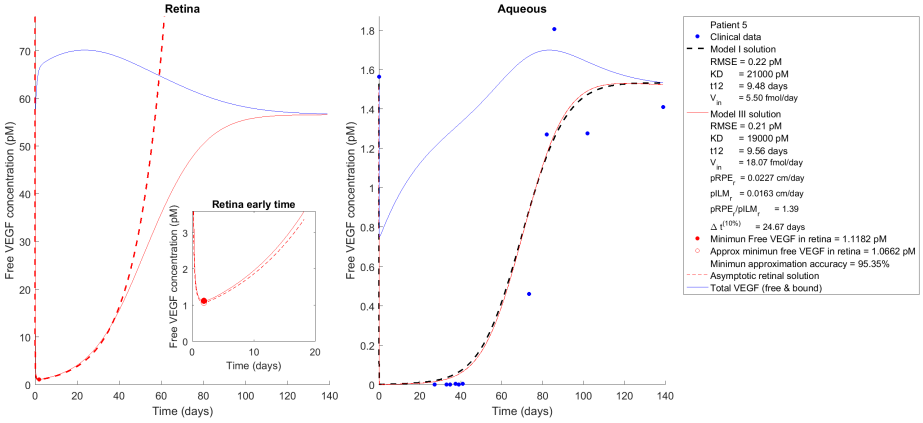

Figure A.12: Patient 5

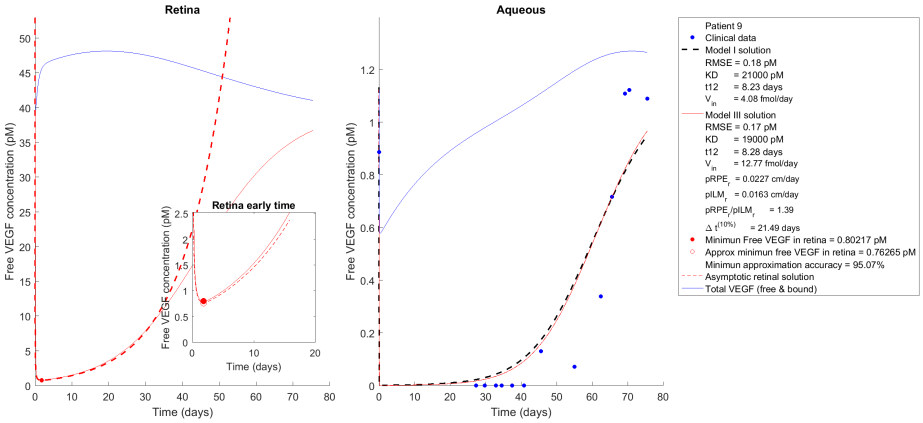

Figure A.13: Patient 9

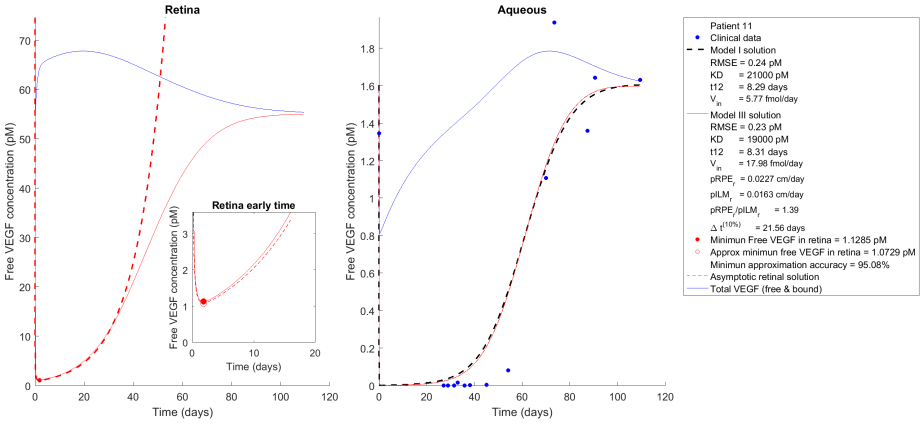

Figure A.14: Patient 11

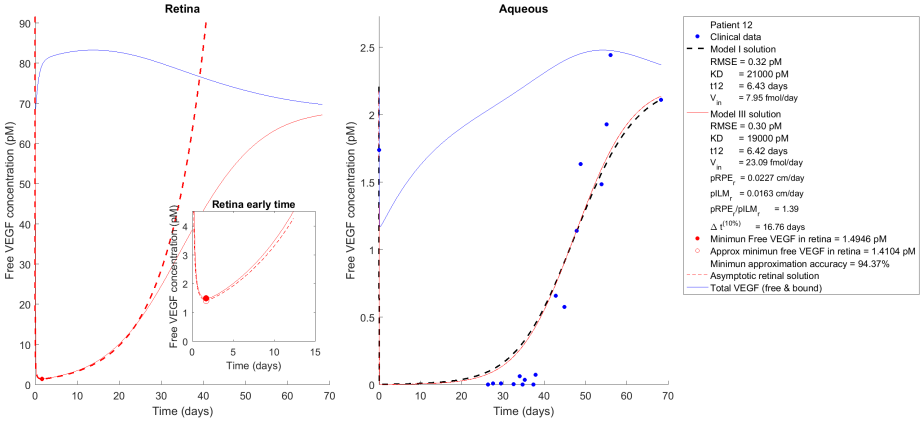

Figure A.15: Patient 12

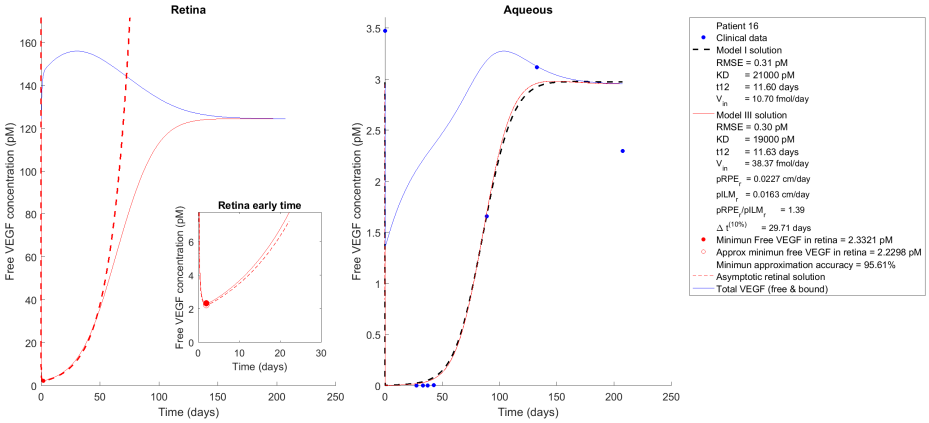

Figure A.16: Patient 16

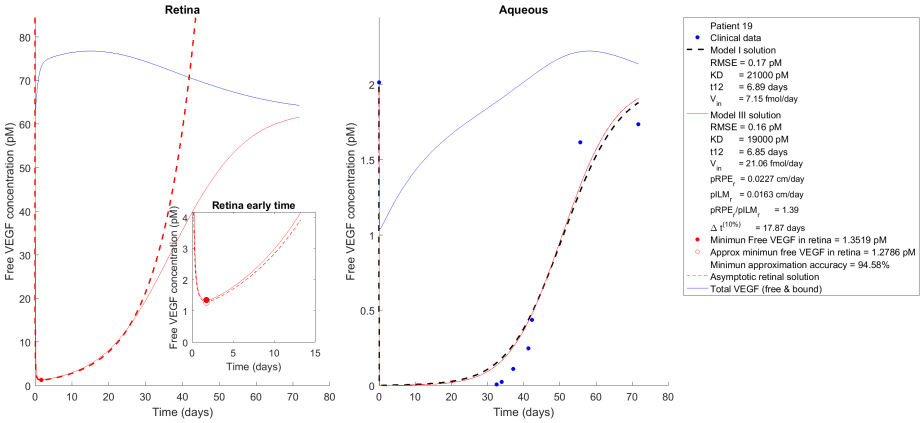

Figure A.17: Patient 19

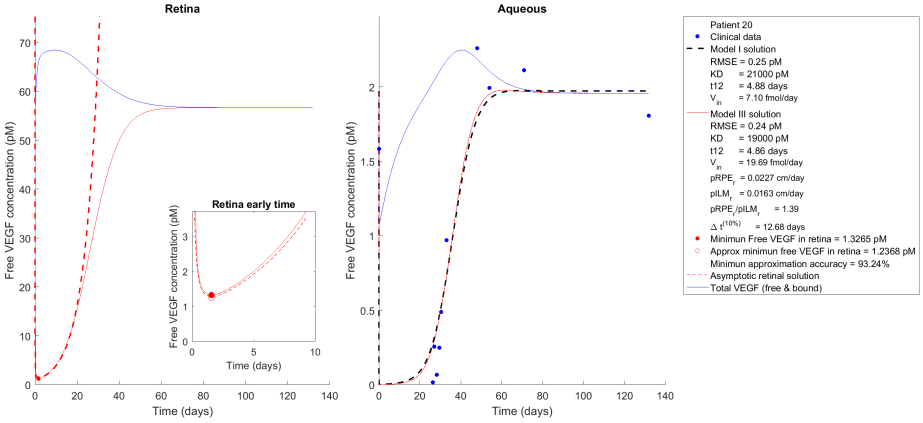

Figure A.18: Patient 20

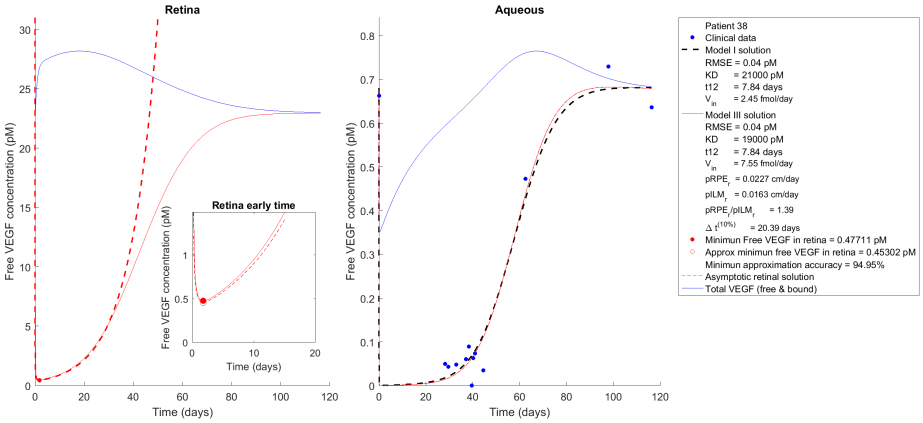

Figure A.19: Patient 38

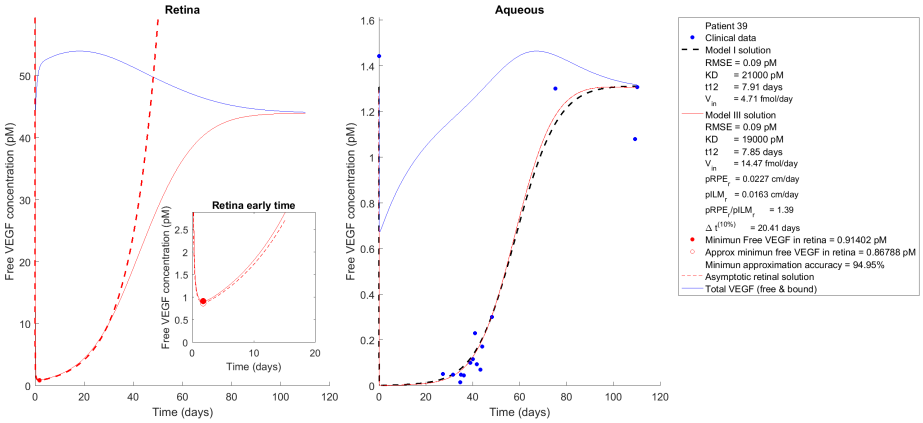

Figure A.20: Patient 39

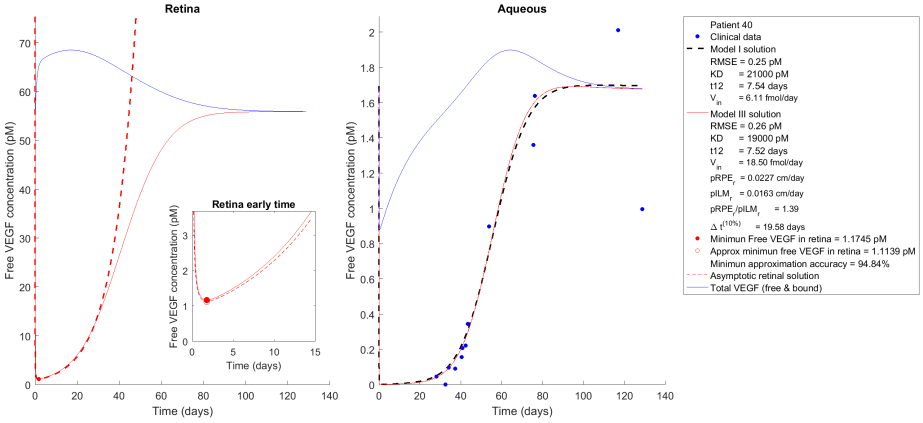

Figure A.21: Patient 40

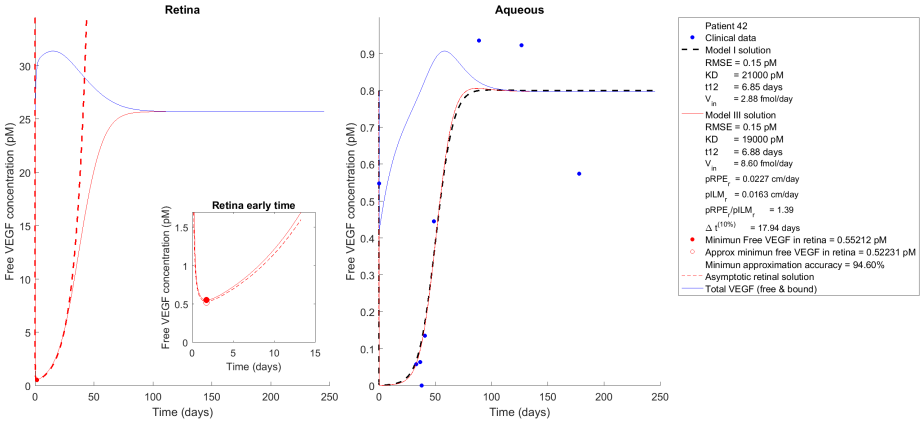

Figure A.22: Patient 42

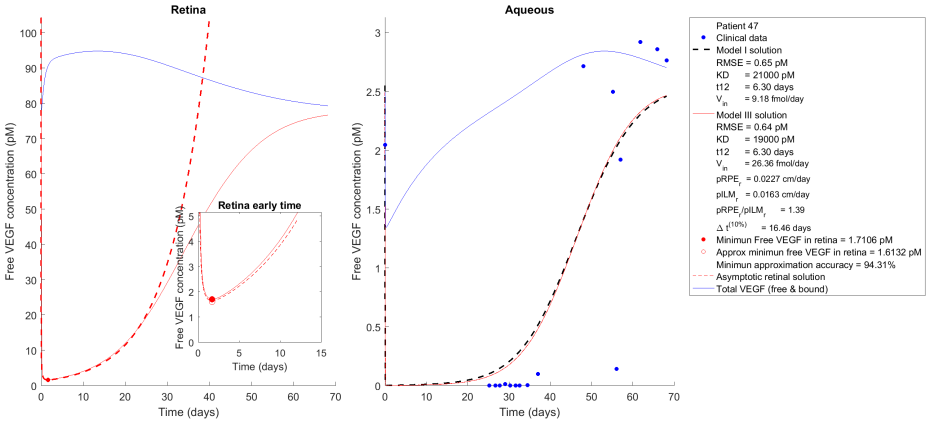

Figure A.23: Patient 47

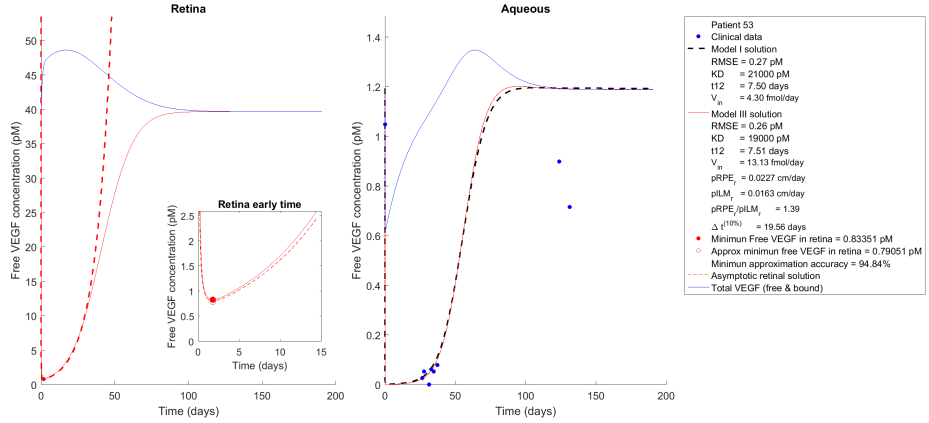

Figure A.24: Patient 53

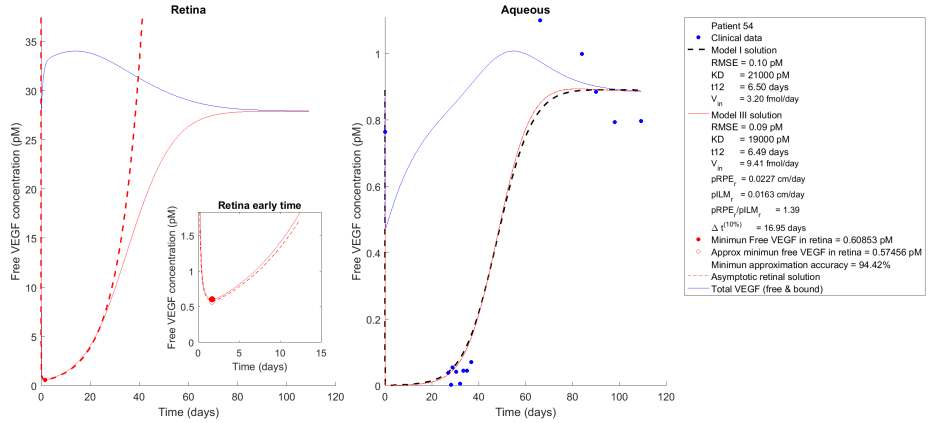

Figure A.25: Patient 54

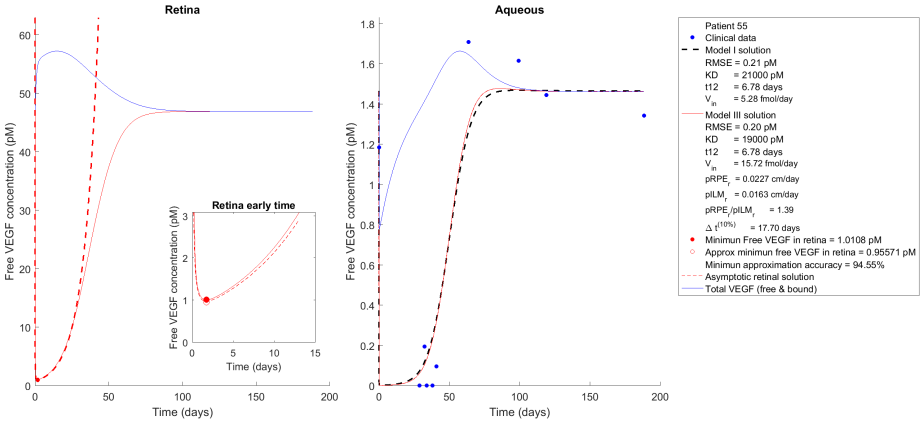

Figure A.26: Patient 55

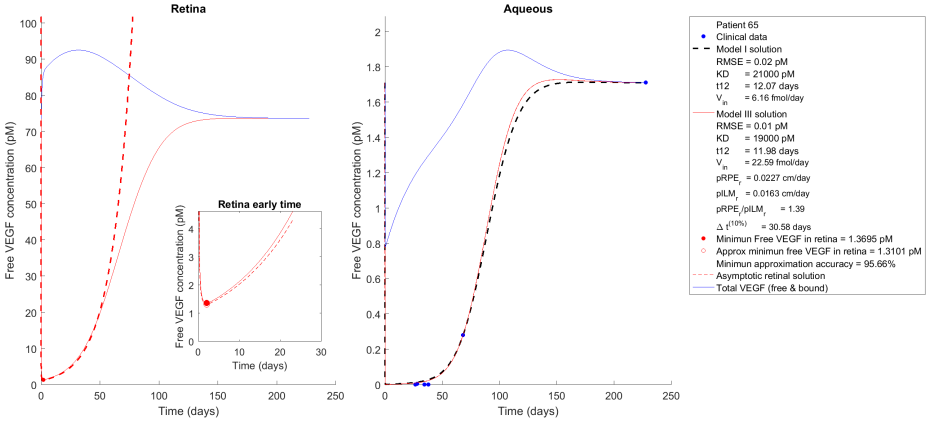

Figure A.27: Patient 65

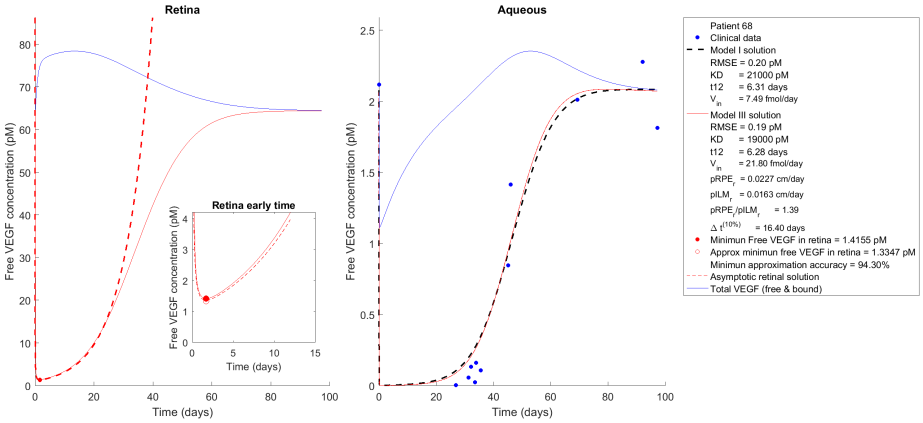

Figure A.28: Patient 68

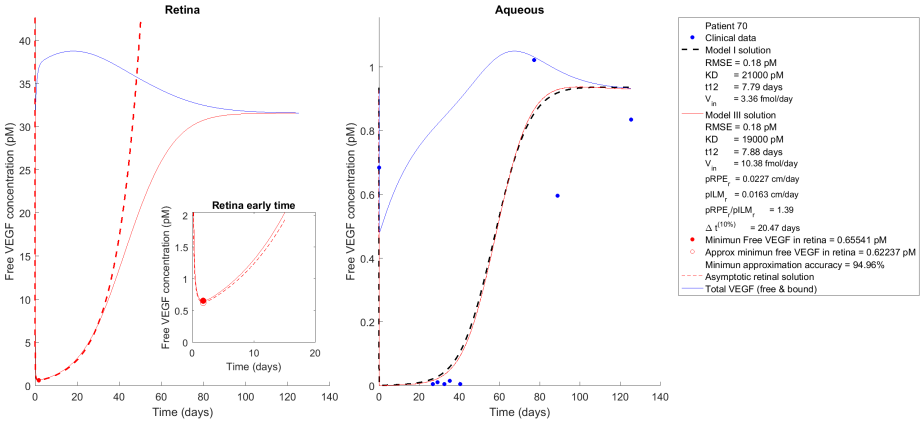

Figure A.29: Patient 70

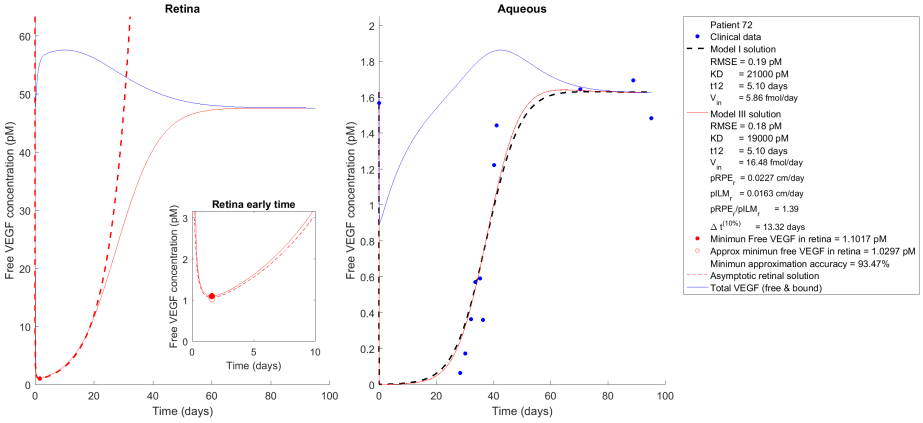

Figure A.30: Patient 72

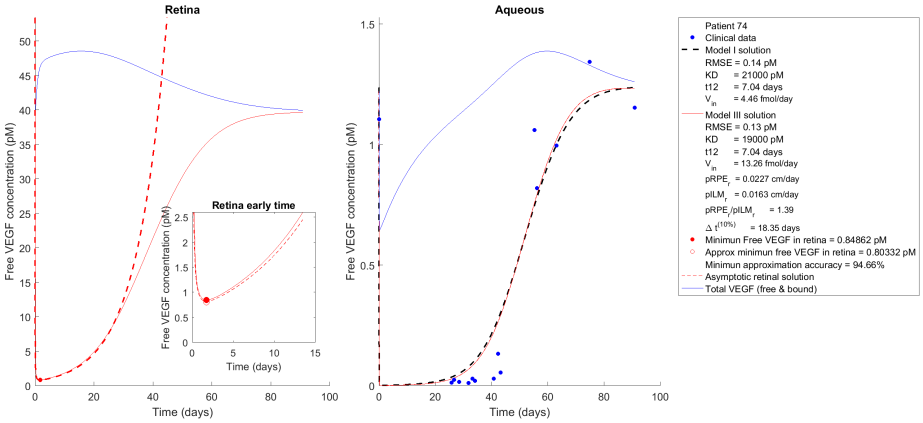

Figure A.31: Patient 74

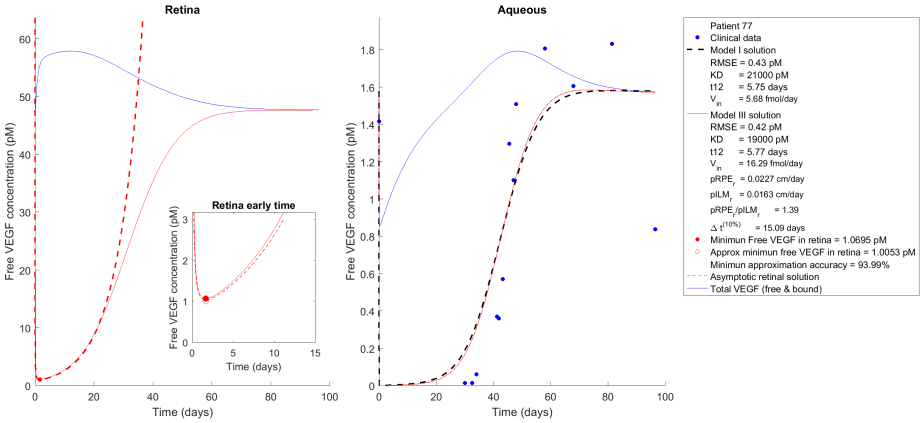

Figure A.32: Patient 77

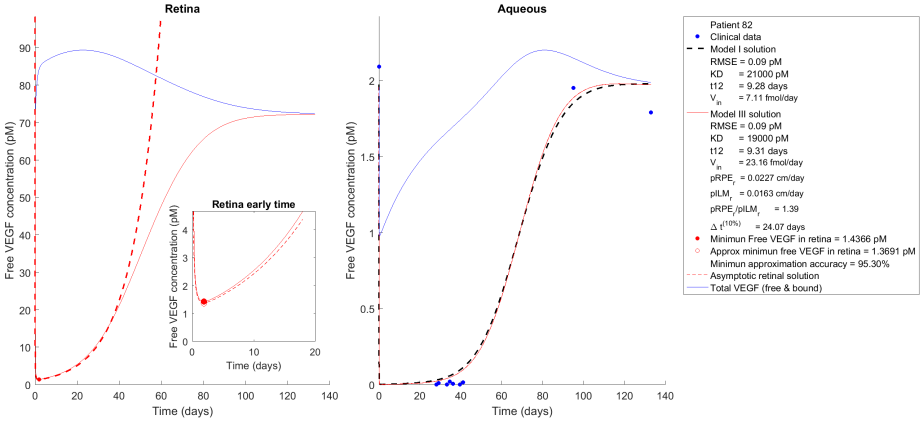

Figure A.33: Patient 82

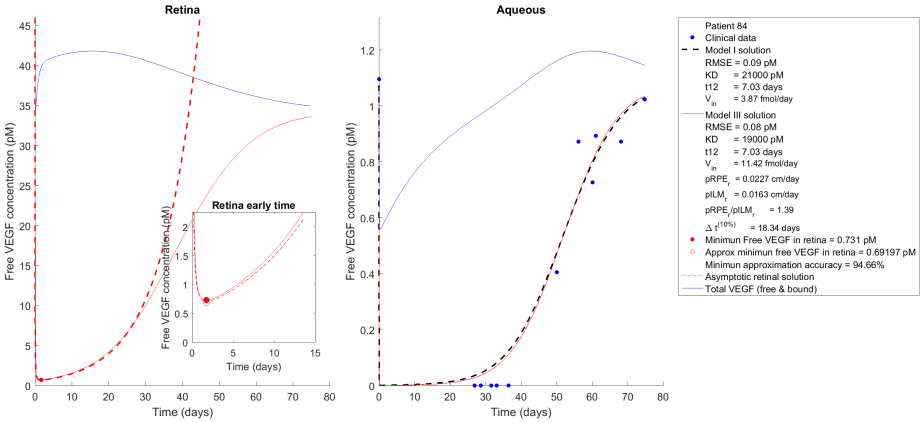

Figure A.34: Patient 84

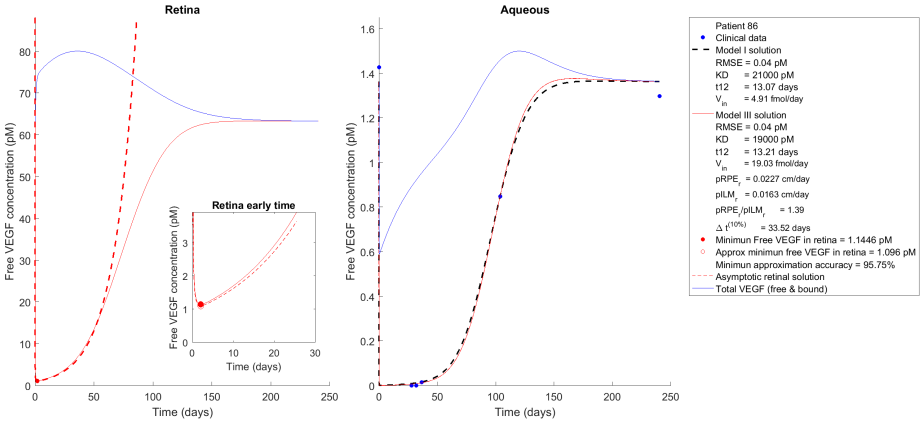

Figure A.35: Patient 86

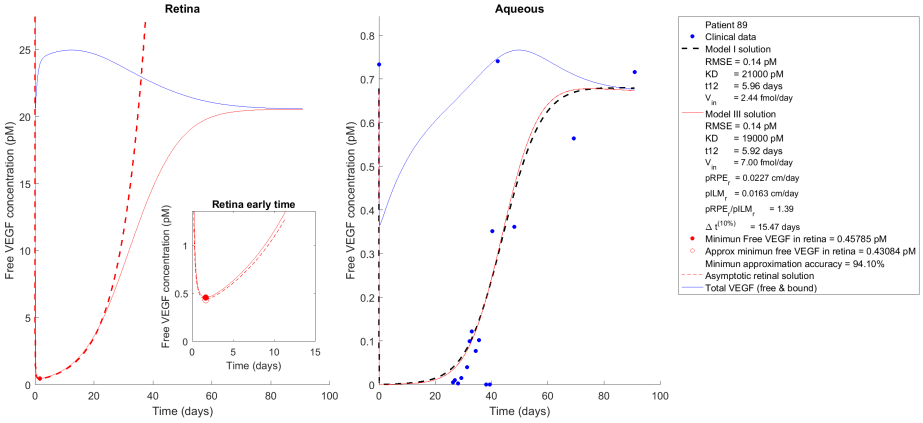

Figure A.36: Patient 89

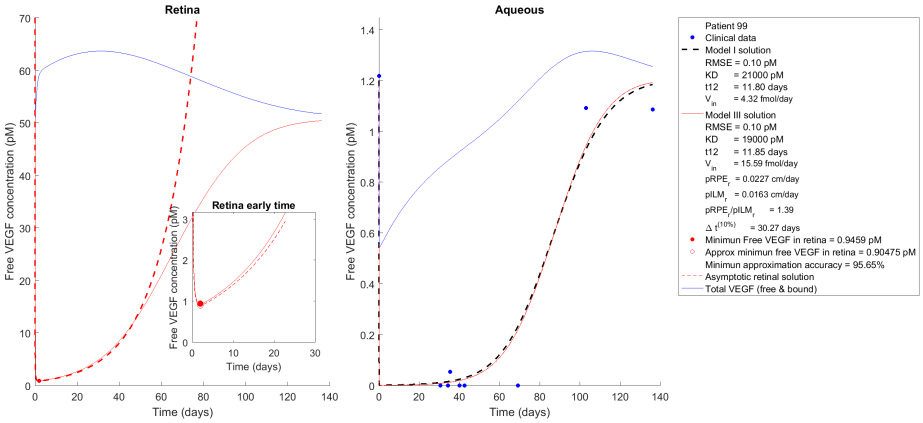

Figure A.37: Patient 99

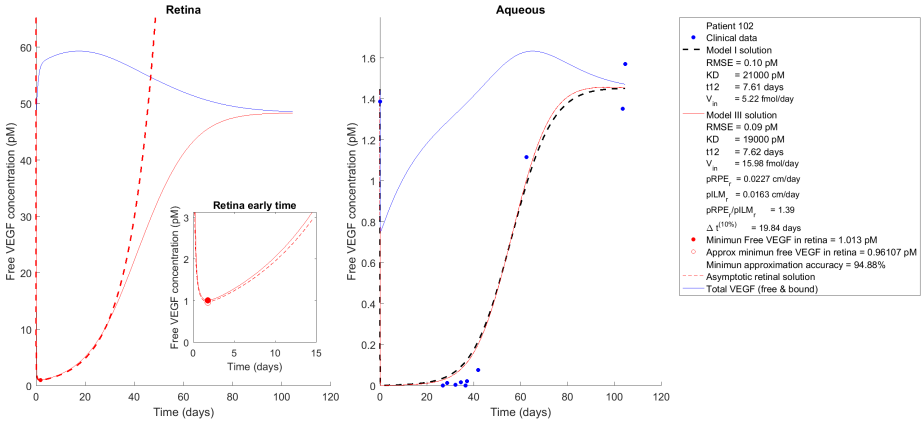

Figure A.38: Patient 102

In order to illustrate the dynamics of total VEGF in the retina and aqueous humour, we present Figure A.39 with an identical format to Figure A.8-A.38 except for the addition of VR and RVR concentration profiles. As drug permeates into the retina and binds VEGF the elimination of total VEGF will decrease due to the smaller permeability of the VEGF-drug complexes. This leads to a transient increase in the total VEGF concentration in the retina, given the constant production of VEGF. In the aqueous humour, which reflects the vitreous, the initial rate of VEGF influx will decrease correspondingly and the total concentration will show a transient fall.

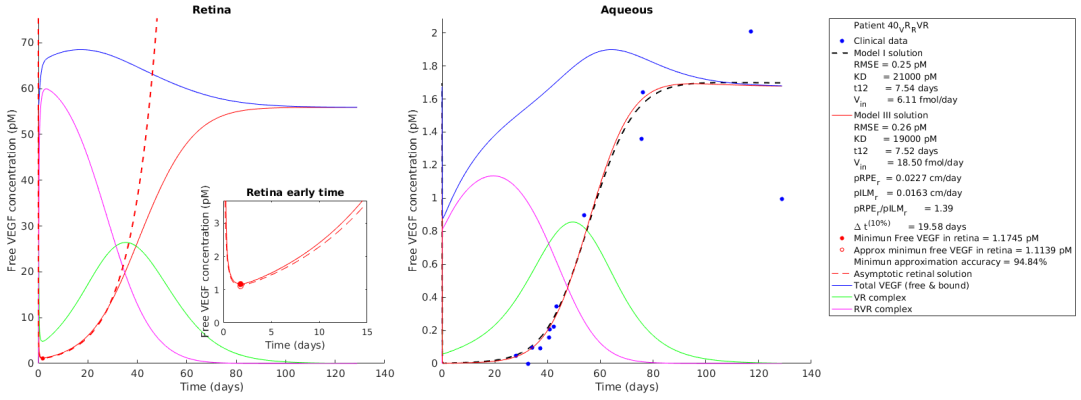

Figure A.39: Patient 40, as in the above plots, with the addition of VEGF-ranibizumab (VR) and ranibizumab-VEGF-ranibizumab (RVR), profiles.

A.9 Chapter 2 lemma 1

Lemma A.1. *If we let* $\alpha \ll 1$*, and we take:*

$$x := \left(\frac{1}{\alpha}\right)^{\frac{1}{1-\alpha}}, \tag{A.30}$$

then we may approximate x by:

$$x \simeq \frac{1}{\alpha} - \log\alpha + O\left(\frac{\alpha}{2}\log^2\alpha\right), \qquad \textit{as } \alpha \to 0, \tag{A.31}$$

where the error tends to zero as $\alpha \to 0$.

Proof. From the definition of x we find:

$$\begin{aligned}
x &= \left(\frac{1}{\alpha}\right)^{\frac{1}{1-\alpha}} && (A.32)\\
&= \left(\frac{1}{\alpha}\right)\left(\frac{1}{\alpha}\right)^{\frac{\alpha}{1-\alpha}} && (A.33)\\
&= \frac{1}{\alpha}\exp\left\{\left(-\frac{\alpha}{1-\alpha}\right)\log\alpha\right\} && (A.34)\\
&= \frac{1}{\alpha}\left[1 - \frac{\alpha}{1-\alpha}\log\alpha + O\left(\frac{\alpha^2}{2(1-\alpha)^2}\log^2\alpha\right)\right] && \text{as } \alpha \to 0 \quad (A.35)\\
&= \frac{1}{\alpha} - \frac{1}{1-\alpha}\log\alpha + O\left(\frac{\alpha}{2(1-\alpha)^2}\log^2\alpha\right) && \text{as } \alpha \to 0 \quad (A.36)\\
&\simeq \frac{1}{\alpha} - \log\alpha + O\left(\frac{\alpha}{2}\log^2\alpha\right) && \text{as } \alpha \to 0. \quad (A.37)
\end{aligned}$$

Notice that the error term tends to zero as $\alpha \searrow 0$, by setting $\alpha = \beta^2$ we find

$$\begin{aligned}
\lim_{\alpha\to 0}\left(\frac{\alpha}{2}\log^2\alpha\right) &= \frac{1}{2}\lim_{\beta\to 0}\left(\beta^2\log^2\beta^2\right) && (A.38)\\
&= 2\lim_{\beta\to 0}\left(\beta\log\beta\right)^2 && (A.39)\\
&= 0. && (A.40)
\end{aligned}$$

□

A.10 Caricature model conservation of mass

Recall that the governing equations for x_1, z_1, x_2 and z_2, as defined by Equations 4.91-4.96 of Chapter 4, are given by:

Compartment Ω_1

$$\varepsilon\frac{\mathrm{d}x_1}{\mathrm{d}\tau} = (\varepsilon z_1 - x_1 y_1) - \varepsilon(p+q)x_1 + \varepsilon\delta p x_2 + \varepsilon a, \tag{A.41}$$

$$\varepsilon\frac{\mathrm{d}z_1}{\mathrm{d}\tau} = -(\varepsilon z_1 - x_1 y_1) - \varepsilon(p+q)z_1 + \varepsilon\delta p z_2, \tag{A.42}$$

Compartment Ω_2

$$\varepsilon\frac{\mathrm{d}x_2}{\mathrm{d}\tau} = (\varepsilon z_2 - x_2 y_2) + \varepsilon\left(\frac{\omega p}{\delta}\right) x_1 - \varepsilon\left(\omega p + k\right) x_2, \tag{A.43}$$

$$\varepsilon\frac{\mathrm{d}z_2}{\mathrm{d}\tau} = -\left(\varepsilon z_2 - x_2 y_2\right) + \varepsilon\left(\frac{\omega p}{\delta}\right) z_1 - \varepsilon\left(\omega p + k\right) z_2. \tag{A.44}$$

Therefore by summing the governing equations for x and z, within their respective compartments, gives:

$$\frac{\mathrm{d}}{\mathrm{d}\tau}\left(x_1 + z_1\right) = -(p+q)(x_1 + z_1) + \delta p(x_2 + z_2) + a \tag{A.45}$$

$$\frac{\mathrm{d}}{\mathrm{d}\tau}\left(x_2 + z_2\right) = \left(\frac{\omega p}{\delta}\right)\left(x_1 + z_1\right) - \left(\omega p + k\right)\left(x_2 + z_2\right). \tag{A.46}$$

By letting

$$X = x_1 + z_1, \quad Y = x_2 + z_2, \tag{A.47}$$

$$A = p + q, \quad B = \delta p, \quad C = \frac{\omega p}{\delta}, \quad D = \omega p + k, \quad E = a, \tag{A.48}$$

we can rewrite the system as

$$\frac{\mathrm{d}X}{\mathrm{d}\tau} = -AX + BY + E \tag{A.49}$$

$$\frac{\mathrm{d}Y}{\mathrm{d}\tau} = CX - DY \tag{A.50}$$

where $X(0) = 1$ and $Y(0) = 1$. Letting

$$\vec{X} = \begin{pmatrix} X \\ Y \end{pmatrix}, \qquad M = \begin{pmatrix} -A & B \\ C & -D \end{pmatrix}, \qquad \vec{E} = \begin{pmatrix} E \\ 0 \end{pmatrix} \tag{A.51}$$

gives

$$\frac{\mathrm{d}\vec{X}}{\mathrm{d}\tau} = M\vec{X} + \vec{E}. \tag{A.52}$$

We assume the solution has the form

$$\vec{X} = \vec{X}_h + \vec{X}_p, \tag{A.53}$$

where

$$\frac{\mathrm{d}\vec{X}_h}{\mathrm{d}\tau} = M\vec{X}_h. \tag{A.54}$$

Therefore $\vec{X}_h$ must be of the form

$$\vec{X}_h = \vec{v}_1 e^{-\bar{\lambda_1}\tau} + \vec{v}_2 e^{-\bar{\lambda_2}\tau}, \tag{A.55}$$

as the eigenvalues of M are $\bar{\lambda_1}$ and $\bar{\lambda_2}$. As $\vec{v}_1$ and $\vec{v}_2$ are eigenvectors, letting $\vec{v}_i \propto (v_i, 1)^T$ gives

$$M\vec{v}_i = -\lambda_i \vec{v}_i \qquad \Rightarrow \qquad \begin{pmatrix} -Av_i + B \\ Cv_i - D \end{pmatrix} = -\begin{pmatrix} \bar{\lambda} v_i \\ \bar{\lambda} \end{pmatrix} \tag{A.56}$$

$$\Rightarrow \qquad \begin{pmatrix} B \\ Cv_i \end{pmatrix} = \begin{pmatrix} (A - \bar{\lambda}_i) v_i \\ D - \bar{\lambda}_i \end{pmatrix}, \tag{A.57}$$

$$\therefore \quad v_i = \frac{D - \bar{\lambda}_i}{C} = \frac{B}{A - \bar{\lambda}_i}. \tag{A.58}$$

Therefore we note that

$$v_i = \frac{k + \omega p - \bar{\lambda}_i}{\frac{\omega p}{\delta}}, \tag{A.59}$$

$$\Rightarrow \qquad \delta v_i = 1 + \frac{k - \bar{\lambda}_i}{\omega p}. \tag{A.60}$$

Note that looking for eigenvectors of the form $\vec{v}_i \propto (v_i, -1)^T$ gives

$$v_i = \frac{\bar{\lambda}_i - D}{C}, \tag{A.61}$$

$$\Rightarrow \qquad \delta v_i = \frac{\bar{\lambda}_i - k}{\omega p} - 1. \tag{A.62}$$

Therefore $\bar{\lambda}_1$ and $\bar{\lambda}_2$ have eigenvectors $(K_1/\delta, 1)^T$ and $(K_2/\delta, -1)^T$, respectively. Therefore

$$\vec{X}_h = c_1 \begin{pmatrix} K_1/\delta \\ 1 \end{pmatrix} e^{-\bar{\lambda_1}\tau} + c_2 \begin{pmatrix} K_2/\delta \\ -1 \end{pmatrix} e^{-\bar{\lambda_2}\tau}, \tag{A.63}$$

where c_1 and c_2 are constants to be determined. Let us now consider $\vec{X}_p$ as follows

$$\vec{X}_p = \begin{pmatrix} x_0 \\ y_0 \end{pmatrix} \qquad \Rightarrow \qquad \vec{0} = \begin{pmatrix} -AX_0 + BY_0 \\ CX_0 - DY_0 \end{pmatrix} + \begin{pmatrix} E \\ 0 \end{pmatrix} \tag{A.64}$$

$$\Rightarrow \qquad \begin{pmatrix} X_0 \\ Y_0 \end{pmatrix} = \frac{E}{\det M} \begin{pmatrix} C \\ D \end{pmatrix}. \tag{A.65}$$

Therefore

$$\vec{X} = c_1 \begin{pmatrix} K_1/\delta \\ 1 \end{pmatrix} e^{-\bar{\lambda_1}\tau} + c_2 \begin{pmatrix} K_2/\delta \\ -1 \end{pmatrix} e^{-\bar{\lambda_2}\tau} + \begin{pmatrix} X_0 \\ Y_0 \end{pmatrix}. \tag{A.66}$$

Let us consider $\vec{X}_0$ - we find

$$\vec{X}_0 = \underbrace{\frac{P_\beta S \left(P_\alpha S + K V_2 \left(1 + \frac{P_\alpha}{P_\beta} \right) \right)}{P_\alpha P_\beta S^2 + K P_\alpha S V_2 + K P_\beta S V_2}}_{=1} \begin{pmatrix} 1 \\ 1 \end{pmatrix}. \tag{A.67}$$

Therefore as $\vec{X}_0 = (1, 1)^T$ and $\vec{X}(0) = (1, 1)^T$, c_1 and c_2 must be identically zero. Therefore:

$$\vec{X} = \begin{pmatrix} 1 \\ 1 \end{pmatrix}, \quad \forall \tau > 0, \tag{A.68}$$

therefore we can write:

$$z_1 = 1 - x_1, \qquad z_2 = 1 - x_2. \tag{A.69}$$

A.11 Caricature model solution for a_1 and a_2, and delay analysis

Solution for a_1 and a_2

Equation 4.109, the dimensionless QSS solution for x_1, may be written dimensionally as follows:

$$a_1 = \left[\frac{1 + \frac{k_{\text{off}} V_1 \left(K V_2 + P_\beta S \right)}{P_\beta S \left(P_\alpha S + K V_2 \left(\frac{P_\alpha}{P_\beta} + 1 \right) \right)}}{S(P_\alpha + P_\beta) + k_{\text{off}} V_1 + b_0 k_{\text{on}} V_1 \frac{K_1 K_2}{K_1 + K_2} e^{-\lambda_1 t}} \right] a_{\text{in}}. \tag{A.70}$$

Recalling that

$$\left(\frac{K_1 + K_2}{K_1 K_2} \right) \simeq \frac{V_1}{S P_\beta} \left(\lambda_2 - \lambda_1 \right), \tag{A.71}$$

allows us to write:

$$a_1 = \left[\frac{1 + \frac{k_{\text{off}} V_1 \left(K V_2 + P_\beta S \right)}{P_\beta S \left(P_\alpha S + K V_2 \left(\frac{P_\alpha}{P_\beta} + 1 \right) \right)}}{S(P_\alpha + P_\beta) + k_{\text{off}} V_1 + \frac{S P_\beta b_0 k_{\text{on}}}{\lambda_2 - \lambda_1} e^{-\lambda_1 t}} \right] a_{\text{in}}. \tag{A.72}$$

Additionally noting that

$$a_0 = \frac{S P_\beta + V_2 K}{S P_\beta} \left(\frac{a_{\text{in}}}{S P_\alpha + V_2 K \left(1 + \frac{P_\alpha}{P_\beta} \right)} \right), \tag{A.73}$$

allows us to recast the solution for a_1 in terms of the equilibrium concentration a_0, in the following way:

$$a_1 = \frac{a_{\text{in}} + k_{\text{off}} V_1 a_0}{k_{\text{off}} V_1 + S(P_\alpha + P_\beta) + \frac{S P_\beta b_0 k_{\text{on}}}{\lambda_2 - \lambda_1} e^{-\lambda_1 t}} \tag{A.74}$$

$$= \frac{a_{\text{in}} + k_{\text{off}} V_1 a_0}{k_{\text{off}} V_1 + S P_\beta \left[\left(1 + \frac{P_\alpha}{P_\beta} \right) + \frac{b_0 k_{\text{on}}}{\lambda_2 - \lambda_1} e^{-\lambda_1 t} \right]}. \tag{A.75}$$

Next, noting that $\lambda_1 \ll \lambda_2$ and λ_2 can be approximated by:

$$\lambda_2 \simeq \frac{S P_\beta}{V_1} \left(1 + \frac{P_\alpha}{P_\beta} \right), \tag{A.76}$$

allows us to finally express a_1 as:

$$a_1 \simeq \frac{a_{\text{in}} + k_{\text{off}} V_1 a_0}{k_{\text{off}} V_1 + S(P_\alpha + P_\beta) + V_1 b_0 k_{\text{on}} e^{-\lambda_1 t} / \left(1 + \frac{P_\alpha}{P_\beta} \right)}. \tag{A.77}$$

Let us next consider the chemical equilibrium solution for a_2:

$$a_2 = \frac{\varepsilon \delta a_0}{\varepsilon + y_2} \tag{A.78}$$

$$= \frac{\delta a_0 K_{\mathrm{D}} \left(\lambda_2 - \lambda_1\right) e^{\lambda_1 t}}{\left(\lambda_2 - K - P_\beta S/V_2\right) b_0 + K_{\mathrm{D}} \left(\lambda_2 - \lambda_1\right) e^{\lambda_1 t}}. \tag{A.79}$$

$$\lambda_1 \ll \lambda_2 \quad \Rightarrow \quad a_2 \simeq \frac{\delta a_0 K_{\mathrm{D}} \lambda_2 e^{\lambda_1 t}}{\left(\lambda_2 - K - P_\beta S/V_2\right) b_0 + K_{\mathrm{D}} \lambda_2 e^{\lambda_1 t}} \tag{A.80}$$

$$= \frac{a_0 \delta e^{\lambda_1 t}}{\frac{b_0}{K_{\mathrm{D}}} \left\{1 - \left(\frac{V_1 K}{P_\beta S} + \frac{V_1}{V_2}\right) / \left(1 + \frac{P_\alpha}{P_\beta}\right)\right\} + e^{\lambda_1 t}}. \tag{A.81}$$

$$V_1 \ll V_2 \quad \Rightarrow \quad a_2 \simeq \frac{\delta a_0}{1 + \frac{b_0}{K_{\mathrm{D}}} \left\{1 - \frac{V_1 K}{P_\beta S} / \left(1 + \frac{P_\alpha}{P_\beta}\right)\right\} e^{-\lambda_1 t}}. \tag{A.82}$$

Therefore, in summary, we have for a_1 and a_2:

$$a_1 \simeq \frac{a_{\mathrm{in}} + k_{\mathrm{off}} V_1 a_0}{k_{\mathrm{off}} V_1 + S(P_\alpha + P_\beta) + V_1 b_0 k_{\mathrm{on}} e^{-\lambda_1 t} / \left(1 + \frac{P_\alpha}{P_\beta}\right)}, \tag{A.83}$$

$$a_2 \simeq \frac{\delta a_0}{1 + \frac{b_0}{K_{\mathrm{D}}} \left\{1 - \frac{V_1 K}{P_\beta S} / \left(1 + \frac{P_\alpha}{P_\beta}\right)\right\} e^{-\lambda_1 t}}. \tag{A.84}$$

Delay analysis

Using the solutions for a_1 and a_2 we define the following:

$$a_1\left(t_1^{(\alpha\%)}\right) = \alpha a_0 \tag{A.85}$$

$$a_2\left(t_2^{(\alpha\%)}\right) = \alpha \delta a_0, \tag{A.86}$$

where $\alpha \in [0, 1]$. The suppression delay between Ω_1 and Ω_2 is then described by:

$$\Delta t^{(\alpha\%)} = t_2^{(\alpha\%)} - t_1^{(\alpha\%)}. \tag{A.87}$$

We may then use the solutions for a_1 and a_2 to solve for $t_1^{(\alpha\%)}$ and $t_2^{(\alpha\%)}$. Therefore solving for $t_1^{(\alpha\%)}$ we find:

$$\alpha a_0 = \frac{a_{\mathrm{in}} + k_{\mathrm{off}} V_1 a_0}{k_{\mathrm{off}} V_1 + S(P_\alpha + P_\beta) + V_1 b_0 k_{\mathrm{on}} e^{-\lambda_1 t_1^{(\alpha\%)}} / \left(1 + \frac{P_\alpha}{P_\beta}\right)}, \tag{A.88}$$

$$\Rightarrow \quad \frac{a_{\mathrm{in}} + k_{\mathrm{off}} V_1 a_0}{\alpha a_0} = k_{\mathrm{off}} V_1 + S(P_\alpha + P_\beta) + \frac{V_1 b_0 k_{\mathrm{on}}}{1 + \frac{P_\alpha}{P_\beta}} e^{-\lambda_1 t_1^{(\alpha\%)}}, \tag{A.89}$$

$$\Rightarrow \quad e^{-\lambda_1 t_1^{(\alpha\%)}} = \frac{1 + \frac{P_\alpha}{P_\beta}}{V_1 b_0 k_{\mathrm{on}}} \left\{\frac{a_{\mathrm{in}} + k_{\mathrm{off}} V_1 a_0}{\alpha a_0} - k_{\mathrm{off}} V_1 - S(P_\alpha + P_\beta)\right\}, \tag{A.90}$$

$$\Rightarrow \quad -\lambda_1 t_1^{(\alpha\%)} = \log\left(\frac{1 + \frac{P_\alpha}{P_\beta}}{V_1 b_0 k_{\mathrm{on}}} \left\{\frac{a_{\mathrm{in}} + k_{\mathrm{off}} V_1 a_0}{\alpha a_0} - k_{\mathrm{off}} V_1 - S(P_\alpha + P_\beta)\right\}\right), \tag{A.91}$$

and similarly for $t_2^{(\alpha\%)}$:

$$\frac{1}{\alpha} = \frac{b_0}{K_\mathrm{D}}\left\{1 - \frac{V_1 K}{P_\beta S}\Big/\left(1+\frac{P_\alpha}{P_\beta}\right)\right\} e^{-\lambda_1 t_2^{(\alpha\%)}} + 1, \tag{A.92}$$

$$\Rightarrow \quad e^{\lambda_1 t_2^{(\alpha\%)}} = \frac{b_0}{K_\mathrm{D}}\left(\frac{\alpha}{1-\alpha}\right)\left\{1 - \frac{V_1 K}{P_\beta S}\Big/\left(1+\frac{P_\alpha}{P_\beta}\right)\right\}, \tag{A.93}$$

$$\Rightarrow \quad \lambda_1 t_2^{(\alpha\%)} = \log\left(\frac{b_0}{K_\mathrm{D}}\left(\frac{\alpha}{1-\alpha}\right)\left\{1 - \frac{V_1 K}{P_\beta S}\Big/\left(\frac{P_\alpha}{P_\beta}+1\right)\right\}\right). \tag{A.94}$$

Therefore:

$$\lambda_1 \Delta t^{(\alpha\%)} = \lambda_1\left(t_2^{(\alpha\%)} - t_1^{(\alpha\%)}\right) \tag{A.95}$$

$$= \log\left(\left(\frac{\alpha}{1-\alpha}\right)\frac{1+\frac{P_\alpha}{P_\beta} - \frac{V_1 K}{P_\beta S}}{V_1 k_\mathrm{off}}\left\{\frac{a_\mathrm{in} + k_\mathrm{off} V_1 a_0}{\alpha a_0} - k_\mathrm{off} V_1 - S(P_\alpha + P_\beta)\right\}\right) \tag{A.96}$$

$$= \log\left(\left(\frac{\alpha}{1-\alpha}\right)\frac{1+\frac{P_\alpha}{P_\beta} - \frac{V_1 K}{P_\beta S}}{V_1 k_\mathrm{off}}\left\{\frac{a_\mathrm{in} + k_\mathrm{off} V_1 a_0}{\alpha a_0} - k_\mathrm{off} V_1 - S(P_\alpha + P_\beta)\right\}\right). \tag{A.97}$$

Therefore in summary we have the following approximations:

$$a_1 \simeq \frac{a_\mathrm{in} + k_\mathrm{off} V_1 a_0}{k_\mathrm{off} V_1 + S(P_\alpha + P_\beta) + V_1 b_0 k_\mathrm{on} e^{-\lambda_1 t}\Big/\left(1+\frac{P_\alpha}{P_\beta}\right)}, \tag{A.98}$$

$$a_2 \simeq \frac{\delta a_0}{1 + \frac{b_0}{K_\mathrm{D}}\left\{1 - \frac{V_1 K}{P_\beta S}\Big/\left(1+\frac{P_\alpha}{P_\beta}\right)\right\} e^{-\lambda_1 t}}. \tag{A.99}$$

If

$$a_1\left(t_1^{(\alpha\%)}\right) = \alpha a_0, \tag{A.100}$$

$$a_2\left(t_2^{(\alpha\%)}\right) = \alpha\delta a_0, \tag{A.101}$$

then

$$-\lambda_1 t_1^{(\alpha\%)} = \log\left(\frac{1+\frac{P_\alpha}{P_\beta}}{V_1 b_0 k_\mathrm{on}}\left\{\frac{a_\mathrm{in} + k_\mathrm{off} V_1 a_0}{\alpha a_0} - k_\mathrm{off} V_1 - S(P_\alpha + P_\beta)\right\}\right), \tag{A.102}$$

$$\lambda_1 t_2^{(\alpha\%)} = \log\left(\frac{b_0}{K_\mathrm{D}}\left(\frac{\alpha}{1-\alpha}\right)\left\{1 - \frac{V_1 K}{P_\beta S}\Big/\left(1+\frac{P_\alpha}{P_\beta}\right)\right\}\right), \tag{A.103}$$

and, where $\Delta t^{(\alpha\%)} = t_2^{(\alpha\%)} - t_1^{(\alpha\%)}$, we find:

$$\lambda_1 \Delta t^{(\alpha\%)} = \log\left(\left(\frac{\alpha}{1-\alpha}\right)\frac{1+\frac{P_\alpha}{P_\beta} - \frac{V_1 K}{P_\beta S}}{V_1 k_\mathrm{off}}\left\{\frac{a_\mathrm{in} + k_\mathrm{off} V_1 a_0}{\alpha a_0}\right.\right. \tag{A.104}$$

$$\left.\left. - k_\mathrm{off} V_1 - S(P_\alpha + P_\beta)\right\}\right). \tag{A.105}$$

Let us now consider the difference between the function inside the logarithm and 1, in order to consider when the delay between compartments 1 and 2 is zero. Let us define the term within the logarithm as

$$f \coloneqq \left(\frac{\alpha}{1-\alpha}\right)\frac{1+\frac{P_\alpha}{P_\beta}-\frac{V_1K}{P_\beta S}}{V_1 k_{\text{off}}}\left\{\frac{a_{\text{in}}+k_{\text{off}}V_1a_0}{\alpha a_0}-k_{\text{off}}V_1-S(P_\alpha+P_\beta)\right\},$$

such that $\lambda_1\Delta t^{(\alpha\%)}=\log(f)$. Therefore let us consider the difference between this function and 1, i.e. if we let $f=g+1$ then we consider $g=f-1$, such that

$$\lambda_1\Delta t^{(\alpha\%)}=\log\left(1+g\right), \tag{A.106}$$

where:

$$g=\frac{P_\alpha}{P_\beta}-\frac{V_1K}{P_\beta S}+\frac{1}{(1-\alpha)V_1k_{\text{off}}}\left(1+\frac{P_\alpha}{P_\beta}-\frac{V_1K}{P_\beta S}\right)\left[\frac{a_{\text{in}}}{a_0}-\alpha S(P_\alpha+P_\beta)\right]. \tag{A.107}$$

A.12 Caricature model plots: Effect of parameter variation on delay

The plots in this Appendix depict the toy model, detailed in Section 4.1.6, solved over baseline, and variation from baseline, parameters (given in Table 4.5). Each plot depicts the numerical (solid, Equations 4.81-4.86) and approximate analytic solution (dashed Equations 4.110-4.111). Solid dots denote exact $t^{\alpha\%}$ values, whereas empty dots are generated via Equations 4.115-4.116, similarly for $\Delta t^{\alpha\%}$, where the approximate value is generated from Equation 4.117. Percentage accuracies of these approximate formulae are given in the figure legends.

The first set of plots, Figures A.40-A.47, under the heading *'Caricature model parameter variation study'*, study the effect on suppression lag time by varying $k_{\text{off}}, k_{\text{on}}, K_{\text{D}}, P_\alpha, P_\beta$ and K, whereas the second set, Figures A.48-A.55, under the heading *'Caricature model, 3-compartment model comparison'*, considers a comparison between the caricature model, and the full 3-compartment model, solved using parameters for Fab molecules, given in Section 4.1.1 (where all molecules in the caricature model are assumed to have transport rates associated with Fab molecules).

In this section, the arrows the plots exhibit the change from the baseline for both the retina and the vitreous compartments and both the 3-compartment PK/PD model and the caricature model.

Caricature model parameter variation study

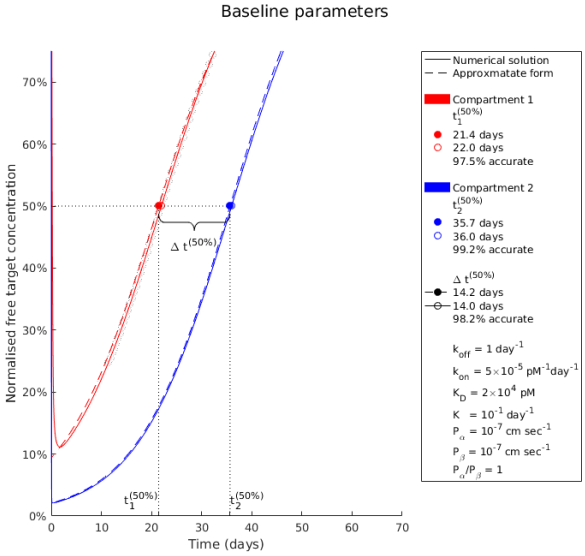

Figure A.40: Baseline parameter values

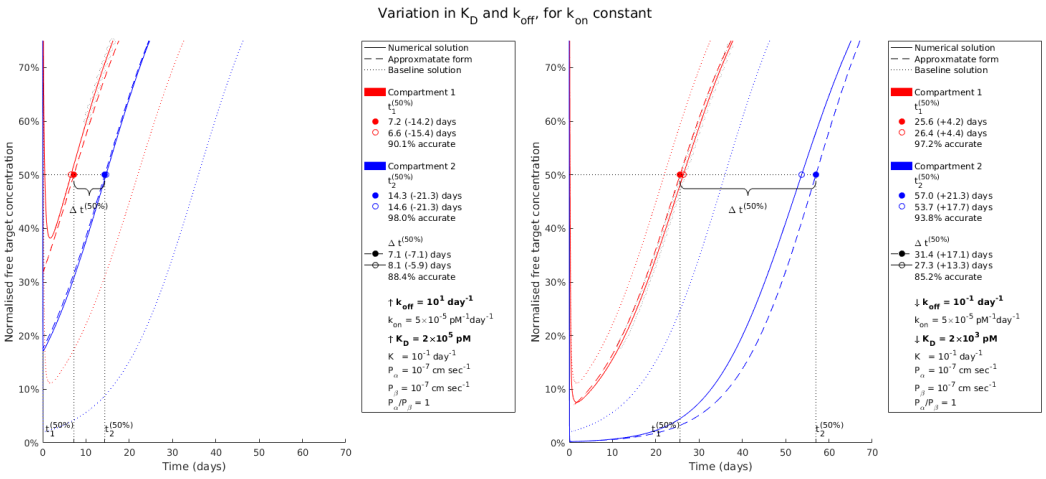

Figure A.41: Variation in k_{off} and K_{D} with k_{on} constant.

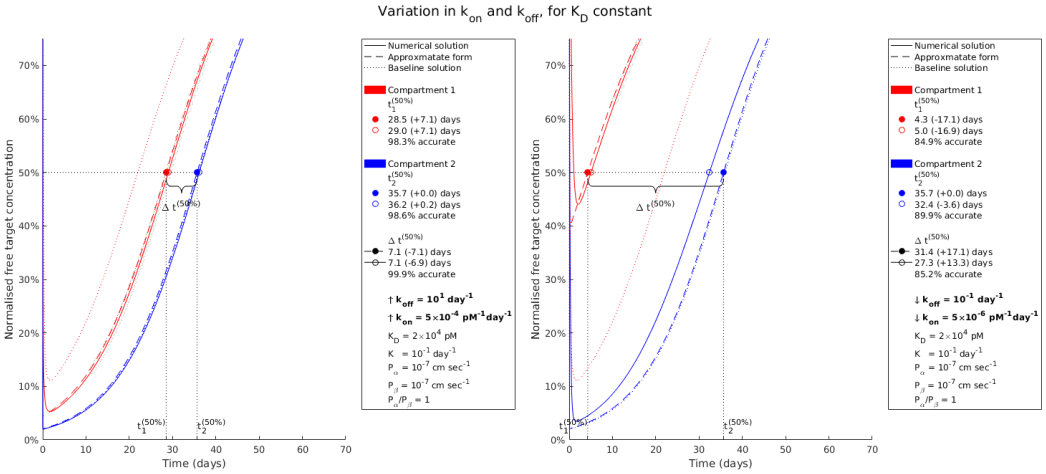

Figure A.42: Variation in k_{off} and k_{on} with K_{D} constant.

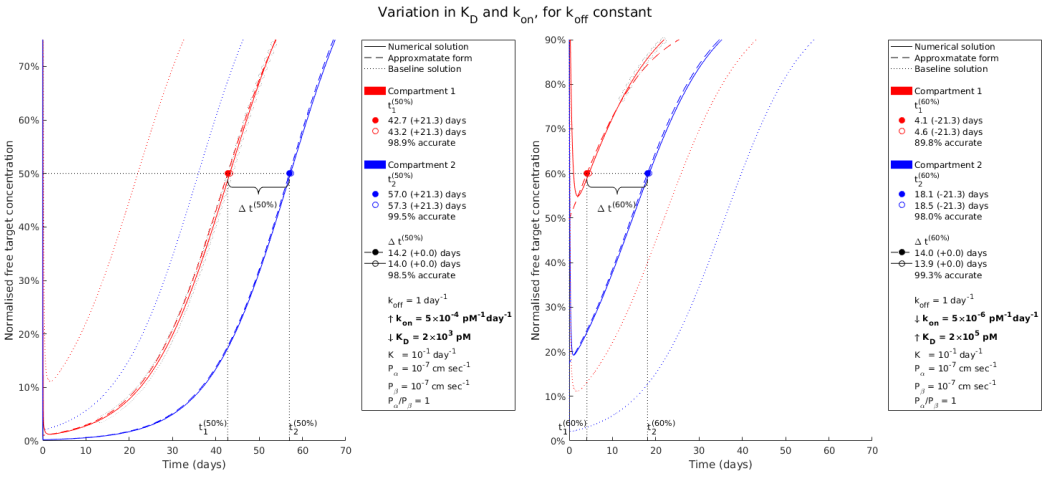

Figure A.43: Variation in k_{on} and K_{D} with k_{off} constant.

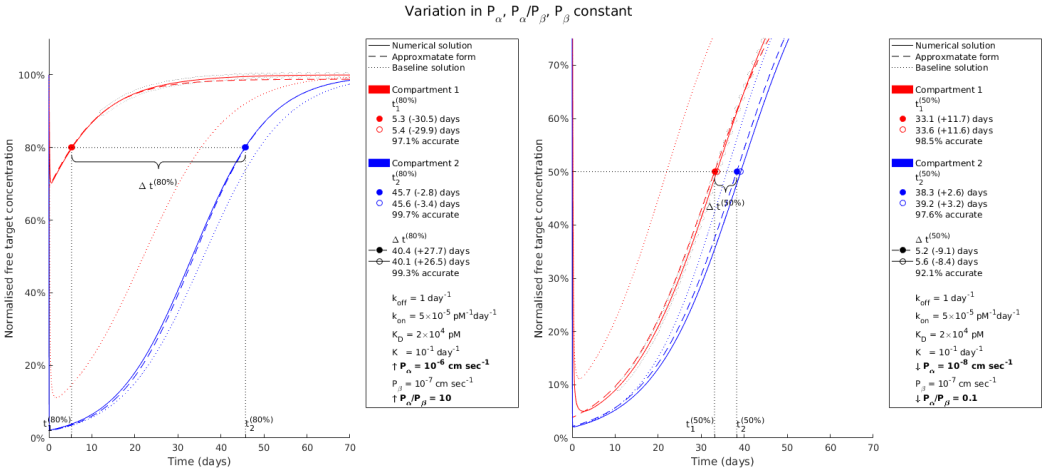

Figure A.44: Variation in P_α and P_α/P_β with P_β constant.

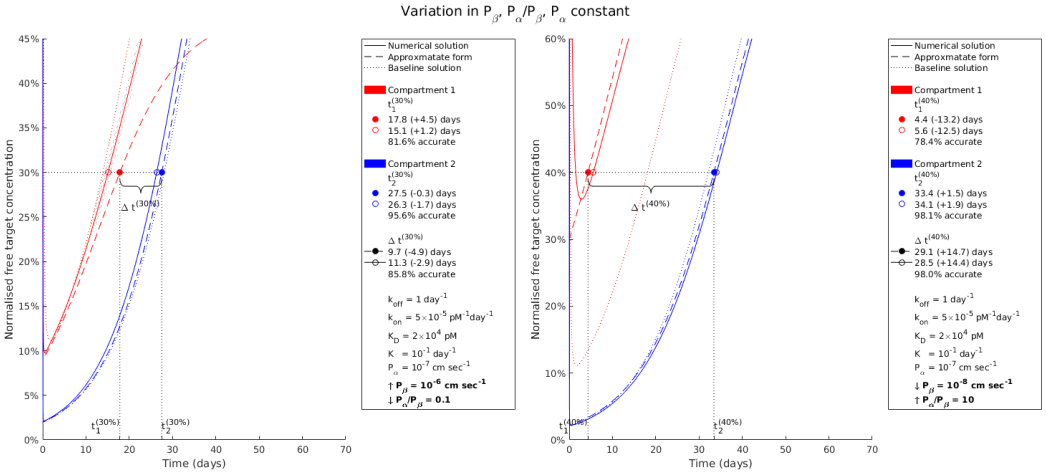

Figure A.45: Variation in P_β and P_α/P_β with P_α constant.

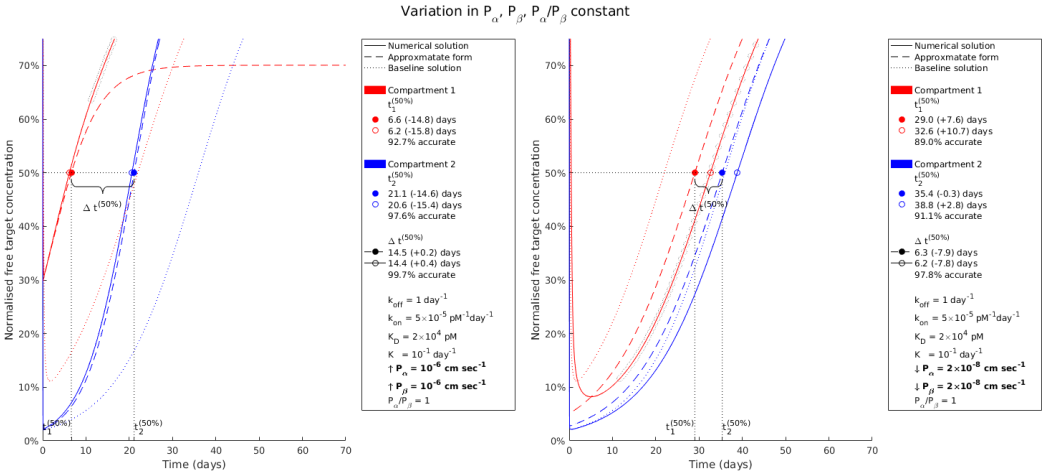

Figure A.46: Variation in P_α and P_β with P_α/P_β constant.

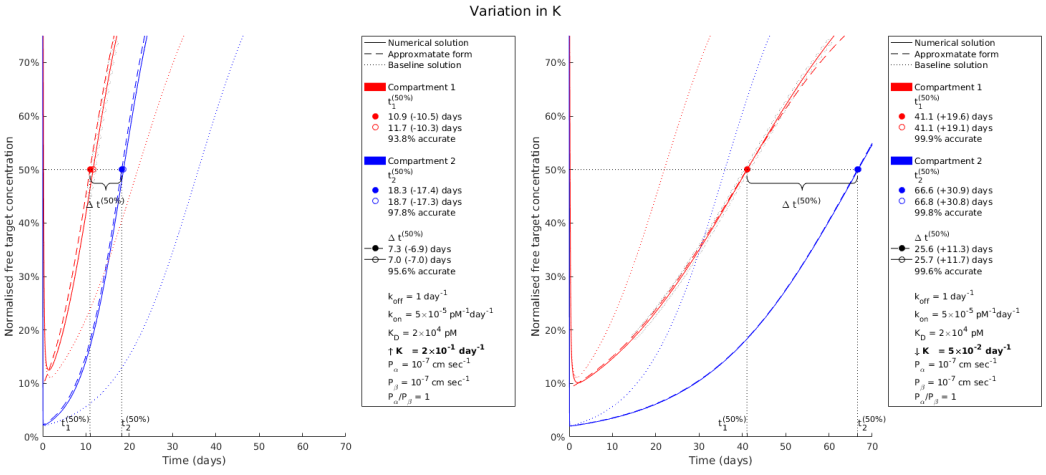

Figure A.47: Variation in K.

Caricature model, 3-compartment model comparison

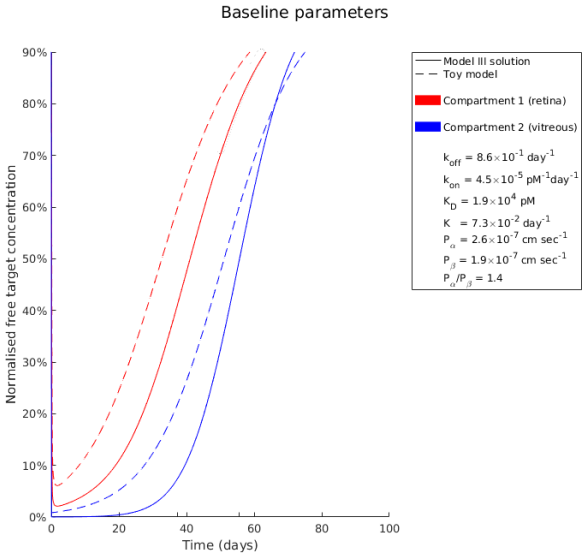

Figure A.48: Baseline parameter values

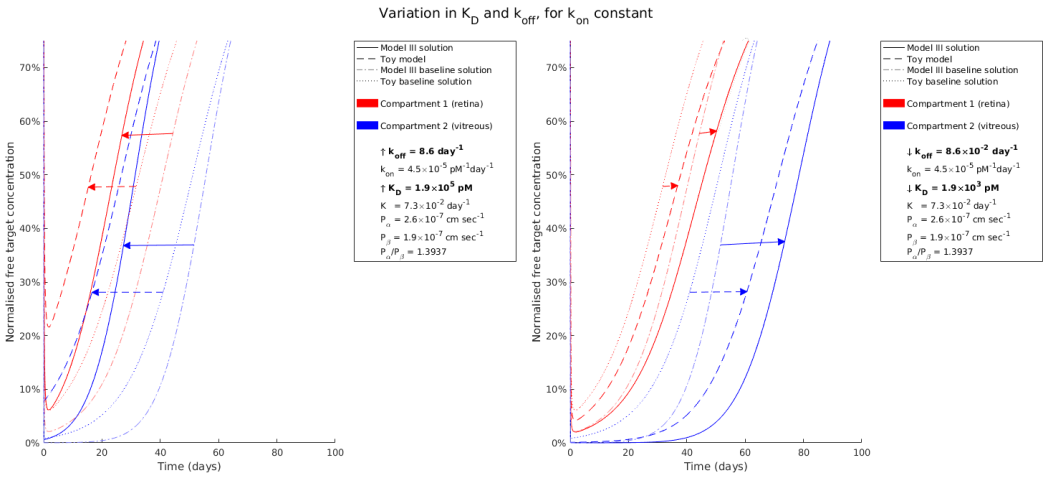

Figure A.49: Variation in k_{off} and K_{D} with k_{on} constant.

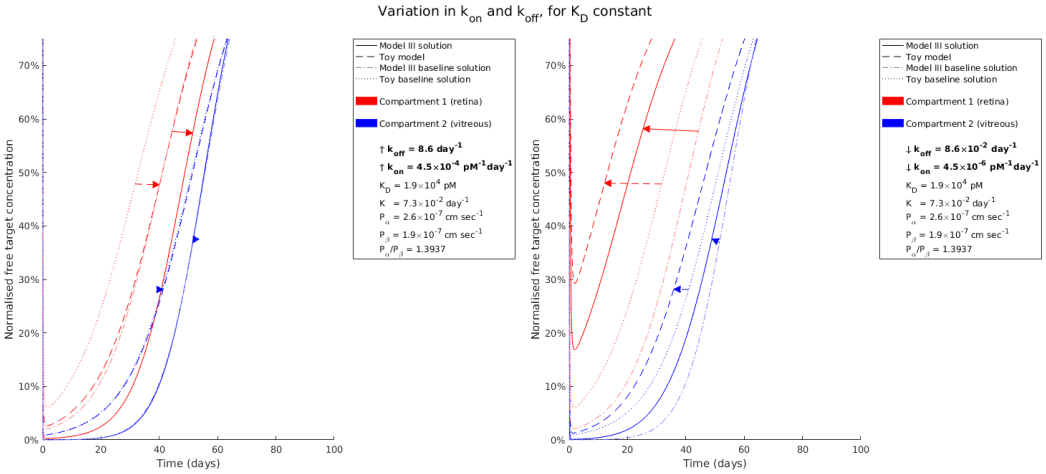

Figure A.50: Variation in k_{off} and k_{on} with K_{D} constant.

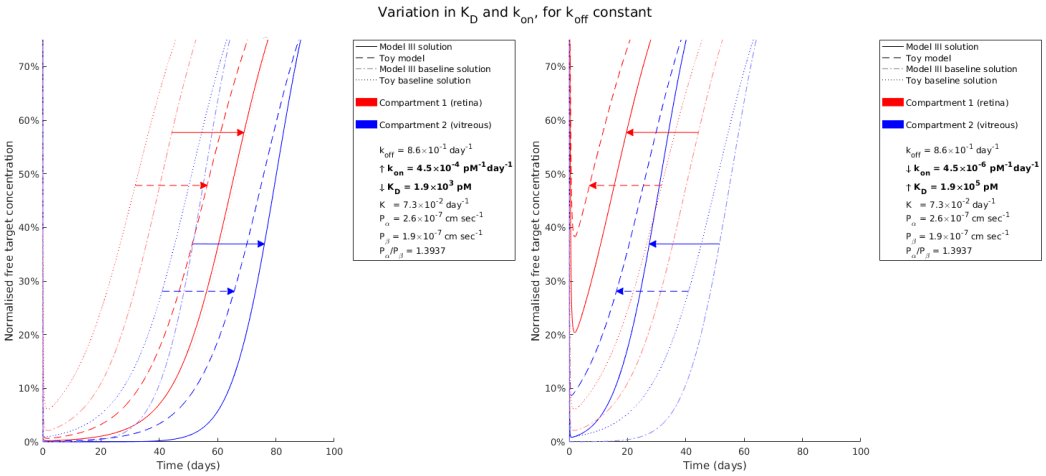

Figure A.51: Variation in k_{on} and K_{D} with k_{off} constant.

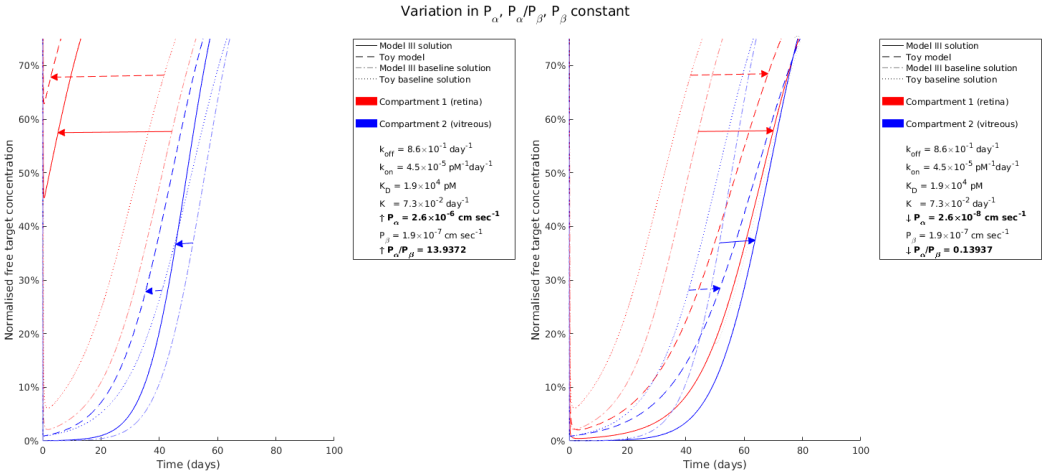

Figure A.52: Variation in P_α and P_α/P_β with P_β constant.

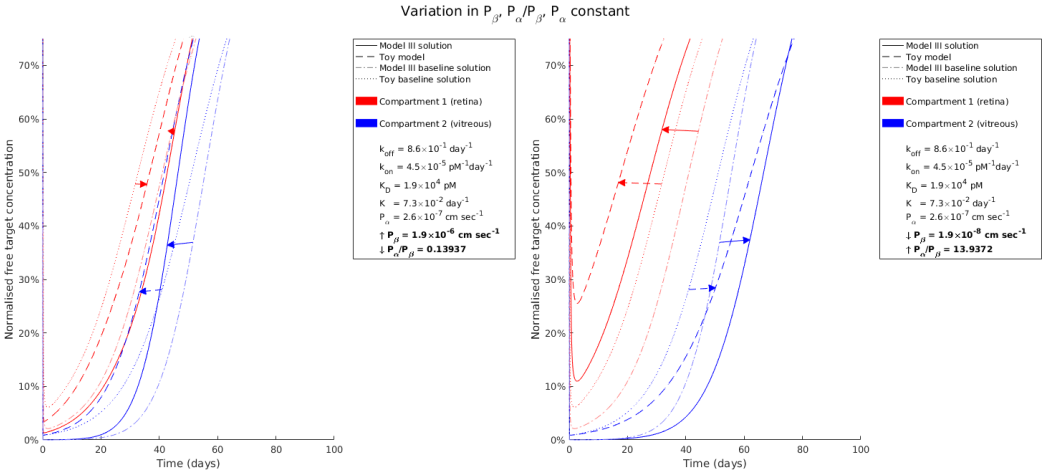

Figure A.53: Variation in P_β and P_α/P_β with P_α constant.

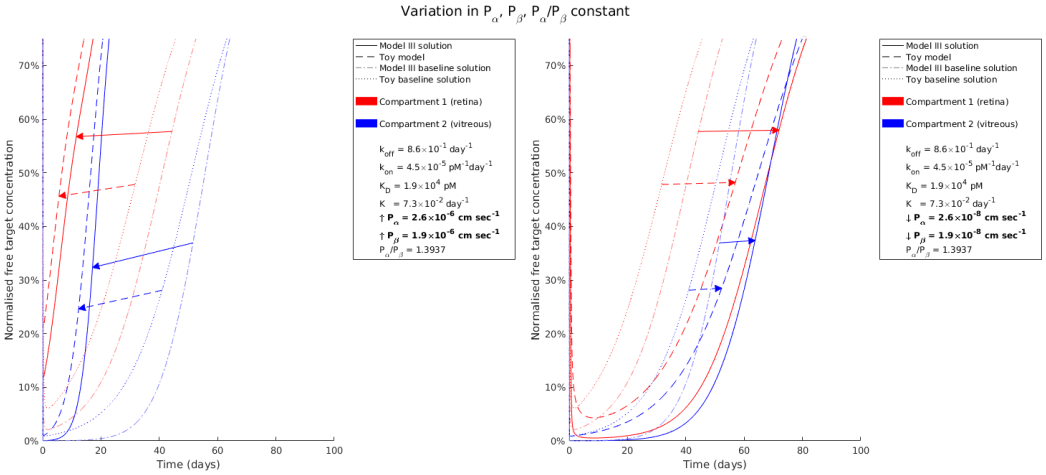

Figure A.54: Variation in P_α and P_β with P_α/P_β constant.

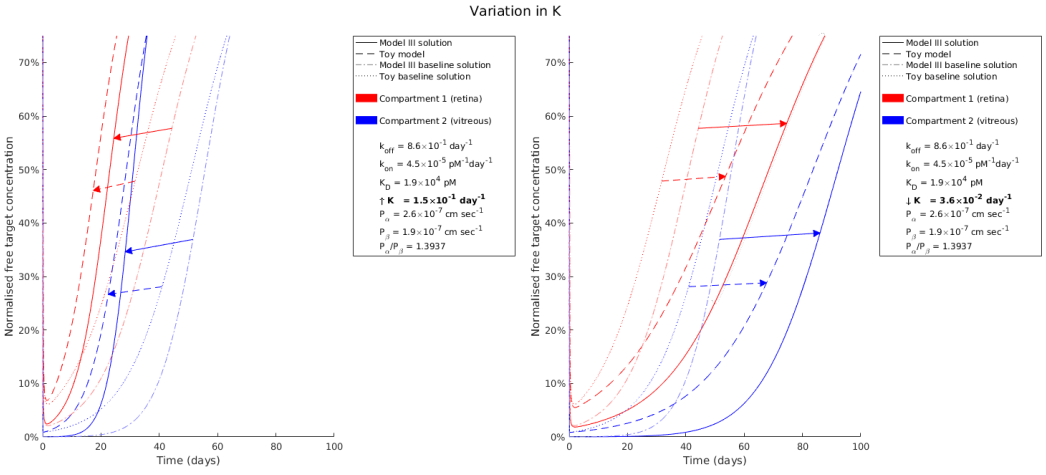

Figure A.55: Variation in K.

A.13 Chapter 3 lemmas

Lemma A.2. *Assuming chemical equilibrium, if $n = K_D^{(n)}$ then 50% of C molecules are bound to N, additionally if $K_D^{(n)}/n \ll 1 \Rightarrow c \sim c_0$, and $K_D^{(n)}/n \gg 1$ then $c \ll c_0$.*

Proof. The fraction of C bound at any point is given by the following:

$$\text{Fraction of C bound } = \frac{b}{c+b} \tag{A.108}$$

$$= \frac{1}{c/b+1}. \tag{A.109}$$

If the system is in a state of chemical equilibrium then we have that $K_{\mathrm{D}}^{(n)} b = cn$, hence:

$$\text{Fraction of C bound } = \frac{1}{K_{\mathrm{D}}^{(n)}/n+1}. \tag{A.110}$$

Therefore if $n = K_{\mathrm{D}}^{(n)}$ we find:

$$\text{Fraction of C bound} = \frac{1}{2}, \tag{A.111}$$

and hence 50% of C molecules are bound. Additionally we find:

$$\lim_{K_{\mathrm{D}}^{(n)}/n \to 0} \{\text{Fraction of C bound}\} = 1, \qquad \lim_{K_{\mathrm{D}}^{(n)}/n \to \infty} \{\text{Fraction of C bound}\} = 0, \tag{A.112}$$

thus proving $K_{\mathrm{D}}^{(n)}/n \ll 1 \Rightarrow c \sim c_0$, and $K_{\mathrm{D}}^{(n)}/n \gg 1 \Rightarrow c \ll c_0$. □

Lemma A.3. *ζ, as defined by Equation 5.88, can be written as*

$$\zeta = \frac{1}{2}\left[1 + \alpha + \beta - \sqrt{(\alpha+\beta)^2 + 2(\beta-\alpha) + 1}\right], \tag{A.113}$$

where

$$\alpha = \frac{c_0}{n_0}, \qquad \beta = \frac{K_D^{(n)}}{n_0}, \tag{A.114}$$

and ζ is bounded such that:

$$\zeta \in (0, 1). \tag{A.115}$$

Additionally β can be expressed in terms of ζ and α in the following way:

$$\beta = \frac{\zeta^2 - (1+\alpha)\zeta + \alpha}{\zeta} \tag{A.116}$$

$$= \zeta - (\alpha + 1) + \frac{\alpha}{\zeta}. \tag{A.117}$$

Proof. First let us recall that:

$$y_0 = \frac{1}{2}\left[\left\{1 - \left(\frac{n_0 + K_{\mathrm{D}}^{(n)}}{c_0}\right)\right\} + \sqrt{\frac{4n_0K_{\mathrm{D}}^{(n)}}{c_0^2} + \left\{1 - \left(\frac{n_0 - K_{\mathrm{D}}^{(n)}}{c_0}\right)\right\}^2}\right], \tag{A.118}$$

therefore from Equation 5.88:

$$\zeta = \frac{c_0}{n_0}\left(1 - \frac{1}{2}\left[\left\{1 - \left(\frac{n_0 + K_{\mathrm{D}}^{(n)}}{c_0}\right)\right\} + \sqrt{\frac{4n_0K_{\mathrm{D}}^{(n)}}{c_0^2} + \left\{1 - \left(\frac{n_0 - K_{\mathrm{D}}^{(n)}}{c_0}\right)\right\}^2}\right]\right) \tag{A.119}$$

$$= \frac{1}{2}\left[1 + \left(\frac{c_0 + K_{\mathrm{D}}^{(n)}}{n_0}\right) - \sqrt{\frac{4K_{\mathrm{D}}^{(n)}}{n_0} + \left\{\left(\frac{c_0 + K_{\mathrm{D}}^{(n)}}{n_0}\right) - 1\right\}^2}\right] \tag{A.120}$$

$$= \frac{1}{2}\left[1 + \left(\frac{c_0}{n_0}\right) + \left(\frac{K_{\mathrm{D}}^{(n)}}{n_0}\right) - \sqrt{4\left(\frac{K_{\mathrm{D}}^{(n)}}{n_0}\right) + \left\{\left(\frac{c_0}{n_0}\right) + \left(\frac{K_{\mathrm{D}}^{(n)}}{n_0}\right) - 1\right\}^2}\right] \tag{A.121}$$

$$= \frac{1}{2}\left[1 + \alpha + \beta - \sqrt{4\beta + (\alpha + \beta - 1)^2}\right] \tag{A.122}$$

$$= \frac{1}{2}\left[1 + \alpha + \beta - \sqrt{(\alpha + \beta)^2 + 2(\beta - \alpha) + 1}\right]. \tag{A.123}$$

To consider the bounds of this function suppose $\zeta \geq 1$. Then:

$$\zeta \geq 1 \quad \Rightarrow \quad 2\zeta - 1 \geq 1 \tag{A.124}$$

$$\Rightarrow \quad \left(\frac{c_0 + K_{\mathrm{D}}^{(n)}}{n_0}\right) - \sqrt{\frac{4K_{\mathrm{D}}^{(n)}}{n_0} + \left\{\left(\frac{c_0 + K_{\mathrm{D}}^{(n)}}{n_0}\right) - 1\right\}^2} \geq 1 \tag{A.125}$$

$$\Rightarrow \quad \left\{\left(\frac{c_0 + K_{\mathrm{D}}^{(n)}}{n_0}\right) - 1\right\}^2 \geq \frac{4K_{\mathrm{D}}^{(n)}}{n_0} + \left\{\left(\frac{c_0 + K_{\mathrm{D}}^{(n)}}{n_0}\right) - 1\right\}^2 \tag{A.126}$$

$$\Rightarrow \quad \frac{4K_{\mathrm{D}}^{(n)}}{n_0} \leq 0, \tag{A.127}$$

which cannot occur, therefore $\zeta < 1$. Consider now $\zeta \leq 0$, we find:

$$\zeta \leq 0 \quad \Rightarrow \quad 2\zeta - 1 \leq -1 \tag{A.128}$$

$$\Rightarrow \quad \left(\frac{c_0 + K_{\mathrm{D}}^{(n)}}{n_0}\right) - \sqrt{\frac{4K_{\mathrm{D}}^{(n)}}{n_0} + \left\{\left(\frac{c_0 + K_{\mathrm{D}}^{(n)}}{n_0}\right) - 1\right\}^2} \leq -1 \tag{A.129}$$

$$\Rightarrow \quad \left\{\left(\frac{c_0 + K_{\mathrm{D}}^{(n)}}{n_0}\right) + 1\right\}^2 \leq \frac{4K_{\mathrm{D}}^{(n)}}{n_0} + \left\{\left(\frac{c_0 + K_{\mathrm{D}}^{(n)}}{n_0}\right) - 1\right\}^2 \tag{A.130}$$

$$\Rightarrow \quad \frac{c_0 + K_{\mathrm{D}}^{(n)}}{n_0} \leq \frac{K_{\mathrm{D}}^{(n)}}{n_0} \tag{A.131}$$

$$\Rightarrow \quad c_0 \leq 0, \tag{A.132}$$

which also cannot occur. Therefore

$$\zeta \in (0, 1). \tag{A.133}$$

Finally notice that we can rearrange Equation A.123 to derive an expression for β, giving:

$$\beta = \frac{\zeta^2 - (1+\alpha)\zeta + \alpha}{\zeta} \tag{A.134}$$

$$= \zeta - (\alpha + 1) + \frac{\alpha}{\zeta}. \tag{A.135}$$

□

Lemma A.4. *The following holds:*

$$\frac{\partial t_{1/2}^{(init)}}{\partial \beta} = 0 \quad \iff \quad A(\zeta; \alpha) = g(\zeta), \tag{A.136}$$

where $A(\zeta;\alpha)$ and $g(\zeta)$ are defined as:

$$A(\zeta; \alpha) \coloneqq \frac{\alpha - \zeta}{\alpha - \zeta^2}, \tag{A.137}$$

$$g(\zeta) \coloneqq \frac{(1-\zeta)(2-\zeta)\zeta - (2-\zeta)^2 \log(2-\zeta)}{\zeta(\zeta-4)(\zeta-1)^2}. \tag{A.138}$$

Proof. By partially differentiating $t_{1/2}^{(\text{init})}$ (Equation 5.89) with respect to β we find:

$$\frac{1}{t_{1/2}^0} \frac{\partial t_{1/2}^{(\text{init})}}{\partial \beta} = \frac{\partial}{\partial \beta}\left(\frac{1}{\beta} f(\zeta)\right) \tag{A.139}$$

$$= \frac{1}{\beta}\frac{\partial}{\partial \beta}(f(\zeta)) - \frac{1}{\beta^2} f(\zeta). \tag{A.140}$$

Therefore by setting $\partial t_{1/2}^{(\text{init})}/\partial\beta = 0$ we find:

$$\frac{\partial t_{1/2}^{(\text{init})}}{\partial \beta} = 0 \quad \Rightarrow \quad \beta \frac{\partial}{\partial \beta}(f(\zeta)) = f(\zeta). \tag{A.141}$$

Next, considering the derivative of $f(\zeta)$ (Equation 5.90) with respect to β we find:

$$\log 2 \frac{\partial}{\partial \beta}(f(\zeta)) = \frac{\partial}{\partial \beta}(\log(2-\zeta)) - \frac{\partial}{\partial \beta}\left[\left(\frac{1-\zeta}{2-\zeta}\right)\zeta\right] \tag{A.142}$$

$$= \left\{\frac{\zeta}{(2-\zeta)^2} - 1\right\}\frac{\partial \zeta}{\partial \beta}. \tag{A.143}$$

We proceed by recalling that:

$$\zeta = \frac{1}{2}\left[1 + \alpha + \beta - \sqrt{(\alpha+\beta)^2 + 2(\beta - \alpha) + 1}\right], \tag{A.144}$$

and hence consider $\partial\zeta/\partial\beta$, which evaluates to:

$$2\frac{\partial\zeta}{\partial\beta} = 1 - \frac{1+\alpha+\beta}{\sqrt{(\alpha+\beta)^2 + 2(\beta-\alpha)+1}}. \tag{A.145}$$

Noting that:

$$\sqrt{(\alpha+\beta)^2 + 2(\beta-\alpha)+1} = 1+\alpha+\beta-2\zeta, \tag{A.146}$$

we find we may express $\partial\zeta/\partial\beta$ as follows:

$$\frac{\partial\zeta}{\partial\beta} = -\frac{\zeta}{1+\alpha+\beta-2\zeta}. \tag{A.147}$$

Therefore:

$$\frac{\partial}{\partial\beta}\left(f\left(\zeta\right)\right) = \frac{1}{\log 2}\left\{1 - \frac{\zeta}{(2-\zeta)^2}\right\}\frac{\zeta}{1+\alpha+\beta-2\zeta}. \tag{A.148}$$

Hence, returning to our expression generated by setting $\partial t_{1/2}^{(\text{init})}/\partial\beta = 0$, we find:

$$\beta\frac{\partial}{\partial\beta}\left(f\left(\zeta\right)\right) = f\left(\zeta\right) \tag{A.149}$$

$$\Rightarrow \quad \frac{\beta}{1+\alpha+\beta-2\zeta} = \frac{(2-\zeta)^2\log\left(2-\zeta\right) - (1-\zeta)(2-\zeta)\zeta}{\zeta(\zeta-4)(\zeta-1)}. \tag{A.150}$$

Next, by recalling β may be expressed in terms of α and ζ as follows:

$$\beta = \frac{\zeta^2 - (1+\alpha)\zeta + \alpha}{\zeta}, \tag{A.151}$$

we find:

$$\frac{\beta}{1+\alpha+\beta-2\zeta} = \frac{(\zeta-1)(\zeta-\alpha)}{\alpha-\zeta^2}, \tag{A.152}$$

and hence, finally, we find:

$$\frac{\partial t_{1/2}^{(\text{init})}}{\partial\beta} = 0 \quad \Rightarrow \quad \underbrace{\frac{\alpha-\zeta}{\alpha-\zeta^2}}_{A(\zeta;\alpha):=} = \underbrace{\frac{(1-\zeta)(2-\zeta)\zeta - (2-\zeta)^2\log\left(2-\zeta\right)}{\zeta(\zeta-4)(\zeta-1)^2}}_{g(\zeta):=} \tag{A.153}$$

$$\Rightarrow \quad A(\zeta;\alpha) = g(\zeta). \tag{A.154}$$

□

A.14 Analysis of the PK/PD of bispecific anti-VEGF vitreal binding macromolecules using a PDE model

In this appendix we consider the PDE analogue of the ODE model presented in Chapter 6. We extend the SVB PDE PK model of Section 5.2 to additionally include interactions between the SVB molecule and VEGF, in an analogous manner to that in which we extended the SVB PK ODE model into the SVB PK/PD model in Section 6. Sections 3.2, 4.2 and 5.2 have all demonstrated the similarities and predictive equivalence of ocular ODE models relative to their PDE analogues. Therefore, finally, to supplement our previous PDE analysis we present this analysis as a verification of continued equivalence between ODE and PDE ocular models. In this section we will compare the PK/PD of ODE and PDE SVB models over the large parameter range ($K_{\mathrm{D}}^{(n)} \in [10^0, 10^{10}]$ and $n_0 \in [10^4, 10^{10}]$), in an analogous manner as Chapter 5, Section 5.2.

A.14.1 Model Formulation and Numerical Solution

In order to formulate the SVB PK PDE model we will extend Equations 5.151-5.159 of Section 5.2, which define the retina-vitreous SVB PDE PK model. The model is then defined by the Equations A.155-A.192:

VEGF (V, $\mathrm{v}(\vec{x},t)$)

$$\frac{\partial v_{\mathrm{ret}}}{\partial t} = D_{\mathrm{ret}}^{(v)}\nabla^2 v_{\mathrm{ret}} + (k_{\mathrm{off}}^{(v)} c_{\mathrm{ret}} - 2k_{\mathrm{on}}^{(v)} v_{\mathrm{ret}} r_{\mathrm{ret}}) + \frac{V_{\mathrm{in}}}{V_{\mathrm{ret}}}\delta_{\vec{x}}(\Omega_M) \qquad \text{for } \vec{x} \in \Omega_{\mathrm{ret}}, \tag{A.155}$$

$$\frac{\partial v_{\mathrm{vit}}}{\partial t} = D_{\mathrm{vit}}^{(v)}\nabla^2 v_{\mathrm{vit}} + (k_{\mathrm{off}}^{(v)} c_{\mathrm{vit}} - 2k_{\mathrm{on}}^{(v)} v_{\mathrm{vit}} r_{\mathrm{vit}}) + \left(k_{\mathrm{off}}^{(v)} f - 2k_{\mathrm{on}}^{(v)} v_{\mathrm{vit}} m\right) \qquad \text{for } \vec{x} \in \Omega_{\mathrm{vit}}, \tag{A.156}$$

$$-D_{\mathrm{ret}}\vec{n}\cdot\nabla v_{\mathrm{ret}} = p_{\mathrm{ILM}}^{(v)}(v_{\mathrm{ret}} - v_{\mathrm{vit}}) \qquad \text{for } \vec{x} \in \partial\Omega_1, \tag{A.157}$$

$$-D_{\mathrm{ret}}\vec{n}\cdot\nabla v_{\mathrm{ret}} = p_{\mathrm{RPE}}^{(v)} v_{\mathrm{ret}} \qquad \text{for } \vec{x} \in \partial\Omega_1^*, \tag{A.158}$$

$$-D_{\mathrm{vit}}\vec{n}\cdot\nabla v_{\mathrm{vit}} = p_{\mathrm{ILM}}^{(v)}(v_{\mathrm{vit}} - v_{\mathrm{ret}}) \qquad \text{for } \vec{x} \in \partial\Omega_1, \tag{A.159}$$

$$-D_{\mathrm{vit}}\vec{n}\cdot\nabla v_{\mathrm{vit}} = p_{\mathrm{HYA}}^{(v)} v_{\mathrm{vit}} \qquad \text{for } \vec{x} \in \partial\Omega_2, \tag{A.160}$$

$$-\vec{n}\cdot\nabla v_{\mathrm{vit}} = 0 \qquad \text{for } \vec{x} \in \partial\Omega_3, \tag{A.161}$$

Drug (R, $\mathrm{r}(\vec{x},t)$)

$$\frac{\partial r_{\text{ret}}}{\partial t} = D_{\text{ret}}^{(r)} \nabla^2 r_{\text{ret}} + (k_{\text{off}}^{(v)} c_{\text{ret}} - 2k_{\text{on}}^{(v)} v_{\text{ret}} r_{\text{ret}}) \qquad \text{for } \vec{x} \in \Omega_{\text{ret}}, \tag{A.162}$$
$$+ (2k_{\text{off}}^{(v)} h_{\text{ret}} - k_{\text{on}}^{(v)} c_{\text{ret}} r_{\text{ret}})$$

$$\frac{\partial r_{\text{vit}}}{\partial t} = D_{\text{vit}}^{(r)} \nabla^2 r_{\text{vit}} + (k_{\text{off}}^{(v)} c_{\text{vit}} - 2k_{\text{on}}^{(v)} v_{\text{vit}} r_{\text{vit}}) \qquad \text{for } \vec{x} \in \Omega_{\text{vit}}, \tag{A.163}$$
$$+ (2k_{\text{off}}^{(v)} h_{\text{vit}} - k_{\text{on}}^{(v)} c_{\text{vit}} r_{\text{vit}})$$
$$+ \left(k_{\text{off}}^{(n)} m - k_{\text{on}}^{(n)} r_{\text{vit}} n\right)$$
$$+ \left(k_{\text{off}}^{(v)} g - k_{\text{on}}^{(v)} r_{\text{vit}} f\right)$$

$$-D_{\text{ret}} \vec{n} \cdot \nabla r_{\text{ret}} = p_{\text{ILM}}^{(r)} (r_{\text{ret}} - r_{\text{vit}}) \qquad \text{for } \vec{x} \in \partial\Omega_1, \tag{A.164}$$

$$-D_{\text{ret}} \vec{n} \cdot \nabla r_{\text{ret}} = p_{\text{RPE}}^{(r)} r_{\text{ret}} \qquad \text{for } \vec{x} \in \partial\Omega_1^*, \tag{A.165}$$

$$-D_{\text{vit}} \vec{n} \cdot \nabla r_{\text{vit}} = p_{\text{ILM}}^{(r)} (r_{\text{vit}} - r_{\text{ret}}) \qquad \text{for } \vec{x} \in \partial\Omega_1, \tag{A.166}$$

$$-D_{\text{vit}} \vec{n} \cdot \nabla r_{\text{vit}} = p_{\text{HYA}}^{(r)} r_{\text{vit}} \qquad \text{for } \vec{x} \in \partial\Omega_2, \tag{A.167}$$

$$-\vec{n} \cdot \nabla r_{\text{vit}} = 0 \qquad \text{for } \vec{x} \in \partial\Omega_3, \tag{A.168}$$

VEGF-drug (VR, $\mathrm{c}(\vec{x}, t)$)

$$\frac{\partial c_{\text{ret}}}{\partial t} = D_{\text{ret}}^{(c)} \nabla^2 c_{\text{ret}} - (k_{\text{off}}^{(v)} c_{\text{ret}} - 2k_{\text{on}}^{(v)} v_{\text{ret}} r_{\text{ret}}) \qquad \text{for } \vec{x} \in \Omega_{\text{ret}}, \tag{A.169}$$
$$+ (2k_{\text{off}}^{(v)} h_{\text{ret}} - k_{\text{on}}^{(v)} c_{\text{ret}} r_{\text{ret}})$$

$$\frac{\partial c_{\text{vit}}}{\partial t} = D_{\text{vit}}^{(c)} \nabla^2 c_{\text{vit}} - (k_{\text{off}}^{(v)} c_{\text{vit}} - 2k_{\text{on}}^{(v)} v_{\text{vit}} r_{\text{vit}}) \qquad \text{for } \vec{x} \in \Omega_{\text{vit}}, \tag{A.170}$$
$$+ (2k_{\text{off}}^{(v)} h_{\text{vit}} - k_{\text{on}}^{(v)} c_{\text{vit}} r_{\text{vit}})$$
$$+ \left(k_{\text{off}}^{(n)} f - k_{\text{on}}^{(n)} c_{\text{vit}} n\right)$$
$$+ \left(k_{\text{off}}^{(v)} g - k_{\text{on}}^{(v)} c_{\text{vit}} m\right)$$

$$-D_{\text{ret}} \vec{n} \cdot \nabla c_{\text{ret}} = p_{\text{ILM}}^{(c)} (c_{\text{ret}} - c_{\text{vit}}) \qquad \text{for } \vec{x} \in \partial\Omega_1, \tag{A.171}$$

$$-D_{\text{ret}} \vec{n} \cdot \nabla c_{\text{ret}} = p_{\text{RPE}}^{(c)} c_{\text{ret}} \qquad \text{for } \vec{x} \in \partial\Omega_1^*, \tag{A.172}$$

$$-D_{\text{vit}} \vec{n} \cdot \nabla c_{\text{vit}} = p_{\text{ILM}}^{(c)} (c_{\text{vit}} - c_{\text{ret}}) \qquad \text{for } \vec{x} \in \partial\Omega_1, \tag{A.173}$$

$$-D_{\text{vit}} \vec{n} \cdot \nabla c_{\text{vit}} = p_{\text{HYA}}^{(c)} c_{\text{vit}} \qquad \text{for } \vec{x} \in \partial\Omega_2, \tag{A.174}$$

$$-\vec{n} \cdot \nabla c_{\text{vit}} = 0 \qquad \text{for } \vec{x} \in \partial\Omega_3, \tag{A.175}$$

Drug-VEGF-drug (RVR, $\mathrm{h}(\vec{x}, t)$)

$$\frac{\partial h_{\text{ret}}}{\partial t} = D_{\text{ret}}^{(h)} \nabla^2 h_{\text{ret}} - (2k_{\text{off}}^{(v)} h_{\text{ret}} - k_{\text{on}}^{(v)} c_{\text{ret}} r_{\text{ret}}) \qquad \text{for } \vec{x} \in \Omega_{\text{ret}}, \tag{A.176}$$

$$\frac{\partial h_{\text{vit}}}{\partial t} = D_{\text{vit}}^{(h)} \nabla^2 h_{\text{vit}} - (2k_{\text{off}}^{(v)} h_{\text{vit}} - k_{\text{on}}^{(v)} c_{\text{vit}} r_{\text{vit}}) \qquad \text{for } \vec{x} \in \Omega_{\text{vit}}, \tag{A.177}$$

$$+ \left(k_{\text{off}}^{(n)} g - 2k_{\text{on}}^{(n)} h_{\text{vit}} n\right)$$

$$-D_{\text{ret}} \vec{n} \cdot \nabla h_{\text{ret}} = p_{\text{ILM}}^{(h)} (h_{\text{ret}} - h_{\text{vit}}) \qquad \text{for } \vec{x} \in \partial\Omega_1, \tag{A.178}$$

$$-D_{\text{ret}} \vec{n} \cdot \nabla h_{\text{ret}} = p_{\text{RPE}}^{(h)} h_{\text{ret}} \qquad \text{for } \vec{x} \in \partial\Omega_1^*, \tag{A.179}$$

$$-D_{\text{vit}} \vec{n} \cdot \nabla h_{\text{vit}} = p_{\text{ILM}}^{(h)} (h_{\text{vit}} - h_{\text{ret}}) \qquad \text{for } \vec{x} \in \partial\Omega_1, \tag{A.180}$$

$$-D_{\text{vit}} \vec{n} \cdot \nabla h_{\text{vit}} = p_{\text{HYA}}^{(h)} h_{\text{vit}} \qquad \text{for } \vec{x} \in \partial\Omega_2, \tag{A.181}$$

$$-\vec{n} \cdot \nabla h_{\text{vit}} = 0 \qquad \text{for } \vec{x} \in \partial\Omega_3, \tag{A.182}$$

Binding site (N, $\text{n}(\vec{x}, t)$)

$$\frac{\partial n}{\partial t} = + \left(k_{\text{off}}^{(n)} m - k_{\text{on}}^{(n)} r_{\text{vit}} n\right) \qquad \text{for } \vec{x} \in \partial\Omega_2, \tag{A.183}$$

$$+ \left(k_{\text{off}}^{(n)} f - k_{\text{on}}^{(n)} c_{\text{vit}} n\right) \tag{A.184}$$

$$+ \left(k_{\text{off}}^{(n)} g - 2k_{\text{on}}^{(n)} h_{\text{vit}} n\right) \tag{A.185}$$

Drug-binding site (RN, $\text{m}(\vec{x}, t)$)

$$\frac{\partial m}{\partial t} = - \left(k_{\text{off}}^{(n)} m - k_{\text{on}}^{(n)} r_{\text{vit}} n\right) \qquad \text{for } \vec{x} \in \partial\Omega_2, \tag{A.186}$$

$$+ \left(k_{\text{off}}^{(v)} f - 2k_{\text{on}}^{(v)} v_{\text{vit}} m\right) \tag{A.187}$$

$$+ \left(k_{\text{off}}^{(v)} g - k_{\text{on}}^{(v)} c_{\text{vit}} m\right) \tag{A.188}$$

VEGF-drug-binding site (VRN, $\text{f}(\vec{x}, t)$)

$$\frac{\partial f}{\partial t} = - \left(k_{\text{off}}^{(n)} f - k_{\text{on}}^{(n)} c_{\text{vit}} n\right) \qquad \text{for } \vec{x} \in \partial\Omega_2, \tag{A.189}$$

$$- \left(k_{\text{off}}^{(v)} f - 2k_{\text{on}}^{(v)} v_{\text{vit}} m\right) \tag{A.190}$$

$$+ \left(k_{\text{off}}^{(v)} g - k_{\text{on}}^{(v)} r_{\text{vit}} f\right) \tag{A.191}$$

Drug-VEGF-drug-binding site (RVRN, $g(\vec{x},t)$)

$$\frac{\partial g}{\partial t} = -\left(k_{\text{off}}^{(n)} g - 2k_{\text{on}}^{(n)} h_{\text{vit}} n\right) \qquad \text{for } \vec{x} \in \partial\Omega_2, \tag{A.192}$$

$$-\left(k_{\text{off}}^{(v)} g - k_{\text{on}}^{(v)} c_{\text{vit}} m\right) \tag{A.193}$$

$$-\left(k_{\text{off}}^{(v)} g - k_{\text{on}}^{(v)} r_{\text{vit}} f\right) \tag{A.194}$$

We solve the model for a dose of 0.5 mg, $R_{\text{h}} = 3.04$ nm, over human geometry, as defined in Figure 3.5 and Table 3.6. All parameters, aside from $k_{\text{off}}^{(n)}, k_{\text{on}}^{(n)}$ and n_0, are generated in the same manner as in the PDE PK/PD model, as defined in Section 4.2. As in Section 5.1 the binding off rate between the SVB and the vitreal binding site, $k_{\text{off}}^{(n)}$, is taken to be much greater than the decay rate of the system such that $k_{\text{off}}^{(n)} \sim O(10)$. We then fix $K_{\text{D}}^{(n)}$ and generate the binding on rate via $k_{\text{on}}^{(n)} = k_{\text{off}}^{(n)}/K_{\text{D}}$. Similarly to $K_{\text{D}}^{(n)}$, the total concentration of binding sites, n_0, is set arbitrarily. Initial conditions for all drug-VEGF and drug-binding sites complexes are initially zero, and the drug is assumed only to be initially present in the vitreous, with uniform concentration corresponding to the initial dose. Initially the concentrations of VEGF in the retina and vitreous are set to the steady state solution in the absence of drug.

As in Section 4.2 we explore the effects of heterogeneous versus homogeneous VEGF production within the retina, by considering VEGF production limited to the macula region of the retina only. Additionally, we also consider the effects of varying the binding affinity between the SVB molecule and VEGF, and how this impacts the PDE model relative to the ODE model.

A.14.2 Predictive comparison between the ODE and PDE model

In order to compare the SVB PK/PD PDE model to the ODE model discussed in Section 6, as in Section 5.2, we modify the value of k_{el} so as to generate the same PK (specifically the $t_{1/2}$ of the system) in the absence of vitreal binding, i.e. when $k_{\text{on}}^{(n)} = 0$. We do this so that when comparing the ODE and PDE models over various parameter values, we may analyse the variation in free VEGF suppression due solely to the introduction of vitreal binding. The ODE model is then solved using the same $K_{\text{D}}^{(v)}$, $K_{\text{D}}^{(n)}$ and n_0 values as the PDE, over $K_{\text{D}}^{(n)} \in [10^0, 10^{10}]$ and $n_0 \in [10^4, 10^{10}]$, where all remaining parameters are set in the same manner as in Chapter 6. Additionally the VEGF production rate, V_{in}, is also set in the ODE model to match the average steady state free VEGF concentrations of the PDE. The free VEGF concentrations in the retina and vitreous are then normalised relative to their

respective free VEGF steady state concentrations, for each each model.

Figure A.56 shows the percentage error between the ODE and PDE SVB PK models retinal and vitreal solutions. The error was calculated by considering the relative magnitude of the spatially averaged PDE solution to the ODE model at equally spaced intervals. We solved the system over $K_{\mathrm{D}}^{(n)} \in [10^0, 10^{10}]$ pM and $n_0 \in [10^4, 10^{10}]$ pM, at equally spaced logarithmic intervals, totalling 1232 combinations (44 $K_{\mathrm{D}}^{(n)}$ values, 28 n_0 values). As can be seen from Figure A.56 the error across $\left(K_{\mathrm{D}}^{(n)}, n_0\right)$ parameter space between the ODE and PDE retinal and vitreal solutions is below 6% and 8%, respectively.

Additionally in Appendix A.15 we present an extreme high/low value comparison of concentrations of free VEGF in the retina and vitreous, of the macula/standard SVB ODE/PDE PK/PD models, for values of $K_{\mathrm{D}}^{(v)}$, $K_{\mathrm{D}}^{(n)}$ and n_0. From this analysis we can see that in all combinations generated by taking extremely high and low physically reasonable values for these three parameters, the ODE, standard PDE and macula PDE models do not vary greatly either quantitatively or qualitatively - in line with errors found over the high resolution sweep of Figure A.56. Given this high fidelity between the ODE and PDE models we will limit our analysis to that conducted for the ODE model presented in Chapter 6.

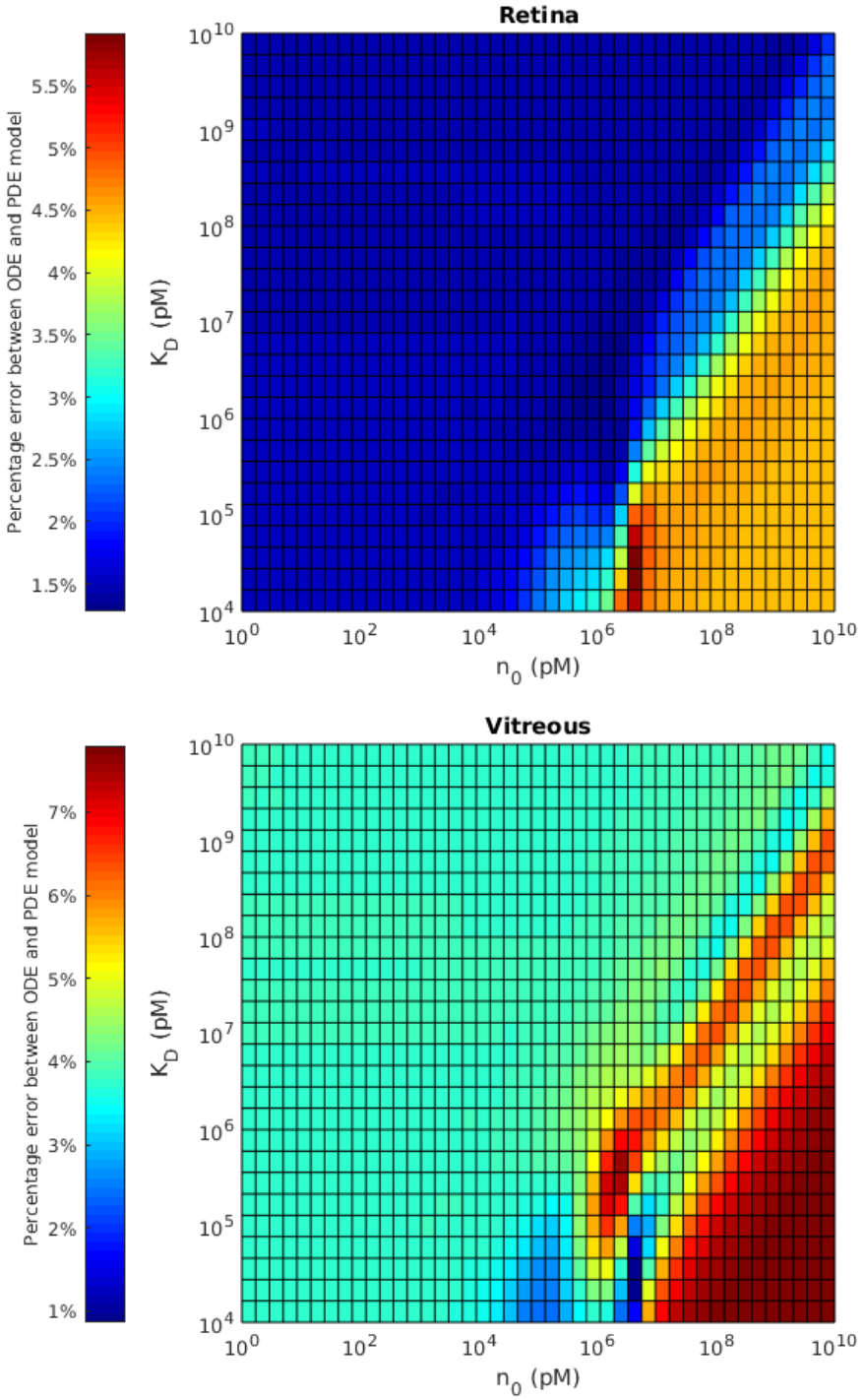

Figure A.56: Percentage error between the ODE (Equations 6.4-6.15) and PDE (Equations A.155-A.192) SVB PK models. Calculated by considering the relative magnitude of the spatially averaged PDE solution to the ODE model at equally spaced intervals. Solved over $K_{\mathrm{D}}^{(n)} \in [10^0, 10^{10}]$ pM and $n_0 \in [10^4, 10^{10}]$ pM, at equally spaced logarithmic intervals, totalling 1232 combinations.

A.15 Extreme parameter value comparison of the ODE and PDE PK/PD static vitreal binding model

Following from Appendix A.14 we present in Figures A.57-A.64 an extreme value parameter comparison of the normalised concentrations of free VEGF in the retina and vitreous, of the macula/standard SVB ODE/PDE PK/PD models. We compare the 8 combinations generated by taking extremely high and low values for $K_{\mathrm{D}}^{(v)}$, $K_{\mathrm{D}}^{(n)}$ and n_0. Models are otherwise solved as outlined in Appendix A.14.

Except for Figures A.58, A.62 and marginally A.64, there is good agreement between the models highlighting the effectiveness of the ODE model even with most parameter extremes. The exceptions are characterised by extreme values of n_0 and do not exhibit behaviours suitable for prospective therapeutic interventions and thus typically would not be considered further.

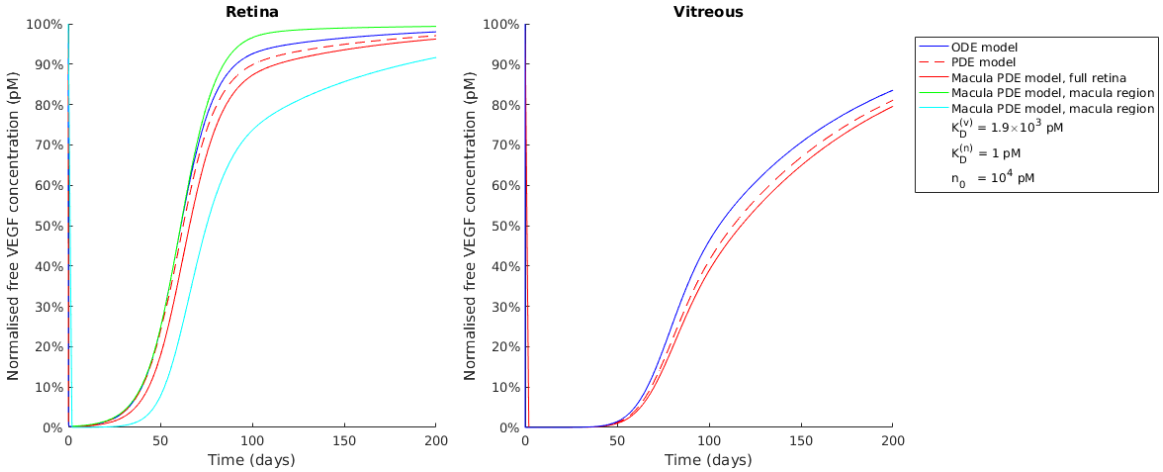

Figure A.57: Macula/standard SVB PK/PD PDE model (Equations A.155-A.192) solved for $K_{\mathrm{D}}^{(v)} = 1.9 \times 10^3$ pM, $K_{\mathrm{D}}^{(n)} = 1$ pM, $n_0 = 10^4$ pM, plotted alongside the 3-compartment PK/PD ODE model (Equations 4.3-4.18).

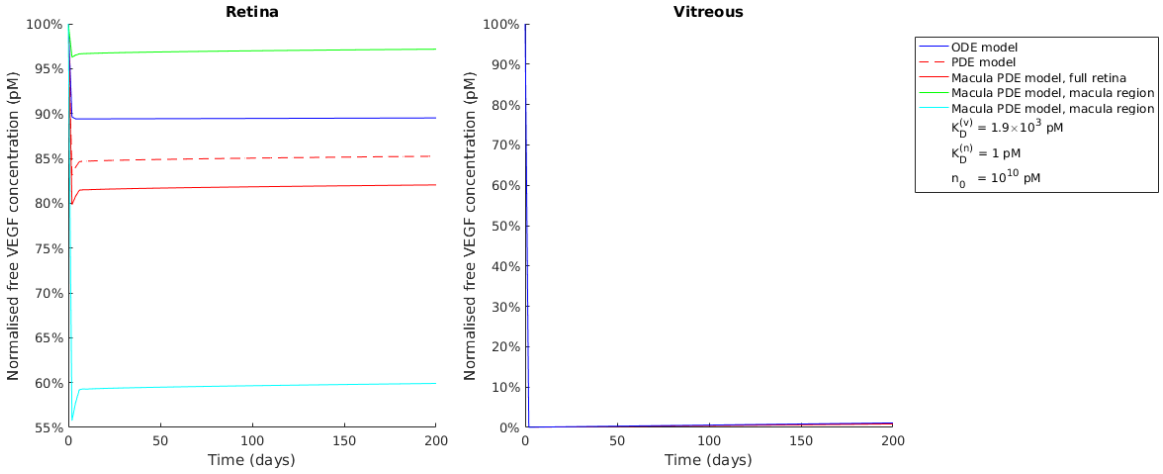

Figure A.58: Macula/standard SVB PK/PD PDE model (Equations A.155-A.192) solved for $K_{\mathrm{D}}^{(v)} = 1.9 \times 10^3$ pM, $K_{\mathrm{D}}^{(n)} = 1$ pM, $n_0 = 10^{10}$ pM, plotted alongside the 3-compartment PK/PD ODE model (Equations 4.3-4.18).

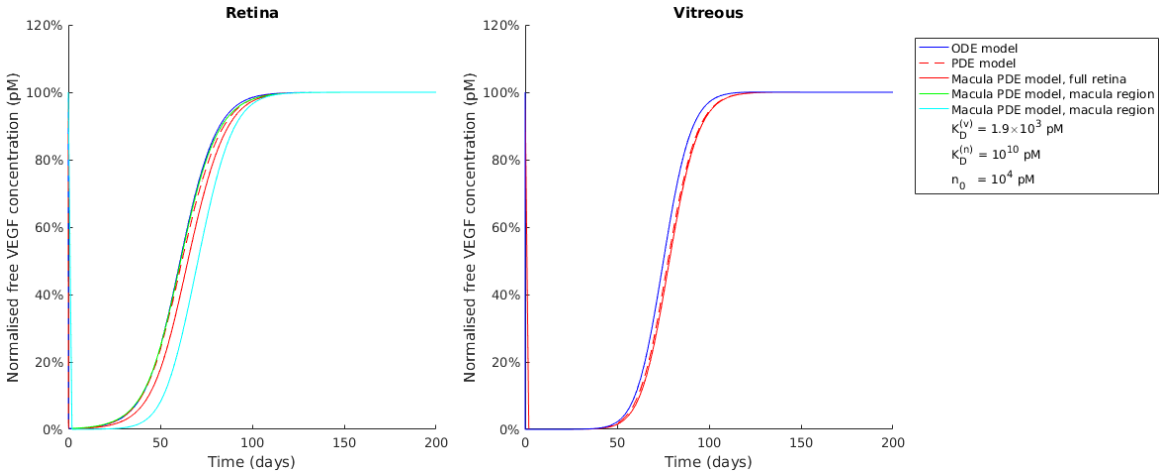

Figure A.59: Macula/standard SVB PK/PD PDE model (Equations A.155-A.192) solved for $K_{\mathrm{D}}^{(v)} = 1.9 \times 10^3$ pM, $K_{\mathrm{D}}^{(n)} = 10^{10}$ pM, $n_0 = 10^4$ pM, plotted alongside the 3-compartment PK/PD ODE model (Equations 4.3-4.18).

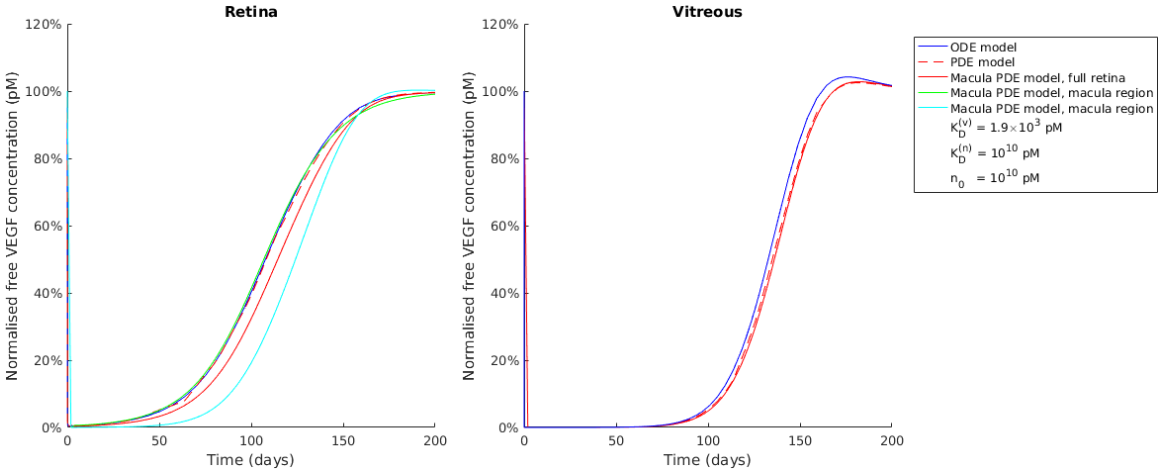

Figure A.60: Macula/standard SVB PK/PD PDE model (Equations A.155-A.192) solved for $K_{\mathrm{D}}^{(v)} = 1.9 \times 10^3$ pM, $K_{\mathrm{D}}^{(n)} = 10^{10}$ pM, $n_0 = 10^{10}$ pM, plotted alongside the 3-compartment PK/PD ODE model (Equations 4.3-4.18).

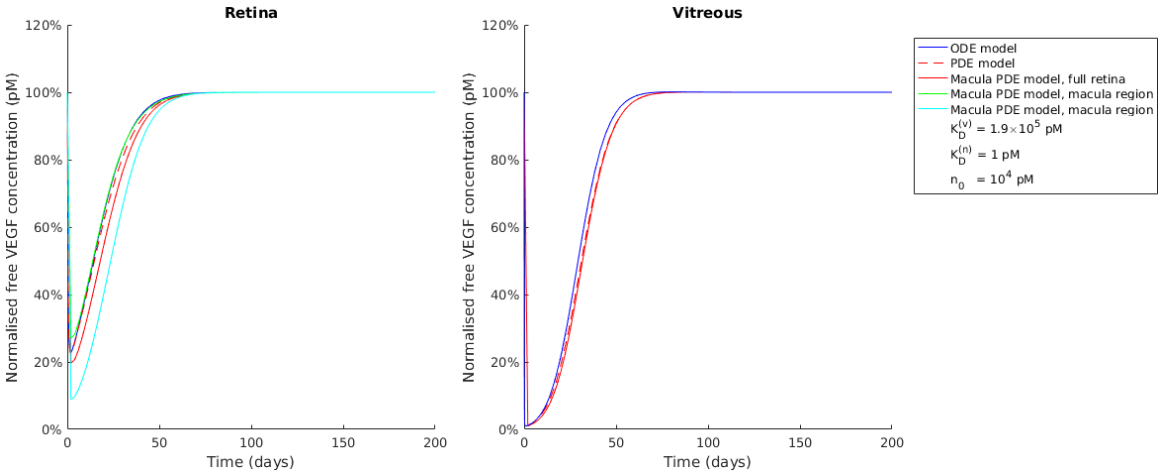

Figure A.61: Macula/standard SVB PK/PD PDE model (Equations A.155-A.192) solved for $K_{\mathrm{D}}^{(v)} = 1.9 \times 10^5$ pM, $K_{\mathrm{D}}^{(n)} = 1$ pM, $n_0 = 10^4$ pM, plotted alongside the 3-compartment PK/PD ODE model (Equations 4.3-4.18).

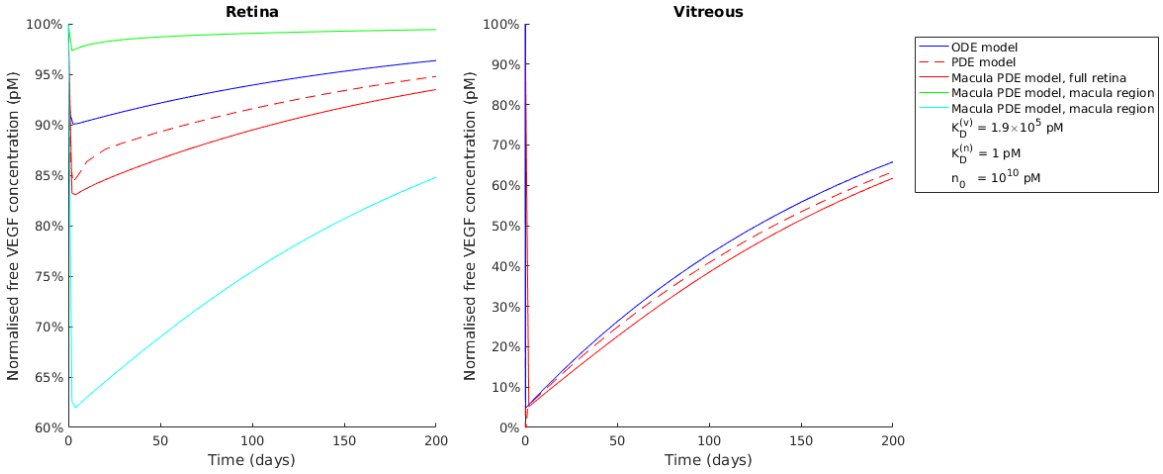

Figure A.62: Macula/standard SVB PK/PD PDE model (Equations A.155-A.192) solved for $K_{\mathrm{D}}^{(v)} = 1.9 \times 10^5$ pM, $K_{\mathrm{D}}^{(n)} = 1$ pM, $n_0 = 10^{10}$ pM, plotted alongside the 3-compartment PK/PD ODE model (Equations 4.3-4.18).

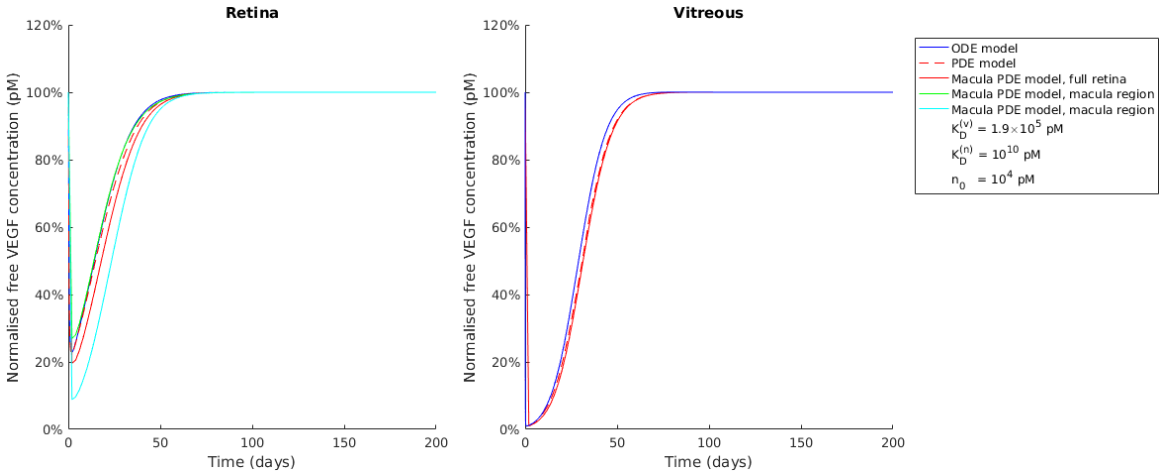

Figure A.63: Macula/standard SVB PK/PD PDE model (Equations A.155-A.192) solved for $K_{\mathrm{D}}^{(v)} = 1.9 \times 10^5$ pM, $K_{\mathrm{D}}^{(n)} = 10^{10}$ pM, $n_0 = 10^4$ pM, plotted alongside the 3-compartment PK/PD ODE model (Equations 4.3-4.18).

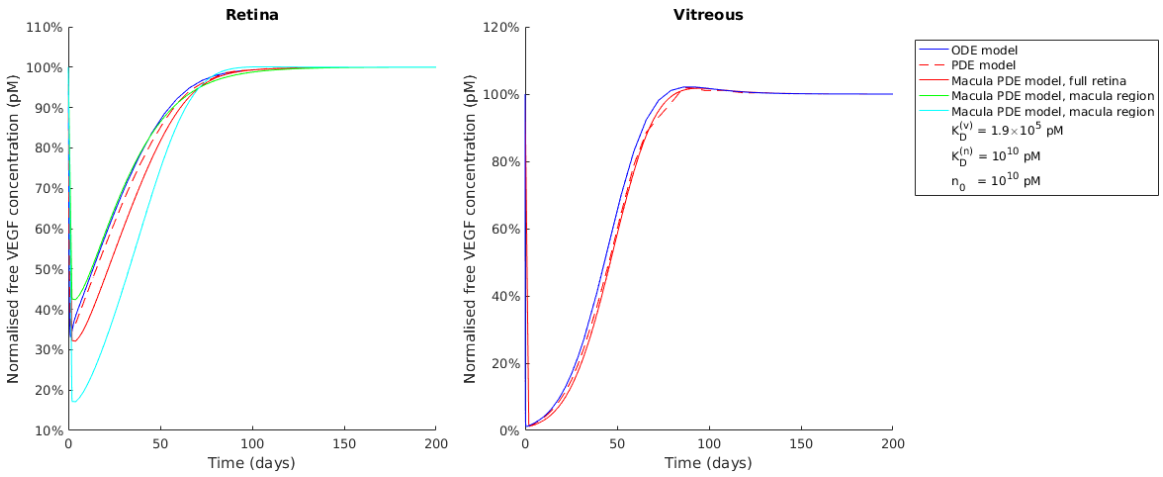

Figure A.64: Macula/standard SVB PK/PD PDE model (Equations A.155-A.192) solved for $K_{\mathrm{D}}^{(v)} = 1.9 \times 10^5$ pM, $K_{\mathrm{D}}^{(n)} = 10^{10}$ pM, $n_0 = 10^{10}$ pM, plotted alongside the 3-compartment PK/PD ODE model (Equations 4.3-4.18).

Bibliography

[1] Felicia Marie Knaul, Paul E. Farmer, Eric L. Krakauer, Liliana De Lima, Afsan Bhadelia, Xiaoxiao Jiang Kwete, Hctor Arreola-Ornelas, Octavio Gómez-Dantés, Natalia M. Rodriguez, George A.O. Alleyne, Stephen R. Connor, David J. Hunter, Diederik Lohman, Lukas Radbruch, Mara del Rocío Sáenz Madrigal, Rifat Atun, Kathleen M. Foley, Julio Frenk, Dean T. Jamison, and M. R. Rajagopal. Alleviating the access abyss in palliative care and pain relief - an imperative of universal health coverage: the Lancet Commission report. *The Lancet*, 391:1391454, 2018.

[2] Juan J.L. Lertora and Konstantina M. Vanevski. Introduction to pharmacokinetics and pharmacodynamics. *Small Molecule Therapy for Genetic Disease*, pages 35–54, 2010.

[3] Derek J. Saunders, Philipp S. Muether, and Sascha Fauser. A model of the ocular pharmacokinetics involved in the therapy of neovascular age-related macular degeneration with ranibizumab. *The British Journal of Ophthalmology*, 99(11):1554–9, 2015.

[4] Neil M. Bressler. Age-related macular degeneration is the leading cause of blindness. *Arch Ophthalmol*, 291(15):1900–1901, 8 2004.

[5] Jayakrishna Ambati and Benjamin Fowler. Mechanisms of age-related macular degeneration. *Neuron*, 75(1):26–39, 2012.

[6] David R. Guyer, Stuart L. Fine, Maureen G. Maguire, Barbara S. Hawkins, Sarah L. Owens, and Robert P. Murphy. Subfoveal choroidal neovascular membranes in age-related macular degeneration. *Archives of Ophthalmology*, 104(5):702, 1986.

[7] Tien Wong, Usha Chakravarthy, Ronald Klein, Paul Mitchell, Gergana Zlateva, Ronald Buggage, Kyle Fahrbach, Corey Probst, and Isabella Sledge. The natural history and prognosis of neovascular age-related macular degeneration. A systematic review of the literature and meta-analysis. *Ophthalmology*, 115(1):116–127, 2008.

[8] Aimee V. Chappelow and Peter K. Kaiser. Neovascular age-related macular degeneration: potential therapies. *Drugs*, 68(8):1029–1036, 2008.

[9] Menno van Lookeren Campagne, Jennifer LeCouter, Brian L. Yaspan, and Weilan Ye. Mechanisms of age-related macular degeneration and therapeutic opportunities. *The Journal of Pathology*, 232(2):151–164, 2014.

[10] Leo A. Kim and Patricia A. D'Amore. A brief history of anti-VEGF for the treatment of ocular angiogenesis. *American Journal of Pathology*, 181(2):376–379, 2012.

[11] Ryan M. Rich, Philip J. Rosenfeld, Carmen A. Puliafito, Sander R. Dubovy, Janet L. Davis, Harry W. Flynn, Serafin Gonzalez, William J. Feuer, Richard C. Lin, Geeta A. Lalwani, Jackie K. Nguyen, and Gaurav Kumar. Short-term safety and efficacy of intravitreal bevacizumab (Avastin) for neovascular age-related macular degeneration. *Retina*, 26(5):495–511, 2006.

[12] Napoleone Ferrara, Lisa Damico, Naveed Shams, Henry Lowman, and Robert Kim. Development of ranibizumab, an anti-vascular endothelial growth factor antigen binding fragment, as therapy for neovascular age-related macular degeneration. *Retina (Philadelphia, Pa.)*, 26(8):859–870, 2006.

[13] F. Semeraro, F. Morescalchi, S. Duse, F. Parmeggiani, E. Gambicorti, and C. Costagliola. Aflibercept in wet AMD: Specific role and optimal use. *Drug Design, Development and Therapy*, 7:711–722, 2013.

[14] Lihui Zou, Huiying Lai, Qi Zhou, and Fei Xiao. Lasting controversy on ranibizumab and bevacizumab. *Theranostics*, 1:395–402, 2011.

[15] Rupert R.A. Bourne, Gretchen A. Stevens, Richard A. White, Jennifer L. Smith, Seth R. Flaxman, Holly Price, Jost B. Jonas, Jill Keeffe, Janet Leasher, Kovin Naidoo, Konrad Pesudovs, Serge Resnikoff, and Hugh R. Taylor. Causes of vision loss worldwide, 1990-2010: A systematic analysis. *The Lancet Global Health*, 1(6):339–349, 2013.

[16] Wan Ling Wong, Xinyi Su, Xiang Li, Chui Ming G. Cheung, Ronald Klein, Ching Yu Cheng, and Tien Yin Wong. Global prevalence of age-related macular degeneration and disease burden projection for 2020 and 2040: A systematic review and meta-analysis. *The Lancet Global Health*, 2(2):106–116, 2014.

[17] AMD Alliance International. The global economic cost of visual impairment. Technical Report March, 2010.

[18] Nigel Hawkes. Cost of hospital prescribing rose 15% in a year owing to new rheumatoid arthritis and cancer drugs. *BMJ (Clinical research ed.)*, 349, 2014.

[19] Rajvardhan Azad, Parijat Chandra, and Ritesh Gupta. The economic implications of the use of anti-vascular endothelial growth factor drugs in age-related macular degeneration. *Indian Journal Of Ophthalmology*, 55(6):441–3, 2007.

[20] Tim U. Krohne, Zengping Liu, Frank G. Holz, and Carsten H. Meyer. Intraocular pharmacokinetics of ranibizumab following a single intravitreal injection in humans. *American Journal of Ophthalmology*, 154(4):682–686, 2012.

[21] Lu Xu, Tong Lu, Lisa Tuomi, Nelson Jumbe, Jianfeng Lu, Steve Eppler, Peter Kuebler, Lisa A. Damico-Beyer, and Amita Joshi. Pharmacokinetics of ranibizumab in patients with neovascular age-related macular degeneration: A population approach. *Investigative Ophthalmology and Visual Science*, 54(3):1616–1624, 2013.

[22] Robert L. Avery, Alessandro A. Castellarin, Nathan C. Steinle, Dilsher S. Dhoot, Dante Joseph Pieramici, Robert See, Stephen Couvillion, Ma'an A. Nasir, Melvin D. Rabena, Kha Le, Mauricio Maia, and Jennifer E. Visich. Systemic pharmacokinetics following intravitreal injections of ranibizumab, bevacizumab or aflibercept in patients with neovascular AMD. *The British Journal Of Ophthalmology*, 98(12):1636–41, 2014.

[23] Carsten H. Meyer, Tim U. Krohne, and Frank G. Holz. Intraocular pharmacokinetics after a single intravitreal iinjection of 1.5 mg versus 3.0 mg of bevacizumab in humans. *Retina*, 31(9):1877–1884, 2011.

[24] Tim U. Krohne, Nicole Eter, Frank G. Holz, and Carsten H. Meyer. Intraocular pharmacokinetics of bevacizumab after a single intravitreal injection in humans. *American Journal of Ophthalmology*, 146(4):508–12, 10 2008.

[25] The CATT Research Group. Ranibizumab and bevacizumab for neovascular age-related macular degeneration. *New England Journal*, 364(20):1897–1908, 2011.

[26] Uday B. Kompella and Henry F. Edelhauser. *Drug Product Development For The Back Of The Eye*. Springer, 2011.

[27] David M. Brown, Eric Chen, Angeline Mariani, and James C. Major. Super-dose anti-VEGF (SAVE) trial: 2.0 mg Intravitreal ranibizumab for recalcitrant neovascular macular degeneration-primary end point. *Ophthalmology*, 120(2):349–354, 2013.

[28] Kapil Gadkar, Cinthia V. Pastuskovas, Jennifer E. Le Couter, J. Michael Elliott, Jianhuan Zhang, Chingwei V. Lee, Sarah Sanowar, Germaine Fuh, Hok Seon Kim, T. Noelle Lombana, Christoph Spiess, Makia Nakamura, Phil Hass, Whitney Shatz, Y. Gloria Meng, and Justin M. Scheer. Design and pharmacokinetic characterization

of novel antibody formats for ocular therapeutics - supp. 2. *Investigative Ophthalmology & Visual Science*, 56(9):5390–5400, 2015.

[29] The Angiogenesis Foundation. Treatment of wet AMD, date accessed 14-09-2018, http://www.scienceofamd.org/treat/.

[30] Deepak Thassu and Gerald J. Chader. *Ocular Drug Delivery Systems*. CRC Press, 2013.

[31] Paul N. Bishop. Structural macromolecules and supramolecular organisation of the vitreous gel. *Progress in Retinal and Eye Research*, 19(3):323–344, 2000.

[32] J. S. Penn, A. Madan, R. B. Caldwell, M. Bartoli, R. W. Caldwell, and M. E. Hartnett. Vascular endothelial growth factor in eye disease. *Progress in Retinal and Eye Research*, 27(4):331–371, 2008.

[33] Rubin M. Tuder, Yasanori Kasahara, and Norbert F. Voelkel. Inhibition of vascular endothelial growth. *Arch Ophthalmology*, 114:66–71, 1996.

[34] Gregory S. Robinson, Eric A. Pierce, Susan L. Rook, Elliot Foley, Ruth Webb, and Lois E. H. Smith. Oligodeoxynucleotides inhibit retinal neovascularization in a murine model of proliferative retinopathy. *Proceedings of the National Academy of Sciences of the United States of America*, 93(10):4851–6, 1996.

[35] Lloyd P. Aiello, Eric A. Pierce, Eliot D. Foley, Hitoshi Takagi, Helen Chen, Lavon Riddle, Napoleone Ferrara, George L. King, and Lois E. H. Smith. Suppression of retinal neovascularization in vivo by inhibition of vascular endothelial growth factor (VEGF) using soluble VEGF-receptor chimeric proteins. *Proceedings of the National Academy of Sciences of the United States of America*, 92(23):10457–61, 1995.

[36] Hiroaki Ozaki, Man Seong Seo, Keiko Ozaki, Haruhiko Yamada, Eri Yamada, Naoyuki Okamoto, Francesco Hofmann, Jeanette M. Wood, and Peter A. Campochiaro. Blockade of vascular endothelial cell growth factor receptor signaling is sufficient to completely prevent retinal neovascularization. *American Journal of Pathology*, 156(2):697–707, 2000.

[37] Harold F. Dvorak, Lawrence F. Brown, Michael Detmar, and Ann M. Dvorak. Vascular permeability factor/vascular endothelial growth factor and the significance of microvascular hyperpermeability in angiogenesis. *American Journal of Pathology*, 149(5):1029–1039, 1999.

[38] Marie Louise Farecki, Matthias Gutfleisch, Henrik Faatz, Kai Rothaus, Britta Heimes, Georg Spital, Albrecht Lommatzsch, and Daniel Pauleikhoff. Characteristics of type 1 and 2 CNV in exudative AMD in OCT-Angiography. *Graefe's Archive for Clinical and Experimental Ophthalmology*, 255(5):913–921, 2017.

[39] Hiroyuki Nomoto, Fumio Shiraga, Noriyuki Kuno, Erika Kimura, Shinobu Fujii, Katsuhiko Shinomiya, Alex K. Nugent, Kazuyuki Hirooka, and Tetsuya Baba. Pharmacokinetics of bevacizumab after topical, subconjunctival, and intravitreal administration in rabbits. *Investigative Ophthalmology and Visual Science*, 50(10):4807–4813, 2009.

[40] Eva M. del Amo, Anna-Kaisa Rimpelä, Emma Heikkinen, Otto K. Kari, Eva Ramsay, Tatu Lajunen, Mechthild Schmitt, Laura Pelkonen, Madhushree Bhattacharya, Dominique Richardson, Astrid Subrizi, Tiina Turunen, Mika Reinisalo, Jaakko Itkonen, Elisa Toropainen, Marco Casteleijn, Heidi Kidron, Maxim Antopolsky, Kati-Sisko Vellonen, Marika Ruponen, and Arto Urtti. Pharmacokinetic aspects of retinal drug delivery. *Progress in Retinal and Eye Research*, 57:134–185, 2016.

[41] Ripal Gaudana, Hari Krishna Ananthula, Ashwin Parenky, and Ashim K. Mitra. Ocular drug delivery. *The AAPS Journal*, 12(3):348–360, 2010.

[42] Yvonne S. Lin, Cindy Nguyen, Jose-Luis Mendoza, Enrique Escandon, David Fei, Y. Gloria Meng, and Nishit B. Modi. Preclinical pharmacokinetics, interspecies scaling, and tissue distribution of a humanized monoclonal antibody against vascular endothelial growth factor. *The Journal Of Pharmacology And Experimental Therapeutics*, 288(1):371–378, 1999.

[43] Qi Zhu, Focke Ziemssen, Sigrid Henke-Fahle, Olcay Tatar, Peter Szurman, Sabine Aisenbrey, Nicole Schneiderhan-marra, Xun Xu, and Salvatore Grisanti. Vitreous levels of bevacizumab and vascular endothelial growth factor-A in patients with choroidal neovascularization. *American Academy of Ophthalmology*, 115:1750–1756, 2008.

[44] Philip Rosenfeld, Andrew Moshfeghi, and Carmen Puliafito. Optical coherence tomography findings after an intravitreal injection of bevacizumab (avastin) for neovascular age-related macular degeneration. *Ophthalmic Surgery, Lasers and Imaging Retina*, 36(4):331–335, 2005.

[45] Sophie J. Bakri, Melissa R. Snyder, Joel M. Reid, Jose S. Pulido, and Ravinder J. Singh. Pharmacokinetics of intravitreal bevacizumab (avastin). *Ophthalmology*, 114(5):855–859, 2007.

[46] Kisaburo Yamada, Kenichi Kimoto, Hirofumi Kono, and Toshiaki Kubota. Switching from intravitreal ranibizumab to bevacizumab for age-related macular degeneration. *ISRN Ophthalmology*, 232(3):149–155, 2011.

[47] Lorenzo Moja, Ersilia Lucenteforte, Koren H. Kwag, Vittorio Bertele, Annalisa Campomori, Usha Chakravarthy, Roberto DAmico, Kay Dickersin, Laurent Kodjikian, Kristina Lindsley, Yoon Loke, Maureen Maguire, Daniel F. Martin, Alessandro Mugelli, Bernd Mühlbauer, Isabel Püntmann, Barnaby Reeves, Chris Rogers, Christine Schmucker, Manju L. Subramanian, and Gianni Virgili. Systemic safety of bevacizumab versus ranibizumab for neovascular age-related macular degeneration. *Cochrane Database of Systemic Reviews*, 2014.

[48] Kimberly Spooner, Thomas Hong, Wijeyanthy Wijeyakumar, and Andrew A. Chang. Switching to aflibercept among patients with treatment-resistant neovascular age-related macular degeneration: a systematic review with meta-analysis. *Clinical Ophthalmology (Auckland, N.Z.)*, 11:161–177, 2017.

[49] Jos Costa, Joo Nascimento, Susana Teixeira, and Rufino Silva. AMD Future Perspectives: New promising drugs, date accessed 14-09-2018, http://www.amdbook.org/content/amd-future-perspectives-new-promising-drugs.

[50] Genentech. Study of the efficacy and safety of the ranibizumab port delivery system (RPDS) for sustained delivery of ranibizumab in participants with subfoveal neovascular age-related macular degeneration (AMD) (LADDER), 2015.

[51] Roman G. Rubio. Long-acting anti-VEGF delivery. *Retina Today*, pages 78–80, 2014.

[52] Ulrich Brinkmann, Remko Griep, Anita Kavlie, Christian Klein, and Head Oncology Programs. Antibodies against human angiopoietin 2. *World Intellectual Property Organisation*, 2010.

[53] ClinicalTrials.gov. A proof-of-concept study of RO6867461 in participants with choroidal neovascularization (CNV) secondary to age-related macular degeneration (AMD) (AVENUE), date accessed 14-09-2018, https://clinicaltrials.gov/ct2/show/NCT02484690.

[54] Usha Chakravarthy, Clare Bailey, David Brown, Peter Campochiaro, Mark Chittum, Karl Csaky, Adnan Tufail, Paul Yates, Patrick Cech, Mylene Giraudon, Paul Delmar, Piotr Szczesny, Jayashree Sahni, Anne Boulay, Sandra Nagel, Sabine Fürst-Recktenwald, and Dietmar Schwab. Phase I trial of antivascular endothelial growth

factor/anti-angiopoietin 2 bispecific antibody RG7716 for neovascular age-related macular degeneration. *Ophthalmology Retina*, 1(6):474–485, 2017.

[55] Jorg T. Regula, Peter Lundh von Leithner, Richard Foxton, Veluchamy A. Barathi, Chui Ming Gemmy Cheung, Sai Bo Bo Tun, Yeo Sia Wey, Daiju Iwata, Miroslav Dostalek, Jorg Moelleken, Kay G. Stubenrauch, Everson Nogoceke, Gabriella Widmer, Pamela Strassburger, Michael J. Koss, Christian Klein, David T. Shima, and Guido Hartmann. Targeting key angiogenic pathways with a bispecific CrossMAb optimized for neovascular eye diseases. *EMBO Molecular Medicine*, 8(11):1265–1288, 2016.

[56] Christian Klein, Wolfgang Schaefer, and Jorg T. Regula. The use of CrossMAb technology for the generation of bi- and multispecific antibodies. *mAbs*, 8(6):1010–1020, 2016.

[57] Roche. Investor Update: Phase II data support potential for Roches novel anti-VEGF/anti-angiopoietin-2 bispecific antibody, RG7716, for people with diabetic macular edema, 2018.

[58] Joy G. Ghosh, Andrew A. Nguyen, Chad E. Bigelow, Stephen Poor, Yubin Qiu, Nalini Rangaswamy, Richard Ornberg, Brittany Jackson, Howard Mak, Tucker Ezell, Vania Kenanova, Elisa De La Cruz, Ana Carrion, Bijan Etemad-Gilbertson, Roxana Garcia Caro, Kan Zhu, Vinney George, Jirong Bai, Radhika Sharma-Nahar, Siyuan Shen, Yiqin Wang, Kulandayan K. Subramanian, Elizabeth Fassbender, Michael Maker, Shawn Hanks, Joanna Vrouvlianis, Barrett Leehy, Debby Long, Melissa Prentiss, Viral Kansara, Bruce Jaffee, Thaddeus P. Dryja, and Michael Roguska. Long-acting protein drugs for the treatment of ocular diseases. *Nature Communications*, 8:1–10, 2017.

[59] Holger Fuchs and Frederik Igney. Binding to ocular albumin as a half-life extension principle for intravitreally injected drugs: evidence from mechanistic rat and rabbit studies. *Journal of Ocular Pharmacology and Therapeutics*, 33(2):115–122, 2017.

[60] Anat Loewenstein. Breaking the burden: a new way to deliver anti-VEGF, date accessed 14-09-2018, https://www.reviewofoptometry.com/article/breaking-the-burden-a-new-way-to-deliver-antivegf. *Review of Optometry*, 2018.

[61] Danny S. Ng, Yolanda W. Yip, Malini Bakthavatsalam, Li J. Chen, Tse K. Ng, Timothy Y. Lai, Calvin P. Pang, and Mrten E. Brelén. Elevated angiopoietin 2 in aqueous of patients with neovascular age related macular degeneration correlates with disease severity at presentation. *Scientific Reports*, 7:1–6, 2017.

[62] ClinicalTrials.gov. Study to evaluate RO6867461 (RG7716) for extended durability in the treatment of neovascular age related macular degeneration (nAMD) (STAIRWAY). Technical report, 2018.

[63] ClinicalTrials.gov. A study of RO6867461 in participants with center-involving diabetic macular edema (BOULEVARD). Technical report, 2018.

[64] Joyce Mordenti, R. Andrew Cuthbertson, Napoleone Ferrara, Karen Thomsen, Celia R. Valverde, Y. Gloria Meng, David T. W. Fei, Kathleen M. Fourre, and Anne M. Ryan. Comparisons of the intraocular tissue distribution, pharmacokinetics, and safety of 125 I-labeled full-length and Fab antibodies following intravitreal administration. *Toxicologic Pathology*, 27(5):536–544, 1999.

[65] Jacques Gaudreault, David Fei, Jeriza Rusit, Pamela Suboc, and Vanessa Shiu. Preclinical pharmacokinetics of ranibizumab (rhuFabV2) after a single intravitreal administration. *Investigative Ophthalmology and Visual Science*, 46(2):726–733, 2005.

[66] Leonid Gibiansky, Kha N. Le, Jeremy Good, Teresa Davancaze, Menno van Lookeren Campagne, Kelly M. Loyet, Alyssa Morimoto, Jin Jin, Lisa A. Damico-Beyer, and William D. Hanley. A mechanistic PK/PD model of factor D inhibition in cynomolgus monkeys by lampalizumab for the treatment of geographic atrophy. *Journal of Pharmacology and Experimental Therapeutics*, 355(2):288–296, 2015.

[67] Sang Jun Park, Yewon Choi, Young Mi Na, Hye Kyoung Hong, Ji Yeon Park, Kyu Hyung Park, Jae Yong Chung, and Se Joon Woo. Intraocular pharmacokinetics of intravitreal aflibercept (eylea) in a rabbit model. *Investigative Opthalmology & Visual Science*, 57(6):2612, 2016.

[68] Stuart Friedrich, Bradley Saville, and Yu-ling Cheng. Drug distribution in the vitreous humor of the human eye: the effects of aphakia and changes in retinal permeability and vitreous diffusivity. *Journal of Ocular Pharmacology and Therapeutics*, 13(5):445–459, 10 1997.

[69] Paul J. Missel. Simulating intravitreal injections in anatomically accurate models for rabbit, monkey, and human eyes. *Pharmaceutical Research*, 29(12):3251–3272, 2012.

[70] Hyuncheol Kim, Martin J. Lizak, Ginger Tansey, Karl G. Csaky, Michael R. Robinson, Peng Yuan, Nam Sun Wang, and Robert J. Lutz. Study of ocular transport of drugs released from an intravitreal implant using magnetic resonance imaging. *Annals of Biomedical Engineering*, 33(2):150–164, 2005.

[71] Sreevani Kotha and Lasse Murtomäki. Virtual pharmacokinetic model of human eye. *Mathematical Biosciences*, 253(1):11–18, 2014.

[72] J. A. Ferreira, Paula de Oliveira, P. M. da Silva, and R. Silva. Mathematics of aging: Diseases of the posterior segment of the eye. *Computers and Mathematics with Applications*, 73(1):11–26, 2017.

[73] Marko Lamminsalo, Ella Taskinen, Timo Karvinen, Astrid Subrizi, and Lasse Murtomäki. Extended pharmacokinetic model of the rabbit eye for intravitreal and intracameral injections of macromolecules: quantitative analysis of anterior and posterior elimination pathways. *Pharmaceutical Research*, 35(8):1–14, 2018.

[74] Laurence A. Hutton-Smith, Eamonn A. Gaffney, Helen M. Byrne, Philip K. Maini, Dietmar Schwab, and Norman A. Mazer. A mechanistic model of the intravitreal pharmacokinetics of large molecules and the pharmacodynamic suppression of ocular VEGF levels by ranibizumab in patients with neovascular age-related macular degeneration. *Molecular Pharmaceutics*, 13(9):2941–2950, 2016.

[75] Laurence A. Hutton-smith, Eamonn A. Gaffney, Helen M. Byrne, Philip K. Maini, Kapil Gadkar, and Norman A. Mazer. Ocular pharmacokinetics of therapeutic antibodies given by intravitreal injection: estimation of retinal permeabilities using a 3 compartment semi-mechanistic model. *Molecular Pharmaceutics*, pages 1–9, 2017.

[76] Laurence A. Hutton-Smith, Eamonn A. Gaffney, Helen M. Byrne, Antonello Caruso, Philip K. Maini, and Norman Alan Mazer. Theoretical insights into the retinal dynamics of VEGF in patients treated with ranibizumab, based on an ocular pharmacokinetic/pharmacodynamic model. *Molecular Pharmaceutics*, 15(7):2770–2784, 2018.

[77] Carsten H. Meyer, Tim U. Krohne, and Frank G. Holz. Concentrations of unbound bevacizumab in the aqueous of untreated fellow eyes after a single intravitreal injection in humans. *Acta Ophthalmologica*, 90(1):68–70, 2012.

[78] Joyce Mordenti, Karen Thomsen, Vojtech Licko, Lea Berleau, Jeanne W. Kahn, R. Andrew Cuthbertson, Eileen T. Duenas, Anne M. Ryan, Cheryl Schofield, Terrance W Berger, Y. Gloria Meng, and Jeffrey Cleland. Intraocular pharmacokinetics and safety of a humanized monoclonal antibody in rabbits after intravitreal administration of a solution or a PLGA microsphere formulation. *Toxicological Sciences : An Official Journal of the Society of Toxicology*, 52(1):101–106, 11 1999.

[79] Sophie J. Bakri, Melissa R. Snyder, Joel M. Reid, Jose S. Pulido, Mohamed K. Ezzat, and Ravinder J. Singh. Pharmacokinetics of intravitreal ranibizumab (lucentis). *Ophthalmology*, 114(12):2179–2182, 2007.

[80] Lan-Hsin Chuang, Wei-Chi Wu, Ling Yeung, Nan-Kai Wang, Yih-Shiou Hwang, Kuan-Jen Chen, Jane Zea-Chin Kuo, and Chi-Chun Lai. Serum concentration of bevacizumab after intravitreal injection in experimental branch retinal vein occlusion. *Ophthalmic Research*, 45(1):31–35, 2011.

[81] Philipp S. Muether, Manuel M. Hermann, Ulrike Viebahn, Bernd Kirchhof, and Sascha Fauser. Vascular endothelial growth factor in patients with exudative age-related macular degeneration treated with ranibizumab. *American Academy of Ophthalmology*, 119(10):2082–2086, 2012.

[82] Philipp S. Muether, Manuel M. Hermann, Katharina Dröge, Bernd Kirchhof, and Sascha Fauser. Long-term stability of vascular endothelial growth factor suppression time under ranibizumab treatment in age-related macular degeneration. *American Journal of Ophthalmology*, 156(5), 2013.

[83] Nicholas Papadopoulos, Joel Martin, Qin Ruan, Ashique Rafique, Michael P. Rosconi, Ergang Shi, Erica A. Pyles, George D. Yancopoulos, Neil Stahl, and Stanley J. Wiegand. Binding and neutralization of vascular endothelial growth factor (VEGF) and related ligands by VEGF Trap, ranibizumab and bevacizumab. *Angiogenesis*, 15(2):171–185, 2012.

[84] Jihong Yang, Xiangdan Wang, Germaine Fuh, Lanlan Yu, Eric Wakshull, Mehraban Khosraviani, Eric S. Day, Jun Liu, Steven J. Shire, Napoleone Ferrara, and Sandeep Yadav. Comparison of binding characteristics and in vitro activities of three inhibitors of vascular endothelial growth factor A. *Molecular Pharmaceutics*, 11:3421–3430, 2014.

[85] Y. Harpaz, M. Gerstein, and C. Chothia. Volume changes on protein folding. *Structure.*, 2(7):641–649, 1994.

[86] The MathWorks Inc. Matlab user guide R2015b: global optimization toolbox, 2015.

[87] William Tasman and Edward A. Jaeger. *Duane's Ophthalmology 2013.* Lippincott Williams & Wilkins, 2013.

[88] Scott T. Fontana and Richard F. Brubaker. Volume and depth of the anterior chamber in the normal aging human eye. *Archives of Ophthalmology*, 98:1803–1808, 1980.

[89] Carol B. Toris, Michael E. Yablonski, Yun-Liang Wang, and Carl B. Camras. Aqueous humor dynamics in the aging human eye. *American Journal of Ophthalmology*, 127(4):407–412, 1999.

[90] Edward Stuttfeld. *The Structural and Functional Characterization of the Extracellular Domain of Vascular Endothelial Growth Factor Receptors: Their Role in Receptor Activation and Use as Therapeutic Targets (Doctoral Dissertation, University of Basel)*. PhD thesis, 2012.

[91] Marie Reille-Seroussi, Jean-Franois Gaucher, Claudia Desole, Nathalie Gagey-Eilstein, Franck Brachet, Isabelle Broutin, Michel Vidal, and Sylvain Broussy. Vascular endothelial growth factor peptide ligands explored by competition assay and isothermal titration calorimetry. *Biochemistry*, 54(33):5147–5156, 2015.

[92] Geetanjali Davuluri, Virginia Espina, Emanuel F. Petricoin, Mark Ross, Jianghong Deng, Lance A. Liotta, and Bert M. Glaser. Activated VEGF receptor shed into the vitreous in eyes with wet AMD. *Arch Ophthalmology*, 127(5):613–621, 2009.

[93] Veli-Pekka Ranta, Eliisa Mannermaa, Kirsi Lummepuro, Astrid Subrizi, Antti Laukkanen, Maxim Antopolsky, Lasse Murtomaki, Margit Hornof, and Arto Urtti. Barrier analysis of periocular drug delivery to the posterior segment. *Journal of Controlled Release*, 148:42–48, 2010.

[94] David M. Maurice. Protein dynamics in the eye studied with labelled proteins. *American Journal of Ophthalmology*, 47(1):361–368, 1959.

[95] Aapo Tervonen, Iina Vainio, Soile Nymark, and Jari Hyttinen. Prediction of passive drug permeability across the blood-retinal barrier. *Pharmaceutical Research*, pages 1–15, 2014.

[96] Shannon E. Boye, Sanford L. Boye, Alfred S. Lewin, and William W. Hauswirth. A comprehensive review of retinal gene therapy. *Molecular Therapy*, 21(3):509–519, 2013.

[97] Leena Pitkanen, Veli-Pekka Ranta, Hanna Moilanen, and Arto Urtti. Permeability of retinal pigment epithelium: Effects of permeant molecular weight and lipophilicity. *Investigative Ophthalmology and Visual Science*, 46(2):641–646, 2005.

[98] Eva M. del Amo, Anna-Kaisa Rimpela, Emma Heikkinen, Otto K. Kari, Eva Ramsay, Tatu Lajunen, Mechthild Schmitt, Laura Pelkonen, Madhushree Bhattacharya,

Dominique Richardson, Astrid Subrizi, Tiina Turunen, Mika Reinisalo, Jaakko Itkonen, Elisa Toropainen, Marco Casteleijn, Heidi Kidron, Maxim Antopolsky, Kati-Sisko Vellonen, Marika Ruponen, and Arto Urtti. Progress in retinal and eye research pharmacokinetic aspects of retinal drug delivery. *Progress in Retinal and Eye Research*, 12(1), 2016.

[99] Whitney Shatz, Philip E. Hass, Mary Mathieu, Hok Seon Kim, Kim Leach, Michelle Zhou, Yongping Crawford, Amy Shen, Kathryn Wang, Debby P. Chang, Mauricio Maia, Susan R. Crowell, Leslie Dickmann, Justin M. Scheer, and Robert F. Kelley. Contribution of antibody hydrodynamic size to vitreal clearance revealed through rabbit studies using a species-matched Fab. *Molecular Pharmaceutics*, 13(9):2996–3003, 2016.

[100] Ernst Bárány and V. Everett Kinsey. The rate of flow of aqueous humor. *American Journal of Ophthalmology*, 32(6):177–188, 1949.

[101] Harvey Motulsky and Arthur Christopoulos. Fitting models to biological data using linear and nonlinear regression. *PRISM Manual*, 2003.

[102] Bradley Efron and Robert Tibshirani. *An Introduction to the Bootstrap*. Chapman & Hall, 1994.

[103] Ophlie Vacca, Marie Darche, David V. Schaffer, John G. Flannery, Jos-Alain Alain Sahel, Alvaro Rendon, and Deniz Dalkara. AAV-mediated gene delivery in Dp71-null mouse model with compromised barriers. *Glia*, 62(3):468–476, 2014.

[104] J. Fraser Wright, Tannie Le, Joseph Prado, Jennifer Bahr-Davidson, Peter H. Smith, Zhu Zhen, Jurg M. Sommer, Glenn F. Pierce, and Guang Qu. Identification of factors that contribute to recombinant AAV2 particle aggregation and methods to prevent its occurrence during vector purification and formulation. *Molecular Therapy*, 12(1):171–178, 2005.

[105] Jaime A. Yáñez, Connie M. Remsberg, Casey L. Sayre, M. Laird Forrest, and Davies M. Neal. Flip-flop pharmacokinetics delivering a reversal of disposition: challenges and opportunities during drug development. *Future Science*, 2(5):643–672, 2012.

[106] W. Halfter, S. Dong, A. Dong, A.W. Eller, and R. Nischt. Origin and turnover of ECM proteins from the inner limiting membrane and vitreous body. *Eye (London, England)*, 22(10):1207–1213, 2008.

[107] Driton Vllasaliu, Franco H. Falcone, Snjezana Stolnik, and Martin Garnett. Basement membrane influences intestinal epithelial cell growth and presents a barrier to the movement of macromolecules. *Experimental Cell Research*, 323(1):218–231, 2014.

[108] Hiroto Terasaki, Taiji Sakamoto, Makoto Shirasawa, Naoya Yoshihara, Hiroki Otsuka, Shozo Sonoda, Toshio Hisatomi, and Tatsuro Ishibashi. Penetration of bevacizumab and ranibizumab through retinal pigment epithelial layer in vitro. *Retina*, 35(5):1007–1015, 2015.

[109] Juyoung Park, Peter M. Bungay, Robert J. Lutz, James J. Augsburger, Ronald W. Millard, Abhijit Sinha Roy, and Rupak K. Banerjee. Evaluation of coupled convective-diffusive transport of drugs administered by intravitreal injection and controlled release implant. *Journal of Controlled Release*, 105(3):279–295, 2005.

[110] Stuart Friedrich, Yu-Ling Cheng, and Bradley Saville. Finite element modeling of drug distribution in the vitreous humor of the rabbit eye. *Annals of Biomedical Engineering*, 25(2):303–14, 1997.

[111] Paul J. Missel. Hydraulic flow and vascular clearance influences on intravitreal drug delivery. *Pharmaceutical Research*, 19(11):1636–1647, 2002.

[112] Stuart Friedrich, Yu-Ling Cheng, and Bradley Saville. Drug distribution in the vitreous humor of the human eye: the effects of intravitreal injection position and volume. *Current Eye Research*, 16(7):663–669, 1997.

[113] Jing Xu, JeffreyJ. Heys, Victor H. Barocas, and Theodore W. Randolph. Permeability and diffusion in vitreous humor: implications for drug delivery. *Pharmaceutical Research*, 17(6):664–669, 2000.

[114] Ardith W. El-Kareh, Samuel L. Braunstein, and Timothy W. Secomb. Effect of cell arrangement and interstitial volume fraction on the diffusivity of monoclonal antibodies in tissue. *Biophysical Journal*, 64(5):1638–1646, 1993.

[115] Feilim Mac Gabhann, Anna Maria Demetriades, Tye Deering, Jonathan D. Packer, Syed Mahmood Shah, Elia Duh, Peter A. Campochiaro, and Aleksander S. Popel. Protein transport to choroid and retina following periocular injection: Theoretical and experimental study. *Annals of Biomedical Engineering*, 35(4):615–630, 2007.

[116] Hubert Stanley Wall. *Analytic theory of continued fractions*. AMS Chelsea Publishing, 1948.

[117] Olds C.D. *Continued fractions*. John Wiley & Sons, 1978.

[118] Sascha Fauser and Philipp S. Muether. Clinical correlation to differences in ranibizumab and aflibercept vascular endothelial growth factor suppression times. *The British Journal of Ophthalmology*, 100(11):1494–1498, 2016.

[119] Napoleone Ferrara. Vascular endothelial growth factor and age-related macular degeneration: from basic science to therapy. *Nature Publishing Group*, 16(10):1107–1111, 2010.

[120] Sanford Bolton and Charles Bon. *Pharmaceutical Statistics: Practical and Clinical Applications*. Dekker Media, 4th edition, 2004.

[121] Peter Heiduschka, Heike Fietz, Sabine Hofmeister, Sigrid Schultheiss, Andreas F. Mack, Swaantje Peters, Focke Ziemssen, Birgit Niggemann, Sylvie Julien, Karl Ulrich Bartz-Schmidt, and Ulrich Schraermeyer. Penetration of bevacizumab through the retina after intravitreal injection in the monkey. *Investigative Ophthalmology and Visual Science*, 48(6):2814–2823, 2007.

[122] Robert D. Tilton. The conformation of the poly(ethylene glycol) chain in mono-pegylated lysozyme and mono-pegylated human growth hormone. *Bioconjugate Chemistry*, 22:2317–2323, 2011.

[123] Johannes Waltenberger, Lena Claesson-Welsh, Agneta Siegbahn, Masabumi Shibuya, and Carl-Henrik Heldin Heldin. Different signal-transduction properties of KDR and Flt1, 2 receptors for vascular endothelial growth-factor. *Journal of Biological Chemistry*, 269(43):26988–26995, 1994.

[124] Veli-Matti Leppanen, Andrea E. Prota, Michael Jeltsch, Andrey Anisimov, Nisse Kalkkinen, Tomas Strandin, Hilkka Lankinen, Adrian Goldman, Kurt Ballmer-Hofer, and Kari Alitalo. Structural determinants of growth factor binding and specificity by VEGF receptor 2. *Proceedings of the National Academy of Sciences*, 107(6):2425–2430, 2010.

[125] Timothy P. Quinn, Kevin G. Peters, Carlie De Vries, Napoleone Ferrara, and Lewis T. Williams. Fetal liver kinase 1 is a receptor for vascular endothelial growth factor and is selectively expressed in vascular endothelium. *Proceedings of the National Academy of Sciences of the United States of America*, 90(16):7533–7537, 1993.

[126] Allen C. Ho, Brandon G. Busbee, Carl D. Regillo, Mark R. Wieland, Sherri A. Van Everen, Zhengrong Li, Roman G. Rubio, and Phillip Lai. Twenty-four-month efficacy and safety of 0.5 mg or 2.0 mg ranibizumab in patients with subfoveal neovascular age-related macular degeneration. *Ophthalmology*, 121(11):2181–2192, 2014.

[127] Rama D. Jager, William F. Mieler, and Joan W. Miller. Age-related macular degeneration. *The New England Journal of Medicine*, 358(24):2606–2617, 2008.

[128] Istvan Lengyel and Irving R. Epstein. A chemical approach to designing Turing patterns in reaction-diffusion systems. *Proceedings of the National Academy of Sciences of the United States of America*, 89(9):3977–3979, 1992.

[129] Giovanni Staurenghi, Timothy Y.Y. Lai, Paul Mitchell, Sebastian Wolf, Andreas Wenzel, Jun Li, Amitabha Bhaumik, and Philip G. Hykin. Efficacy and safety of ranibizumab 0.5 mg for the treatment of macular edema resulting from uncommon causes. Twelve-month findings from PROMETHEUS. *Ophthalmology*, 125(6):850–862, 2018.

[130] Ting Zhao, Yang Yang, Aizhen Zong, Haining Tan, Xinlei Song, Shuo Meng, Chunxia Song, Guangli Pang, and Fengshan Wang. N-terminal PEGylation of human serum albumin and investigation of its pharmacokinetics and pulmonary microvascular retention. *BioScience Trends*, 6(2):81–88, 2012.

[131] Endre A. Balazs and Janet L. Denlinger. Aging changes in the vitreous. *New York: Alan R. Liss.*, pages 45–57, 1982.

[132] Ben Goldacre. *Bad Pharma: How Drug Companies Mislead Doctors and Harm Patients*. Fourth Estate, 2012.

[133] GaBI Journal Editor. Patent expiry dates for biologicals. *Generics and Biosimilars Initiative Journal*, 6(1):27–30, 3 2017.

[134] Philip J. Rosenfeld. Avastin in ophthalmology: a global phenomenon. *American Academy of Ophthalmology*, 2006.

[135] A.K. Shalaby, K. Lewis, K. Bush, P.R. Meredith, S. Di Simplicio, and A.J. Lockwood1. Licence to save: A UK survey of anti-VEGF use for the eye in 2015. *Eye*, 30:1404–1406, 2016.

[136] Robert Steinbrook. The price of sight ranibizumab, bevacizumab, and the treatment of macular degeneration. *New England Journal of Medicine*, 355(14):1409–1412, 2006.

[137] O. Sha and W.H. Kwong. Postnatal developmental changes of vitreous and lens volumes in sprague-dawley rats. *Neuroembryology and Aging*, 4(4):183–188, 2006.

[138] Liisa M. Hirvonen, Gilbert O. Fruhwirth, Nishanthan Srikantha, Matthew J. Barber, James E. Neffendorf, Klaus Suhling, and Timothy L. Jackson. Hydrodynamic radii of ranibizumab, aflibercept and bevacizumab measured by time-resolved phosphorescence anisotropy. *Pharmaceutical Research*, 33(8):2025–2032, 2016.

[139] J. K. Armstrong, R. B. Wenby, H. J. Meiselman, and T. C. Fisher. The hydrodynamic radii of macromolecules and their effect on red blood cell aggregation. *Biophysical Journal*, 87(6):4259–4270, 2004.

[140] Muppalla Sukumar, Brandon L. Doyle, Jessica L. Combs, and Allen H. Pekar. Opalescent appearance of an IgG1 antibody at high concentrations and its relationship to noncovalent association. *Pharmaceutical Research*, 21(7):1087–1093, 2004.

[141] Ondrea Bermudez and Daniel Forciniti. Aggregation and denaturation of antibodies: A capillary electrophoresis, dynamic light scattering, and aqueous two-phase partitioning study. *Journal of Chromatography B: Analytical Technologies in the Biomedical and Life Sciences*, 807(1):17–24, 2004.

[142] Kapadiya Nidhi, Singhvi Indrajeet, Mehta Khushboo, Karwani Gauri, and Dhrubo Jyoti Sen. Hydrotropy: A promising tool for solubility enhancement: A review. *International Journal of Drug Development and Research*, 3(2):26–33, 2011.

[143] Torsten Deckert, Bo Feldt-Rasmussen, Rene Djurup, and Maria Deckert. Glomerular size and charge selectivity in insulin-dependent diabetes mellitus. *Kidney International*, 33(1):100–106, 1988.

[144] Jeeyun Ahn, Hyuncheol Kim, Se Joon Woo, Ji Hyun Park, Sunyoung Park, Duck Jin Hwang, and Kyu Hyung Park. Pharmacokinetics of intravitreally injected bevacizumab in vitrectomized eyes. *Journal Of Ocular Pharmacology And Therapeutics : The Official Journal Of The Association For Ocular Pharmacology And Therapeutics*, 29(7):612–8, 2013.

[145] Christos I. Sinapis, John G. Routsias, Angelos I. Sinapis, Dimitrios I. Sinapis, George D. Agrogiannis, Alkistis Pantopoulou, Stamatis E. Theocharis, Stefanos Baltatzis, Efstratios Patsouris, and Despoina Perrea. Pharmacokinetics of intravitreal bevacizumab (Avastin®) in rabbits. *Clinical Ophthalmology*, 5(1):697–704, 2011.

[146] Francis Perrin. Mouvement Brownien d'un ellipsoide (II). Rotation libre et dépolarisation des fluorescences. Translation et diffusion de molécules ellipsoidales. *Journal de Physique et le Radium*, 7(1):1–11, 1936.

[147] Napoleone Ferrara and William J. Henzel. Pituitary follicular cells secrete a novel heparin-binding growth factor specific for vascular endothelial cells. *Biochemical and Biophysical Research Communications*, 160(2):851–858, 1989.

[148] FDA. Lucentis (ranibizumab injection) label. Technical report, FDA, 2006.

[149] Daniele Venturoli and Bengt Rippe. Ficoll and dextran vs. globular proteins as probes for testing glomerular permselectivity: effects of molecular size, shape, charge, and deformability. *American Journal Of Physiology. Renal Physiology*, 288(4):605–613, 2005.